FLAW GROWTH AND FRACTURE

Proceedings of the Tenth National Symposium on Fracture Mechanics

ASTM STP 631

AMERICAN SOCIETY FOR TESTING AND MATERIALS

FLAW GROWTH AND FRACTURE

Proceedings of the
Tenth National Symposium
on Fracture Mechanics

A symposium sponsored by
ASTM Committee E-24 on
Fracture Testing of Metals
American Society for
Testing and Materials
Philadelphia, Pa., 23–25 Aug. 1976

ASTM SPECIAL TECHNICAL PUBLICATION 631
J. M. Barsom, symposium chairman

List price $49.75
04-631000-30

AMERICAN SOCIETY FOR TESTING AND MATERIALS
1916 Race Street, Philadelphia, Pa. 19103

Library of Congress Catalog Card Number: 77-73543

NOTE
The Society is not responsible, as a body,
for the statements and opinions
advanced in this publication.

Printed in Baltimore, Md.
October 1977

Foreword

This publication, *Flaw Growth and Fracture,* contains papers presented at the Tenth National Symposium on Fracture Mechanics which was held 23–25 August 1976 at Philadelphia, Pa. The American Society for Testing and Materials' Commitee E-24 on Fracture Testing of Metals sponsored the symposium. J. M. Barsom, U. S. Steel Corporation, Monroeville, Pa., served as symposium chairman.

Related ASTM Publications

Properties of Materials for Liquefied Natural Gas Tankage, STP 579 (1975), $39.75 (04-579000-30)

Mechanics of Crack Growth, STP 590 (1976), $45.25 (04-590000-30)

Fractography—Microscopic Cracking Process, STP 600, (1976), $27.50 (04-600000-30)

A Note Of Appreciation to Reviewers

This publication is made possible by the authors and, also, the unheralded efforts of the reviewers. This body of technical experts whose dedication, sacrifice of time and effort, and collective wisdom in reviewing the papers must be acknowledged. The quality level of ASTM publications is a direct function of their respected opinions. On behalf of ASTM we acknowledge with appreciation their contribution.

ASTM Committee on Publications

Editorial Staff

Jane B. Wheeler, *Managing Editor*
Helen M. Hoersch, *Associate Editor*
Ellen J. McGlinchey, *Senior Assistant Editor*
Kathleen P. Zirbser, *Assistant Editor*
Sheila G. Pulver, *Assistant Editor*

Contents

Introduction

Significant progress has been achieved in the field of fracture mechanics since its inception two decades ago. This progress has been recorded, in part, in various ASTM special technical publications (STP). This publication presents the Proceedings of the Tenth National Symposium on Fracture Mechanics which is sponsored by ASTM Committee E-24 on Fracture Testing of Metals. The papers in this publication indicate the large interest by the international scientific and engineering community in fracture mechanics and the present and near future areas of primary research in this field.

The symposium represents the 1976 state of the art in the analytical and experimental research conducted in the field of fracture mechanics, and, thus, it should be useful to scientists and engineers in keeping abreast of recent developments in this field.

The contents of this volume show that research is continuing in the areas of elastic-plastic behavior, toughness characterization of low-strength, high-toughness materials, environmental and residual-stress effects on crack initiation and propagation, and crack propagation under variable-amplitude loading. Fracture and fatigue behavior for cracks in regions of strain concentrations (holes and notches) and correlation between fracture-mechanics data and data obtained from rapid, inexpensive tests are areas of research receiving increased emphasis. These problem areas will continue to occupy a significant portion of future research efforts, and progress in these frontiers of research should increase our understanding and capabilities to ensure the safety and reliability of engineering structures.

The success of the Tenth National Symposium on Fracture Mechanics is evidenced by the papers in this volume, and the publication of its proceedings is due to the tireless efforts of many people. The contributions of the authors, the reviewers, the members of the Symposium Organizing Committee, J. J. Palmer and Jane B. Wheeler of ASTM and their staff are gratefully acknowledged. The worldwide interest in this symposium, as demonstrated by the papers in this volume and by the attendance at the symposium, is a tribute to the scientists and engineers who have contributed to the development of the field of fracture mechanics.

J. M. Barsom
United States Steel Corporation Research Laboratory, Monroeville, Pa.; symposium chairman.

P. C. Paris[1]

Fracture Mechanics in the Elastic-Plastic Regime

REFERENCE: Paris, P. C., **"Fracture Mechanics in the Elastic-Plastic Regime,"** *Flaw Growth and Fracture, ASTM STP 631,* American Society for Testing and Materials, 1977, pp. 3-27.

ABSTRACT: The objective of this paper is to present, as simply as possible, an explanation of the J-integral methods of elastic-plastic fracture mechanics. Its rationale as an extension of the linear-elastic fracture mechanics is emphasized. Other methods, such as crack-opening displacement and equivalent-energy methods, are contrasted with the J-integral methods for both analysis and applications to material characterization. Finally, the broad applicability and usefulness of the J-integral methods are also emphasized.

KEY WORDS: crack propagation, fractures (materials), fatigue (materials), creep properties, plastic properties

In recent years several attempts have been made to extend fracture mechanics into the elastic-plastic regime. These began with plasticity corrections to linear-elastic fracture mechanics (LEFM) with modest success. However, these corrections proved insufficient to handle analytical modeling of many practical cracking problems from large-scale crack tip plasticity into fully plastic regimes.

The first attempt at developing elastic-plastic models is termed the crack opening stretch (COS) method. It did not attract the attention of many researchers simply because it lacked a flexible analytical basis, and its rational physical basis was not well understood. Measurements and applications were thus left unclear as compared to the more rigorous context of LEFM.

More recently, a method called equivalent energy (EE) arose which was somewhat lacking in a rational physical and analytical basis and methods of application. Moreover, since COS and EE methods lacked certain aspects of an analytical basis, their limitations were not made clear, and, therefore, their application was always suspect.

Most important over the past ten years, has been the development of

[1]Professor of mechanics, Washington University, St. Louis, Mo. 63130; formerly, visiting professor of engineering, Brown University, Providence, R.I.

the J-integral method of analysis. It can be viewed as a direct extension of the methods of LEFM into the elastic-plastic and fully plastic regimes. It possesses an analytical basis and rational physical basis equally as powerful as LEFM. Indeed, the LEFM, COS, and EE methods can be regarded as simply special cases of the more general J-integral method, each with its own special limitations. Moreover, the limitations of the other less powerful methods have remained unclear until the J-integral method has provided an analytical basis within which they can be assessed. Therefore, it might be reasoned that if it is chosen to apply one of the less powerful special-case methods then the J-integral method should also be included to assess limitations, if for no other reason.

In summary it will be reviewed herein that:

1. J may be viewed as the intensity parameter for the crack-tip stress field for the elastic-plastic regime (the same role as K for the linear-elastic regime).
2. J may be evaluated via its analytical basis using the path independent integral form, or nonlinear compliance form or other equivalent methods for special cases (such as $J = \mathcal{G} = K^2/E$ for linear-elastic cases).
3. J may be estimated for various problems by making use of approximation methods developed from its analytical basis.
4. J may be used to characterize material behavior by reasoning that equal J values mean equal intensities of surrounding crack-tip stress fields of identical form for a given material. Thus, equivalent internal response—that is, for the onset and early stages of crack growth—is expected (other conditions equivalent, such as environment, rate of loading, etc., the same hypothesis on which all of LEFM is based).
5. J may be used to attempt to develop rational parameters to describe cracking behavior for various material behaviors such as nonlinear elastic, creep, fatigue, etc., as well as elastic-plastic material behavior.

Further, the elements of the J-integral method (with LEFM as a special case) will be presented herein in as simple a fashion as possible in order to attempt to explain the rational basis and utility of the method. It will also be compared to other methods to show its comprehensive nature, that is, viewing others as limited special cases. In each area, references will be provided for comprehensive presentations of background; therefore, only essential details in outline format will be provided.

J-Integral—What Is It?

Reading the literature on the J-integral is admittedly difficult for the average engineer; therefore, a simple interpretation of that literature seems to be in order. Rice, in the middle and late 1960s, was interested in energy approaches to crack-analysis problems. He discovered that a

certain line integral, the so-called J-integral, has some interesting properties [*1,2*].[2] Simply let the J-integral be defined as (Fig. 1)

$$J = \oint_{\Gamma} \left(Wdy - T_i \frac{\partial u_i}{\partial x} ds \right)$$

where

$$W = \int \sigma_{ij} d\epsilon_{ij}$$

Now, assume deformation theory of plasticity is in order, that is, assuming the stress and strains in a plastic (or elastic-plastic) body are the same as for a nonlinear elastic body with the same stress-strain curve. This is a very reasonable assumption if no unloading occurs, and later in this discussion it will be noted that even with deliberate unloading such as fatigue it will still be reasonable in some cases. Under deformation theory:

W = strain-energy density (nonlinear elastic),
Γ = path of the integral,
ds = increment of distance along the path or contour,
T_i = traction on the contour (if cut out as a free body),
u_i = displacement in the direction of T_i, and
x,y = rectangular coordinates as noted.

Now, using equilibrium, the usual strain-displacement relationships (small strains and rotations) and using the Green-Gauss theorem, that is

$$\int (n_x F_x + n_y F_y) ds = \int \left(\frac{\partial F_y}{\partial x} - \frac{\partial F_x}{\partial y} \right) dA$$

where n_i are the components of the outward unit normal to Γ, Rice showed for any closed path within a body (not jumping across the crack) $J = 0$. A closed path ($\Gamma + \Gamma' +$ along the crack surface) is shown in Fig. 2.

Since along a crack surface, $dy = 0$ and $T_i = 0$, then the contribution to J is zero as noted from the integral. Thus, $J_\Gamma + J_{\Gamma'} = J_{\text{closed path}} = 0$ or

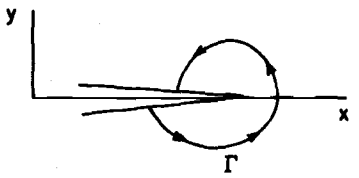

FIG. 1—*The J-integral.*

[2]The italic numbers in brackets refer to the list of references appended to this paper.

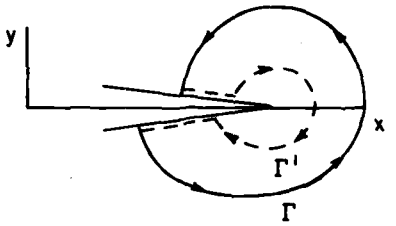

FIG. 2—*A closed path* ($\Gamma + \Gamma' +$ *along the crack surface*).

$J_\Gamma = J_{\Gamma'}$ (with reversed direction). This result shows that J is path independent when applied around a crack tip from one crack surface to another. Thus the J-integral value can be computed by evaluating this integral along any contour around the crack tip from very small to encompassing the outside boundaries of the specimen or body.

Result—This allows evaluation of J from stress analysis (such as finite element analysis) using stress and strain results where they are more accurately known away from the crack-tip region.

But as yet, J is noted only to be a path independent integral (which is by itself not too interesting), but its nature should be further explored. The fact that it is path independent implies that it is a crack-tip parameter, that is, its value on a contour immediately adjacent to the crack tip can be evaluated on a larger contour from conditions faraway. But further physical definition is desired (Fig. 3).

Consider J around some contour Γ at a crack tip where crack extension a distance, da, takes place carrying the contour with it. If

$$J = \oint_\Gamma W dy - \oint_\Gamma T_i \frac{\partial u_i}{\partial x} ds$$

then multiplying each term by da,

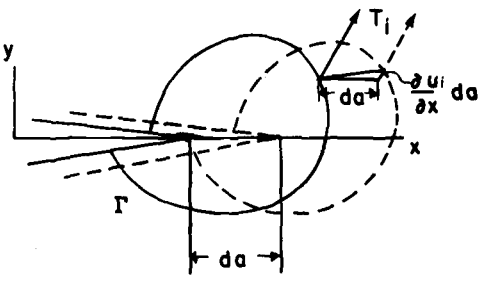

FIG. 3—J *around contour* Γ *at a crack tip.*

$\oint W dy\, da$ = the strain-energy gained (and lost) by moving to the new contour (for nonlinear elasticity) and

$\oint T_i \frac{\partial u_i}{\partial x} ds\, da$ = work done by tractions on the contour in moving.

Thus, $J\ da$ is the total energy coming through the contour for a crack extension, da. This is the same amount of energy for all contours down to one just surrounding the crack point, because of the path independence of J.

Result—For nonlinear or linear elasticity, J is the energy being made available at the crack tip per unit increase in crack area, da (per unit thickness) or $J = \mathcal{G}$ (the Griffith energy).

Result—For linear elasticity then in addition

$$J = \mathcal{G} = \frac{K^2}{E'}$$

Result—For plasticity, W is not strain-energy density, that is, energy is dissipated within material elements; thus, J is not the Griffith energy, $\mathcal{G}$, that is, it is not energy made available at the crack tip for crack extension processes. (This result is negative but should not be regarded as discouraging! Later, J will be interpreted as a crack-tip stress-strain field intensity under elastic-plastic conditions.)

Rice [*1,2*] also pointed up, again using deformation theory, that the J-integral can be evaluated in an alternate way. Consider a body with a crack subjected to a load, P, where, δ_p, is the work producing component of displacement of the load point (see Fig. 4). Choosing for the moment

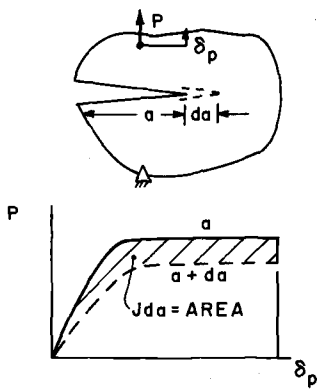

FIG. 4—*A body with a crack subjected to a load.*

(without loss of later generality) the nonlinear elastic interpretation of deformation theory, the work done in loading the body, $\int P d\delta_P$, is different for crack lengths, a, and $a + da$ where da will be regarded as an increment of crack extension. The difference under nonlinear elastic conditions is energy made available for crack extension or (as noted on the P-δ_P curve): Jda = area. But this interpretation is also true for plastic bodies, since both J and the load displacement curves for a and $a + da$ will be the same for nonlinear elastic and plastic material bodies with the same stress-strain relation. Therefore, an alternate, equally valid definition for J for both nonlinear elastic and elastic-plastic conditions is

$$J = \frac{\text{area}}{da} = -\int \frac{\partial P}{\partial a} d\,\delta_P = \int \frac{\partial \delta_P}{\partial a} \cdot dP$$

Result—Thus, J may be evaluated from load versus load-point-displacement relationships for slightly different crack sizes (by the previous forms).

This result allowed Begley and Landes [*3,4*] to do the first experimental evaluations of J (and also to examine material response). They simply experimentally determined load-displacement relationships for different crack lengths in test specimens which otherwise are identical. Moreover, from this alternate form, various approximations or estimates of J (versus displacement, δ_P) are found [*5,6*]. These approximations for computing J are of interest in practical application of the analysis which will be discussed later.

Thus, definitions of J have been presented, and useful resulting special case interpretations developed. Nevertheless, for the elastic-plastic material case an interpretation of J has not yet been presented here upon which sound fracture theories may be based. The discussions must proceed to particular views of, and the analysis of, crack-tip stress and strain fields in order to provide such an interpretation.

Finally, the definitions and methods of evaluation of J here have been based on deformation theory. Deformation theory is regarded as "exact" for nonlinear elastic conditions. As a plasticity theory in such a use as this, it is regarded as very accurate if properly applied. Experimental results provide verification, as well as comparisons with other methods of analysis. Results using the alternative incremental theory of plasticity [*7,8*] agree very well indeed with deformation theory results. This was not unexpected but provides additional confidence in J-integral analysis.

But let the discussion now proceed into the area of crack-tip stress and strain fields in order to provide the rational basis for J-integral analysis of fracture phenomena. In anticipation, it is relevant to know that elastic-plastic crack-tip fields are completely analogous to the linear-elastic crack-tip fields which have been well known for the past 20 years and upon

which the rationale of LEFM has been developed. Thus, in order to establish the usefulness of, and confidence in, the J-integral method, the similarities in linear-elastic and elastic-plastic analyses will be emphasized.

Indeed in the discussion to follow, if consideration is restricted to analysis of elastic-plastic fields which exist within linear-elastic fields, then it can be noted that it is appropriate to perform J-integral analysis within a region surrounded by another region in which LEFM applies. In this way, the two can be clearly seen to be analogous. Moreover, in this case the integral interpretation of J is equally appropriate both for paths, Γ, within the elastic-plastic field and also for paths, Γ, entirely in the linear-elastic field. Then subsequently, it can be noted that the J-integral analysis is equally valid without having a surrounding linear-elastic field. Careful consideration of such viewpoints is recommended for development of a full understanding of J-integral analysis, its powers, its possibilities, and also its limitations.

Crack-Tip Stress and Strain Fields

The general applicability of the J-integral (as with $\mathcal{G}$ and K in LEFM) comes from viewing the stress and strain fields surrounding the crack tip with an appropriate rationale.

Consider three distinct levels of viewing the surrounding field as noted in Fig. 5. They are (1) elastic, (2) elastic-plastic, and (3) an intensely nonlinear (large strains and rotations) zone (incapable of full analysis cur-

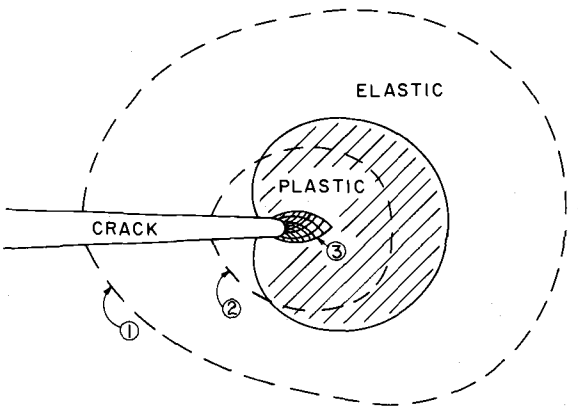

VIEW ①: AN ELASTIC FIELD SURROUNDING THE CRACK TIP
VIEW ②: AN ELASTIC-PLASTIC FIELD SURROUNDING THE CRACK TIP.
VIEW ③: AN INTENSE ZONE OF DEFORMATION

FIG. 5—*Crack-tip stress and strain fields surrounding the crack tip.*

rently). The elastic view, (1) may be appropriately used only if the crack-tip plastic zone is small compared to planar distances to other boundaries (or load points, etc.). That is to say for small-scale yielding, LEFM is appropriate. Lacking small-scale yielding, an elastic-plastic view, (2) must be adopted for the so-called elastic-plastic fracture mechanics regime. However, we must remain aware of limitations that the intensely nonlinear zone, (3), should then remain small compared to planar distances to boundaries. Now if zone (3) is comparatively small, then view (2) may be regarded as an elastic-plastic field, surrounding the crack tip (and the intensely nonlinear zone), which lends itself to analysis by usual plasticity theories. It is emphasized that this viewing procedure is completely analogous to LEFM wherein if the whole plastic zone is comparatively small, then view (1) may be regarded as a linear-elastic field, surrounding the crack tip (and plastic zone), which lends itself to analysis by theory of elasticity. Now proceed to consider and compare each view in more detail.

Linear-Elastic Crack-Tip Stress and Strain-Fields

The elastic view (1) is presented in Fig. 6. First, viewing the plastic zone as small compared to the extent of surrounding elastic material, linear elasticity is applied to obtain the elastic-field equations surrounding the near neighborhood of the crack tip. The distribution of stresses, σ_{ij}, and strains, ϵ_{ij}, have the characteristic of $1/\sqrt{r}$ singularity (higher order terms have been ignored). The equations given on the figure are the usual form for LEFM analysis, and K is the parameter describing the intensity of the field. K is thus determined from loads and body dimensions including crack size using the solution of the elastic boundary value problem for the configuration of interest.

If the plastic zone has significant size, w, the crack size should be taken to be an equivalent elastic crack size, including part of the plastic zone for effective analysis. However, such a correction, though frequently useful, approaches an elastic-plastic problem with significant plasticity using basically elastic analysis. Thus, for more generality and assured accuracy one must proceed to an elastic-plastic analysis; that is to say, we must proceed then to view the field as an elastic-plastic field.

Elastic-Plastic Crack-Tip Stress and Strain Fields

The fully elastic-plastic view, (2), is illustrated in Fig. 7. The view is taken that an elastic-plastic field (with small strains and rotations) surrounds the crack tip within the region denoted by (2), but outside the intensely nonlinear zone. Using plasticity theory for power hardening material Hutchinson [*9*] and Rice and Rosengren [*10*] obtained (with as-

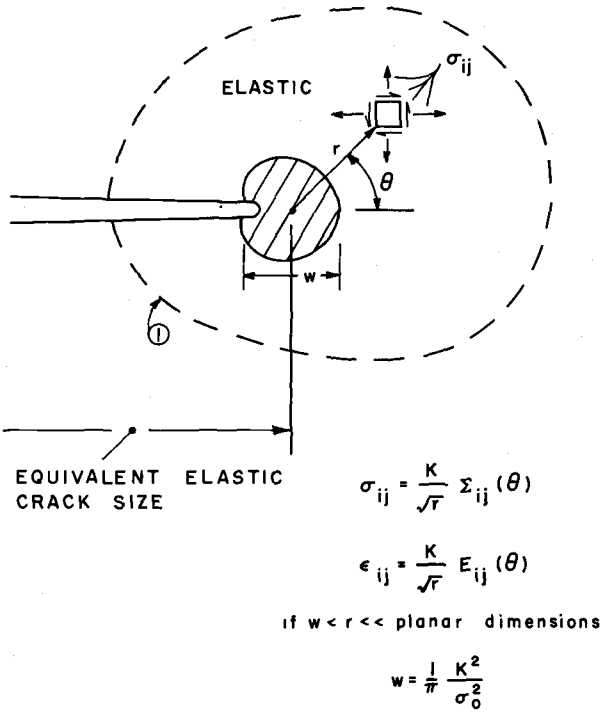

FIG. 6—*Linear-elastic crack-tip stress and strain fields.*

sistance from the earlier work of L. McClintock) the form of the stress, σ_{ij}, and strain, ϵ_{ij}, fields.

First, note the similarity to Fig. 6 which illustrated the linear-elastic case (1). Indeed for the linear-elastic case, $N = 1$, the plastic-field equations reduce to the linear-elastic field equations, that is, the $1/\sqrt{r}$ singularity reappears, $\bar{\Sigma}_{ij} = \Sigma_{ij}$, $\bar{E}_{ij} = E_{ij}$ and as a consequence, noting $\epsilon_0 = \sigma_0/E$ then

$$J = \frac{K^2}{E}$$

This was noted previously upon defining J. But this result is just for linear-elastic interpretations.

Indeed, it is more general to state that given the material properties, σ_0, ϵ_0, and N then a unique elastic-plastic stress and strain field exists which is further described, only by its intensity, J.

Result—J is the intensity of the elastic-plastic field surrounding the crack tip (playing the same role as K, the intensity of the surrounding elastic field, for the LEFM case).

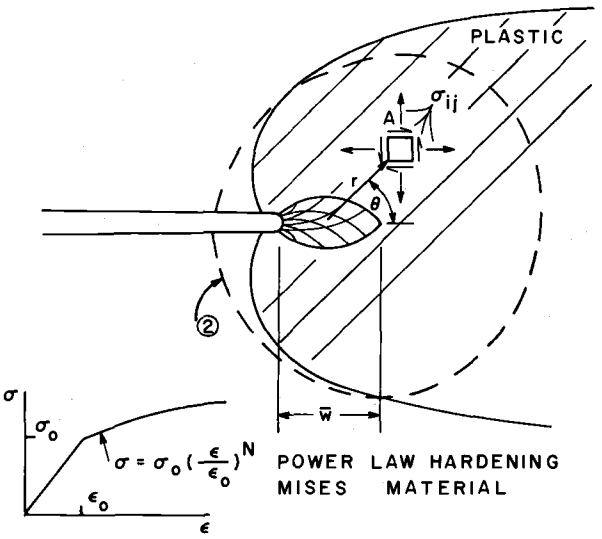

$$\sigma_{ij} = \sigma_0 \left(\frac{J}{r\sigma_0\epsilon_0}\right)^{\frac{N}{1+N}} \bar{\Sigma}_{ij}(\theta, N)$$

$$\epsilon_{ij} = \epsilon_0 \left(\frac{J}{r\sigma_0\epsilon_0}\right)^{\frac{1}{1+N}} \bar{E}_{ij}(\theta, N)$$

if $\bar{w} < r << $ planar dimensions

FIG. 7—*Elastic-plastic crack-tip stress and strain fields.*

Thus, J is seen to be an equivalent field parameter to its elastic analog K (or $\mathcal{G}$) and the LEFM analysis is extended fully into the elastic-plastic regime by the J-integral as an equally powerful and rational method. Indeed, LEFM is seen to be just a special case of the J-integral method.

However, within the elastic-plastic regime cautions about limitations should be followed, as with the linear-elastic case. Specifically, the zone of intense nonlinearity must be small compared to other planar dimensions, etc. Thus, the discussion proceeds to view that zone.

The Intensely Deformed Nonlinear Zone

Analysis of the details of the intensely deformed nonlinear zone at the crack tip is illustrated in Fig. 8 as view (3). Rice and Johnson [*11*] have considered analysis of this region using slip-line theory and more recently large strain, etc., finite element analysis (recent work of Rice and McMeeking). At this size scale representations through current plasticity theories

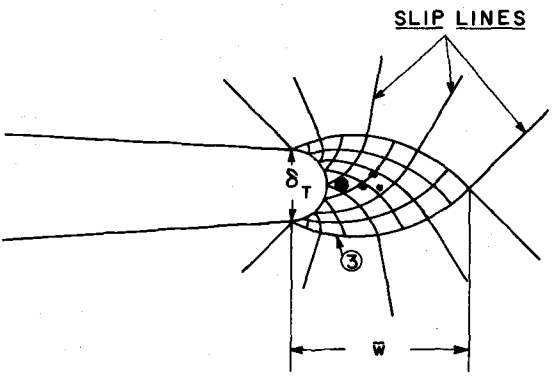

FIG. 8—*The intensely deformed nonlinear zone.*

are weak. Moreover, the development of holes, tearing (shown as black dots), and other fracture processes cause additional disturbances not taken into account in the analysis.

However, some general conclusions may be reached. Within this zone, (3), near the crack tip, hydrostatic stress conditions cause stress of the order of 3 σ_0 (three times the simple tensile flow stress) to be present. Thus, it seems evident that it is within this zone where fracture processes take place. Thus, in order to assure similarity of fracture conditions, it is this zone which must be surrounded by similar fields, such as controlled by J in view (2). The size of the zone, $\bar{w}$, must be small compared to planar dimensions if the analysis by J is to be relevant, that is, [*12*]

$$\bar{w} \cong 2 \frac{J}{\sigma_0} \ll \text{planar dimensions}$$

Moreover, if plane-strain fracture processes are to be maintained, then this zone size $\bar{w}$ should be small compared to thickness, B. Consistent with LEFM considerations, it is suggested in the elastic-plastic field analysis that [*12*]

$$B \geq 25 \frac{J}{\sigma_0} \text{ (for plane strain)}$$

Additional analysis of the level of view (3) proceeds in attempts at examining mechanisms and processes of fracture. This is not yet done.

Lacking this, then currently the J-integral method may be regarded as the only complete theory upon which fracture analysis, measurements, etc., may be based, with an equally rational basis and analytical tools equivalent to LEFM but in the elastic-plastic regime.

J-Integral Analysis for Monotonic Loading with Abrupt Failure or Stable Tearing

Begley and Landes [*3,4*], as mentioned earlier, developed an experimental method of measuring J from load displacement records for slightly different crack lengths in otherwise identical specimens. They applied this first to rotor steel (and other steel) at temperatures where abrupt failure (cleavage) occurs prior to any stable tearing. They showed that the J values for abrupt failure with full plasticity of a small specimen corresponded to the K values for abrupt failure in large standard (ASTM Test for Plane-Strain Fracture Toughness of Metallic Materials E 399-74) linear-elastic plane-strain fracture toughness tests. The comparison was made reasoning that the critical J in the elastic test computed by

$$J(\text{elastic test}) = \frac{K^2}{E}$$

might be the same as the critical J in the fully plastic test and indeed that is what was found, that is

$$J_{Ic}\,(\text{plastic test}) = J_{Ic}\,(\text{elastic test}) = \frac{K_{Ic}{}^2}{E}$$

Actually, it was only after obtaining this result that it was reasoned that for identical J values the implication was that identical elastic-plastic fields would be surrounding the crack tips. Therefore, the onset of abrupt failure was occurring within identical stress and strain fields with identical intensities, prior to stable crack extension in both types of tests.

Now, stable crack extension prior to failure implies unloading in material bypassed by the crack tip. There were worries that unloading might cause error due to violation of J-integral analysis assumptions (deformation plasticity). Moreover, stable crack extension in the standard K_{Ic} test (ASTM E 399-74) causes the measurement point for K_{Ic} to be a 2 percent effective crack extension (an approximately but variable 1 percent actual crack extension with uncertain plasticity effects being the balance) in a large enough but otherwise unspecified specimen size. So with stable crack extension this additional point requiring clarification arose.

However, in later work Landes and Begley [*13*] and Logsdon [*14*] showed that even with stable tearing, the values of J—for a crack growth comparable with the standard K_{Ic} test—gave comparable J_{Ic} (plastic test)

values (using compact or bend-plastic tests because occasionally center-crack specimens gave some as yet unexplained differences). Thus, confidence was gained that J-integral analysis was still sound even with the unloading implied by limited amounts of stable tearing.

Finally, since stable tearing (in at least limited amounts) does not seem to bother the J-integral analysis, then it was reasoned that J could be used as the loading (field intensity) parameter to characterize stable tear crack extensions, Δa. Again, Begley and Landes [*13*] and later Logsdon [*14*] and others [*15*] simply plotted applied field intensity, J, versus Δa to characterize the materials response (or R-curve). Recently, Paris and Clarke [*16*] have gone so far as to analyze transition temperature phenomena, the interchanging roles of cleavage and stable tearing, for a medium strength steel. The J-integral R-curve method is convenient and provides unusual detail in doing such work.

In summary, five years of testing experience give convincing data that J-integral analysis is an appropriate method for describing crack-extension behavior and properties under monotonic loading. Limitations, such as the previously mentioned $\bar{w}$, size limit, and limitations on other details of the analysis are not fully understood but are resolved well enough to sustain high confidence in using J-integral analysis for elastic-plastic situations.

J-Integral Rate for Time-Dependent Plasticity

For linear time-dependent plasticity or creep (linear viscoelastic), the stresses, σ_{ij}, and internal (or external) tractions, T_i, remain constant with time (approximately) for steady loading. The tractions and stresses also remain constant for steady-state loading for purely viscous material behavior. With these special cases in mind, the time derivative of J or J-integral rate may be computed as follows

$$J^* = \frac{dJ}{dt} = \oint_\Gamma W^* dy - T_i \frac{\partial \dot{u}_i}{\partial x_i} ds$$

where

$$W^* = \int \sigma_{ij}\, d\dot{\epsilon}_{ij} \text{ and } \dot{\sigma}_{ij} = 0, \text{ and } \dot{T}_i = 0.$$

Under such conditions, J^* may be thought of as the rate of deformation within the plastic field at a crack tip (Fig. 9).

Landes and Begley have applied J^* to correlation of creep cracking data on a material [*17*]. Their results on the figure show that J^* correlates data on the time-rate of crack growth for two different configurations

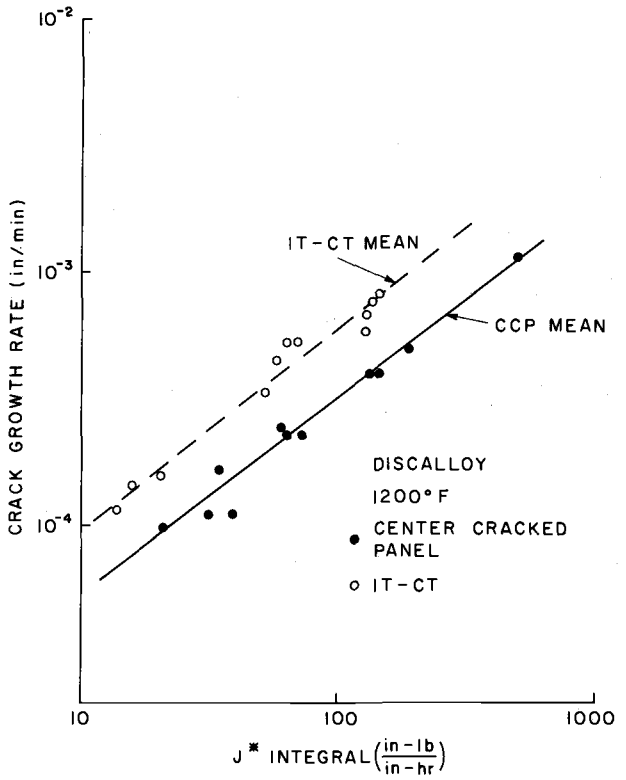

FIG. 9—*Creep crack-growth rate versus J* integral.*

within a factor of about 2. However, the linear time-dependency or fully viscous assumptions as yet have not been fully explored, thus, the method has great promise but requires further verification.

Nevertheless, it might be thought quite surprising that any correlations exist at all on the basis of using J^*, since the original assumption of J-integral analysis was deformation theory of plasticity. Here, we have time dependency on top of crack motion which implies unloading. An assumption of deformation theory applied to plasticity is no unloading, but perhaps a better perspective can be drawn for this assumption.

Any unloading which is occurring is situated behind the crack tip as it progresses, that is, behind the region where cracking processes are taking place. On the other hand, in the region immediately ahead of the tip of the (moving) crack where the processes preceding separation are occurring, deformation intensities are increasing enormously, especially as compared to deformation in any unloading process. Thus, perhaps the J^* is evaluating reasonably the rates of the enormously intensifying deformations which are causing separation, whereas unloading becomes of

little consequence in the analysis. Indeed, this is proposed as a reasonable explanation of the success of Begley and Landes' correlation of data.

Moreover, undoubtedly their material was neither perfectly linear viscoelastic nor purely viscous, and, in addition, steady state may not have been achieved in their tests. Their successful correlation of data, then, might imply that relaxation of other assumptions also might be possible. But prudence dictates that before speculating further, careful experimentation should be employed to evaluate effects of stretching these assumptions. This experimentation remains to be done, but at least it can be stated here that it may be approached with optimism for using J^* for creep phenomena.

Application of J-integral Analysis to Fatigue Crack Growth

In view of the previously cited no unloading assumption of deformation theory of plasticity, it might seem on first reaction ludicrous to suggest even considering cyclic loading J analysis with alternating plasticity. However, this is an area with important practical consequences in many applications problems. For that reason, Dowling [*18*] made the attempt which netted (astounding for some) success.

Figure 10 shows data compiled on A533B steel by Dowling using the usual LEFM correlation method of plotting ΔK, the range of cyclic stress field intensity, versus da/dN, the crack extension per cycle. He then reasoned that the crack growth occurs during loading and evaluated the increase in J, that is, ΔJ, for the loading portion of cycles on elastic-plastic specimens and corresponding da/dN values. He did this for both center cracked (CC) and compact tension (CT) specimens and plotted the data as shown in the Fig. 10, superimposed on the elastic test (and analysis) data. As before, correspondence between linear-elastic and elastic-plastic analysis is found through

$$\Delta J \text{ (plastic test)} = \Delta J \text{ (elastic test)} = \frac{(\Delta K)^2}{E}$$

The correlation is very good and is especially clear upon noting overlapping of the data for two full log cycles of growth rates, da/dN. Similar results have been compiled by Dowling for other material.

Certainly, the correlation of overlapping data for elastic and plastic tests is not just fortuitous. Even with cyclic unloading the J-analysis must still be applicable. In hindsight, it can be reasoned to be logical, as follows.

At the high end of the growth rate curve, the crack tip moves ahead during each cycle into relatively virgin material in terms of plastic deformations, compared to the intense deformations it will sustain (right at the crack tip) during the next cycle. (Refering back to the elastic-plastic

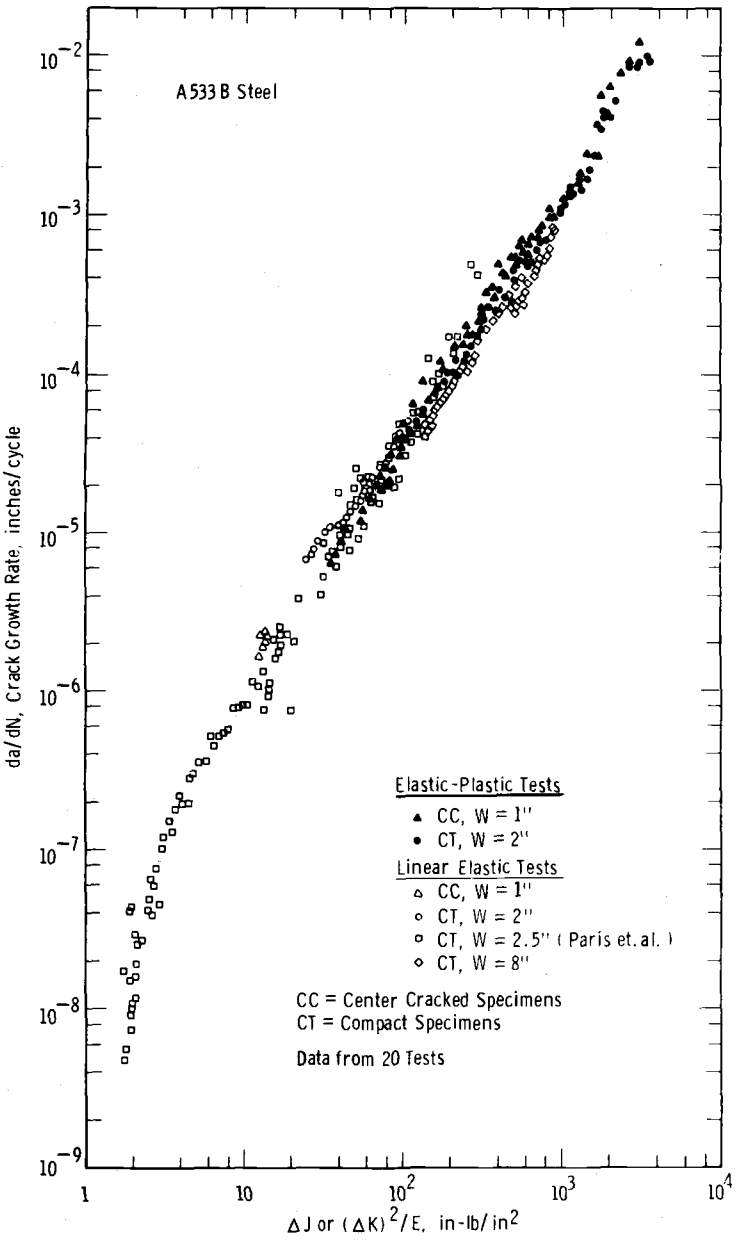

FIG. 10—*Fatigue crack-growth rate versus cyclic J for various geometries.*

field equations the strain singularity is to the inverse $1/(N + 1)$ power of distance from the tip, r.) Thus, during the next cycle past history (previous loading and unloading) will not be significant compared to the loading, ΔJ, which is then being sustained. Thus, as long as a moving crack is considered, it may be possible to neglect past history including unloading in a J-integral analysis and characterization of material behavior phenomena.

Whether this explanation is correct or not the data correlations stand secure. Therefore another broad area of applicability of J-integral analysis has been illustrated here. Moreover, initial assumptions, such as no unloading, for mathematical convenience are not always strict limitations as is seen here (sometimes "Mother Nature" is not too harsh after all). But then limitations should be assessed carefully and considered frequently, which leaves much to be explored in the application of J to fatigue crack growth.

Computation Methods and Estimates for J Determination

The original path independent integral form for J, that is

$$J = \oint_\Gamma W dy - T_i \frac{\partial u_i}{\partial x} ds$$

and the equally valid nonlinear compliance form for J, that is

$$J = -\int \frac{\partial P}{\partial a} d\delta_P = \int \frac{\partial \delta_P}{\partial a} dP$$

give the basis for equally applicable methods of determining J for a given configuration and crack and a given loading (or deformation) state. Both forms are considered to be exact as analytical tools.

If an elastic-plastic solution giving the stresses and strains is known for a crack problem of interest, then the first integral form may be used to compute J using any contour enclosing the crack tip (but not enclosing the applied loads). Thus, if a solution is known in analytic form or numerical form (such as finite element results), J may be computed around many contours to check or average its evaluation. Experience dictates that the portion of the stress-strain solutions right at or nearby the crack tip are of worst accuracy, and, thus, the possibility of evaluation of J on contours away from the crack-tip region is a decided and valuable advantage.

Moreover, if stress-strain solutions can be made available for two slightly differing crack sizes in the form of load versus load-point-displacement then the second, nonlinear compliance, form may be adopted. Since the load-point-displacements tend to average the effects of the stress-

strain state throughout the body, this method is equally attractive for analysis.

Other methods also can be devised based on a full knowledge of stress-strain solutions and indeed are of interest. Consequently, it is evident that for an application where the full stress-strain solution is known, J can be computed. Moreover, finite-element analysis is always available; so for the price of the analysis, J can be evaluated and prospects or effects of fracture characterized. However, costs of such analysis are high and numerical evaluations (finite element) often do not assist much in parametrically understanding a problem (without repeated runs and multiplying costs). Therefore, it is relevant to discuss possibilities of analysis simplifications or estimating methods or both for J for cases of some interest.

For example, if it is desired to evaluate J after developing fully plastic conditions and continued plastic deformations, then rigid-plastic (nonhardening) analysis is often appropriate. In such a case, the load versus load-point-displacement relationship neglects original elastic behavior (rigid) and the relationship is increasing (unlimited) displacement, δ_P, at limit load, P_L. Now, considering the second, nonlinear compliance, form for J previously mentioned then

$$J = -\int_0^{\delta_P} \frac{\partial P}{\partial a}\, d\delta_P = \frac{-\partial P_L}{\partial a} \times \delta_P$$

Since loads stay constant at limit loads, P_L, (that is, they are not functions of displacement), then it is noted $\partial P/\partial a$ goes outside the integral sign.

Result—J simply becomes the rate of change of limit load with respect to crack size times, the work producing component of load point displacement under conditions appropriate for rigid-plastic analysis.

Now, limit loads and their changes with crack size are relatively easy to compute (using slip-field analysis), so a decided simplification has been developed. Moreover, it is readily apparent that J depends linearly on displacements and linearly on the rate of decrease of limit loads with crack size, giving the intuitive parametric tools for simplified thinking about J.

Thus, for example it is expected that rigid-plastic conditions are appropriate for analysis, but, with work hardening occurring approximately linearly with displacements, then the preceding results assist considerations. If the limit loads, P_L, harden (increase) linearly with displacement, but at different rates for different crack sizes, then J will increase with δ_P by a squared term and a linear term in displacement. Other examples are added easily for visualizing effects.

For the elastic-plastic (nonhardening) case, similar considerations may be made on the form of increase of J with displacement, δ_P, by considering

the nature of load versus load-point-displacement relationships [5] and their changes with crack size. During the early part of loading, a cracked body is predominately elastic during which J is equal to $\mathcal{G}$ or proportional to δ_P^2. During the later stages of load after limit loads are developed, J depends linearly on δ_P. In between, a transition (elastic-large-scale yielding) occurs but this is a brief and smooth change from squared to linear dependancy on δ_P. For the purpose of developing accurate estimates of J versus δ_P (or load P) behavior, the elastic portion can be estimated using LEFM and the transition using plastic zone corrected LEFM and final later plastic behavior from limit analysis [5]. Thus, it is easy and relevant to develop estimating procedures for J, based on the original mathematical-physical nature of J-integral definitions, that is, the path independent integral and nonlinear compliance forms.

In addition to these general procedures for estimating or computing J for quite arbitrary configurations, the analytical nature of J permits certain simplifications for special configurations. In particular, Rice [6] has shown that such simplifications exist for configurations with a single characteristic length dimension involving the crack size. An already classical example is the case of a half plane, cracked from infinity perpendicular to the edge with the remaining uncracked ligament, b, transmitting pure bending loads in the form of a moment, M (per unit thickness). Then the work producing displacement, the relative rotation, θ, of the moments must be by dimensional analysis considerations a function of M over b^2, that is

$$\theta = f\left(\frac{M}{b^2}\right)$$

This is because throughout the elastic-plastic range the only other parameters to enter this relationship are material parameters which are nondimensional or have dimensions of force over length squared (that is, elastic modulus, flow stress, strain hardening coefficient, etc.). With this clue as to the key factor in Rice's analysis his original handwritten note on this analysis is included here as Fig. 11.

His analysis proceeded to make use of the nonlinear compliance form of J, where finally

$$J = \frac{2}{b} \times \text{area (of the } M \text{ versus } \theta \text{ or load-displacement curve)}$$

The area under this curve is the work done by loading, or

$$J = \frac{2}{b} \times \text{work}$$

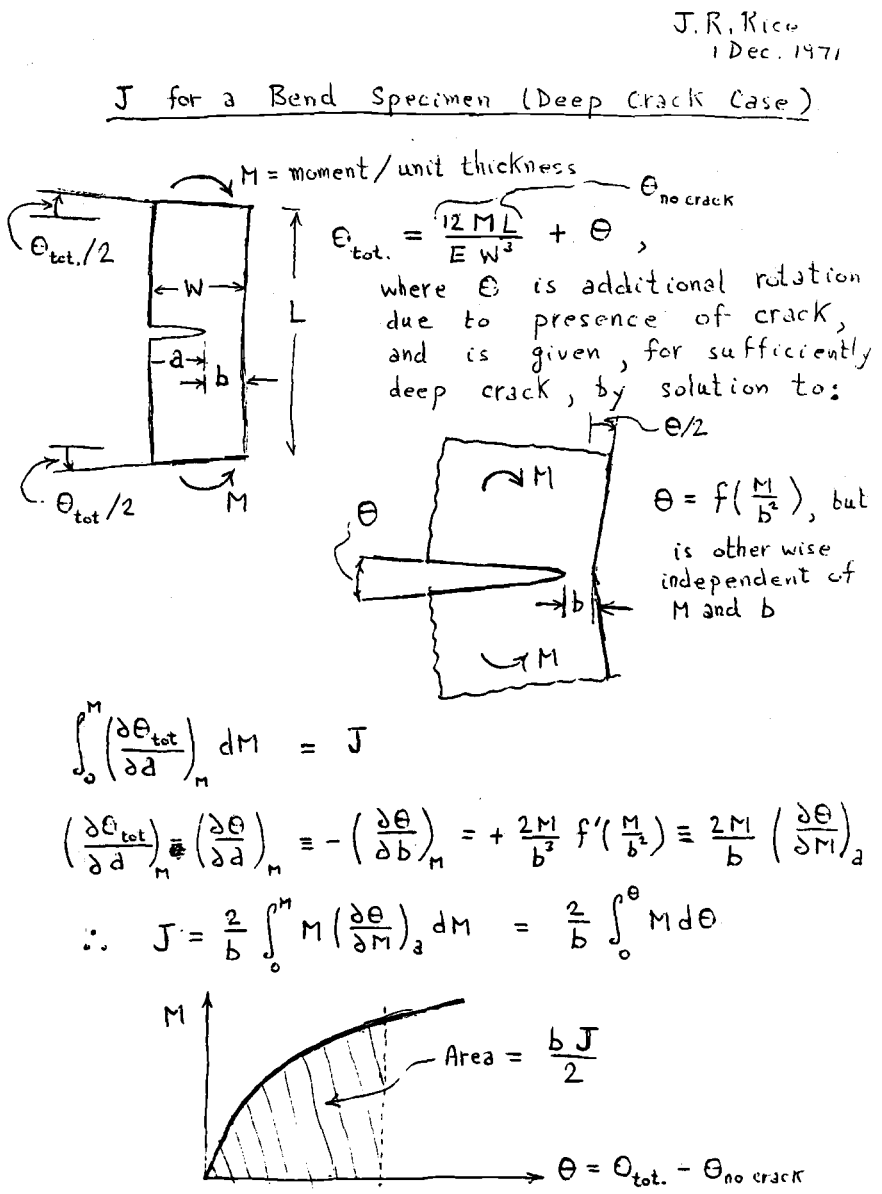

FIG. 11—J *for a bend specimen (deep crack case).*

Now, in order to apply this analysis to finite size specimens with small remaining ligaments, *b*, some additional considerations are required. As implied in Rice's analysis on the figure, the analysis holds only if the displacements with no crack (or notch) are removed. With small ligaments

remaining, the loads which can be sustained, as limited by full plasticity for the ligament, could cause only elastic action of the specimen with no crack. Therefore, it is possible to subtract these undesired displacements, using elastic analysis to assess their size, that is, this presents no difficulty.

Thus, applying the analysis to deeply cracked bend bars subject to four-point bending (pure bending at the cracked section) appears to present no difficulty. The work to be used in the computation of J is simply that done by the loading, less that for an elastic specimen with no crack (which could be experimentally determined). How deep is a deep enough crack is answered simply by saying deep enough so that the plasticity is confined to the remaining ligament so that a wider specimen with the same ligament would display the same patterns of plasticity (that is, confined to the ligament region, etc.).

With a three-point bending specimen the main loading point is opposite the crack (or notch), so that local stresses caused by this load might alter the plasticity effects at the ligament. However, this seems to be no problem and is dropped from the discussion here. On the other hand for a deeply cracked compact (tension) specimen, tension as well as bending exists on the ligament, but this effect is small (and disappears entirely in the limit of very deep precracking). By measuring displacements directly across on the crack (or notch) surface at the load line, the measurement is directly the work producing displacement of the loads due only to having a crack present. Thus, indeed the deeply cracked compact specimen is very convenient and accurate for J-integral testing. For more extensive analysis of test method, see Refs *3,4,6,13,14,15,* etc.

Now, the Rice analysis of pure bending has other ramifications. For example the Charpy test is a bend test measuring energy loss or work for failure so it may be regarded as a crude J test. However, even the so-called instrumented Charpy test is not instrumented well enough to analyze data as quantitatively acceptable as in K_{Ic} or J testing. And moreover, size limitations as cited for J analysis earlier are not met by lower strength-higher toughness materials in the standard Charpy test size, but, at least, this analysis gives some clues as to why Charpy tests are sometimes qualitatively correlated to J results or K_{Ic} tests or both.

Finally, the Rice analysis can be applied to any configuration with a single characteristic (ligament ahead of the crack) dimension. Moreover, except for the case of pure bending it can be shown J is not just proportional to work done in loading. This result implies that EE is applicable to bending but not to other configurations in general (though to some other configurations if rigid-plastic analysis is appropriate). Therefore, it has been illustrated that some simple and direct analysis methods can be developed to improve understanding applications of the J-integral analysis. Undoubtedly, other such simplifications will be forthcoming in the future to make analysis even simpler and clarify both the understanding

of material behavior and the cracking behavior of structural components in the elastic-plastic regime.

Summary of the Comprehensive Nature of J-Integral Analysis

Table 1 gives a resume of applicability of J-integral analysis to various categories of elastic through plastic behavior. In each regime, its assumptions are indicated and relationships to (normal) fracture mechanics analysis and other fields of mechanics are noted. Finally, analysis tools required (or normally used) to compute J or equivalent parameters are listed.

Thus, this table gives a concise impression of the comprehensive nature of J analysis. Detailed application to each of the indicated areas is pos-

TABLE 1—*Comprehensive nature of J-integral analysis of cracking phenomena.*

Behavior (material)	Assumptions	Relationship to J	Analysis Methods
Nonlinear elastic	deformation theory: crack-tip fields	$J = \mathcal{G}$ (Griffith theory) exact	solutions to deformation theory problems
Linear elastic	elasticity theory: crack-tip fields	$J = \mathcal{G} = K^2/E$ exact	usual LEFM solutions for K and estimates
Elastic small-scale yielding	elasticity theory: crack-tip fields: correction for plastic zone	$J = \mathcal{G} = K^2/E$ corrected crack length approximate	usual LEFM solutions for K and estimates plus plastic zone corrections
Elastic plastic	deformation theory: crack-tip fields[a]	J = integral or compliance form (identity)	plasticity solutions for J and estimates
Rigid plastic	limit analysis: slip-line fields	$J = (\partial P_L/\partial a)\delta_P$ exact	limit load analysis with cracks and estimating
Time-dependent plastic creep	deformation theory: linear rate dependence or purely viscous-crack-tip fields	$^*J$ = integral or compliance form $^*J = dJ/dt$ approximate	used experimentally only to date
Cyclic plasticity (fatigue)	deformation theory: no unloading history effects crack-tip fields	ΔJ = compliance form	ΔJ plays same role as $\Delta K^2/E$ in elastic case: used experimentally only to date

NOTE—$\mathcal{G}$ = energy per unit area made available for crack extension,
E = effective modulus of elasticity,
P_L = load limit,
δ_P = load point displacement, and
t = time.

[a]Agreement with incremental theory is good.

sible, although since the method is relatively new and undeveloped, many particular applications will require further development. On the other hand, considering that LEFM analysis has been available for almost 20 years and many of its applications developed only in the last 10 years, J-integral analysis seems to be developing on a more rapid application schedule than was so for LEFM.

Note that this table is at best a very simplified presentation. It is especially relevant to acknowledge that limitations are omitted for brevity in the table but have been outlined in the previous text and are discussed in many of the listed references, as well as in other recent works in this field. Nevertheless, this table represents a listing of the general behavior areas where successful applications of the J-integral method are already accomplished.

Comparative Applicability of J-Integral and Other Methods

The relative appropriateness of applications of J compared to LEFM, COS, and EE methods to various problems has been the subject of various discussions [*2,6,19*]. In addition to lacking an analytical basis, the COS and EE methods lack clear indication of their limitations within their methodology. Nevertheless, on Table 2 they are listed as applicable if known limitations do not prohibit their use in the regimes considered.

Table 2 clearly illustrates the comprehensive nature of the J-integral approach when compared to other methods.

TABLE 2—*A comparison of alternate methods.*

Behavior (material)	LEFM	COS	EE
Nonlinear elastic	not applicable	not applicable	not applicable
Linear elastic	applicable	not applicable	applicable
Elastic small-scale yielding (requiring plasticity correction)	applicable	$\delta_T = (M\mathcal{S}/\sigma_0)$ applicable but poor approximation	applicable but poor approximation except for bending
Elastic plastic	not applicable	$\delta_T = M(J/\sigma_0)$ applicable	not applicable, except for bending
Rigid plastic	not applicable	applicable δ_T proportional to load point displacements, δ_P, through slip-line solutions	applicable but limited to certain configurations
Time-dependent plastic	not applicable	not applicable	not applicable

Conclusions

1. The J-integral analysis method, to date, is the most general and fundamentally sound method for analyzing fracture in the elastic-plastic regime.

2. The rationale of the J-integral method in application is that J is the intensity of the elastic-plastic crack-tip field, which is completely analogous to (just as sound as) LEFM.

3. The J-integral method has a flexible analytical (mathematical) basis leading to general and tractable computation methods and direct experimental methods for evaluating J.

4. Simplified methods for estimating J also may be developed along with intuitive methods for considering elastic-plastic cracking behavior based on the analytic approach of the J-integral method.

5. J-integral methodology has been developed to characterize plane-strain fracture toughness behavior (cleavage and stable tearing) for material (from small specimens compared to K_{Ic} tests).

6. Initial successful applications of J-integral methodology for characterizing cracking behavior are areas such as (*a*) time-dependent plasticity (creep), (*b*) cyclic full plasticity (fatigue), and (*c*) transition phenomena.

7. Linear-elastic, nonlinear elastic, and elastic small-scale yield fracture mechanics analyses are all shown to be special cases of the J-integral method, that is, treatable by the more general J-integral method if desired for generality.

8. The J-integral method is a relatively new analysis method (with demonstrated advantages); therefore, it is expected that many aspects of its technology are not yet developed. Substantial improvements may be expected.

9. The J-integral method has limitations which tend to be defined more easily and clearly because of its analytical nature. However, for many applications, the limitations are not well explored nor sufficiently understood, and caution is recommended.

10. Other methods of elastic-plastic fracture mechanics are less well developed, have serious limitations, or lack the analytical basis of J-integral methods or both.

Acknowledgments

This task was initiated by the Westinghouse Electric Corporation (through ERDA Contract E-3045 Task VI) and supported by the Materials Research Laboratory at Brown University funded by the National Science Foundation. The encouragement and assistance of many individuals in preparing this discussion are gratefully acknowledged, including especially J. D. Landes, G. A. Clarke, and E. T. Wessel of Westinghouse; J. R.

Rice of Brown University; J. W. Hutchinson of Harvard University; and J. A. Begley of Ohio State University.

References

[1] Rice, J. R., *Journal of Applied Mechanics*, 1968, pp. 379–386.
[2] Rice, J. R., *Fracture*, Vol. 2, 1968, pp. 191–311.
[3] Begley, J. A. and Landes, J. D., in *Fracture Toughness, ASTM STP 514*, 1972, pp. 1–23.
[4] Landes, J. D. and Begley, J. A., in *Fracture Toughness, ASTM STP 514*, 1972, pp. 24–39.
[5] Bucci, R. J., Paris, P. C., Landes, J. D., and Rice, J. R., in *Fracture Toughness, ASTM STP 514*, 1972, pp. 40–69.
[6] Rice, J. R., Paris, P. C., and Merkel, J. G., *Progress in Flaw Growth and Fracture Toughness Testing, ASTM STP 536*, 1973, pp. 231–245.
[7] Hayes, D., Ph.D. thesis, Imperial College, London, England, 1972.
[8] Harvard University by Hutchinson, Shih, and co-workers; and Westinghouse Research by W. K. Wilson, 1972 to 1975, private communications.
[9] Hutchinson, J. W., *Journal of Mechanics and Physics of Solids*, 1968, pp. 13–31; pp. 337–347.
[10] Rice, J. R. and Rosengren, *Journal of Mechanics and Physics of Solids*, 1968, pp. 1–12.
[11] Rice, J. R., and Johnson, M. A., *Inelastic Behavior of Solids*, McGraw Hill, 1970.
[12] Paris—discussion of ref 3 and 4.
[13] Begley, J. A. and Landes, J. D., in *Fracture Analysis, ASTM STP 560*, 1974, pp. 170–186.
[14] Logsdon, W. A., in *Mechanics of Crack Growth, ASTM STP 590*, 1976, pp. 43–61.
[15] Andrews, W., Clarke, G., Faris, P. C., and Schmidt, D., in *Mechanics of Crack Growth, ASTM STP 590*, 1976, pp. 27–43.
[16] Paris, P. C. and Clarke, G., "Slow Tearing and Cleavage Properties of a Medium Steel Through The Transition Range," submitted to the International Congress of Theoretical and Applied Mechanics, Delft, 1976.
[17] Begley, J. A. and Landes, J. D., in *Mechanics of Crack Growth, ASTM STP 590*, 1976, pp. 128–148.
[18] Dowling, N., and Begley, J. A., in *Mechanics of Crack Growth, ASTM STP 590*, 1976, pp. 82–103.
[19] Begley, J. A. and Landes, J. D., in *Progress in Flaw Growth and Fracture Toughness Testing, ASTM STP 536*, 1973, pp. 246–263.

R. M. McMeeking

Path Dependence of the J-Integral and the Role of *J* as a Parameter Characterizing the Near-Tip Field

REFERENCE: McMeeking, R. M., **"Path Dependence of the J-Integral and the Role of *J* as a Parameter Characterizing the Near-Tip Field,"** *Flaw Growth and Fracture, ASTM STP 631,* American Society for Testing and Materials, 1977, pp. 28–41.

ABSTRACT: The J-integral has significant path dependence immediately adjacent to a blunted crack tip under small-scale yielding conditions in an elastic-plastic material subject to mode I loads and plane-strain conditions. Since the J-integral, evaluated on a contour remote from the crack tip, can be used as the one fracture-mechanics parameter required to represent the intensity of the load when small-scale yielding conditions exist, *J* retains its role as a parameter characterizing the crack-tip stress fields, at least for materials modelled by the von Mises flow theory. Some results obtained using both the finite-element method and the slip-line theory are suggestive of a situation in which an outer field parameterized by a path-independent value of *J* controls the deformation in an inner or crack-tip field in which *J* is path dependent. The outer field is basically the solution to the crack problem when large deformation effects involved in the blunting are ignored. Thus, the conventional small-strain approaches in which the crack-tip deformation is represented by a singularity have been successful in characterizing such features as the crack-tip opening displacement in terms of a value of the J-integral on a remote contour. An interesting deduction concerns a nonlinear elastic material with characteristics in monotonic stressing similar to an elastic-plastic material. Since *J* is path independent everywhere in such a material, the stress and strain fields near the crack tip in such a material must differ greatly from those arising in the elastic-plastic materials studied so far. This result is of significance because it is believed that such nonlinear elastic constitutive laws can represent the limited strain-path independence suggested by models for plastic flow of polycrystalline aggregates based on crystalline slip within grains.

KEY WORDS: crack propagation, J-integral, path dependence, tip field, plasticity, blunting, fractures (materials)

The utility of the J-integral [*1*][2] in fracture mechanics would seem to depend on its role as a parameter characterizing the near-tip field. If the

[1] Presently, acting assistant professor, Division of Applied Mechanics, Stanford University, Stanford, Calif. 94305; formerly, research assistant, Division of Engineering, Brown University, Providence, R. I. 02912.

[2] The italic numbers in brackets refer to the list of references appended to this paper.

value of J, computed on a contour remote from the crack tip, directly controls the near-tip stress and strain distribution and magnitudes before the onset of fracture, then J can be used to characterize the mechanics of fracture initiation. Apart from linear-elastic materials, the most obvious cases in which J parameterizes the near-tip field are power law hardening deformation plastic materials as analyzed by Rice and Rosengren [2] and Hutchinson [3]. In these cases, the crack tip is modelled as a singular point for strain. The strength of the singularity is determined by the hardening characteristics, and the amplitude of the singularity is controlled by the path independent J. The angular characteristics of the stress and strain fields are determined basically by the hardening characteristics.

These analyses would seem to be quite accurate models for the near-tip behavior in incrementally plastic materials. Thus, the near-tip strain in incrementally plastic materials has a singular behavior dependent on the hardening characteristics of the material, which also sets the angular stress and strain distribution. The amplitude of the singularity is governed by a value of the J-integral evaluated on a contour shrunk onto the tip. Since there is no guarantee of path-independence of J in incrementally plastic materials, there would seem to be no certainty that a value of J computed on a remote contour would control the near-tip stress and strain state in these materials. If, however, the tip value of J were equal to the remote value (that is, path-independence of J actually does occur) or if the tip value were some constant function of the remote value, then the near-tip field would be characterized by a remote value of J. According to the small-strain finite element analyses of Rice and Tracey [4] and Tracey [5] using singular crack-tip elements and flow theory plasticity, the J-integral is path independent, at least under conditions of small-scale yielding. There is some uncertainty in this work concerning the path dependence of J in the crack-tip elements. However, Parks [6] has analyzed the same problems by the same methods but using a deformation theory of plasticity. He also found J to be path dependent in the crack-tip element despite the nonlinear elastic constitutive law he used. In view of this, it would seem that there is a defect in the crack-tip element as far as path independence of J in the deformation theory is concerned. This does not rule out the possibility of a path dependence of J very close to the crack tip in the flow theory materials when conventional small-strain assumptions are made. However, according to the results of Rice and Tracey [4,5], if J is path dependent, the tip value of J is a numerical constant times the remote value of J, at least in small-scale yielding. The results for small-scale yielding are, in general, in agreement with the well-known, one-parameter characterization of fracture initiation that is the plane-strain fracture toughness.

However, a recent finite-element study of the blunting of crack tips in elastic-plastic materials in small-scale yielding by McMeeking [7] has re-

vealed a significant path dependence of J, very close to the crack tip, on contours of radius comparable in size to a few times the crack-tip opening displacement. There would seem to be no functional dependence of the tip J values on the remote J values. Indeed, the tip value would appear to be zero. If the one-parameter characterization of the initiation of fracture in small scale yielding is dependent on the remote value of the J-integral controlling the tip value of the J-integral and on this, in turn, controlling the tip stress and deformation state, then one-parameter characterization of the initiation of fracture in small-scale yielding should not work. It would appear, however, that an outer field, characterized by a path-independent value of J, controls the deformation in an inner, or crack-tip, field in which J is path dependent. Thus, the remote value of J parameterizes the near-tip field while the tip value of J is possibly zero.

The comments about the flow-theory materials have been restricted to the case of small-scale yielding. The more important questions about the role of J as a parameter characterizing the near-tip field concern the cases of large-scale yielding and fully-plastic conditions as have been investigated by Begley and Landes [*8*]. With continuous hardening, as in a power law hardening material, it seems likely that a characteristic near-tip field similar to the Hutchinson [*3*], Rice-Rosengren [*2*] near-tip field arises, at least when conventional small-strain assumptions are used. Since this field is dependent on the tip value of the J-integral, it would be of value, as far as characterizing fracture initiation is concerned, to understand the way the tip value of J depends on the remote value of J in flow-theory materials in conditions of large-scale yielding or full plasticity. If there is no hardening at all, there is known to be a gross nonuniqueness of crack-tip stress and deformation fields in full plasticity of flow theory materials, as illustrated by the slip-line solutions discussed by McClintock and Irwin [*9*]. In terms of the analysis of the mechanics of fracture initiation, it is desirable to know how soon beyond small-scale yielding conditions the nonuniqueness sets in. Once the nonuniqueness arises, it is impossible for the J-integral to characterize fracture initiation uniquely. Similarly, it is desirable to understand the relationship between fully plastic solutions for nonhardening materials and solutions for materials which have some hardening but which eventually experience a saturation to a constant flow stress after large strain.

Definition of the J-Integral

In view of the large deformations which occur near the tip of a blunted crack, it is necessary to define the J-integral, following Eshelby [*10*], as

$$J = \int_{\Gamma} \left[W dX_2 - \mathbf{T} \cdot \frac{\partial \mathbf{u}}{\partial X_1} ds \right] \tag{1}$$

where Γ is a path in the undeformed state of the material from the bottom surface of the notch through material to the upper surface of the notch, $\mathbf{X}$ is the position of a material point in the undeformed configuration, $\mathbf{u}$ is displacement, $\mathbf{T} = \mathbf{n} \cdot \mathbf{t}$ where $\mathbf{n}$ is the outward normal to the integration path and $\mathbf{t}$ is the nominal (first Piola-Kirchhoff) stress tensor as in $t_{ij} = |F| \sigma_{pj} \partial X_i / \partial x_p$, where $|F|$ is the ratio of the volume of a material element in the deformed state to its volume in the undeformed state, σ is the true stress, and $\mathbf{x} = \mathbf{u} + \mathbf{X}$. In addition, ds is an element of path length and

$$W = \int_0^{\partial u_i / \partial X_j} t_{ji} d(\partial u_i / \partial X_j)$$

Note that the definition of W means that it can also be expressed as

$$\int_0^{t_f} |F| \sigma_{ij} D_{ij} dt$$

where t is a loading parameter which is zero in the undeformed configuration and t_f in the deformed state for which W is to be computed. The tensor $\mathbf{D}$ is the rate of deformation tensor with components given by

$$D_{ij} = \frac{1}{2} (\partial v_i / \partial x_j + \partial v_j / \partial x_i)$$

where $\mathbf{v}$ is velocity. The explicit loading history of the material point for which W is to be calculated is used in the computation, although this requirement becomes immaterial in a nonlinear elastic material. The J-integral is path independent in elastic materials when defined according to Eq 1. The definition of J coincides with the usual small-strain definition when the difference between deformed and undeformed configurations can be neglected.

Path Dependence of the J-Integral

Path dependence of the J-integral was detected when a finite-deformation analysis of plane-strain, notch-tip opening with contained yielding was carried out using the finite-element method [7]. A notch with a semicircular tip was opened up until the width of the notch at the tip, b, was about fives times b_0, the undeformed width of the notch. The J-integral was computed on various contours around the notch tip at several levels of notch-tip opening. The results are plotted in Fig. 1, in which J_∞ is the value of the J-integral computed on a contour remote from the crack tip.

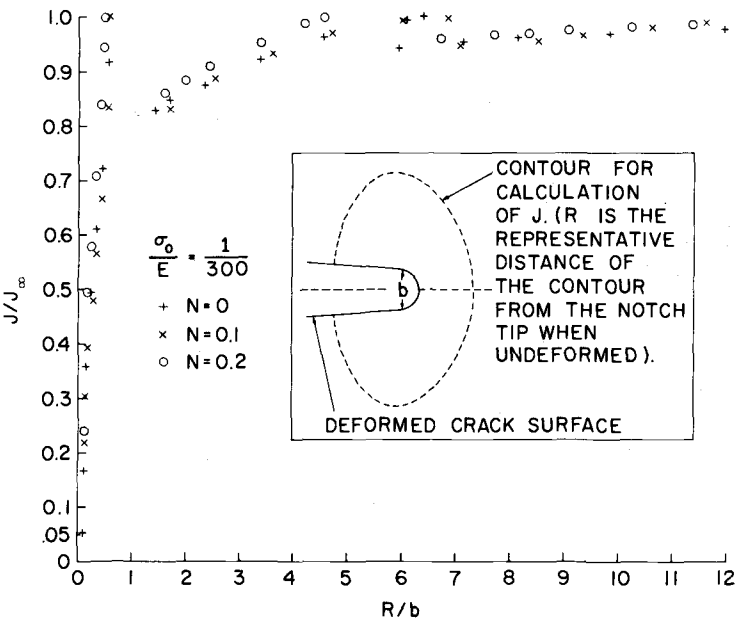

FIG. 1—*Plot of J-integral, computed from the finite element results for the blunting of a notch with contained yielding, versus the distance from the notch tip of the eontour on which* J *is calculated.*

As indicated in the figure, the results are for three Prandtl-Reuss type, elastic-plastic materials with the same ratio of yield stress in tension, σ_0, to Young's modulus, E. The materials, however, have differing hardening properties as characterized by N. The term N is the hardening exponent in a power law hardening relationship of the form

$$(\bar{\tau}/\sigma_0)^{1/N} = \bar{\tau}/\sigma_0 + 3G\bar{\epsilon}^P/\sigma_0$$

where

$$\bar{\tau}^2 = \frac{3}{2}\tau_{ij}'\tau_{ij}',$$

$\boldsymbol{\tau}'$ = Kirchhoff stress deviator,

$\boldsymbol{\tau} = |F|\boldsymbol{\sigma}$,

G = elastic shear modulus, and

$$\bar{\epsilon}^P = \int \left(\frac{2}{3}D_{ij}^P D_{ij}^P\right)^{1/2} dt,$$ where $\mathbf{D}^P$ is the plastic part of $\mathbf{D}$.

The nonhardening material has $N = 0$.

As can be seen in Fig. 1, the J-integral is only significantly path dependent when the contour is less than about five deformed notch widths

from the notch tip. Indeed, further from the notch tip than about ten current notch widths, J is path independent. The value of J in this area of path independence is J_∞, and the current notch width has been shown as a function of J_∞ for each material in Fig. 2. A very approximate fit to the lines in Fig. 2 is

$$J_\infty = (b - b_0) f_N \sigma_0 \tag{2}$$

where b is greater than about $2b_0$. The term f_N is a nonzero constant chosen to match the gradient of the line for each hardening material ($f_0 = 1.8$, $f_{0.1} = 2.4$ and $f_{0.2} = 3.7$).

On the other hand, the values of J in Fig. 1 for $R/b < 0.5$ are very dependent on path. It would appear that a very rough fit to the results for $J/J_\infty < 0.5$ is

$$J_i/J_\infty = \ln(b/b_0)/[(b/b_0 - 1)f_0] \tag{3}$$

where J_i is just a value of J very close to, but not on, the crack-tip surface, and $R = 0.66b_0$ for all the points with $J/J_\infty < 0.5$. Presently, there will be an attempt to give some physical basis for this result. First, attention will be paid to the implications of the result for very large values of b/b_0.

An important feature of the finite-element solution is that for values of b/b_0 larger than about three, a self-similar sequence of solutions develops. This is reflected in the fact that Fig. 3, a plot of the near-tip stress and deformation states for one particular material, is based on results

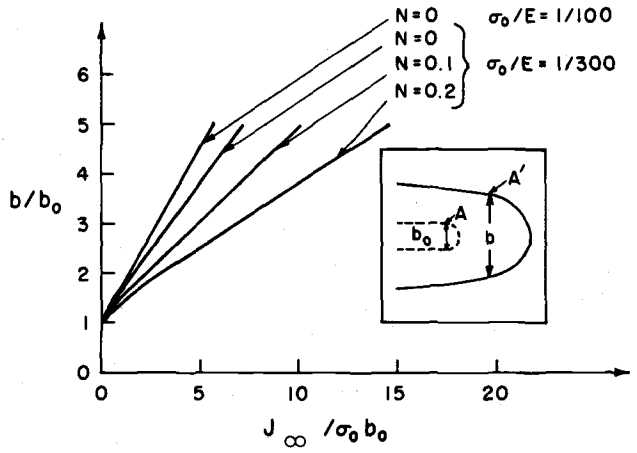

FIG. 2—*Plot of notch width,* b, *versus the value of the J-integral,* J_∞, *computed on a remote contour around the notch tip.*

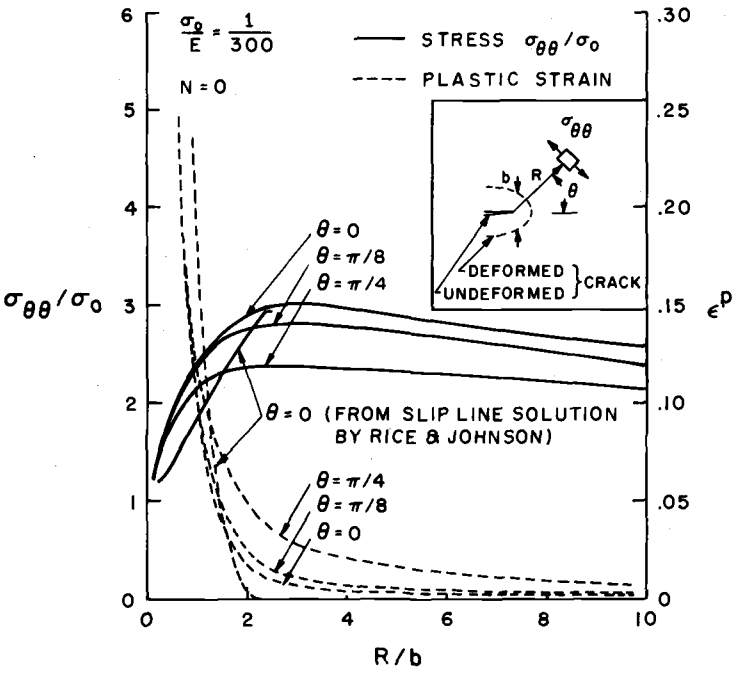

FIG. 3—*Plot of stress $\sigma_{\theta\theta}/\sigma_0$ and plastic strain around the blunted notch for $\sigma_0/E = 1/300$ and N = 0. Note σ_0 is the yield stress in tension and R and θ are defined for the position of the material in the undeformed configuration.*

from several steps of deformation. The crack tip similarly develops into a steady state shape, and the influence of the original shape becomes negligible. As a result, when b/b_0 is sufficiently large, the solution serves as an approximation to the smooth blunting of a sharp crack in an elastic-plastic material in contained yielding conditions. In particular, if the solution for the opening of the notch were processed to arbitrarily large amounts of opening, the approximation could, presumably, be driven arbitrarily close to the solution for the sharp crack. If opening the notch to five times its original width is sufficient to indicate the trend as $b/b_0 \rightarrow \infty$, then the limit of Eq 3 as $b/b_0 \rightarrow \infty$ would seem to give the solution for the tip value of J for a sharp crack. It is simple to see from Eq 3 that

$$\lim_{b/b_0 \rightarrow \infty} J_i/J_\infty = 0$$

The characteristic length in the self-similar solution is b. However, according to Eq 2, $b = b_0 + (J_\infty/\sigma_0)f_n$. It seems reasonable to use this relationship with $b_0 = 0$ as the relationship between J_∞ and b for an origi-

nally sharp crack [7]. Thus, the length J_∞/σ_0 is a length parameter which characterizes the stress and deformation field around a blunted crack tip, even though the tip value of the J-integral seems to be zero.

Path Dependence of the J-Integral in a Rigid-Plastic Model

As a confirmation of the path dependence of J, the rigid-plastic, nonhardening, deeply cracked, double-edge notched, thick specimen was studied using slip-line theory. There is no unique flow field for this specimen. The field of slip lines and the state of stress near the crack tip is unique, however, and shown in Fig. 4. The term τ_0 is the flow stress in shear and $\tau_0 = \sigma_0/\sqrt{3}$. The field of displacements chosen from among the nonunique flow fields for this specimen is shown in Fig. 5. This field was chosen because there are no discontinuities of velocity at the slip line separating A and C and C and B. This means, that with respect to this and to the near-tip stress field, the left-hand notch experiences the same conditions as the notch in small-scale yielding analyzed through the slip-line method by Rice [1]. The velocities near the tip in the fans above and below the left-hand notch in the fully plastic double-edge notched panel are not the same as the velocities near the tip deduced by Rice for the crack in small-scale yielding. However, the velocities are not very different, and the results of a contour integral calculation of J very close to the tip in the double-edge notched panel will be of some relevance to the result for small-scale yielding. Notable features of the strain field chosen for the double-edge notched panel are that the regions A, B, D, and E are nondeforming, and there is a tangential velocity discontinuity at the slip line between B and E.

At the scale of Figs. 4 and 5, the details of the notch tip are obscured. This would be so as long as $b/a \ll 1$, where a is the ligament between the notch tips. Attention is henceforth restricted to values of Δ/a small enough for this to remain true. It then follows that there are negligible differences

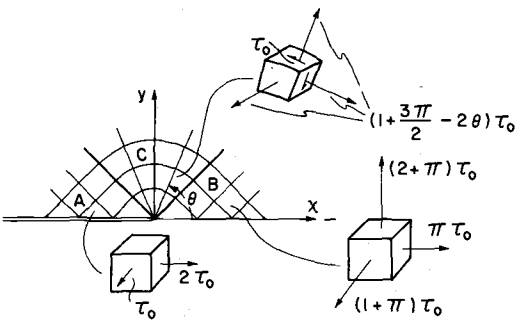

FIG. 4—*Near tip stress state and slip lines for rigid-plastic model.*

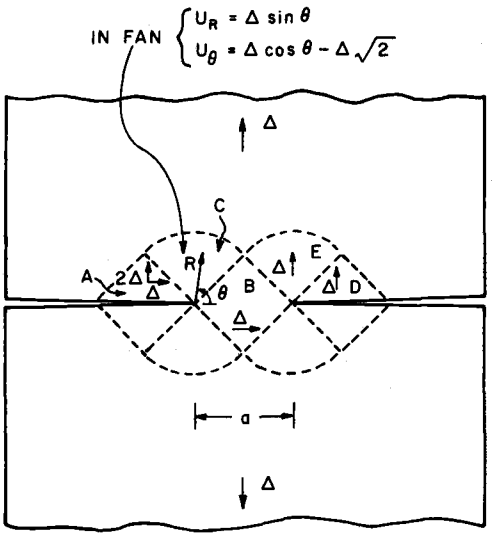

FIG. 5—*Displacements for rigid-plastic model.*

between the deformed and undeformed positions of material points near the top of fan C. Thus, the conventional small-strain definition of the J-integral may be used on a circular contour near the top of the fan. Following Rice's [*11*] calculation of J in this flow field, the value of J around the left-hand notch tip on a contour remote from the tip is

$$J_\infty = 2(2 + \pi)\tau_0\Delta \tag{4}$$

In order to compute J on a contour on the notch tip, we need the details of the slip-line field around it as given by Rice and Johnson [*12*]. The details are shown in Fig. 6. On the scale of Fig. 6, fan C is noncentered, and area B is not adjacent to the notch tip. Adjacent to the notch tip is a region of spiral slip lines in which intense strains occur. The normal velocity on the slip lines from S to the notch tip is just the radial velocity in the fan C, and so is $\dot{\Delta}\sin\theta$. Using this boundary condition, Rice and Johnson solved the slip-line equations numerically for the displacements on the notch tip in terms of Δ and the original notch shape. In particular, the equivalent plastic strains $\bar{\epsilon}^p$ on the notch tip can be computed.

The definition of the J-integral on a contour on a semicircular notch tip of diameter b_0 is

$$J_{\text{tip}} = \frac{b_0}{2}\int_{-\pi/2}^{\pi/2} W(\theta)\cos\theta\, d\theta \tag{5}$$

where θ is the polar angle from the X-axis, based on an origin at the center of the undeformed semicircular notch tip. For a rigid perfectly plastic von Mises type material, $W = \sqrt{3}\,\tau_0\bar{\varepsilon}^p$. Using the equivalent plastic strains on an originally semicircular notch tip from the Rice and Johnson solution, a value J_{tip} for the J-integral on the notch tip may be computed. For example, when $b = 5b_0$, $J_{tip} = 3.771\tau_0 b_0$. Noting that $\Delta = (b - b_0)/4$, J_∞ is seen to have a value of $10.283\tau_0 b_0$ when $b = 5b_0$ and $J_{tip}/J_\infty = 0.367$. As b/b_0 is increased, the value J_{tip}/J_∞ drops. In addition, the ratios are similar to the results for J_i/J_∞ obtained by finite elements at the same b/b_0, although allowance has to be made for the fact that the contour for J_i did not lie on the tip. As before, $J_{tip}/J_\infty \to 0$ as $b/b_0 \to \infty$, but this condition is subject to $a/b \to \infty$.

A feature of the solution is that the shape of the notch tip can be obtained from the shape of a sharp crack blunted by the same amount, Δ, by adding the original notch shape to the sharp crack blunted shape. This procedure is equivalent to the superposition in Henky nets discussed by Hill [*13*]. As a result, the solution for the blunt notch approaches the solution for the sharp crack arbitrarily closely as b/b_0 is made arbitrarily large. The solution for the originally sharp crack is a sequence of self-similar states in which all lengths scale according to b [*12*]. For example, the point S lies $1.9b$ from the crack-tip surface. Since $b = 4\Delta$ in the case of an originally sharp crack, it follows that in the self-similar solution all lengths scale by J_∞/τ_0 or, equivalently, J_∞/σ_0. As before, the value of J on a remote contour characterizes the near-tip field, while J_{tip} seems to be zero.

Of course, these comments concerning J as a characterizing parameter in fully plastic rigid-plastic materials must be treated with care. In the right-hand notch in Fig. 5, the contributions to the J-integral arise entirely from the discontinuities in displacement between B and E. The value of the J-integral on a remote contour is, as before, $2(2 + \pi)\tau_0\Delta$. However, the flow field around this notch tip is very different from that around the left-hand notch tip, so J_∞ only characterizes the left-hand notch from one

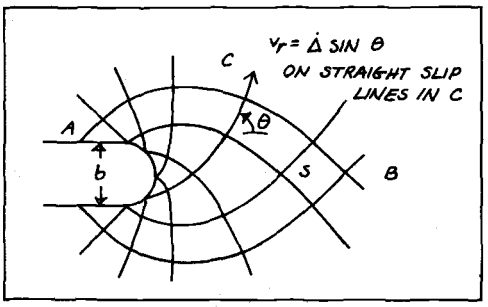

FIG. 6—*Slip-line field around a blunt notch with velocities in* C *corresponding to the left-hand notch in Fig. 5.*

state of deformation to another in the given flow field. It does not necessarily characterize one notch as compared to another. For example, a single-edge notch in a fully plastic specimen would have an even different stress state at the notch tip compared with the double-edge notched specimen [*9*]. This difficulty is not present in the small-scale yielding of elastic-plastic materials. Since the rigid-plastic model is the limiting behavior of an elastic-plastic material, the question of the extent to which J_∞ uniquely characterizes the deformation and stress around any notch as small-scale yielding conditions are exceeded is important to *J*-fracture toughness testing.

Crack and Notch-Tip Blunting

It would seem that when a proper account is taken of the blunting of crack or notch tips, a path dependence of the J-integral can be detected. This is illustrated quite readily by the rigid-plastic model so far discussed. If the crack or notch tip is modelled by a point centering fans carrying singular shear strains above and below the tip, then the J-integral is path independent all the way into the crack or notch tip. This would apply to the rigid-plastic model with the flow field given in Fig. 5, and this type of field is discussed in a more general way by Rice [*1*]. However, when the analysis takes account of blunting, as in the work of Rice and Johnson [*12*] and illustrated in Fig. 6, the path dependence of *J* is detected. The path dependence of *J* would seem to be associated with the area near the blunted crack tip in which large strains occur. This inner field of large deformations is surrounded by the outer field, as deduced using the crack tip as a point of singular strain. The J-integral is path independent in the outer field as long as the contour on which it is computed is sufficiently faraway from the crack tip. Note that so far no analysis has been carried out in the region between remote contours and crack-tip contours in the rigid-plastic model.

The same features of inner and outer field are present in the finite-element results concerning blunting of a notch tip with contained yielding [*7*]. Sufficiently faraway from the notch tip, the stresses and deformations become similar to those deduced by Rice and Tracey [*4*] and Tracey [*5*] for the same problem. They modelled the crack tip as a singular point for strain using special crack-tip finite elements. Parks [*6*] has noted that the J-integral was path independent in the solutions of Refs *4* and *5* except in the crack-tip elements. However, this path dependence of *J* in the crack-tip element persisted when a deformation plastic material was analyzed, suggesting that the path dependence was a defect in the crack-tip singular element. Path dependence of *J* arises in the region of intense deformations near the notch tip in the solution of notch blunting by finite elements, and *J* becomes path independent away from the notch tip in the

region of the solution where the Rice and Tracey results are approached.

These results are suggestive of a situation in which an outer field in which J is path independent with value J_∞ controls the deformation on an inner field in which J is path dependent. The outer field is basically the solution to the crack problem when large deformation effects involved in the blunting are ignored. For this reason, the approaches to crack problems—such as those of Rice [*1*], for nonhardening deformation plastic materials, Rice and Rosengren [*2*] and Hutchinson [*3*], for deformation plastic, power law hardening materials, Rice and Tracey [*4*], for nonhardening elastic-plastic materials, and Tracey [*5*], for power law hardening elastic-plastic materials—have been successful in characterizing, for example, the crack-tip opening displacement in terms of a value of the J-integral on a remote contour, although they ignore the effect of blunting.

Deformation Near Notch Tips in Incremental and Deformation Theory Materials

We have noted that in the incremental theory of elastic-plastic materials, a path dependence of the J-integral can arise at the notch tip. However, no such path dependence of J can arise in a deformation theory, since these materials are actually nonlinear elastic. This implies some difference between the crack-tip deformations of these two materials.

If the stretch ratio tangential to the notch-tip surface of material lying on the notch-tip surface is λ, then W is approximately $2\sigma_0(\ln\lambda)/\sqrt{3}$ after strains large compared to yield and dilational strain have accumulated on the notch tip in a nonhardening material. This applies to both the incremental and deformation theories of plasticity. It follows from Eq 5 that

$$J_{\text{tip}} = \frac{b_0\sigma_0}{\sqrt{3}} \int_{-\pi/2}^{\pi/2} [\ln\lambda(\theta)] \cos\theta \, d\theta \tag{6}$$

on a contour lying on the tip of an originally semicircular notch of diameter b_0.

Recalling from Eqs 2 and 3 that in an incremental theory the value of the J-integral on a contour close to the crack tip in a nonhardening material seems to be approximated well by

$$J_i = b_0\sigma_0 \ln(b/b_0) \tag{7}$$

when b/b_0 is sufficiently large, we note that if Eq 7 applies approximately to the contour on the notch tip, then

$$\int_{-\pi/2}^{\pi/2} [\ln\lambda(\theta)]\cos\theta \, d\theta \approx \sqrt{3} \ln(b/b_0)$$

One way in which this relationship could arise is if $\lambda(\theta)$ were equal to b/b_0 everywhere on the notch tip; the approximation would then involve the difference between 2 and $\sqrt{3}$. Indeed, the true strains on the notch tip in the finite-element solution seem to agree very roughly with this, being about $\ln(b/b_0)$ at $\theta = 0$ and falling to $1/2 \ln(b/b_0)$ at $\theta = \pi/2$.

Turning now to the deformation theory material, we note that the J-integral must be path independent, and, according to the finite-element results in Eq 2, the value would seem to be $1.8(b - b_0)\sigma_0$ for the non-hardening material when b/b_0 is sufficiently large. Of course, this value for J was computed on a contour remote from the notch tip in an incremental theory material. However, the experience of Parks [*6*] in comparing the deformation theory with the incremental theory in the outer field is that the deformations and stresses are the same. Hence, we will assume that the value of J in the outer field of the analysis including the effects of blunting will be given by Eq 2. This value is equated with the expression for J on a contour on the notch tip, and so

$$\int_{-\pi/2}^{\pi/2} [\ln\lambda(\theta)]\cos\theta \, d\theta \approx 3.12 \, (b/b_0 - 1)$$

Thus, the notch-tip strains in the deformation theory material must differ from those of the incremental theory material. In addition, the strains on the notch tip in both materials must be compatible with the opening ratio b/b_0.

This result for deformation plastic materials is important because of the relationship between deformation theory plasticity and models for polycrystalline multislip during almost radial straining. For example, the model of Batdorf and Budiansky [*14*] leads to an exact equivalence with deformation theory under moderately nonradial loading. In this model, the strain rate of the polycrystal is computed as the average, over all orientations, of the strain rate in a single crystal subject to the macroscopic stress state. On the other hand, the self-consistent model of Hutchinson [*15*] leads to an approximate equivalence with deformation theory. In this model, individual crystals are modelled as spheres lying within homogenous material which has the net constitutive properties of the polycrystal. The stress state in the polycrystal is computed as the average stress rate in the crystal over all orientations of crystal relative to the homogenous material. Applying this self-consistent model to uniaxial tensile stressing of an elastically isotropic, nonhardening polycrystalline face centered cubic material, Hutchinson found that the moduli for subsequent increments of shear strain fall as strain is accumulated. In an incremental macroscopic theory for plasticity, the moduli for increments of shear strain, due to a state of uniaxial stress, are constant. This is because a shear-strain rate is tangential to the yield surface representing a state of

uniaxial stress. In the polycrystalline model, Hutchinson found that the drop in the moduli for subsequent shear strains is approximated well by the appropriate moduli in a deformation theory of plasticity.

These models imply a deformation theory constitutive law only when the loading is at the most moderately nonradial. But near the blunting crack tip there can be very nonradial loading. However, it seems reasonable to assume that the polycrystalline models for slip will lead to a macroscopic flow theory somewhat intermediate to von Mises flow theory and deformation plasticity. In that case, the near-tip deformations would be significantly different from those already worked out for an incremental theory of plasticity by McMeeking [7] and Rice and Johnson [12].

Acknowledgments

The author is indebted to Professor J. R. Rice for helpful discussions of this topic. The work was carried out at Brown University, and the author received support from the U.S. Energy Research and Development Administration under Contract E(11-1)3084 and from the National Science Foundation Materials Research Laboratory.

References

[1] Rice, J. R., *Journal of Applied Mechanics*, Vol. 35, 1968, pp. 379–386.
[2] Rice, J. R. and Rosengren, G. F., *Journal of the Mechanics and Physics of Solids*, Vol. 16, 1968, pp. 1–12.
[3] Hutchinson, J. W., *Journal of the Mechanics and Physics of Solids*, Vol. 16, 1968, pp. 13–31.
[4] Rice, J. R. and Tracey, D. M. in *Numerical and Computer Methods in Structural Mechanics*, S. J. Fenves et al, Eds., Academic Press, New York, 1973, pp. 585–623.
[5] Tracey, D. M., *Transactions*, Series H, American Society for Mechanical Engineers, Vol. 98, 1976, p. 146.
[6] Parks, D. M., "Some Problems in Elastic-Plastic Finite Element Analysis of Cracks," Ph.D. dissertation, Brown University, Providence, R. I., 1975.
[7] McMeeking, R. M., "Finite Deformation Analysis of Crack Tip Opening in Elastic-Plastic Materials and Implications for Fracture Initiation," Technical Report E(11-1) 3084/44, Division of Engineering, Brown University, Providence, R. I., May 1976; *Journal of the Mechanics and Physics of Solids*, to be published.
[8] Begley, J. A. and Landes, J. D. in *Fracture Toughness, ASTM STP 514*, American Society for Testing and Materials, 1972, p. 1.
[9] McClintock, F. A. and Irwin, G. R. in *Fracture Toughness Testing and its Applications, ASTM STP 381*, American Society for Testing and Materials, 1965, pp. 84–113.
[10] Eshelby, J. D. in *Inelastic Behavior of Solids*, M. F. Kanninen et al, Eds., McGraw-Hill, New York, 1970, p. 77.
[11] Rice, J. R. in *Mechanics and Mechanisms of Crack Growth*, Proceedings of April 1973 Conference, Cambridge, England, M. J. May, Ed., British Steel Corporation, Physical Metallurgy Center Report, 1975, p. 14.
[12] Rice, J. R. and Johnson, M. A. in *Inelastic Behavior of Solids*, M. F. Kanninen et al, Eds., McGraw-Hill, New York, 1970, pp. 641–670.
[13] Hill, R., *Journal of the Mechanics and Physics of Solids*, Vol. 15, 1967, p. 255.
[14] Batdorf, S. B. and Budiansky, B., *Journal of Applied Mechanics*, Vol. 21, 1954, p. 323.
[15] Hutchinson, J. W., *Proceedings*, Royal Society, Series A, Vol. 319, 1970, pp. 247–272.

S. N. Atluri,[1] *Michihiko Nakagaki,*[1] *and Wen-Hwa Chen*[1]

Fracture Analysis Under Large-Scale Plastic Yielding: A Finite Deformation, Embedded Singularity, Elastoplastic Incremental Finite-Element Solution

REFERENCE: Atluri, S. N., Nakagaki, Michihiko, and Chen, Wen-Hwa, **"Fracture Analysis Under Large-Scale Plastic Yielding: A Finite Deformation, Embedded Singularity, Elastoplastic Incremental Finite-Element Solution,"** *Flaw Growth and Fracture, ASTM STP 631,* American Society for Testing and Materials, 1977, pp. 42–61.

ABSTRACT: The potential of the well-known J-integral as a fracture initiation criterion has been demonstrated in recent experiments by Begley and Landes and others. This paper deals with a numerical procedure for the estimation of J-integral and for arbitrary strain-hardening materials, in general situations of ductile fracture under large-scale yielding conditions. A finite-deformation analysis is employed to study the effects of crack-tip blunting. An incremental "tangent modulus" finite-element method has been used to account for both the geometric nonlinearity and the elastoplastic strain-hardening material behavior. A kinematic hardening law was used to describe the incremental plastic flow. Strain and stress singularities, corresponding to the material model, have been embedded in finite elements near the crack tip. Displacement and traction continuities between these near-tip elements and the surrounding elements have been enforced through the hybrid-displacement, finite-element model. This numerical procedure has been used to solve the case of a three-point bend specimen of Ni-Cr-Mo-V steel for which experimental results are also available. Excellent correlation between the present results and available experimental results has been established for the J versus δ (load-point displacement) relationship. To characterize the effect of crack-tip blunting, the present example also has been solved using a small-deformation theory, and solutions are compared with those from the present finite-deformation analysis. The implication of the results in predicting crack-growth initiation and its stability in ductile materials is discussed. By using the modified definition of J-integral as valid for finite deformation, it has been found that approximate path independence of J is maintained, accurately, even for a contour closest to the crack tip.

KEY WORDS: crack propagation, fractures (materials), finite-deformation effects, finite-element method, strain hardening

[1]Professor, postdoctoral fellow, and graduate student, respectively, School of Engineering Science and Mechanics, Georgia Institute of Technology, Atlanta, Ga. 30332.

In recent experiments, Begley and Landes [*1*][2] have demonstrated the potential of the J-integral as a fracture-initiation criterion in the large-scale plastic yielding range. In experimentally determining critical J in elastic-plastic problems, Begley and Landes utilized the interpretation of J as the rate of change with respect to the crack length of the area under the load versus the load-point displacement curves of standard fracture test specimens such as the three-point bend specimen and the compact tension specimen. Thus, the original experimental protocol [*1*] calls for testing virgin specimens with different crack sizes. For fracture test specimens such as those cited previously where the only geometric dimension of interest is the uncracked ligament length, Rice et al [*2*] have shown that the J-integral can be evaluated from single specimen test data for the load displacement relation. Merkle and Corten [*3*] have also presented improved empirical relations for estimating J from single tests of compact tension specimens. In the large-scale yielding analysis of single fracture test specimens, simple approximate procedures for estimation of J have been used by Bucci et al [*4*] who "extrapolate" from small-scale yielding range to fully plastic range using Irwin's "plasticity corrections." The material description used [*4*] is elastic-perfect plastic.

The objective of this paper is to present an accurate numerical procedure to estimate J directly in arbitrary plane problems of ductile fracture with arbitrary boundaries, under arbitrary loading conditions, and when the material properties can be characterized as elastic plastic with arbitrary strain hardening.

An incremental elastic-plastic, finite-element procedure for estimation of J for arbitrary strain-hardening material, but based on a small deformation theory, has been presented earlier by Atluri and Nakagaki [*5*]. The procedure [*5*] was based on an "initial stress" type incremental elastic-plastic, finite-element procedure.

In this paper, a consistently formulated finite-deformation analysis procedure is considered to account for large geometry changes near the crack tip. To account for this geometrical nonlinearity as well as the arbitrary strain-hardening, elastic-plastic behavior, an incremental "tangent modulus" method of analysis is considered. The incremental plastic flow has been described by a Prager-Ziegler type kinematic hardening law.

This procedure also employs circular-sector shaped "embedded-singularity" elements near the crack tip. The dominant singular behavior, for stresses/strains, corresponding to the now well-known Hutchinson-Rice-Rosengren solution is embedded in each of these near-tip singular elements [*5*]. Continuity of displacements and tractions between these near-tip elements with singular field assumptions and the neighboring elements with regular field assumptions was enforced through a hybrid

[2]The italic numbers in brackets refer to the list of references appended to this paper.

displacement finite-element model as was done by the authors in the linear-elastic problem [*6, 7*].

The developed finite-deformation analysis procedure is used to solve the problem of three-point bend bars of Ni-Cr-Mo-V steel for which experimental results have been reported by Begley and Landes [*1*]. This two-dimensional, finite-element model does not involve the thickness of the bend bar specimen except for the "either-or" choice of plane stress or plane strain. Based on the arguments of Bucci et al [*4*] for the dimensions of this specimen, plane-stress conditions were invoked. Excellent correlation of the presently computed J versus δ relation with the reported experimental results is noted.

Finally, to delineate the effect of finite geometry changes near the crack tip, this problem also is solved by using the small-deformation analysis procedure reported earlier [*5*] and compared with the present finite-deformation analysis results. Detailed results for the bend bar specimen, using both the finite-deformation and small-deformation analysis are presented.

Brief Description of Formulation

Finite Deformation, Elastoplastic, Embedded-Singularity, Incremental Finite Element Method Based on Hybrid-Displacement Model.

To start with, we used circular-sector shaped singular elements near the tip (Fig. 1) with assumptions for displacement, as described in detail in Ref *5*, to correspond to stress/strain singularities (for strain-hardening materials) of the well-known Hutchinson-Rice-Rosengren type. These singular elements are surrounded by regular eight-node isoparametric quadrilateral elements (Fig. 2). Compatibility of displacements and continuity of tractions between these regular and singular elements is enforced through a Lagrangean multiplier technique as shown next.

The incremental analysis of the present finite-deformation problem is based on a continuously updated Lagrangean (coordinate-system) formu-

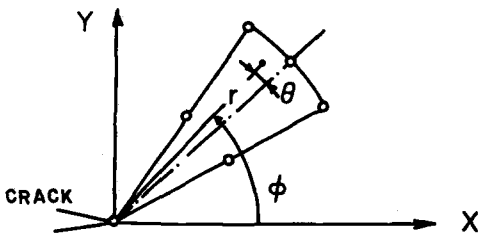

FIG. 1—*Nomenclature for a singular element.*

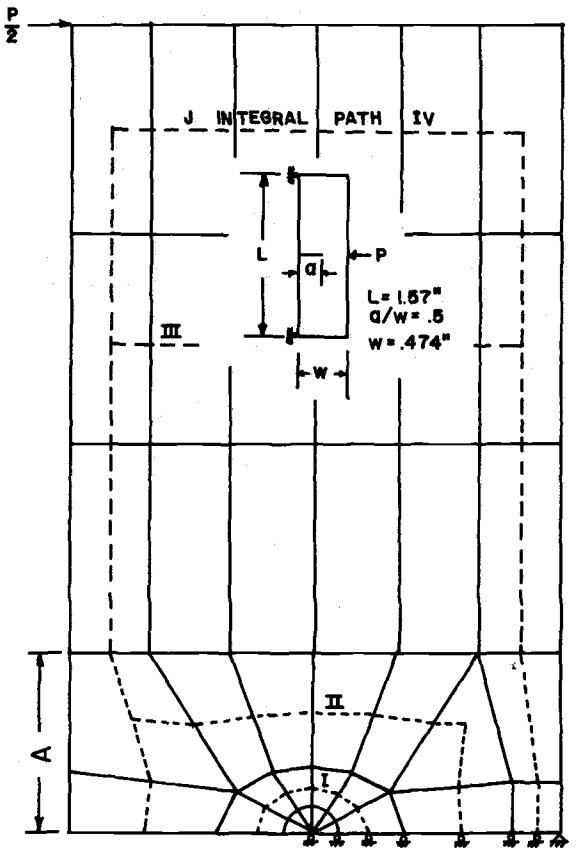

FIG. 2—*Finite-element model of three-point bend bar (shown in insert) and J-integral paths.*

lation. In the following, for simplicity, we consider the formulation in the context of a general three-dimensional problem and present only the essential mathematical details due to space limitations. We consider a fixed cartesian coordinate system, and consider C_N to be the state (namely, deformation, strain, and stress) of the structure before the addition of the N^{th} load increment. Let x_i be the material coordinates of a point in the initial, undeformed and unstressed configuration, C_1. Let u_i^N be the displacement, measured in the fixed cartesian system, of a point in C_1 to the deformed state C_N. The new coordinates of the material point in C_N then become $X_i^N = x_i + u_i^N$. Let the (symmetric) Eulerean (true) stress tensor in C_N be τ_{ij}^N, measured per unit area in C_N and in the metric of the fixed cartesian system. Let the body forces per unit volume in C_N be F_i^N and prescribed surface tractions per unit area in C_N be T_i^{-N}.

Let additional body forces ΔF_i (per unit C_N volume) and additional surface tractions $\Delta \bar{T}_i$ (per unit C_N area) be applied during the movement of the structure from C_N to C_{N+1}. Let additional cartesian displacements of the material point in moving from C_N to C_{N+1} be Δu_i; thus, $X_i^{N+1} = X_i^N + \Delta u_i$ are the new coordinates of a material point in C_{N+1}. The incremental Green strain $\Delta^* g_{ij}$ from C_N to C_{N+1}, with reference to the metric in C_N, can be written as

$$\Delta^* g_{ij} = \frac{1}{2}\left[\frac{\partial \Delta u_i}{\Delta X_j^N} + \frac{\partial \Delta u_j}{\partial X_i^N}\right] + \frac{1}{2}\left[\frac{\partial \Delta u_K}{\partial X_i^N}\frac{\partial \Delta u_K}{\Delta X_j^N}\right] \equiv \Delta e^*_{ij} + \Delta \eta^*_{ij} \tag{1}$$

During the motion from C_N to C_{N+1}, the state C_N is treated as one with initial stresses. The new stresses in C_{N+1} due to the additional incremental loading, will be represented by the symmetric Kirchhoff-Trefftz stress tensor $S_{ij(N)}^{N+1}$, which is measured per unit area in C_N but in the deformed-metric in C_{N+1}. Thus

$$S_{ij(N)}^{N+1} = \tau_{ij}^N + \Delta^* S_{ij} \tag{2}$$

Assuming the material has yielded, the relation between the incremental stress $(\Delta^* S_{ij})$[3] and the incremental strain $\Delta^* g_{ij}$ will be written as

$$\Delta^* S_{ij} = E_{ijkl}^{\prime}(\tau_{ij}^N)\,\Delta^* g_{kl} \tag{3}$$

where $E_{ijkl}^{\prime}$ is the current constitutive property, as modified by plasticity, and is a function of current true stress, τ_{ij}^N. Such a constitutive relation, based on the well-known Huber-Mises-Hencky yield criteria, Drucker's normality condition, and a Prager-Ziegler type kinematic hardening law has been derived for the present plane-stress conditions following the procedure described in Ref 5, and further details are omitted here.

Based on this, it can be shown that the variational principle governing the equilibrium of state C_{N+1} is $\delta \Delta \pi_{HD} = 0$ where

$$\Delta \pi_{HD}(\Delta u_i, \Delta v_i, T_{Li}) = \sum_{m=1}^{P}\left\{\int_{\Omega_m}\left[\left(\tau_{ij}^N + \frac{1}{2}\Delta^* S_{ij}\right)\Delta^* e_{ij} + \frac{1}{2}\tau_{ij}^N \Delta u_{k,i}\Delta u_{k,j}\right.\right.$$

[3]The stress increment $\Delta^* S_{ij}$ is referred to commonly as the Truesdell stress increment.

$$- (F_i^N + \Delta F_i)\Delta u_i \Big] da - \int_{\partial\Omega_m} T_{Li}(\Delta u_i - \Delta v_i)\, ds - \int_{S_{\sigma m}} (\bar{T}_i + \Delta \bar{T}_i)\, \Delta v_i\, ds \Big\} \tag{4}$$

where

Ω_m = domain of the m^{th} finite element,
$\partial\Omega_m$ = boundary of the m^{th} finite element,
$S_{\sigma m}$ = a portion of $\partial\Omega_m$ where tractions are prescribed,
τ_{ij}^N = true (Euler) stress in C_N, measured per unit area in C_N and in the fixed cartesian metric,
$F_i^N, \bar{T}_i$ = body force and surface traction, per unit volume and per unit area, respectively, in C_N,

$$\Delta e^*_{ij} = \frac{1}{2}\left[\frac{\partial \Delta u_i}{\partial X_j^N} + \frac{\partial \Delta u_j}{\partial X_i^N}\right]; \quad \Delta S^*_{ij} = E_{ijkl}^t(\tau_{ij}^N)\Delta e^*_{kl} \tag{5}$$

Δu_i = arbitrarily assumed displacements, in each element, that need not satisfy interelement compatibility *a priori* (in elements surrounding the crack tip, displacements corresponding to the Hutchinson-Rice-Rosengren singularities for hardening materials are included),
Δv_i = independently assumed displacements at the element boundary, $\partial\Omega_m$, which inherently satisfy interelement compatibility criteria,
T_{Li} = Lagrange multiplier to enforce the compatibility condition, $\Delta u_i = \Delta v_i$ at $\partial\Omega_m$, and
$\Delta F_i, \Delta \bar{T}_i$ = prescribed increments of body forces and surface tractions, respectively, measured unit volume and unit area, respectively in C_N.

The Euler equations corresponding to $\delta\Delta\pi\ (\delta\Delta u_i,\ \delta\Delta v_i,\ \delta T_{Li}) = 0$ lead to

$$\Delta^* S_{kj,j} + (\tau_{ij}^N \Delta u_{k,j}),_i + \Delta \bar{F}_k + \{\tau_{kj,j}^N + \bar{F}_k\} = 0 \tag{6}$$

$$(\tau_{kj}^N + \Delta^* S_{kj})\, n_j + \tau_{ij}^N \Delta u_{k,j}\, n_i = T_{Lk} \text{ at } \partial\Omega_m \tag{7}$$

$$\bar{T}_i + \Delta \bar{T}_i = T_{Li} \text{ at } S_{\sigma_m} \tag{8}$$

and

$$\Delta u_i = \Delta v_i \text{ at } \partial\Omega_m \tag{9}$$

In the previous equations, a comma followed by an index such as i, is meant to designate a partial differentiation with respect to the cartesian

coordinate, X_i^N. Equation 6 refers to the equilibrium of the total Kirchhoff-Trefftz stress $S_{ij(N)}{}^{N+1}$ in C_{N+1}. If state C_N was in true equilibrium, the last two bracketed terms in Eq 6 would be equal to zero. However, because of the inherent numerical errors in the incremental solution process, the state C_N may not be truly equilibrated. Thus, retaining the last two terms in Eq 6 leads to an "equilibrium-check" iteration process similar to the one described in detail by Hofmeister et al [9]. Equation 7 states that the tractions derived from the assumed incremental interior displacements match the independently assumed boundary tractions, T_{Li}. Finally, Eq 9 is the statement of interelement displacement compatibility that is enforced in the present method, by means of Lagrange multipliers, T_{Li}.

Because of the advantages of the previously described hybrid-displacement model, and the convenience of the conventional finite-element displacement model, a combination of both the methods is used in this formulation. Thus, one can visualize the domain of the cracked structure to be divided into two regions—(*a*) a small region near the crack tip where the singular, near field solution is predominant and (*b*) a region away from the crack tip where the effect of the singularity is not dominant. In these calculations, a hybrid-displacement model is used to derive the stiffness properties of the near-tip sector elements, and the conventional displacement model is used to derive the stiffness properties of the far-field, eight-node isoparametric elements.

Consider first the development of the properties of the near-tip, circular-sector shaped singular elements, wherein the three independent variables Δu_i, Δv_i, and T_{Li} are assumed as follows[4]

$$\Delta u_i = \boldsymbol{A}\,\boldsymbol{\beta},\ \Delta v_i = \boldsymbol{L}\,\Delta q;\ \boldsymbol{T}_{Li} = \boldsymbol{R}\,\boldsymbol{\alpha} \tag{10}$$

where $\boldsymbol{\beta}$ and $\boldsymbol{\alpha}$ are unknown independent parameters, and Δq are increments of nodal displacements during the generic load step, $C_N \rightarrow C_{N+1}$. The functions $\boldsymbol{A}$ and $\boldsymbol{R}$ are arbitrary. However, $\boldsymbol{L}$ are functions at the boundary of the circular-sector element such that they uniquely interpolate for Δv at the boundary in terms of the relevant $\Delta \mathbf{q}$ at the boundary and, in addition, ensure displacement compatibility with the surrounding eight-noded isoparametric quadrilateral elements (see Fig. 2).

For far-field regular elements, as mentioned earlier, the conventional compatible displacement finite-element model is used. The incremental energy functional corresponding to this model can be expressed as

$$\Delta\pi_{CD}(\Delta u_i) = \sum_{m=p+1}^{m} \left\{ \int_{\Omega_m} \left(\frac{1}{2} E_{ijkl}\,\Delta\epsilon_{kl}\Delta\epsilon_{ij} + \frac{1}{2}\,\tau_{ij}{}^{N}\Delta u_{k,i}\Delta u_{k,j} \right.\right.$$

[4]The usual bold face is used to denote a column vector, and bold face italic is used to denote a matrix.

$$- \Delta\bar{F}_i \Delta u_i) da - \int_{S_{\sigma_m}} \Delta\bar{T}_i \Delta u_i ds + \int_{\Omega_m} (\tau_{ij}{}^N\Delta u_{i,j} - \bar{F}_i{}^N\Delta u_i) da - \int_{S_{\sigma_m}} \bar{T}_i{}^N\Delta u_i ds \Big\} \tag{11}$$

The finite-element approximations for a far-field regular element are considered as

$$\Delta u = D\Delta q \tag{12}$$

from which the strains and deformation gradients are derived as

$$\Delta\epsilon = B\,\Delta q \quad \Delta u_{k,j} = W_k\,\beta \tag{13}$$

For purposes of convenience of notation we consider that, out of a total of M finite elements, $m = 1, p$ are the so-called singular elements and $m = p+1 \ldots M$ are the far-field regular elements.

The assumptions for the field variables as in Eq 10 for elements $m = 1, \ldots p$ are substituted into Eq 4 and the first variation of π_{HD} with respect to the parameters α and β is set to zero, to obtain, for elements $m = 1, p$, that

$$\alpha = P^{-T}(H + C_g)P^{-1}\,G\,\Delta q + P^{-T}C_e - P^{-T}F_4 \tag{14}$$

$$\beta = P^{-1}G\,\Delta q \tag{15}$$

where

$$\Delta\epsilon = W\beta, \quad \Delta u_{k,i} = W\beta \tag{16}$$

$$H = \int_{\Omega_m} W^T E\, W dA \tag{17}$$

$$P = \int_{\partial\Omega_m} R^T A ds \tag{18}$$

$$G = \int_{\partial\Omega_m} R^T L ds \tag{19}$$

$$\boldsymbol{C}_g = \int_{\Omega_m} (\boldsymbol{W}_1^T \boldsymbol{\tau}_{ij}^N \boldsymbol{W}_1 + \boldsymbol{W}_2^T \boldsymbol{\tau}_{ij}^N \boldsymbol{W}_2) dA \tag{20}$$

and

$$\boldsymbol{C}_e = \int_{\Omega_m} \boldsymbol{W}^T \boldsymbol{\tau}^N dA \tag{21}$$

Substituting for $\boldsymbol{\alpha}$ and $\boldsymbol{\beta}$ from Eqs 14 and 15 into Eq 4, one can express $\Delta\pi_{HD}$ in terms of $\Delta\boldsymbol{q}$ only, as

$$\Delta\pi_{HD} = \sum_{m=1}^{P} \frac{1}{2} \Delta\boldsymbol{q}^T (\boldsymbol{K} + \boldsymbol{K}_g) \Delta\boldsymbol{q} - \Delta\boldsymbol{q}^T \Delta\boldsymbol{Q} - \Delta\boldsymbol{q}^T \Delta\boldsymbol{Q}_C \tag{22}$$

where

$$\boldsymbol{K} = (\boldsymbol{P}^{-1}\boldsymbol{G})^T \boldsymbol{H} (\boldsymbol{P}^{-1}\boldsymbol{G}) \tag{23}$$

$$\boldsymbol{K}_g = (\boldsymbol{P}^{-1}\boldsymbol{G})^T \boldsymbol{C}_g (\boldsymbol{P}^{-1}\boldsymbol{G}) \tag{24}$$

$$\Delta\boldsymbol{Q} = \boldsymbol{F}_2 = \int_{S_{\sigma_m}} \boldsymbol{L}^T \Delta\bar{\boldsymbol{T}}\, ds \tag{25}$$

and

$$\Delta\boldsymbol{Q}_c = (\boldsymbol{P}^{-1}\boldsymbol{G})^T (\boldsymbol{F}_4 - \boldsymbol{C}_e) \tag{26}$$

Likewise, the assumptions for the field variable in Eq 12 for elements $m = p + 1 \ldots M$ are substituted into Eq 11 to obtain $\Delta\pi_{cD}$, for elements $m = p + 1 \ldots M$, as

$$\Delta\pi_{cD} = \sum_{p+1}^{M} \frac{1}{2} \Delta\boldsymbol{q}^T (\boldsymbol{K}^R + \boldsymbol{K}_g^R) \Delta\boldsymbol{q} - \Delta\boldsymbol{q}^T \boldsymbol{F}_2^R - \Delta\boldsymbol{q}^T (\boldsymbol{F}_4^R + \boldsymbol{C}_e^R) \tag{27}$$

where

$$\boldsymbol{K}^R = \int_{\Omega_m} \boldsymbol{B}^T \boldsymbol{E}' \boldsymbol{B}\, dA \tag{28}$$

$$\boldsymbol{K}_g^R = \int_{\Omega_m} (\boldsymbol{W}_1^T \boldsymbol{\tau}_{ij}^N \boldsymbol{W}_1 + \boldsymbol{W}_2^T \boldsymbol{\tau}_{ij}^N \boldsymbol{W}_2)\, dA \tag{29}$$

$$\boldsymbol{C}_e^R = \int_{\Omega_m} \boldsymbol{B}^T \boldsymbol{\tau}^N \, dA \tag{30}$$

$$\boldsymbol{F}_2^R = \int_{S_{\sigma_m}} \boldsymbol{D}^T \Delta \bar{\boldsymbol{T}} \, ds \tag{31}$$

and

$$\boldsymbol{F}_4^R = \int_{S_{\sigma_m}} \boldsymbol{D}^T \bar{\boldsymbol{T}}^N \, ds \tag{32}$$

Combining Eqs 22 and 27, the total energy functional for the system, $\Delta\pi$, can be written as

$$\Delta\pi = \sum_{m=1}^{P} \left[\frac{1}{2} \Delta\boldsymbol{q}^T (\boldsymbol{K} + \boldsymbol{K}_g) \Delta\boldsymbol{q} - \Delta\boldsymbol{q}^T \Delta\boldsymbol{Q} - \Delta\boldsymbol{q}^T \Delta\boldsymbol{Q}_c \right]$$

$$+ \sum_{m=p+1}^{M} \left[\frac{1}{2} \Delta\boldsymbol{q}^T (\boldsymbol{K}^R + \boldsymbol{K}_g^R) \Delta\boldsymbol{q} - \Delta\boldsymbol{q}^T \Delta\boldsymbol{Q}^R - \Delta\boldsymbol{q}^T \Delta\boldsymbol{Q}_C{}^R \right] \tag{33}$$

where

$$\Delta\boldsymbol{Q}^R = \boldsymbol{F}_2^R; \text{ and } \Delta\boldsymbol{Q}_c{}^R = \boldsymbol{F}_4^R + \boldsymbol{C}_e^R \tag{34}$$

By expressing the element incremental nodal displacements $\Delta\boldsymbol{q}$ in terms of independent generalized global displacements $\Delta\boldsymbol{q}^*$, and using the condition of stationarity of $\Delta\pi$ with respect to $\Delta\boldsymbol{q}^*$, one obtains the final expression

$$[K(q_N, P_N)]\{\Delta q^*\}_{N+1} = \{\Delta Q(q_N, P_N)\} + \{\Delta Q_{ec}\} \tag{35}$$

where

$\{q\}_N$ = generalized nodal displacements in state C_N (with loads P_N),

$[K(q_N, P_N)]$ = the tangent stiffness matrix at state C_N which includes the effects of initial stresses, displacements, and the influence of plastic yielding at state C_N,

$\{\Delta q^*\}_N^{N+1}$ = incremental displacements of the structure from C_N to C_{N+1},
$\{\Delta Q(q_N, P_N)\}$ = incremental loads, and
$\{\Delta Q_{ec}\}$ = residual nodal forces to check the equilibrium of state C_N.

The solution of Eq 35 with a Newton-Raphson type equilibrium correction iteration is similar essentially to that presented by Hofmeister et al [9], and further details are omitted for lack of space. Finally, we note that in order to carry out the incremental solution from C_{N+1} to C_{N+2}, the Kirchhoff-Trefftz stresses $S_{ij(N)}^{N+1}$ are converted to Euler (true) stresses in C_{N+1}, using the relation

$$\tau_{ij}^{N+1} = \frac{1}{\det\left[\dfrac{\partial X_i^{N+1}}{\partial X_j^N}\right]} \frac{\partial X_i^{N+1}}{\partial X_K^N} \frac{\partial X_j^{N+1}}{\partial X_l^N} S_{kl(N)}^{N+1} \tag{36}$$

Problem Definition

Detailed results are presented in the following for a three-point bend specimen made of Ni-Cr-Mo-V steel with dimensions of $W = 0.474$ in., $S = 1.5$ in., $w/a = 0.5$, thickness $B = 0.394$ and 0.788 in. (see Fig. 2) whose material properties are shown in Fig. 3. The Westinghouse experimental results for the J-δ curve for this specimen can be found in Refs *1* and *4*.

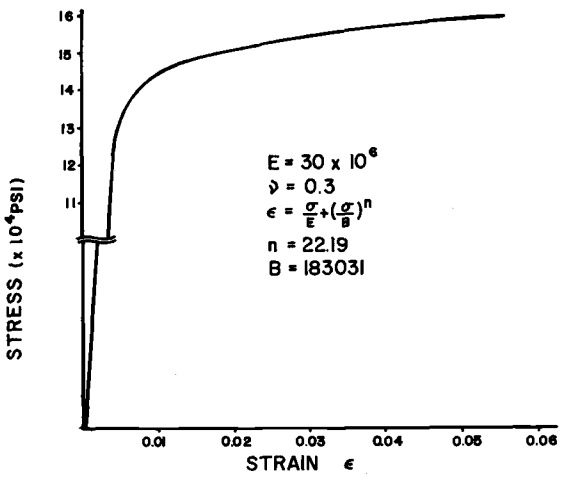

FIG. 3—*Uniaxial stress-strain curve for Ni-Cr-Mo-V steel.*

Results for J-Integral

At this point, we define the J-integral appropriate to the finite-deformation analysis of planar cracks [*10*] which is a counterpart of the J-integral applicable to infinitesimal deformations as introduced by Rice. For finite deformations, the modified J-integral can be written as

$$J = \int_\Gamma \left[wdy - t_K \frac{\partial u_K}{\partial x} ds \right] \tag{37}$$

where t_K are Piola-Lagrange tractions derived from the unsymmetric Piola-Lagrange stress tensor, t_{ij}. Thus, $t_K = t_{kl} n_l$, where n_l are the direction cosines of a unit normal to Γ in the initial configuration. The unsymmetric Piola-Lagrange stress tensor t_{Kl} is related to the symmetric Kirchhoff-Trefftz stress (S_{ij}) and symmetric Euler stress (τ_{ij}) through the relations

$$t_{mj}{}^N = \tau_{ij}{}^N J \frac{\partial x_m}{\partial X_i^N} = S_{mn(1)}{}^N \frac{\partial X_j^N}{\partial x_n} \tag{38}$$

where

$\tau_{ij}{}^N$ (Euler) and $S_{mn(1)}{}^N$ (Kirchhoff-Trefftz) = stresses in state C_N,
X_i^N = coordinates of a material point in C_N,
x_n = material coordinates in C_1, and
J = determinant of the Jacobian matrix, $[\partial X_j^N / \partial x_i]$.

In the present computations a 5 by 5 product Gaussian integration procedure is used numerically to evaluate the stiffness and other properties of each finite element, while, in the singular near-tip elements, appropriate transformations of variables were employed to eliminate the singularities in the integrands. The stress, strain, and deformation states were monitored at each of the 25 integration points in each element, and, depending on the stress state of each point, the current constitutive law was changed at each point. Thus, in the present computations, part of the element can yield while the remainder can stay elastic, thus, allowing for a more precise definition of yield zones in the cracked specimen at various load levels as shown in Fig. 4. By properly evaluating the stress-working density W and the Piola-Lagrange tractions at each step, the J-integral was evaluated at each load and load-point displacement level using Eq 37. The J-integral paths were made to traverse through the middle of each element, where a much smoother stress data can be expected rather than

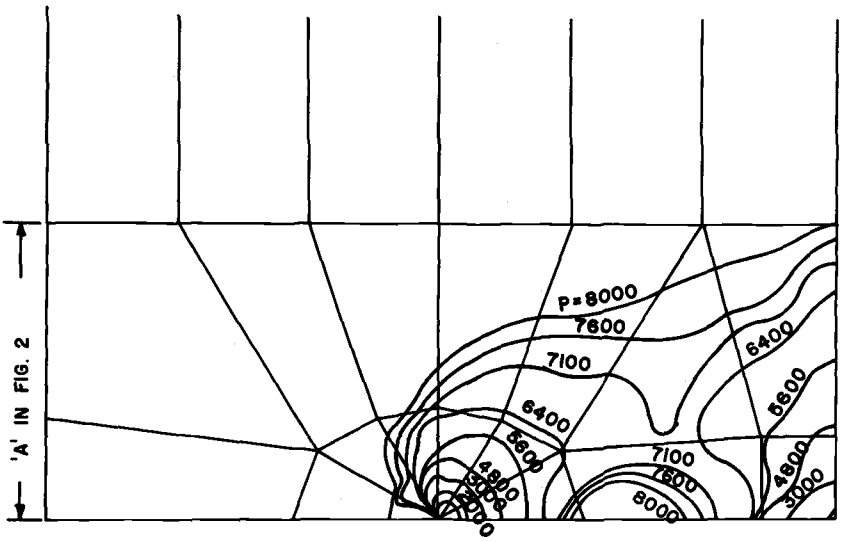

FIG. 4—*Yield zones at various load levels (finite deformation analysis).*

through the interelement boundaries where it is well known that discontinuities in stresses/tractions can arise in the usual finite element displacement method. Since there are five Gaussian integration points on the middle line of each isoparametric element, where the stress/strain data are stored as mentioned previously, these are used as Gaussian integration points for each segment (within each element) of the J-contour.

Figure 5 shows the computed P versus δ curve. Also shown for comparison purposes are (*a*) the curve based on linear-elastic theory, (*b*) the curve based on a small-deformation elastic-plastic analysis reported in Atluri and Nakagaki [*5*], and (*c*) the estimate given by Bucci, Paris, Landes, and Rice [*4*]. The J versus δ curve is shown in Fig. 6. The J-integral was calculated using Eq 37 on four different paths as shown in Fig. 2. In this finite-deformation analysis, the value of J was found to be almost path independent (+ 1.5 percent variation). Also shown in Fig. 6 for comparison purposes are (*a*) J-integral estimation based on a linear-elastic analysis, (*b*) directly computed J-integral using the small-deformation elastoplastic analysis of Ref *5*, (*c*) the J-integral estimates given by Bucci et al [*4*], and (*d*) the Westinghouse experimental data [*4*] for bend specimens of thickness 0.374 and 0.788 in., respectively, and (*e*) the estimation of J from the presently computed P versus δ curves using the empirical relation of Rice, Paris and Merkle [*2*]. Excellent correlation between the present finite deformation results and the referenced experimental results can be noticed. As reported in Ref *4*, for both the single and double thickness bend bars, Westinghouse experimentally determined

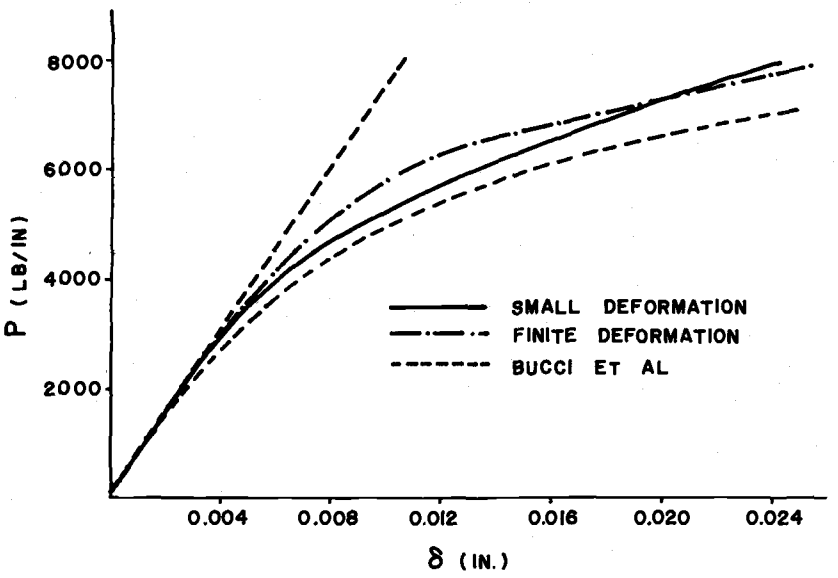

FIG. 5—*Load versus load-point displacement for three-point bend bar.*

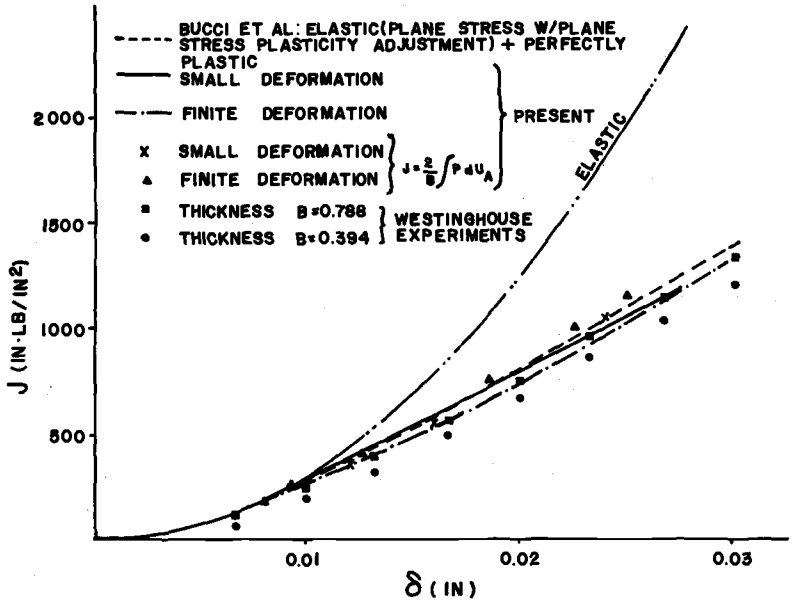

FIG. 6—*J-integral versus δ curve for three-point bend bar.*

displacement, δ, at fracture ranged between 0.022 and 0.024 in. for a/w ratios of magnitude comparable to 0.5. Under the present finite-deformation analysis, for the previously mentioned experimentally determined fracture displacements, the computed J is almost in between the Westinghouse experimental results as can be seen from Fig. 6. For the same critical δ range, both small-deformation analysis [5] results and those of Bucci et al [4] for J, are about 6 to 10 percent higher.

It is also interesting to note that in the small-deformation analysis even though path independence was noticed for paths 2, 3, and 4 (Fig. 2), this was not the case for path 1, which is immediate to the crack tip (the path 1 value J different by about 9 to 11 percent from those of paths 2, 3, and 4). However, more accurate path independence was noticed for all paths 1 through 4 (with only ± 1.5 percent variation) in the present finite-deformation analysis. In the present analysis, it is speculated that since finite-geometry changes are more important near the crack tip the use of Eq 37 for J under finite deformations leads to this more accurate path independence for the contour immediately adjacent to the crack tip.

Figure 4 shows the yield zones in the specimens under the finite deformation analysis, and Fig. 7 shows the yield zones under small-deformation analysis at various load levels. Figure 8 shows the crack-surface deformation profiles for various load levels under both the finite-deformation analysis and small-deformation analysis. Figures 9 and 10 show the distribution of the effective strain ahead of the crack tip in the uncracked ligament under finite-deformation and small-deformation

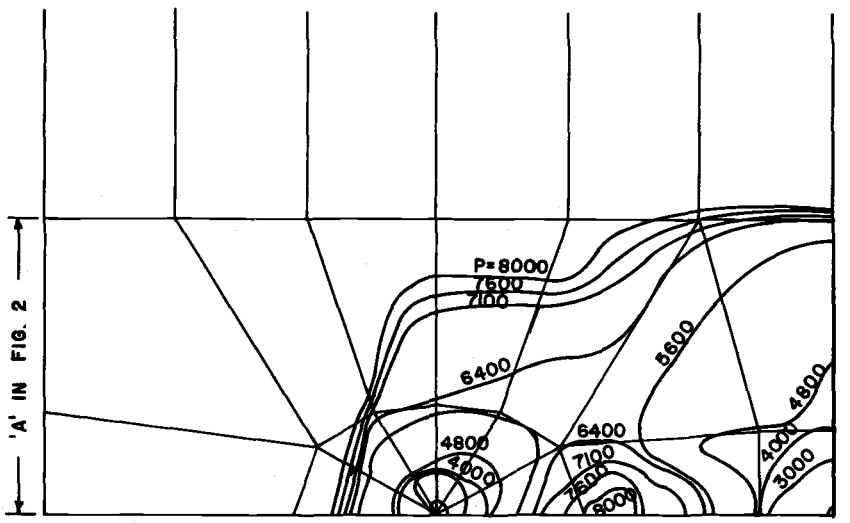

FIG. 7—*Yield zones at various load levels (small deformation analysis).*

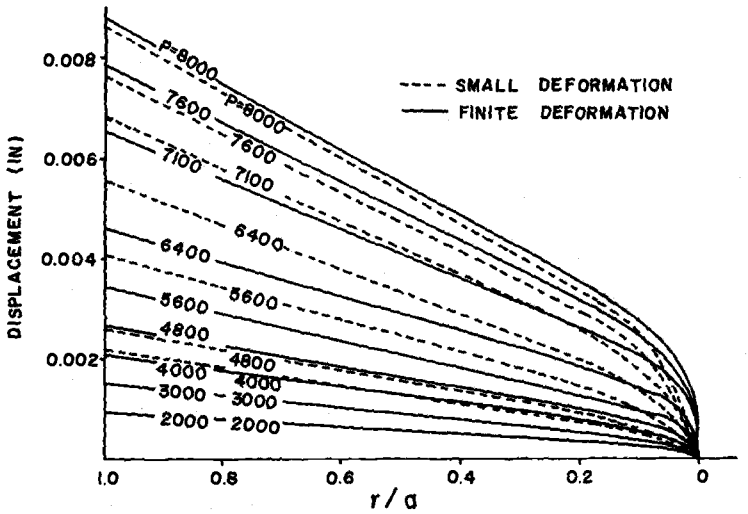

FIG. 8—*Crack-surface deformation profiles at various load levels.*

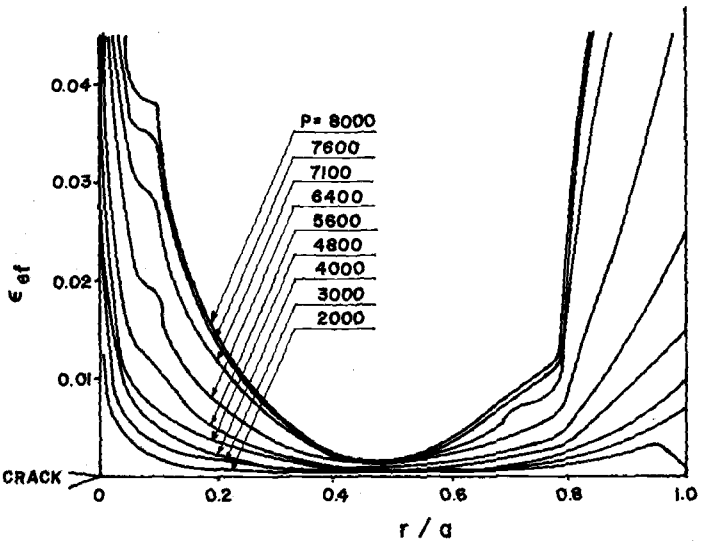

FIG. 9—*Effective strain distribution in the uncracked ligament (finite deformation analysis).*

analysis, respectively. Likewise, Figs. 11 and 12 show the distribution of effective stress in the uncracked ligament for the finite-deformation and small-deformation analysis, respectively. Extended discussions of Figs. 4 and 7 through 12 are omitted for want of space. However, the primary observation can be made that even though the effect of finite geometry

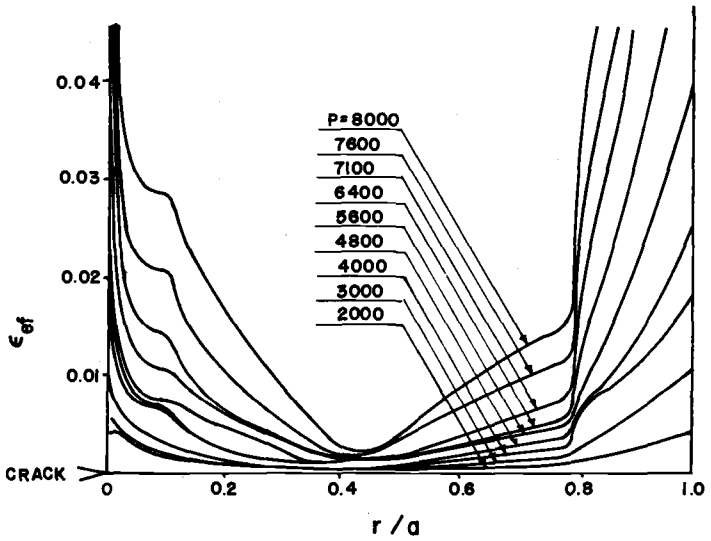

FIG. 10—*Effective strain distribution in the uncracked ligament (small deformation analysis).*

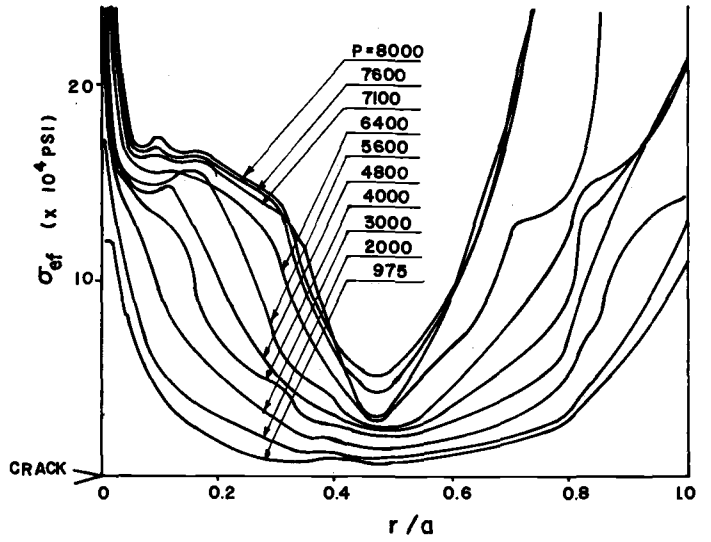

FIG. 11—*Effective stress distribution in the uncracked ligament (finite deformation analysis).*

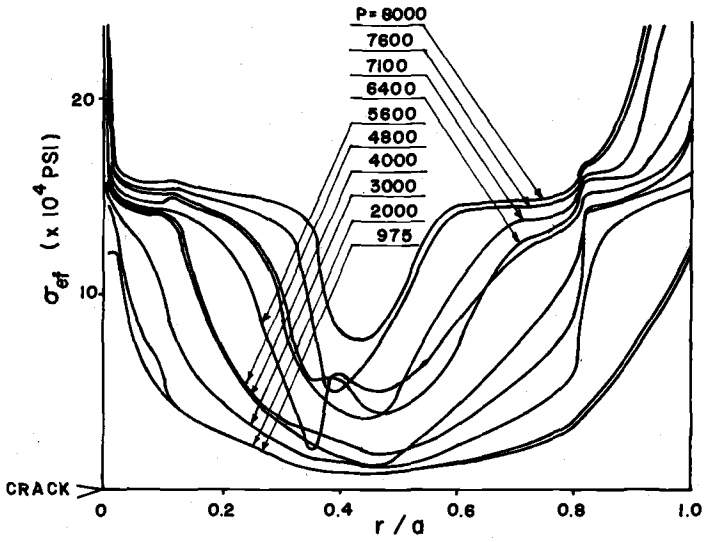

FIG. 12—*Effective stress distribution in the uncracked ligament (small deformation analysis).*

changes near the crack tip may alter the detailed results for stresses, strains, and displacements, the J-integral remains a valid parameter that is relatively insensitive to the variation in the details of the solution.

The previously developed procedure also was applied to the case of a center notch test specimen of Ni-Cr-Mo-V steel and of dimensions identical to those in Fig. 16 of Ref *4*. At first, it was observed that the presently computed results differed from those of Ref *1* by nearly a factor of two. However, it was subsequently learned [*11*] that the results in Ref *1* for center cracked tension specimens contained seemingly compensating errors. As noted in Ref *11*, these involved a missing factor of two in determining J from compliance measurements and a measurement point for J_{Ic} at maximum load, which had been observed to coincide with the onset of crack growth in the bend specimens [*1*] but had been assumed incorrectly to do so in the tension specimens as well. When these errors were accounted for, once again, an excellent correlation between the presently computed results and those of Ref *1* was noticed for the J values.

After the present computations were performed, further improvements to the previously described elastic-plastic finite-element procedure were attempted. These include (*a*) incorporation of a "knee-correction" to properly account for and improve the convergence near the point of discontinuity or of acute slope variation in the given material uniaxial stress-strain curve, (*b*) further improvements in the elastic-plastic incremental constitutive law to more properly account for finite-deformation effects,

and (*c*) shifting the point of measurement of r (as in the $r^{-n/n+1}$ type Hutchinson-Rice-Rosengren strain singularity) to the center of curvature of the blunted crack tip so that near the tip of the blunted crack only a large but finite strain concentration may result. The details of the knee-correction are essentially similar to those in Zienchiewicz and Nayak [*12*]. At each load step, the radius of curvature of the blunted crack tip was calculated, and the center of curvature of the blunted crack-tip profile was taken as the origin to measure r to be used in the assumed Hutchinson-Rice-Rosengren type singular functions. The effects of these improvements were noted to be (*a*) better convergence during each equilibrium-check and iteration especially under fully developed plasticity and (*b*) better path-independence (within ± 1.4 percent) as well as improved numerical value for J. These improved results for J are reported in Ref *13*. Also, the crack-surface deformation profiles for the bend bar, with the above modifications to the procedure, were noticeably more blunted at the root of the notch. These improved crack-surface deformation profiles for the bend bar, detailed results for J, stress and strain state, etc., for the case of a compact tension specimen, and the correlations for J and crack opening displacement for several test specimen geometries are the subject of a forthcoming paper [*14*].

Conclusions

Excellent correlation was found for the numerical results, obtained using a finite deformation, embedded singularity, elastic-plastic incremental finite-element method with available experimental results for the J versus δ relation for a three-point bend bar. The empirical formula of Rice, Paris, and Merkle to compute J from a single specimen test data for P versus δ curve is found to be valid in the case of a bend bar. Using the modified definition of the J-integral to account for finite deformations, it has been found that more accurate path independence is maintained also for a contour immediately close to the crack tip. Even though the effect of crack-tip blunting, as seen from the present finite deformation analysis, is to alter the detailed solution for stresses/strains/displacements, it is felt that the J-integral still remains a valid parameter to characterize fracture initiation under large-scale plastic yielding.

This analysis considers only the problem of crack-growth initiation. An analysis of the stability of such crack growth, involving the translation of the entire set of singular near-tip elements and consideration of global energy balance is currently being completed and will be reported in a forthcoming paper.

Acknowledgments

This work was initiated under support by the AFOSR under grant 74-2667, and has also been supported by NSF under grant 74-ENG-21346. We gratefully acknowledge these supports and the encouragement received from Dr. W. J. Walker.

References

[1] Begley, J. A. and Landes, J. D. in *Fracture Toughness, ASTM STP 514,* American Society for Testing and Materials, 1972, pp. 1–20.

[2] Rice, J. R., Paris, P. C., and Merkle, J. G. in *Progress in Flaw Growth and Fracture Toughness Testing, ASTM STP 536,* American Society for Testing and Materials, 1973, pp. 231–245.

[3] Merkle, J. G. and Corten, H. T., *Journal of Pressure Vessel Technology,* Vol. 9, Nov. 1974, pp. 286–292.

[4] Bucci, R. J., Paris, P. C., Landes, J. D., and Rice, J. R. in *Fracture Toughness, ASTM STP 514,* American Society for Testing and Materials, 1972, pp. 40–70.

[5] Atluri, S. N. and Nakagaki, M., "J-Integral Estimates for Strain Hardening Materials in Ductile Fracture Problems," *Proceedings, AIAA/ASME/SAE 17th Structures, Structural Dynamics, and Materials Conference,* Valley Forge, Pa., May 1976.

[6] Atluri, S. N., Kobayashi, A. S., and Nakagaki, M., *International Journal of Fracture,* Vol. 11, No. 2, 1975, pp. 251–271.

[7] Atluri, S. N., Kobayashi, A. S. and Nakagaki, M., *American Institute of Aeronautics and Astronautics Journal,* Vol. 13, No. 6, 1975, pp. 734–740.

[8] Chen, W. H., "Finite Deformation Analysis of Planar Cracks," Ph.D. thesis, Georgia Institute of Technology, to be published.

[9] Hofmeister, L. D., Greenbaum, G. A., and Evensen, D. A., *American Institute of Aeronautics and Astronautics Journal,* Vol. 9, No. 7, 1971, pp. 1248–1254.

[10] Knowles, J. K. and Sternberg, Eli, "An Asymptotic Finite-Deformation Analysis of the Elasto-Static Field Near the Tip of a Crack," Technical Report 27, Division of Engineering and Applied Science, California Institute of Technology, Pasadena, Calif., Jan. 1973.

[11] Rice, J. R., "Elastic-Plastic Fracture Mechanics" in *The Mechanics of Fracture,* F. Erdogan, Ed., Vol. 19, American Society of Mechanical Engineers, 1976, pp. 23–55.

[12] Nayak, G. C. and Zienckiewicz, O. C., *International Journal for Numerical Methods in Engineering,* Vol. 5, 1972, pp. 113–135.

[13] Atluri, S. N. and Nakagaki, M., "Stress Analysis of Cracks in Elasto-Plastic Range" to be presented at the *4th International Conference on Fracture,* Waterloo, Ont., Canada, June 1977 and to appear in the *Proceedings.*

[14] Atluri, S. N., Nakagaki, M., and Chen, W. H., "Fracture Initiation in Plane Ductile Fracture Problems: An Elasto-Plastic Finite Element Analysis" to be presented at the *3rd International Conference on Pressure Vessel Technology,* Tokyo, Japan, April 1977, and to appear in the *Journal of Pressure Vessel Technology; Transactions,* American Society of Mechanical Engineers.

J. P. Hickerson, Jr.[1]

Comparison of Compliance and Estimation Procedures for Calculating J-Integral Values

REFERENCE: Hickerson, J. P., Jr., **"Comparison of Compliance and Estimation Procedures for Calculating J-Integral Values,"** *Flaw Growth and Fracture, ASTM STP 631,* American Society for Testing and Materials, 1977, pp. 62–71.

ABSTRACT: Methods for J-integral fracture toughness testing are new and, therefore, not well established. Compliance methods developed by Begley and Landes provide accurate data but require extensive specimen testing and analysis. Estimation procedures that allow the calculation of J_c from a single test are convenient to use but are of unknown accuracy. In order to compare these two techniques, compact tension specimen test data from seven alloys were analyzed by both methods. A comparison of the results showed that estimated values of J_c by the Rice, Paris, and Merkle equation agreed best with compliance data when $a/w > 0.75$ but always tended to underestimate J_c. An equation derived from an improved analysis by Merkle and Corten tended to overestimate J_c.

KEY WORDS: crack propagation, fractures (materials), cracking (fracturing), crack initiation, fracture tests, toughness, mechanical properties, loads (forces)

Recent experiments have shown the J-integral to be a satisfactory fracture criterion for metals deforming in an elastic-plastic fashion [*1–8*].[2] This has made it possible to extend concepts of fracture mechanics and fracture toughness testing to structures and materials that fail only after substantial plasticity; however, because of limited experience with this new concept, those applying the J-integral to laboratory testing have yet to define the most appropriate procedures for performing tests and reducing the resultant data. This paper discusses a comparison of two methods currently being used to conduct tests and reduce experimental data.

Experimental difficulties with J-integral methodology come from several sources. The definition of J as a line integral [*9*] (Fig. 1)

[1] Member of the technical staff, Physical Metallurgy Division 5835, Sandia Laboratories, Albuquerque, N. M. 87115.

[2] The italic numbers in brackets refer to the list of references appended to this paper.

$$J = \int_{\Gamma} \left(W dy - \vec{T} \frac{\partial \vec{u}}{\partial x} ds \right) \tag{1}$$

does not lend itself to straightforward analysis of specimen data. The alternate definition of J as a change in nonlinear elastic potential energy by

$$J = \frac{-\partial \Pi}{\partial A} \tag{2}$$

where

Π = potential energy and
A = crack surface area

suggests compliance methods[3] for evaluating J [*1,10*]. While methods such as these have been successfully used and are rigorously correct, they are cumbersome to apply and require extensive specimen testing and considerable data reduction.

In hopes of simplifying these difficulties, estimation procedures have

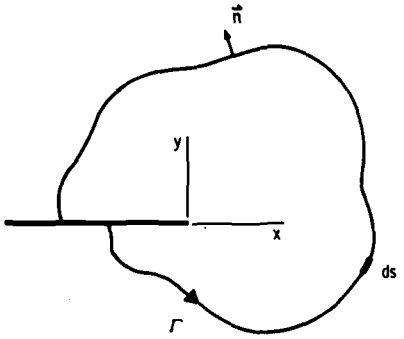

FIG. 1—*Definition of the J-integral.*

[3]The author recognizes that these are not strictly compliance methods because of the presence of large-scale yielding; however, because a succinct and descriptive definition does not exist for these tests, compliance methods are used hereafter to mean methods of analyzing families of load-displacement curves such as those applied by Begley and Landes [*1*] and the author in the text.

been proposed which would allow the calculation of critical values of J from a single specimen [*11,12*]. The simplest and most commonly used method is that proposed by Rice, Paris, and Merkle [*12*] for deeply cracked three-point bend and compact specimens. By assuming that loading conditions approach pure bending of the remaining ligament they show that J will be given by (Fig. 2)

$$J = \frac{2A}{Bb} \tag{3}$$

where

A = area under the load-displacement curve at a given displacement,
B = specimen thickness, and
b = $(W - a)$, the remaining uncracked ligament if W is the specimen width and a is the crack length.

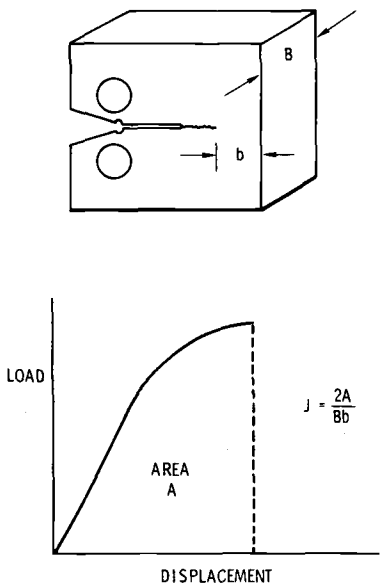

FIG. 2—*Illustration of the Rice, Paris, and Merkle* [12] *method for estimating* J *values from compact specimen data.*

Equation 3 is applied commonly to the reduction of test data although Merkle and Corten [*13*] have produced evidence that it probably underestimates J values measured on compact specimens. Their results obtained from an elastic fully plastic limit analysis that included axial forces indicate that a more appropriate form of Eq 3 would be

$$J = \frac{\lambda A}{Bb}$$
$$\lambda = \lambda(a) \tag{4}$$

Values of λ decline from 2.55 at $a/W = 0.3$ to 2.31 at $a/W = 0.7$. Predictions of λ past $a/W = 0.7$ were not made.

Srawley also has shown that Eq 3 may not represent all combinations of crack length and elastic-plastic behavior [*14*]. He has demonstrated that in the general case the value of λ given in Eq 4 will be related to the work done on the test specimens at fixed displacements, U, by

$$\lambda = \left[\frac{\partial \ln U}{\partial \ln b}\right]_{b,V} \tag{5}$$

For the extremes of linear-elastic and rigid-plastic behavior, λ was found to have a value near 2.0 in three-point bend specimens when a/W exceeded 0.5. A similar analysis of the compact specimen was not performed.

During a recent experimental program, critical values of the J-integral were obtained on seven alloys by both compliance and estimation methods applied to compact specimens. A comparison of the results obtained is the subject of this paper.

Procedures

The details of the experimental procedures are given in Ref *8* and will be summarized here only. The experiments involved fracture tests on seven commercial alloys listed in Tables 1 and 2. All alloys were in sheet form and heat treated to produce a condition of high-fracture toughness. By conventional methods of fracture toughness testing, it would be difficult, if not impossible, to obtain valid linear-elastic data on all these alloys.

In order to obtain sufficient data for a compliance analysis of J-integral values, nine to ten compact specimens having $W = 101.6$ mm (4.0 in.) of each alloy were tested. Each series of specimens was prepared by fatigue precracking to neighboring crack sizes ranging from 60 mm $\leq a \leq$ 89 mm; $0.59 \leq a/W \leq 0.88$. Test specimens were loaded to fracture during which time autographic records of load versus displacement of loading points were taken. Since specimens were in sheet form, stable cracking usually preceded failure; however, it was possible to use optical methods to detect the onset of crack extension. Critical conditions were defined as 0.13 mm (0.005 in.) of crack growth and values of $J = J_c$ were calculated based on loading curves up to that point.

TABLE 1—*General data on the alloys tested.*

Materials	Commercial Alloy Designation	Nominal Composition, weight percent	Metallurgical Condition	Nominal Sheet Thickness, mm
Aluminum	6061-0	0.25Cu, 0.6Si, 0.1Mn, 0.25Cr, remainder Al	mill annealed	3.18
Aluminum	7075-0	1.6Cu, 2.5Mg, 5.6Zn, 0.3Cr, remainder Al	mill annealed	3.18
Brass	70/30	70.0Cu, 30.0Zn	cold rolled annealed, 510°C/30 min	3.18
Magnesium	AZ31B	3.0Al, 1.0Zn, remainder Mg	annealed, 343°C/30 min	4.01
Steel	1018	0.18C, 0.75Mn, remainder Fe	hot rolled	3.00
Steel	4130	0.30C, 0.50Mn, 0.25Si, 1.0Cr, 0.20Mo, remainder Fe	mill normalized	3.00
Steel	HP9-4-20	9.0Ni, 4.5Co, 0.18C, 0.75Mo, 0.75Cr, 0.10V, remainder Fe	quenched and tempered, 566°C/6 h	2.06

As stated earlier, both compliance and estimation methods were used to reduce the data. The compliance method made use of the definition [*12*]

$$J = \frac{1}{BW} \int_0^V - \left(\frac{\partial P}{\partial R}\right)_V dV \tag{6}$$

where

V = displacement,
P = applied load, and
$R = a/W$.

The graphical steps in the process are illustrated in Fig. 3. From load-displacement curves of all test specimens, families of P versus R-curves at given displacements are constructed. The slopes of these curves at fixed values of R provide $-[\partial P/\partial R]_V$ data that can be plotted against V as shown. Measurement of the area under resulting curves out to the critical displacement, V_c, gives the value of the integral

$$\int_0^{V_c} - \left[\frac{\partial P}{\partial R}\right]_{V_c} dV$$

and allows calculation of J_c by means of Eq 6.

The estimation procedure was the currently popular method of Rice, Paris, and Merkle (Eq 3, Fig. 2). Estimated values of J_c obtained by this

TABLE 2—*Longitudinal and transverse tensile properties of the alloys tested.*

Alloy	Orientation[a]	0.2 Percent Offset Yield Strength		Ultimate Strength		Uniform Elongation, %	Total Elongation in 25 mm, %
		MPa	ksi	MPa	ksi		
6061-0	L	62	9.0	132	19.1	21.5	29.2
	T	64	9.3	131	19.0	22.1	29.1
7075-0	L	90	13.0	197	28.6	16.3	21.5
	T	92	13.3	205	29.7	16.7	20.9
70/30	L	110	16.0	341	49.5	55.0	~60.0
	T	112	16.2	339	49.2	54.0	55.2
AZ31B	L	175	25.4	264	38.3	21.2	32.2
	T	199	28.9	268	38.9	19.5	30.3
1018	L	277	40.2	380	55.1	31.0	43.9
	T	309	44.8	388	56.3	29.2	41.4
4130	L	664	96	800	116	8.5	19.1
	T	696	101	827	120	8.9	18.1
HP9-4-20	L	1276	185	1331	193	7.9	17.8
	T	1296	188	1345	195	8.1	16.8

[a] L = longitudinal and T = transverse.

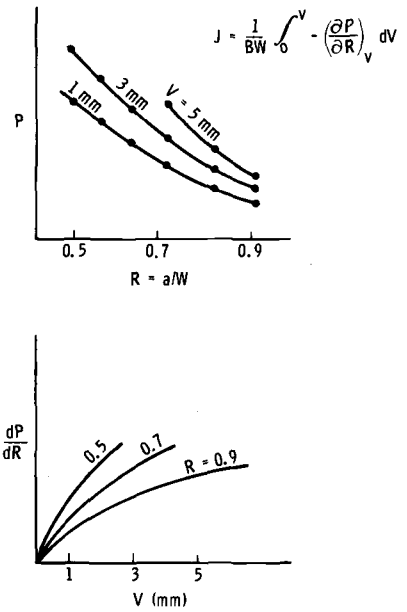

FIG. 3—*Illustration of the steps in the graphical method used to obtain J values from compliance data.*

method were compared directly with data obtained by the compliance method on a specimen by specimen basis.

In actual practice, the compliance data were reduced in a two-step process that separately calculated the contribution to J of data prior to general yield and added this result to the contribution obtained after general yield. The steps described previously were applied manually to P versus R data collected prior to general yield. Curves and slopes were fit by eye, and the areas defined by displacements at general yield were calculated by a trapezoidal method applied to closely spaced data points. The contribution of data beyond general yield was best measured by curve fitting P versus R data. The resulting equations were generally found to be within a 3 percent agreement with actual data points. By differentiating these equations with respect to R and integrating the result with respect to V, the contribution of data beyond general yield was obtained and added to that measured prior to general yield to give the values of J_c subsequently reported.

Measurement of J_c by the Rice, Paris, and Merkle method was performed with the aid of a precision planimeter which was used to measure areas under load-displacement curves. The accuracy and repeatability of such measurements has been found to be within one percent.

Results and Discussion

The data resulting from J_c calculations by compliance and estimation procedures is summarized in Table 3 and Fig. 4. From the data presented in the table it is seen that the estimation procedure consistently produces values that are less than those measured by the compliance technique. The figure shows that on a specimen by specimen basis the disagreement is greatest at short-crack lengths and tends to reduce as the crack length increases. For a/W greater than 0.75, the differences between compliance data and estimated data are generally less than 5 percent.

While the Rice, Paris, and Merkle procedure consistently underestimates

TABLE 3—*Comparison of mean values of* J_c *as calculated by compliance and estimation procedures.*

	J_c from Compliance		$2A/Bb$		$2A/Bb$
Alloy	J/mm^2	lb/in.	J/mm^2	lb/in.	J_c
6061-0 aluminum	0.123	703	0.115	657	0.935
7075-0 aluminum	0.072	412	0.069	395	0.959
70/30 brass	0.283	1615	0.261	1488	0.921
AZ31B magnesium	0.043	245	0.043	243	0.992
1018 steel	0.334	1910	0.297	1698	0.889
4130 steel	0.205	1168	0.191	1090	0.933
HP9-4-20 steel	0.235	1343	0.220	1257	0.936

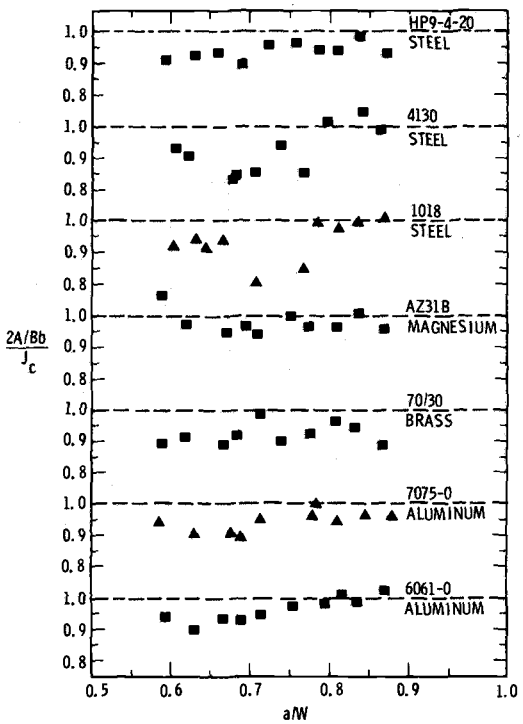

FIG. 4—*Ratio of compliance and estimation results for* J_c *as a function of crack length.*

values of J_c, it does considerably better than the 15 percent discrepancy one might predict from the Merkle and Corten analysis. Making use of the observation of Srawley that

$$\lambda = \left[\frac{\partial \ln U}{\partial \ln b} \right]_{b,V} \tag{7}$$

values of λ were obtained graphically for each alloy at four to six displacements (both elastic and after ligament yielding) by plotting ln U versus ln b. Although the Merkle and Corten analysis would predict a slight curvature in these data, none were observed. A linear regression analysis was used to measure the slopes and, thus, obtain values of λ given in Table 4.

Except for AZ31B magnesium, all values of λ exceed 2.0. If, for reasons to be discussed later, one neglects the magnesium data, a mean value of λ from the other materials is found to be 2.18 ± 0.010. It should be noted, however, that the range in λ is great enough to suggest a slight material

TABLE 4—*Values of* λ *obtained from graphical application of Eq 5.*

Alloy	Mean Value, λ	Standard Deviation
6061-0 aluminum	2.07	± 0.06
7075-0 aluminum	2.12	± 0.07
70/30 brass	2.32	± 0.08
AZ31B magnesium	1.92	± 0.11
1020 steel	2.16	± 0.01
4130 steel	2.21	± 0.06
HP9-4-20 steel	2.21	± 0.04

dependency in its value. The precision of the measurement is probably not great enough to establish this conclusively.

The magnesium data was not included in the previous discussion because of its anisotropic yield behavior. The compressive yield strength of annealed AZ31B is approximately two thirds the tensile yield strength [*15*]. In the compact specimen at limit load, the back edge of the specimen yields in compression. Substantially lowering the compressive yield strength would tend to reduce the limit load and move the apparent hinge point about which the specimen arms rotate nearer to the crack tip. The Merkle-Corten analysis suggests that this would tend to reduce λ to a value less than that calculated for a material with an isotropic yield surface. For this reason, the magnesium data should probably be considered separately from that of the other alloys.

Conclusions

Based on the comparison of data and the previous discussion, the following conclusions are drawn.

1. If one expresses J for the compact specimen as

$$J = \frac{\lambda A}{Bb}$$

then values of λ for the specimens tested should lie between 2.0 (as predicted by the Rice, Paris, and Merkle equation) and 2.4 (the upper limit for $a/W \cong 0.6$ from the Merkle-Corten analysis).

2. Measured values of λ averaged 2.18 which is consistent with the observation that the Rice, Paris, and Merkle equation produced J_c estimates that averaged 4 to 11 percent lower than compliance measured values.

3. Measured values of λ appeared independent of crack length between $0.6 \leqslant a/W \leqslant 0.9$, suggesting a single valued form for λ would be appropriate.

4. As crack length increased, J_c estimates by the Rice, Paris, and Merkle method approached compliance measured values of J_c. The best agreement was obtained when $a/W > 0.75$.

5. The low value of $\lambda = 1.92$ obtained from AZ31B magnesium data was attributed tentatively to its anisotropic yield surface which permits large amounts of compressive yielding at the specimen back edge.

In summary, it appears that the currently accepted practice of using the Rice, Paris, and Merkle method to estimate J_c values from single tests on compact specimens is slightly in error. The tendency will be to underestimate J_c by about 10 percent if $a/W < 0.75$, thus, also underestimating K_c by about 5 percent.

References

[1] Begley, J. A. and Landes, J. D. in *Fracture Toughness, ASTM STP 514*, American Society for Testing and Materials, 1972, pp. 1–20.

[2] Landes, J. D. and Begley, J. A. in *Fracture Toughness, ASTM STP 514*, pp. 24–39.

[3] Loss, F. J. and Gray, R. A., Jr., "J-Integral Characterization of Irradiated Stainless Steels," Naval Research Laboratories Report 7565, 1973.

[4] Landes, J. D. and Begley, J. A. in *Fracture Analysis, ASTM STP 560*, American Society for Testing and Materials, 1974, pp. 170–186.

[5] Kobayashi, A. S., Chiu, S. T., and Beeuwkes, R., *Engineering Fracture Mechanics*, Vol. 5, 1973, pp. 293–305.

[6] Logsdon, W. L., "Elastic-Plastic Fracture Toughness Values," presented to the 1974 National Symposium on Fracture Mechanics, Providence, R.I., 26–28 Aug. 1974.

[7] Yoder, G. R. and Griffis, C. A., "Application of the J Integral to the Initiation of Crack Extension in a Titanium 6Al-4V Alloy," presented to the 1974 National Symposium on Fracture Mechanics, Providence, R.I., 26–28 Aug. 1974.

[8] Hickerson, J. P., "Experimental Confirmation of the J Integral as a Thin Section Fracture Criterion," *Engineering Fracture Mechanics*, to be published.

[9] Rice, J. R., *Journal of Applied Mechanics*, Vol. 35, 1968, pp. 379–386.

[10] Rice, J. R. in *Fracture, An Advanced Treatise*, Vol. II, H. Liebowitz, Ed., Academic Press, New York 1968, pp. 191–311.

[11] Bucci, R. J., Paris, P. C., Landes, J. D., and Rice, J. R. in *Fracture Toughness, ASTM STP 514*, American Society for Testing and Materials, 1972, pp. 40–69.

[12] Rice, J. R., Paris, P. C., and Merkle, J. G., *Progress in Flaw Growth and Fracture Toughness Testing, ASTM STP 536*, American Society for Testing and Materials, 1973, pp. 231–245.

[13] Merkle, J. G. and Corten, H. T., *Journal of Pressure Vessel Technology*, Vol. 96, 1974, pp. 286–292.

[14] Srawley, J. E., *International Journal of Fracture*, Vol. 12, 1976, pp. 470–474.

[15] *Military Standardization Handbook*, Metallic Materials and Elements for Aerospace Vehicle Structures, MIL-HDBK-5B, Vol. I, Aug. 1974.

B. Marandet[1] *and G. Sanz*[1]

Evaluation of the Toughness of Thick Medium-Strength Steels by Using Linear-Elastic Fracture Mechanics and Correlations Between K_{Ic} and Charpy V-Notch

REFERENCE: Marandet, B., and Sanz, G., **"Evaluation of the Toughness of Thick Medium-Strength Steels by Using Linear-Elastic Fracture Mechanics and Correlations Between K_{Ic} and Charpy V-Notch,"** *Flaw Growth and Fracture, ASTM STP 631,* American Society for Testing and Materials, 1977, pp. 72-95.

ABSTRACT: Fracture toughness of medium strength steels (A533B, 2.25Cr-1Mo, electroslag welds, cast steels ...) with different heat treatments was investigated by using big compact specimens.

The comparison of Charpy V and K_{Ic} transition curves shows that a very good correlation exists between the transition temperatures defined by these two tests. By defining TK_{Ic} as the temperature at which K_{Ic} = 100 MPa$\sqrt{m}$ and TK 28 as the temperature at which Charpy V-notch (CVN) = 28 J, the relationship is

$$TK_{Ic} = 9 + 1.37\ TK\,28 \quad (°C)$$

The fact that the slope of this straight line is not one makes the existence of a direct correlation between K_{Ic} and CVN impossible. Nevertheless, this relationship may be used to predict accurately K_{Ic} from CVN. If one shifts the K_{Ic} versus temperature curves in order for TK_{Ic} and TK 28 to coincide, K_{Ic} and CVN are related by

$$K_{Ic} = 19\,(KV)^{1/2}\ (\text{MPa}\sqrt{m},\ \text{J})$$

Predicting K_{Ic} versus temperature curve from the Charpy V transition curve can thus be achieved in several steps.

KEY WORDS: crack propagation, fracture, steels, impact tests

During the fabrication or the service life of a metallic structure, there are many circumstances capable of giving rise to the appearance of "defects" (cracking related to welding, corrosion, fatigue, etc.). If the size of

[1]Institut de Recherches de la Sidérurgie Francaise, Saint Germain En Laye, France.

these defects reaches a critical value, an unstable fracture of the structure may occur at a nominal stress lower than the yield stress of the material.

Linear-elastic fracture mechanics make it possible to establish quantitative relationships between the size of these defects, applied stress, and fracture toughness (K_{Ic}) of the material. Recent developments in this theory, associated with modern computing methods, may be used to predict the conditions under which the fracture of a real structure will occur.

In the case of medium-strength steels, the determination of toughness under plane-strain conditions (K_{Ic}) requires thick specimens (several hundreds of millimetres) [*1–5*].[2] Substantial experimental facilities must be used for cracking and breaking them. The safety requirements for big thick-walled welded vessels (nuclear reactor vessels, synthesis reactor bodies, etc.) justify such tests, but, for metallurgical control in steel plants, simpler tests (such as the Charpy test) are preferable.

The purpose of this study was to measure the toughness (K_{Ic}) of various grades of medium-strength steels used as thick plates for heavy vessel fabrication: A533B, 2.25Cr-1Mo, and corresponding submerged arc and electroslag welds.

Unlike very high-strength steels, these steels exhibit a well-defined ductile-brittle transition. For each state considered, we measured the variation of K_{Ic} from liquid nitrogen temperature to the highest temperature compatible with the thickness of the specimen.

This study was mainly conducted to enable us to answer the following questions: Does the measurement of K_{Ic} provide a good differentiation of the resistance of mild steels against fracture? Is there a correlation between the K_{Ic} "transition temperature" and the Charpy V transition temperature? Is it possible to find close correlations between K_{Ic} values and Charpy V-notch (CVN) values?

The existence of such correlations would be of obvious practical value, because it would then be possible to estimate the toughness (K_{Ic}) of a material on the basis of data obtained by means of a test as simple and economic as the Charpy test.

Steels Studied—Heat Treatments

The tests covered a few grades of medium-strength steels frequently used in heavy vessel fabrication (10CD 9-10, A533B), a C-Mn steel and a Mn-Mo-V cast steel (15MDV 04-03-M). The chemical compositions of these steels are given in Table 1.

For each steel grade, one or more heat treatments were studied. In the case of the steels 10CD 9-10 reference B and A533B reference C, the toughness of welded joints also was measured (submerged arc or elec-

[2]The italic numbers in brackets refer to the list of references appended to this paper.

TABLE 1—*Chemical compositions.*

Reference	Steel grade	C	Mn	Si	P	S	Al	Ni	Cr	Mo	Cb	V
A	E 36	0.120	1.27	0.34	0.016	0.020	0.058	...	...	...	0.016	0.041
B	10CD 9-10	0.140	0.57	0.24	0.010	0.010	0.007	...	2.35	1.01	...	...
C	18MDN 5-05 (ASTM: A533B)	0.190	0.138	0.28	0.009	0.013	...	0.59	...	0.59	...	...
D	10CD 9-10	0.125	0.425	0.26	0.012	0.017	...	...	2.35	0.99	...	...
E	15 MDV 04-03 M (cast steel)	0.140	1.50	0.50	<0.02	<0.02	<0.02	...	...	0.3	...	0.06
F	10CD 9-10	0.110	0.455	0.275	0.014	0.025	0.010	0.115	2.10	1.05	...	...

troslag welding). The relevant heat treatment conditions are given in Table 2. Mechanical properties at room temperature are given in Table 3.

Carbon-Manganese Steel (Reference A)

The first tests dealt with a Nb-V microalloyed steel which we chose deliberately to investigate in a brittle state in order to facilitate the adjustment of testing equipment and methods. The steel was delivered in the form of blocks measuring 420 by 300 by 160 mm^3 cut from a plate in the as-rolled condition.

Steel 10CD 9-10 (Reference B)

This steel was melted in an electric furnace and vacuum degassed. It was received in the form of a plate measuring 1500 by 1000 by 170 mm^3. The plate was then divided into coupons of smaller dimensions which received the following treatments.

1. Austenitization for 5 h at 950°C, followed by cooling in air (simulation of hot forming operations).
2. A second austenitization at 925°C for 5 h, followed by spray quenching (cooling from 850 to 300°C in less than 12 min).
3. Tempering for 12 h at 640°C (reference B1) which represents the most unfavorable treatment to which a hydrocracking vessel can be subjected during its fabrication. The usual treatment temperature is in fact 655°C, but, in view of the relatively poor temperature control on an industrial furnace (± 15°C), it may be feared that certain parts of the system will be kept at the minimum temperature of 640°C throughout the treatment. The cooling of the coupon took place on the hearth outside of the furnace.

We also investigated a normalizing treatment (reference B4) to represent the case of a vertically electroslag welded shell, normalized and cooled horizontally in still air.

Finally, we measured the toughness of welded joints. The welding processes used for these follow:

Submerged Arc Welding (Reference B3)—This process was used on coupons 170-mm thick in the quenched and tempered (2 h at 640°C) condition. After welding, a stress relief treatment of 10 h at 640°C was carried out.

Electroslag Welding in the Vertical Position (Reference B2)—This was carried out on plates 170-mm thick having undergone treatment to simulate hot forming (5 h at 950°C/air cooled). Welding conditions were welding speed: 0.79 miles/h; preheating of starting bead at 150°C; and postheating for 2 h at 200°C and then cooling under asbestos.

TABLE 2—*Heat treatments.*

Steel	Heat Treatment [a]
A (thickness 150 mm)	as rolled
B (thickness 170 mm)	
B1	950 °C 5 h/AC + 925 °C 5 h/WQ + 640 °C 12 h/AC
B2	950 °C 5 h/AC—Electroslag welding + 950 °C 5 h/WQ + 640 °C 12 h/AC
B3	950 °C 5 h/AC + 925 °C 5 h/WQ + 640 °C 2 h/AC + submerged arc welding + 640 °C 10 h/AC
B4	950 °C 5 h/AC + 925 °C 5 h/AC + 640 °C 12 h/AC
C (thickness 170 mm)	
C1	950 °C 5 h/AC + 925 °C 5 h/WQ + 650 °C 3 h/AC + 625 °C 20 h/AC
C2	950 °C 5 h/AC + 925 °C 5 h/WQ + 650 °C 3 h/AC + submerged arc welding + 625 °C 20 h/AC
D (thickness 110 mm)	
D1	925 °C 1 h/WQ + 600 °C 1 h/AC
D2	925 °C 1 h/WQ + 620 °C 1 h/AC
D3	925 °C 1 h/WQ + 640 °C 1 h/AC
D4	925 °C 1 h/WQ + 660 °C 1 h/AC
D5	925 °C 1 h/WQ + 680 °C 1 h/AC
D6	925 °C 1 h/WQ + 700 °C 1 h/AC
E (thickness 100 mm)	960 °C 4 h/AC + 650 °C 3 h/AC
F (thickness 110 mm)	
F1	925 °C 1h/WQ + 700 °C 1h/AC
F2	925 °C 1h/WQ + 700 °C 1 h/AC + 675 °C 4 h/AC

[a]AC: air cooled; WQ: water quenched

TABLE 3—*Results of the tension tests at room temperature.* [a]

	R_e		R_m			
Steel	N/mm^2	ksi	N/mm^2	ksi	A, %	Z, %
A	303	43.9	515	74.7	29	67.6
B1	572	82.9	689	99.9	21.2	80.8
B2	584	84.7	703	101.9	20.4	78.5
B4	274	39.7	537	77.9	28.9	83.2
C1	458	66.4	609	88.3	26.7	83.4
D1	820	118.9	927	134.4	20.1	69.0
D2	673	97.6	780	113.1	21.6	71.7
D3	593	86.0	706	102.4	24.9	77.7
D4	597	86.6	720	104.4	26.0	76.9
D5	526	76.3	655	95.0	26.8	77.5
D6	521	75.5	645	93.5	26.5	78.8
E	377	54.7	523	75.8	24.1	43.7
F1	510	74.0	641	92.9	24.0	76.8
F2	494	71.6	624	90.5	24.3	75.9

[a]R_e = yield strength.
R_m = Ultimate Tensile Strength.
A = elongation.
Z = reduction in area.

The weld specimen dimensions were 2200 by 500 by 170 mm^3. It then underwent austenitization for 5 h at 925 °C followed by quenching in agitated water and tempering for 12 h at 640 °C.

Steel A533B (Reference C)

This steel was made in an electric furnace and vacuum degassed. It was received in the form of a plate measuring 1500 by 1000 by 160 mm^3. To simulate hot forming operations, austenitization was carried out at 950 °C for 5 h followed by cooling on the hearth outside of the furnace. After a further austenitization at 925 °C for 5 h followed by spray quenching (850 to 300 °C in less than 12 min), the plate underwent tempering for 3 h at 650 °C and was then stress relieved for 25 h at 625 °C. This procedure is representative of the treatments carried out on a nuclear reactor vessel. The cooling rate after stress relief was programmed at 30 °C/h to correspond to the practical conditions (reference C1).

Finally, we measured the toughness (K_{Ic}) of a submerged arc weld (reference C2). This was carried out on plates 160-mm thick having undergone treatments for hot forming simulation (950 °C, 5 h/air), spray quenching, and tempering (650 °C, 3 h/air). After welding, stress relief was carried out for 20 h at 625 °C.

X-ray, ultrasonic, and magnetic particle inspections were performed on all the welded coupons. The existence of some zones rich in inclusions was observed on two of them. A map of the defects made it possible to choose the location of the test specimens intended for K_{Ic} measurements.

Steel 10CD 9-10 (Reference D)

This steel was also melted in an electric furnace, vacuum degassed, and cast in two flat ingots from which master plates were obtained measuring 3800 by 1500 by 110 mm^3 which underwent a softening treatment after rolling. Ultrasonic inspection made it possible to check the homogeneity of these plates which were then cut so as to provide blocks measuring 1500 by 300 by 110 mm^3.

After austenitization at an average temperature of 940 °C, the blocks were quenched in agitated water for about 10 min. Under these conditions, the internal cooling rate is estimated at 700 °C/h.

The tempering treatment was carried out on pieces of smaller dimensions (250 by 240 by 110 mm^3). References D1 to D6 correspond to holding times of 1 h at temperatures ranging from 600 to 700 °C in steps of 20 °C.

Steel 10CD 9-10 (Reference F)

Another heat of the same steel was made, shaped, cut, and heat treated

under the same conditions described previously. A comparison was made between a sample in a tempered condition (1 h at 700 °C) and a sample in a tempered and stress-relieved condition (stress relief at 675 °C for 4 h).

Steel 15MDV 04-03 M (Reference E)

This is a weldable cast steel grade with a high-yield strength. Oblong blocks capable of providing compact specimens of 100-mm thickness were cast to these dimensions, normalized for 4 h at 940 °C and tempered for 3 h at 650 °C.

For each of the states considered, we measured the variation in toughness (K_{Ic}), yield strength, and CVN as a function of temperature. The description of the experimental methods we used to measure K_{Ic} with thick specimens (100 and 150 mm) in a wide temperature range (−196 °C to +100 °C) is given in Ref *6*. The tests were achieved in agreement with ASTM Test for Plane-Strain Fracture Toughness of Metallic Materials (E 399-74).

Experimental Results

The evolution of the toughness as a function of temperature is shown in Figs. 1 through 15 for each of the steels and heat treatments considered. Most of the K_{Ic} versus temperature curves obtained were interrupted in the transition range because the increase in toughness is such that the results were not valid according to the ASTM E 399-74 standard (thickness, crack length, P_{max}/P_Q ratio). Toughness measurements which did not fulfill the conditions defined by the ASTM E 399-74 standard are indicated by bracketed points on the curves.

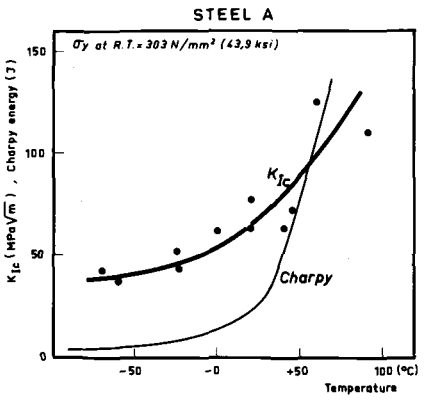

FIG. 1—*Variation of* K_{Ic} *and Charpy with temperature for steel A.*

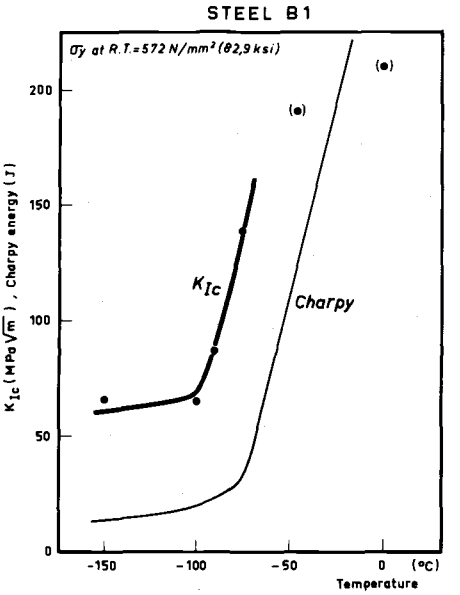

FIG. 2—*Variation of* K_{Ic} *and Charpy energy with temperature for steel B1.*

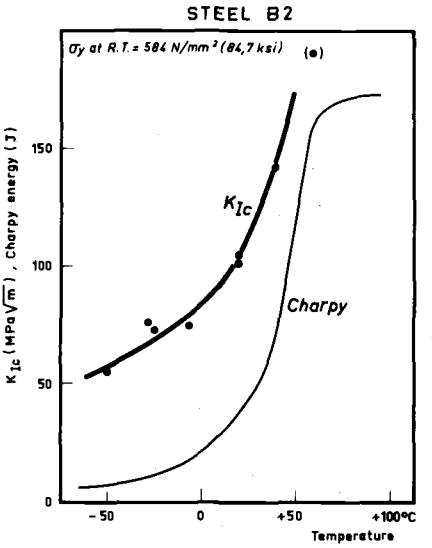

FIG. 3—*Variation of* K_{Ic} *and Charpy energy with temperature for steel B2.*

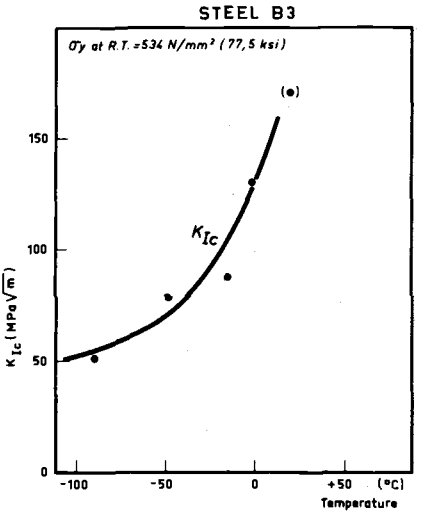

FIG. 4—*Variation of* K_{Ic} *with temperature for steel B3.*

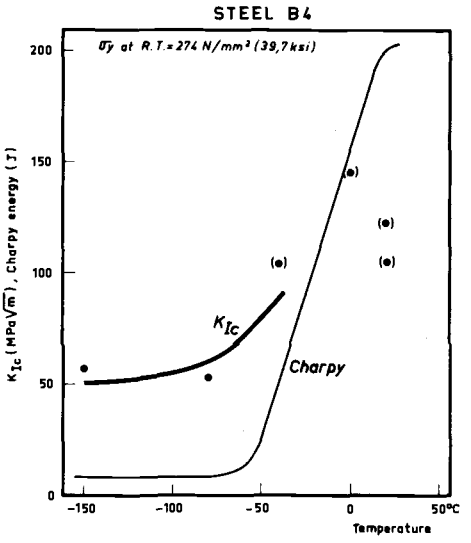

FIG. 5—*Variation of* K_{Ic} *and Charpy energy with temperature for steel B4.*

To identify the position of K_{Ic} transition curves on the temperature scale, we had to define a transition temperature. We decided to characterize the temperature over which toughness increases rapidly with temperature. An examination of the 15 curves obtained in this study and the

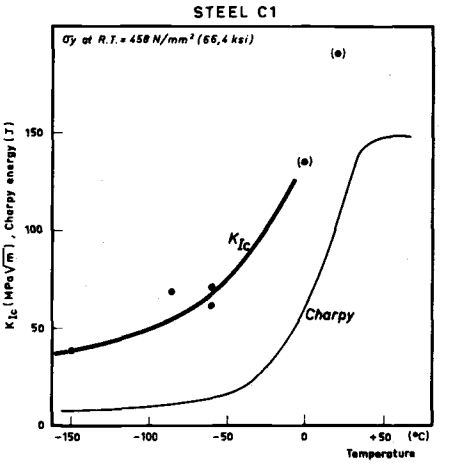

FIG. 6—*Variation of* K_{Ic} *and Charpy energy with temperature for steel C1.*

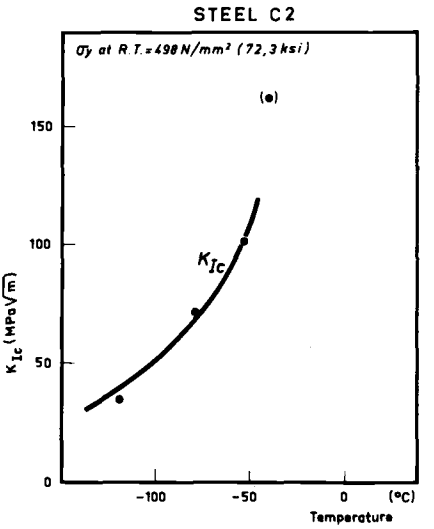

FIG. 7—*Variation of* K_{Ic} *with temperature for steel C2.*

results of the literature shows that this rapid increase in K_{Ic} occurs for K_{Ic} values between 60 and 100 MPa·m$^{1/2}$. We have, thus, defined the toughness transition temperature TK_{Ic} as being the temperature at which K_{Ic} has a value of 100 MPa·m$^{1/2}$.

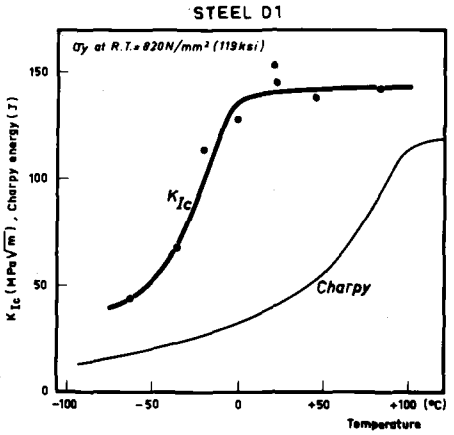

FIG. 8—*Variation of* K_{Ic} *and Charpy energy with temperature for steel D1.*

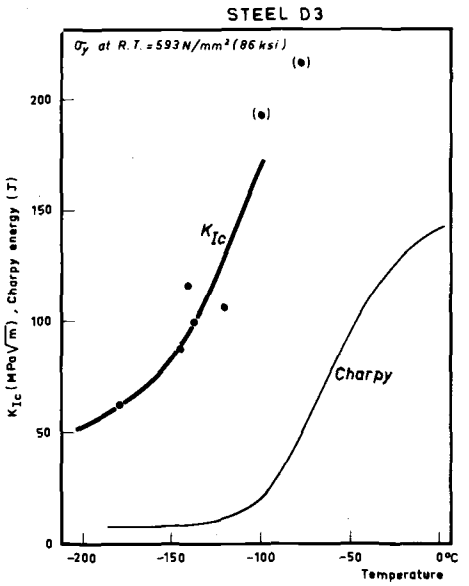

FIG. 9—*Variation of* K_{Ic} *and Charpy energy with temperature for steel D3.*

Carbon-Manganese Steel (Reference A)

In the as-rolled conditions, this steel is fairly brittle (T*K* 28 = +25 °C[3]; fracture appearance transition temperature (FATT) = +17 °C) (Fig. 1).

[3]T*K* 28 = temperature at which *KV* = 28 J (CVN = 20 ft·lb).

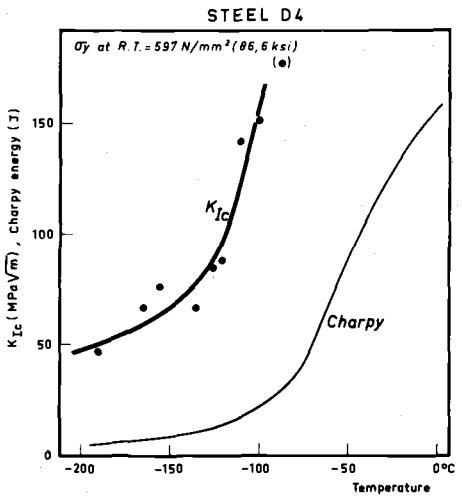

FIG. 10—*Variation of* K_{Ic} *and Charpy energy with temperature for steel D4.*

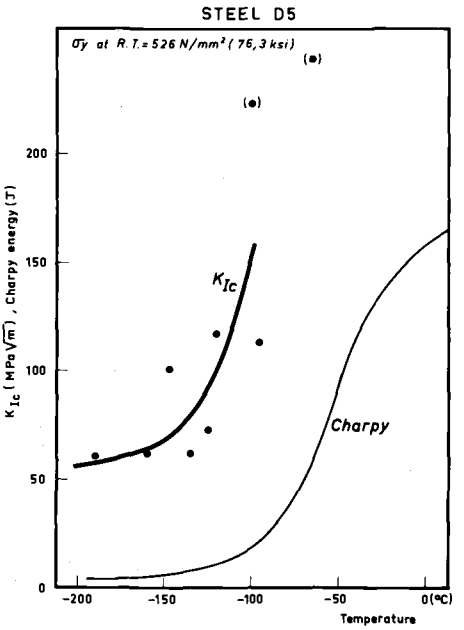

FIG. 11—*Variation of* K_{Ic} *and Charpy energy with temperature for steel D5.*

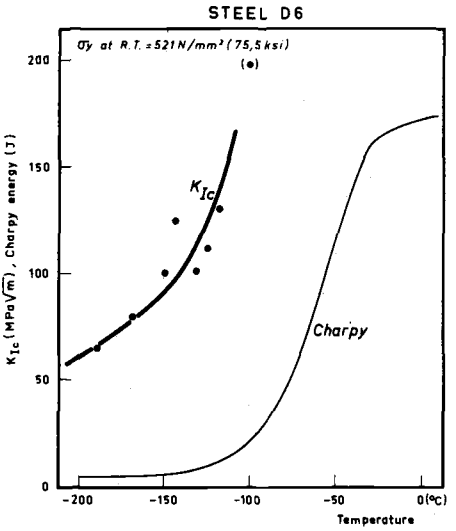

FIG. 12—*Variation of* K_{Ic} *and Charpy energy with temperature for steel D6.*

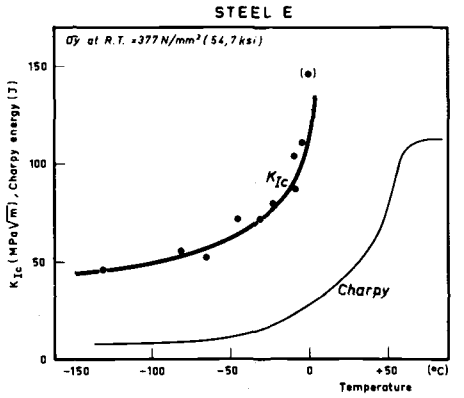

FIG. 13—*Variation of* K_{Ic} *and Charpy energy with temperature for steel E.*

This brittleness is due to the large ferritic grain size resulting from a low cooling rate after rolling (plate 160-mm thick).

Steel 10CD 9-10 (Reference B)

Parent Metal—The results obtained are given in Figs. 2 and 5. The toughness transition of the steel 10CD 9-10 occurs at a lower temperature for the quenched and tempered condition ($TK_{Ic} = -90\,°C$) than for the

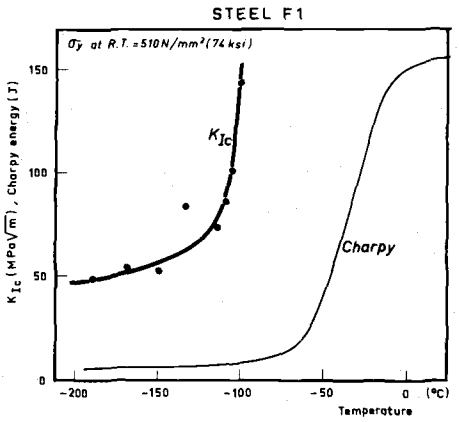

FIG. 14—*Variation of* K_{Ic} *and Charpy energy with temperature for steel F1.*

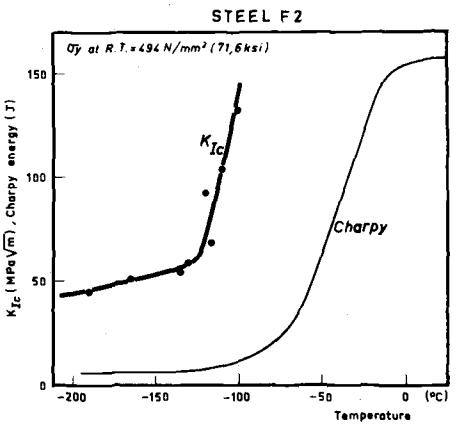

FIG. 15—*Variation of* K_{Ic} *and Charpy energy with temperature for steel F2.*

normalized-tempered condition ($TK_{Ic} \leqq -25\,°C$). Impact tests give similar results as appears in Table 4.

The difference in the transition temperature for the two treatments considered is of the order of 15 to 35 °C depending on the criterion adopted for defining the impact transition temperature. Let us note that the measurements of K_{Ic} have led to a difference of much greater amplitude ($\Delta TK_{Ic} \sim 65\,°C$).

Submerged Arc Weld—The K_{Ic} versus temperature curve relative to submerged arc weld (reference B3) is given in Fig. 4. If we compare this curve with the one obtained for the base metal (reference B1, Fig. 2), we see that the submerged arc weld is more brittle than the parent metal since the toughness transition temperature TK_{Ic} is about 65 °C higher. Be-

TABLE 4—*Transition temperatures obtained for steel B (2.25Cr-1 Mo) after two different heat treatments.*

Heat Treatment \ Impact Transition Temperatures	TK 28, °C	FATT, °C
Quenched-tempered (reference B1)	−80	−20
Normalized-tempered (reference B4)	−45	− 5

cause of the limited quantity of metal it was not possible to determine the Charpy V transition curve for this weld.

Electroslag Weld—The K_{Ic} versus temperature curve relative to electroslag welding (reference B2) is given in Fig. 3. The brittleness of this type of weld is even more pronounced. In fact, the TK_{Ic} temperature is located precisely at room temperature. It exceeds that of the submerged arc weld by 35 °C and that of the base metal by 110 °C.

Steel A533B (Reference C)

Parent Metal—The results obtained are given in Fig. 6. They are in good agreement with those found by Wessel [*5*] on a steel of the same grade having received comparable heat treatment.

Submerged Arc Weld—Unlike what we found for the steel 10CD 9-10, the toughness of the multipass weld of the A533B steel is slightly higher than that of the base metal (Fig. 8). The difference in the transition temperatures TK_{Ic} is about 25 °C. Our measurements are also in good agreement with those of Wessel [*3*].

As for the submerged arc weld corresponding to the 10CD 9-10 steel, it was not possible to determine the Charpy V transition curve for this metal.

Steel 10CD 9-10 (Reference D)

The six structural states studied are those obtained following water quenching from 940 °C and tempering for 1 h at a temperature between 600 and 700 °C (in steps of 20 °C). The results obtained for five of these six states (references D1, D3 to D6) are given in Figs. 8 to 12. It is noted that the brittleness of the steel decreases considerably as the tempering temperature increases.

Tempering at the lowest temperature (600 °C for 1 h in air) gives the steel a relatively low-toughness and a high-yield strength (see Fig. 8). Under these conditions, we were able to record the upper shelf value of the transition curve with specimen thicknesses of 100 mm. The toughness

measured at room temperature is located just at the beginning of this plateau (about 140 MPa $\sqrt{m}$).

When the tempering temperature of the steel is increased up to 640 °C, the K_{Ic} transition curve is offset considerably towards lower temperatures. Between 640 and 700 °C, tempering has no further significant effect on the position of the transition curve (see Figs. 10 to 12).

Tempering at 620 °C falls within the region of rapid variation of transition temperature with tempering temperature. This explains the wide scatter in the K_{Ic} measurements carried out on this state and the fact that it was not possible to draw a significant K_{Ic} versus temperature curve through the experimental points.

Table 5 indicates the values of TK_{Ic} and impact transition temperatures found for each heat treatment. The extreme tempering conditions (600 °C

TABLE 5—*Transition temperatures obtained for steel D (2.25Cr-1 Mo) after different heat treatments.*

Reference	TK_{Ic}, °C	Impact Strength	
		TK 28, °C	FATT °C
D1	− 15	− 15	+ 70
D2	≃ − 100	≃ − 70	≃ + 5
D3	− 140	− 95	− 25
D4	− 130	− 90	− 20
D5	− 125	− 90	− 30
D6	− 140	− 100	− 30

for 1 h, reference D1 and 700 °C for 1 h, reference D6) are differentiated by an offset in the impact transition temperature which varies from 85 to 100 °C depending on the criterion adopted. For the toughness transition temperature, the same states are differentiated by an offset of about 125 °C.

Steel 10CD 9-10 (Reference F)

On this grade, we investigated the influence of stress relief treatment for 4 h at 675 °C (reference F2) on the toughness of the steel in the tempered condition (1 h at 700 °C) (reference F1).

The results obtained on these two states are presented in Figs. 14 and 15. The stress relief treatment causes practically no change in the yield strength or the value of K_{Ic}. As can be seen by examining the results given in Table 6, the toughness and impact transition temperatures are not modified substantially.

TABLE 6—*Transition temperatures obtained for steel F (2.25Cr-1 Mo) after two different heat treatments.*

Reference	TK_{Ic}, °C	Impact Strength	
		TK 28, °C	FATT °C
F1	−105	−60	−20
F2	−110	−75	−20

Steel 15MDV 04-03 M (Reference E)

The curves of the variation in yield strength and toughness (K_{Ic}) as a function of temperature are given in Fig. 13.

Correlations Between K_{Ic} and Other Brittleness Parameters

The classical tests normally used to characterize the brittle fracture resistance of medium-strength steels (impact, Pellini, drop weight tear test (DWTT), etc.) are simpler and cost much less than tests designed to measure K_{Ic}. For this reason, several workers have attempted to establish correlations between K_{Ic} values determined experimentally on big specimens and the values of the fracture energy of Charpy specimens. The better known of these correlations are those proposed by Barsom and Rolfe [*7–9*], Sailors and Corten [*10*], and Begley and Logsdon [*11*].

Before undertaking a study of direct correlations between K_{Ic} values and impact values (KV), we have attempted to compare the transition temperature defined by these two types of tests. This had led us to propose a correlation method in two steps, the validity of which was checked out on measurements carried out within the framework of this study as well as on published measurements of other authors.

Correlations Between Transition Temperatures

One of the most important findings of the impact tests on medium-strength steels is the existence of a transition characterized by a very rapid rise in K_{Ic} with test temperature.

We have sought to determine whether the temperature at which K_{Ic} begins to increase rapidly can be correlated with the temperature above which impact strength also increases rapidly. The transition temperatures considered are

TK_{Ic}—temperature for which $K_{Ic} = 100$ MPa·m$^{1/2}$

TK_{28}—temperature for which CVN = 28 J

To generalize our results, we looked in the literature for studies dealing both with K_{Ic} versus temperature curves and impact transition curves. We took results from Greenberg, Wessel, and Pryle [*12*], Wessel [*3*], Barsom and Rolfe [*7*] and Dahl [*13*].

We have plotted in Fig. 16 all K_{Ic} versus temperature curves that we examined. Steels G to M are taken from Ref *12*, steels N and O are taken from Ref *3*, steel P is taken from Ref *7*, and steels Q and R are taken from Ref *13*.

It can be seen from Fig. 17 that there is a very good correlation between TK_{Ic} and T*K* 28. The results can be expressed in terms of the following linear regression equation

$$TK_{Ic} = 9 + 1.37\ TK\ 28$$

(correlation coefficient = 0.97 for 26 points)

For the steels considered here (maybe not for steel P for which we had not sufficient information), the crystallinity of Charpy specimens at the temperature T*K* 28 is always greater than 80 to 85 percent. It has been checked that the results obtained by Dahl [*13*] for the correlation presented here is not valid for materials that do not present this behavior, in particular for steels having low values of the upper shelf energy. The fact that the slope of the regression line is clearly higher than 1.0 calls for certain remarks.

1. The toughness test provides a better differentiation of brittle fracture sensitivity than the impact test. In fact, the correlation only provides figures for the observations made earlier. It should be pointed up that the range of the TK_{Ic} values for the steels studied is 225°C (see Fig. 16), whereas it is only 180°C for the T*K* 28 criterion.

2. It is possible, if one knows the K_{Ic} and impact transition curves for a given state, to predict very simply the new K_{Ic} versus temperature curve

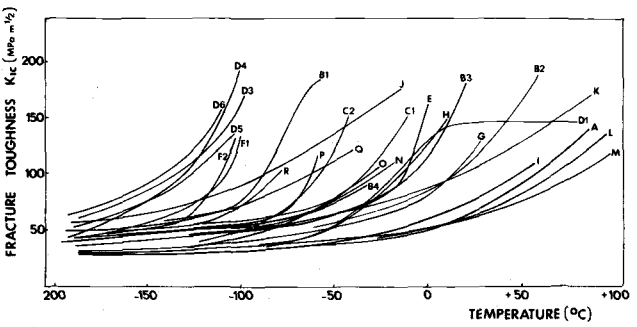

FIG. 16—*Variation of* K_{Ic} *with temperature for the different steels of this study.*

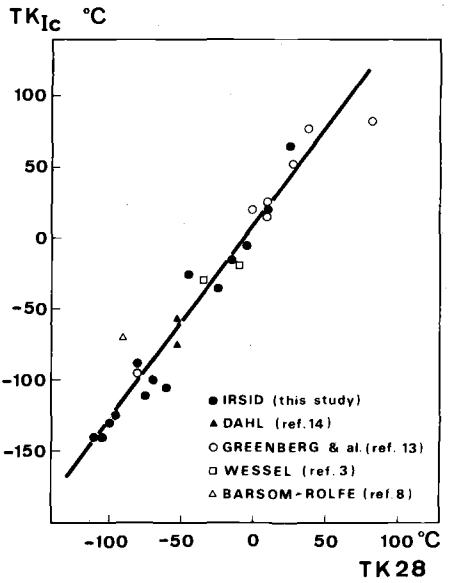

FIG. 17—*Correlation between* TK_{Ic} *(temperature at which* K_{Ic} *= 100 MPa* $\sqrt{m}$*) and Charpy transition temperature TK 28 (temperature at which CVN = 28J).*

resulting from another heat treatment or from embrittlement on the basis of the new impact transition curve. In fact, it is sufficient to shift the K_{Ic} versus temperature curve by a quantity ΔT equal to 1.37 times the offset of the T*K* 28 temperatures. We verified that such a shift is in perfect agreement with the experimental values of K_{Ic}.

3. For certain applications, the existence of this correlation makes it possible to determine at which temperature the impact tests must be carried out in order to ensure that a defect of a given size does not cause brittle fracture.

It is not surprising to find that the slope of the linear relationship between TK_{Ic} and T*K* 28 is different from one. Former studies on the correlations between results of various brittle fracture tests have in fact shown that a slope of one could be fortuitous only and that a slope higher than one means that the test which is being compared with the Charpy test is more similar than the latter to a pure crack initiation test [*14*].

Calculation of K_{Ic} *From Impact Strength* KV

We have seen that there is a very close relationship between TK_{Ic} and T*K* 28 with a slope higher than one. Figure 18 illustrates an additional consequence which may be drawn from this observation. We have plotted K_{Ic} and impact strength transition curves for two states which are very

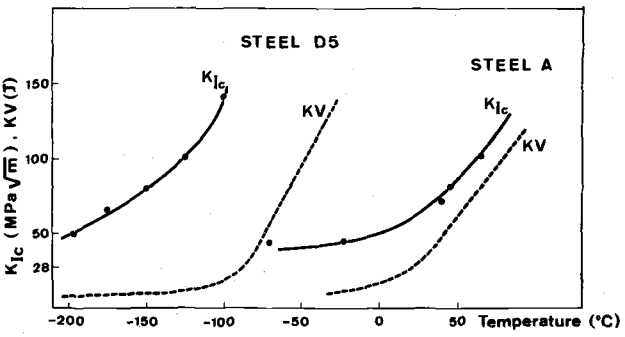

FIG. 18—*Comparison of* K_{Ic} *versus temperature and CVN (KV) versus temperature curves for two steels having very different toughnesses.*

different from a brittleness viewpoint (A and D5). It is noted that the relative position of the K_{Ic} transition curve and the impact curve is not the same for the two steels. There can thus be no direct correlation between K_{Ic} and KV, at least when one compares static K_{Ic} and classical dynamic Charpy.

However, it would appear that, if the K_{Ic} versus temperature curves are shifted so that they always occupy the same position in relation to the impact curve, it will then be possible to obtain a good correlation between K_{Ic} and KV. The simplest idea consists in making TK_{Ic} coincide with TK 28.

If the K_{Ic} versus temperature curves are shifted in order for TK_{Ic} to coincide with TK 28, one obtains the following relationship between K_{Ic} and KV verified for $KV < 50$ J for all the grades considered in this study

$$\frac{K_{Ic}^2}{E} = 1.75\,(KV)\left[\frac{K_{Ic}^2}{E} \text{ in. N/mm; } KV \text{ in J}\right]$$

or

$$K_{Ic} = 19\,(KV)^{1/2}\,[K_{Ic} \text{ in. MPa} \cdot \text{m}^{1/2};\ KV \text{ in J}]$$

The calculation of the K_{Ic} versus temperature curve on the basis of the impact transition curve is then carried out as follows.

1. Determination of impact transition curve;
2. Calculation of K_{Ic} versus temperature curve on the basis of the impact curve by the previous relationship [$K_{Ic} = 19\,(KV)^{1/2}$];
3. Calculation of TK_{Ic} from TK 28 [$TK_{Ic} = 9 + 1.37\,TK$ 28]; and
4. Shifting of the calculated K_{Ic} versus temperature curve so that it passes through the point of coordination $T = TK_{Ic}$, $K_{Ic} = 100$ Mpa·m$^{1/2}$.

By way of example, we have noted in Fig. 19 the comparison of the experimental points with the K_{Ic} versus temperature curves calculated in

this manner for four conditions leading to different brittleness (references A, E, B2, and D4). It is not materially possible in this paper to give this comparison for all the states studied, but we have verified that agreement between calculation and experimentation is as correct for the other states as for those of Fig. 19.

Comparison with Existing Correlations

The analysis presented in Fig. 18 demonstrates that there can be no direct correlation between K_{Ic} and KV since the impact transition curves and the curves of the variation of K_{Ic} with temperature do not always have the same position with respect to each other. Apart from the correlation presented here which takes this phenomenon into account, it may, thus, be expected that the previously established correlations (8 to 12) will yield good results only in certain brittleness ranges.

To check out this point, we have considered three steels having different brittle fracture behaviors.

1. Steel A is characterized by a high value of the parameter TK 28 (+30°C) and, hence, a calculated value of +50°C for TK_{Ic}. In this case, $TK_{Ic} > TK$ 28.

2. Steel E which has a TK 28 value of − 5°C and, hence, a calculated value of + 2°C for TK_{Ic} is very close to the TK 28 value.

3. Steel D4 which has an impact transition at a very low temperature (TK 28 = − 90°C, and, hence, it has a calculated value of − 115°C for TK_{Ic}). For this steel, $TK_{Ic} < TK$ 28.

Use was made of the correlations established by Barsom-Rolfe, Sailors-Corten, Begley-Logsdon, and ourselves in this study to predict the variation of K_{Ic} with temperature for these three steels which have very dif-

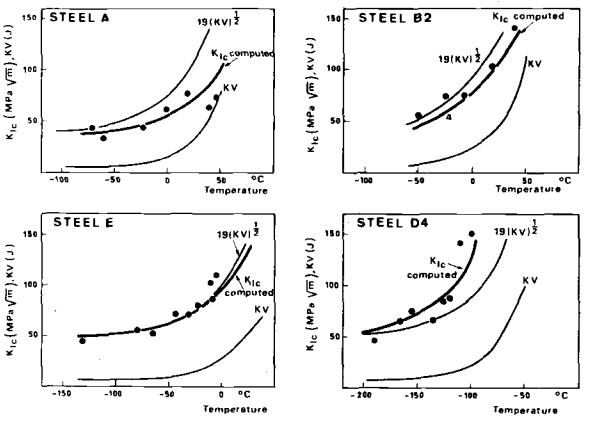

FIG. 19—*Comparison of the* K_{Ic} *temperature computed curves with experimental points.*

ferent brittle fracture behavior. As predicted, the correlations of Barsom-Rolfe, Sailors-Corten, and Begley-Logsdon show a good agreement between the K_{Ic} versus temperature curves and the experimental points only in certain brittleness ranges.

Figure 20, in fact, brings out the following points. The correlation 1 of Barsom-Rolfe gives good results when the impact transition temperature T*K* 28 is high (steel A: T*K* 28 = + 30°C). As this temperature drops, the correlation gives K_{Ic} values which are increasingly low (steels E and D4).

The correlation 2 of Barsom-Rolfe (this correlation takes into account the difference in strain rate between Charpy and K_{Ic} tests) leads to K_{Ic} values in good agreement with the real values when the T*K* 28 temperature is near −20°C (for a yield strength value near 400 N/mm²). It gives K_{Ic} values which are too high when T*K* 28 is higher than 20°C and too low when the T*K* 28 temperature is low.

The correlation of Sailors and Corten gives predictions comparable to

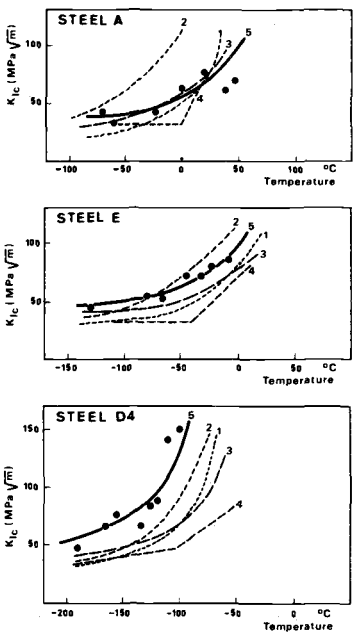

1. Barsom-Rolfe n°1;
2. Barsom-Rolfe n°2;
3. Sailors-Corten;
4. Begley-Logsdon;
5. this study;
•. experimental points.

FIG. 20—*Comparison of the different methods used to calculate* K_{Ic} *versus temperature curves from Charpy tests with actual* K_{Ic} *values.*

the correlation 1 of Barsom and Rolfe. This is not surprising because Sailors and Corten used the same experimental data as the latter researchers.

The correlation of Begley and Logsdon gives K_{Ic} values which are too low for the three brittleness ranges. The difference between real values and calculated values is small for steel A (transition at high temperature); it increases as the transition temperature T*K* 28 decreases.

These examples confirm that the agreement between the experimental points and the K_{Ic} versus temperature curves calculated in accordance with the method described in this paper is excellent whatever the brittleness of the material.

Conclusions

In this study, we determined the toughness K_{Ic} of a steel of the C-Mn type, three steels of the 10CD 9-10 type in different heat treatment conditions, a steel of the Mn-Mo-Ni type (A533B), a cast steel of the 15MDV 04-03 M type, and three electroslag or submerged-arc welds of 100 or 150 thickness.

The plotting of K_{Ic} versus temperature curves shows that the measurement of K_{Ic} provides a very good differentiation of fracture resistance of materials.

The comparison of impact curves and K_{Ic} versus temperature curves shows that there is a very good correlation between the transition temperatures defined by the K_{Ic} test and the impact test. By defining TK_{Ic} as the temperature at which $K_{Ic} = 100$ MPa·m$^{1/2}$, the relationship is written

$$TK_{Ic} = 9 + 1.37\ TK\ 28 \text{ (in. °C)}$$

T*K* 28 being the impact transition temperature at the level $KV = 28$ J.

The existence of this correlation between the transition temperatures makes it possible to calculate the K_{Ic} versus temperature curve as follows.

1. Determine the impact transition curve;
2. Calculate the K_{Ic} values from KV by the relationship $K_{Ic} = 19\ (KV)^{1/2}$ and plot the K_{Ic} versus temperature curve;
3. Calculate TK_{Ic} from T*K* 28; and
4. Shift the preceding K_{Ic} versus temperature curve so that it passes through the point of coordinates $T = TK_{Ic}$, $K_{Ic} = 100$ MPa·m$^{1/2}$ (shifting of quantity $TK_{Ic} - TK\ 28$).

The curves of the variation of K_{Ic} with temperature calculated by this method are in excellent agreement with the experimental values of K_{Ic}, if the crystallinity of the Charpy specimens at the temperature T*K* 28 is greater than 80 to 85 percent.

Acknowledgments

The results given in this paper were obtained within the framework of four research contracts entered into with the European Communities Commission, the French Délégation Générale à la Recherche Scientifique et Technique, Babcock-Atlantique, and the French Centre Technique des Industries de la Fonderie (CTIF).

We extend our particular thanks to MM. Leymonie and Cadiou of Babcock-Atlantique, MM. Dollet, Boulisset, and Ponsot of Creusot-Loire and M. Detrez of CTIF for their help in the supply, heat treatment, and cutting of blocks capable of serving as fracture mechanics specimens. We also extend our thanks to all the people at IRSID who took part in this study and in particular to MM. Bertoletti and Wyseur who carried out most of the tests, and M. Aupée for his contribution to the development of the experimental technique.

References

[1] Wessel, E. T., *Engineering Fracture Mechanics,* Vol. 1, No. 1, June 1968, pp. 77–103.

[2] Wessel, E. T., Clark, W. G., and Pryle, W. H., "Fracture Mechanics Technology Applied to Heavy Section Steel Structures," *Proceedings,* Second International Conference on Fracture, Brighton, England, 13–18 April 1969, paper 72.

[3] Wessel, E. T., "Linear Elastic Fracture Mechanics for Thick-Walled Welded Steel Pressure Vessels: Material Property Considerations," *Practical Fracture Mechanics for Weldable Structural Steels,* United Kingdom Atomic Energy Authority, Risley, England, 29–30 April 1969, 1969.

[4] Clark, W. G., and Wessel, E. T., in *Review of Developments in Plane Strain Fracture Toughness Testing, ASTM STP 463,* American Society for Testing and Materials, 1970, pp. 160–190.

[5] Wessel, E. T., and Mager, T. R., "The Fracture Mechanics Approach to Reliability in Nuclear Pressure Vessels," *The Technology of Pressure Retaining Components,* M. S. Wechsler, Ed. The Metallurgical Society of American Institute of Mechanical Engineers.

[6] Marandet, B. and Sanz G., *Revue de Métallurgie,* April 1976, pp. 359–383.

[7] Barsom, J. M. and Rolfe, S. T., in *Impact Testing of Metals, ASTM STP 466,* American Society for Testing and Materials, 1970, pp. 281–302.

[8] Barsom, J. M., "The Development of AASHTO Fracture-Toughness Requirements for Bridge Steels," U.S. Steel Report, presented at the U.S. Japan Cooperative Science Seminar, Tohoku University, Sendai, Japan, 12–16 Aug. 1974; *Engineering Fracture Mechanics,* Vol. 7, No. 3, Sept. 1975, pp. 605–618.

[9] Rolfe, S. T., *International Metallurgical Reviews,* Vol. 19, 1974, pp. 183–198.

[10] Sailors, R. H. and Corten, H. T., in *Fracture Toughness, ASTM STP 514,* American Society for Testing and Materials, 1972, pp. 164–191.

[11] Begley, J. A. and Logsdon, W. A., "Correlation of Fracture Toughness and Charpy Properties for Rotor Steels," Westinghouse Scientific Paper 71-1E7-MSLRF-P 1, 16.7., 1971.

[12] Greenberg, H. D., Wessel, E. T., and Pyrle, W. H., *Engineering Fracture Mechanics,* Vol. 1, 1970, pp. 653–674.

[13] Dahl, W., Vergleich der Aussagen der Verschiedenen Sprödbruchprüfuerfahren, Final Report on VDEh for the Research EEC 6210-55/1/50, March 1975.

[14] Cheviet, A., Grumbach, M., Prudhomme, M., and Sanz, G., *Revue de Métallurgie,* March 1970, pp. 217–236.

A. Baus,[1] *H. P. Lieurade,*[1] *G. Sanz*[1] *and M. Truchon*[1]

Correlation Between the Fatigue-Crack Initiation at the Root of a Notch and Low-Cycle Fatigue Data

REFERENCE: Baus, A., Lieurade, H. P., Sanz, G., and Truchon, M., "**Correlation Between the Fatigue-Crack Initiation at the Root of a Notch and Low-Cycle Fatigue Data,**" *Flaw Growth and Fracture, ASTM STP 631,* American Society for Testing and Materials, 1977, pp. 96–111.

ABSTRACT: Fatigue-crack initiation was investigated by testing high-strength steels (AFNOR 35 NCD 16 and 35 CD 4) with 0.6-in. (15-mm) thick ASTM compact specimens having various notch-root radii between 0.003 in. (0.07 mm) and 0.04 in. (1 mm).

Measuring devices were used to detect flaws with a surface area of only a few square millimetres in their propagation planes.

In order to calculate the number of cycles required to initiate a crack, notch root behavior was investigated through several parameters. – $\Delta K/\sqrt{\rho}$, from linear-elastic fracture mechanics, which concentrate results when the initiation time is large; – K_f^{EP}, an experimental parameter derived from low-cycle fatigue data when $N_i < 10^5$ cycles. In this case, the ratio between theoretical and experimental values of the initiation time is between one and two for a given nominal stress.

KEY WORDS: crack propagation, cracking (fracturing), fractures (materials), notched specimens

Conventional fatigue tests (for example, plotting of Wöhler curves) give gross information on the fatigue resistance of a material (initiation + propagation + fracture) but are difficult to use when precise information is desired regarding the life of a structural element subjected to fatigue.

Conventional fracture mechanics have made it possible to quantify the slow propagation phase of a crack subjected to cyclic loading, as well as the fracture phase, when the stress-intensity factor is known. Unfortunately, it is still impossible to quantify separately the initiation phase of a crack.

The purpose of this study was to provide a reply to this problem. We examined more particularly the following points.

1. Development of a means of detecting crack initiation;

[1]Institut de Recherches de la Sidérurgie Francaise, Saint Germain en Laye, France.

2. Choice of a parameter, which is a function of the metal and defect geometry, capable of providing information on the initiation phase; and
3. Calculation of the number of cycles necessary to initiate a fatigue crack in a part or a structure with a known defect (notch, groove, etc.).

Materials

The steels examined were two high-strength steels of the 35 NCD 16 and 35 CD 4 types, with the chemical compositions listed in Table 1. The heat treatments for these steels may be found in Table 2. The mechanical properties obtained after these different treatments are given in Table 3.

TABLE 1—*Materials' chemical composition.*

Steel	C	Mn	Si	Ni	Cr	Mo	P	
35 NCD 16	0.373	0.399	0.291	4.5	1.8	0.515	0.009	< 0.005
35 CD 4	0.349	0.83	0.317	...	1.06	0.24	0.021	0.028

TABLE 2—*Materials' heat treatment.*

Steel	Reference	Heat treatment
35 NCD 16	R 200	875°C 30 min/air + liquid N_2 25 min + 200°C 2 h/air
35 NCD 16	R 200 γ	875°C 30 min/furnace 100°C + 200°C 2 h/air
35 NCD 16	R 500	875°C 30 min/air + liquid N_2 25 min + 500°C 2 h/air
35 CD 4	35 CD 4	850°C 45 min/oil + 550°C 4 h/air

TABLE 3—*Materials' tensile properties.*

Steel	Reference	$R_e(\sigma_y)$ (N/mm^2)	$R_e(\sigma_y)$ (ksi)	R_m (ultimate tensile strength) (N/mm^2)	R_m (ultimate tensile strength) (ksi)	Elongation (%)	RA[a] (%)
35 NCD 16	R 200	1635	237	2015	292	11.5	52
35 NCD 16	R 200 γ	1025	149	2040	296	12.1	42
35 NCD 16	R 500	1320	191	1580	229	13.0	55
35 CD 4	35 CD 4	1020	148	1150	167	18.4	63

[a]RA = reduction in area.

Experiments

Specimens

In this study, we used compact specimens 15-mm thick (ASTM Test for Plane-Strain Fracture Toughness of Metallic Materials E 399-74)). The geometrical characteristics of the notch were varied by choosing two depths a_0 and five notch-root radii ρ machined mechanically by longitudinal grinding. The configurations studied are shown in Table 4.

The corresponding stress concentration factors K_t, were calculated by determining the values of σ_{max} using the finite elements method in the case where $a_0/W = 1/3$. Thus, it was possible to verify that the stress σ_{max} calculated in this way corresponded to within better than 5 percent to the value

$$\sigma_{max} = \frac{2K_I}{\sqrt{\pi\rho}}$$

in which K_I is the stress-intensity factor calculated by taking the depth of the mechanical notch a_0 for the value of the crack length. This confirms the conclusions of Heckel and Wagner [*1*][2] and Clark [*2*] who consider that there is no significant difference between the results given by these two methods in the range of high K_t values. The K_t values of these different specimens are given in Table 5.

All crack initiation testing was conducted on a servo-hydraulic fatigue machine of ± 100 kN, under tension-to-tension loading conditions at a stress ratio

$$R_S = \frac{\sigma_{min}}{\sigma_{max}} \text{ of } 0.1$$

and at a frequency of 20 Hz.

Crack detection

In order to detect crack initiation in the center of the specimen, we used

TABLE 4—*Specimen configuration used.*

a_0/W \ ρ (mm)	0.07	0.1	0.25	0.5	1.0
1/3	x	x	x	x	x
1/2	...	x	...	...	x

[2]The italic numbers in brackets refer to the list of references appended to this paper.

TABLE 5—*Elastic stress concentration factor.*

a_0/W \ ρ (mm)	0.07	0.1	0.25	0.5	1.0
⅓	13.0	11.3	7.4	5.3	4.0
½	...	9.4[a]	...	...	3.0[a]

[a]Derived from formula $\sigma_{max} = 2K_t/\sqrt{\pi\rho}$.

two techniques concurrently—specimen compliance measurement method and potential-drop method.

Compliance Measurement—In this method, one rectifies the signal coming from a clip-on gage which measures the reciprocal displacement of the edges of the mechanical notch.

Potential-Drop Method—With a device developed at Institut de Recherches de la Sidérurgie (IRSID), the variation in the electrical resistance of the specimen during crack initiation and propagation is measured. Two identical specimens are supplied with an alternating current of 30 A under 600 mV. One of the specimens is mounted on the machine by means of electrically insulated yokes; the other, which is not stressed, is used as a reference. The two specimens are mounted in a Thomson bridge balanced at the beginning of the test, and one records the variation in the electrical potential on the edges of the mechanical notch during the test. This technique also has been used for the determination of J_{Ic} [*3*].

These two methods proved to be very helpful while crack initiation takes place in the center of the specimen and while the crack shape is strongly dependent on the root-radius value in the early stage of propagation—long-shallow for smallest root radii and short-deep for largest ones (Fig. 1).

Figure 2 shows a typical curve obtained on the *x-y* recorder coupled to the measurement system. The criterion chosen for crack initiation is the number of cycles, N_i, corresponding to a measurable deviation of the electrical signal recorded during the test.

Several specimens tested in the same experimental conditions were broken a few cycles after initiations, up to different values of the crack detector output (10, 20, 30 mV). It was checked in this way that the defect area corresponding to crack detector output zero deviation is about 1 mm^2.

Results of Initiation Tests

Raw data relating $\Delta\sigma_{nom}$ and N_i are shown in Fig. 3. In this figure, $\Delta\sigma_{nom}$ is the nominal stress amplitude at the notch root calculated according to Ref *2*, and N_i is the number of initiation cycles measured according to the criterion defined previously.

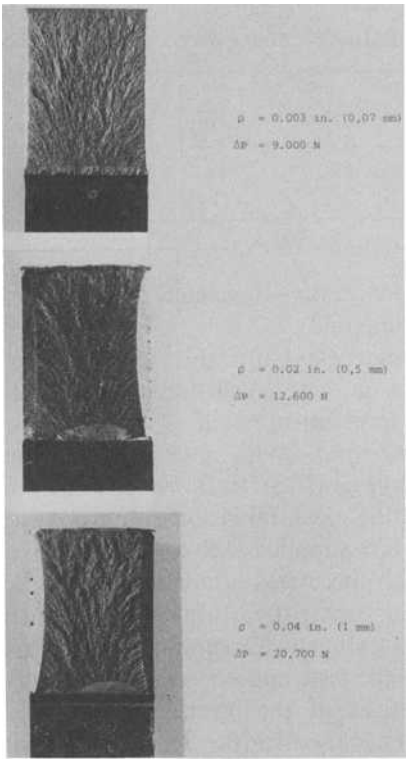

FIG. 1—*Fatigue crack initiation defects corresponding to 10 mV crack detector output deviation (compliance method).*

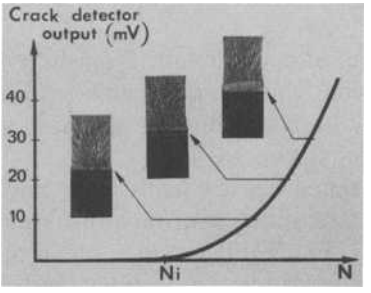

FIG. 2—*Typical curve obtained with an initiation test.*

It is noted in Fig. 3 that, for the same notch-root radius, the test points lie on a straight line, and, if the number of initiation cycles, N_i, is to be kept constant, a higher load amplitude must be applied to the specimen as the notch-root radius increases.

Results expressed in this way show that initiation is very sensitive to

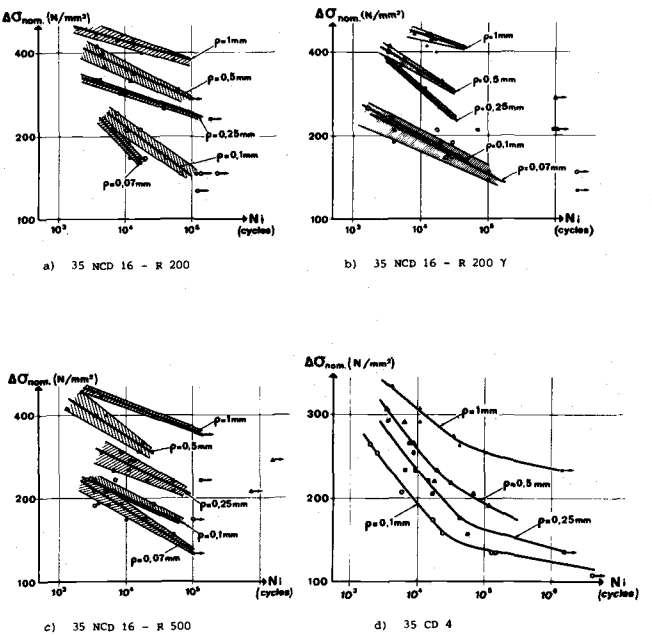

FIG. 3—*Results of fatigue crack initiation tests.*

notch-root sharpness. In fact, the nominal stress provides information only on the overall stress condition of the specimen. The finite element computation which gives a first approximation to the real behavior shows, however, that there is a significant stress gradient in the vicinity of the mechanical-notch root. Dixon [*4*] and Kuguel [*5*], among others, have already investigated the influence of this gradient on the fatigue behavior of structures or specimens. The local aspect of the initiation phenomenon, thus, appears to be decisive, and it is the reason why we have analysed the behavior of the metal at the notch root.

Behavior of Metal at Notch Root

We have adopted the following initial hypotheses.

1. The time necessary for a fatigue crack to initiate is determined by the stress and strain field at the notch root.
2. There is a measurable criterion which characterizes this field.
3. This criterion can be related simply to the amplitude of the nominal load applied to the specimen.

As we shall point out in the following paragraphs, the phenomenon has been considered from different points of view and this has led us to introduce different possible characteristic parameters.

Elastic Analysis of Stress Concentration

Use of Fracture Mechanics—Certain authors [*1,6,7*] have conducted an analysis of stresses in the vicinity of a notch having a measurable root radius ρ. Thus, they were led to establish a relationship between stress distribution at notch root and the ratio $\Delta K/\sqrt{\rho}$ which is then considered to be an initiation criterion. ΔK is calculated using the length of the mechanical notch as the crack length, and ρ is the notch root radius.

Jack and Price [*8,9*], Barsom [*10*], and Clark [*2*] used this parameter for analysing the results of fatigue initiation tests which they carried out on specimens having notches of different radii, generally larger than those chosen for this study. In Fig. 4, we have given the results expressed in this manner in the case of the steels used in this work.

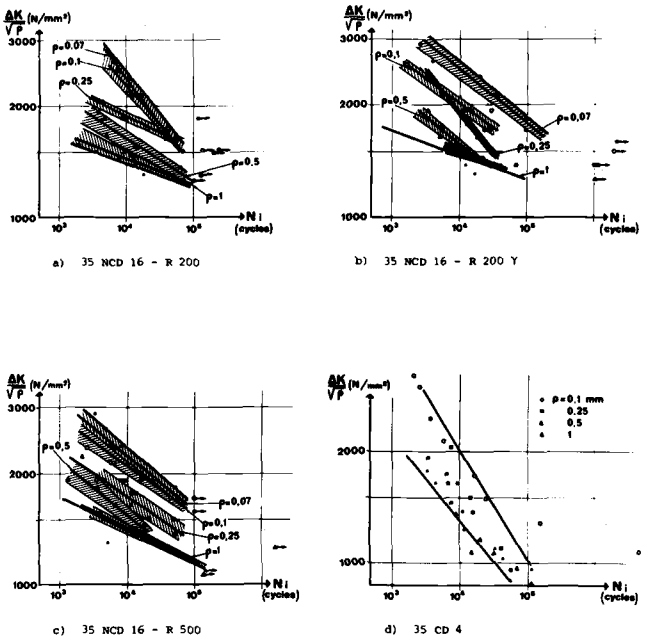

FIG. 4—*Application of fracture mechanics concepts to the results of fatigue crack initiation tests.*

As the diagrams are bilogarithmic, the points still lie on straight lines at constant notch-root radius, but the corresponding $\Delta K/\sqrt{\rho}$ levels decrease as the radius ρ increases. The scatter bands converge when the number of cycles is large, and this agrees with the observations made by Barsom and McNicol [*10*].

Use of the Stress Concentration Factor K_t—In the calculation of K_t, we demonstrated that it was possible to write

$$K_t = \frac{1}{\sigma_{nom}} \times \frac{2K_1}{\sqrt{\pi\rho}}$$

The parameter K_t and the criterion $\Delta K/\sqrt{\rho}$ are issued from the same elastic analysis, and it is obvious they will have the same effect on the test data.

Use of Fatigue Notch Factor

Many authors have noted that the preceding analysis gives exaggerated results regarding fatigue especially for small notch-root radii. For this reason, in fatigue, use is made of an experimental fatigue-notch factor which is characteristic of both the mechanical notch and the material. It is called K_f and defined as the ratio of the fatigue limits of an unnotched specimen and a notched specimen determined during tests of the same type.

As it is not possible to carry out a comparison with tests on unnotched specimens when the notched ones are compact, we determined this coefficient by means of an empirical formula established by Neuber [*11*]

$$K_f^N = 1 + \frac{K_t - 1}{1 + \sqrt{A/\rho}}$$

the index N indicating the origin of the coefficient thus determined.

From rotation-bending test data, we adjusted the constant A at the value of 0.01 which is approximately that recommended by the author in the case of martensitic steels. The calculated values are given in Table 6. Knowing K_f^N, it is possible to calculate in each case the amplitude of the maximum stress at the notch root by the formula

$$\Delta\sigma_{max}^N = K_f^N \times \Delta\sigma_{nom}$$

The test results treated in this way are shown in Fig. 5. It is noted that the results are better grouped than previously. It is no longer possible to plot the lines relative to each radius without complicating the graph—one observes only a band which converges as the number of cycles is large.

Elastoplastic Analysis of Stress Concentration Under Fatigue

Preliminary Remarks—As the experimental conditions were set for the crack initiation to occur between 10^3 and 10^5 cycles, it was thought that the notch-root behavior could be related to low-cycle fatigue laws. In this case, the modified Neuber rule [*12*] is a powerful means of expressing notch-root stress-strain behavior

$$K_f^2 = K_\sigma \times K_\epsilon$$

where

K_f = the fatigue notch factor,
K_σ = the stress concentration factor in an elastoplastic model of the behavior of the material ($K_\sigma = \Delta\sigma/\Delta\sigma_{nom}$), and
K_ϵ = the deformation concentration factor in the same model ($K_\epsilon = \Delta\epsilon/\Delta\epsilon_{nom}$).

For a notched specimen tested under a nominal stress amplitude $\Delta\sigma_{nom}$

TABLE 6—*Fatigue notch factors according to Neuber* [11].

ρ (mm)	$a_0/W = 1/3$	$a_0/W = 1/2$
0.07	9.7	...
0.10	8.8	7.4
0.25	6.3	...
0.50	4.8	...
1.00	3.7	2.8

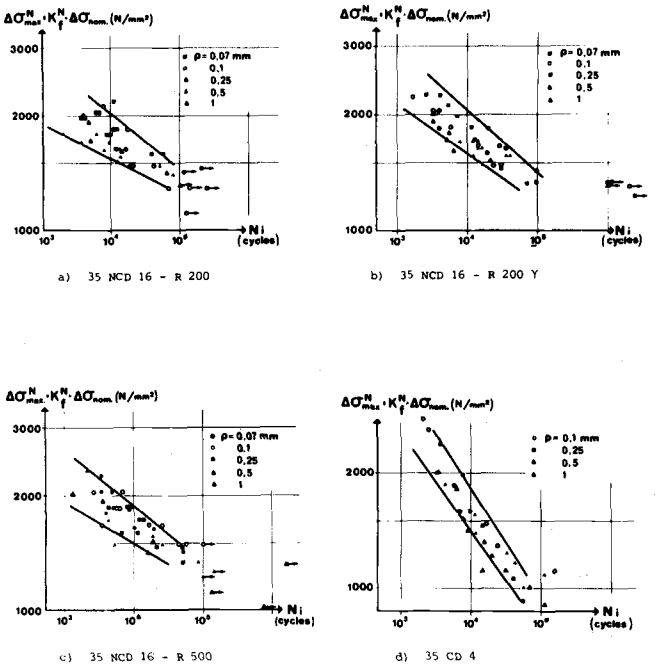

FIG. 5—*Application of Neuber's formula to the results of fatigue crack initiation tests.*

lower than the yield strength, the development of this formula leads to the following relationship

$$\Delta\sigma \times \Delta\epsilon = \frac{(K_f \times \Delta\sigma_{nom})^2}{E}$$

This formula shows that when a fatigue test is carried out at a constant loading amplitude on a notched specimen, the volume of the metal located at the notch root undergoes "stress-strain" cycles which comply with the following rule

$$\Delta\sigma \times \Delta\epsilon = \text{constant}$$

For simulation tests on plain specimens, Morrow, Wetzel, and Topper [*13,14*] showed that the product $\Delta\sigma \times \Delta\epsilon$ at the notch root determines the fatigue behavior of notched specimens provided that the crack-propagation phase is negligible in relation to the life of the specimen.

In this study, the quantity $\sqrt{E\,\Delta\sigma\,\Delta\epsilon}$ was adopted as a criterion because it is expressed simply as a function of the nominal stress amplitude

$$\sqrt{E\,\Delta\sigma\,\Delta\epsilon} = K_f \times \Delta\sigma_{nom}$$

Application to Crack Initiation—We can relate the metal at the notch root to the metal in an unnotched low-cycle fatigue specimen by taking the number of cycles to initiation as equivalent to the number of cycles to failure of the low-cycle fatigue specimen. This is valid because Gallet and Lieurade [*15*] showed that, in a low-cycle fatigue test, the propagation phase is negligibly short and corresponds to a defect size of the same order of magnitude as in our crack-initiation tests. The behavior of the metal at the notch root is stabilized very quickly [*15*], and it may be considered that in addition to the product $\Delta\sigma \times \Delta\epsilon$, the amplitude $\Delta\epsilon$ remains constant at the notch root. The same authors also have shown that the ratio $R_\epsilon = \epsilon_{min}/\epsilon_{max}$ has no influence on the low-cycle fatigue results of the 35 NCD 16 steel.

In light of this, the Manson-Coffin curve and the cyclic stress-strain curve of each material (see Appendix) make it possible to establish a correlation between the number of initiation cycles, N_i, and the value of the criterion $\sqrt{E\Delta\sigma\,\Delta\epsilon}$ in accordance with the diagram of Fig. 6. For each material, this theoretical correlation is represented graphically by the elastoplastic theoretical curve (EPTC) (Fig. 7).

After each initiation test, we verified that for a given material and a given value of K_t, the ratio $\sqrt{E\,\Delta\sigma\,\Delta\epsilon}/\Delta\sigma_{nom}$ remained constant whatever the value of N_i (Fig. 8) with only a small scatter in the values around an average value which we call K_f^{EP}.

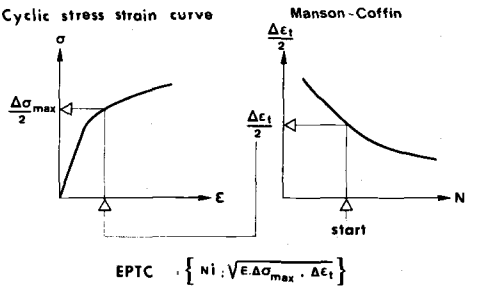

FIG. 6—*Step by step determination of the elastoplastic theoretical curve of a material.*

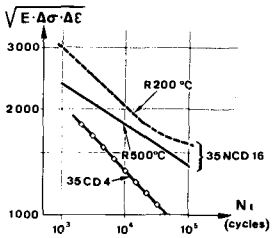

FIG. 7—*Elastoplastic theoretical curves for materials of this work.*

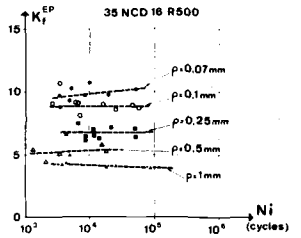

FIG. 8—*Elastoplastic initiation parameter variation with number of cycles to crack initiation.*

Thus, it is possible to establish a correspondence between K_t and K_f^{EP} (Fig. 9). It should be noted that this correspondence is not affected by the notch depth, as shown by the curve relative to the steel 35 NCD 16-R 200 on which are plotted points corresponding to two different notch depths. The correspondence which relates K_t and K_f^{EP} is thus a one-to-one correspondence and depends only on the material. Knowing the values of K_f^{EP} for each material and each notch configuration, we have presented the test results relating $K_f^{EP} \times \Delta\sigma_{nom}$ and N_i (Fig. 10).

The results are grouped in a narrow band which converges at large

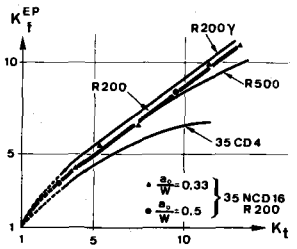

FIG. 9—*Elastoplastic initiation parameter variation with notch acuity and material.*

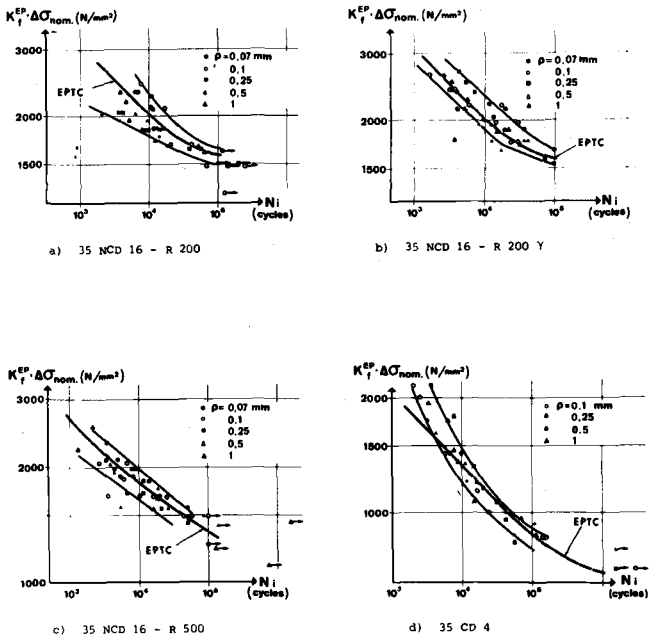

FIG. 10—*Application of elastoplastic analysis to the results of fatigue crack initiation tests.*

values of number of cycles. The EPTC of the material also was plotted. Thus, a good correspondence is observed between the theoretical law and the experimental data.

Calculation of the Duration of the Initiation Phase

Figure 11 summarizes the procedure to be followed.

1. For a given geometrical configuration, it is always possible to calculate the coefficient K_t by using, for example, the tables of Peterson [*16*].

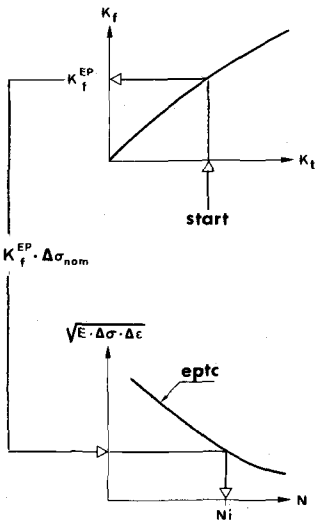

FIG. 11—*Determination of the fatigue crack initiation period by the elastoplastic method.*

2. For the materials of this study, we know the correspondence between K_f^{EP} and K_t.

3. Knowing the cyclic characteristics of the material, the quantity $K_f^{EP} \times \Delta\sigma_{nom}$ is entered into the diagram ($\sqrt{E\,\Delta\sigma\,\Delta\epsilon}$; N_i), and the number of cycles N_i necessary for the initiation of a fatigue crack is thus derived.

For a given nominal stress amplitude, the ratio between theoretical duration and experimental results varies between one and two at the maximum.

Comparison of Different Analyses

Let us consider the differences between the results obtained with the different criteria at a crack-initiation value of 10^4 cycles. For this purpose, in each case, one measures the half width of the scatter band at 10^4 cycles and divides this half width by the average value of the scatter band at the same location. Thus, one obtains the percentage of scattering around the average value of the scatter band (Table 7).

From these calculations, it appears that the parameter which best groups the results of initiation tests is the parameter K_f^{EP} which is also the parameter which best takes into account the properties of the steel and, particularly, its capacity to harden or soften under cyclic loading.

Narrowing of the experimental scatter band is not the only advantage of elastoplastic analysis over other analyses. As shown in Fig. 10, the scatter band of experimental data overlaps the EPTC of the material

TABLE 7—*Scatter hand width at* $N_a = 10^4$ *cycles obtained with different analyses.*

Parameter \ Grade	R 200, %	R 200 α, %	R 500, %	35 CD 4, %
$\Delta K/\sqrt{\rho}$	± 28	± 29	± 26	± 21
$\Delta\sigma_{max}{}^{N}$	± 14	± 12	± 12	± 13
$K_f{}^{EP} \times \Delta\sigma_{nom}$	± 11	± 10	± 10	± 10

under consideration. Among the analyses considered, this analysis is the only one which corresponds to a theoretical law of the initiation behavior of a notched specimen immediately derivable from conventional laws for the low-cycle fatigue behavior of the material used.

Conclusions

In this study, we attempted to determine whether it was possible to predict the number of cycles necessary for the initiation of a fatigue crack at the root of a defect showing a radius ρ and subjected to cyclic loading. Consequently, we carried out fatigue-crack initiation tests on compact tension 15 specimens in 35 NCD 16 and 35 CD 4 steels showing different notch-root radii ρ ($0.07 < \rho < 1$ mm). The study included three parts.

1. We first investigated different systems making it possible to determine, *a priori,* the initiation of a crack from a notch root. Two systems proved satisfactory. One uses a clip-on gage together with suitable processing of the measured signal, and the other uses the measurement of the electrical resistance of the specimen.

2. We then examined the parameters capable of predicting the value of, N_i, the number of cycles for crack initiation. Thus, we analysed the results from $\Delta K/\sqrt{\rho}$ (where ΔK is the variation in the stress-intensity factor during a cycle, and ρ is the notch-root radius), $K_f{}^{N}$, the fatigue notch factor, and $K_f{}^{EP}$, elastoplastic initiation parameter which is calculated from the Manson-Coffin curve and the cyclic stress-strain curve of the material. These parameters do not all yield the same accuracy for the calculation of the number of cycles N_i.

On one hand, our results are in good agreement with Barsom's [*10*] which show that the elastic $\Delta K/\sqrt{\rho}$ approach is very helpful when $N_i > 10^6$ cycles, because it defines a threshold value under which no crack initiation occurs, and that can be used in the same way as the fatigue limit in the conventional fracture tests.

On the other hand, the $K_f{}^{EP}$ approach shows that there exists a good correlation between fatigue crack initiation when $N_i < 10^5$ cycles and material's low-cycle fatigue behavior.

Acknowledgments

This work was supported by French "Délégation à la Recherche Scientifique et Technique" under Contract 73-7-1573.

APPENDIX

Low-cycle fatigue data used in this work from Ref *15*.

$\Delta\sigma/2$ (N/mm^2)	$\Delta\epsilon/2$ (%)	N_f (cycles)
	35 NCD 16-R 200 and R 200 γ	
1796	1.7	117
1786	1.619	154
1656	1.313	258
1452	1.088	599
1382	0.838	1 320
1290	0.688	2 925
1358	0.656	2 528
1023	0.568	9 094
900	0.460	35 000[a]
750	0.400	420 000[a]
	35 NCD 16-R 500	
1204	1.54	230
1248	1.44	255
1204	1.21	390
1175	0.99	683
1129	0.78	1 522
973	0.563	4 661
884	0.456	15 271
	35 CD 4	
792	1.41	360
763	0.98	665
686	0.76	1 457
568	0.462	7 431
629	0.33	12 259
487	0.26	68 384

[a]Constant stress-amplitude tests.

References

[*1*] Heckel, K. and Wagner, R., *International Journal of Fracture*, Vol. 11, 1975, pp. 135–140.

[*2*] Clark, W. G., *Fracture Toughness and Slow-Stable Cracking, ASTM STP 559*, American Society for Testing and Materials, 1974, pp. 205–224.

[*3*] Marandet, B. and Sanz, G., "Characterization of the Fracture Toughness of Steels by the Measurement with a Single Specimen of J_{Ic} and the Parameter K_{Bd}," IRSID

Report, Institut de Recherches de la Sidérurgie Française, St-Germain-en-Laye, Feb., 1976, p. 252; this publication, pp. 462–476.

[4] Dixon, J. R., *Journal of Mechanics and Physics of Solids,* Vol. 10, 1962, pp. 253–263.

[5] Kuguel, R., *Proceedings,* American Society for Testing and Materials, 1961, pp. 732–748.

[6] Malkin, J. and Tetelman, A. S., *Engineering Fracture Mechanics,* Vol. 3, 1971, pp. 151–167.

[7] Forman, R. G., *Engineering Fracture Mechanics,* Vol. 4, 1972, pp. 333–345.

[8] Jack, A. R. and Price, A. T., *International Journal of Fracture Mechanics,* Vol. 6, No. 4, Dec. 1970, pp. 401–409.

[9] Jack, A. R. and Price, A. T., *Acta Metallurgica,* Vol. 20, July 1972, pp. 857–866.

[10] Barsom, J. M. and McNicol, R. C., *Fracture Toughness and Slow-Stable Cracking, ASTM STP 559,* American Society for Testing and Materials, 1974, pp. 183–204.

[11] Neuber, H., *Theory of Notch Stresses,* J. W. Edwards Co, Ann Arbor, Mich., 1946.

[12] Neuber, H., *Journal of Applied Mechanics,* Vol. 28, No. 4, Dec. 1961, pp. 544–560.

[13] Morrow, J., Wetzel, R. M., and Topper, T. H., *Effects of Environment and Complex Load History on Fatigue Life, ASTM STP 462,* American Society for Testing and Materials, 1970, pp. 74–91.

[14] Stadnick, S. J. and Morrow, J., *Testing for Prediction of Material Performance in Structures and Components, ASTM STP 515,* American Society for Testing and Materials, 1972, pp. 229–252.

[15] Gallet, G. and Lieurade, H.-P. "Influence de la Structure Métallographique d'un acier au Nickel-Chrome-Molybdène sur son Comportement en Fatigue Plastique," IRSID Report RE 236, Institut de Recherches de la Sidérurgie Française, St-Germain-en-Laye, Nov. 1974.

[16] Peterson, R. E., *Stress Concentration Factors,* Wiley, New York, 1973.

J. A. Begley,[1] *W. A Logsdon,*[1] *and J. D. Landes*[1]

Ductile Rupture Blunt-Notch Fracture Criterion

REFERENCE: Begley, J. A., Logsdon, W. A., and Landes, J. D., **"Ductile Rupture Blunt-Notch Fracture Criterion,"** *Flaw Growth and Fracture, ASTM STP 631,* American Society for Testing and Materials, 1977, pp. 112-120.

ABSTRACT: A blunt-notch fracture criterion is proposed. The criterion is shown to be applicable for the initiation of ductile tearing in the plane-strain regime. Elastic to fully plastic behavior can be treated. Experiments have shown ductile crack initiation to occur at a J-integral value which is only a function of notch root radius. Two specimen geometries have been tested using a nickel-chromium-molybdenum-vanadium-rotor steel. The onset of ductile tearing from the notch tip was measured using the multiple specimen heat tinting resistance curve technique. Notch-root radii for blunt-notch compact-toughness specimens and center-notched panels varied from 0.10 in. (0.25 cm) to that of a fatigue precrack. Results are also presented for blunt-notch toughness tests of aluminum alloy 6061-T651 using compact-toughness specimens.

KEY WORDS: crack propagation, fractures (materials), cracking (fracturing), bursting, notch

The flaw tolerance of engineering materials can be reasonably well described using the concepts of fracture mechanics. A conservative assumption of crack-like defects permits single parameter characterizations of both elastic and plastic stress and strain fields for the near-tip region. Hence, a wide range of material behavior has been characterized in terms of K, J, or crack opening displacement (COD) from fracture, fatigue, and stress-corrosion cracking to creep crack-growth rates.

Real defects in engineering structures do not always have a crack-like acuity. Flaws which cannot be treated as cracks would seem to preclude the concept of a singular near-tip field and, thus, prevent a convenient field characterization of the near-tip mechanical environment. Correlation and prediction of mechanical behavior then passes to point parameters such as a critical stress or strain. Such point parameters may be

[1] Mechanics Department, Westinghouse Research Laboratories, Pittsburgh, Pa. 15235; J. A. Begley is now professor, Department of Metallurgical Engineering, Ohio State University, Columbus, Ohio 43210.

modified by requiring action over a distance related to the metallurgical structure.

A critical strain or strain over a characteristic distance are attractive criteria for ductile rupture [*1–4*].[2] Experiments were conducted to further evaluate the critical strain concept. Emphasis was placed on the J-integral, reflecting the fact that the J-integral as first presented by Rice [*5*] was envisioned as an analytic tool in the approximate analysis of strain concentrations at notches and cracks.

As discussed in this paper, the initiation of ductile tearing from a blunt notch of a given root radius was found to occur at a J value which was otherwise independent of specimen geometry. This provides a useful engineering approach to evaluate the flaw tolerance of structures containing defects which do not possess a crack-like, notch-tip acuity.

Experimental Procedures

Blunt-notch toughness tests were conducted on 1.0-in. (2.5-cm) thick compact-toughness specimens and center-notched panels. Specimen geometries and pertinent dimensions are illustrated in Fig. 1. Four notch-root radii were examined for each specimen geometry including a fatigue precrack. The nickel-chromium-molybdenum-vanadium (NiCrMoV) rotor steel specimens were removed from a 44 in. (112 cm) diameter rotor forging and oriented with the notch direction as near radial as possible (orientation C-R according to ASTM Test for Plane-Strain Fracture Toughness of Metallic Materials (E 399-74)). The 6061-T651 aluminum compact-toughness specimens were machined from a 1.0-in. (2.5-cm) thick plate in the L-T orientation. Conventional mechanical properties of these alloys are listed in Table 1. To ensure a ductile tearing mode of fracture, the nickel-chromium-molybdenum-vanadium rotor steel specimens were tested at 300 °F (149 °C) which is well onto the Charpy upper shelf. The 6061-T651 aluminum specimens were tested at 75 °F (24 °C).

A multiple specimen heat tinting resistance curve technique was utilized to determine the initiation of fracture from the notch root for the NiCrMoV rotor steel specimens. The aluminum specimens were anodized in lieu of heat tinting. A thorough description of the J resistance curve technique is given in Ref *6*. Briefly, the testing procedure is to (*a*) load the compact-toughness specimen or center-notched panel to a predetermined J level in the region where crack extension is anticipated, (*b*) unload and heat tint or anodize the specimen to mark the crack advancement, and (*c*) pull the specimen apart and measure crack growth (Δa) from the exposed fracture surface. For both the compact-toughness specimens and center-notched panels, J was calculated from the load-displacement record and specimen dimensions using approximations of Rice et al [*7*] as shown next.

[2] The italic numbers in brackets refer to the list of references appended to this paper.

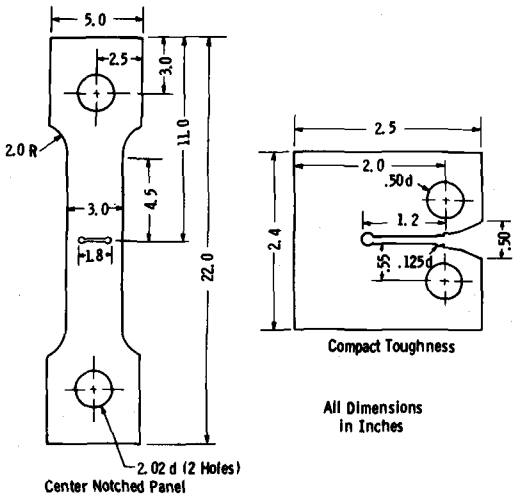

FIG. 1—*Blunt notch toughness specimens (1-in. thick).*

$$\text{Compact-toughness specimen:} \quad J = \frac{2A}{B(w - a)}$$

$$\text{Center-notched panel:} \quad J = (1 - \nu^2)\frac{K^2}{E} + \frac{2A}{B(w - 2a)}$$

Here A is an area under the load-displacement record as shown in Fig. 2,

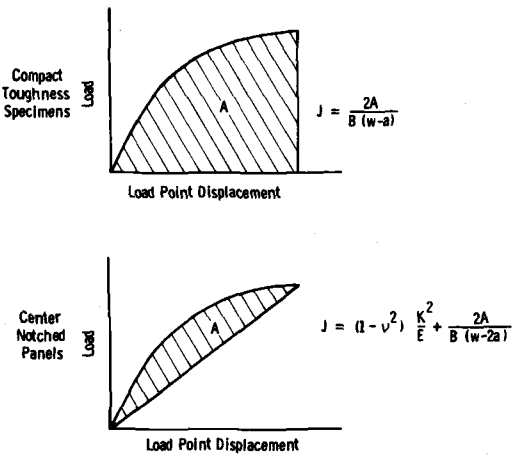

FIG. 2—*Description of the graphical evaluation of* J *from load versus load point displacement records.*

TABLE 1—*Mechanical properties of ASTM A471 NiCrMoV rotor steel and 6061-T651 aluminum alloy.*

Alloy	Orientation	0.2% Yield Strength		Ultimate Strength		Elongation, %	Reduction in Area, %
		ksi	MPa	ksi	MPa		
A471	ID	109.9	757.7	129.7	894.2	15.55	42.35
(NiCrMoV)	OD	111.6	769.5	129.5	892.9	20.64	61.12
6061-T651[a]	L	41.7	287.5	45.7	315.1	19	52
Aluminum	T	40.0	275.8	47.0	324.1	14	32

[a]Estimated properties.

B is the specimen thickness, w is the specimen width, ν is Poisson's ratio and E is Young's modulus. Total crack length for the center-notched panel is denoted by $2a$ while crack length for the compact geometry is given by a. The J value for center-notched panels is broken into elastic and plastic components. The elastic term

$$(1 - \nu^2)\frac{K^2}{E}$$

is computed from a stress-intensity value based on the maxium load.

Results of a test series were plotted in terms of applied J level versus crack advancement, Δa. Extrapolation of this curve to zero crack growth provides the J value for the initiation of fracture at the notch root. For fatigue precracked specimens this J value is termed J_{Ic}.

Results

Resistance curves based on J are shown in Figs. 3 through 5 for compact-toughness specimens and center-notched panels of the NiCrMoV rotor steel and 6061-T651 aluminum alloy. Curves for the blunt-notch specimens are parallel to those for the fatigue precracked specimens. Beyond initiation, the notch tip does not influence the resistance to continued crack propagation.

Figure 6 illustrates the J resistance curves for fatigue precracked specimens of the two NiCrMoV test geometries. The J_{Ic} values are identical reflecting the dominance of the crack-tip plastic singularity. Slope of the J versus Δa curve for the center-cracked panels, however, is considerably

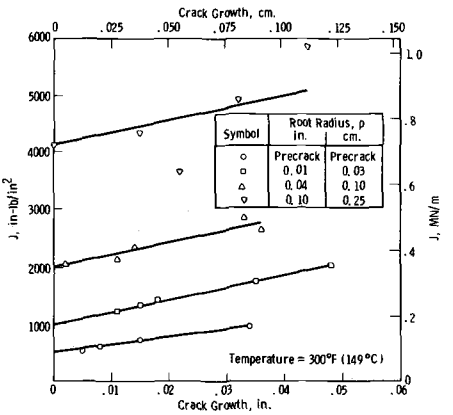

FIG. 3—J *resistance curves for ASTM A471 NiCrMoV rotor steel compact toughness specimens with various root radii.*

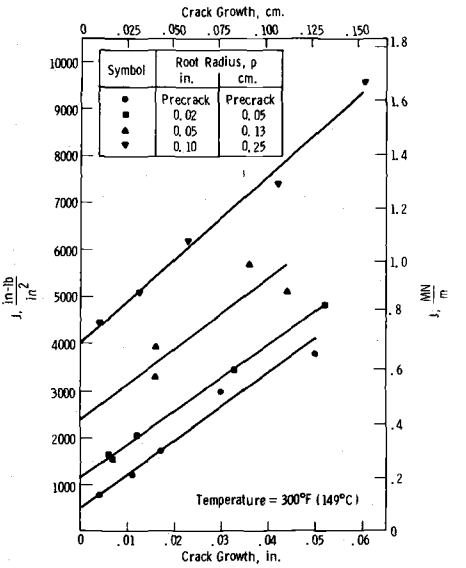

FIG. 4—J *resistance curves for ASTM A471 NiCrMoV rotor steel center notched panels with various root radii.*

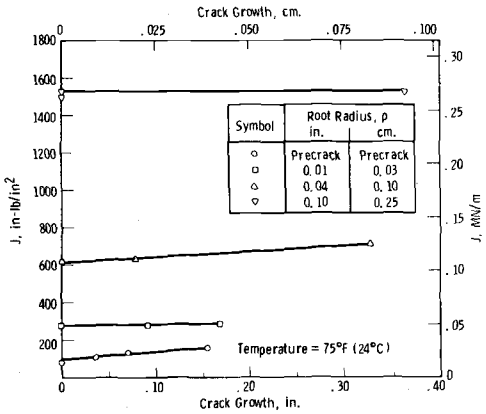

FIG. 5—J *resistance curves for 6061-T651 aluminum compact toughness specimens with various root radii.*

steeper than that of the compact-toughness specimens. This is caused by a difference in the crack propagation path. For the center-cracked panels, tearing proceeds along the rigid plastic slip lines at 45 deg to the original crack plane. The crack path for compact-toughness specimens is coplanar with the fatigue crack plane. While the initiation of crack growth is dominated by the singular plastic crack-tip stress-strain field, the direction of continued tearing is influenced greatly by the slip-line field.

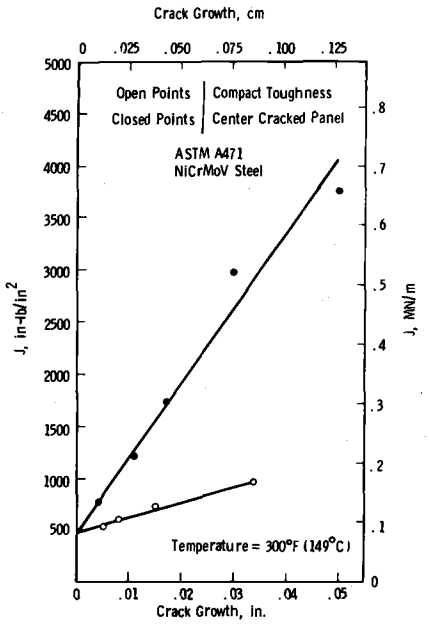

FIG. 6—J *resistance curves for precracked ASTM A471 NiCrMoV rotor steel compact toughness specimens and center cracked panels.*

The effect of notch-root radius on the J level for crack initiation is summarized in Fig. 7 for both the NiCrMoV rotor steel and 6061-T651 aluminum alloy. Here, the *J* level for crack initiation is plotted versus notch-root radius. The center-notched panel results fall along the same line as those for the compact-toughness specimens. These results clearly substantiate a two-parameter, blunt-notch fracture criterion based on the notch-root radius and the J-integral. Armed with this information, one can predict the behavior of defects with finite root radii.

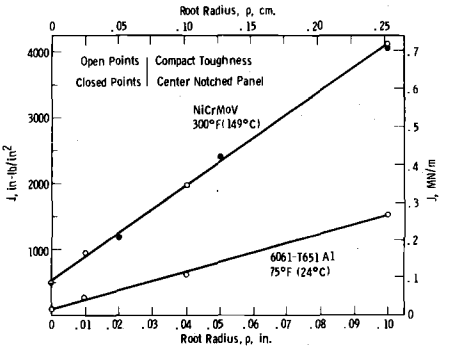

FIG. 7—*Critical* J *versus root radius* (ρ).

Discussion

While Fig. 7 lends support to a two-parameter, blunt-notch criterion, it also raises some interesting questions regarding a critical strain theory. Rice [5] indicates that the notch-root strain is given by

$$\varepsilon = \varepsilon_y \left[\frac{\left(N + \frac{1}{2}\right)\left(N + \frac{3}{2}\right)\Gamma\left(N + \frac{1}{2}\right)}{\Gamma\left(\frac{1}{2}\right)\Gamma(N + 1)} \frac{J}{\sigma_y \varepsilon_y \rho} \right]^{1/(1+N)}$$

where σ_y is the yield stress, ε_y is the yield strain, and the relationship between stress and strain beyond the yield limit is given by

$$\sigma = \sigma_y (\varepsilon/\varepsilon_y)^N$$

To a good approximation, a critical notch-root strain fracture theory leads to a linear plot of J versus notch-root radius which passes through the origin. The lines in Fig. 7 are straight but extrapolate to the J_{Ic} level rather than the origin. This is in conflict with both the critical strain theory and the concept of an effective root radius of a fatigue crack.

A possible explanation of this behavior is that J is a field parameter which characterizes the stress and strain field in the region around the notch tip. The initiation of stable cracking from the notch tip commences when this field parameter reaches a critical value. This is virtually the same as the characterization of stable fracture from a fatigue crack at a critical K_{Ic} or J_{Ic} value.

Summary and Conclusions

1. Blunt-notch, fracture-toughness tests have been performed using various specimen geometries and notch root radii for an A471 NiCrMoV rotor steel and a 6061-T651 aluminum alloy.

2. Ductile tearing from these blunt notches occurs at a geometry independent J value for a given notch-root radius.

3. The previously mentioned findings provide a convenient engineering technique to predict the fracture behavior of engineering structures containing notch-like defects of a finite-root radius.

4. A critical notch-root strain theory is not consistent with experimental findings.

References

[1] McClintock, F. A., "Local Criteria for Ductile Rupture," *International Journal of Fracture Mechanics*, Vol. 4, 1968.

[2] McClintock, F. A., "Ductile Fracture Instability in Shear," *Journal of Applied Mechanics,* Vol. 25, 1958.

[3] Smith, R. F. and Knott, J. F., "Crack Opening Displacement and Fibrous Fracture in Mild Steel," Conference on Practical Application of Fracture Mechanics to Pressure Vessel Technology, London, May 1971, Institution of Mechanical Engineers, London, 1971.

[4] Mohamed, S. A. and Tetelman, A. S., "Strain and Stress Distribution in Fully Plastic Notched Bars and the Criterion for Ductile Rupture Initiation," Third International Conference on Fracture, Munich, Germany, April 1973.

[5] Rice, J. R., "A Path Independent Integral and the Approximate Analysis of Strain Concentration by Notches and Cracks," *Journal of Applied Mechanics,* Vol. 35, 1968.

[6] Landes, J. D. and Begley, J. A. in *Fracture Analysis, ASTM STP 560,* American Society for Testing and Materials, 1974, pp. 170–186.

[7] Rice, J. R., Paris, P. C. and Merkle, J. C. in *Progress in Flaw Growth and Fracture Toughness Testing, ASTM STP 536,* American Society for Testing and Materials, 1973, pp. 231–245.

W. G. Clark, Jr.[1]

Stress-Corrosion Crack Initiation in High-Strength Type 4340 Steel

REFERENCE: Clark, W. G., Jr., **"Stress-Corrosion Crack Initiation in High-Strength Type 4340 Steel,"** *Flaw Growth and Fracture, ASTM STP 631,* American Society for Testing and Materials, 1977, pp. 121–138.

ABSTRACT: The stress-corrosion, crack-initiation properties of two high-strength (180 ksi, 1240 MPa and 215 ksi, 1480 MPa yield strength) American Iron and Steel Institute type 4340 steels were evaluated with blunt-notch test specimens exposed to hydrogen sulfide (H_2S) gas (that is, an accelerated test environment). Results show that the initiation of a stress-corrosion crack from a blunt notch depends primarily upon the notch-tip strain which, in turn, can be related to the elasticity calculated maximum notch-tip stress and the notch-tip radius. A test method and analytical procedure is proposed which can be used to predict the critical strain required to develop stress-corrosion cracking at a blunt notch.

KEY WORDS: crack propagation, stress corrosion, corrosion, fracture, notch, steels, cracks, stresses

Existing linear-elastic fracture mechanics technology provides a unique quantitative approach to the evaluation of environment induced subcritical crack growth (stress-corrosion cracking) in structural alloys. Specifically, it has been shown that the critical combination of defect size and applied stress required to induce stress-corrosion cracking as well as the subsequent rate of crack growth can be characterized in terms of the fracture mechanics crack-tip, stress-intensity factor, K_I [*1,2*].[2] From knowledge of the appropriate fracture-mechanics material parameters, it is possible to determine if, and how fast, a preexisting crack-like defect will grow to the critical size for failure. However, it is well known that a preexisting crack is not required to induce stress-corrosion cracking, and there are many service failures that clearly demonstrate this fact. In these instances, the development of stress-corrosion cracking is usually associated with a stress concentration of some type, and, once a crack develops,

[1]Fellow engineer, Mechanics Department, Westinghouse Research Laboratories, Pittsburgh, Pa. 15235.

[2]The italic numbers in brackets refer to the list of references appended to this paper.

the time to failure can be relatively short. Consequently, in such applications, crack initiation becomes a primary design consideration.

Over the years, many attempts have been made to characterize the crack-initiation performance of structural alloys. Although much of this effort has focused on fatigue behavior, some consideration has been given to stress-corrosion crack initiation [*3*]. Unfortunately, the limited amount of data currently available are applicable only to specific loading conditions, and the results are qualitative in nature.

Recent developments and advances in the areas of fracture mechanics and stress analysis now provide techniques whereby it is possible to analyze more accurately the stress/strain conditions associated with crack-initiation behavior. Consequently, it appears feasible to develop a more quantitative approach to this phenomenon. Recent studies have produced substantial evidence which indicates that the stress-intensity concept of fracture-mechanics technology may apply to the evaluation of crack-initiation behavior in the presence of notches [*4–6*]. Since the stress-intensity factor is essentially a measure of the magnitude of stresses and strains in the vicinity of a stress concentration and since crack initiation obviously depends upon these parameters, it is reasonable to assume that a relationship may exist between the applied stress-intensity factor and crack-initiation behavior. Data are available which show that such a correlation does in fact exist, and considerable success has been achieved in attempts to correlate fatigue-crack initiation performance with an effective blunt-notch, stress-intensity factor. Clark and Barsom and McNicol as well as others have demonstrated that within limits, the number of loading cycles required to develop a fatigue crack at a blunt-notch stress concentration can be related to the parameter $\Delta K_I/\sqrt{r}$ (cyclic stress-intensity range divided by the square root of the notch radius) which in turn, is an estimate of the maximum elastic-notch stress, σ_{max} [*4–6*]. Although substantially more testing is required to evaluate this relationship thoroughly and fully characterize the limitations as a practical design tool, the potential advantages make it reasonable to consider this relationship in the evaluation of stress-corrosion crack initiation.

This paper presents the results of an investigation designed to evaluate the blunt-notch stress corrosion crack initiation performance of high-strength (180 ksi, 1240 MPa and 215 ksi, 1480 MPa yield strength) 4340 steel and the applicability of fracture-mechanics concepts to the characterization of such behavior. Three widely different toughness test specimen geometries (tension, bend, and compact toughness specimens) containing blunt notches with radii ranging from 0.003 (0.008 cm) to 0.160 in. (0.41 cm) were subjected to slow-rate, rising load stress corrosion testing in a 50 psi (345 kPa gage) hydrogen sulfide (H_2S) gas environment. The onset of stress-corrosion cracking was evaluated as a function of the blunt-notch radius and the results expressed in terms of the elastically

calculated notch stress determined from fracture-mechanics considerations. A quantitative approach to the characterization of stress-corrosion cracking in the presence of blunt notches is proposed and further analyses and testing required to confirm the procedure and extend the concept to fatigue performance is recommended.

Material and Specimen Preparation

The material involved in this investigation consisted of quenched and tempered American Iron and Steel Institute (AISI) type 4340 steel, heat treated to 180 ksi (1240 MPa) and 215 ksi (1480 MPa) yield-strength levels. The 180 ksi (1240 MPa) yield-strength material was obtained as a 3-in. (7.62-cm) thick forged plate, and the 215 ksi (1480 MPa) yield-strength material was obtained as 7.5-in. (14.05-cm) diameter forged bar stock. The nominal chemical composition, heat treatment, and room-temperature tensile properties of the forgings are summarized in Table 1. The room-temperature fracture toughness determined in accordance with ASTM Test for Plane-Strain Fracture Toughness of Metallic Materials (E 399-74) is 150 ksi$\sqrt{\text{in.}}$ (165 MPa$\sqrt{\text{m}}$) and 75 ksi$\sqrt{\text{in.}}$ (82.4 MPa$\sqrt{\text{m}}$) for the 180 ksi (1240 MPa) and 215 ksi (1480 MPa) yield-strength material, respectively. The K_{Iscc}[3] for these materials in a 50 psi (345 kPa gage) H_2S

TABLE 1—*Chemical composition, heat treatment and room-temperature tensile properties of materials investigated.*

Material	Chemical Composition, Weight Percent								
	C	Mn	Si	P	S	Ni	Cr	Mo	V
180 ksi yield (1241 MPa)	0.36	0.63	0.25	0.010	0.010	2.54	0.86	0.39	0.093
215 ksi yield (1482 MPa)	0.41	0.81	0.27	0.006	0.009	1.88	0.91	0.37	...
	Heat Treatment								
180 ksi yield (1241 MPa)	Austenitized 4 h at 1560°F (849°C), water quenched; double tempered 4 h at 1080°F (582°C) and furnace cooled.								
215 ksi yield (1482 MPa)	Austenitized 2 h at 1500°F (816°C), oil quenched; tempered 10 h at 600°F (316°C) and air cooled.								
	Tensile Properties at 75°F (23.9°C)								
	Tensile Strength, ksi (MPa)		Yield Strength (0.2 percent offset), ksi (MPa)		Elongation in 2 in. or 50 mm, percent		Reduction in Area, percent		
180 ksi yield (1241 MPa)	194 (1338)		179 (1234)		14		46		
215 psi yield (1482 MPa)	250 (1724)		215 (1482)		10		38		

[3] K_{Iscc} = the value of the plane-strain, stress-intensity factor below which an existing crack will not grow due to stress corrosion.

gas environment measured as the result of both long-time constant displacement and rising load tests is 26 ± 5 ksi$\sqrt{in.}$ (28.6 ± 5.5 MPa$\sqrt{m}$) for the 180 ksi (1240 MPa) yield material and 17 ± 3 ksi$\sqrt{in.}$ (18.7 ± 3.3 MPa$\sqrt{m}$) for the 215 ksi (1480 MPa) yield material [7].

Figures 1, 2, and 3 show the three toughness specimen geometries used in this investigation. In all cases, the test specimens were taken from the "as received" material such that the plane of the notch was parallel to the long-transverse direction of the plate (radial plane of the bar) and perpendicular to the major axis of the forging. Figures 1 and 2 show the three blunt-notch configurations used for the edge-notched-tension and three-point-bend tests. Note that the notch depth is the same for each of the three notches in a given specimen. Figure 3 shows the multiple notch compact-toughness specimen tested in this investigation [6]. The use of this specimen involves conducting a test with the original notch and then saw cutting to the first hole and repeating the test with the new notch. This procedure is then repeated for the next hole. In addition to the three-notch radii shown in Fig. 3, tests also were conducted with specimens containing 0.003 in. (0.008 cm) and 0.16 in. (0.41 cm) radii notches.

Experimental Procedure

All of the stress-corrosion, crack-initiation testing involved in this investigation was conducted at room temperature (80°F, 26.7°C) in a 50

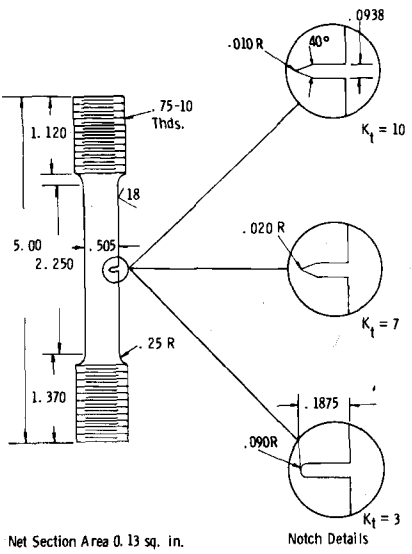

FIG. 1—*Notched tensile bar used for crack-initiation studies.*

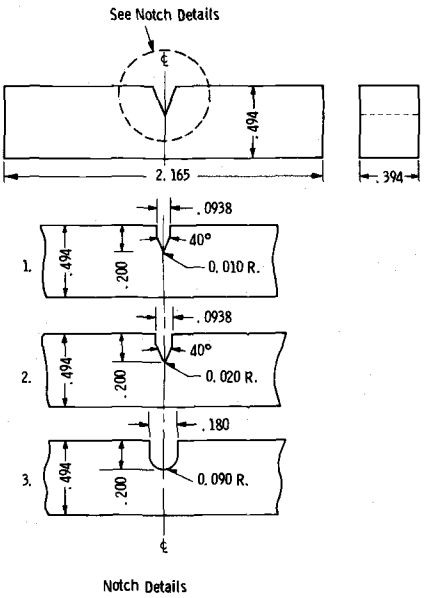

FIG. 2—*Notched bend specimen used for crack initiation studies.*

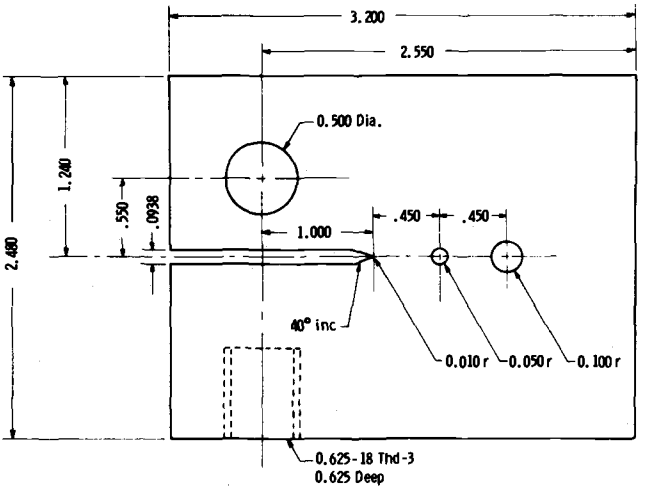

FIG. 3—*Mulitple radius crack initiation test specimen.*

psig (345 kPa gage) H_2S gas[4] environment in accordance with the rising load accelerated stress-corrosion test procedure described by Clark and Landes [*8*]. Specifically, the notched-test specimens were subjected to slow-rate tensile loading in the H_2S gas and the load corresponding to the

[4]99.6 volume percent (liquid phase) H_2S, typically 31 ppm water.

onset of stress-corrosion cracking determined. Two techniques were used to monitor the initiation of a crack at the notch tip. In one case, the notched area of the specimen was examined visually with a low-magnification (×15) microscope focused through a view port in the test chamber. In the other case, the load-deflection record developed in the H_2S gas environment was compared to an air environment load-deflection record developed for an identical test specimen and the load corresponding to the point of deviation between the two test records used to estimate the load at crack initiation. The load-deflection record comparison method of estimating the crack-initiation load permits one to distinguish between deviation on the load-deflection record caused by plastic deformation and that caused by the onset of cracking. Although each of these crack-initiation detecting techniques have been used successfully to determine the load corresponding to crack initiation [surface cracks in the notch as small as 0.03 in. (0.08 cm) long by 0.01 in. (0.025 cm) deep could be detected], such instrumentation was not required in any of the tests involved in this investigation. Because of the extremely rapid rate of crack growth associated with stress-corrosion cracking in the material-environment system involved here (high-strength 4340 steel exposed to H_2S gas), the load associated with the initiation of a crack essentially was identical to the load required to cause failure of the test specimen. In fact, for the multiple notch compact toughness tests (Fig. 3), it was necessary to establish displacement limits on the test machine to prevent the first crack from growing through the next blunt notch.

Figure 4 presents a schematic illustration of the environment chamber used to conduct the tension tests. The test chamber details and a description of the test procedures associated with the three-point-bend and compact-toughness tests are given in Refs *7* and *8*, respectively.

Analysis of Blunt-Notch Specimens

As noted previously, the results of the blunt-notch, crack-initiation testing involved in this investigation are expressed in terms of the elastically calculated maximum notch stress, σ_{max}, as determined from fracture-mechanics considerations. The general equation used to compute σ_{max} is given below

$$\sigma_{max} = \frac{2K_I}{(\pi r)^{1/2}} \tag{1}$$

This expression is derived from the basic relationship between the stress-intensity factor for a sharp crack with a length corresponding to the depth of the blunt notch being considered (K_I), the notch-root radius (r), and the maximum stress at the notch root (σ_{max}) as given next [*9*]

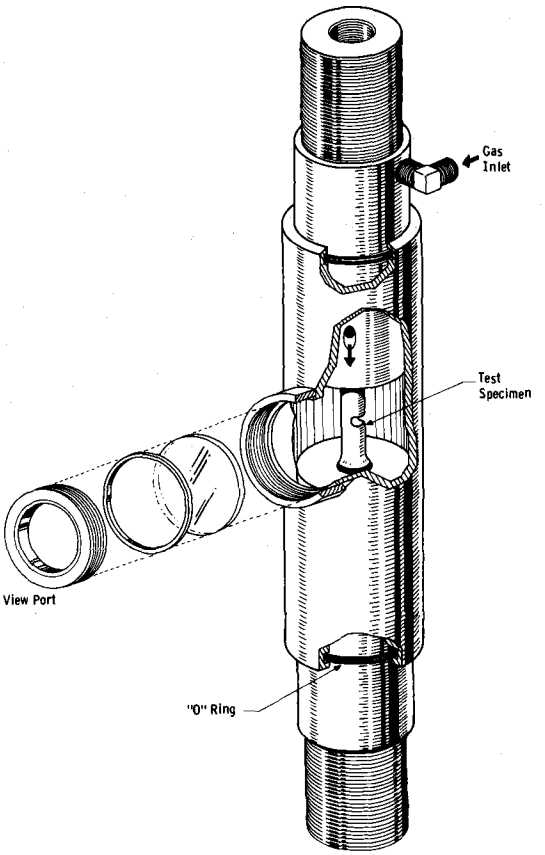

FIG. 4—*Environment chamber used for crack initiation testing (tension specimens).*

$$K_I = \lim_{r \to 0} \frac{(\pi)^{1/2}}{2} (r)^{1/2} \sigma_{max} \tag{2}$$

The stress-intensity factors associated with the edge-notched 0.505-in. (1.28-cm) diameter tension tests were computed in accordance with the experimentally determined K calibration shown in Fig. 5. Note that this calibration is applicable only to 0.505-in. (1.28 cm) diameter tension specimens. The stress-intensity factors computed for the three-point-bend tests (1.6-in., 4.06-cm span) were determined from the expression developed by Gross and Srawley [*10,11*]. The K expression developed by Wilson was used to compute K_I for the compact-toughness specimens [*11,12*]. Table 2 presents a summary of the stress intensity and maximum notch-stress expressions in terms of the applied load, P, for the specific notch radii and test specimen geometries involved in this study. Note that

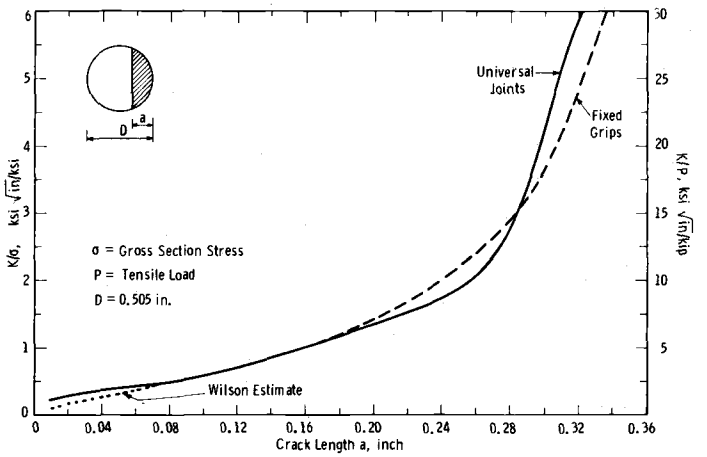

FIG. 5—K *calibration for a 0.505-in.-diameter round tensile bar with an edge crack.*

for the case of the compact toughness specimens the notch depth, a as well as the notch radius, r, vary among specimens. Table 2 also includes the net section stress, σ_N, relationship with applied load for the test specimens involved in this investigation. The values of σ_N for the tension and bend specimen were determined from the conventional force-equilibrium equations involving net section area and outer fiber bending stress (at the notch surface), respectively. The value of σ_N for the compact-toughness specimens was computed from the nominal stress equation developed by Wilson [*13*]

$$\sigma_N = \left[\frac{3(W + a)}{W - a} + 1 \right] \frac{P}{(W - a)} \tag{3}$$

where W is the test specimen length measured from the centerline of loading (2.55 in. or 6.48 cm in this case).

Experimental Results

Figures 6, 7, and 8 present the results of the blunt-notch, H_2S gas environment, stress-corrosion, crack-initiation testing for each of the three test specimen geometries and the two steels involved in this investigation. Data generated with fatigue precracked test specimens ($r \rightarrow 0$) also are included for reference purposes. The test results are expressed in terms of the net section failure stress (also, in this case, the stress associated with the onset of cracking at the notch tip) versus the square root of the notch-tip radius. This method of presenting the data was chosen primarily to provide a convenient graphical display (rather than plotting failure load versus

TABLE 2—*Summary of blunt-notch analyses.*

Edge-Notched Tensile Specimen 0.505 in. (1.28 cm) diameter 0.188 in. (0.48 cm) deep notch	$\sigma_N = 7.7P$	$K_I = 7.0P$	$\sigma_{max} = 7.9P/\sqrt{r}$
		$r = 0.01$ in. (0.025 cm)	$79P$
		$r = 0.02$ in. (0.051 cm)	$56P$
		$r = 0.09$ in. (0.228 cm)	$26P$
Edge-Notched Three-Point Bend Specimen 0.4 in. (1.0 cm) x 0.5 in. (1.27 cm) 1.6 in. (4.06 cm) span 0.200 in. (0.51 cm) deep notch	$\sigma_N = 67P$	$K_I = 2.24P$	$\sigma_{max} = 25.3P/\sqrt{r}$
		$r = 0.01$ in. (0.025 cm)	$253P$
		$r = 0.02$ in. (0.051 cm)	$180P$
		$r = 0.09$ in. (0.228 cm)	$84P$

Compact Toughness Specimen 1 in. (2.54 cm) thick WOL	σ_N	K_I	σ_{max}
$r = 0.003$ in. (0.007 cm), $a = 0.767$ in. (1.96 cm)	$3.7P$	$4.1P$	$84P$
$r = 0.010$ in. (0.025 cm), $a = 1$ in. (2.54 cm)	$5.0P$	$5.0P$	$56P$
$r = 0.050$ in. (0.127 cm), $a = 1.5$ in. (3.81 cm)	$12P$	$8.2P$	$41P$
$r = 0.100$ in. (0.254 cm), $a = 2.0$ in. (5.08 cm)	$47P$	$22.2P$	$79P$
$r = 0.160$ in. (0.406 cm), $a = 2.0$ in. (5.08 cm)	$47P$	$22.2P$	$62P$

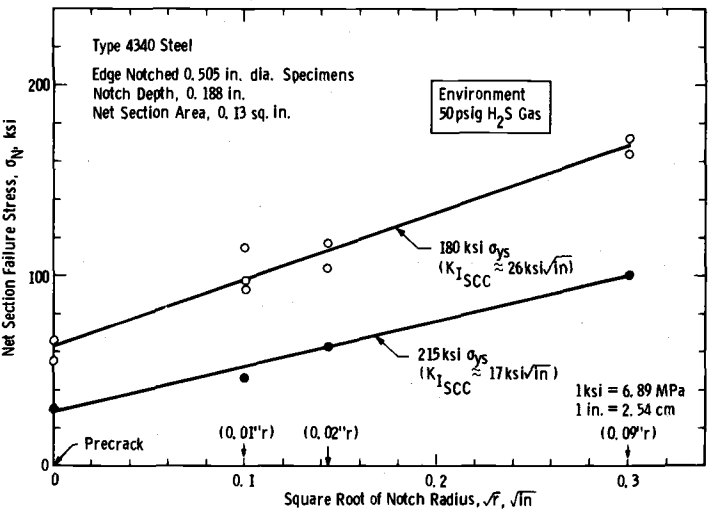

FIG. 6—*Net section failure stress versus* $\sqrt{r}$, *tension specimens.*

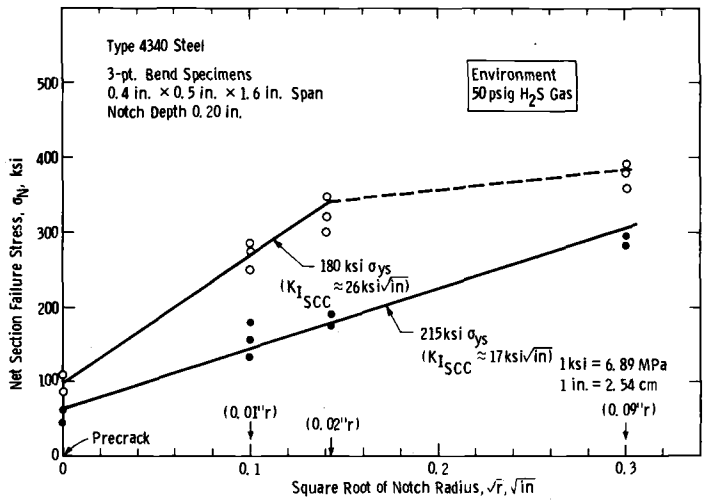

FIG. 7—*Net section failure stress versus* $\sqrt{r}$, *bend specimens.*

notch radius). Since both the tension and bend bar test specimens had constant notch depths, the actual failure load, P, for each test can be determined easily by dividing σ_N by the appropriate factor given in Table 2 (7.7 and 67 for the tensile and bend bars, respectively). The compact-toughness specimens involved various notch radii as well as various notch depths; thus, P cannot be determined from Fig. 8. Table 3 presents a summary of the compact-toughness specimen test results.

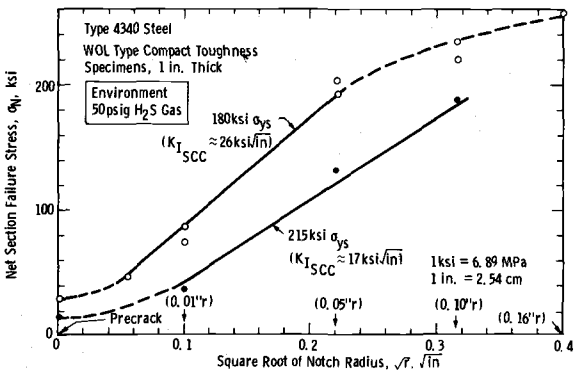

FIG. 8—*Net section (nominal) failure stress versus* $\sqrt{r}$, *compact toughness specimens.*

Note that all of the blunt-notch data (excluding the precracked wedge opening load (WOL) tests) generated with the 215 ksi (1480 MPa) yield-strength material exhibit a linear relationship between σ_N and $\sqrt{r}$. This is not the case for the 180 ksi (1240 MPa) yield-strength material. Specifically, deviation from the general linear behavior is encountered with the larger notch-radii tests conducted with the bend bars and compact toughness specimens (dotted line behavior in Figs. 7 and 9). This deviation behavior reflects the "limit load" (the load at which a specimen becomes fully plastic) characteristics of the specific test specimen geometries being considered [*14*]. In general, a tension specimen reaches limit load at a nominal stress approximately equal to the materials yield strength. For the case of a bend bar, limit load is reached at 1.5 to 2 times the materials yield strength. The limit load for the compact-toughness specimen, which includes both a bending and tension component, is expected to be somewhere between that of a tension specimen and a bend specimen. Based on these limit load considerations and the data presented in Figs. 6, 7, and 8, we can conclude that below limit load conditions, a linear relationship exists between the net section stress required to develop a stress-corrosion crack at the tip of a blunt notch and the square root of the notch radius. Note, however, that this relationship is specimen dependent. Specifically, for a given notch radius, the net section failure stress varies considerably with specimen type. Obviously, a quantitative characterization of blunt-notch stress corrosion performance cannot be based on nominal stress considerations.

Figure 9 presents the results of this investigation expressed in terms of the elastically calculated maximum notch stress, σ_{max}, determined from fracture-mechanics considerations as described previously (Table 2) and the square root of the notch radius. Note that for a given material and given notch radius, the minimum value of maximum notch stress required

TABLE 3—*Summary of compact toughness specimen test results.*

Specimen Identification	Notch Radius, r, in. (cm)	Notch Length, a, in. (cm)	Crack Initiation [a] Load, P, kip (MN)	Nominal [a] Stress, σ_N, ksi (MPa)	Maximum [a] Notch Stress, ksi (MPa)
		180 ksi (1241 MPa) Yield Strength Material			
4-35	0.003 (0.008)	0.767 (1.95)	12.8 (56.9)	47.4 (326)	1075 (7525)
3-35	0.010 (0.025)	1.000 (2.54)	17.7 (78.7)	88.5 (610)	991 (6937)
3-36	0.010 (0.025)	1.000 (2.54)	15.0 (66.7)	75.0 (525)	840 (5880)
3-34	0.050 (0.127)	1.50 (3.81)	17.0 (75.6)	204 (1428)	680 (4760)
3-36	0.050 (0.127)	1.50 (3.81)	16.0 (71.2)	192 (1344)	640 (4480)
3-34	0.100 (0.254)	2.00 (5.08)	5.0 (22.2)	235.0 (1645)	395 (2765)
3-35	0.100 (0.254)	2.00 (5.08)	4.7 (21.0)	220.0 (1540)	371 (2600)
4-35	0.160 (0.406)	2.00 (5.08)	5.5 (20.9)	258.0 (1806)	341 (2387)
		215 ksi (1482 MPa) Yield Strength Material			
169-19	0.010 (0.025)	1.00 (2.54)	7.75 (34.4)	38.8 (272)	434 (3038)
169-19	0.050 (0.127)	1.50 (3.81)	11.0 (48.9)	132.0 (924)	451 (3151)
169-15	0.100 (0.254)	2.00 (5.08)	4.0 (17.8)	188.0 (1316)	316 (2212)

[a]At onset of cracking at notch.

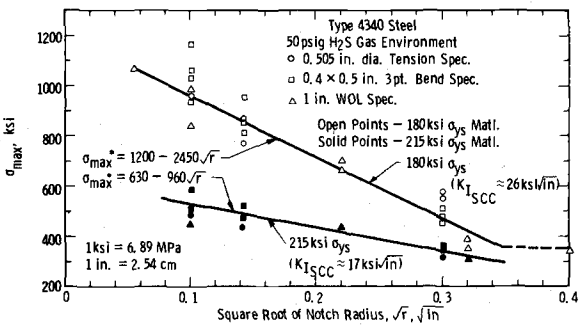

FIG. 9—*Maximum failure stress versus* $\sqrt{r}$.

to develop a stress-corrosion crack (designated here as σ_{max}*) is essentially independent of the specific test specimen geometry. Also note, however, that an inverse linear relationship exists between σ_{max}* and $\sqrt{r}$ for notch radii ranging from 0.003 in. (0.008 cm) to 0.100 in. (0.254 cm). These data clearly demonstrate that the onset of stress-corrosion cracking at a blunt notch is not dependent on σ_{max} alone. Specifically, the maximum notch stress required to initiate a stress-corrosion crack from a blunt notch increases as the notch radius decreases. The specific relationships between σ_{max}* and $\sqrt{r}$ for the two steels evaluated in this investigation are noted in Fig. 9.

Figure 9 also shows that based on a single data point at a notch radius of 0.160 in. (0.41 cm) developed for the 180 ksi (1240 MPa) yield-strength material, a minimum value of σ_{max} may exist below which stress-corrosion crack initiation will not occur.

Discussion

The results of this investigation clearly demonstrate that the onset of stress-corrosion cracking at a blunt notch depends upon both the elastically calculated maximum notch stress and the specific notch radius being considered. Similar behavior has been noted by Barsom and McNicol in the evaluation of fatigue-crack initiation performance [*5*]. Specifically, Barsom and McNicol found that at relatively low-applied stress levels, the number of cycles required to develop a fatigue crack, N_i, was dependent directly upon the elastically calculated maximum notch stress; however, as the applied stress level increased, the relationship between σ_{max} and N_i became dependent upon the notch radius being considered. This interaction between the maximum stress required to develop a crack at a blunt notch and the notch radius has been explained in an extensive elastic-plastic analysis of blunt-notched compact toughness specimens conducted by Wilson [*13*]. Figure 10 presents a schematic representation of Wilson's

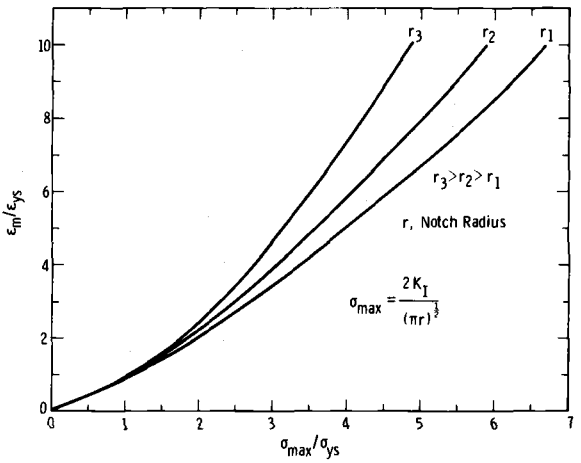

FIG. 10—*Schematic representation of maximum total strain versus maximum elastic-notch stress.*

analytical results showing the maximum total strain versus the maximum elastic-notch stress for three specimens with various notch radii. Note that as the notch radius increases, the total strain corresponding to a given maximum stress also increases. Note also that at a constant total strain level, the maximum notch stress decreases with increasing notch radius. Consideration of this analysis and the fact that the maximum notch stress required to develop a crack decreases with increasing r (Fig. 9 and Ref 5) clearly implies that crack initiation (both stress corrosion and fatigue initiation) is primarily a strain-dependent phenomenon.

Although the foregoing analysis shows that the notch-tip strain, rather than stress, is likely to be the most sensitive parameter for the characterization of crack-initiation performance, it is often extremely difficult, if not impossible, to determine the magnitude of strains at the tip of a narrow notch. Consequently, it is generally more realistic to consider other parameters which can be related to the notch-tip strains. As noted previously, the parameter σ_{max} can be used for this purpose when the notch-stress levels involved in the development of a crack are relatively small (on the order of the materials tensile strength or less). However, for the case of stress-corrosion crack initiation the σ_{max} levels will generally be higher than the materials tensile strength;[5] thus, it is necessary to consider both σ_{max} and $\sqrt{r}$ in the development of a correlation with the notch-tip strain. The same situation would apply to the consideration of low-cycle fatigue performance.

[5]Note that even for the low-stress corrosion resistant, high-strength 4340 steel evaluated in this program, notch-tip stresses in excess of the material's tensile strength were required to develop a crack.

The test results developed in this investigation apply specifically to the evaluation of the notch-tip condition below which a stress-corrosion crack will not develop, and no consideration is given to the time required to develop a crack. In fact, the H_2S gas test environment was chosen primarily to eliminate time-dependent phenomena from the evaluation. For such cases where time-dependent phenomena are not being considered, experimental data similar to that shown in Fig. 9 can be used directly as a quantitative estimate of stress-corrosion crack initiation performance. If the material-environment system to be evaluated yields relatively rapid crack initiation, rising load tests (in the environment of interest) representing three different notch radii could be conducted and a σ_{max}* versus $\sqrt{r}$ curve developed as was done in this investigation. This information could then be used to predict the applied stress required to develop a stress-corrosion crack for an actual component where σ_{max} and $\sqrt{r}$ are known. Conversely, such data could be used to evaluate the severity of a given notch geometry (notch depth and radius) in a known stress field. The actual calculations involved in such analyses simply require rewriting Eq 1 and the appropriate stress intensity expressions for the component involved and solving for the parameter of interest.

For the case of a material-environment system where the time required to develop a crack is relatively long and a rising load test does not yield accurate results, it would be necessary to conduct long time tests with a series of specimens representing two or three different notch radii to establish the corresponding maximum notch stress required to develop a crack. A test procedure similar to the cantilever beam stress-corrosion test developed by Brown could be used to find the value of σ_{max} for the various notch radii being evaluated [*15*].

The interaction between σ_{max}, $\sqrt{r}$, and stress-corrosion performance demonstrated in this investigation clearly indicates that an optimum approach to the characterization of blunt-notch crack initiation behavior would be to incorporate both σ_{max} and $\sqrt{r}$ into a single parameter which could then be related to the notch-tip strain. In fact, such a correlation is required to characterize crack-initiation behavior in terms of a time-dependent parameter such as elapsed cycles or crack incubation time. In order to develop a single parameter which relates σ_{max} and $\sqrt{r}$ to notch-tip strain, it is necessary to determine (measure or calculate) the actual strain at the notch tip in a series of simple specimens. Obviously, the relationship between σ_{max} and $\sqrt{r}$ and the notch-tip strain will depend upon the stress-strain characteristics of the material involved, and, if cyclic loading is being considered, the cyclic stress-strain curve must be used. A detailed analysis of the notch-tip strain as a function of the elastically calculated notch-tip stress and the specific notch radius is currently underway, and it is expected that the results of this analysis will yield a simple expression

which can be used to predict the notch-tip strain and, ultimately, the crack-initiation performance of structural materials.

If we assume that stress-corrosion crack initiation is a strain-dependent phenomenon and that a critical value of strain exists below which a stress-corrosion crack will not grow, the relationship between σ_{max} and $\sqrt{r}$ shown in Fig. 9 for each material can be interpreted to represent the combination of σ_{max} and $\sqrt{r}$ required to provide a constant strain level at the notch tip. For the case of the 180 ksi (1240 MPa) yield strength steel, we can estimate the critical value of strain from a Neuber's rule analysis of the compact toughness test with the 0.16 in. (0.41 cm) notch radius (Fig. 9) [*16*]. This analysis yields a critical value of strain on the order of 2.5 percent. Thus, based on the previous assumptions, we can conclude that the σ_{max} versus $\sqrt{r}$ relationship shown in Fig. 9 for the 180 ksi (1240 MPa) yield-strength material represents the combination of σ_{max} and $\sqrt{r}$ required to develop 2.5 percent strain and, consequently, stress-corrosion cracking in the H_2S gas environment.

The stress-corrosion, crack-initiation data generated in this investigation clearly demonstrates that the elastically calculated maximum notch-stress parameter may provide the basis for a truly quantitative approach to the characterization of blunt-notch crack initiation. Obviously, a substantial amount of additional testing and analysis is required to substantiate the use of this parameter further and determine the specific limitations. One additional area of particular concern is the potential applicability of this parameter to wide notch-type stress concentrations such as holes and grooves. Plans are being made currently to evaluate these geometries.

Summary and Conclusions

The stress-corrosion, crack-initiation performance of two high-strength AISI type 4340 steels was evaluated with three widely different blunt-notched toughness specimens subjected to slow-rate, rising load testing in a H_2S gas environment. The onset of stress-corrosion cracking was evaluated as a function of the blunt-notched radius and the results expressed in terms of the elastically calculated notch stress determined from fracture-mechanics considerations. Based on the results of this investigation, a test procedure and analytical method is proposed which can be used to predict the applied stress required to develop stress-corrosion cracking at a blunt notch.

The pertinent conclusions associated with this investigation in which K_{Iscc} was used as the principal measure of stress-corrosion resistance are summarized below.

1. The onset of stress-corrosion cracking from a narrow blunt notch

is dependent upon the elastically calculated maximum notch stress and the notch-tip radius.

2. For notch radii smaller than 0.100 in. (0.254 cm), an inverse linear relationship exists between the maximum notch stress and the square root of the notch radius required to cause stress-corrosion crack initiation.

3. The elastically calculated notch-tip stress and the notch-tip radius can be related to the notch-tip strain which, in turn, is the controlling mechanical parameter for stress-corrosion crack initiation.

4. An experimental test procedure involving the use of relatively simple notched specimens can be used to develop a quantitative measure of stress-corrosion, crack-initiation performance.

Acknowledgments

The author would like to thank J. D. Landes and W. K. Wilson for their helpful discussions and comments on the analysis of the test results.

The experimental work was conducted by P. J. Barsotti and W. H. Halligan under the direction of D. R. Young of the Fracture Mechanics Laboratory. The work was sponsored by the Westinghouse Large Rotating Apparatus Division.

References

[1] Wei, R. P., Novak, S. R., and Williams, D. P., "Some Important Considerations in the Development of Stress Corrosion Cracking Test Methods," *Materials Research and Standards,* Vol. 12, No. 4, 1972.

[2] Johnson, H. H. and Paris, P. C., "Subcritical Flaw Growth," *Engineering Fracture Mechanics,* Vol. 1, No. 1, 1968.

[3] *Stress Corrosion Cracking of Metals—A State of the Art, ASTM STP 518,* American Society for Testing and Materials, 1972.

[4] Jack, A. R. and Price, A. T., "The Initiation of Fatigue Cracks from Notches in Mild Steel Plates," *International Journal of Fracture Mechanics,* Vol. 6, No. 4, 1970.

[5] Barsom, J. M. and McNicol, R. C., in *Fracture Toughness and Slow-Stable Cracking, ASTM STP 559,* American Society for Testing and Materials, 1974, pp. 183–204.

[6] Clark, W. G., Jr., in *Fracture Toughness and Slow-Stable Cracking, ASTM STP 559,* American Society for Testing and Materials, 1974, pp. 205–224.

[7] Clark, W. G., Jr., in *Cracks and Fracture, ASTM STP 601,* American Society for Testing and Materials, 1976, pp. 138–153.

[8] Clark, W. G., Jr. and Landes, J. D. in *Stress Corrosion—New Approaches, ASTM STP 610,* American Society for Testing and Materials, 1976, pp. 108–127.

[9] Paris, P. C. and Sih, G. C., "Stress Analysis of Cracks," *Fracture Toughness Testing and Its Application, ASTM STP 381,* American Society for Testing and Materials, 1965, pp. 30–83.

[10] Gross, B. and Srawley, J. E., "Stress-Intensity Factors for a Single-Edge-Notch Specimen in Bending or Combined Bending and Tension by Boundary Collocation of a Stress Function," NASA Technical Note D-2063, National Aeronautics and Space Administration, Jan. 1965.

[11] Brown, W. F., Jr. and Srawley, J. E., *Plane Strain Crack Toughness Testing of High Strength Metallic Materials, ASTM STP 410,* American Society for Testing and Materials, 1967.

[*12*] Wilson, W. K., "Stress Intensity Factors for Compact Tension Specimens," Westinghouse Research Memo 67-1D6-BTLFR-M1, June 1967.
[*13*] Wilson, W. K., *Journal of Pressure Vessel Technology,* Vol. 96, Nov. 1974, p. 293.
[*14*] Landes, J. D. and Begley, J. A., in *Fracture Toughness ASTM STP 514,* 1972, pp. 24–39.
[*15*] Brown, B. F., "A New Stress-Corrosion Cracking Test for High-Strength Alloys," *Materials Research and Standards,* Vol. 6, No. 3, March 1966.
[*16*] Neuber, H., "Theory of Stress Concentration for Shear Strained Prismatical Bodies with Arbitrary Nonlinear Stress-Strain Law," *Journal of Applied Mechanics,* Dec. 1961.

N. E. Dowling[1]

Fatigue-Crack Growth Rate Testing at High Stress Intensities

REFERENCE: Dowling, N. E., "**Fatigue-Crack Growth Rate Testing at High Stress Intensities,**" *Flaw Growth and Fracture, ASTM STP 631,* American Society for Testing and Materials, 1977, pp. 139–158.

ABSTRACT: Controlled load fatigue-crack growth rate tests are conducted using compact specimens of various widths between 1 and 10 in. Two engineering metals are tested: A533B pressure vessel steel and A469 alloy rotor steel. In these high-toughness materials, the upper limit of data interpretation based on linear-elastic analysis appears to be controlled by fully plastic limit load behavior. This resulted in the largest specimens yielding data at higher stress intensities than can be investigated in the smaller specimens usually employed in fatigue-crack growth rate testing. Test methods and limitations relative to plasticity are discussed, and it is recommended that deflections be monitored during load controlled testing. Some observations also are made concerning the relevance of static fracture toughness to failure following fatigue-crack growth.

KEY WORDS: crack propagation, cracks, fractures (materials)

The stress-intensity parameter, K, is used widely for correlation of fatigue-crack growth rates. As the stress-intensity concept is based on linear-elastic analysis, its use should be limited by plasticity considerations. However, for fatigue-crack growth rate testing, no consensus exists at the present time as to the details of these plasticity limitations, and, often, no such limitations are observed. This is in contrast to the situation for static fracture toughness testing, where the stress-intensity concept is employed subject to the strict plasticity limitations and resulting size requirements of the ASTM Test for Plane-Strain Fracture Toughness of Metallic Materials (E 399-74). For fatigue-crack growth rate testing, an ASTM standard is currently being developed [*1*][2] and, in this development, some consideration must be given to plasticity limitations and possible specimen size requirements.

In this paper, experimental data and discussion which relate to plasticity

[1] Senior engineer, Westinghouse Research Laboratories, Pittsburgh, Pa. 15235.

[2] The italic numbers in brackets refer to the list of references appended to this paper.

limitations and specimen size effects in fatigue-crack growth rate testing at high stress intensities are presented. Two intermediate strength steels are tested using specimens over a range of sizes. Some observations are made concerning the failures which terminated fatigue-crack growth in these tests, and the relevance of static fracture toughness to failure following fatigue-crack growth is discussed. Testing problems occurring just prior to specimen failure, plasticity limitations, and size effects also are considered.

Laboratory Investigation

Materials and Specimens

The two materials tested were A533B pressure vessel steel with 70 ksi yield strength and A469 alloy rotor steel with 96 ksi yield. Additional mechanical properties of these steels are given in Table 1, and their nominal compositions conform to the correspondingly numbered ASTM specifications.

TABLE 1—*Mechanical properties of materials tested.*

ASTM Specification	Yield Strength, ksi	Ultimate Strength, ksi	Elongation in 2 in., %	Reduction in Area, %	Charpy V-Notch Data	
					ft·lb at 75 °F	FATT, °F
A533B, class 1	70	91	28	69	73	95
A469, class 5	96	114	20	58	56	55

Compact specimens of the two types described in Fig. 1*a* were tested. Most specimens (type CT) were of the same proportions as the ASTM Method E 399-74 fracture toughness specimen. A limited number of wedge opening load (WOL) specimens having somewhat different proportions were also tested. This geometry has been employed previously in fracture mechanics testing [*1–3*]. The specific specimen types and sizes tested are listed in Table 2, where, with reference to Fig. 1*a*, the dimension W gives the specimen size. Later, some test data from other sources will be referred to where the thickness of the specimens used did not conform to Fig. 1*a*. In these cases, the B dimension will be given in addition to W.

Test Procedures

All tests were conducted on closed loop electrohydraulic testing equipment. Simple tension to tension constant amplitude load cycling was

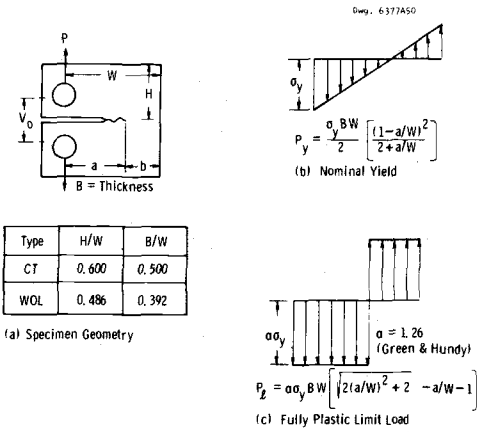

Type	H/W	B/W
CT	0.600	0.500
WOL	0.486	0.392

(a) Specimen Geometry

FIG. 1—*Compact specimen geometry; also, loads and assumed stress distribution in the uncracked ligament for both nominal and fully plastic yielding.*

employed with the specific test loads applied being given in Table 2. A value of $R = P_{min}/P_{max} = 0.025$ was used for all tests. For some tests, the maximum load was sufficiently high for nominal yielding (Fig. 1*b*) to occur in the first cycle. The test loads employed were chosen on the basis of estimated fully plastic limit load failure at the specific crack lengths given in Table 2. Figure 1*c* was used in making these estimates—the constraint factor $\alpha = 1.26$ being taken from the pure bending slip-line field analysis of Green and Hundy [*4,5*].

To obtain data for computing fatigue-crack growth rates, surface crack lengths were monitored visually on both sides of the specimen using two low-power (×20) travelling microscopes. Deflections during cyclic loading were monitored by a clip gage attached to the front face of the specimen over a gage length such as V_0 in Fig. 1*a*. So that crack growth and deflection data could be taken until just prior to specimen failure, the frequency of cycling was decreased several times during each test. This allowed the rate of crack extension with time to be held roughly constant. Initial and terminal values of test frequency are given in Table 2 for each test conducted.

Prior to testing, each specimen was precracked at low stress in a manner generally consistent with the requirements of ASTM Method E 399-74.

Data Reduction

Cyclic crack-growth rates during each test were determined from crack length versus cycles data (*a* versus *N*) by the incremental polynomial procedure described in Ref *1*. In this procedure, a second order polynomial is fitted through the first seven data points. The first derivative of

TABLE 2—*Description of fatigue crack growth rate tests.*

Specimen Description			Maximum Load [a] P_{max}, kips	Estimated Final a/W From Limit Load	Range of "a versus N" Data [b]		Test Frequency, Hz	
No.	Type	W, in.			Initial a/W	Final a/W	Initial	Final
			A533B Pressure Vessel Steel					
1/2T54	CT	1.00	2.17	0.60	0.50	0.64	0.3	0.3
1/2T55	CT	1.00	1.16	0.70	0.50	0.74	5.0	5.0
1T59	CT	2.00	14.3	0.50	0.40	0.53	0.2	0.03
1T51	CT	2.00	8.68	0.60	0.50	0.64	0.3	0.05
1T53	CT	2.00	4.64	0.70	0.50	0.72	2.0	2.0
1T52	CT	2.00	1.95	0.80	0.50	0.82	30	1.0
2T40	CT	4.00	34.7	0.60	0.50	0.62	0.3	0.05
2T41	CT	4.00	18.6	0.70	0.50	0.70	0.5	0.1
4T6	CT	8.00	139	0.60	0.50	0.61	0.2	0.2
4T5	CT	8.00	74.2	0.70	0.50	0.70	0.8	0.8
			A469 Alloy Rotor Steel					
1T37	CT	2.00	11.9	0.60	0.49	0.62	0.3	0.1
1T40	CT	2.00	6.35	0.70	0.49	0.71	0.3	0.05
2T96	CT	4.00	35.6	0.65	0.50	0.63	0.1	0.05
2T70	CT	4.00	17.2	0.75	0.50	0.74	0.3	0.025
4T18	WOL	10.22	182	0.65	0.38	0.54	0.25	0.1
4T16	WOL	10.22	87.8	0.75	0.44	0.65	2.5	2.0

[a] For all tests $R = P_{min}/P_{max} = 0.025$.
[b] Surface crack lengths.

this polynomial is then evaluated at the central data point to obtain a crack-growth rate, da/dN. The same operation is then applied to the second through eighth, third through ninth, etc., data points so as to obtain crack-growth rates at various numbers of cycles during the test.

Values of stress-intensity range, ΔK, suitable for correlating with crack-growth rates were determined from measured crack lengths and load ranges, $\Delta P = P_{max} - P_{min}$, by the usual methods of linear-elastic fracture mechanics. The K-calibration polynomial fit from ASTM Method E 399-74 was used for CT specimens out to dimensionless crack lengths, a/W, of 0.7, and, for WOL specimens, the polynomial given in Refs *1* and *3* was used also out to $a/W = 0.7$. At larger values of a/W, these polynomial fits are not applicable [*6*]; hence, the analysis of Ref *7* was used.

Test Results

The fatigue-crack growth rate versus stress-intensity data obtained are shown in Figs. 2 and 3. Additional data from Refs *8* and *9* also are plotted. In the case of A533B, these additional data are for material having nominally the same mechanical properties and composition as that tested here. All of the A469 data plotted are for material from a single rotor forging. In Figs. 2 and 3, open symbols are used to distinguish data taken

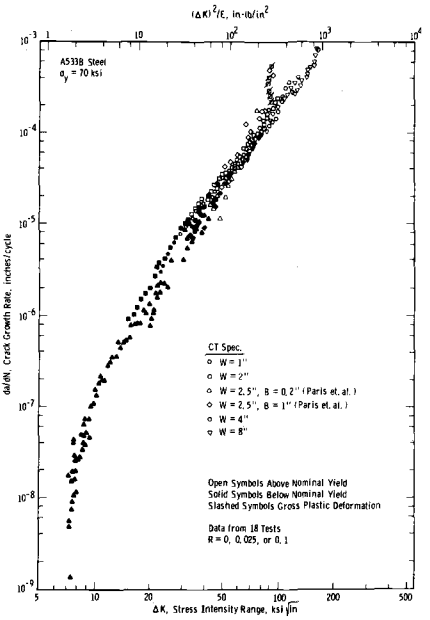

FIG. 2—*Fatigue-crack growth rate versus stress intensity for various size specimens of A533B steel.*

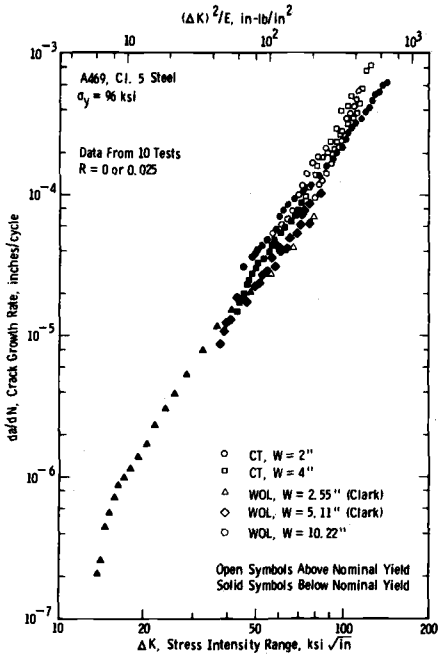

FIG. 3—*Fatigue-crack growth rate versus stress intensity for various size specimens of A469, Class 5 steel.*

at combinations of maximum cyclic load and crack length which exceeded nominal yielding (see Fig. 1*b*).

Typical deflection versus cycles behavior is shown in Fig. 4. For most tests, the behavior was similar to Fig. 4*a* and *b* in that specimen failure was associated with large increase in mean deflection over a relatively small number of cycles. As illustrated qualitatively in terms of loads and deflections in Fig. 5, such deformations cannot be explained in terms of linear-elastic behavior. Linear-elastic deformation would result in the minimum deflection remaining a constant fraction of the maximum deflection, with this fraction being the same as $R = P_{min}/P_{max}$ for the applied loads. Any excess deflection is due to plastic deformation, as illustrated by $V_{plastic}$ in Fig. 5. Such plastic deflections were observed to begin when the crack had grown to a length corresponding approximately to limit load for the applied P_{max}.

The deflection range, ΔV in Fig. 5, never deviated significantly from expectations based on linear elasticity. In other words, the cyclic plasticity, as indicated by the formation of a load versus deflection hysteresis loop, was never observed to be large.

Plastic-deflection behavior was accompanied by a rapid increase in crack-growth rate—more so in the center of the specimen than at the

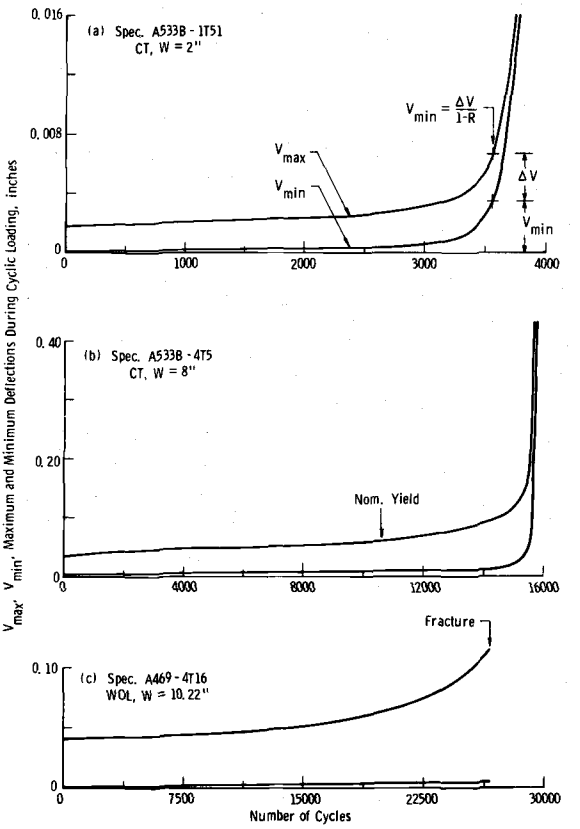

FIG. 4—*Typical deflection versus cycles behavior during fatigue-crack growth.*

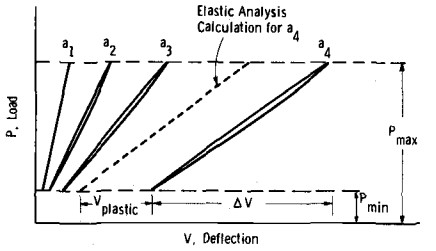

FIG. 5—*Effect of plastic deformation on load versus deflection behavior during fatigue-crack growth rate testing.*

edges. (Prior to the onset of this behavior, most specimens exhibited only slight crack front curvature.) Crack growth during this phase may be identified on the fracture surfaces in Fig. 6 by the dark, usually crescent shaped, areas. This area is especially evident in Fig. 6 for specimen 2T41.

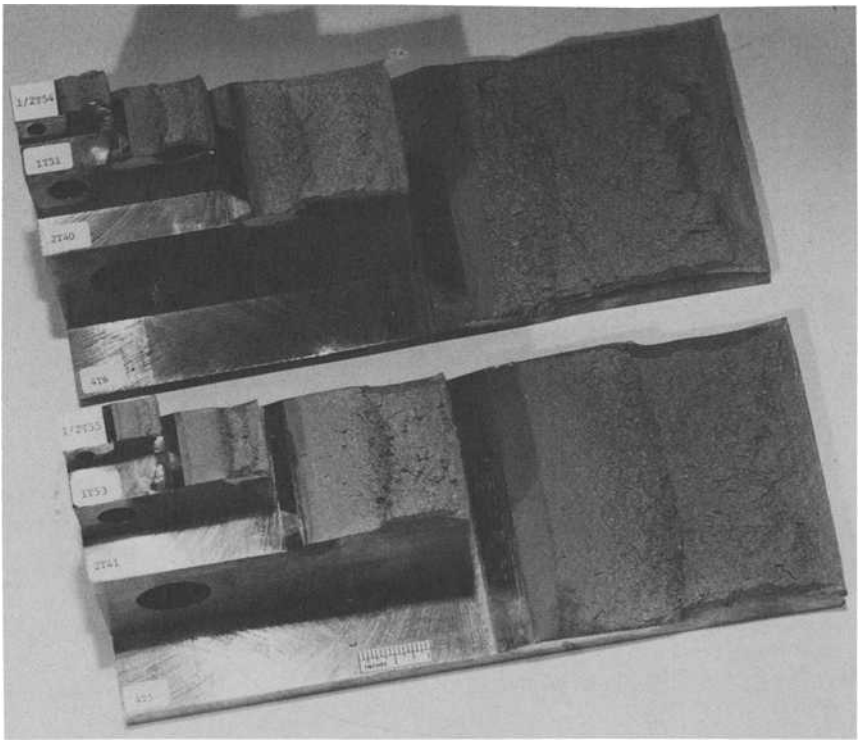

FIG. 6—*Fracture surfaces for limit-load failures following fatigue-crack growth in various size specimens of A533B steel.*

Hence, failure of these specimens occurred incrementally over a number of cycles and involved a tearing sort of propagation for a considerable crack length before final fracture occurred. No meaningful crack-growth rate data could be obtained during the plastic-deflection phase of specimen life.

Contrasting behavior was exhibited by the two large size specimens of A469, where fatigue-crack growth was simply terminated in an abrupt manner by brittle fracture. As illustrated by Fig. 4*c*, no unusual deflection behavior occurred. In one additional specimen, A469-2T96, sudden fracture occurred after a small amount of plastic deflection.

Stress intensities and crack lengths are plotted in Figs. 7 and 8 for failure of all specimens tested. In those tests where final fracture was preceded by tearing and large plastic deflections, failure was arbitrarily defined as the onset of this process. In particular, failure was defined as occurring when the excess minimum deflection due to plastic deformation had increased so that it was equal to the deflection range. With reference to Fig. 5, this arbitrary definition of failure is given by

$$V_{\text{plastic}} = \Delta V$$

which results in

$$V_{\min} = V_{\text{elastic}} + V_{\text{plastic}}$$

$$V_{\min} = \frac{\Delta V}{1 - R}$$

Application of the above is illustrated in Fig. 4*a*.

Lines indicating limit load predictions of failure according to Fig. 1*c* are shown in Figs. 7 and 8. Also shown are static fracture toughness data [*10*] for these two steels. In plotting these fracture toughness data, solid symbols are used for valid ASTM Method E 399-74 plane-strain fracture toughness values, K_{Ic}. Half-solid symbols are used to denote K_Q values which do not meet the size requirements of ASTM Method E 399-74 for plane strain, but which do correspond to linear fracture, that is, complete failure or pop-in prior to the specified 5 percent load-deflection secant line. The slashed symbols indicate values of K_{Ic} calculated from J_{Ic} for plastically deformed specimens analyzed as described in Ref *11*. All of the data of this type that are shown are for tests where sudden cleavage fracture occurred with no previous slow crack extension. Thus, unambiguous

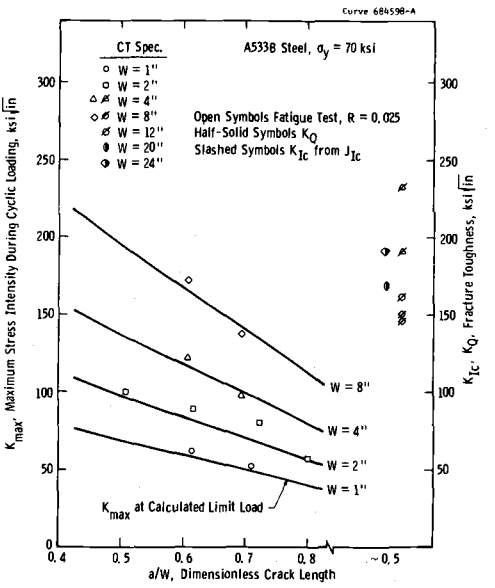

FIG. 7—*Maximum stress intensities for failure following fatigue-crack growth in A533B steel.*

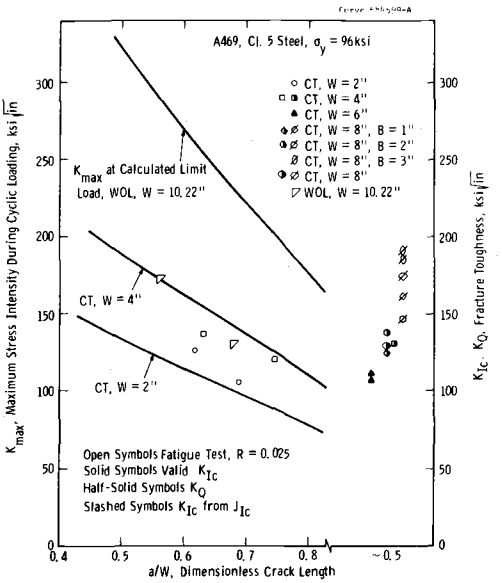

FIG. 8—*Maximum stress intensities for failure following fatigue-crack growth in A469 steel.*

identification of the fracture point was possible even under plastic deformation.

Discussion

Failure Following Fatigue-Crack Growth

From Fig. 7, the onset of the plastic deformation behavior terminating fatigue-crack growth in A533B steel was predicted quite accurately using a simple equation based on fully plastic limit load. Furthermore, the maximum stress intensities attainable were size dependent in a manner clearly consistent with limit-load failure. In one of the large size specimens, the stress intensity reached was within the fracture toughness range. However, limit load failure, even in this case, is not surprising in view of the fact that linear static K_Q fractures in this very high-toughness material require the additional constraint accompanied by an additional doubling of specimen size.

For the two smaller specimen sizes of A469, the agreement with limit-load predictions in Fig. 8 is reasonable, although not as good as for A533B. However, the two largest specimens tested failed in an elastic manner far below limit load. These two failures are consistent with the linear fractures (K_Q and K_{Ic}) which occurred for this material in static tests on specimens of similar and lesser thickness.

These data on A533B and A469 steels suggest that failure terminating fatigue-crack growth is controlled by either limit load or fracture toughness, whichever occurs first. Some additional test data bearing on this subject from exploratory tests by Begley [*12*] are illustrated in Figs. 9 and 10. Figure 9 represents a straightforward case of fracture toughness controlled failures terminating fatigue-crack growth in 7075-T651 aluminum alloy. However, in Fig. 10, contrasting behavior occurred for a low-toughness A470 steel. Surprisingly, the specimens subjected to cyclic loading passed through the static fracture toughness and failed due to fully plastic limit load at much higher stress intensities. Note that linear static K_Q fractures are shown for specimens of the same thickness as those tested in fatigue and that one of the fatigue specimens failed at a low stress intensity when cycling was interrupted by static testing.

Apparently, cyclic loading increased the fracture toughness of the A470 steel of Fig. 10. No case of the reverse behavior, namely, a decrease in fracture toughness due to cyclic loading, is known to the writer. Hopefully, this never occurs, but the possibility cannot be ruled out without knowing the particular physical mechanism causing the unexpected behavior of A470 steel.

It is useful to discuss in some detail the nature of limit-load failure during cyclic loading. For an ideal elastic, perfectly plastic, material, Fig. 11 schematically illustrates the deformations ahead of a growing fatigue crack under tension to tension loading. Consider a point, the position of which changes relative to the crack tip as from 1 to 6 in Fig. 11*b*. When the point is far removed from the crack tip, as at 1 and 2, simple linear-

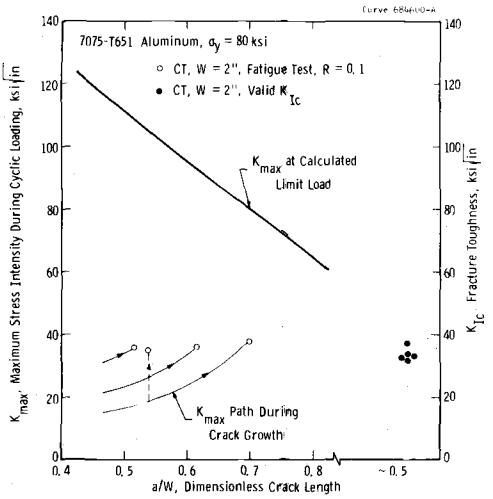

FIG. 9—*Fracture toughness failures terminating fatigue-crack growth in 7075-T651 aluminum* [12].

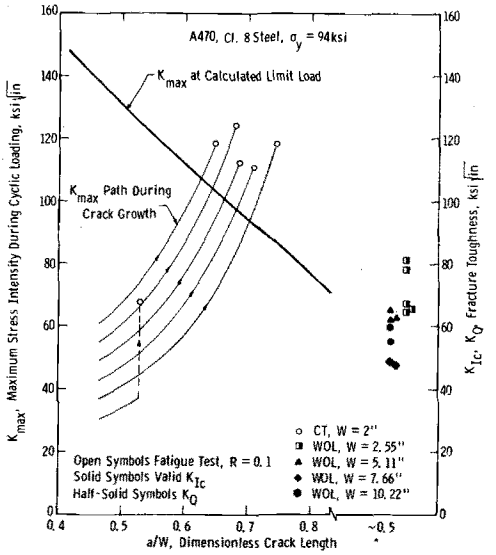

FIG. 10—*Unexpected fully plastic limit load failures following fatigue-crack growth in A470 steel* [12].

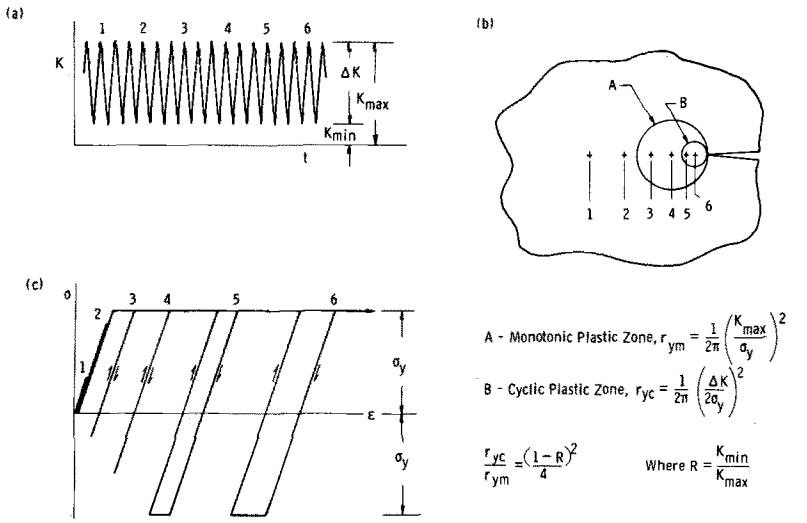

FIG. 11—*Stress-strain behavior at a point being approached by the tip of a growing fatigue crack. In* (c)*, the reversed stresses and strains are shown for selected cycles only.*

elastic, stress-strain behavior occurs. On closer approach of the crack tip, as at 3 and 4, tensile yielding occurs on each cycle, but the reversed deformations are still elastic. For small-scale plasticity, the distance ahead of the crack tip where monotonic tensile yielding first occurs may be estimated by using the maximum cyclic stress intensity with the Irwin plastic zone size equation [*13*].

Reversed yielding does not occur until the crack tip has approached to within a distance determined by the stress-intensity range and the condition that the strain ranges must exceed twice the yield strain. The extent of this zone of cyclic plasticity may be estimated [*14,15*] by an equation of the same form as before, but K_{max} is replaced by ΔK and σ_y by $2\sigma_y$. Note that the cyclic plastic zone is nominally one fourth as large as the monotonic plastic zone for zero to tension loading and even relatively smaller for R values above zero.

Fully plastic limit load is simply the condition of monotonic yielding over the entire uncracked ligament. For compact and other types of specimens where there is a significant bending component, this occurs when the monotonic plastic zone joins with a zone of monotonic compressive yielding extending from the rear surface of the specimen. At limit load in the compact geometries tested here, and for zero to tension loading, the cyclic plastic zone is estimated according to Fig. 11 to occupy a fraction of the uncracked ligament on the order of one tenth. Thus, the overall load-deflection behavior of the member is expected to exhibit only small reversed plasticity. The plastic deformation, being dominated by tensile and compressive straining similar to 3 and 4 in Fig. 11*c*, is apparent mainly as an increasing mean deflection. This explains the observed behavior (see Figs. 4*a* and *b* and 5) for limit-load failure during cyclic loading.

Acceleration of Fatigue-Crack Growth at High Stress Intensities

Many investigators [*1,3,16–19*] have reported a sharp increase at high stress intensities in the fatigue-crack growth rate exponent, that is, a sharp increase in the slope on a *da/dN* versus ΔK plot such as Figs. 2 and 3. It is somewhat puzzling that the data of this investigation do not exhibit such a trend. This is the case despite the following factors—all of which should have increased the likelihood of such behavior being observed. (1) By using large size specimens, data were obtained at higher stress intensities than are normally investigated in materials of similar yield strength. (2) Test frequencies were reduced as crack-growth rates increased to facilitate taking data at high growth rates. (3) The failures terminating fatigue-crack growth were of two types—toughness controlled and fully plastic limit-load controlled.

One possible explanation for this situation is that several different micromechanisms may be involved in fatigue-crack propagation, and

those which cause acceleration of fatigue-crack growth are not operative for the two materials tested here. For example, certain aluminum alloys exhibit a quite distinct change in the fatigue-crack growth rate exponent which is almost certainly a real physical effect [*18,19*]. Also, some data [*16*] on high yield strength steels are quite convincing to the effect that a transition in behavior can occur just prior to toughness failure.

A second possibility is that there are important differences in the test techniques used here compared to those used previously by others. A possible specific cause is suggested by a test result from a previous investigation [*20*] of fatigue-crack growth under gross plasticity. In this test, a specimen from the same heat of A533B steel was cycled as shown in Fig. 12 between zero load and a sloping load versus deflection line. This control condition caused the behavior at combinations of load and crack length approaching limit load to be more stable in that the increases with cycles of the crack-growth rate and mean deflection were gradual, rather than rapid as under simple load control. Thus, it was possible to obtain fatigue-crack growth rates under conditions similar to those existing during limit-load failure. In this test, the stress-intensity range, calculated from the load range and crack length as if there were no plasticity, remained approximately constant. The resulting data, plotted as slashed square symbols in Fig. 2, indicate an acceleration of crack-growth rate not observed in larger size specimens.

In fatigue-crack growth rate tests conducted at constant frequency, large deflections associated with limit-load failure could cause an electrohydraulic testing machine to fail to respond fully to the programmed load. Behavior similar to that in Fig. 12 could occur, and growth rates would be reported that were essentially taken during an extended limit-load failure. Note that such a problem with the programmed loads could easily go undetected near the end of a test, as the test technician must at that time give increased attention to measuring the rapidly accelerating crack. Thus, data obtained near the end of the life in a fatigue-crack growth rate test should be regarded with some suspicion, particularly for a low yield strength metal, and particularly if no special provisions are made to ensure accurate electrohydraulic testing machine response.

Limitations of Linear-Elastic Interpretation of Fatigue-Crack Growth Rate Data

Judging from the requirements of ASTM Method E 399-74 for static fracture toughness testing, two separate factors may necessitate specimen size requirements in fatigue-crack growth rate testing. The first of these is the possibility of state-of-stress effects, specifically of different behavior for plane stress versus plane strain. As the significant size criterion is the ratio of specimen thickness to plastic zone size, state-of-stress effects, if

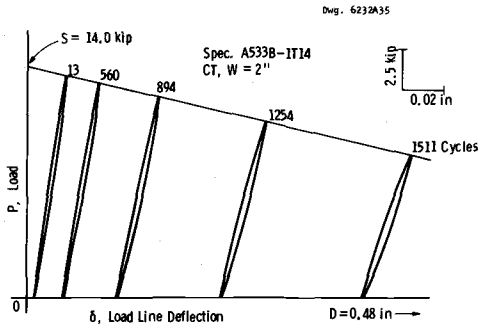

FIG. 12—*Load versus deflection hysteresis loops during load control to a sloping line.*

important, would be expected to cause an influence of specimen thickness on fatigue-crack growth rate.

For data below nominal yield, the plasticity is sufficiently restricted compared to the planar dimensions of the specimen so that any thickness effects which occur are expected to be independent of specimen size. But above nominal yield, interaction between thickness and planar dimension effects is a possibility. However, from Figs. 2 and 3, no trends consistent with a thickness effect occur either above or below nominal yield in the data of this investigation. Note that for A533B the data cover a factor of 20 in thickness and for A469 a factor of four.

Although thickness effects have been reported by some investigators [*3,16,17,21-25*], many data [*1,3,8,16,17,24-28*] suggest that there is no such effect. Where thickness effects are reported, the change in growth rate is generally no greater than a factor of two, and some of the reported effects are associated with general yielding [*24,25*] or final brittle fracture behavior [*16*]. Also, the reported thickness effects are not consistent as to whether faster rates occur in thicker or thinner specimens. Thus, the data of this investigation are consistent with the trend of the existing data in that no significant thickness effects are observed. However, some caution as to thickness effects is advisable, particularly in applications where a small change in growth rate might be critical. For example, in applications involving plate material, limited data might be obtained using specimens of full plate thickness to confirm more extensive data on reduced thickness specimens.

The second factor possibly necessitating specimen size requirements is related to linear elastic fracture mechanics being limited to small-scale plasticity. This is determined primarily by the planar dimensions of the specimen. In particular, the uncracked ligament length must be large compared to the plastic-zone size. Specimen thickness is a secondary variable, being of importance only because the increased constraint of plane strain

elevates the yield strength so that the plastic-zone is reduced by about a factor of three [*13,29*].

If the extent of plasticity is too great, then values of stress intensity, K, have no meaning, and test data interpreted in terms of K are expected to exhibit size effects. In Figs. 2 and 3, no trends in growth rate are apparent which can be attributed to specimen size. However, note that minor effects could be obscured by the scatter in the data.

If plane stress is assumed, ASTM Method E 399-74 requires, in effect, that the uncracked ligament must not be shorter than approximately 16 estimated [*13*] plastic-zone sizes

$$b \geq 2.5 \left(\frac{K}{\sigma_y}\right)^2 = 15.7\, r_y \tag{1}$$

where

$$r_y = \frac{1}{2\pi}\left(\frac{K}{\sigma_y}\right)^2$$

In applying such a limitation to fatigue-crack growth rate testing, it must be decided whether the monotonic or the cyclic plastic zone is critical. These two alternatives are illustrated in Fig. 13 for zero to tension loading.

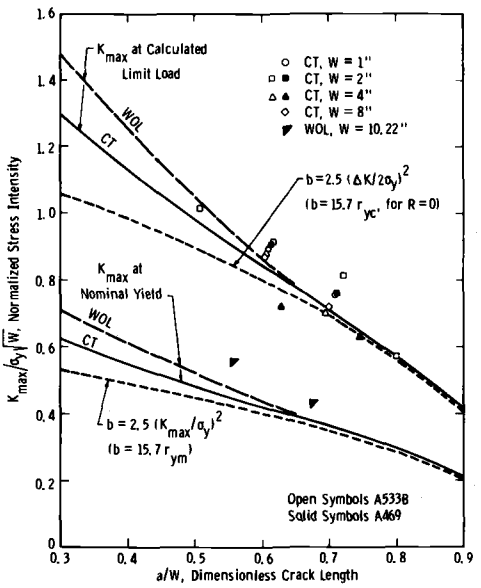

FIG. 13—*Limit load and nominal yield in compact specimens compared with possible requirements on uncracked ligament length.*

The lower dotted line corresponds to a factor of approximately 16 applied to the monotonic plastic-zone size, whereas the upper line is for the same factor applied to the cyclic plastic-zone size. Lines for predicted limit load and nominal yield are also shown, as are the test data for failure following fatigue-crack growth. Note that in Fig. 13 stress intensity is nondimensionalized with respect to yield strength and the square root of the specimen size so as to make a plot that is material and size independent.

From Fig. 13, this factor of 16 when applied to the cyclic plastic zone for compact specimens, results in a limitation that is only slightly more conservative than fully plastic limit load. For R values significantly greater than zero, this requirement is less conservative than fully plastic limit load. Since specimen failure will occur at limit load, this implies that no size limitation is necessary if the cyclic plastic-zone size is thought to control the validity of linear-elastic fracture mechanics for fatigue testing. It is further implied that the only limitation needed is one in terms of specimen deflections, so that no data will be taken during limit-load failure where linear-elastic fracture mechanics obviously has no meaning. (A tentative approach to the interpretation of fatigue-crack growth rate data for general yielding conditions is described in Refs *20* and *30*).

However, it can be argued that the monotonic plastic zone limits the validity of linear-elastic fracture mechanics for cyclic loading. For example, the reduced planar constraint resulting from a monotonic plastic zone that is not small compared to the specimen size could have some effect, such as lowering the crack-closure level. This might result in a secondary effect on growth rate similar to that of an elevated load ratio, R. If such effects occur in the A533B and A469 data of Figs. 2 and 3, they are of the same order as the scatter in the data. Note, from Fig. 13, that a factor of 16 limitation based on the monotonic plastic zone is similar to nominal yield, so that this limitation would invalidate all data plotted as open symbols in Figs. 2 and 3.

The absence of significant size effects in Figs. 2 and 3 suggests that the cyclic plastic-zone size is indeed the controlling parameter, and, further, that size limitations are unnecessary for fatigue testing of compact specimens. However, until size effect data in additional materials become available, some caution in this area is advisable.

The previous discussion applies in its details only to compact specimens. However, similar considerations exist for other specimen geometries, such as center-cracked panels. Laboratory investigation and discussion similar to the foregoing are needed for that specimen geometry.

Conclusions

Based on the experimental data and discussion presented earlier in this paper, the following conclusions and recommendations are made.

1. Failure following fatigue-crack growth occurs when either the fracture toughness or fully plastic limit load is reached, with the fracture toughness sometimes being modified by cyclic loading.

2. Limit load failures are likely in low yield strength metals for the specimen sizes commonly employed, particularly if the fracture toughness is high. Where failure following fatigue-crack growth is due to limit load, the highest stress intensities that can be investigated are proportional to the square root of specimen size.

3. Deflections should be monitored during fatigue-crack growth rate testing. Data which are obtained while the mean deflection is increasing due to plastic deformation should not be interpreted in terms of linear-elastic fracture mechanics. Care is needed in ensuring that electrohydraulic testing machines respond fully to the programmed load, especially near the ends of tests where the deflection may be large.

4. For A533B and A469 steels tested up to very high stress intensities by the use of large size specimens, no transition to an increased fatigue-crack growth rate exponent was observed. It is not certain whether this unexpected behavior was due to the micromechanisms of fracture in these steels or to the special care employed in testing.

5. In agreement with most previous data, no significant thickness effects were observed in the two steels tested, with data over a factor of 20 in thickness being available for A533B. However, some caution as to thickness effects is advised. Whenever possible, extensive data on a different thickness than in a service application should be checked by limited data on a thickness approaching or equaling that of the application.

6. No size effects exceeding the scatter in the data were observed in the two steels tested, with a factor of eight in size being investigated in A533B steel. It is not clear for fatigue loading whether a size requirement similar to that of ASTM Method E 399-74 should be applied to the monotonic or to the cyclic plastic zone. The data of this investigation suggest that the more strict limitation based on monotonic plastic zone size is unnecessary for fatigue-crack growth rate testing of compact specimens.

Acknowledgments

Gratitude is expressed to J. A. Begley and S. J. Hudak, Jr., for their advice and constructive comments. D. R. Young, Jr., aided in planning laboratory tests and in detailed design of experimental apparatus. This work was made possible by the sponsorship of the Large Rotating Apparatus Division of Westinghouse Electric Corporation, with the atmosphere and facilities which resulted in this paper existing largely due to the efforts of E. T. Wessel, Manager of Mechanics of Materials, Westinghouse Research Laboratories.

References

[1] Clark, W. G., Jr., and Hudak, S. J., Jr., *Journal of Testing and Evaluation,* Vol. 3, No. 6, Nov. 1975, pp. 454–476.

[2] Wessel, E. T., *Engineering Fracture Mechanics,* Vol. 1, 1968, pp. 77–103.

[3] Barsom, J. M., Imhof, E. J., and Rolfe, S. T., *Engineering Fracture Mechanics,* Vol. 2, 1971, pp. 301–317.

[4] Green, A. P., *Quarterly Journal of Mechanics and Applied Mathematics,* Vol. VI, Part 2, 1953, pp. 223–239.

[5] Green, A. P. and Hundy, B. B., *Journal of the Mechanics and Physics of Solids,* Vol. 4, 1956, pp. 128–144.

[6] Wilson, W. K., "Stress Intensity Factors for Compact Specimens Used to Determine Fracture Mechanics Parameters," Research Report 73-1E7-FMPWR-R1, Westinghouse Research Laboratories, Pittsburgh, Pa., July 1973.

[7] Wilson, W. K., *Engineering Fracture Mechanics,* Vol. 2, 1970, pp. 169–171.

[8] Paris, P. C., Bucci, R. J., Wessel, E. T., Clark, W. G., Jr., and Mager, T. R., in *Stress Analysis and Growth of Cracks, ASTM STP 513,* American Society for Testing and Materials, 1972, pp. 141–176.

[9] Clark, W. G., Jr., unpublished fatigue crack growth rate data, Westinghouse Research Laboratories, Pittsburgh, Pa., 1969.

[10] Greenberg, H. D., Wessel, E. T., Clark, W. G., Jr., and Pryle, W. H., "Critical Flaw Sizes for Brittle Fracture of Large Turbine Generator Rotor Forgings," Scientific Paper 69-1D9-MEMTL-P2, Westinghouse Research Laboratories, Pittsburgh, Pa., Dec. 1969; presented at the Fifth International Forgemaster Meeting in Terni, Italy, 6–9 May 1970.

[11] Landes, J. D. and Begley, J. A., in *Fracture Analysis, ASTM STP 560,* American Society for Testing and Materials, 1974, pp. 170–186.

[12] Begley, J. A., unpublished cyclic loading fracture data, Westinghouse Research Laboratories, Pittsburgh, Pa., 1972.

[13] Irwin, G. R., *Proceedings,* 7th Sagamore Ordnance Materials Research Conference, Part 4, 1960, pp. 63–71.

[14] Paris, P. C., in *Fatigue—An Interdisciplinary Approach,* Syracuse University Press, 1964, pp. 107–127.

[15] Rice, J. R., in *Fatigue Crack Propagation, ASTM STP 415,* American Society for Testing and Materials, 1967, pp. 247–311.

[16] Carmen, C. M. and Katlin, J. M., *Journal of Basic Engineering,* Dec. 1966, pp. 792–800.

[17] Barsom, J. M., *Journal of Engineering for Industry,* Nov. 1971, pp. 1190–1196.

[18] Crooker, T. W. *Engineering Fracture Mechanics,* Vol. 5, 1973, pp. 35–43.

[19] Clark, W. G., Jr., *Engineering Fracture Mechanics,* Vol. 1, 1968, pp. 385–397.

[20] Dowling, N. E. and Begley, J. A., in *Mechanics of Crack Growth, ASTM STP 590,* American Society for Testing and Materials, 1976.

[21] Clark, W. G., Jr., and Trout, H. E., Jr., *Engineering Fracture Mechanics,* Vol. 2, 1970, pp. 107–123.

[22] Jack, A. R. and Price, A. T., *Acta Metallurgica,* Vol. 20, July 1972, pp. 857–866.

[23] Schijve, J., in *Fatigue Crack Propagation, ASTM STP 415,* American Society for Testing and Materials, 1967, pp. 415–459.

[24] Richards, C. E. and Lindley, T. C., *Engineering Fracture Mechanics,* Vol. 4, 1972, pp. 951–978.

[25] Griffiths, J. R. and Richards, C. E., *Materials Science and Engineering,* Vol. 2, 1973, pp. 305–310.

]26] Clark, W. G., Jr., and Wessel, E. T., in *Review of Developments in Plane Strain Fracture Toughness Testing, ASTM STP 463,* American Society for Testing and Materials, 1970, pp. 160–190.

[27] Brothers, A. J. and Yukawa, S., *Journal of Basic Engineering,* March 1967, pp. 19–27.

[28] Frost, N. E. and Denton, K., *Journal of Mechanical Engineering Science,* Vol. 3, No. 4, 1961, pp. 295–298.

[29] McClintock, F. A. and Irwin, G. R., in *Fracture Toughness Testing and Its Applica-*

tions, ASTM STP 381, American Society for Testing and Materials, 1965, pp. 84–113.
[30] Dowling, N. E., in *Cracks and Fracture, ASTM STP 601,* American Society for Testing and Materials, 1976, pp. 19–32.

B. M. Kapadia[1] *and E. J. Imhof, Jr.*[1]

Fatigue-Crack Propagation in Electroslag Weldments

REFERENCE: Kapadia, B. M. and Imhof, E. J., Jr., **"Fatigue-Crack Propagation in Electroslag Weldments,"** *Flaw Growth and Fracture, ASTM STP 631,* American Society for Testing and Materials, 1977, pp. 159–173.

ABSTRACT: The paper discusses the results of an investigation of fatigue-crack propagation behavior of as-deposited electroslag weldments in two hot-rolled structural steels, ASTM A36 and ASTM A588 Grade A. Fatigue-crack growth tests were conducted on 1T wedge-opening-loading (WOL) specimens machined from six 1-in.-thick and four 4-in.-thick weldments that were representative of electroslag welds for bridges. The testing was done in air at room temperature under tension-to-tension sinusoidal loading. Various orientations and locations of the fatigue crack in relation to the weld geometry were investigated.

The fatigue-crack growth rates (da/dN) in the weldments were similar to, or up to five times slower than, the rate in the base steels. The retardation in crack-growth rate was most pronounced at low values of the stress-intensity factor range (ΔK) and was substantially greater for crack propagation in the coarse-grained heat-affected zone (HAZ) and bond-line regions than in the weld metal. Marked variations in the microstructure of the weld metal and HAZ had no signficant influence on crack-propagation behavior, which appeared to be influenced primarily by the residual stresses in the weldments as discussed in a separate paper.

The results of this study show that the upper bound of the crack-growth behavior for low-strength structural steels may be used as a conservative estimate of the crack-propagation behavior of as-deposited electroslag weldments in such steels. On this basis, the prediction of the service life of electroslag-welded structures subjected to cyclic loads, and the determination of safe inspection intervals, may be made by the same approach as that presently used for standard structural-steel weldments made by other processes.

KEY WORDS: fatigue (materials), crack propagation, electroslag welding, structural steels, retarding

Failures of engineering structures subjected to repeated loads usually are caused by initiation of subcritical cracks and their propagation to critical size at which unstable fracture occurs. These subcritical cracks may be introduced during fabrication, particularly in constrained welded structures and, therefore, could be present when the structure is put into

[1]Associate research consultant and research technician, respectively, U.S. Steel Corporation, Research Laboratory, Monroeville, Pa. 15146.

service. In these cases, the useful life of the structure is governed by the fatigue-crack propagation behavior of the material comprising it. Thus, to predict the service life of many structures and establish safe inspection intervals, an understanding of the rate of fatigue-crack propagation in structural materials is essential.

Considerable work [*1–6*][2] has been done to characterize the crack-propagation behavior of steels, titanium alloys, and aluminum alloys under various test conditions. However, most of these studies have been concerned with the behavior of base metal rather than weldments. A few studies [*7–11*] have investigated crack propagation in weldments produced by gas metal arc, shielded metal arc, submerged arc, and gas-tungsten arc welding processes, but hardly any information is available on the fatigue-crack propagation behavior of electroslag[3] weldments. Moreover, only limited data exist on the fatigue strength (based on *S-N* curve) of electroslag-welded joints [*12,13*].

Therefore, an investigation was conducted at U.S. Steel Research,[4] as part of a research project sponsored under the National Cooperative Highway Research Program,[5] to study the crack-propagation behavior of electroslag weldments in two hot-rolled structural steels commonly used in bridge construction. The results were analyzed by using linear-elastic fracture mechanics and are presented in this paper.

Materials and Experimental Procedure

Materials

Two hot-rolled structural steels—ASTM A36 and ASTM A588 Grade A—and several welding-process variables were investigated in this study and are summarized in Table 1. The fatigue-crack growth tests were conducted on ten production-type electroslag butt welds in the as-deposited condition. Six of these were 1 to 1-in. (2.54-cm) butt joints, and the remaining four were 4 to 4-in. (10.16-cm) butt joints.

[2]The italic numbers in brackets refer to the list of references appended to this paper.

[3]Electroslag welding is a highly efficient and economical process for welding heavy plates with a minimum of distortion.

[4]It is understood that the material in this paper is intended for general information only and should not be used in relation to any specific application without independent examination and verification of its applicability and suitability by professionally qualified personnel. Those making use thereof or relying thereon assume all risk and liability rising from such use or reliance.

[5]The opinions and findings expressed or implied in this paper are those of the authors. They are not necessarily those of the Highway Research Board, the National Academy of Sciences, the Federal Highway Administration, the American Association of State Highway Officials, nor of the individual states participating in the National Cooperative Highway Research Program.

TABLE 1—*Processing details of weldments investigated.*

Weldment No.	Steel	Filler-Metal Feed	Wire	Welding Shoes
		1-In.-Thick Weldments		
1	A36	stationary tube	cored	water cooled
2	A36	oscillating wire	cored	water cooled
6	A588-A	stationary tube	solid	water cooled
13[a]	A36	stationary tube	cored	solid copper
17	A36	stationary tube	solid	water cooled
19	A588-A	stationary tube	solid	water cooled
		4-In.-Thick Weldments		
3	A36	oscillating tube	cored	water cooled
8[b]	A588-A	oscillating tube	solid	water cooled
18	A36	oscillating tube	solid	water cooled
20[b]	A588-A	oscillating tube	cored	water cooled

NOTE—Conversion factor is 1 in. = 2.54 cm.

[a]This weldment was only 24 in. long; all other weldments investigated were 42 in. long.

[b]These two welds were oriented parallel to the plate rolling direction, whereas all the other welds are oriented normal to the plate rolling direction (the most common orientation in bridge fabrication).

The chemical compositions and mechanical properties of the A36 and A588 Grade A steel plates used in the present investigation were typical of the respective steels. All the weldments, except Weldment 13, were 42 in. (107 cm) long and were made by using water-cooled copper shoes. Weldment 13 was made by using solid-copper shoes and was only 24 in. (61 cm) long. The welding procedure was standardized and closely controlled with respect to joint preparation, fixturing, heat input, and travel speed. All weldments were radiographed and examined ultrasonically prior to obtaining test specimens.

Specimen Preparation

The fatigue-crack propagation tests in the present investigation were conducted on 1-in.-thick (2.54 cm) 1T wedge-opening-loading (WOL) specimens. For this specimen, the stress-intensity factor, K_I, at the crack tip is given by the following equation [*14*]

$$K_I = \frac{C_3 P}{B\sqrt{a}} \tag{1}$$

where

P = applied load,
B = specimen thickness,
a = crack length measured from the loading plane, and
C_3 = function of the dimensionless crack length, a/W, where W is the specimen length measured from the loading plane.

The tests were conducted (*a*) with fatigue cracks oriented perpendicular to the plate surface and running parallel to the weld in both the 1 and 4-in.-thick weldments and (*b*) with fatigue cracks oriented perpendicular to the plate surface and parallel to the weld and running in the through-the-thickness direction in only the 4-in.-thick weldments (Fig. 1). Denoting the length direction of the weldment by L, the width direction by T, and the thickness direction by S, the first orientation will be designated, in accordance with convention adopted by ASTM,[6] as the TL orientation and the second as the TS orientation.

Fatigue cracks having TL orientation were located at the midwidth of the weld (weld metal), at the weld-base-metal interface (bond line), and in the coarse-grained region of the HAZ (coarse-grained HAZ), which generally corresponded to a location about 1/16 to 1/8 in. (1.6 to 3.2 mm) from the bond line (Fig. 1). In the 4-in.-thick weldments, these cracks were centered on the midthickness. Cracks having TS orientation (only in the 4-in.-thick weldments) were located at the midwidth of the weld, at the bond line, and adjacent to the weld-bond line such that the crack would be expected to run through the weld, across the bond line, and then into the HAZ, or to follow a reverse course depending on the configuration of the weld cross section (Fig. 1). One specimen was tested for each of the aforementioned conditions. Thus, altogether, three specimens were tested from each of the six 1-in.-thick weldments and six specimens from

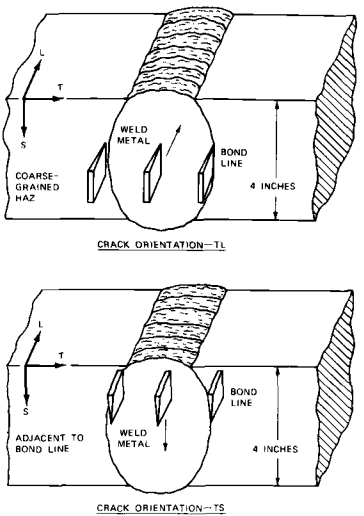

FIG. 1—*Orientations and locations of the fatigue crack in a 4-in.-thick (102-mm) weldment.*

[6]In this system, the first letter indicates the direction normal to the crack plane and the second letter indicates the direction of crack extension.

each of the four 4-in.-thick weldments, resulting in a total of 42 specimens.

Oversized WOL specimen blanks were first machined from the test weldments and were surface ground to the final specimen thickness. The blanks were then etched to reveal the weld metal and the HAZ in order to locate precisely the specimen notch in the appropriate region of the weld. Because of the inherent curvature of the weld bond line and the markedly irregular shape and size of the weld cross section of some of the weldments, great care had to be taken in locating the notch for the HAZ and the bond-line specimens.

The specimens were machined from the blanks to ±0.002-in. (0.05-mm) tolerances on all dimensions. An 0.007-in. (0.18-mm) root radius notch was then made with an electrical-discharge machine (EDM). To provide a means of measuring the rate of crack extension, two rows of diamond-shaped hardness indentations were made on both specimen surfaces (with a Vickers-pyramid-hardness testing machine) parallel to and 0.09 in. (2.3 mm) from the plane of the crack and in the direction of crack extension. The distance between neighboring indentations was 0.01 ± 0.0002 in. (0.25 ± 0.005 mm).

Test Procedure

Testing was done in air at room temperature and at cyclic-stress frequencies of 180 and 300 cpm in two 50-kips (222.4 kN) Materials Testing Systems (MTS) machines.

In all tests the fatigue crack was initiated and propagated under tension-to-tension sinusoidal loading at a constant maximum load of 3600 lb (16 kN) and a constant minimum load of 300 lb (1.33 kN)—both of which were controlled within ±1.0 percent. Thus, the stress ratio, R, was slightly less than 0.10. Prior to making crack-length measurements, the fatigue cracks were extended about 0.23 in. (5.8 mm) from the machined notch root at a frequency of 600 cpm.[7] Thus, at the time crack-length measurements were begun, the total crack length, a, was approximately equal to the specimen thickness of 1 in.

Fatigue-crack extension was measured optically at ×17 magnification with an M-101 Gaertner microscope mounted in a micrometer slide. The accuracy of measurement of any crack length was approximately ±0.002 in. (0.05 mm). Because of generally uneven crack extension along the two sides of the specimen (by up to about 0.05 in. or 1.27 mm for most of the specimens), crack lengths were measured on both sides, and the average value was used in the analysis of crack-growth data. The average crack extension between consecutive measurements was approximately 0.035

[7]This procedure normally is observed in order to minimize the error in neglecting the influence of the machined notch on stress-intensity factor calculations and also to enable the fatigue-crack front to stabilize.

in. (0.89 mm). Crack-growth tests were terminated at a total crack length of about 1.8 in. or 4.6 cm ($a/W = 0.7$) or earlier if the crack deviated outside the course defined by the hardness impressions.

Results and Discussion

Analysis of Results

The crack-propagation rate under cyclic stresses can be empirically related to the instantaneous value of the stress-intensity factor range at the tip of the crack by the following equation [*1,15*]

$$\frac{da}{dN} = A\,(\Delta K)^n \tag{2}$$

where

a = crack length (in.),
N = number of cycles,
ΔK = stress-intensity-factor range, ksi $\sqrt{\text{in.}}$, and
A and n = constants for a given material.

According to this functional relationship based on a linear-elastic fracture-mechanics approach, fatigue-crack propagation is dependent primarily on the stress-intensity factor range and is independent of loading configuration and specimen geometry. A plot of the crack-growth rate, da/dN, versus the stress-intensity factor range, ΔK, on logarithmic coordinates is a linear relationship having a slope equal to the exponent, n, in Eq 2. Superposition of such plots enables direct comparisons of crack-growth behavior over a wide range of ΔK values.

Fatigue-Crack Growth in Base Steels

The fatigue-crack, growth-rate data [*16,17*] presented in Fig. 2 for ASTM A36 and ASTM A588 Grade A steels—the base steels of the weldments investigated—provided a suitable reference with which to compare the fatigue-crack growth behavior of the weldments. The test conditions under which these data were obtained were very similar to those used in the present investigation. Crack-growth measurements were made starting from a total crack length, a, of about 1 in., thereby, virtually eliminating the nonlinearity ("tail") occasionally observed in such plots at very low-ΔK values.

The crack-growth data for both the steels can be represented, as shown in Fig. 2, by a single relatively narrow scatter band whose upper and lower bounds (with respect to crack-growth rate) are expressed as follows

$$\frac{da}{dN} = 1.68 \times 10^{-10} (\Delta K)^{3.3} \tag{3}$$

$$\frac{da}{dN} = 1.09 \times 10^{-10} (\Delta K)^{3.3} \tag{4}$$

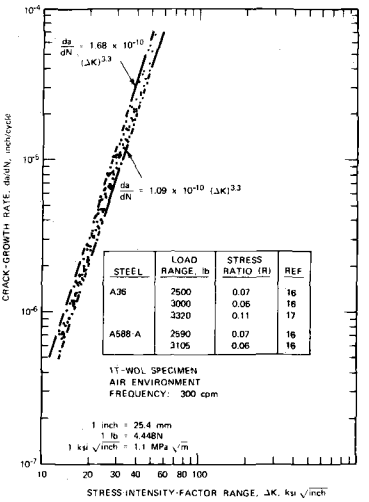

FIG. 2—*Fatigue-crack propagation data for A36 and A588-A steels.*

Fatigue-Crack Growth in Weldments

Crack-growth data, da/dN versus ΔK, for two of the 1-in.-thick weldments (Weldments 1 and 13) representing extremes of crack-growth behavior observed are presented in Figs. 3 and 4. Crack growth in the former weldment was considerably slower than that in the latter at low-ΔK values. Similar data on one of the 4-in.-thick weldments (Weldment 3) for crack propagation in the TL and TS orientations are presented in Fig. 5. The scatter band representing the crack-growth behavior of the base steels, A36 and A588-A, also is included in each figure for comparison.

As a rule, the fatigue-crack growth rates in the weldments were similar to those in the base steels at high-ΔK values but were significantly lower at low-ΔK values. Inasmuch as the crack-growth measurements in the present investigation also were made starting from a total crack length, a, of about 1 in., and the load amplitude was maintained essentially constant during the tests, no nonlinearity effects attributable to either of these causes were expected. Moreover, care was taken to exclude any data points that appeared to be affected by crack-growth delay following an accidental transient overload (for example, such as may be caused during

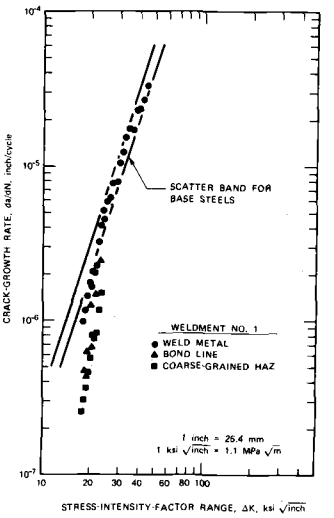

FIG. 3—*Fatigue-crack propagation data for Weldment 1.*

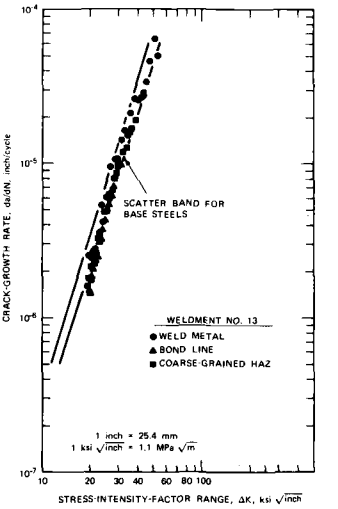

FIG. 4—*Fatigue-crack propagation data for Weldment 13.*

interruption of the test) which was usually evident from a "beach mark" indication on the fracture surface. Therefore, the significantly lower crack-growth rates observed in some of the weldments at low-ΔK values, in relation to those of the base steels, must be interpreted as representing an actual difference in crack-propagation behavior.

On this basis, the following general observations were made for the crack-growth data obtained on the weldments.

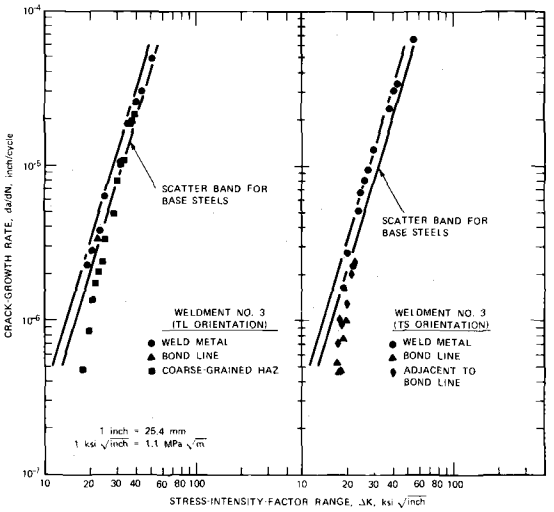

FIG. 5—*Fatigue-crack propagation data for Weldment 3.*

1. Fatigue-crack growth rates in the weldments were similar to, or up to five times slower than, the rate in the base steels.

2. The crack-growth retardation effect in the weldments was most pronounced at low-ΔK values, generally below about 25 ksi $\sqrt{\text{in.}}$ (27.5 MPa$\sqrt{\text{m}}$).

3. In some weldments, the retardation effect was substantially greater in the bond-line or coarse-grained HAZ specimens or both than in the weld-metal specimens (for example, see Fig. 3), but this behavior was rather inconsistent.

Similar crack-growth retardation effects have been observed previously in weldments of ASTM A514 steel [*7*], 5 percent nickel steel (ASTM A645) [*8*], Type 304 stainless steel [*9,10*], and 7005-T6 aluminum alloy [*11*]. However, in all of these, welding processes other than electroslag welding were used. Crack-growth retardation was observed in the HAZ as well as in the weld metal in each of the foregoing examples except one [*11*] in which only the HAZ showed the effect.

The inconsistent crack-growth-retardation behavior of the bond-line and coarse-grained HAZ specimens in this study could have been due to the apparent lack of consistency in the actual crack paths. The machined notches from which the fatigue cracks initiated only could be positioned approximately in the HAZ and bond-line specimens of some of the weldments. This situation was further complicated by the fact that the crack path in many of the bond-line and HAZ specimens (but in none of the weld-metal specimens, with one exception) deviated markedly from the intended course. These crack deviations occurred independent of the observed crack-growth retardation effects. As a rule, crack deviations in

the bond-line and HAZ specimens of the same weldment occurred either toward the weld metal or the base plate, but, on the whole, there did not seem to be any preference for either mode of deviation.

Effect of Microstructure on Crack-Growth Rate

To determine whether the observed crack-growth retardation effects were in fact related to the microstructure of the HAZ and weld metal, all specimens were fractured after completion of the test and the fatigue-crack surfaces examined.

Figures 6 and 7 show demarcation of the weld and HAZ regions traversed by the fatigue crack in each of the 1 and 4-in.-thick weldments, respectively. In general, although the cracks did initiate approximately in the intended region, they almost never exclusively followed that region except for the weld-metal specimens. Therefore, the lack of consistency in the crack-growth behavior of the bond-line and coarse-grained HAZ specimens was not surprising.

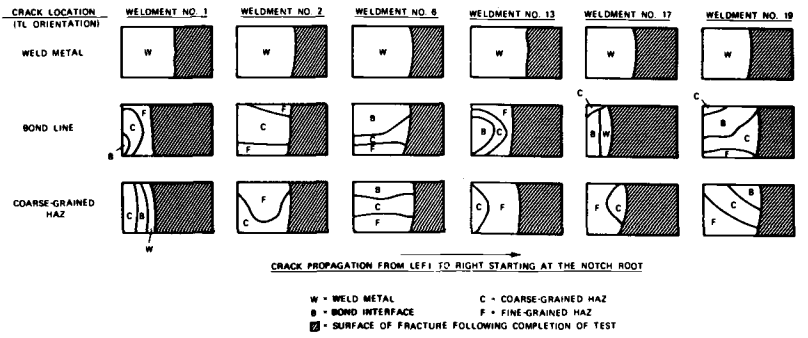

FIG. 6—*Demarcation of weld and HAZ regions transversed by the fatigue crack in 1-in.-thick (35.4-mm) weldments.*

Analysis of crack-growth data with reference to Figs. 6 and 7 indicated that the observed retardation effects could not be correlated consistently with one or more components of microstructure but rather appeared to be characteristic of each specimen as a whole. For example, both the bond-line and coarse-grained HAZ specimens of Weldment 1 exhibited appreciable crack-growth retardation (see Fig. 3) although the fatigue cracks followed quite different paths as seen in Fig. 6. In the bond-line specimen, the crack initiated partly at the bond interface but rapidly deviated toward the base plate, traversing first the coarse-grained and then the fine-grained region of the HAZ; in the coarse-grained HAZ specimen, however, the crack initiated in the coarse-grained HAZ as intended but

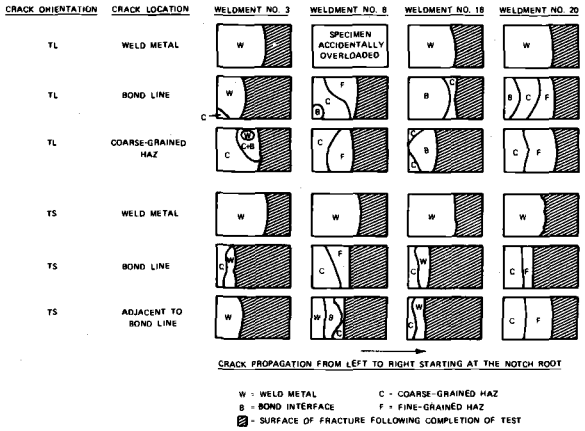

FIG. 7—*Demarcation of weld and HAZ regions transversed by the fatigue crack in 4-in.-thick (102-mm) weldments.*

then propagated along the bond interface and into the weld metal.[8] To illustrate this clearly, the *da/dN* versus ΔK plots for these two specimens are reproduced in Fig. 8 with the microstructural features associated with each data point indicated therein.

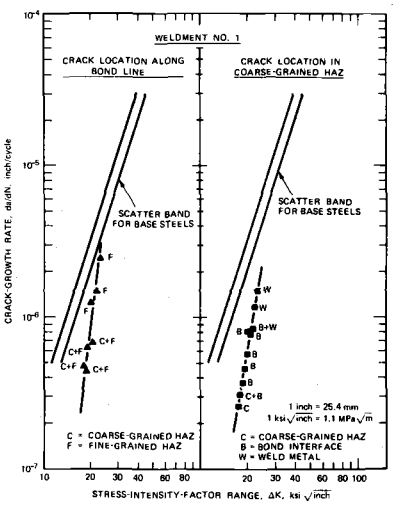

FIG. 8—*Fatigue-crack propagation data for Weldment 1 showing weld and HAZ regions traversed by the fatigue crack.*

[8]The opposing directions of crack deviation in this case were an exception to the earlier general observations.

Macrofractographic Observations

Macrofractographs of bond-line and coarse-grained HAZ specimens from the 1 and 4-in.-thick weldments which exhibited appreciable crack-growth retardation (Figs. 9*A*, *B*, and *C*) clearly show that their fatigue-crack paths were not confined to any particular microstructure. Figure 9*D* shows a typical example of crack propagation along the bond interface, showing characteristic ripple markings associated with the solidification structure of electroslag welds [*18*].

Macrofractographs of the weld-metal specimens which had a microstructure of cast columnar grains with the main dendrite axes initially perpendicular to the bond interface but gradually curving toward the top of the weldment and eventually becoming almost vertical at the midwidth of the weld showed more distinctive features. Figure 10 shows the fatigue-crack surfaces of weld-metal specimens from 1-in.-thick Weldments 19 and 13 in which the direction of crack propagation was along and against the direction of columnar grain growth (toward the top of the weldment), respectively. Despite the marked differences in surface topography, the crack-growth rates of these two specimens were very similar. Figures 11*A* and *B* show the marked differences in surface topography of weld-metal specimens with respect to TL versus TS orientation in 4-in.-thick weldments. A transition in the columnar grain structure from fine to coarse in a 4-in.-thick weldment caused a marked change in the fatigue-crack surface topography as shown in Fig. 11*C* but had no significant influence on the crack-propagation behavior.

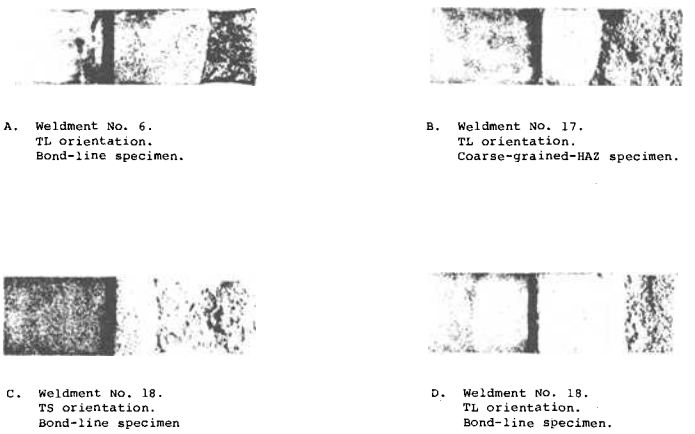

FIG. 9—*Fatigue-crack surfaces of bond-line and coarse-grained-HAZ specimens showing* (A, B, *and* C) *significant differences in microstructures transversed by the fatigue crack in specimens which exhibited appreciable crack-growth retardation, and* (D) *bond interface with ripple markings* (× *0.40*).

A. Weldment No. 19. Crack propagation toward top of weldment.

B. Weldment No. 13. Crack propagation toward bottom of weldment.

FIG. 10—*Fatigue-crack surfaces of weld-metal specimens (TL orientation) from 1-in.-thick (25.4-mm) weldments showing marked differences in surface topography for crack propagation* (A) *along and* (B) *against direction of columnar grain growth* (× *0.40*).

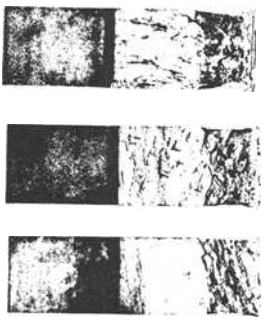

A. Weldment No. 18. TL orientation.

B. Weldment No. 18. TS orientation.

C. Weldment No. 8. TS orientation.

FIG. 11—*Fatigue-crack surfaces of weld-metal specimens from 4-in.-thick (102-mm) weldments showing marked differences in surface topography related to* (A,B) *specimen orientation, and* (C) *transition in columnar grain structure from fine to coarse* (× *0.40*).

Thus, it was concluded that the marked variations in microstructure of electroslag welds resulting from their unique solidification and thermal histories play an insignificant role in fatigue-crack growth behavior.

All but one of the aforementioned studies [*7–11*], in which crack-growth retardation was observed in weldments, considered this effect to be independent of microstructure. The one exception [*10*] concerned a Type 304 stainless-steel weldment with Type 308 filler metal in which crack-growth retardation was attributed to the fine duplex delta ferrite-austenite structure of the weld deposit. The remaining studies [*7,8,9,11*] attributed the observed crack-growth retardation to compressive residual stresses introduced by welding. As discussed in a subsequent paper [*19*], this observation is also applicable to the data obtained in the present study.

Practical Implications

In this investigation, the fatigue-crack growth rate in the weld metal and in the HAZ of electroslag weldments of A36 and A588 Grade A steels was similar to or slower than that in the base metal by as much as five times. These findings are consistent with those of a literature survey [*12*] which indicated that the fatigue strengths of machined electroslag-

welded joints (reinforcement removed) were generally as high as, or higher, than those of the parent material. (The fatigue strengths of unmachined electroslag welds were as high as or higher than those obtainable for butt welds made by other processes.) A subsequent limited study [*13*] of the fatigue and fracture behavior of electroslag weldments in A36 and A588 plates conducted by the Center for Highway Research, University of Texas, also reached similar conclusions.

The observed retardation in crack-growth rate has been attributed in a subsequent paper [*19*] to compressive residual stresses introduced by welding. However, this beneficial effect of the compressive residual stresses does not appear to be a consistent one and, furthermore, would diminish under service conditions of high-tensile mean loads or following a stress-relief heat treatment. Therefore, the upper bound of the scatter band (with respect to crack-growth rate) for the base steels (Fig. 2 and Eq 3) may be used to obtain a conservative estimate of the fatigue-crack growth behavior of as-deposited electroslag weldments in such steels. On this basis, the prediction of the service life of electroslag-welded structures subjected to cyclic loads and the determination of safe inspection intervals may be made by using the same approach as that presently used for standard structural-steel weldments made by other processes.

Summary

The results of this investigation may be summarized as follows.

1. Fatigue-crack growth rates (da/dN) in the electroslag weldments studied were similar to or up to five times slower than the rate in the base steels, A36 and A588 Grade A.

2. The retardation in crack-growth rate was most pronounced at low values of the stress-intensity factor range (ΔK).

3. The retardation effect was substantially greater for crack propagation in the coarse-grained HAZ and bond-line regions than in the weld metal, but this was not observed consistently.

4. The variations in the microstructure of the weld metal and the HAZ caused marked differences in the topography of the fatigue-crack surfaces but had no significant influence on the crack-propagation rate.

5. A conservative estimate of the fatigue-crack propagation rate in electroslag weldments of low-strength structural steels may be made by using the upper bound of the scatter band (with respect to crack-growth rate) of the crack-growth data for the base steels used in this investigation as given by the relationship

$$\frac{da}{dN} = 1.68 \times 10^{-10} (\Delta K)^{3.3}$$

where da/dN is the crack-growth rate in inch per cycle and ΔK is the applied stress-intensity factor range in ksi $\sqrt{\text{in.}}$

Acknowledgments

This work was sponsored by the American Association of State Highway and Transportation Officials, in cooperation with the Federal Highway Administration, and was conducted in the National Cooperative Highway Research Program which is administered by the Transportation Research Board of the National Research Council.

References

[1] Paris, P. C., "The Fracture Mechanics Approach to Fatigue," *Proceedings*, Tenth Sagamore Army Materials Research Conference, Syracuse University Press, 1964.
[2] McEvily, A. J. and Boetner, R. C., "On Fatigue Crack Propagation in FCC Metals," *Acta Metallurgica*, Vol. 11, 1963, p. 725.
[3] Carman, C. M. and J. M. Katlin, "Low Cycle Fatigue Crack Propagation of High-Strength Steels," Technical Report ASME No. 66-MET-3, American Society of Mechanical Engineers, April 1966.
[4] Donaldson, D. R. and Anderson, W. E., *Proceedings*, Crack Propagation Symposium, Cranfield, England, Vol. 2, 1969, p. 375.
[5] Crooker, T. W. and Lange, E. A., "Failure of Structural Alloys by Slow Crack Growth," NRL Report 6944, Naval Research Laboratory, Washington, D.C., Oct. 1969.
[6] Barsom, J. M., Imhof, E. J., and Rolfe, S. T., *Engineering Fracture Mechanics*, Vol. 2, 1971, p. 301.
[7] Parry, M., Nordberg, H., and Hertzberg, R. W., *Welding Journal*, Oct. 1972, pp. 485-490.
[8] Sarno, D. A., Bruner, J. P., and Kampschaefer, G. E., *Welding Journal*, Nov. 1974, pp. 486-494.
[9] James, L. A., *Journal of Testing and Evaluation*, Vol. 1, No. 1, 1973, pp. 52-57.
[10] James, L. A., *Welding Journal*, April 1973, pp. 173-179.
[11] El-Soudani, S. M. and Pelloux, R. M., *Welding Journal*, May 1975, pp. 144-152.
[12] Harrison, J. D., "Fatigue Tests of Electroslag Welded Joints," *Metal Construction and British Welding Journal*, Vol. 1, No. 8, Aug. 1969.
[13] Noel, J. S. and Toprac, A. A., "Static, Fatigue, and Impact Strength of Electroslag Weldments," Technical Report 157-1F, Project 3-5-71-157, Center for Highway Research, Dec. 1972.
[14] Wilson, W. K., "Review of Analysis and Development of WOL Specimen," 67-7D7-BTLPV-R1, Westinghouse Research Laboratory, 8 March 1967.
[15] Paris, P. C. and Erdogan, F., *Transactions*, American Society of Mechanical Engineers, *Journal Basic Engineering*, Series D, Vol. 85, No. 3, 1963, p. 528.
[16] Barsom, J. M. and Novak, S. R., "Subcritical Crack Growth in Steel Bridge Members," Final Report NCHRP 12-14, National Cooperative Highway Research Program, Sept. 1974.
[17] U.S. Steel Research, unpublished data.
[18] Medovar, B. I. and Klyuev, M. M., "The Layer by Layer Solidification of Electroslag Remelted Ingots," *Welding Research Abroad*, Jan. 1968, pp. 67-71.
[19] Kapadia, B. M., "The Role of Residual Stresses in Fatigue-Crack Propagation in Weldments," presented at ASTM Symposium on Fatigue Testing of Weldments, Toronto, Canada, May 1977.

T. A. Cruse,[1] *G. J. Meyers,*[1] *and R. B. Wilson*[1]

Fatigue Growth of Surface Cracks

REFERENCE: Cruse, T. A., Meyers, G. J., and Wilson, R. B., "**Fatigue Growth of Surface Cracks,**" *Flaw Growth and Fracture, ASTM STP 631,* American Society for Testing and Materials, 1977, pp. 174–189.

ABSTRACT: Fatigue-crack growth in gas-turbine engines generally involves surface initiated cracks of semielliptical shape (surface crack) or quarter-elliptical shape (corner crack). Such cracks initiate in regions of locally high stresses and stress gradients. A major aspect of the design system prediction of cyclic growth of these cracks is the development of efficient yet accurate fatigue-crack growth analytical models.

A major advance in modeling accuracy and efficiency has been achieved through the combined use of boundary-integral equation models of three-dimensional crack problems and a weight function representation of elliptical crack growth. Surface and corner crack-fatigue growth data have been compared to the results predicted by the design system analytical model. In general, excellent agreement has been obtained. Some questions concerning the important features of surface and corner-crack growth as well as the weight function method are addressed.

KEY WORDS: crack propagation, fatigue (materials), cracking (fracturing), design, stress analysis

The fatigue life of cracks growing in engine disk structures is modeled using fracture-mechanics analysis. Fatigue-crack growth has been found by experience to fall into two classes: the growth of subsurface or buried cracks from intrinsic defects or the growth of surface cracks initiated by fatigue loading of initially defect-free structural notches. The technology of stress analysis and fracture mechanics has reached the level where the fatigue life of components with buried cracks may be predicted reliably and conservatively. However, the complexity of the stress fields and crack geometry for surface-crack problems in engine structural details, such as rim slots and bolt holes, has precluded the use of fracture mechanics for such problems. Rather, the fatigue life of structural details with stress concentrations has been estimated conservatively by predicting the cycles

[1]Project engineer, analytical engineer, and assistant project engineer, respectively, Pratt & Whitney Aircraft Division, United Technologies Corporation, East Hartford, Conn. 06108.

to initiate a surface crack, ignoring the life which remains in the part until surface-crack growth causes failure.

Linear-elastic fracture-mechanics analysis forms the basis for predicting the residual fatigue life of a cracked structural element. The material is characterized in terms of its crack-growth rate (da/dN) as a function of the cyclic change in the crack-tip, stress-intensity factor (ΔK). The effects of the stress field, the crack size and shape, and the local structural geometry are enveloped by the parameter K. The primary difficulty in analyzing the growth of surface cracks is that no one value of K may be assigned to characterize the entire crack front; further, the stress state near the crack is three dimensional due to crack-front curvature and complex local geometry.

The results presented in this paper concern the evaluation of a design system analytical model for fatigue growth of surface-initiated cracks. A weight function method is used for a simplified model of elliptical cracks in order to account for the effects of locally variable stresses. The underlying fracture-mechanics model of elliptical cracks is based on three-dimensional boundary-integral equation (BIE) analysis. The paper addresses questions of BIE accuracy for predicting local stress-intensity factor data as well as the simplified model used to represent growing elliptical surface and corner cracks.

Two sets of experimental crack-growth data are correlated analytically. The first test is the growth of a surface crack in a nominal tension specimen. Crack-length and depth-growth rate data are obtained and used to calibrate BIE data for surface cracks. The second set of experimental data is taken from a published experimental program for corner-crack growth at a hole in a plate. This second set of data allows for an evaluation of the design system model for corner-crack growth at stress concentrations.

Use of the weight function method for modeling the effects of variable stress fields is reviewed together with the technique for modeling elliptical cracks with two shape (size) degrees of freedom. In order to obtain an efficient design system, it is necessary to reduce the completely general crack shape to an elliptical shape; fatigue growth of surface and corner cracks is modeled by predicting the change in the two ellipse dimensions. Some questions concerning this use of a reduced crack model are reviewed.

Surface Flaw Specimen Correlation

Test Program Description

A primary goal in three-dimensional BIE fracture mechanics analysis research is the development of efficient models for predicting fatigue growth of surface cracks. Two questions arise in this development. How accurately does the analysis method predict the stress-intensity factor

distribution? What criterion governs the fatigue growth of a surface crack? In order to address these two questions, a test program was undertaken in which surface cracks were grown in fatigue.

The test specimen shown in Fig. 1 is adapted from a standard fatigue-crack growth test specimen. A "thumbnail" surface slot was created by electrical-discharge machining (EDM) and shows as the smallest, darkened surface in Fig. 2. The specimen was cycled with a nominal stress of 40 ksi at an R-ratio of 0.0. Surface length measurements were obtained by replication and are given in Fig. 3.

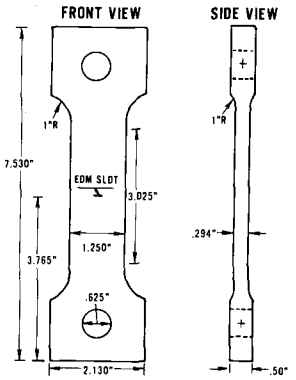

FIG. 1—*Test specimen geometry for surface-crack growth.*

In order to quantify the crack depth and crack shape during fatigue loading (in the absence of striations), the specimen was heat tinted several times. Differential oxidation of the crack surface was accomplished and is seen in Fig. 2; dimensions of these heat-tinted crack shapes are given in Fig. 4. Surface crack depth versus cycle data were then obtained by interpolation of the heat tint data in Fig. 3. Values of crack depth between heat tint depths were taken from a plot of crack aspect ratio, that is, crack depth versus surface length. Finally, it was verified by separate testing that the heat tinting did not effect the fatigue-crack growth rate for control specimens.

Fracture-Mechanics Analysis

The test program was defined in order to achieve the greatest degree of analytical simplicity possible. Thus, the crack was initiated at an EDM slot rather than allowed to initiate by natural, crystallographic cracking. Secondly, the loading is symmetric tension such that Mode I deformation results; generally, all in-service surface cracks grow in Mode I normal to

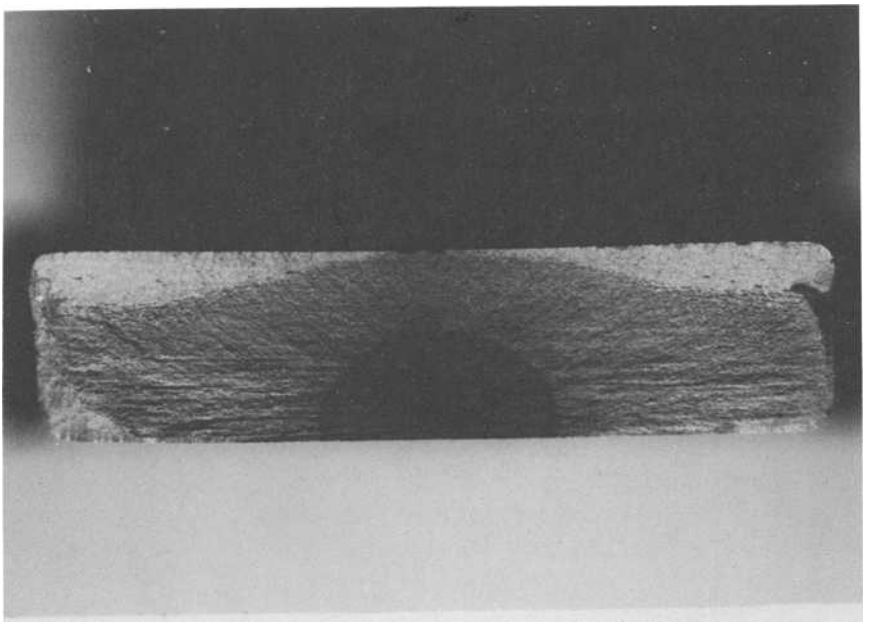

FIG. 2—*Cross-section of failed surface-crack specimen showing heat-tinted crack shapes.*

the surface of the structure. Finally, the specimen was loaded in nominal uniform tension. Nonuniform stress influence is addressed in the next section.

Standard BIE modeling of the symmetric quadrant of the specimen was used to estimate values of crack-front, stress-intensity factor. For details of the modeling procedure the reader is directed to Ref *1*.[2] Actual heat-tint crack shapes were used in the modeling with the exception of the characteristic "turn back" of the crack at the specimen surface seen in Figs. 2 and 4. The model assumed a normal intersection angle as shown in Fig. 4. In all cases, the heat-tint crack shape was quite nearly elliptical with an approximate aspect ratio of $c/a = 1.2$. Elliptical shapes were used in the BIE analyses for the actual crack size and shape.

A major concern in specimen design is the importance of finite specimen dimensions (width and depth) on the stress-intensity factor (K) distribution. An analytical study was performed for the crack shape and size taken from Heat Tint 4; the results are shown in Fig. 5. The lowest curve corresponds to the K-distribution for the nearly infinite body; the upper curves model the finite-depth effect and the combined finite-size effects. It is seen that crack depth is the most important influence for this rather deep crack, and it effects the entire shape of the K-distribution as well as its magnitude. Finite-width effects are small—on the order of a few per-

[2]The italic numbers in brackets refer to the list of references appended to this paper.

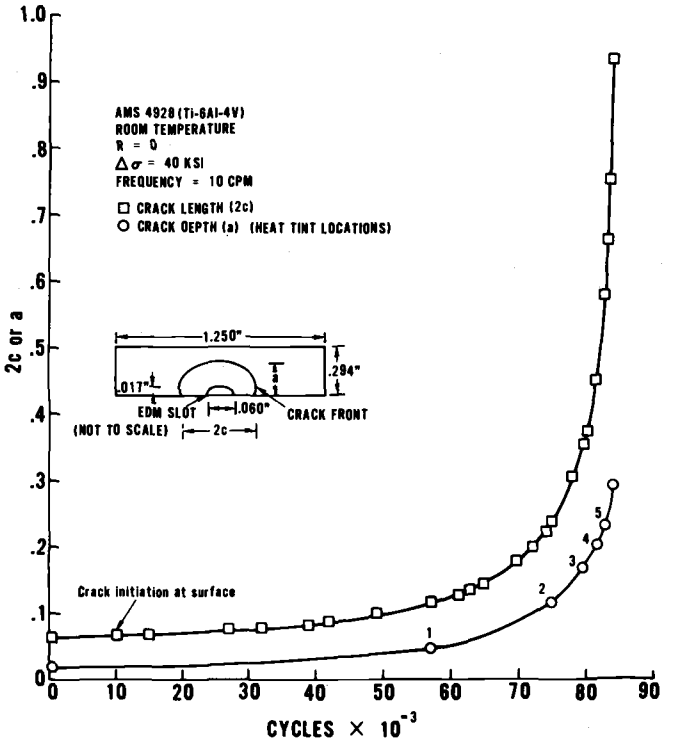

FIG. 3—*Crack-surface length and depth data taken from fatigue test of surface-crack specimen.*

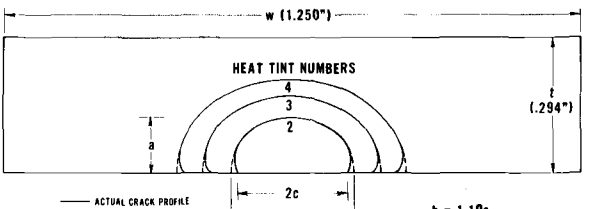

HEAT TINT LOCATIONS

HEAT TINT NUMBER	b/a	a/t	2 c/w	2 b/w
1	1.40	.153	.091	.100
2	1.10	.402	.189	.208
3	1.16	.564	.281	.308
4	1.21	.693	.358	.395
5	1.40	.780	.460	.507

FIG. 4—*Detailed description of surface-crack sizes and shapes at the heat-tint locations.*

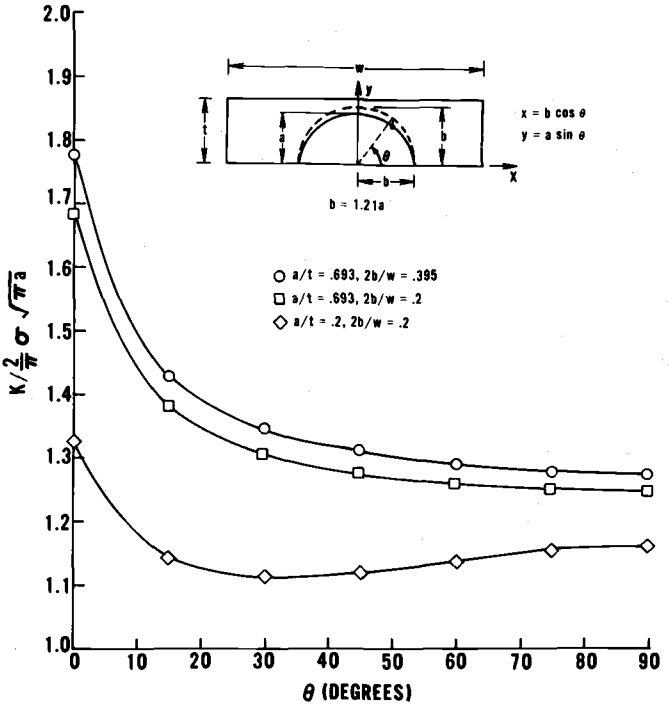

FIG. 5—*Stress-intensity factor distributions for various models of the surface crack at heat tint 4.*

cent. It is, therefore, concluded that the test specimen represented an infinitely wide sheet with thickness being the dominant size scale parameter.

Correlation of Test Data

Crack-growth rate data from Fig. 3 was used in a standard data reduction program to obtain crack-growth rate versus size. Separate calculations were performed for surface length and crack depth. Base line fatigue crack growth rate for this alloy (AMS 4928; 6A1-4V titanium) was taken as

$$da/dN = 3.6 \times 10^{-10} (\Delta K)^{3.5} \tag{1}$$

for $10^{-6} \leq da/dN \leq 10^{-4}$ in./cycle; ΔK has the units of ksi$\sqrt{\text{in.}}$

Empirical values of stress-intensity factors at the surface (ΔK_b) and the crack depth (ΔK_a) locations are obtained from the growth-rate data and Eq 1. The resulting stress-intensity factors are plotted in Fig. 6.

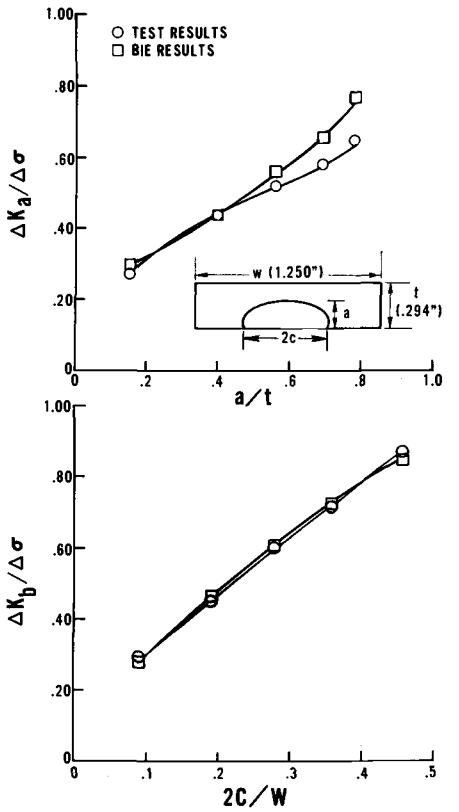

FIG. 6—*Experimentally determined values of stress-intensity factors at two locations for the surface-crack specimen compared to BIE values.*

BIE values of stress-intensity factor at two crack front locations also are plotted in Fig. 6. Good correlation of the analytical data was achieved at the crack depth up to $a/t = 0.5$. For deeper cracks, the correlation is seen to degrade. It is assumed currently that the numerical model does not measure this depth effect which was shown in Fig. 5 adequately. Further numerical analysis is expected to resolve this discrepancy.

A significant difficulty was initially encountered in correlating the free-surface, growth-rate data. Attention was focused on the turn-back zone on the crack front as shown in Fig. 2. Measurements of the size of this zone were made; in all cases, the turn back occurred within 15 deg of elliptical angle (as defined in Fig. 5). Further, it was found that the actual surface length (c) was a nearly constant percentage of the surface length (b) of the superscribed ellipse as shown in Fig. 4.

BIE analysis results showed that the K-distributions for the surface crack specimen were affected by crack turn back only within the 15 deg

turn-back zone. As seen from analyzing Fig. 4 geometries for the aspect ratios encountered, normal motion of the crack front for the semiellipse model is essentially equal over the 15-deg portion of the crack front; this result is accurate to within 1.5 percent. Assuming crack growth in the direction normal to the local crack front is determined by Eq 1 in the absence of free-surface effects, it is deduced that $K(15 \text{ deg}) = K_b$ for the semiellipse. Taking $db/dN = 1.10\ dc/dN$ and Eq 1, the experimental value of K_b is plotted in Fig. 6*b*; BIE data for K (15 deg) is plotted as the analytical estimate of K_b. The good agreement between the estimates in both parts of Fig. 6 verifies the BIE results for crack-front locations below the turn-back zone.

Further BIE investigation of the K-distribution within the crack turn-back zone indicated that the surface value of K (K_c) increased with the amount of turn back. For the amount of turn back shown in Fig. 4, it was estimated roughly that the K_c was 40 percent higher than K (15 deg). This significantly greater value of K is required due to the kinematics of crack opening near the free surface. It should be recalled from Ref *1* that the K data used herein is determined on the basis of crack-opening displacements.

Known residual compressive stresses at the specimen-free surface are a possible means of correlating the turn-back effect. The surface compressive stress will tend to keep the crack tip (at the surface) closed during a part of the cyclic loading, thereby, reducing the cyclic damage for a given amount of remote loading. A model for crack growth with a mean stress correction for this alloy has been given in Ref *2*; the correction is given in terms of $R = K_{\min}/K_{\max}$ by

$$\Delta K_{\text{eff}} = \frac{1.63}{1.73 - R} \Delta K \tag{2}$$

When $R = 0.1$ (base-line testing), Eq 1 is the correct crack-growth model using $\Delta K_{\text{eff}} = \Delta K$ (computed). Using the computed estimate of K_c relative to K_b and the constant ratio of $b/c = 1.10$, Eq 2 gives an estimate of $R = -0.6$. This value of R gives a surface residual compressive stress (normalized to the loading amplitude) of 0.38; X-ray diffraction evaluation of the normalized residual stress at the surface produced an estimate of 0.57 ± 0.3. While this general agreement is certainly not conclusive, it offers some potential insight into the turn-back problem.

Additional surface-crack specimen data were generated, and they confirmed the results cited previously. It is concluded generally that the BIE analysis is accurate for the cases where finite-depth effects are not great. Further, it is possible on the basis of these results to conclude that a reasonable model for fatigue growth of surface cracks can be offered. The model is to treat the crack as having elliptical shape with each crack-

front location moving ahead at a rate dependent on its value of stress-intensity factor. Finally, the turn-back zone is seen as a local adjustment of crack shape which does not effect the results for the majority of the crack front.

Corner Crack Specimen Correlation

Review of the Design Problem

Fatigue-crack growth in gas-turbine engine structures generally involves a surface or corner crack growing in the variable stress field of a stress concentration. Modeling such crack growth must involve the effects of the variable stress loading, the distribution of crack-front, stress-intensity factor as described in the preceding section, and the finite dimensions of the local structure when necessary. Since each notch geometry differs between various structural components, the magnitude of the modeling task appears, at first, to be extremely large.

However, various techniques are available to reduce significantly the amount of analytical support necessary to model surface and corner-crack growth in engineering structures. The weight-function method described in Refs *3* and *4* is one such technique and is reviewed next. Essentially, the technique is based on the use of fracture-mechanics data generated for various crack shapes and sizes for the simple problem of uniform applied stress. Values of K for nonuniform loading are then generated by integrating the local, uncracked stress field with the weight functions for simple tension.

Three-dimensional cracks introduce an additional order of difficulty in the weight-function approach due to the variability of K along the crack front. Efficient three-dimensional modeling therefore requires some simplifying criterion for three-dimensional crack growth. Reference *4* shows that one possible technique is to assume that surface and corner cracks can grow only by changing from one elliptical shape to another such that two crack dimensions (and thus two values of K) define the entire crack front. The following sections attempt to establish the credibility of this approach for corner cracks growing from the edge of a circular hole.

Elements of the Weight-Function Method for Three-Dimensional Cracks

It has been shown in Ref *3* that for a linear-elastic body in plane strain loaded symmetrically about a crack, the Mode I, stress-intensity factor for any load system can be calculated if the stress distribution in the uncracked body is known and the stress-intensity factor and displacement field are known for a single load state. In particular, in the absence of body forces

$$K^{(2)}(l) = \frac{H}{2K^{(1)}(l)} \int_{\Gamma} \mathbf{t}^{(2)} \times \frac{\partial \mathbf{u}^{(1)}}{\partial l} \, d\Gamma \tag{3}$$

where $K^{(2)}$ and $\mathbf{t}^2$ are the stress-intensity factors and surface tractions of Load State 2 and $\mathbf{u}^{(1)}$ is the displacement field for Load State 1. H denotes an elastic modulus, and l is the crack length.

In the case mentioned previously, the crack is one dimensional, and its stress singularity is defined by a single, stress-intensity factor. In the case of a crack in a three-dimensional geometry, the stress-intensity factor is a function of position on the crack face. In principle [*3*], the stress-intensity factor for any load state can be determined in a manner analogous to Eq 3. In practice, the determination of the required information on variations of $\mathbf{u}^{(1)}$ with crack geometry is too difficult.

In order to exploit the weight-function method in three-dimensional problems, it is necessary to reduce the number of degrees of freedom defining the crack shape. The behavior of the surface-crack data just cited makes such an assumption plausible. An approach is to allow two degrees of freedom (the semiaxes a and b) to determine the elliptical crack shape. This approach was followed in Ref *4* and leads to two stress-intensity factors, $\bar{K}_a$ and $\bar{K}_b$, for the two degrees of freedom. These values of $\bar{K}$ can then be related by such models as Eq 1 to independent growth of the two axes of the elliptical crack.

The crack-growth model (Eq 1) for the material is integrated using the averaged stress-intensity factor(s). In the two degrees of freedom model, this leads to a coupled pair of equations since each $\bar{K}$ depends on the current shape of the growing crack.

The two degrees of freedom model for elliptical cracks was used to predict the growth of the surface crack discussed previously. The model predicts the two ellipse dimensions (a, b) given in Fig. 4 by applying the crack-growth rate in Eq 1 to each of the weight-function, stress-intensity factors $\bar{K}_a$, $\bar{K}_b$. Predicted values of the actual surface length (c) are taken to be (b/1.10) to account for the crack turn-back effect. Correlation of the predicted crack size and the experimental data is shown in Fig. 7. Agreement is good (including the slope, da/dN) from Heat Tint 1, which is the initial modeling size, through Heat Tint 3. Beyond Heat Tint 3, the correlation is not as good; however, the $\bar{K}$ computer model data do not currently include finite specimen depth effects. These effects become significant for a/T when they are greater than 0.6 (Heat Tint 3).

The values of $\bar{K}_a$ and $\bar{K}_b$ for the surface-crack problem were found to be essentially equal over the predicted life of the growing crack. In Fig. 5, the normalized value of $\bar{K}/K(a)$ for the aspect ratio is about 1.15 for both $\bar{K}_a$ and $\bar{K}_b$. It is seen from the figure that these values of $\bar{K}$ are representative of the K-distribution inside of the crack turn-back zone (15 deg). The correlation in Fig. 7 indicates that the K-distribution along the interior

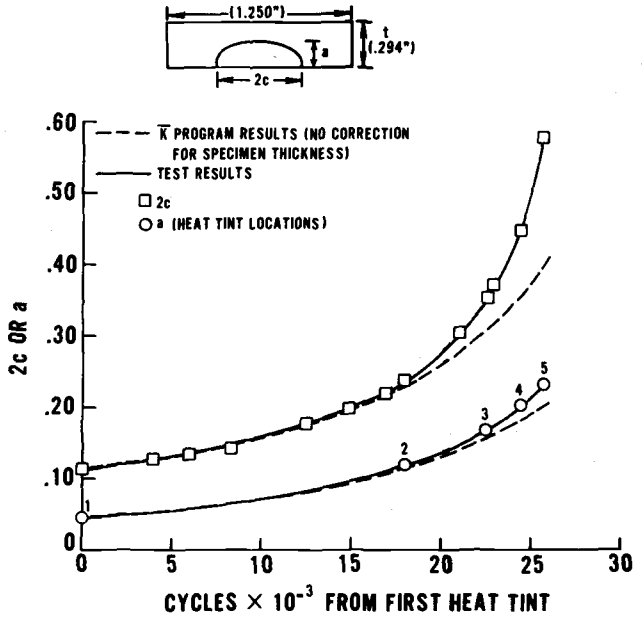

FIG. 7—*Correlation of surface-crack growth data with two degrees of freedom, elliptical surface crack analytical prediction.*

portion of the crack front governs growth, not the stress-intensity factor distribution within the crack turn-back zone.

It, therefore, seems possible to predict surface fatigue-crack growth for the general problem with variable stresses using a weight-function approach. Such fatigue-crack growth modeling is extremely efficient and allows surface crack-life predictions to be made routinely in a design environment.

Correlation of Test Data

Published experimental data for corner cracks grown in plates with circular holes were taken from Ref *5*; the specimen geometry is shown in Fig. 8. The material used in the study was Plexiglas which was characterized by a crack-growth relation given by

$$da/dN = 0.2214 \times 10^{-20} (\Delta K)^{5.591} \tag{4}$$

with da/dN in in./cycle and ΔK in psi$\sqrt{\text{in.}}$ It should be noted at this point that the very high exponent for this Plexiglas data makes predicted values of da/dN very sensitive to errors in the cyclic stress-intensity factor.

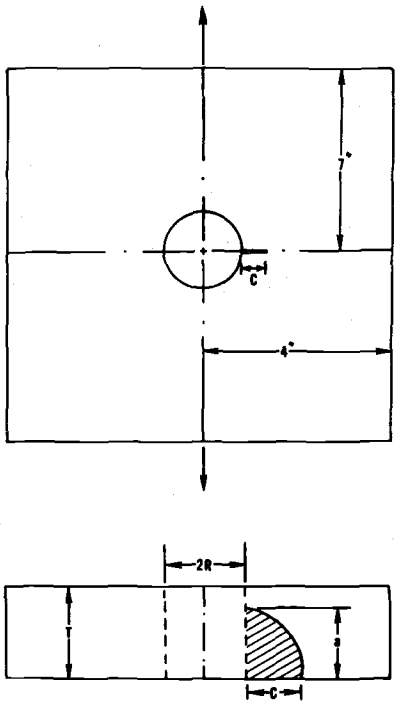

FIG. 8—*Test-specimen geometry for corner-crack testing given in Ref* 5.

Crack growth was modeled using the weight-function data for corner cracks in a cube under simple tension as described in Ref *4*. Thus, the interaction of the crack size and the circular hole are neglected by the usual model; more will be said on this later. Uncracked stresses were obtained by numerical modeling and found to be quite close to the results for an infinite plate with a circular cutout.

Figure 9 shows the K-distribution for a corner crack of aspect ratio equal to 1.5. This value was selected from Ref *1* as it is close to the actual "equilibrium" corner-crack aspect ratio value. The two values of $\bar{K}$ for the elliptical shape under uniform tension loading also are indicated in Fig. 9. It should be noted that these values of $\bar{K}$ closely approximate the local values of K away from the zone of free-surface influence (turn back) discussed previously. Reference *1* data also show that the normalized values of K near dimension a in Fig. 9 are quite insensitive to crack-aspect ratio for values greater than one; the normalized values of K near dimension c are more strongly influenced by crack-aspect ratio.

Initial attempts to correlate the corner crack-growth data in Ref *5* were not successful due to consistent overestimation of the values of $\bar{K}$. It now is concluded that the effects of hole geometry on the weight-function data

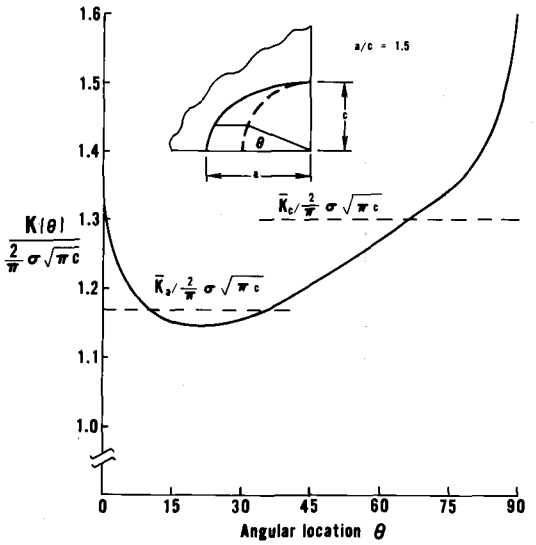

FIG. 9—*Stress-intensity factor distribution for 1.5:1 aspect ratio corner crack.*

cannot be neglected for the crack sizes in Ref *5*. Following the results for through-the-thickness cracks given in Ref *6*, it was decided to reduce the values of K uniformly to account for this effect. In Ref *6*, it is shown for a through-the-thickness crack that K decreased by 20 percent for values of crack length (c) to hole radius (R) ratio greater than 0.2.

While a rigorous three-dimensional solution does not exist for the corner crack on the hole, a reduction in crack-front, stress-intensity factor of 9 percent was used in this study. Both values of $\bar{K}$ were reduced equally, corresponding to a uniform reduction in K along the entire crack front. Reference *6* shows that the reduction in K rapidly assumes a lower limit, constant value for $c/R > 0.2$. It was assumed on the current study that the limiting reduction in K had also been achieved as $c/R > 0.25$.

Figure 10 compares predicted corner crack-growth data for hole surface length (a) and specimen surface length (c) with the experimental data from Ref *5*. In general, the agreement is quite good, particularly in light of the scatter in base-line, crack-growth data (factor of three) reported in Ref *5*. Further, the trends in values of crack-aspect ratio for various initial values as predicted by the two degrees of freedom crack model agreed quite well with experimental data.

Figures 11 and 12 show the results of the study in terms of the two values of $\bar{K}$ computed for the two surface lengths of the corner cracks. Figure 11 shows the expected result, that is, the normalized values of $\bar{K}_a$ at the surface of the hole were essentially independent of aspect ratio. Figure 12 shows the values of $\bar{K}_c$ computed for the specimen surface

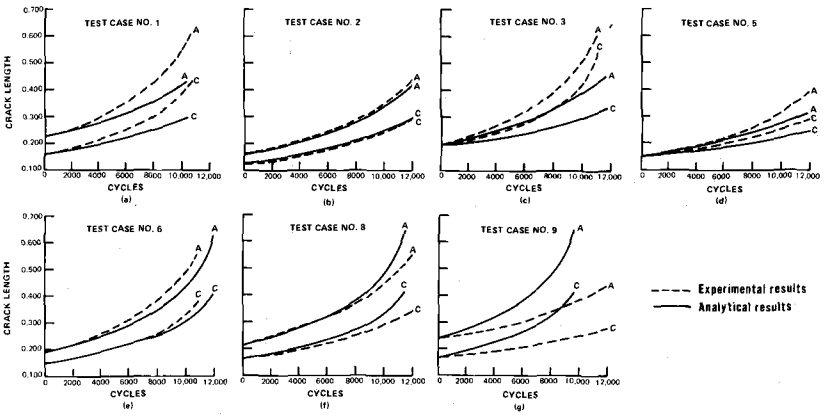

FIG. 10—*Comparison of experimental data for corner cracks to weight function predictions for various initial crack sizes.*

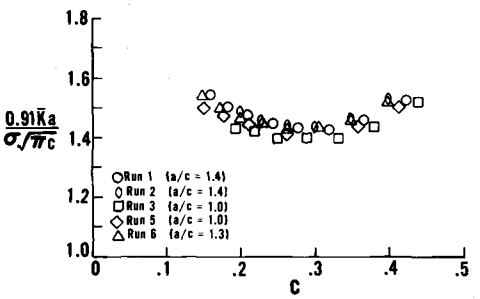

FIG. 11—*Normalized values of stress-intensity factor computed at the hole surface by the weight function method.*

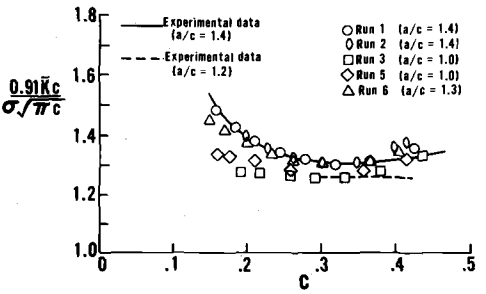

FIG. 12—*Normalized values of stress-intensity factor computed along the specimen surface by the weight function method.*

length. As expected, aspect ratio is seen to effect the values of $\bar{K}_c$. Experimental values of normalized $\bar{K}_c$ for two aspect ratios taken from the data in Ref *6* also are plotted. The agreement between analysis and test is good.

The conclusion that the weight function values of $\bar{K}_a$ and $\bar{K}_c$ adequately account for the local variations in actual values of K below the free-surface locations is further substantiated. The major remaining issue in this study is the need for an independent evaluation of the hole size effect, assumed herein to be essentially a uniform reduction in K. Further analysis is expected to provide this confirmation.

Conclusions

Residual fatigue-life prediction for surface and corner cracks in structures can be reduced to a level of effort appropriate for routine design analysis using the weight-function approach. The reduction occurs through the use of a weight-function approach to modeling local, uncracked-stress variation together with simple elliptical models of the cracks. Three-dimensional, fracture-mechanics analysis performed for simple cracked geometries and loading forms the numerical basis of the system.

Fatigue-growth data from a surface-crack fatigue test have been correlated using both local values of stress-intensity factor as well as two averaged values deduced from the weight-function model of elliptical cracks. Further, fatigue data for corner cracks growing from holes in plates, simulating real structural fatigue problems, have been correlated by the weight-function model. It is seen that these real cracks grow essentially as ellipses with aspect ratios generally less than 1.5. Even in the variable stress-field tests, the cracks tended to a constant, equilibrium value of aspect ratio. Local disturbance of the crack shape at the specimen surface was not found to be an important aspect of the surface and corner crack-fatigue problem. Stress-intensity factor distribution below the surface appears to dictate growth rate.

Finally, the need to develop complex, multidegree of freedom weight-function models for these structural fatigue-crack growth problems does not appear to be justified. Crack area and the leading terms describing the uncracked stress field dominate the fatigue-life calculation. Crack-aspect ratio and higher-order definition of local stresses are, at most, secondary concerns. It now seems clear that fatigue-life prediction for surface and corner cracks may be efficiently accomplished without the need for detailed analysis of the crack-front, stress-intensity factor distribution; this conclusion requires further detailed verification.

Acknowledgments

Portions of this paper are derived from work sponsored by the Air Force Office of Scientific Research (AFSC), United States Air Force, under Contract F44620-74-C-0060 with W. J. Walker (NA) as Project Engineer; the authors further wish to acknowledge the work by P. M. Besuner which forms the basis for the life prediction methodology used in this paper.

References

[1] Cruse, T. A. and Meyers, G. J., "Three-Dimensional Fracture Mechanics Analysis," *Journal of the Structural Division*; American Society of Civil Engineers, Vol. 103, No. ST2, Feb. 1977, pp. 309–320.

[2] Yuen, A., Hopkins, S. W., Leverant, G. R., and Rau, C. A., *Metallurgical Transactions*, Vol. 5, 1974, pp. 1833–1842.

[3] Rice, J. R., *International Journal of Solids & Structures*, Vol. 8, 1972, pp. 751–758.

[4] Cruse, T. A. and Besuner, P. M., *Journal of Aircraft*, Vol. 4, 1975, pp. 369–375.

[5] Snow, J. R., "Stress Intensity Factor Calibration for Corner Flaws at an Open Hole," Technical Report AFML-TR-74-282, Air Force Materials Laboratory, Dayton, Ohio, 1974.

[6] Kobayashi, A. S., Palvanick, N., Emery, A. F., and Love, W. J., "Corner Crack at the Bore of a Rotating Disk," *Journal of Engineering for Power*, Vol. 98, Oct. 1976, pp. 465–470.

C. W. Smith,[1] *M. Jolles,*[1] *and W. H. Peters*[1]

Stress Intensities for Cracks Emanating from Pin-Loaded Holes

REFERENCE: Smith, C. W., Jolles, M., and Peters, W. H., "**Stress Intensities for Cracks Emanating from Pin-Loaded Holes,**" *Flaw Growth and Fracture, ASTM STP 631,* American Society for Testing and Materials, 1977, pp. 190–201.

ABSTRACT: A series of stress freezing photoelastic experiments were conducted on large plates containing central holes with cracks emanating from the edge formed by the intersection of the hole with the plate surface. Loads were applied through rigid pins with neat fits in the holes. Stress-intensity factors (SIF) were estimated by a computer assisted least squares analysis of the photoelastic data taken from slices near the points of intersection of the flaw border with the hole boundary and the plate surface. Results indicate that the local mode of loading changes from Mode I near the hole boundary to mixed mode near the plate surface. The analysis is extended to include mixed mode loading, and results are compared with an existing approximate theory.

KEY WORDS: crack propagation, photoelasticity, fracture mechanics, stress intensity factors, fractures (materials), stresses

Nomenclature

n, t, z	Local rectangular cartesian coordinates along the flaw border (mm)
σ_{ij}, $i,j = n,z$	Stress components in plane normal to flaw surface and flaw border near crack tip (kPa)
σ_{ij}° $i,j = n,z$	Part of regular stress field near crack tip (kPa)
r, θ	Polar coordinates measured from crack tip (mm, rad)
τ_{max}	Maximum shearing stress in plane normal to flaw surface and flaw border near crack tip (kPa)
σ_b	Bearing stress (kPa)
K_I	Mode I stress-intensity factor (kPa·m$^{1/2}$)
K_{II}	Mode II stress-intensity factor (kPa·m$^{1/2}$)

[1]Professor, lecturer, and graduate research assistant, respectively, Department of Engineering Science and Mechanics, Virginia Polytechnic Institute and State University, Blacksburg, Va. 24061.

K^* Combined mode stress-intensity factor $[(K_I \sin \theta + 2K_{II} \cos \theta)^2 + (K_{II} \sin \theta)^2]^{1/2}$ (kPa·m$^{1/2}$)
K_{AP} Mode I apparent stress-intensity factor $[\tau_{max}(8\pi r)^{1/2}]$ (kPa·m$^{1/2}$)
K^*_{AP} Combined mode apparent stress-intensity factor (kPa·m$^{1/2}$)
n' Stress fringe order
f Material fringe value (N/m)
t' Slice thickness (mm)
a Flaw depth (mm)
T Plate thickness (mm)
$\bar{r}$ Hole radius (mm)
c Flaw length (mm)
θ_m Angle defining maximum distance from crack tip to a given fringe (rad)
$\theta_m{}^\circ$ Angle θ_m approaching the crack tip (rad)

Problems associated with cracks emanating from both unfilled and filled holes in plates have been a major concern of stress analysts for several years [*1*][2] and is currently receiving considerable attention from researchers in several industries. Variations of the problem have been studied both analytically and experimentally [*2–5*], but, to date, the problem has proven to be mathematically intractable to even a purely elastic solution due to its complex three-dimensional effects characterized by variations in the stress-intensity factor (SIF) along the flaw border.

In view of these complications, one is led to consider experimental techniques for obtaining SIFs for the problem. Stress freezing photoelasticity is a well-established technique for analyzing three-dimensional problems, and (using an idea of G. R. Irwin [*6*]) the senior author and his associates have developed, over a period of years [*7–22*], a computer assisted stress freezing photoelastic technique for estimating values of the Mode I SIF along the border of cracks in three-dimensional problems. Experimental features of the method and the current analytical approach are described [*23,24*]. It has already been applied successfully to problems of cracks emanating from open holes [*4,5*].

This paper concerns an application of this method to the determination of SIF at prescribed locations along the border of a flaw emanating from the corner formed by the intersection of the surface of a flat plate with the boundary of a pin-loaded hole where the pin is rigid.

Analytical Considerations

The method of analysis for Mode I loading has been described elsewhere [*5,24*] but will be summarized here for convenience.

[2]The italic numbers in brackets refer to the list of references appended to this paper.

Mode I Analysis

It has been shown [*25*] that the singular elastic field surrounding the tip of an elliptically shaped flaw border can be expressed in the same form as for the plane case if a local moving rectangular cartesian coordinate system is employed. For Mode I loading, these stresses can be written in the form

$$\sigma_{nn} = \frac{K_I}{(2\pi r)^{1/2}} \cos\frac{\theta}{2}\left(1 - \sin\frac{\theta}{2}\sin\frac{3\theta}{2}\right) - \sigma_{nn}^{\circ}$$

$$\sigma_{zz} = \frac{K_I}{(2\pi r)^{1/2}} \cos\frac{\theta}{2}\left(1 + \sin\frac{\theta}{2}\sin\frac{3\theta}{2}\right) - \sigma_{zz}^{\circ} \qquad (1)$$

$$\sigma_{nz} = \frac{K_I}{(2\pi r)^{1/2}} \sin\frac{\theta}{2}\cos\frac{\theta}{2}\cos\frac{3\theta}{2} - \sigma_{nz}^{\circ}$$

where the notation, adapted to the current problem, is pictured in Fig. 1. The first terms represent the singular part of the stress field and the σ_{ij}° (following the Irwin approach for the plane problem) represent the contribution of the regular stress field in the form of the first terms of Taylor's series expansions of the regular stress components near the crack tip. Assuming that any flaw border can be represented as locally elliptic in shape [*26*], Eq 1 can be considered as applicable to such flaw-border shapes.

Observation of Mode I fringe patterns (Fig. 2) reveals that the fringes tend to spread in a direction approximately normal to the flaw surface.

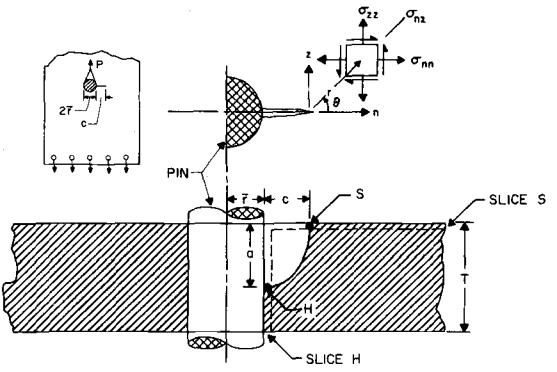

FIG. 1—*Problem geometry and stress notation.*

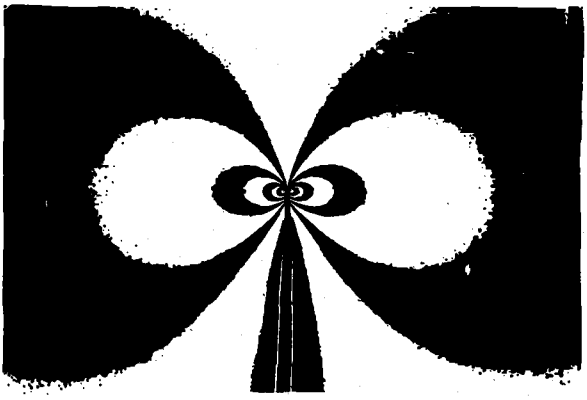

FIG. 2—*Spreading of fringes normal to crack plane (Mode I).*

Thus, best fringe discrimination and accuracy is expected along $\theta = \pi/2$ in Eq 1. Evaluating Eq 1 along $\theta = \pi/2$, computing

$$\tau_{\max} = \frac{1}{2}\left[(\sigma_{nn} - \sigma_{zz})^2 + 4\sigma_{nz}^2\right]^{1/2} \tag{2}^3$$

and truncating to the same order as Eqs 1, one obtains

$$\tau_{\max} = \frac{A}{r^{1/2}} + B \tag{3}$$

where $A = K_I/(8\pi)^{1/2}$ and B = constant containing σ_{ij}°. Rewriting Eq 3 in a normalized form, we have

$$\frac{\tau_{\max}(8\pi r)^{1/2}}{\sigma_b(\pi a)^{1/2}} = \frac{K_I}{\sigma_b(\pi a)^{1/2}} + \frac{B(8\pi r)^{1/2}}{\sigma_b(\pi a)^{1/2}} \tag{4}$$

or

$$\frac{K_{Ap}}{\sigma_b(\pi a)^{1/2}} = \frac{K_I}{\sigma_b(\pi a)^{1/2}} + \frac{B(8)^{1/2}}{\sigma_b}\left(\frac{r}{a}\right)^{1/2} \tag{5}$$

where $K_{Ap} = \tau_{\max}(8\pi r)^{1/2}$ is defined as an "apparent SIF. Equation 5, when plotted as

$$\frac{K_{Ap}}{\sigma_b(\pi a)^{1/2}} \text{ versus } \left(\frac{r}{a}\right)^{1/2}$$

[3]Also, from the stress optic law $\tau_{\max} = n'f/2t'$.

yields a straight line which when extrapolated to the origin will yield $K_I/\sigma_b(\pi a)^{1/2}$, the normalized SIF.

Since the foregoing approach utilizes a two-parameter (A,B) model and such an approach was suggested originally only for the case where the remote stress field was uniform and no surfaces other than the crack surfaces were present, one expects the size of the zone dominated by Eqs 3 through 5 to be constricted when such additional effects are present. However, if the linear zone of Eq 5 can be located experimentally, the two-parameter approach can still be used. If one cannot locate such a zone experimentally, then additional terms leading to an equation of the form

$$\tau_{max} = \frac{A}{r^{1/2}} + \sum_{n=0}^{m} B_n r^{n/2} \tag{6}$$

with suitable truncation criteria must be considered. Since such criteria are not yet established, this latter approach is avoided where possible and was not necessary in the studies described next.

Mixed Mode Analysis

The equations for the mixed-mode analysis containing only inverse square root singular terms were presented in Ref *9* and appear to be adequate for many two-dimensional problems. However, for three-dimensional problems, one needs to include additional terms in the same fashion as was done for Mode I. In the sequel, the development of these equations is traced, and the application of the technique to mixed-mode problems is described.

When a cracked body is subjected to mixed-mode loadings, one can write, following Eq 1

$$\sigma_{nn} = \frac{K_I}{(2\pi r)^{1/2}} \cos\frac{\theta}{2}\left[1 - \sin\frac{\theta}{2}\sin\frac{3\theta}{2}\right]$$

$$- \frac{K_{II}}{(2\pi r)^{1/2}} \sin\frac{\theta}{2}\left[2 + \cos\frac{\theta}{2}\cos\frac{3\theta}{2}\right] - \sigma_{nn}^{\circ}$$

$$\sigma_{zz} = \frac{K_I}{(2\pi r)^{1/2}} \cos\frac{\theta}{2}\left[1 + \sin\frac{\theta}{2}\sin\frac{3\theta}{2}\right]$$

$$+ \frac{K_{II}}{(2\pi r)^{1/2}} \sin\frac{\theta}{2}\cos\frac{\theta}{2}\cos\frac{3\theta}{2} - \sigma_{zz}^{\circ} \tag{7}$$

$$\sigma_{nz} = \frac{K_I}{(2\pi r)^{1/2}} \sin\frac{\theta}{2}\cos\frac{\theta}{2}\cos\frac{3\theta}{2}$$

$$+ \frac{K_{II}}{(2\pi r)^{1/2}} \cos\frac{\theta}{2}\left[1 - \sin\frac{\theta}{2}\sin\frac{3\theta}{2}\right] - \sigma_{nz}^{\circ}$$

where the notation again refers to Fig. 1 for the problem at hand. Now, proceeding exactly as before with Eqs 2 and 3, but without specifying a value for θ, we obtain for the coefficients in Eq 3

$$A = \left\{\frac{1}{8\pi}\left[(K_I \sin\theta + 2K_{II}\cos\theta)^2 + (K_{II}\sin\theta)^2\right]\right\}^{1/2}$$
$$B = B[\theta, K_I, K_{II}, \sigma_{ij}^{\circ}] \tag{8}$$

Now, in general, the effect of σ_{ij}° involves both a folding and a change in eccentricity of the fringe loops [*11*]. If folding occurs, θ_m, the angle, along which the distance to a fringe from the crack tip is greatest, will vary with the fringe order n', and one must plot θ_m versus r/a and extrapolate to the origin in order to obtain θ_m°—the value of θ_m associated with K_I and K_{II}. In the present problem, θ_m was constant over the data range in the fashion indicated qualitatively by Fig. 3. Upon computing

$$\lim_{\substack{r\to 0\\ \theta\to\theta_m^{\circ}}}\left\{(8\pi r)^{1/2}\frac{\partial\tau_{max}(K_I, K_{II}, r, \theta, \sigma_{ij}^{\circ})}{\partial\theta}\right\} = 0 \tag{9}$$

one obtains

$$\left[\frac{K_{II}}{K_I}\right]^2 - \frac{4}{3}\left[\frac{K_{II}}{K_I}\right]\cot 2\theta_m^{\circ} - \frac{1}{3} = 0 \tag{10}$$

By inserting the measured value of θ_m° into Eq 10, $[K_2/K_1]$ can be computed. Then, by combining the stress-optic law with a modified form of Eq 3

$$\tau_{max} = \frac{n'f}{2t'} = \frac{K^*_{Ap}}{(8\pi r)^{1/2}} \tag{11}$$

where

$$K^*_{Ap} = [(K_{IAp}\sin\theta_m + 2K_{IIAp}\cos\theta_m)^2 + (K_{IIAp}\sin\theta_m)^2]^{1/2}$$

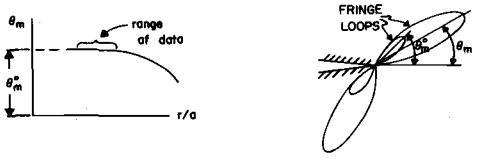

FIG. 3—*Determination of* θ_m° *from* θ_m.

we can solve for the individual values of K_I and K_{II}. In order to do this, we must obtain

$$K^* = [(K_I \sin \theta_m^\circ + 2K_{II} \cos \theta_m^\circ)^2 + (K_{II} \sin \theta_m^\circ)^2]^{1/2}$$

from K^*_{Ap} by plotting a normalized $K^*_{Ap} = \tau_{max}(8\pi r)^{1/2}$ versus $(r/a)^{1/2}$, identifying a linear zone and extrapolating to the origin as was done for the Mode I case.

Experiments

Stress freezing tests on eight separate models were conducted. These models were constructed from fringe free cast plates of PSM-8, a high-quality stress freezing material manufactured by Photolastic, Inc., which is free of time edge[4] and surface tension effects. Model making procedure consisted of the following steps.

1. Drill and ream circular hole in center of long, wide plate.
2. Tap in starter crack with sharp edge at hole-surface interface.
3. Insert aluminum pin (neat fit) and mount model in a dead loading rig.
4. Heat above critical temperature, apply remote tension normal to flaw surface, grow crack to the desired size, remove load, and cool to room temperature.
5. Heat above critical temperature, apply live load through pin, and cool to room temperature.
6. Slice as indicated in Fig. 1.

Figure 1 shows the crack geometry and slice locations. The geometries tested are shown in the upper part of Table 1. These slices are thick (approximately 2.5 mm) relative to crack-root radius (approximately 2.5×10^{-3} mm) and are believed to yield nearly plane-strain averages not significantly affected by boundary-layer [*27*] effects.

Slices were analyzed by the Tardy method in a crossed circular polariscope at $\times 10$. Typical fringe patterns near *S* and *H* (see Fig. 1) are shown in Figs. 4*a* and *b*, respectively. Data extracted from fringe patterns such as Fig. 4 are shown on Fig. 5. A least squares digital computer program was used to obtain a best fit line for the data in the linear zone. Results are tabulated in the center of Table 1.

The dysymmetry of the fringes about the crack plane in Fig. 4*a* reveals the presence of mixed mode behavior near *S* [*9*] while the symmetric fringe geometry in Fig. 4*b* reveals only Mode I near *H*. This striking feature was present in all tests. Values of K_{II} were found to be from 11 to 22 percent of K_I (Table 1). In fact, the fringe patterns at *S* (Fig. 4*a*) revealed a zero fringe order along a direction normal to θ_m°, indicating that the minimum value of $\tau_{max} \approx 0$ and K_{II} contributed a negligible amount to the stresses

[4]Fringes resulting from absorption or desorption of moisture near edges.

TABLE 1—*Test geometry and SIF values.* [a]

Test Number	1P	2P	3P	4P [b]	5P [b]	6P	7P	8P
Hole radius ($\bar{r}$), mm	6.67	6.67	3.18	3.18	3.18	6.67	3.18	6.67
Plate depth (T), mm	13.21	12.95	13.21	12.95	13.46	12.85	13.72	12.95
Crack length (c), mm	2.29	3.30	2.79	2.79	2.79	4.57	5.33	6.60
Crack depth (a), mm	2.54	3.56	4.83	5.59	5.84	7.11	10.92	11.43
Bearing stress (σ_b), kPa	265.	270.	557.	568.	547.	273.	536.	193.
a/T	0.19	0.28	0.37	0.43	0.43	0.55	0.80	0.88
a/c	1.11	1.08	1.69	2.00	2.08	1.56	2.04	1.73
c/r	0.34	0.50	0.88	0.88	0.88	0.69	1.68	0.99
$2\bar{r}/T$	1.01	1.03	0.48	0.49	0.47	1.04	0.46	1.03
Stress Intensity Factors at S K_I (or K_{II})$_{exp}/\sigma_b(\pi a)^{1/2}$								
K_I	0.181	0.129	0.165	0.156	0.132	0.181	0.091	0.211
K_{II}	0.020	0.029	0.034	0.026		0.030	0.017	0.036
Stress Intensity Factors at H								
$K_I/\sigma_b(\pi a)^{1/2}$ Exp	0.376	0.386	0.243	0.225	0.205	0.215	0.117	0.285
$(K_{IS} + K_{IH})/2\sigma_b(\pi a)^{1/2}$	0.279	0.258	0.204	0.191	0.169	0.198	0.104	0.248
Theoretical Stress Intensity Factors $K_I/\sigma_b(\pi a)^{1/2}$								
(At S), Shah	0.355	0.289	0.198	0.190	0.188	0.237	0.123	0.182
(At H), Shah	0.474	0.442	0.289	0.240	0.256	0.312	0.254	0.305
Newman	0.370	0.298	0.164	0.157	0.155	0.224	0.086	0.166

[a] All plates were 178 mm wide $\sigma_b = P/2\bar{r}T$.

[b] Tests 4P and 5P were intended as approximate replications; however, the crack growth in 5P was small and at an angle to the initial flaw, invalidating the data for K_{II}.

along this line. Fringe data were taken normal to this direction, and it was found that θ_m was constant over the zone where data were gathered, indicating that the data were sufficiently close to the crack tip so that $\theta_m \approx \theta_m°$ (Fig. 3).

It has been shown analytically [*24*] that a graph such as Fig. 5 should yield linear data in the zone dominated by the stress singularity, and, hence, only this part of the data are used in this work. Values of K^* were obtained at both S and H (where $K_{IIAp} = 0$) by fitting a straight line to the data, as is shown in Fig. 5, and extrapolating to the origin. At H, $K^* = K_I$. At S, K* was used in Eqs 3 and 8 with Eq 10 to obtain values of K_I and K_{II}. Values of K_H were significantly larger than values of K_{IS} for all geometries tested as shown by Table 1. Tests 4 and 5 were for nearly identical geometries, and results are seen to differ by 10 percent. On the basis of this and prior experience with the method, the authors conjecture that experimental scatter is of the order of ± 5 to ± 7 percent.

Reference *5* contains tests on geometries similar to those of Tests 1P, 6P, and 7P. Comparing the results for pin loads with those where the hole contained no pin, it was found that K_{IS} with pin was about two to four times the value without pin, and K_H with pin was two to five times the value of K_H without pin.

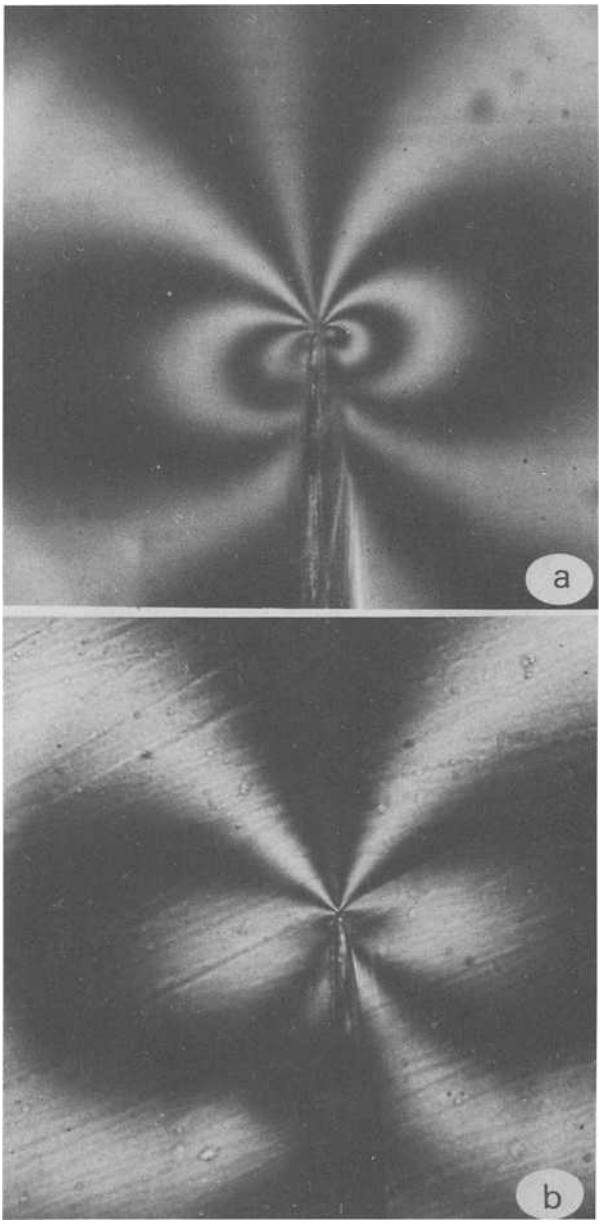

FIG. 4—(*a*) *Typical fringe pattern for surface slice bright field;* (*b*) *typical fringe pattern for hole slice dark field.*

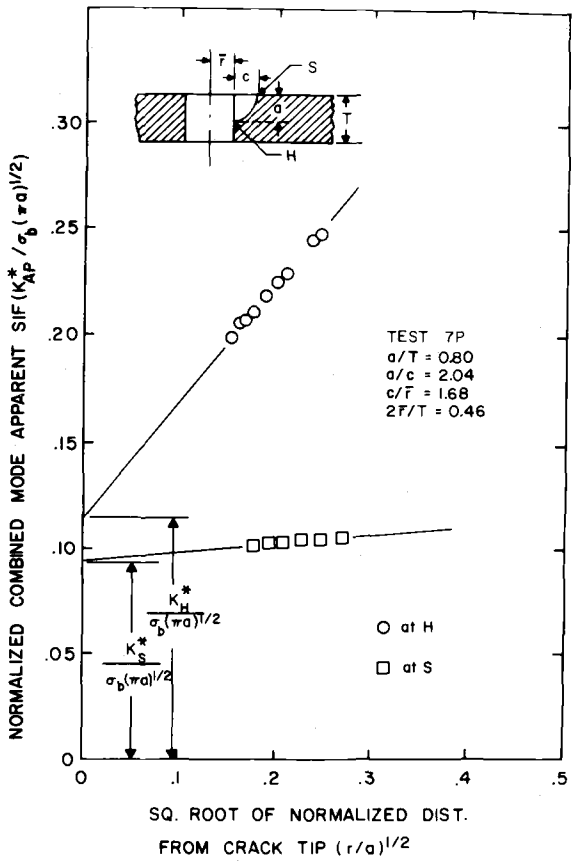

FIG. 5—*Typical set of data and* K* *determination.*

The authors are aware of one published approximate theory [*2*] for predicting SIF distributions for the problem which they investigated here. Comparisons are made with that theory, developed by Shah, in Table 1. In making comparisons, results from the Shah theory were computed at the midpoint of each specimen slice. At *S*, the Shah theory overestimated K_I by 20 to 125 percent except for Test 8 ($a/t \approx 0.88$) where an apparent boundary-layer effect caused $K_{S(\text{Exp})}$ to be greater than $K_{S(\text{Th})}$. At *H*, the Shah theory again overestimated experimental values by 10 to 110 percent. However, the larger discrepancies occurred only for the deep flaws ($a/t > 0.5$), and this may be due to a load transfer effect noted by the authors in prior work [*28*] on open holes for deep flaws.

In addition to the work of Shah, Newman [*29*] has adapted an approximate theory for the average K_I along the flaw border to the case of a hole with a concentrated force applied to the internal hole boundary normal

to the flaw border. Comparisons of results using his theory with the average of the normalized experimental results $(K_{IS} + K_{IH})/2\sigma_b(\pi a)^{1/2}$ show that his results vary some 25 percent or so from the average experimental results. However, the largest differences occur when $K_{IH}/2\sigma_b(\pi a)^{1/2}$ is 50 to 300 percent greater than $K_{IS}/2\sigma_b(\pi a)^{1/2}$ suggesting that the average of $(K_{IS} + K_{IH})/2\sigma_b(\pi a)^{1/2}$ may not be an accurate approximation to the integrated average value of K_I around the flaw border. Better agreement might result if intermediate experimental values were available.

Conclusions

On the basis of the studies described herein, the following is concluded.

1. Stress intensities for cracks emanating from rigid pin-loaded holes are several hundred percent higher than those obtained for remote loading of open holes.

2. The available design theory of Shah overestimates SIF, in general, for the pin-loaded holes with cracks.

3. Mixed mode effects are present near the intersection of the crack front with the plate surface in all tests.

4. More values are needed to compare with an integrated average K_I value such as given by Newman.

These results are believed to provide reasonable estimates for a complex three-dimensional problem for a prescribed range of geometries. Extrapolation of results to other geometries is not recommended.

Acknowledgments

The authors wish to acknowledge the support of the staff and facilities of the Department of Engineering Science and Mechanics at Virginia Polytechnic Institute and State University, the suggestions of Dr. J. C. Newman, Jr., and the support of NASA Langley under Grant No. NSG 1024.

References

[1] Hall, L. R. and Finger, R. W., "Fracture and Fatigue Growth of Partially Embedded Flaws," Proceedings of the Air Force Conference on Fatigue and Fracture of Aircraft Structures and Materials, AFFDL-TR-70-144, U.S. Air Force Systems Command, Wright-Patterson AFB, Ohio, Sept. 1970, pp. 235-262.

[2] Shah, R. C. in *Mechanics of Crack Growth, ASTM STP 590,* American Society for Testing and Materials, 1975, pp. 429-459.

[3] Kobayashi, A. S., Polvanich, N., Emery, A. B., and Love, W. J., "Corner Crack at the Bore of a Rotating Disk," Technical Report 75WA/GT-18, American Society of Mechanical Engineers, 1975.

[4] McGowan, J. J. and Smith, C. W. in *Mechanics of Crack Growth, ASTM STP 590,* American Society for Testing and Materials, 1975, pp. 460-476.

[5] Smith, C. W., McGowan, J. J., and Jolles, M., *Proceedings,* Twelfth Annual Meeting of Society for Engineering Science, 1975, pp. 353-362.

[6] Irwin, G. R., *Proceedings,* Society for Experimental Stress Analysis, Vol. 16, No. 1, 1958, pp. 92-96.
[7] Smith, D. G. and Smith, C. W., *International Journal of Fracture Mechanics,* Vol. 6, No. 3, Sept. 1970, pp. 305-318.
[8] Smith, D. G. and Smith, C. W., *Journal of Experimental Mechanics,* Vol. 11, No. 9, Sept. 1971, pp. 394-401.
[9] Smith, D. G. and Smith, C. W., *Journal of Engineering Fracture Mechanics,* Vol. 4, No. 2, June 1972, pp. 357-366.
[10] Marrs, G. R. and Smith, C. W. in *Stress Analysis and Growth of Cracks, ASTM STP 513,* American Society for Testing and Materials, 1972, pp. 22-36.
[11] Schroedl, M. A., McGowan, J. J., and Smith, C. W., *Journal of Engineering Fracture Mechanics,* Vol. 4, No. 4, Dec. 1972, pp. 801-809.
[12] Schroedl, M. A. and Smith, C. W. in *Progress in Flaw Growth and Fracture Toughness Testing, ASTM STP 536,* American Society for Testing and Materials, 1973, pp. 45-63.
[13] Schroedl, M. A., McGowan, J. J., and Smith, C. W., *Journal of Experimental Mechanics,* Vol. 14, No. 10, Oct. 1974, pp. 392-399.
[14] Harns, A. E. and Smith, C. W., *Recent Advances in Engineering Science, Vol. 7* (Part II of Proceedings of Tenth Anniversary Meeting of the Society of Engineering Science), Scientific Publishers, Boston, 1976, pp. 59-66.
[15] Schroedl, M. A. and Smith, C. W. in *Fracture Analysis, ASTM STP 560,* American Society for Testing and Materials, 1974, pp. 69-80.
[16] Smith, C. W., *Proceedings,* Third International Congress on Experimental Mechanics, Dec. 1974, pp. 287-292.
[17] Schroedl, M. A., McGowan, J. J., and Smith, C. W., "Use of a Taylor Series Correction Method in Photoelastic Stress Intensity Determinations," Technical Report VPI-E-73-34, Virginia Polytechnic Institute and State University, Blacksburg, Va., Nov. 1973.
[18] Mullinix, B. R. and Smith, C. W., *International Journal of Fracture,* Vol. 10, No. 3, Sept. 1974, pp. 337-352.
[19] McGowan, J. J. and Smith, C. W., *International Journal of Fracture,* Vol. II, No. 6, Dec. 1975, pp. 977-988.
[20] Schroedl, M. A. and Smith, C. W., *Journal of Engineering Fracture Mechanics,* Vol. 7, 1975, pp. 341-355.
[21] Jolles, M., McGowan, J. J., and Smith, C. W., *Journal of Engineering Materials and Technology,* Vol. 97, Series H, No. 1, Jan. 1975, pp. 45-51.
[22] Jolles, M., McGowan, J. J., and Smith, C. W., "Effects of Artificial Cracks and Poisson's Ratio Upon Photoelastic Stress Intensity Determination" *Journal of Experimental Mechanics,* Vol. 16, No. 5, May 1976, pp. 188-193.
[23] Kobayashi, A. E., Ed., *Experimental Fracture Mechanics II,* Society for Experimental Stress Analysis Monograph Series, Iowa State Press, October 1975, pp. 1-58.
[24] Jolles, M., McGowan, J. J., and Smith, C. W., "Use of a Hybrid, Computer Assisted Photoelastic Technique for Stress Intensity Determination in Three Dimensional Problems," *Computational Fracture Mechanics* (*Second National Congress on Pressure Vessels and Piping*), ASME (SP), June 1975, pp. 83-102.
[25] Sih, G. C. and Kassir, M., *Journal of Applied Mechanics,* Vol. 33, No. 3, Sept. 1966, pp. 601-611; *Transactions* American Society of Mechanical Engineers, Vol. 88, Series E, 1966.
[26] Sih, G. C. and Liebowitz, H. O., "Mathematical Theories of Brittle Fracture," *Fracture Vol. II Mathematical Fundamentals,* Academic Press, New York, 1968, pp. 68-188.
[27] Sih, G. C., *International Journal of Fracture Mechanics,* Vol. 7, No. 1, March 1971, pp. 39-59.
[28] Jolles, M., McGowan, J. J., and Smith, C. W., *Proceedings,* Twelfth Annual Meeting of the Society for Engineering Science, Oct. 1975, pp. 353-362.
[29] Newman, J. C., Jr., "Predicting Failure of Specimens with Either Surface Cracks or Corner Cracks at Holes," Technical Report NASA-TN D-8244, National Aeronautics and Space Administration, June 1976.

J. Lanteigne,[1] *M. N. Bassim,*[1] *and D. R. Hay*[1]

Dependence of J_{Ic} on the Mechanical Properties of Ductile Materials

REFERENCE: Lanteigne, J., Bassim, M. N., and Hay, D. R., "**Dependence of J_{Ic} on the Mechanical Properties of Ductile Materials,**" *Flaw Growth and Fracture, ASTM STP 631,* American Society for Testing and Materials, 1977, pp. 202-216.

ABSTRACT: Application of the relation $J_{Ic} = K_{Ic}^2/E$ yields values of J_{Ic} which are different from those measured directly. This difference is attributed to the plasticity of the crack tip. A more accurate relation for evaluation of J_{Ic} which takes into consideration the mechanical properties of the material such as the yield stress and Young's modulus, and based on compliance tests, is formulated. Experimental tests which demonstrate the validity of this equation are presented.

KEY WORDS: crack propagation, fractures (materials), ductility

The J-integral, developed by Rice [*1,2*],[2] is a fracture criterion for ductile materials. Such materials develop a considerable plasticity at the crack tip, and the size of the plastic zone is of an order of magnitude larger than that encountered in brittle materials. The J-integral has been evaluated experimentally for several materials [*3-7*], and a standard procedure for its determination has been proposed [*8*]. Also, the independence of the J_{Ic} on specimen geometry has been demonstrated [*9*].

While experimental results in the literature have shown that J-integral testing reduces the size of fracture-mechanics specimens to a large extent, the correlation between J_{Ic}—defined as the J-integral at the fracture point—and the stress-intensity factor, K_{Ic}, still has a certain degree of discrepancy. The deviation between K_{Ic} measured directly using the ASTM Test for Plane-Strain Fracture Toughness of Metallic Materials (E 399-74) and that obtained from measuring J_{Ic} and applying the relation

$$J_{Ic} = \frac{K_{Ic}^2}{E} \tag{1}$$

[1]Graduate student, assistant research professor, and research professor, respectively, Department of Metallurgical Engineering, Ecole Polytechnique, Montreal, Quebec, Canada.

[2]The italic numbers in brackets refer to the list of references appended to this paper.

where E (Young's modulus) is on the average 10 percent and could be as high as 40 percent for ductile steels (for the case of the nickel-chromium-molybdenum-vanadium (Ni-Cr-Mo-V) rotor steel tested by Begley and Landes [*9*] at room temperature). This deviation in results can be attributed to the fact that, while the J-integral is developed primarily for materials with some ductility, it is formulated using the principles of linear-elastic fracture mechanics. Namely, that at the fracture point, J_{1c} is equal to the crack-extension force G_{1c}. This leads to Eq 1.

In this study, a relation between J_{1c} and other mechanical properties of ductile materials is developed. Essentially, a more accurate expression than that of Eq 1 is formulated which includes the yield strength and the plasticity at the crack tip. Experimental data are presented which demonstrate the accuracy of this relation in describing the behavior of a variety of ductile alloys of aluminum, titanium, and steels. This relation is confirmed also using previous data from the literature. A model describing the size of the plastic zone at the crack tip also is presented.

J-Integral as a Function of Compliance

In this analysis, we assume fracture under prescribed loading. The load-point displacement is given as

$$\delta = \delta_e + \delta_c \tag{2}$$

where δ_e is the elastic deformation of an uncracked specimen, and δ_c is the displacement due to the crack opening. For elastic displacement, Hooke's law for a single-edge notched specimen is applied, namely

$$\delta_e = \frac{8DP}{BEw} \tag{3}$$

where

B = specimen thickness,
w = width measured from the load axis,
D = half the distance between the two points of loading, and
P = applied load.

The crack extension force G_1 is related to the stress-intensity factor K_1 by

$$G_1 = \frac{K_1^2}{E} \tag{4}$$

and to the compliance C with the equation

$$G_1 = \frac{P^2}{2B}\frac{\partial C}{\partial a} \tag{5}$$

where a is the crack length in the specimen.

Substituting δ/P for C in Eq 5 and following the analysis of Adams and Munro [*5*], we obtain

$$\delta_c = \frac{P}{BE} f^*(a/w) \tag{6}$$

with $f^*(a/w)$ a function of the specimen geometry. By substitution of Eqs 6 and 3 into Eq 2, the displacement can be expressed as

$$\delta = \frac{1}{BE}\left(\frac{8D}{w} + f^*(a/w)\right) P \tag{7}$$

or

$$\delta = \frac{1}{BE} f\,(a/w)\, P \tag{8}$$

with

$$f\,(a/w) = \frac{8D}{w} + f^*\,(a/w)$$

$f\,(a/w)$ is a compliance function to be determined experimentally for a given geometry by measuring the inverse of the slope of the relation between load and load-point displacement for a material with known E. Equation 7 also can be used to describe the elastic-plastic behavior of a ductile material. In this case, a plastic-zone correction is necessary. Thus, we replace a by a_p which is defined as

$$a_p = a + \gamma_y \tag{9}$$

with γ_y being the plastic-zone correction [*10*], and it is defined in the next section. Equation 7 then becomes

$$\delta = \frac{1}{BE} f(a_p/w)\, P \tag{10}$$

Under prescribed loading, the potential energy U of a body loaded to P' is given as

$$U = -\int_0^{P'} \delta\, dP \tag{11}$$

substituting for δ in Eq 11 by Eq 10, we obtain

$$U = -\frac{1}{BE}\int_0^{P'} f(a_p/w)\, PdP$$

and J_{1c} will then be equal to

$$J_{1c} = \frac{1}{B^2Ew}\int_0^{P_f}\left(\frac{df(a_p/w)}{d(a/w)}\right) PdP \tag{12}$$

with P_f being the fracture load.

Plastic Zone Correction γ_y

Westergaard [*11*] has shown that for an infinite elastic body subjected to a load in the y-direction and containing a crack along the x-direction a solution is found in terms of the Airy function

$$\phi = \mathrm{Re}\bar{\bar{Z}} + y\,\mathrm{Im}\bar{Z}$$

with $\bar{Z} = d\bar{\bar{Z}}/dz$, $Z = d\bar{Z}/dz$, and Z is an analytical function of the complex variable $z = x + iy$. The normal stress σ_{yy} is given as

$$\sigma_{yy} = \frac{\partial^2\phi}{\partial x^2} = \mathrm{Re}Z + y\,\mathrm{Im}Z'$$

with $Z' = dZ/dz$.

In the plane of the crack ($y = 0$)

$$\sigma_{yy} = \mathrm{Re}Z$$

The solution is in the form

$$Z = \frac{a_0 + a_1z + a_2z^2 + a_3z^3 + \ldots}{\sqrt{z}}$$

which leads to

$$\sigma_{yy} = \frac{K_1}{\sqrt{6\pi r}} + a_1\sqrt{r} + a_2r^{3/2} + a_3r^{5/2} + a_4r^{7/2} + \ldots \tag{13}$$

at $\theta = 0$, with $r = x$ and $a_0 = K_1/\sqrt{6\pi}$ in plane strain.

According to the model of Irwin [*12*], the plastic zone at the crack tip is obtained, as r approaches zero

$$\lim_{r \to 0} \sigma_{yy} = \frac{K_I}{\sqrt{6\pi r}}$$

At $\sigma_{yy} = \sigma_y$, r becomes r_y leading to the relation

$$r_y = \frac{1}{6\pi}\left(\frac{K_I}{\sigma_y}\right)^2 \tag{14}$$

with σ_y being the yield stress. We define a translation vector such as $\gamma_y = R - r_y$ with

$$R = \frac{1}{\sigma_y}\int_0^{r_y} \sigma_{yy}\, dr \tag{15}$$

Thus, the elastic singularity at $r = 0$ is translated to $r = \gamma_y$. More generally from Eq 13, r_y can be written as

$$r_y = \left[\frac{K_I}{\sqrt{6\pi}\,\sigma_y} + \frac{a_1}{\sigma_y} r_y + \frac{a_2}{\sigma_y} r_y^2 + \frac{a_3}{\sigma_y} r_y^3 + \frac{a_4}{\sigma_y} r_y^4 + \cdots\right]^2$$

with $a_1 r_y$, $a_2 r_y^2$, $a_3 r_y^3 \cdots$ much smaller than K_I. Then, using the approximation r_y in Eq 14, we obtain

$$r_y = \frac{K_I^2}{6\pi\sigma_y^2} + A_1 K_I^3 + A_2 K_I^4 + A_3 K_I^5 + A_4 K_I^6 + A_5 K_I^7 + \cdots \tag{16}$$

with

$$A_1 = \frac{2a_1}{(6\pi)^{1/2}\sigma_y^4}, \quad A_2 = \frac{a_1^2}{36\pi^2\sigma_y^6}$$

$$A_3 = \frac{2a_2}{(6\pi)^{1/2}\sigma_y^6}, \quad A_4 = \frac{2a_1 a_2}{(6\pi)^3\sigma_y^8}, \quad A_5 = \frac{2a_3}{(6\pi)^{1/2}\sigma_y^8} \cdots$$

Integrating Eq 15, substituting Eq 13 and using the Irwin approximation for r_y, we obtain

$$R = \frac{1}{3\pi}\left(\frac{K_I}{\sigma_y}\right)^2 + \frac{2a_1}{3(6\pi)^{1/3}\sigma_y{}^4} K_I{}^3 + \frac{2a_2}{5(6\pi)^{1/3}\sigma_y{}^6} K_I{}^5$$

$$+ \frac{2a_3}{7(6\pi)^{1/3}\sigma_y{}^8} K_I{}^7 + \cdots \tag{17}$$

and from Eqs 16 and 17

$$\gamma_y = R - r_y = \frac{1}{6\pi}\left(\frac{K_I}{\sigma_y}\right)^2 + \alpha_1 K_I{}^3 + \alpha_2 K_I{}^4 + \alpha_3 K_I{}^5 \tag{18}$$

$$+ \alpha_4 K_I{}^6 + \alpha_5 K_I{}^7 + \cdots$$

with

$$\alpha_1 = \frac{-4a_1}{3(6\pi)^{1/3}\sigma_y{}^4}, \qquad \alpha_2 = \frac{-a_1{}^2}{36\pi^2\sigma_y{}^6}, \qquad \alpha_3 = \frac{-8a_2}{5(6\pi)^{1/3}\sigma_y{}^6}$$

$$\alpha_4 = \frac{-2a_1a_2}{(6\pi)^3\sigma_y{}^8}, \qquad \alpha_5 = \frac{-12a_3}{7(6\pi)^{1/3}\sigma_y{}^8} \qquad \cdots$$

Dependence of J_{Ic} on the Mechanical Properties

For a single-edge notched specimen, the stress-intensity factor K_I is given as

$$K_I = \frac{P}{B\sqrt{w}} F(a/w) \tag{19}$$

Where the function $F(a/w)$ is given for a standard geometry, Eq 12 can be written as

$$J_{Ic} = \frac{1}{B^2Ew} \int_0^{P_f} \frac{\partial f(a_p/w)}{\partial (a_p/w)} \times \frac{\partial (a_p/w)}{\partial (a/w)} PdP$$

$$= \frac{1}{B^2Ew} \int_0^{P_f} \frac{\partial f(a_p/w)}{\partial (a_p/w)} \times \left(1 + \frac{1}{w} \frac{\partial \gamma_y}{\partial K_I} \frac{\partial K_I}{\partial (a/w)}\right) PdP$$

It is now possible to write J_{Ic} as a function of K_{Ic}, E, and σ_y using Eq 19. Assuming that at the fracture load, K_I corresponds to K_{Ic}, we obtain

$$J_{Ic}(K_{Ic}, E, \sigma_y) = \frac{1}{E(F(a/w))^2} \int_0^{K_{Ic}} \frac{\partial f(a_p/w)}{\partial (a_p/w)} \times \left(1 + \frac{1}{w} \frac{\partial \gamma_y}{\partial K_I} \frac{\partial K_I}{\partial (a/w)}\right) K_I dK_I \quad (20)$$

σ_y is included implicitly in the term $\partial \gamma_y / \partial K_I$. Equation 20 shows the dependence of J_{Ic} on the mechanical properties of materials exhibiting elastic-plastic behavior.

For a brittle material, $\gamma_y \rightarrow 0$ and $a_p \rightarrow a$. Equation 20 becomes

$$J_{Ic}(K_{Ic}, E, \sigma_y) = \frac{1}{E(F(a/w))^2} \frac{\partial f(a/w)}{\partial (a/w)} \int_0^{K_{Ic}} K_I dK_I \quad (21)$$

$$= \frac{1}{2E(F(a/w))^2} \frac{\partial f(a/w)}{\partial (a/w)} K_{Ic}^2$$

From Eqs 4, 5, and 7

$$\frac{K_I^2}{E} = \frac{1}{2} \frac{P}{Bw} \frac{\partial \delta}{\partial (a/w)}$$

$$= \frac{P^2}{2B^2 Ew} \frac{\partial f(a/w)}{\partial (a/w)}$$

Substituting Eq 19, we obtain

$$2(F(a/w))^2 = \frac{\partial f(a/w)}{\partial (a/w)} \quad (22)$$

By substitution in Eq 21, Eq 1 is obtained as predicted from linear-elastic fracture mechanics.

Experimental Results

The experimental part of this study deals with the evaluation of the compliance function $f(a/w)$ of Eq 8 and the coefficients a_i of Eq 18 for a given specimen geometry. The material used was a tool steel, D6, in the annealed state. The composition and mechanical properties of this alloy are given in Table 1. The microstructure of this alloy consists of a large precipitate of chromium and iron carbides in a ferritic matrix.

Compact tension fracture-mechanics specimens 12.7 mm (½ in.) thick were sufficient to obtain plane-strain fracture. These specimens were

TABLE 1—*Composition and properties of D6 tool steel.*

		Composition		
C	Cr	W	Mn	Si
2.05	12.5	1.3	0.75	0.3
		Microstructure		
Precipitates				
maximum size		20 μm		
minimum size		2 μm		
composition		$(Fe, Cr)_3 C$, $(Fe, Cr)_7 C_3$		
Grain size		0.20 μm		
Matrix		ferrite		
		Mechanical Properties		
Elongation at fracture		8 percent		
Yield stress		480 MN/m^2		
Ultimate tensile stress		765 MN/m^2		
Young's modulus		19 790 kgf/mm^2		
K_C		60 MN·m$^{-3/2}$		
$\Delta K_{\text{threshold}}$		6 MN·m$^{-3/2}$ [at $da/dn = 10^{-6}$mm/cycle]		
Hardness		22 RC (240 HB)		

fatigued to different crack lengths so that at the final stage of precracking the stress-intensity factor K_I was always less than 15 Mn·m$^{-3/2}$. This was followed by compliance tests in which the specimen was loaded elastically in tension while the load P versus load-point displacement δ was recorded. After unloading, the crack was marked by forming a thin oxide layer using a burner. The crack was further propagated to a new length by fatigue with K_I in the final stage less than 15 MN·m$^{-3/2}$, and the compliance test was repeated at room temperature with the load incremented by 1000 kg/min to fracture. Figure 1 gives the load versus load-point displacement curves to the fracture load P_f for specimens with different values of a/w.

In Fig. 1, the compliance C is the inverse of the slope of the linear part of each of the curves. It also is written as

$$C = \frac{f(a/w)}{BE} \tag{23}$$

Substituting for E (19 790 kgf/mm^2) and B (12.7 mm), $f(a/w)$ is determined for each crack length. Figure 2 shows the dependence of $f(a/w)$ on the crack length a. A polynomial regression yields the function

$$f(a/w) = 2.2 + 291.82(a/w) - 820.79(a/w)^2 + 963.14(a/w)^3 \tag{24}$$

according to Eq 8, $8D/w$ is equal to 2.2 and

$$f^*(a/w) = 291.82(a/w) - 820.79(a/w)^2 + 963.14(a/w)^3$$

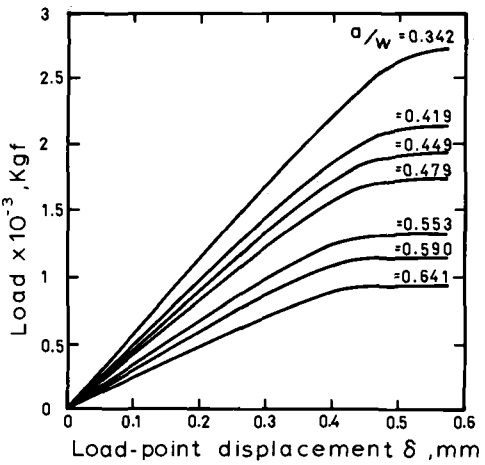

FIG. 1—*Load-load point displacement curves under prescribed loading for compact tension specimens of D6 tool steel with different crack length.*

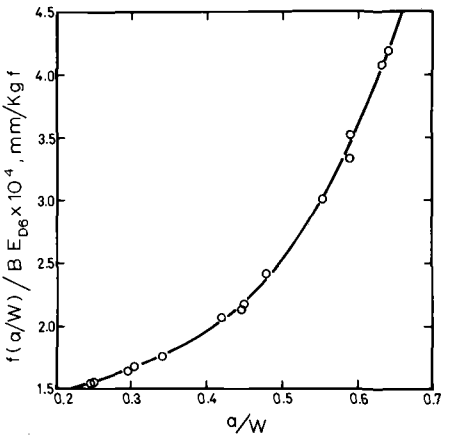

FIG. 2—*The dependence of* f(a/w) *on the crack length expressed as* (a/w).

Equation 24 was verified for two other materials—one is SAE 1045 steel with E = 19 800 kgf/mm^2 and a/w = 0.54 and titanium 6 aluminum-4 vanadium (Ti 6Al-4V) with a/w = 0.5 and E = 13 070 kgf/mm^2. Experimental P-δ curves for these two materials are given in Fig. 3. The inverse of the slope of the linear part of the experimental curves corresponds very closely with that calculated using Eq 23 with a deviation of only 3.5 percent for the steel and 2 percent for the titanium alloy.

In order to evaluate the coefficient a_i of Eq 18, the set of α_i which is a solution to the equation

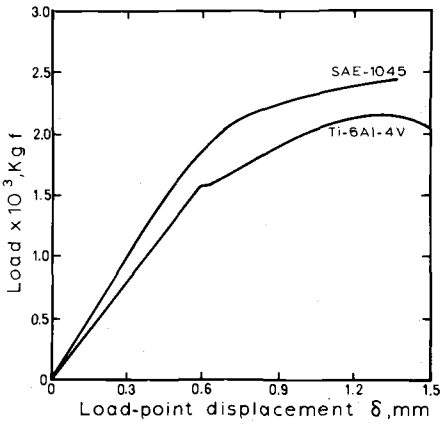

FIG. 3—*Load-load point displacement curves under prescribed loading for an SAE 1045 steel and Ti 6A1-4V specimens.*

$$\delta = \frac{f[(a + \gamma_y)/w]P}{BE}$$

obtained by combining Eqs 9 and 10 and determined in such a way that the difference between the experimental and theoretical load-load point displacement curves is minimized for every value of a/w. The equation

$$\gamma_y = 2.278 \times 10^{-4} K_I^2 + 10^{-7} K_I^3 - 2.47 \times 10^{-11} K_I^4 + 5 \times 10^{-10} K_I^5 - 2.058 \times 10^{-13} K_I^6 + 5 \times 10^{-13} K_I^7 \quad (25)$$

is obtained. In this analysis K_I is given by ASTM Method E 399-74 for compact tension specimens.

This equation is shown in Fig. 4 with γ_y in millimetres and K in MN·m$^{-3/2}$. The first term of this equation corresponds to the Irwin plastic-zone correction and the higher order coefficients respect the constraints imposed by Eq 18. Using the yield strength of D6 (480 MN/m^2) and applying Eq 18, we obtain

$$\begin{aligned} a_1 &= -0.333 \text{ MN·m}^{-3/2}/\text{mm} \\ a_2 &= -6.092 \text{ MN·m}^{-3/2}/\text{mm}^2 \\ a_3 &= -24.97 \text{ MN·m}^{-3/2}/\text{mm}^3 \end{aligned} \quad (26)$$

From Eqs 24, 25, and 18 and from ASTM Method E 399-74, we obtain the function $\partial f(a_p/w)/\partial(a_p/w)$, $\partial\gamma/\partial K_I$, and $\partial F(a/w)/\partial(a/w)$, respec-

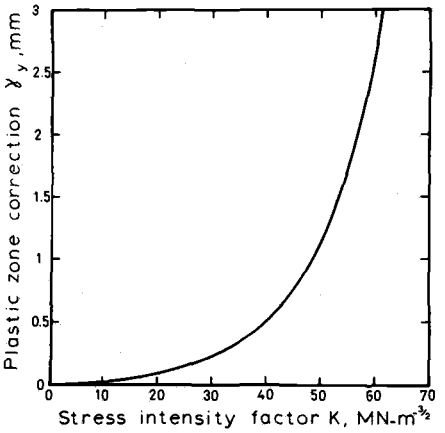

FIG. 4—*The dependence of* γ_y *on the stress intensity factor* K_I.

tively. It is now possible to apply Eq 20 and obtain J_{Ic} for any material as a function of σ_y, E, and K_{Ic}.

For aluminum alloys, taking E = 8085 kgf/mm^2 we obtain the curves in Fig. 5 where J_{Ic} is given as a function of σ_y and K_{Ic} on a logarithmic scale. The curve corresponding to σ_y = 250 MN/m^2 is obtained at values of $\gamma_y = \gamma_{yc}$ up to 3 mm with γ_{yc} evaluated from Eq 18 at $K_I = K_{Ic}$.

Similarly, for alloy steels, with E = 19 800 kgf/mm^2, the dependence of J_{Ic} on σ_y and K_{Ic} is shown in Fig. 6, while for titanium, taking E = 13 070 kgf/mm^2, we obtain the data in Fig. 7. In Fig. 7, the highest values of γ_{yc} is 1 mm while for the alloy steels in Fig. 6, it is equal to 3 mm.

In Figs. 5 to 7, it is noticed that as γ_{yc} tends to zero, that is, for brittle materials which do not exhibit much plasticity at the crack tip, we obtain a straight line with a slope equal to two which corresponds to Eq 1. Also, the relation between J_{Ic} and σ_y is a horizontal line indicating the independence of J_{Ic} on the yield strength in Eq 1, as discussed later in connection with Fig. 8.

The results shown in Figs. 5 to 7, which were obtained from Eq 20 and compliance tests on the tool steel, correspond remarkably with the published data in the literature. For the aluminum alloy 2024-T351, with E = 8085 kgf/mm^2 and σ_y = 334 MN/mm^2, Yoder and Griffis [*6*] have found K_{Ic} = 36.3 MN·m$^{-1/2}$ and J_{Ic} = 1.7 kgf/mm. From Fig. 5, we obtain J_{Ic} = 1.7 kgf/mm. For Ti6A1-4V with E = 13 070 kgf/mm^2 and σ_y = 855 MN/m^2 with K_{Ic} = 66 MN·m$^{-1/2}$, Yoder and Griffis [*7*] found values of J_{Ic} ranging from a minimum of 3.5 kgf/mm to a maximum of 4.4 kgf/mm. Figure 7 gives a value of 3.7 kgf/mm. Finally, for the Ni-Cr-Mo-V rotor steel, Begley and Landes [*9*] have found a value of J_{Ic} = 17 kgf/mm. In Fig. 6, with σ_y = 916 MN/m^2 and K_{Ic} = 132 MN·m$^{-1/2}$, we obtain J_{Ic} = 13 kgf/mm.

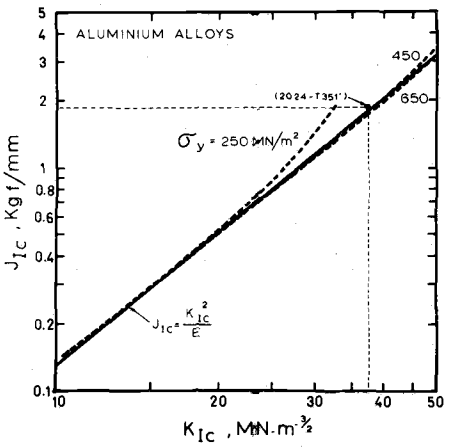

FIG. 5—*The relation between* J_{Ic}, K_{Ic}, *and* σ_y *for aluminum alloys* (E *taken as 8085* kgf/mm^2).

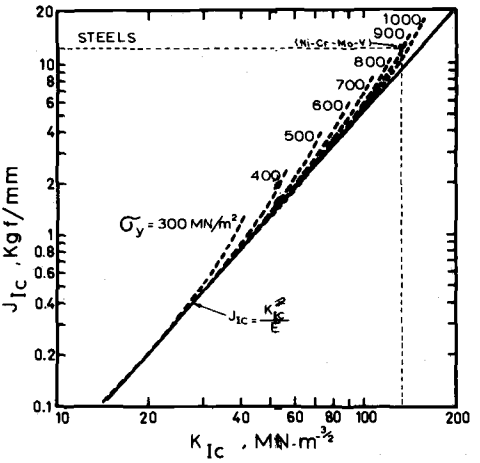

FIG. 6—*The relation between* J_{Ic}, K_{Ic}, *and* σ_y *for alloy steels with* E = *19 800* kgf/mm^2.

Discussion

In ductile materials with considerable plasticity at the crack tip, application of linear-elastic fracture mechanics necessitates the use of very thick specimens. Other criteria such as the J-integral and the crack opening displacement (COD) are needed to characterize the fracture toughness of such materials. Evaluation of these criteria can be obtained with much smaller specimens and, thus, could be affected by the ductility of the material as the size of the plastic zone ahead of the crack becomes large. The relation between J_{Ic} and K_{Ic} commonly used and given in Eq 1 is based

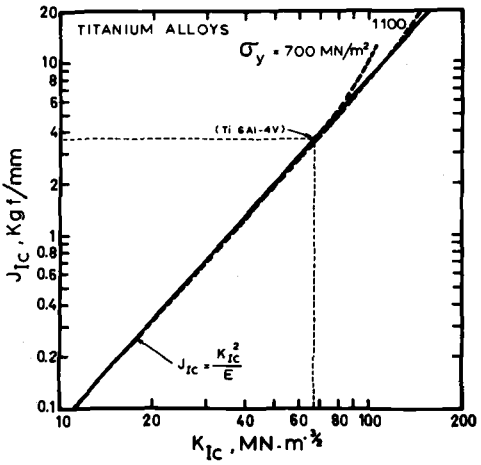

FIG. 7—*The relation between* J_{Ic}, K_{Ic}, *and* σ_y *for titanium alloys with* E = *13 070 kgf/mm*^{2}.

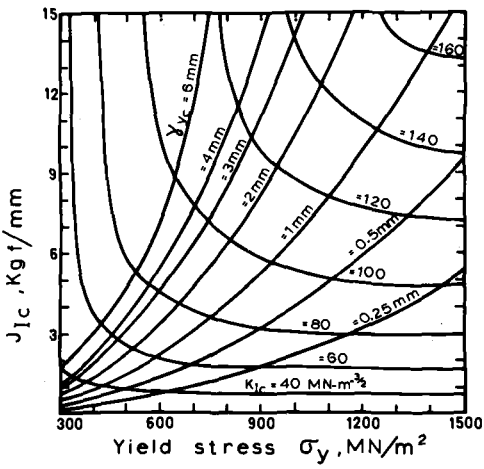

FIG. 8—*The dependence of* J_{Ic} *on the yield stress and either fracture toughness or the critical plastic zone correction for alloy steels* (E = *19 800 kgf/mm*^{2}).

on the concepts of linear-elastic fracture mechanics and does not take into consideration the contribution of the material ductility. In some cases [*9*], there is a large difference between J_{Ic} evaluated experimentally and that calculated from Eq 1. Theoretically, according to Eq 1, two steels—one more ductile than the other—might have the same K_{Ic} and are expected to have the same J_{Ic} when measured in plane strain with specimens with appropriate thickness. Experimental results might show that this is not generally true, since with smaller thickness the ductility of one material will cause higher values of J_{Ic}.

Criteria of fracture have to be formulated in terms of mechanical properties of the material and particularly its ductility expressed in terms of the plastic-zone correction γ_y—the latter describing more accurately the plasticity at the crack tip than the model of Irwin. Consider Eq 20, the relation between J_{Ic}, E, and σ_y represents a volume in space where every cross section belongs to a certain material or alloy. In these cross sections, we have lines of constant plasticity (constant γ_{yc}) and others of constant toughness (constant K_{Ic}). An example for such a cross section for steels, at $E = 19\,800$ kgf/mm is shown in Fig. 8. In this diagram, it is evident that for two steels with the same toughness K_{Ic} but with different ductility, represented by γ_{yc}, we have different values of J_{Ic}. This conclusion is not at all evident if Eq 1 was applied and discrepancies between experimental J_{Ic} measurements and that obtained from Eq 1 would have become apparent. For brittle materials with little plasticity at the crack tip, the formulation in this study reduces to that cited previously in the literature and confirms the validity of Eq 1.

It is interesting to note that the data in Figs. 5 to 8 for a variety of alloys ranging from aluminum to steels were obtained from compliance tests on a material which does not have too much in common with these alloys. This indicates that the role of the tool steel used was only to supply the data for a compliance and the plastic-zone correction, γ_y, and that the derivation of Eq 20 is general regardless of which material was used as the reference for generating the experimental data.

Results like those in Figs. 5 to 7, and particularly those in Fig. 8, serve to obtain J_{Ic} if the plasticity at the tip of a crack in a structure is known. If the plastic zone is measured by metallography or by microhardness, together with the yield stress of the material, J_{Ic} can be evaluated quite readily and, as demonstrated, with a high degree of accuracy.

Summary and Conclusions

1. An expression for J_{Ic} as a function of the compliance is formulated. In this equation, the crack length is expressed in terms of a plastic-zone correction.

2. This plastic-zone correction is derived from the work of Westergaard for a crack in an infinite elastic body and the elastic singularity at $r = 0$ translated to a point $r = \gamma_y$ which is dependent on the yield stress.

3. J_{Ic} is then obtained as a function of the yield stress, Young's modulus, and the critical plastic-zone correction or the fracture toughness K_{Ic}.

4. Experimental results were obtained using a tool steel, D6. Compliance measurements to determine $f(a/w)$ and γ_y were conducted.

5. The expression for J_{Ic} was verified for aluminum and titanium alloys and also on steel and was found to be in good agreement with data published in the literature.

6. The effect of plasticity at the crack tip on J_{Ic} was determined. A plot of J_{Ic} versus σ_y and K_{Ic} or γ_{yc} for alloy steel was obtained which could be used to determine J_{Ic} from measurement of the size of the plastic zone ahead of the crack.

7. The equations derived are quite general and do not depend on the material used in the compliance measurements.

Acknowledgments

The authors would like to acknowledge the National Research Council of Canada, the Canadian Department of Defence, and the Steel Company of Canada for their support of this investigation.

References

[1] Rice, J. R., *Transactions,* American Society of Mechanical Engineers, *Journal of Applied Mechanics,* Vol. 35, 1968, pp. 379-386.

[2] Rice, J. R., "Mathematical Analysis in the Mechanics of Fracture," *Fracture, An Advanced Treatise,* H. Liebowitz, Ed., Academic Press, New York, 1968.

[3] Begley, J. A. and Landes, J. D. in *Fracture Toughness, Part II, ASTM STP 514,* American Society for Testing and Materials, 1972, pp. 1-20.

[4] Bucci, R. J., Paris, P. C., Landes, J. D., and Rice, J. R. in *Fracture Toughness, Part II, ASTM STP 514,* American Society for Testing and Materials, 1972, pp. 40-69.

[5] Adams, N. J. I. and Munro, H. G., *Engineering Fracture Mechanics,* Vol. 6, 1974, pp. 119-132.

[6] Griffis, C. A. and Yoder, G. R., Technical Report 7676, Naval Research Laboratory, 1974.

[7] Griffis, C. A. and Yoder, G. R., *Eighth National Symposium on Fracture Mechanics,* Brown University, 1974.

[8] Landes, J. D. and Begley, J. A. in *Fracture Analysis, ASTM STP 560,* American Society for Testing and Materials, 1974, pp. 170-186.

[9] Landes, J. D. and Begley, J. A. in *Fracture Toughness, Part II, ASTM STP 514,* American Society for Testing and Materials, 1972, pp. 24-39.

[10] Lanteigne, J., Bassim, M. N., and Hay, D. R., *International Journal of Fracture,* Vol. 12, 1976, pp. 485-487.

[11] Westergaard, H. M., *Transactions,* American Society of Mechanical Engineers, Vol. 61, 1939, pp. A49-A53.

[12] Irwin, G. R., *Proceedings,* Seventh Sagamore Ordnance Materials Research Conference, Aug. 1960, Syracruse University Press, Met E 661-611/F.

H. P. Keller[1] *and D. Munz*[1]

Effect of Specimen Size on J-Integral and Stress-Intensity Factor at the Onset of Crack Extension

REFERENCE: Keller, H. P. and Munz, D., "**Effect of Specimen Size on J-Integral and Stress-Intensity Factor at the Onset of Crack Extension,**" *Flaw Growth and Fracture, ASTM STP 631,* American Society for Testing and Materials, 1977, pp. 217-231.

ABSTRACT: For a nickel-chromium-molybdenum steel and the aluminum alloy 7475, linear-elastic fracture mechanics can be applied to determine the stress-intensity factor at the onset of crack extension K_{Io} for specimens with $(W - a)_c > 0.4\,(K_{Io}/\sigma_y)^2$. For smaller specimens, K_{Io} can be calculated from the J-integral J_{Io} at the onset of crack extension, whereas linear-elastic fracture mechanics yield values which are too low. Below a minimum thickness $B \leq 50\,J_{Io}/\sigma_y$ an increase of J_o was observed.

KEY WORDS: crack propagation, fracture properties, steels, aluminum alloys

Nomenclature

a	Crack length
Δa	Crack extension
Δa_{knee}	Δa at the knee point of the J-Δa-curve
B	Specimen thickness
$B_{pl\,st}$	Minimum thickness of a specimen with plane-strain region in the center
B_{LE}	Minimum thickness of a proportional sized specimen for which linear-elastic fracture mechanics can be applied
COS	Crack-tip opening displacement (crack-opening stretch)
E	Young's modulus
J	J-integral
J_o	J at the onset of crack extension
J_{Io}	J at the onset of crack extension, evaluated with the pseudo compliance method, $J = -1/B\,\partial U/\partial a$

[1]Research engineer and division head, respectively, Deutsche Forschungs-und Versuchsanstalt für Luft-und Raumfahrt, Cologne, Germany.

J_{2o} J at the onset of crack extension, evaluated from $J = 2U/B \times (W - a)$
J_{1o} J at the onset of crack extension under plane strain
$J_{f\max}$ J for the maximum fatigue load
K_o Stress-intensity factor at the onset of crack extension calculated according to linear-elastic fracture mechanics
K^*_o Stress-intensity factor at the onset of crack extension, calculated according to linear-elastic fracture mechanics with plasticity correction
K_{1o} Stress-intensity factor at the onset of crack extension under plane strain and $r_{pl} \ll W - a$
K_{1c} Stress-intensity factor at the onset of unstable crack extension under plane strain and $r_{pl} \ll W - a$
K_Q Stress-intensity factor with the 5 percent secant method
$K_{f\max}$ Stress-intensity factor from the maximum fatigue load
K_{J1o} Stress-intensity factor calculated from J_{1o}
K_{J2o} Stress-intensity factor calculated from J_{2o}
r_{pl} Plastic zone correction, $1/6\pi\,(K/\sigma_y)^2$
U Deformation energy (area under the load deformation curve)
U_{crack} Deformation energy due to the crack
δ Load point displacement
δ_o Load point displacement at the onset of crack extension
λ Plane-strain region at the crack tip

The J-integral, introduced by Rice in fracture mechanics considerations, describes the singularity at the crack tip irrespective of the size of the plastic zone. It was, therefore, suggested that J at the onset of crack extension can be used as a fracture criterion in elastic-plastic fractures. Besides, it is hoped to evaluate fracture toughness K_{1c} with small specimens, which are not suitable for linear-elastic fracture mechanics (LEFM), by measuring J at the onset of crack extension and calculating K from J using linear-elastic relations. In the last few years, the experimental technique for J-integral determination was improved, and approximation methods were developed to evaluate J from one load-displacement curve. In this paper, some results on the effect of specimen size on the critical J at the onset of crack extension are reported.

General Remarks on the Effect of Specimen Size

Minimum Thickness for Plane Strain

Plane-strain fracture toughness K_{1c} can be determined if the specimen size is sufficiently large to make sure that the plastic zone size at fracture

is small enough compared with the ligament $W - a$, and, along the crack front, the plane-strain region predominates, requiring a minimum thickness B.

In Fig. 1, σ_{zz}, the principal stress in the direction of the crack (z-axis) is plotted against z in a schematic manner. The region $B - \lambda$, which is not in plane strain, is not known exactly. According to Robinson and Tetelman [*1*],[2] the relation between $B - \lambda$ and the crack-tip opening displacement COS is

$$B - \lambda = 25 \text{ COS} \tag{1}$$

The minimum thickness, in the specimen center below which no plane-strain region exists, therefore is given by $B_{\text{pl st}} = 25$ COS. Within the scope of LEFM, the relation between COS and stress-intensity factor K is given by

$$\text{COS} = C \frac{K^2 (1 - \nu^2)}{E \sigma_y} \tag{2}$$

There are some discussions about the factor C in the literature. Robinson [*2*] has found $C = 1$ for some materials, leading to

$$B_{\text{pl st}} = \frac{25 (1 - \nu^2)}{E} \frac{K^2}{\sigma_y} \tag{3}$$

Stress-Intensity Factor at the Onset of Stable and Unstable Crack Extension

Now, it is well established that stable crack growth can also occur under plane-strain conditions [*2–5*]. Therefore, two critical stress-intensity factors are necessary to describe the fracture behavior—that is, K_{1o} at the onset of stable crack extension, and K_{1c} at the onset of unstable crack extension.

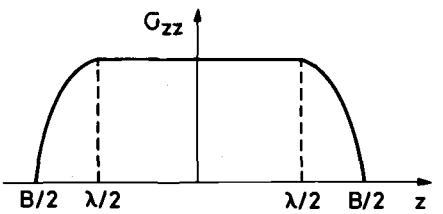

FIG. 1—*Distribution of the principal stress σ_{zz} along the z-axis.*

[2]The italic numbers in brackets refer to the list of references appended to this paper.

If the specimen size is large enough to fulfill both requirements just mentioned—small plastic zone size compared with $W - a$ and plane strain in the specimen center—K_o is independent of size and is called K_{Io}. The stress-intensity factor at the onset of unstable crack extension, however, can be size dependent also under plane-strain conditions, if a rising R-curve exists [*6,7*]. With the ASTM Test for Plane-Strain Fracture Toughness of Metallic Materials (E 399-74), K_{Ic} is determined either at the onset of crack extension (pop-in behavior), that is, $K_{Ic} = K_{Io}$, or at a crack extension of about 2 percent (secant method) that is, $K_{Ic} = K_{\Delta a = 2\ \text{percent}}$. In that case, K_{Ic} increases with increasing size of the specimens [*3*].

J-Integral at the Onset of Crack Extension

In Fig. 2, the expected effect of specimen size on the critical values of K and J at the onset of crack extension, K_o and J_o, is shown. It is assumed that specimens with a fixed ratio of W (width), B (thickness), and a (crack length) are used. Below a critical specimen size, characterized by B_{LE}, the ratio of plastic-zone size to ligament $W - a$ exceeds a critical value, and LEFM can no longer be applied. Therefore, K_o decreases below K_{Io}. In the midsection of the specimen there is still a plane-strain region. Therefore, J at the onset of crack extension has its size-independent values J_{Io} for $B < B_{LE}$. For $B < B_{pl\ st}$, the triaxial stress state breaks down and therefore $J_o > J_{Io}$.

If Fig. 2 is correct, then K_{Io} can be determined in the region $B_{pl\ st} < B < B_{LE}$ by measuring J_{Io} and calculating K_{Io} with the relation valid in LEFM

$$K_{Io}^2 = \frac{EJ_{Io}}{1 - \nu^2} \tag{4}$$

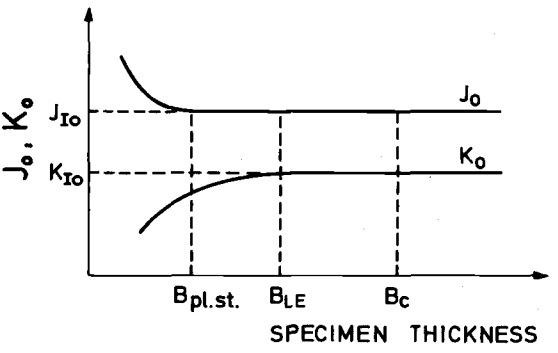

FIG. 2—*Effect of specimen size on* J_o *and* K_o *at the onset of crack extension.*

There are only few results concerning the effect of specimen size on J_0 [*8–12*]. Size-independent J_0 was found for the aluminum alloy 2024 [*10,11*] and for some steels [*9,12*]. K_{Io}, calculated from J_0 according to Eq 4, is mostly compared with K_{Ic}, determined according to the secant method using large specimens. No comparisons were made with K_{Io}, calculated with the load at the onset of crack extension.

The lower limit of B below which J_0 increases is not known exactly. The factor of 25 in Eq 3 is not well established by experimental results.

Materials and Experimental Procedure

Material

The aim of this investigation was to contribute to the determination of the limits of LEFM and of J-integral analysis for fracture-toughness evaluation ($B_{pl\ st}$ and B_{LE} in Fig. 2). Therefore, the materials were not used in the usual heat treatment but in a condition suitable to find one or both of these limits with the available size of the plates. Two materials were investigated.

Aluminum Alloy 7475—The material was received as a plate with a thickness of 63 mm in the condition T 7351. To obtain a more ductile behavior, the material was annealed for 15 h at 180°C. The yield strength was 326 N/mm² in the annealed condition.

Nickel-Chromium-Molybdenum Steel—The steel had the composition: 0.32C, 4.2Ni, 1.68Cr, 0.43Mo, 0.41Mn, 0.28Si, 0.016P, and 0.014S. Bars with a cross section of 100 by 250 mm were obtained in a wrought and afterwards annealed condition. From tension tests σ_y = 497 N/mm², σ_u = 728 N/mm², and $E = 2.07 \times 10^5$ N/mm² was determined.

Specimens

Compact specimens of various sizes were used (Table 1 and 2). The load point displacement was determined with a clip gage which was placed in the load line. For the steel specimens with B = 13 mm and W = 28 mm, this method could not be applied. Hence, for these specimens, the load was plotted against the displacement of the grippings. The deformation of the grippings was corrected.

J-Integral Determination

For the aluminum alloy, J was determined by means of two methods.

1. The method proposed by Begley and Landes [*8*] in their first paper using the equation

$$J_1 = \frac{-1}{B}\frac{\partial U}{\partial a} \tag{5}$$

where U is the deformation energy (area under the load-deformation curve).

2. The approximation method proposed by Landes and Begley [*9*]

$$J_2 = \frac{2U}{B(W - a)} \tag{6}$$

It could be shown [*13*] that this equation agrees better with Eq 5 than the equation proposed by Rice et al [*14*] where U is replaced by U_{crack}. For the steel, only Method 2 was used.

TABLE 1—*Results for the aluminum alloy 7475.*

B, mm	W, mm	W/B	J_{1o}, N/mm	J_{2o}, N/mm	K_{J1o}, $MNm^{-3/2}$	K_{J2o}, $MNm^{-3/2}$	K_o, $MNm^{-3/2}$	K^*_o, $MNm^{-3/2}$	K_Q, $MNm^{-3/2}$
50	100	2	24.5	20	43.6	39.4	42.9	44.6	54.9
25	50	2	...	22.5	...	41.8	42.6	46.2	43.0
15	50	3.3	27.5	22.5	46.2	41.8	42.7	46.2	41.5
5	50	10	24.4	22	43.5	41.3	39.5	42.1	31.9

TABLE 2—*Results for the steel 35NiCrMo16.*

B, mm	W, mm	W/B	J_{2o}, N/mm	$J_2{}^a$, N/mm	K_{J2o}, $MNm^{-3/2}$	K_o, $MNm^{-3/2}$	K^*_o, $MNm^{-3/2}$	K_Q, $MNm^{-3/2}$
90	200	2.22	155	256	190	169	194	125
49	100	2.04	150	170	187	141	171	89
24	50	2.08	150	182	187	114	148	59
13	28	2.15	135	139	177	87	111	57
5	50	10	240	247	236	103	125	55

[a]From the intersection with $J = 2\,\sigma_{fl} \times \Delta a$.

Determination of J_o

To determine J at the onset of crack extension, different fatigue-precracked specimens were subjected to different loads and, after unloading, fatigued again. The amount of stable crack extension could be measured on the fracture surface between the fatigue cracks in a scanning electron microscope (see Fig. 3). For the aluminum alloy, load point displacement δ was plotted against crack extension Δa and δ_o obtained by extrapolation to $\Delta a = o$. Then J_o was obtained from the J-δ-curves. Besides this pro-

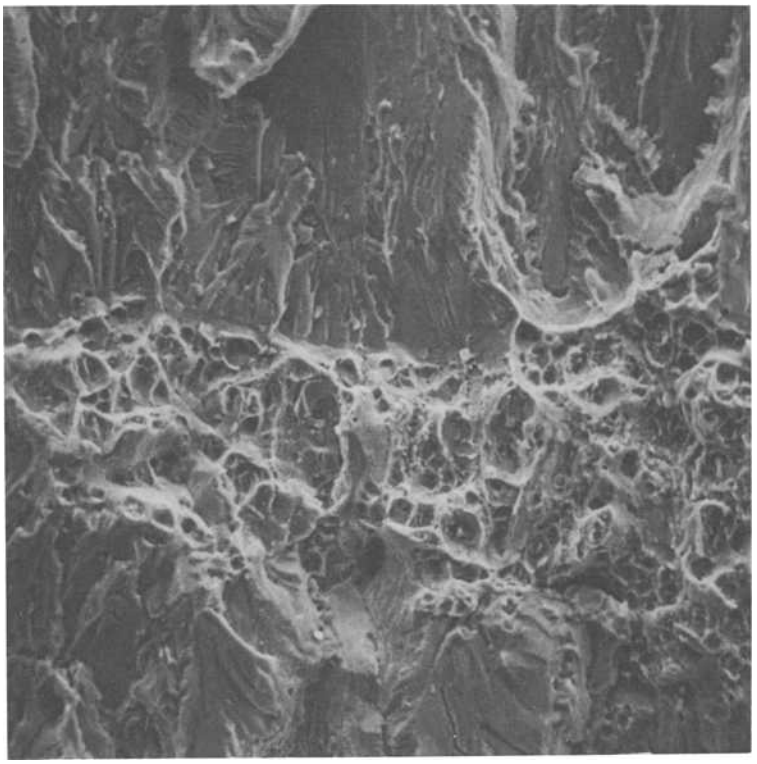

FIG. 3—*Dimple structure between fatigue cracks (7475).*

cedure, J_o was obtained by plotting J, determined with Eq 6, against Δa and by extrapolation to Δa = o. For the steel, J_o was determined only from the J-Δa-curves.

Experimental Results

Aluminum Alloy 7475

From load-displacement curves, measured for specimens with different crack lengths of about a/W = 0.4, 0.5, 0.6, 0.7, and 0.8, J-δ-curves were obtained. J_o at the onset of crack extension was determined for a/W = 0.6. In Fig. 4, displacement δ is plotted against crack extension Δa. In the

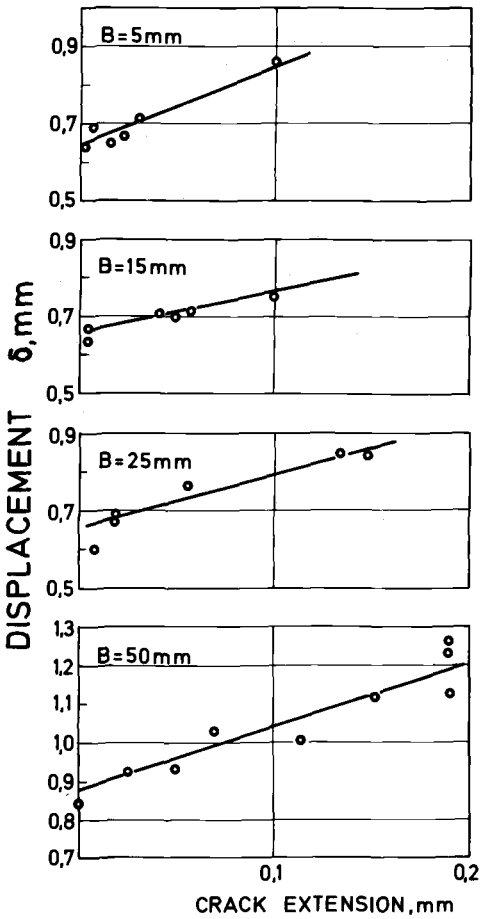

FIG. 4—*Displacement versus crack extension for 7475.*

scanning electron microscope, the stable crack extension could be separated easily from the stretched zone (Fig. 3).

Therefore, Δa is the real crack extension and extrapolation to $\Delta a = 0$ could be done in an unequivocal manner to obtain δ_0. J_{1o} obtained from δ_0 and the J-δ-curves are included in Table 1.

In Fig. 5, J_2 calculated with Eq 6 is plotted against Δa. Again extrapolation to $\Delta a \simeq 0$ is possible. The extrapolation value J_{2o} is also included in Table 1 and Fig. 6.

From Fig. 6, it can be seen that J_0 is independent of specimen thickness and that J_{2o}, obtained with Eq 6, is about 20 percent lower than J_{1o} obtained with Eq 5.

Calculations of J for linear-elastic behavior have shown that for a/W

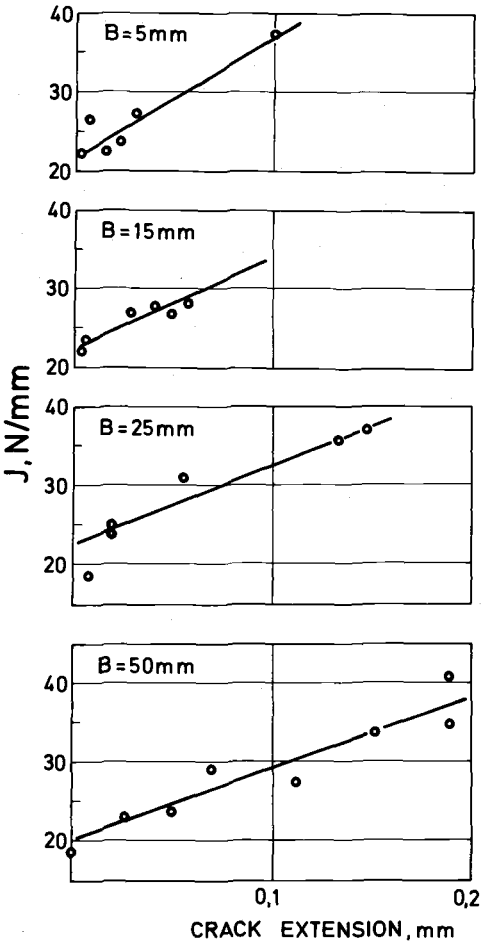

FIG. 5—J_2 *versus crack extension for 7475.*

= 0.6 the simplified formula, Eq 6, yields about 10 percent lower values than Eq 5 [*13*]. For elastic-plastic behavior, the difference is smaller.

Five different stress-intensity factors were calculated from the experimental results (see Table 1 and Fig. 7). That is, K_{J1o} from J_{1o} with Eq 4 (E = 6.92, 10^4N/mm^2, ν = 0.33); K_{J2o} from J_{2o} with Eq 4; K_o calculated according to LEFM with the load F_o at the onset of crack extension, and F_o was obtained from δ_o and the F-δ-curve; K^*_o as K_o, with the plasticity correction, replacing crack length a by $a + 1/6\pi \times (K_o/\sigma_y)^2$; and K_Q determined with the 5 percent secant method.

From Table 1 and Fig. 7, the following can be seen.

1. For all specimen sizes there is a good agreement between K_{J1o} calcu-

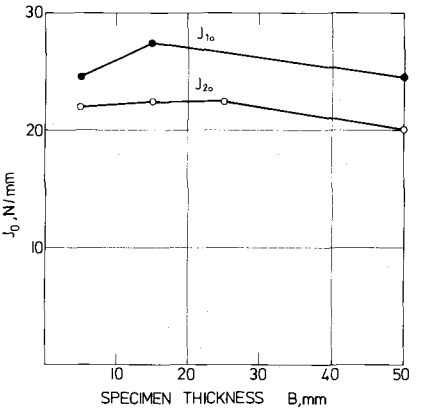

FIG. 6—J_o *versus specimen thickness for 7475.*

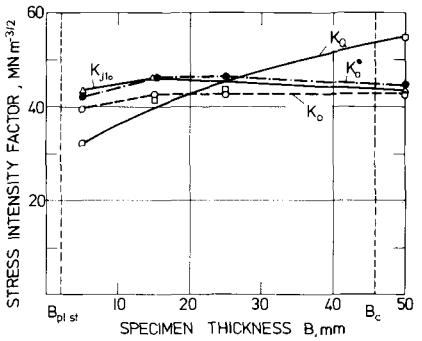

FIG. 7—*Stress intensity factors versus specimen thickness for 7475;* K_o *calculated with LEFM,* K^*_o *calculated with LEFM using plasticity correction,* K_{J1o} *calculated from* J_{1o}.

lated from J_{1o} and K^*_o, calculated with LEFM, whereas K_{J2o} is smaller than K^*_o.

2. While K_o, K^*_o, and K_{J1o} are almost independent of specimen size, K_Q increases with increasing thickness.

3. For specimens with $B = 50$ mm, crack extension starts below K_Q at the beginning of the deviation from the linear part of the F—COD-curve.

4. For specimens with $B = 5$ mm, crack extension starts after considerable deflection of the F-COD curve ($K_o > K_Q$). Nevertheless, LEFM gives nearly the same value for K_o as for the specimens with $B = 50$ mm.

The thickness independent $K^*_o = K_{J1o}$, is the plane-strain stress-intensity factor K_{1o} at the onset of crack extension. With $K_{1o} = 44$ MN/m$^{-3/2}$ and $\sigma_y = 326$ N/mm^2, the critical crack size according to ASTM Method

E 399-74 is $B_c = (W - a)_c = 2.5\,(K_{1o}/\sigma_y)^2 = 45.5$, and, according to Eq 3, $B_{pl\,st} = 1.9$ mm.

Steel

For the steel, it was difficult to separate the stretched zone from the dimple structure in the scanning electron microscope. Therefore, in contrast to the aluminum alloy, the measured crack extension contains both stretched zone and dimple structure.

In Fig. 8, J-Δa-curves are shown for the specimens with $W/B \sim 2$ (B = 13 mm, 24 mm, 49 mm, 90 mm). For each specimen size, two straight lines are drawn through the measured values. It is assumed that the steep line for small crack extension corresponds to the stretched zone. These straight lines do not go through the origin. There is an intersection with the J-axis between J = 40 N/mm and J = 65 N/mm.

From a physical point of view, the intersection between the two lines should be defined as J_o. The intersection of the J-Δa-curves with the straight line $J = (\sigma_y + \sigma_u)\,\Delta a$, as proposed by Landes and Begley [*9*], is somewhat higher. The results for the specimens with B = 5 mm, W = 50 mm are shown in Fig. 9.

In Table 2 and Fig. 10, J_{2o}, K_o, K^*_o, K_Q, and K_{J2o} are shown. For the steel specimens, only J_{2o} was determined. Because of the large plastic deformation at the onset of crack extension, the difference between J_{1o} and J_{2o} should be smaller than for the aluminum alloy [*13*].

The results can be summarized as follows.

1. In the range 13 mm < B < 90 mm, J_o is independent of specimen thickness. Between B = 5 mm and B = 13 mm, J_o increases.

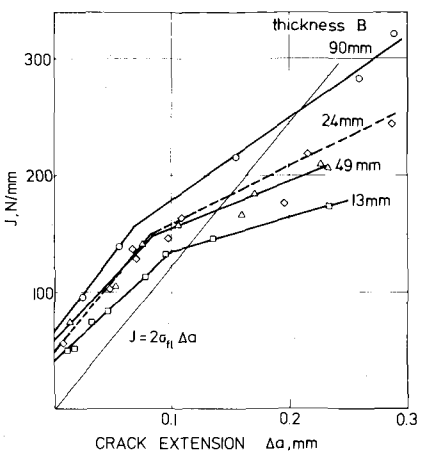

FIG. 8—J_2 *versus crack extension for specimens with* W/B ≦ *2 (NiCrMo steel).*

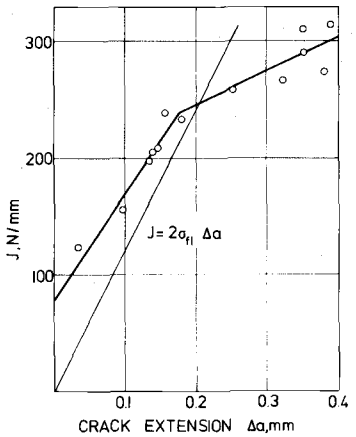

FIG. 9—J_2 *versus crack extension for specimens with* W = *50 mm,* B = *5 mm* (*NiCrMo steel*).

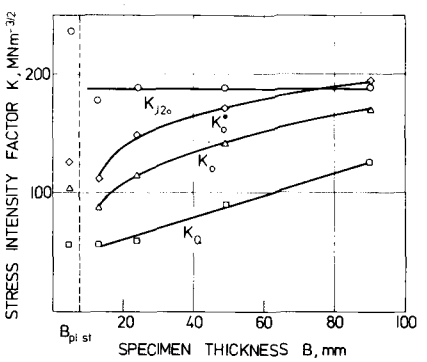

FIG. 10—*Stress intensity factor versus specimen thickness for NiCrMo steel* (*same notation as in Fig. 7*) B = *5 mm:* W/B = *10;* B > *5 mm:* W/B ≦*2.*

2. For B > 13 mm, K_o and K^*_o increase with increasing thickness. For B = 70 mm there is $K^*_o = K_{J2o}$. For B = 90 mm, K^*_o is somewhat higher than K_{J2o}. This may be due either to the scatter of the results or a too large plasticity correction. For very large specimens with linear load-displacement curve until crack extension, K^*_o, K_o, and K_{Jo} have to be identical.

3. For all specimen sizes, there is $K_Q < K_o$.

4. From Fig. 8, it can be seen that for Δa = constant, J increases with increasing thickness. From this behavior, it follows that J at the intersection with $J = 2\sigma_{fl} \times \Delta a$ also increases with thickness, whereas J_o at the knee of the J-Δa-curves is independent of thickness.

The thickness independent K_{J2o} is the plane-strain stress-intensity factor

at the onset of crack extension. The minimum thickness according to ASTM Method E 399, calculated with $K_{J2o} = K_{Io} = 188$ MNm$^{-3/2}$ and $\sigma_y = 497$ N/mm^2 is $B_c = 358$ mm. The minimum thickness for which plane strain exists in the specimen center calculated with Eq 3 is $B_{pl\ st} = 7.6$ mm.

Conclusions

The purpose of this investigation was to provide a contribution to the solution of two problems:

1. What is the minimum specimen size for which LEFM can be applied under plane-strain conditions?
2. Is it possible to determine K_{Io} with smaller specimens by means of J-integral determination, and what is the minimum specimen size to determine J_{Io}?

The application of LEFM is limited by a critical ligament $W - a$. The plane-strain condition is limited by a critical thickness. The following conclusions can be drawn from the experimental results.

K_{Io}, the stress-intensity factor at the onset of crack extension under plane-strain conditions, can be determined with specimens smaller than those calculated from $(W - a)_c = 2.5\ (K_{Io}/\sigma_y)^2$. From Fig. 10, it can be seen that for the steel specimens with $W/B = 2$, there is agreement between K_{J2o} and K^*_o for $B > 70$ mm. This leads to $(W - a)_{LE} = 56$ mm for $W/B = 2$ and $a/W = 0.6$ or

$$(W - a)_{LE} = 0.4 \left(\frac{K_{Io}}{\sigma_y} \right)^2 \tag{7}$$

Further experiments are necessary to prove whether the factor 0.4 can be used as a general rule or whether the factor is dependent on the material.

For the aluminium alloy there is $(W - a)_c = 45.5$ mm. Also, for specimens with $W - a = 20$ mm ($W = 50$ mm, $a/W = 0.6$), K_{Io} could be determined with LEFM. If the factor 0.4 in Eq 7 is used, then $(W - a)_{LE} = 7.3$ mm.

For the steel, there exists a broad range of specimen sizes for which K_{Io} can be determined using J-integral, but not with the LEFM ($K_o < K_{Io}$). The lower limit of the specimen thickness is between 5 and 13 mm. Equation 3 leads to a minimum thickness of $B_{pl\ st} = 7.6$ mm. Landes and Begley [9] have proposed for the minimum thickness $B = \alpha\ J_o/\sigma_y$, with $\alpha = 25$, which is identical with Eq 3. Later on in guidelines of the ASTM task group "elastic-plastic fracture criteria," $\alpha = 50$ was recommended. With $B = 13$ mm for the steel, we obtain $\alpha = 43$.

As to the evaluation method of J_0, it can be concluded that the scatter in the J-Δa or the δ-Δa-curve is reduced if a scanning electron microscope is used to determine crack extension.

Where a clear separation between dimple structure and stretched zone is possible, only the dimple region should be measured. Then J_0 should be determined by extrapolation to $\Delta a = 0$. If such a separation is not possible, J_0 has to be determined after some crack extension. The suggestion of Landes and Begley [*9*] to determine the intersection of the J-Δa-curve with the straight line $J = 2\sigma_{fl} \times \Delta a$ yields somewhat higher values than the intersection of the two straight lines in Figs. 8 and 9.

It is not easy to understand the intersection of the first part of the J-Δa-curve, corresponding to the stretched zone formation, with the J-axis between 40 and 65 N/mm. It should be expected that the stretched zone formation begins if the maximum fatigue load of the precracking is exceeded. In terms of J, the maximum fatigue load is about $J_{f\max} = 7$ N/mm and, therefore, below the intersection of the J-Δa-curve with the J-axis.

A rough estimation of K_{Io} also can be made in the following way. It is assumed that the stretched zone is formed during the loading between the maximum fatigue load $F_{f\max}$ and the load corresponding to J_0 at the knee on the J-Δa-curve.

Crack-tip opening displacement at J_0 is roughly twice the measured crack extension Δa_{knee} at J_0. Using Eq 2, the following relation exists between K and COS

$$K_{Io} - K_{f\max} = \left[\frac{2E \times \sigma_y \times \Delta a_{knee}}{1 - \nu^2}\right]^{1/2} \tag{7}$$

In Table 3, Δa_{knee}, $K_{f\max}$, and K_{Io} calculated with Eq 7 are given. There is excellent agreement between K_{Io} calculated from Δa_{knee} and from J_0.

TABLE 3—*Comparison of* K_{J0} *calculated from J-integral and* K_{Io} *calculated from stretched zone for the steel 35NiCrMo16.*

B, mm	Δa_{knee}, μm	$K_{f\max}$, MNm$^{-3/2}$	K_{Io}, MNm$^{-3/2}$	K_{Jo}, MNm$^{-3/2}$
90	67	48	172	190
49	85	47	187	187
24	82	46	183	184
13	100	22	174	177
5	180	40	244	236

Acknowledgments

We wish to thank J. Eschweiler for his help during the performance of the tests and H. Schleicher for the preparation of the specimens. The fi-

nancial support of the Deutsche Forschungsgemeinschaft is acknowledged gratefully.

References

[1] Robinson, J. N. and Tetelman, A. S., *International Journal of Fracture,* Vol. 11, 1975, pp. 453–468.

[2] Robinson, J. N., "The Critical Crack Tip Opening Displacement and Microscopic Fracture Criteria for Metals, Ph.D. thesis, University of California, Los Angeles, Calif., 1973.

[3] Munz, D., Galda, K. H., and Link, F. in *Mechanics of Crack Growth, ASTM STP 590,* American Society for Testing and Materials, 1976, pp. 219–234.

[4] Green, G. and Knott, J. F., *Journal of the Mechanics and Physics of Solids,* Vol. 23, 1975, pp. 167–183.

[5] Rice, J. R., in *Mechanics and Mechanisms of Crack Growth,* British Steel Corporation, 1973, pp. 14–39.

[6] Srawley, J. E. and Brown, W. F. in *Fracture Toughness Testing and its Application, ASTM STP 381,* American Society for Testing and Materials, 1965, pp. 133–198.

[7] Clausing, D. P., *International Journal of Fracture Mechanics,* Vol. 5, 1969, pp. 211–227.

[8] Begley, J. A. and Landes, J. D. in *Fracture Toughness, ASTM STP 514,* American Society for Testing and Materials, 1972, pp. 1–23.

[9] Landes, J. D. and Begley, J. A. in *Fracture Analysis, ASTM STP 560,* American Society for Testing and Materials, 1974, pp. 170–186.

[10] Griffis, C. A. and Yoder, G. R., "Application of the J-Integral to Crack Initiation in a 2024-T351 Aluminium Alloy," NRL Report 7676, Naval Research Laboratory, Washington, D.C., April 1974.

[11] Griffis, C. A. and Yoder, G. R., *Journal of Engineering Materials and Technology,* 1974.

[12] Ricardella, P. C. and Swedlow, J. L. in *Fracture Analysis, ASTM STP 560,* American Society for Testing and Materials, 1974, pp. 134–154.

[13] Keller, H. P. and Munz, D., "Comparison of Different Equations for Calculation of J-Integral from one Load-Displacement Curve," Report DLR-FB 76-56, DFVLR, Cologne, Germany.

[14] Rice, J. R., Paris, J. G. and Merkle, J. G. in *Progress in Flaw Growth and Fracture Toughness Testing, ASTM STP 536,* American Society for Testing and Materials, 1973, pp. 231–245.

H. Kitagawa[1] *and H. Ishikawa*[1]

Determination of Stress Intensities of Through-Cracks in a Plate Structure Under Uncertain Boundary Conditions by Means of Strain Gages

REFERENCE: Kitagawa, H. and Ishikawa, H., **"Determination of Stress Intensities of Through-Cracks in a Plate Structure Under Uncertain Boundary Conditions by Means of Strain Gages,"** *Flaw Growth and Fracture, ASTM STP 631,* American Society for Testing and Materials, 1977, pp. 232-244.

ABSTRACT: It is often required to determine the values of the stress-intensity factors at a tip of a given two-dimensional through-crack even when some of the boundary conditions are not exactly given.

A new method is proposed for determination of this kind of stress-intensity factor by combining experimental stress-analysis techniques, fracture mechanics, and variational methods.

In this paper, the stresses on the boundary of a small domain surrounding a crack tip were measured by electric resistance strain gages, and the stress-intensity factors were calculated by variational method. Sufficient accuracy was obtained. For convenience of applications, a method by means of a calculating table was proposed.

KEY WORDS: crack propagation, fractures (materials), stress analysis

A new method is proposed for determination of the stress-intensity factors at a tip of a two-dimensional through-crack by a combination of resistance strain-gage measurement and a variational method, even in the case when the mechanical-boundary conditions are not given.

In this stage of progress of the application of fracture mechanics, it is important to find the methods to determine the value of the stress-intensity factor (K) of a through-crack in a structure or a specimen.

There are many methods for the analysis of stress-intensity factors. In most of these, however, all of the distribution of external loads or boundary displacements and the exact configuration of the cracked body are

[1]Professor and graduate student, respectively, Tokyo University, Tokyo, Japan.

required to be given in advance. Often in actual structures, however, an exact distribution of the loads or displacements at the outer boundary of the structures, or the exact distribution of stiffness, can not be evaluated easily. Even in the case of a simple specimen, an exact distribution of loads or displacements at its clamped ends is not given usually, which sometimes causes a significant error in evaluation of stress-intensity factors [*1,2*].[2] In these cases, most existing methods or solutions can not be available effectively.

A practical solution for this problem will be given in this paper. First, a domain is assumed, which is surrounding the specified tip of a given or prepared two-dimensional through-crack in a given structure or specimen. Next, the mechanical-boundary conditions of the assumed domain are determined by one of the experimental stress-analysis techniques, for example, resistance strain gages in this paper. Finally, the stress-intensity factors are analyzed under the boundary conditions determined previously by a variational method given in this paper. (As a method for this purpose, other methods including finite-element method will be expected to be available.)

Fracture mechanics and experimental stress analysis have progressed independently from each other. This paper is one of the trials for the purpose of combining the gains of these two.

Procedures of Analysis

The procedures of our analysis are shown in Fig. 1. The procedures will be outlined as follows.

1. In the given cracked body, a domain (*D*) surrounding a specified tip of a through-crack is assumed, as shown in Fig. 2.
2. Mechanical-boundary conditions are determined by means of the

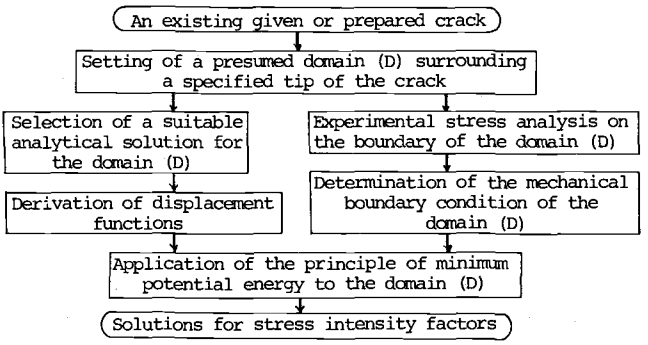

FIG. 1—*Procedures of analysis.*

[2]The italic numbers in brackets refer to the list of references appended to this paper.

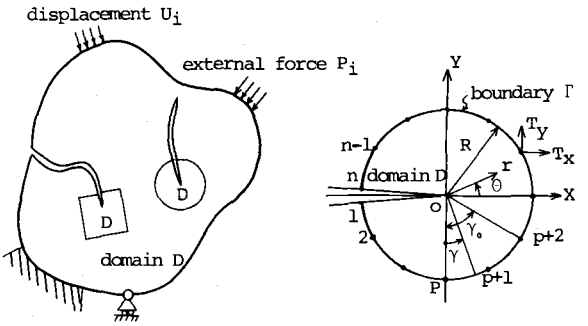

FIG. 2—*A domain* (D) *surrounding a crack tip and coordinate system.*

results of measurements by strain gages at several points on the outer boundary of the domain (*D*) and some interpolation.

3. A suitable analytical solution for the domain (*D*) is selected according to the given conditions, and displacement functions are derived.

4. By means of the displacement functions and the boundary conditions given previously, a potential energy in the domain (*D*) is brought to a minimum value by a variational method, and the values of K can be obtained from the coefficient matrix determined as the displacement matrix.

Determination of Boundary Condition

At first a domain (*D*), such as a circular or rectangular domain, is assumed to be surrounding the tip of a given through-crack in the given structural component, as shown in Fig. 2. In this paper, a circular domain is assumed. The boundary conditions of the domain, in this study, are prescribed in terms of traction forces. In this paper, the measurement by one of the experimental stress analyses or electric resistance strain gage is carried out at several specified discrete points (n points) on the boundary (Γ) of the domain. As the values of stress components (σ_x, σ_y, τ_{xy}) at the $(p)^{th}$ point on the boundary (Γ) can be calculated from the measured values at the point, the prescribed values of traction forces $\{T\}_p^T = [T_x T_y]_p$ is obtained from the relation between traction forces and stress components, that is given by

$$\{T\}_p = \begin{Bmatrix} T_x \\ T_y \end{Bmatrix}_p = \begin{Bmatrix} l_x\sigma_x + l_y\tau_{xy} \\ l_x\tau_{xy} + l_y\sigma_y \end{Bmatrix}_p \tag{1}$$

where l_x and l_y are the direction cosines of the unit normally drawn outwards on the boundary (Γ). And, referring to the paper by Tong, Pian,

and Lasry [3], traction force $\{\bar{T}\}$ at the arbitrary point on the boundary (Γ) is assumed in such a way that $\{\bar{T}\}$ varies quadratically between a set of three consecutive points, that is, $(p)^{\text{th}}$, $(p + 1)^{\text{th}}$ and $(p + 2)^{\text{th}}$ point, as follows

$$\{\bar{T}\} = \begin{Bmatrix} \bar{T}_x \\ \bar{T}_y \end{Bmatrix} = [M]\{Q\} \tag{2}$$

$$[M] = \begin{bmatrix} (1 - \gamma/\gamma_0)(1 - 2\gamma/\gamma_0) & 0 & 4(\gamma/\gamma_0) \times (1 - \gamma/\gamma_0) & & \\ 0 & (1 - \gamma/\gamma_0)(1 - 2\gamma/\gamma_0) & 0 & 4(\gamma/\gamma_0) \times (1 - \gamma/\gamma_0) & \\ & & 0 & (\gamma/\gamma_0) \times (2\gamma/\gamma_0 - 1) & 0 \\ & & & 0 & (\gamma/\gamma_0) \times (2\gamma/\gamma_0 - 1) \end{bmatrix} \tag{3}$$

$$\{Q\}^T = [T_{x,p} T_{y,p} T_{x,p+1} T_{y,p+1} T_{x,p+2} T_{y,p+2}] \tag{4}$$

where

$[M]$ = interpolation function matrix that varies quadratically,
γ_0 = angle between line O $-$ p and line O $-(p + 2)$, and
γ = angle measured anticlockwise from line O $-$ p,

where O is the origin or the center of the circular domain and coincides with the tip of the crack (see Fig. 2).

$\{\bar{T}\}$ shown in Eq 2 is used as the mechanical-boundary condition of the domain, the boundary value of which is prescribed in terms of traction forces.

Analytical Solution for the Domain (D)

In this paper, the domain with an edge crack is adopted, because this kind of domain is convenient for following the growing tip of the various cracks in actual structures, such as a crack initiated at the edge of a plate or a crack grown from a welded zone, and the region of variable stiffness in actual structures.

To analyze the domain with an edge crack, an analytical solution for a semiinfinite crack in an infinite plate is used.

Now, let $\phi(z)$ and $\psi(z)$ be Muskhelishvili's complex stress functions. Displacements u_x and u_y can be expressed generally by $\phi(z)$ and $\psi(z)$ as follows

$$2\mu(u_x + iu_y) = \eta\phi(z) - z\overline{\phi'(z)} - \overline{\psi(z)} \tag{5}$$

where

$\mu = E/2(1 + \nu)$,
$\eta = 3 - \nu$ for plane strain and $\eta = (3 - \nu)/(1 + \nu)$ for plane stress,
E and ν = Young's modulus and Poisson's ratio, respectively,
$(\,)'$ = differentiation,
$\overline{(\,)}$ = the complex conjugate, and
$z = re^{i\theta}$ with $i^2 = -1$.

Substituting the result of the eigen-function expansion [*4,5*] of $\phi(z)$ and $\psi(z)$ about the tip of a semiinfinite crack, whose surfaces are traction free, into Eq 5, we have

$$\{u\} = \begin{Bmatrix} u_x \\ u_y \end{Bmatrix} = \sum_{m=1}^{\infty} A_{\mathrm{I}m} \begin{Bmatrix} f_{x\mathrm{I}}{}^m \\ f_{y\mathrm{I}}{}^m \end{Bmatrix} + \sum_{m=1}^{\infty} A_{\mathrm{II}m} \begin{Bmatrix} f_{x\mathrm{II}}{}^m \\ f_{y\mathrm{II}}{}^m \end{Bmatrix} \tag{6}$$

$$f_{x\mathrm{I}}{}^m = \frac{1}{2\mu}\left[\left\{\eta + \frac{m}{2} + (-1)^m\right\} \cos\left(\frac{m\theta}{2}\right) - \frac{m}{2}\cos\left(\frac{m}{2} - 2\right)\theta\right] r^{m/2}$$

$$f_{y\mathrm{I}}{}^m = \frac{1}{2\mu}\left[\left\{\eta - \frac{m}{2} - (-1)^m\right\} \sin\left(\frac{m\theta}{2}\right) + \frac{m}{2}\sin\left(\frac{m}{2} - 2\right)\theta\right] r^{m/2} \tag{7}$$

$$f_{x\mathrm{II}}{}^m = \frac{1}{2\mu}\left[\left\{-\eta - \frac{m}{2} - (-1)^m\right\} \sin\left(\frac{m\theta}{2}\right) + \frac{m}{2}\sin\left(\frac{m}{2} - 2\right)\theta\right] r^{m/2}$$

$$f_{y\mathrm{II}}{}^m = \frac{1}{2\mu}\left[\left\{\eta - \frac{m}{2} + (-1)^m\right\} \cos\left(\frac{m\theta}{2}\right) + \frac{m}{2}\cos\left(\frac{m}{2} - 2\right)\theta\right] r^{m/2}$$

where $A_{\mathrm{I}m}$ and $A_{\mathrm{II}m}$ are real numbers and related to deformation Mode I and Mode II, respectively.

Application of Energy Principle

In order to analyze the edge-crack domain under the mechanical-boundary condition just mentioned using the analytical solution, we employ the principle of minimum potential energy as a variational principle. Then, in this paper, displacements in Eq 6 are the argument functions of the functional of the variational principle. Choosing the m in the series of Eq 6 as $m = N$, the displacements are written in a matrix form as follows

$$\{u\} = [U]\{\alpha\} \tag{8}$$

$$\{\alpha\}^T = [A_{\mathrm{I}1} \ldots A_{\mathrm{I}N} A_{\mathrm{II}1} \ldots A_{\mathrm{II}N}] \tag{9}$$

$$[U] = \begin{bmatrix} f_{x\mathrm{I}}{}^1 \ldots f_{x\mathrm{I}}{}^N f_{x\mathrm{II}}{}^1 \ldots f_{x\mathrm{II}}{}^N \\ f_{y\mathrm{I}}{}^1 \ldots f_{y\mathrm{I}}{}^N f_{y\mathrm{II}}{}^1 \ldots f_{y\mathrm{II}}{}^N \end{bmatrix} \tag{10}$$

The strain $\{\epsilon\}$ corresponding to the displacement in Eq 8 can be written by means of the strain-displacement relation as follows

$$\{\epsilon\} = [B]\{\alpha\} \tag{11}$$

We substitute Eqs 8 and 11 into the functional of the variational principle. (In this paper, we deal with only the case that the body force is equal to zero.) Then, from the minimum condition of the functional, we have

$$\{\alpha\} = [H]^{-1}[G]\{Q\} \tag{12}$$

where

$$[H] = \int_S [B]^T [D_e] [B] \, dS \tag{13}$$

$$[G] = \int_\Gamma [U]^T [M] \, d\Gamma \tag{14}$$

where

$[D_e]$ = matrix for the stress $\{\sigma\}$-strain $\{\epsilon\}$ relation, $\{\sigma\} = [D_e]\{\epsilon\}$,
S = area of the cracked domain, and
Γ = outer boundary of S.

It is clear from Eqs 6 and 7 that the first element $A_{\mathrm{I}1}$ and the $(N + 1)^{\mathrm{th}}$ element $A_{\mathrm{II}1}$ in a column vector $\{\alpha\}$ correspond to the singular terms of stresses, and so stress-intensity factors, K_{I} and K_{II}, are given by Eq 15

$$K_{\mathrm{I}} = \sqrt{2\pi} A_{\mathrm{II}} \quad K_{\mathrm{II}} = \sqrt{2\pi} A_{\mathrm{III}} \tag{15}$$

Calculating Table for Stress-Intensity Factors

If we can obtain the values of stress-intensity factors directly from only the several measured values without the foregoing calculation, it is very convenient for practical purpose.

Equation 12 shows that the column vector $\{\alpha\}$ is obtained from the product of the matrix, $[H]^{-1}[G]$, that is dependent on the size and the configuration of the domain (D), and the column vector $\{Q\}$, that is given by the results of experimental-stress analyses. Therefore, the matrix $[H]^{-1}[G]$ was calculated beforehand for various kinds of sizes, and the configuration of the domain and the efficient table of matrix for the calculation of the stress-intensity factor was made. As an example, Table 1 shows the table of matrix in case of a circular domain with $n = 13$ and $N = 20$. In this table, H_α^1 and H_α^{N+1} are first and the $(N+1)^{\text{th}}$ row of $[H]^{-1}[G]$, respectively, and they can be related to stress-intensity factors, K_{I} and K_{II}, as follows

$$\begin{Bmatrix} K_{\mathrm{I}} \\ K_{\mathrm{II}} \end{Bmatrix} = \sqrt{2\pi R} \begin{Bmatrix} A_{\mathrm{II}} \\ A_{\mathrm{III}} \end{Bmatrix} = \sqrt{2\pi R} \begin{bmatrix} H_\alpha^1 \\ \mathrm{H}_\alpha^{N+1} \end{bmatrix} \{Q\} \tag{16}$$

where R is the radius of the circular domain.

The calculating table is not dependent on material constants. Then, it is used for various kinds of materials.

Examination of Accuracy of the Present Calculation

Accuracy of the calculation with the present method was examined by means of an infinite plate with a single crack. In this calculation, the thickness of a plate is taken as a unit.

In this paper, the mixed mode crack, as shown in Fig. 3, will be examined. By means of Muskhelishvili's complex stress functions [6], the stress components $\{\sigma\}_p$ at the point p (see Fig. 2) on the outer boundary (Γ) of the domain (D) was calculated. The values of K_{I} and K_{II} were obtained from the $\{\sigma\}_p$ as input data. The effects of the numbers of terms N in Eqs 6 and 7, the numbers of the points of measurement n, and the dimensionless radius R/a of the circular domain (D) on these values of K_{I} and K_{II} were examined, as shown in Figs. 4, 5, and 6; a is a half crack length.

According to Fig. 4, the values of K_{I} and K_{II} do not show apparent convergence with increase of the numbers of terms N. Their errors are

TABLE 1—*Calculating table for stress-intensity factors.*

$$\begin{bmatrix} H_\alpha^{\,1} \\ H_\alpha^{\,N+1} \end{bmatrix}^T = \begin{bmatrix} 0.01310 & 0.07178 \\ -0.27639 & 0.02340 \\ 0.37482 & 0.24640 \\ -0.96427 & 0.06923 \\ 0.33827 & 0.10692 \\ -0.37031 & 0.01159 \\ 0.70273 & 0.25462 \\ -0.35648 & 0.01799 \\ 0.30114 & 0.15292 \\ 0.00382 & 0.03834 \\ 0.35721 & 0.19412 \\ 0.06654 & 0.22260 \\ 0.09363 & 0.0 \\ 0.0 & 0.16366 \\ 0.35721 & -0.19412 \\ -0.06654 & 0.22260 \\ 0.30114 & -0.15292 \\ -0.00382 & 0.03834 \\ 0.70273 & -0.25462 \\ 0.35648 & 0.01799 \\ 0.33827 & -0.10692 \\ 0.37031 & 0.01159 \\ 0.37482 & -0.24640 \\ 0.96427 & 0.06923 \\ 0.01310 & -0.07178 \\ 0.27639 & 0.02340 \end{bmatrix}$$

almost constant and are less than about 3 percent for N greater than five. This is due to the quadratical approximation of traction force on the domain boundary, as shown in Eq 3. Then, as the numbers of terms N, four or five are enough for the accuracy which is better than 3 percent.

From Fig. 5, it is found that as the numbers of points of measurement n, greater than thirteen, gives the better accuracy than 2 percent in case of both K_I and K_{II}.

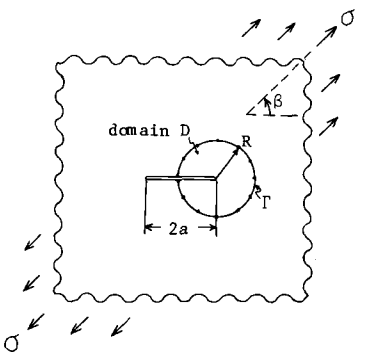

FIG. 3—*Mixed mode deformation.*

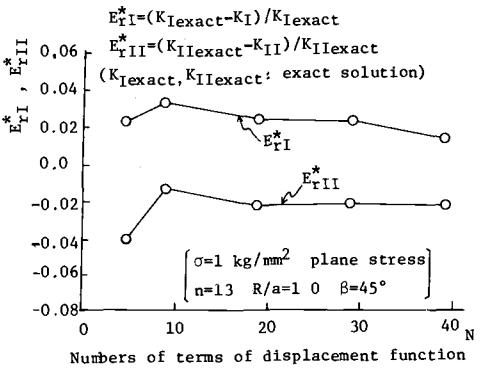

FIG. 4—*Effect of numbers* (N) *of terms of displacement function on stress-intensity factors* (K_I *and* K_{II}).

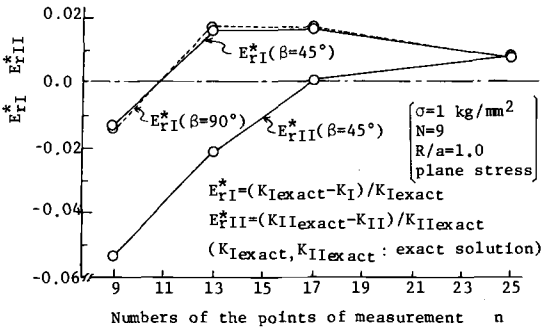

FIG. 5—*Effect of numbers* (n) *of the points of measurement on stress-intensity factors* (K_I *and* K_{II}).

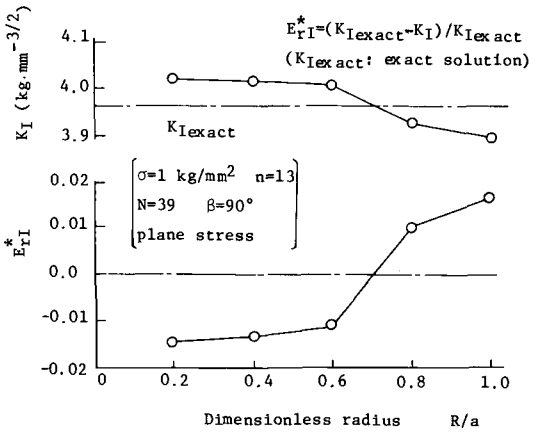

FIG. 6—*Effect of dimensionless radius* (R/a) *of a domain on stress intensity factor* (K_I).

As shown in Fig. 6, in case of the first mode deformation ($\beta = 90$ deg), the error of K_I just varies within 2 percent for R/a of $0.2 \leq R/a \leq 1.0$. This slight effect of R/a also is due to the same approximation as in the case of Fig. 4. Then, in case of the first mode deformation, even the cracks close complex boundaries will possibly be analyzed with a small domain at the relevant tip with good accuracy. In case of mixed mode deformation ($\beta \neq 90$ deg), this has not been ensured, and examinations are now under consideration.

Examples of Determination of K by the Experiments of Strain Measurement and Examination of Availability of the Present Method

Some examples of the determination carried out by the present method, including the experiments of strain-gage measurement, will be shown, and, in addition, the availability of this method will be experimentally examined.

The specimens as cracked bodies were made of a mild steel (SPC1), and the configuration and the sizes of one of them are shown in Fig. 7. The electric resistance strain gages used are eleven three-axes gages (Rosette gages) and two ordinary single-axis gages. All of their gage lengths are 2 mm. The locations of gages are shown in the right figure in Figs. 7 and 8. A uniaxial tensile loading was applied to the specimen, in which a

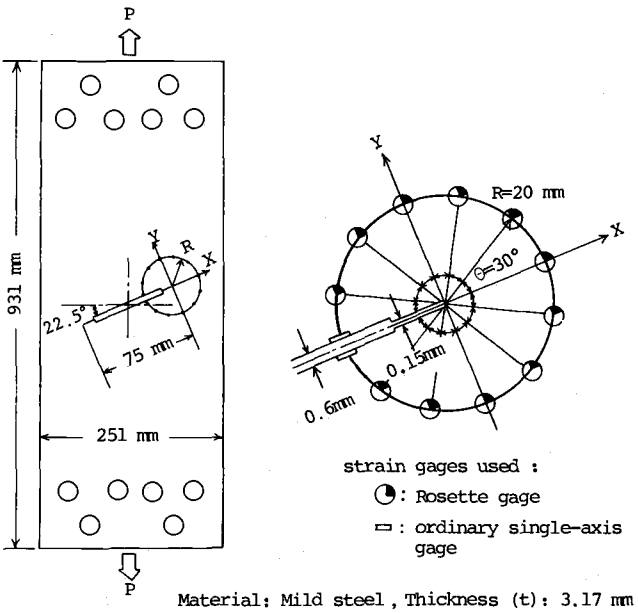

FIG. 7—*Configuration and sizes of specimen and locations of strain gages.*

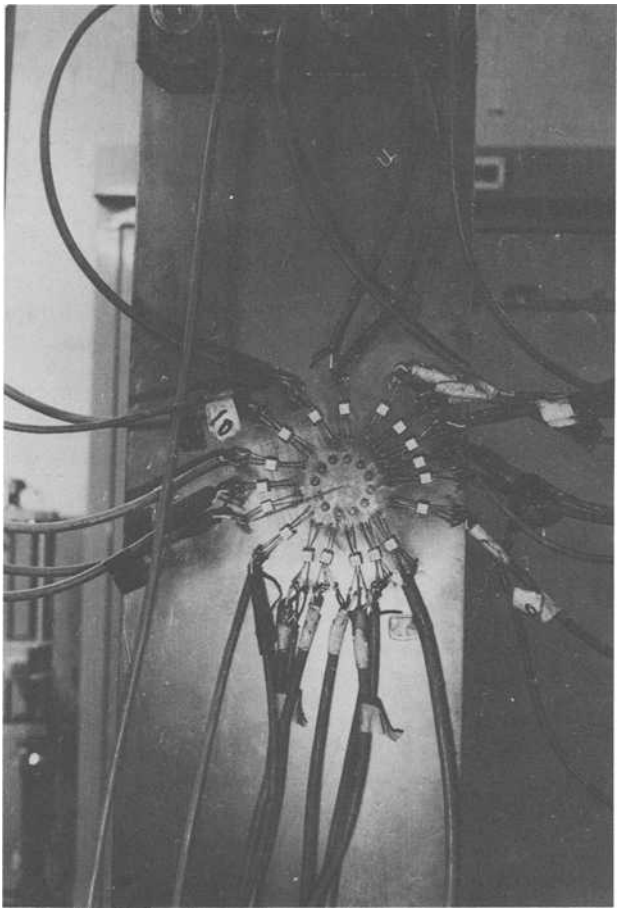

FIG. 8—*Photograph of specimen.*

straight crack-like notch was performed. The notch-tip radius is 0.075 mm. By means of the results of strain measurements and Table 1, the values of K_I and K_{II} were calculated. The results from the experiments, K^*_I and K^*_{II}, were compared with the almost exact reference values [7], K_I and K_{II}, by collocation method, and their errors, E_{rI} and E_{rII}, were evaluated. Some of the results are shown in Table 2. The values of K were obtained with fairly good accuracy.

Summary

Determination of the stress-intensity factors of a given crack or the crack with uncertain boundary conditions is important practically.

TABLE 2—*Experimental results of determination of* K *and their errors.*

Load	Stress Intensity Factor				Error	
	Experimental Value		Reference Value[a]			
P, kg	K^*_{I}, kg·mm$^{-3/2}$	K^*_{II}, kg·mm$^{-3/2}$	K_{I}, kg·mm$^{-3/2}$	K_{II}, kg·mm$^{-3/2}$	$E_{rI} = (K_I - K^*_I)/K_I$	$E_{rII} = (K_{II} - K^*_{II})/K_{II}$
2000	24.93	9.43	24.83	9.81	−0.004 = −0.4%	0.038 = 3.8%
3000	37.89	14.88	37.24	14.71	−0.017 = −1.7%	−0.012 = −1.2%

[a]Obtained by collocation method [7].

Applying a minimum potential energy principle to an assumed domain (D) surrounding a tip of a crack, a method of determination of the stress-intensity factor of a two-dimensional through-crack by experimental strain analyses has been proposed, and the possibility of general availability of this method has been examined. For practical use, a convenient calculating table of the K-matrix was prepared.

Experiments with electric resistance strain gages were carried out for the cases of the mixed mode crack. The values of K were obtained with fairly good accuracy, which will be an experimental assurance of the availability of our present method.

Acknowledgments

The authors would like to express their hearty acknowledgments to the kind and valuable suggestions or discussions given by Professor K. Oi of University of Tokyo, Professor T. H. H. Pian of Massachusetts Institute of Technology, Assistant Professor K. Watanabe of University of Tokyo, and T. Ohira of University of Tokyo.

References

[1] Isida, M., *International Journal of Fracture Mechanics,* Vol. 7, No. 3, Sept. 1971, p. 301.
[2] Kitagawa, H., Watanabe, K., and Hisada, T., *Preprint of Japan Society of Mechanical Engineers,* No. 750-1, April 1975, p. 255.
[3] Tong, P., Pian, T. H. H., and Lasry, S. J., *International Journal for Numerical Methods in Engineering,* Vol. 2, 1970, p. 73.
[4] Sih, G. C., and Liebowitz, H., *Fracture II,* H. Liebowitz, Ed., Academic Press, New York, 1968.
[5] Williams, M. L., *Journal of Applied Mechanics,* Vol. 24, Sept. 1957 p. 109.
[6] Muskhelishvili, N. I., *Some Basic Problems in the Mathematical Theory of Elasticity,* 4th Ed., 1963, noordhoff.
[7] Kitagawa, H., and Yuuki, R., *Preprint of Japan Society of Mechanical Engineers,* No. 760-12, Oct. 1976, p. 25.

D. E. McCabe[1]

Determination of R-Curves for Structural Materials Using Nonlinear Mechanics Methods

REFERENCE: McCabe, D. E., **"Determination of R-Curves for Structural Materials Using Nonlinear Mechanics and Methods,"** *Flaw Growth and Fracture, ASTM STP 631,* American Society for Testing and Materials, 1977, pp. 245-266.

ABSTRACT: The crack line wedge loaded method of test, originally intended for R-curve determination of ultrahigh strength sheet materials is now being used to evaluate the toughness of low-strength, high-toughness steels. The testing technique and equipment used is described in detail. Use is made of an elastic return slope concept on specimens under dominant plastic conditions to determine the extent of slow-stable crack extension. A crack-tip opening displacement (CTOD) approach, incorporating plastic hinge modeling, is used to determine K_R values. Also, a J_R approximation technique is introduced for comparison to K_R determined by the CTOD approach. R-curves typical of structural grades of steel are presented and examples of instability condition predictions are cited.

KEY WORDS: crack propagation, fractures (materials), R-curves, elastic properties

Recent efforts in the application of fracture mechanics based methods of test to low-strength, high-toughness materials have been concentrated on the development of single-value parameters such as K_{Ic}, J_{Ic}, and crack-tip opening displacement (CTOD). Generally, these values are determined in laboratory specimens at an event corresponding to the beginning of crack-tip extension. An implicit assumption in the application of these values to critical condition predictions in service components, therefore, is that incipient crack growth constitutes the instability event. This is generally recognized as a valid assumption when plane-strain conditions do in fact exist at the crack tip. Ultrahigh-strength materials are applied frequently in situations which satisfy such a requirement, and the application of single-value parameters has been quite clear in such cases. However, valid plane-strain, crack-tip constraint conditions are not often encountered in ordinary structural grades of plates or forgings since the required wall

[1]Senior engineer, Westinghouse Electric Corporation, Research and Development, Pittsburgh, Pa. 15235.

thicknesses would have to be of the order of 5 to 18 in., depending upon yield strength and toughness.

Experience in testing ultrahigh-strength sheet materials under conditions of dominant plane stress has revealed that slow-stable crack growth oftentimes precedes the instability event and that crack growth proceeds under increased crack-growth resistance. The so-called K_c instability value may lie well above the K value of incipient crack growth, depending upon specimen size and initial crack length. Since similar plane-stress conditions most certainly prevail for many structural materials in service, slow-stable crack growth with increasing crack-growth resistance also is to be expected. Examples to support this assertion are available from experiences in controlled experiments on purposely flawed gas transmission line pipes. Test pipes loaded under monotonically increased load have been observed to suffer slow-stable crack growth as much as 15 to 36 percent of the initial crack length prior to instability [*1*].[2] In cases where slow-stable crack growth has been demonstrated, the fracture toughness is more appropriately represented in terms of crack-growth resistance (R-curves) which can be applied to the prediction of instability conditions.

Although slow-stable crack growth has oftentimes been observed in tests on laboratory size specimens of high-toughness materials, little interest has been shown in evaluation of the data in terms of R-curves. From the standpoint of testing procedure, the reluctance to incorporate R-curve analysis is understandable because of a lack of availability of a standardized test method. In addition, the relatively small fracture mechanics types of specimens used in K_{Ic}, J_{Ic}, and CTOD work normally do not contain sufficient crack path to provide full R-curve data. Usually net section plastic flow intercedes early in the loading history, and this in combination with the slow-stable crack growth complicates the analysis.

The purpose of this paper, therefore, is to describe how a test method originally designed to develop R-curves on high-strength materials was modified to accommodate R-curve determinations on structural materials. The crucual point of the modification is the incorporation of nonlinear mechanics methods of analysis, such that reasonable size laboratory specimens can be used to develop full R-curves. The procedure used is the crack line wedge loading technique (CLWL) shown conceptually in Fig. 1. The specimen is loaded along the crack line using a wedge and split pin arrangement. All information necessary to make computations is obtained from the measurement of displacements at two locations along the crack line. Both crack length and applied wedge load are computed using prior determined compliance calibration curves. The procedure, as it was applied to testing of ultrahigh-strength sheet materials, has been reported in earlier publications [*2*].

[2] The italic numbers in brackets refer to the list of references appended to this paper.

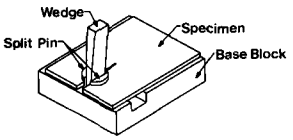

FIG. 1—*Crack-line loaded specimen with displacement controlled wedge loading.*

Specimen

The CLWL specimen design has been revised from the wedge opening load (WOL) configuration of earlier work to the compact specimen (CS) geometry of the ASTM Test for Plane-Strain Fracture Toughness of Metallic Materials (E 399-74) (Fig. 2). The specimen is modified from the K_{Ic} specimen to the extent that it is loaded on the crack line instead of using the recommended two loading hole arrangement. For R-curve work, material thickness is not specified, and the tests are usually made in the as-received thickness.

If the largest specimen indicated in Fig. 2 is used, the machining tolerances can be quite liberal, and the specimen could be produced economically to tolerance merely by careful saw cutting of most edges. This is permissible if straightness of the cut can be maintained within 1/16 in. However, the usual practice is to mill the back edge to provide a good reference surface for positioning and machining of the loading hole. The initial flaw is a saw cut, sharpened at the end with a honed hacksaw blade, followed by fatigue cracking an additional 0.05 to 0.1 in.

Equipment

The specimen is placed horizontally on a 1-1/4-in.-thick stainless steel base plate which is surface ground for optimum flatness, since it serves as

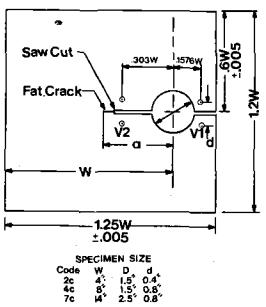

FIG. 2—*Crack-line wedge-loaded specimens.* (Note—*The specimens that actually were used conform to the proportionalities shown here but differ by a small amount from the sizes stipulated by the code convention.*)

a reference surface to clamp down specimens for prevention of buckling (Fig. 3). Planar dimensions of 17-1/2 by 20-1/2 in. is just sufficient to handle the 7C size specimen indicated in Fig. 2. The plate is supported in front on a pedestal made of 4-in. diameter heavy wall pipe which provides a direct reaction force to the downward thrust load from the wedge during loading. With this arrangement, no bending forces are transmitted through the base plate, as would be the case with remotely located reaction supports. The pipe flange is bolted very loosely to the underside of the base plate such that when the wedge is withdrawn after completion of the test or at intermediate steps, all the restraint against raising the specimen and split pins is taken up by a special framework designed for this task. Alignment of the base plate with respect to the horizontal plane is accomplished using an adjustable support under the back edge of the base plate.

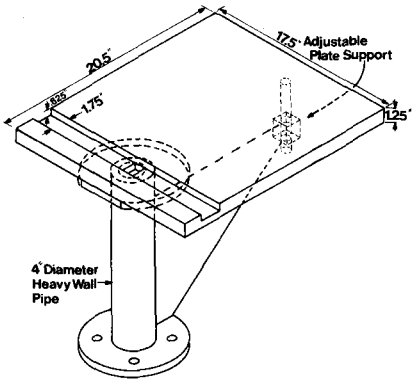

FIG. 3—*Base plate and supporting pipe for CLWL testing.*

A 1-3/4 in. wide by 5/8 in. deep slot is machined into the base plate in order to contain two sliding retainer blocks which are shown in Fig. 4. They provide vertical support for the split pins and will slide in the base plate slot to accommodate the increased cross section of the wedge as it is driven downward during tests. The segmented split pins sit in a recessed section of the blocks. The downward thrust load of the wedge is transmitted through the segments and will tend to cause the sliding blocks to teeter into the pipe cavity. The needed reaction force is provided by the specimen, and possible vertical displacement of the specimen is controlled easily by firm back-up support from a suitable hold-down system.

The wedge and split pin arrangement used to load the specimen is shown schematically in Fig. 5. The split pins are segmented and have centrally located pivot points to accommodate developing angularity as the specimen is wedged open. The segments are free to rotate about the pivot points; thus, the load line is maintained throughout the test. They are made to be 1/32 in. smaller in diameter than the hole in the specimen to

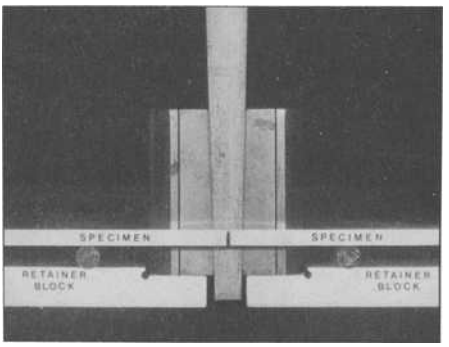

FIG. 4—*Front view of loading system as removed from the base plate.*

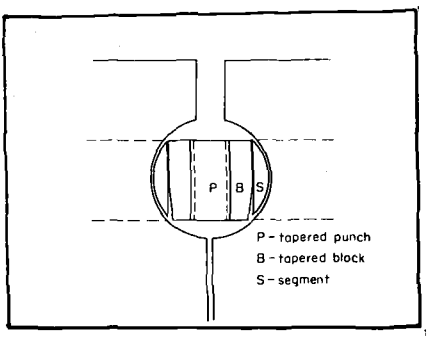

FIG. 5—*Plan view of punch and dies for wedge loading.*

help concentrate the forces at the theoretical load line. Some brinelling of the specimen may occur as a result of this when the test proceeds, but this has not been found to have an adverse effect on the overall behavior of the specimen. The segments are made of a 300 grade maraging steel for combined high strength and toughness. The tapered blocks are made of an air hardenable tool steel since only high hardness is needed. The wedge is also made of tool steel with a 20 to 1 taper ratio, and the surfaces are chrome plated for wear and corrosion resistance. Before each test, both the wedge and split pins are lubricated with a Teflon spray followed by light polishing with a molybdenum disulfide powder. The load advantage realized after friction losses is about 5 to 1. The wedge is mounted to the shaft of a 15 ton capacity piston by a 1½-in. diameter pin connection. With this integral system, it is equally convenient to insert or withdraw the wedge. In order to prevent withdrawal of the split pin, blocks, and segments, along with the wedge, a framework which is shown in Fig. 6, is inserted between the upper cylinder head and the split pins. The span of the framework is adjustable through the use of two 3/4-in. bolts threaded into the top. During loading in test, these bolts are periodically snugged up

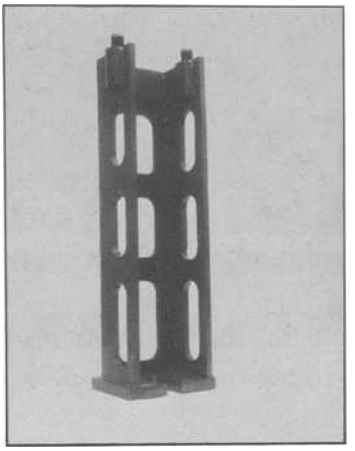

FIG. 6—*Framework used to prevent withdrawal of split pins.*

to compensate for any compressive displacement of the pipe pedestal. The framework bears on steel blocks (Fig. 7) which serve as extension arms. This places the framework above the area where an environment chamber for low-temperature work is placed. The purpose is to avoid extending a massive framework into a region where it also would have to be cooled along with the specimen.

Specimens are restrained against buckling during testing using a hold-down framework system shown in Fig. 8. The framework is bolted to the sides of the base plate and is removable for ease of installation of test specimens. Bolts distributed throughout the framework contact hold-down

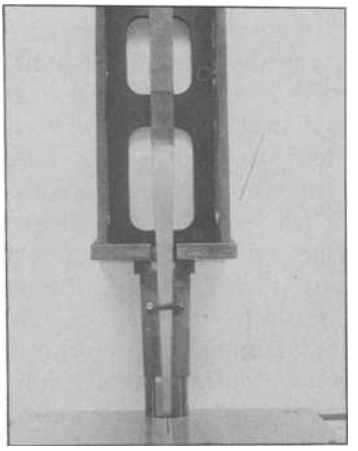

FIG. 7—*Assembly photo of support system used to prevent lifting of the split pins on wedge withdrawal.*

plates. Ball bearing pads shown in Fig. 9 are sandwiched between the plates and the specimen to reduce friction.

These ball bearings pads, or parallels, with 3/8-in. diameter balls are used commonly in machine shops and, hence, are obtainable from commercial suppliers. With such an arrangement, it is also possible to apply pressure to flatten slightly warped specimens and still retain good lateral freedom of motion.

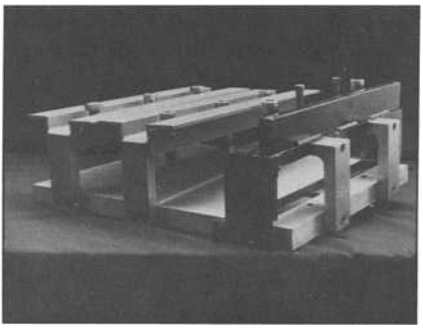

FIG. 8—*Specimen hold-down framework mounted over the base plate.*

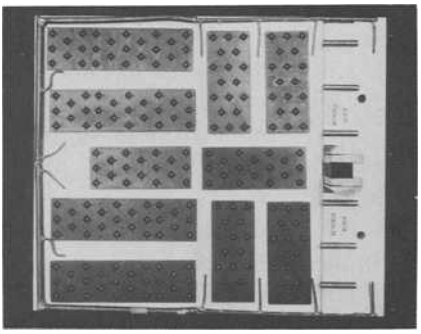

FIG. 9—*Overhead view of base plate with ball bearing pads distributed throughout; note LN feed lines for cryogenic temperature testing.*

Cryogenic Tests

Because of the self-contained instrumentation features of the CLWL method, R-curves can be conveniently made at temperatures down to −300°F. The main additional effort involves the encapsulation of the test jig with an insulating box and the provision of a liquid nitrogen (LN) feed and control system shown in Fig. 10. The LN is introduced through a distribution system of small diameter copper tubes (Fig. 9) on to the base plate which acts as a heat sink to vaporize the LN. The feed system is on-

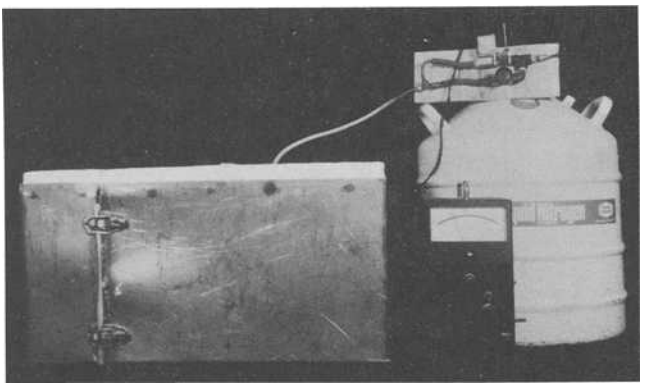

FIG. 10—*Photo of additional equipment needed for cyrogenic tests; insulating box, LN feed system, and millivoltmeter controller.*

off controlled by a millivoltmeter type controller which operates a solenoid valve in the LN feed line. The temperature is controlled from a thermocouple attached directly to the specimen. This sytem is then used for unattended cooldown to test temperature. At control temperature, the on-off system causes temperature sweeps of about 10°F. Immediately before test, the LN feed is augmented with a needle valve bypass system installed in parallel to the solenoid valve which gives an even flow temperature control during tests to a nearly constant value.

At cryogenic temperatures, the effectiveness of lubricants used on the wedge is reduced due to lubricant hardening, and, instead of the quiet uniform motion of the wedge seen at room temperature, a slight chatter can develop. In order to minimize this chatter, the insertion of the wedge can be delayed until immediately before the start of loading, and the retained heat in the wedge is then sufficient to sustain the effectiveness of the lubricant until the test is complete.

Instrumentation

Displacement is measured at the two locations indicated in Fig. 2, using clip gages designated V1 and V2. These gages are extra large, in comparison to the conventional ASTM Method E 399-74 gages, in order to provide the needed extra working range (Fig. 11). The gages are calibrated to be accurate to 2 percent over the linear working range of 0.6 in. for V1 and 0.3 in. for V2. They respond to movements of less than 0.0001 in. and display nearly equivalent accuracy in the initial part of a test. A point contact system of attachment to gage blocks, attached to the specimen with screws, is favored presently for the best reproducible control. Rockwell diamond indentation marks on the blocks provide the needed point

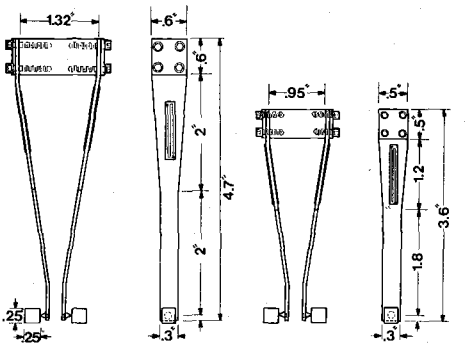

FIG. 11—*Front and side views of V1 and V2 clip gages.*

positioning capability. The objective of the system is to minimize error in displacement indication resulting from the hinge-like rotation of the specimen upon loading.

Two independent d-c power supplies are used to supply excitation voltage to the 1000 ohm strain gage bridges. The power input is kept as low as possible, consistent with the amplification capability of the *x-y* recorder, to obtain $\times 100$ and $\times 200$ displacement magnification. In cryogenic work, the clip gage output is a function of temperature because the gage factor increases at lower temperature. The adjustment for this temperature effect is made through reduction of the excitation voltage. With a relatively low-excitation voltage provided to the strain gage bridge, it was determined experimentally that the low-temperature calibration will plateau out below -100°F, and this has been found to be convenient for conducting most cryogenic tests.

The clip gage outputs are autographically plotted on an *x-y* recorder at $\times 100$ (V1) and $\times 200$ (V2), an example of which is shown in Fig. 12. The

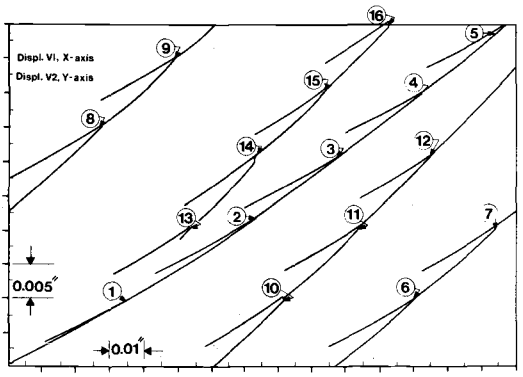

FIG. 12—*Test record for line pipe steel, 7C specimen.*

plotter has pen position reset capability which is used to accommodate the rather large total displacements usually encountered in testing high-toughness materials. The record shows four reset events to selected locations. There are 16 locations along the record where the wedging was stopped and the specimen was partially unloaded. The purpose for this will be covered in a later section.

Test Procedure

Elastic Small-Scale Plastic Determination Method

In the initial stages of tests on specimens of low-strength, high-toughness materials, the effective stress field will be dominantly elastic (depending upon specimen size and yield strength), and the conventional computational procedures that have been applied to ultrahigh-strength materials can be used. For any selected point along the V1-V2 test record, the ratio between the two displacements can be used to determine crack length. The double compliance calibration curve used to make this determination is given in Fig. 13. This calibration is good over all specimen sizes and materials so long as the planar proportionality of the specimens and clip

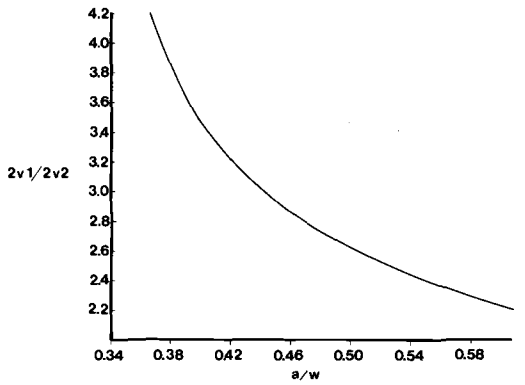

FIG. 13—*Double compliance calibration curve for compact specimen.*

gage locations are maintained. The crack length, a, determined by compliance contains a component which models the relaxation effect of the plastic zone. This plastic zone adjusted crack is referred to as effective crack length, a_{eff}. In order to determine the applied load, P, from the wedge, the calibration curve of Fig. 14 is used. Here, the abscissa is entered using the effective crack length obtained from double compliance. Given the corresponding compliance, the applied load can be determined using the V1 gage displacement. Crack driving force, K, which is equal to the crack-growth resistance is then calculated [*2*] from

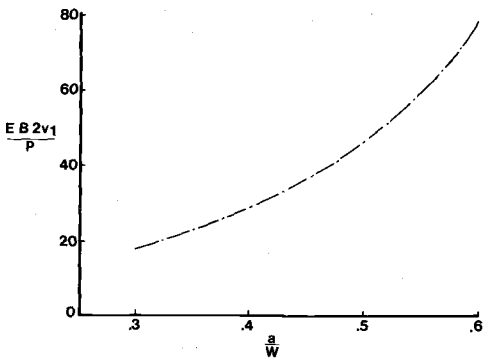

FIG. 14—*Compliance calibration for compact CLWL specimen.*

$$K = P/BW^{3/2}[f(a/w)]$$

where

$$f(a/w) = 29.6(a/w)^{1/2} - 185.5(a/w)^{3/2} + 655.7(a/w)^{5/2} - 1017(a/w)^{7/2} + 638.9(a/w)^{9/2} \quad (1)$$

Note—Factor a is set equal to a_{eff}. The R-curve of K_R versus crack growth ($a_{eff} - a_o$) can then be plotted up to the point where the specimen transcends into dominant plastic flow. A strain gage bonded to the back edge of the specimen is used to indicate incipient large-scale plastic flow. Experience in testing a wide range of materials indicates that when the measured compressive strain equals $\sigma_{ys}/E + 2000$ μ-in., nonlinear mechanics procedures can be introduced.

Plastic Analysis

The study of the mechanics of yielding in notched specimens has been developed beginning with the early work in slip-line analysis of Green and Hundy [*3*]. Through efforts which have been concentrated mainly in the United Kingdom, a fracture technology based on CTOD measurements has been developed into a working practice, which is modified here to apply to R-curve generation. Generally, it has been recognized that specimens of the three-point bend or compact type will displace by a plastic hinging mechanism when loaded beyond net section yield. For ordinary structural materials, the hinging is reported to take place about a mythical point located very close to the midpoint of the uncracked ligament. This rotation point location is frequently identified in terms of a rotation constant, n, expressed as the fraction of the distance from the crack tip to

the hinge point divided by the remaining uncracked ligament. In physical terms, hinging means that displacements measured along the crack line tend to be a linear function of the distance from the hinge point. This is demonstrated by Fig. 15*a*, from the work of Harrison on three-point-bend specimens [*4*]. The linearity also was supported later in finite-element calculations made by Turner and Hayes [*5*]. To demonstrate the hinging action in compact specimens, Fig. 15*b* gives an example for the CLWL specimen of this work. In Fig. 15*a*, plastic hinging begins at displacement level *C*, and the rotation constant, *n*, is about 0.33. As the test proceeds, the rotation constant increases, finally converging at about 0.45 which is the value suggested in slip-line work. In preliminary studies for the present method development, rotation constants were determined for several materials of widely varying strength levels (Fig. 16). The results indicate that the rotation constant tends to be material dependent and that the converging model of 0.45 (*W-a*) for the hinge point applies only to certain grades of steels.

In order to determine crack opening stretch (COS) which is defined here as CTOD at the physical crack tip, it was necessary to develop a suitable means of following slow-stable crack growth. The double compliance procedure as outlined earlier is intended for use under dominant elastic conditions, and errors in effective crack length prediction can be expected under dominant plastic conditions. However, use can be made of a working hypothesis that plastically deformed bodies unload with an apparently restored fully elastic behavior. Hence, if the CLWL specimens are partially unloaded at selected points during the test, the return slopes,

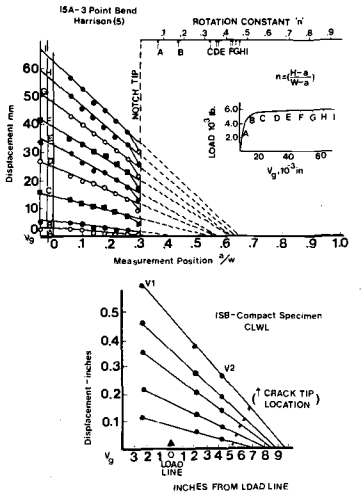

FIG. 15—*Displacement versus measurement position for loading increments; 15A—3 point bend, and 15B—compact specimen.*

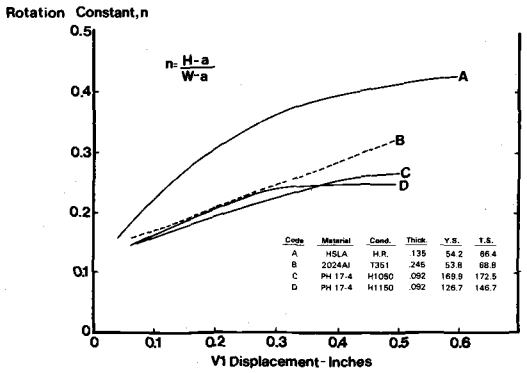

FIG. 16—*Variation in rotational factor,* A, *with front displacement V1.*

Δ2V1/Δ2V2, will correspond to the existing physical crack lengths. A typical V1-V2 displacement test record showing this periodic partial unloading was given earlier in Fig. 12. The physical crack lengths are determined using the elastic double compliance curve of Fig. 13. COS is then determined, as is outlined in Fig. 17, by locating the hinge point using V1

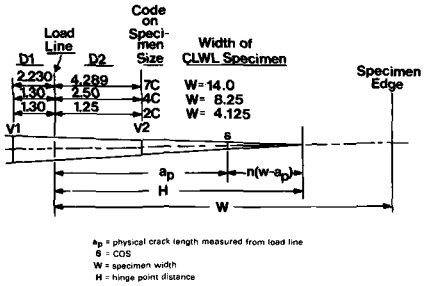

FIG. 17—*Plastic hinge point model for CLWL specimens.*

and V2 displacements and then calculating the COS from linear interpolation to the physical crack tip

$$\text{COS} = \text{V2}\left(\frac{H - a_p}{H - \text{D2}}\right) \tag{2}$$

COS is then converted into stress-intensity factor using the expression [6]

$$K_R = \sqrt{E \times \text{COS} \times \sigma_{ys}} \tag{3}$$

H = hinge point distance from the load line = $a_p + n\,(W - a_p)$,
a_p = physical crack length,

W = specimen width,
n = rotational constant, and
V2 = V2 clip gage displacement.

Plastic Analysis—J-Integral

An alternate approach of recent interest for handling large-scale yielding is the J-integral method. As with the CTOD approach, a problem develops in the handling of slow-stable crack growth, but, in this case, the appropriateness of the determination is in question as well. J-integral analysis is limited normally to determinations at incipient crack growth because error is introduced when the specimen unloads at the crack tip due to the crack-extension process. The analysis is presently limited to similarly loaded bodies with neighboring crack lengths, and a single calibration curve expressing J as a function of load-line displacement, δ_l, will suffice.

An alternate method suggested here is to accommodate slow-stable crack growth by using a family of calibration curves (J versus δ_l) covering the range of expected crack growth. J could then be determined from a calibration curve corresponding to an instantaneously existing crack length and displacement in the R-curve specimen. The calibration curves are developed through the use of the following operational definition of J-integral

$$J = -\frac{1}{B}\frac{\partial U}{\partial a} \tag{4}$$

where

U = potential energy,
a = crack length, and
B = material thickness.

The experimental procedure is to prepare several calibration specimens with blunted crack tips so as to prevent crack extension up to maximum or limit load and having varied crack lengths covering the crack-growth range expected in R-curve development. The family of J versus δ calibration curves is then generated after the procedure outlined by Begley and Landes [*7,8*] (Fig. 18). The basis of the adaptation is that specimens which have undergone crack growth in an R-curve test will have nearly the same J value as specimens loaded to the same displacement with the same fixed crack length.

Example Results

The raw data extracted from Fig. 12 are listed in Table 1 for the purpose of demonstrating the typical K_R curve data development. The first five

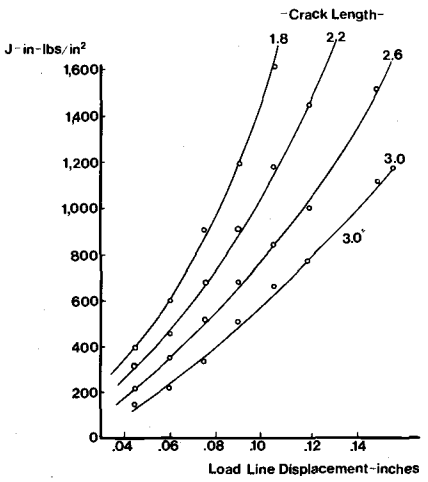

FIG. 18—*J-integral calibration curve, 2024AL ¼ in. thick, 2C specimens.*

data sets represent K_R determined by conventional elastic analysis. Beyond general yield, the physical crack length, as determined by return slope compliance and overall V1 and V2 displacements, are used to determine K_R in terms of COS. The resulting R-curve is given in Fig. 19. Smoothly rising R-curves of this type are common to structural grades of thin plate when tested in the upper shelf transition-temperature range. Slow-stable crack growth usually starts at K_R levels well below the maximum toughness capability of the material. The actual size of the elastic-plastic border as determined by surface strain measurements is of the order of 4 to 5 in. in diameter at the upper shelf on the K_R curve. Effective plastic zones obtained by subtracting physical crack length from effective crack determined by compliance, range from about 1 to 2 in. Although the effect of specimen size on the R-curve has not been systematically studied at this time, the presence of these large plastic zones suggest that the smaller fracture-toughness specimens used in other methods may not be suitable for complete and accurate R-curve development.

Structural materials traditionally have been evaluated in terms of transition-temperature curves using impact tests. It, therefore, was considered of interest to view the transition-temperature effect in terms of R-curves. The results of an experiment on a quenched and tempered carbon-manganese steel is given in Fig. 20. The R-curve appears to be insensitive to temperature down to −150°F, representative of the upper shelf for this material. The loss in toughness was found to occur within a very narrow temperature range and is manifested through sudden crack instability and departures from the fully ductile R-curve. The Charpy transition curve inserted in the figure confirms the existence of the sharp transition range.

TABLE 1—*Data and calculations for a typical CLWL test line pipe steel, 74.7 ksi yield strength.*

$$K_R = (P/BW^{1/2})f(a/w)$$

$$K_R = (E\sigma_y \text{ COS})^{1/2}$$

	V1	V2	V1/V2	$\Delta V1/\Delta V2^a$	a_e/w^b	a_p/w^b	P^c	Δa_e	Δa_p	K_R	COS
1	0.0364	0.0100	3.64	3.80	0.394	0.385	20.2	0.131	0	71.2	
2	0.0673	0.0200	3.65	3.70	0.413	0.390	34.5	0.398	0.080	127.8	
3	0.0953	0.0300	3.18	3.68	0.429	0.391	45.7	0.626	0.096	176.4	
4	0.1218	0.0400	3.04	3.60	0.443	0.396	55.1	0.816	0.165	220.6	
5	0.1455	0.0495	2.94	3.55	0.455	0.400	62.5	0.990	0.210	258.4	
					Start of Plastic Hinge						
6	0.1705	0.0598		3.52		0.402			0.239	288.1	0.037
7	0.1934	0.0696		3.45		0.406			0.307	309.8	0.0428
8	0.2273	0.0846		3.39		0.411			0.370	342.6	0.0523
9	0.2496	0.0948		3.33		0.416			0.437	361.3	0.0582
10	0.2809	0.1094		3.25		0.423			0.532	385.8	0.0664
11	0.3020	0.1196		3.20		0.427			0.595	402.0	0.0721
12	0.3229	0.1298		3.10		0.437			0.733	411.2	0.0754
13	0.3533	0.1450		3.09		0.438			0.748	438.7	0.0859
14	0.3729	0.1547		3.02		0.446			0.855	447.1	0.0892
15	0.3925	0.1650		2.97		0.451			0.937	458.6	0.0938
16	0.4119	0.1745		2.92		0.458			1.024	466.4	0.0970
17	0.4313	0.1847		2.90		0.460			1.060	480.4	0.1029

NOTE—a_e = effective crack length.
a_p = physical crack length.
W = specimen width.

[a] Unloading slope.
[b] From Fig. 14.
[c] From Fig. 15 using a_e/w.

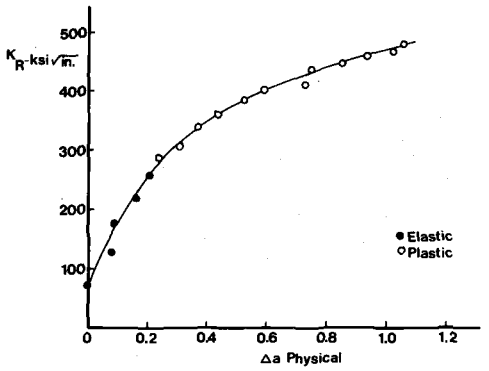

FIG. 19—*R-curve for gas transmission line pipe steel; data from Table 1.*

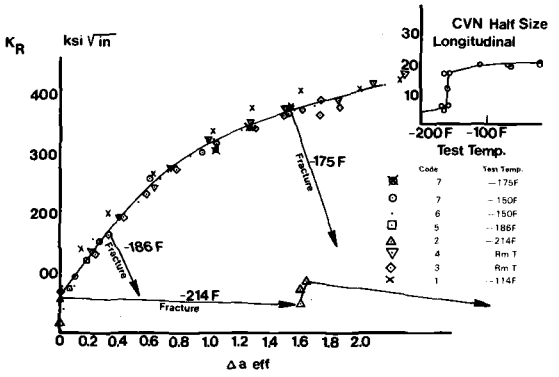

FIG. 20—*R-curve determined over a temperature range for a quenched and tempered steel plate.*

An R-curve which typifies the behavior of a cryogenic grade nickel steel is shown in Fig. 21. The test was conducted in the transition-temperature range where instead of the rapid toughness degradation, seen with carbon-manganese grades, we note the development of a crack pop-in characterization. This behavior is believed to be a characteristic of nickel steels which have long, shallow transition temperatures as indicated by the inserted Charpy transition curve. Crack-growth resistance development is accompanied by sudden bursts of crack extension, the severity of which depends upon the location within the transition range. At temperatures within the lower plataeu range, the first pop-in results in unarrested crack growth. With increased temperature through the transition range, the pop-in severity diminishes, and, at upper shelf, the R-curve is smooth—similar to that for the low-alloy steel of Fig. 19.

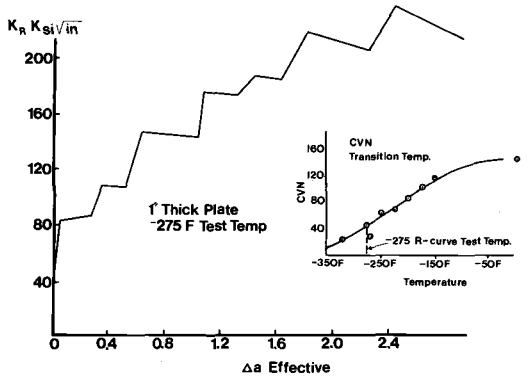

FIG. 21—*R-curve for an experimental nickel alloy steel tested in the transition temperature region.*

Utilization of R-Curves

R-curves made on structural materials can be utilized to make instability condition predictions by applying the failure prediction principles demonstrated for ultrahigh-strength materials [*9*]. The usual practice is to match crack driving force curves of the cracked configuration to R-curves plotted in terms of Δa effective. In the case of tough materials, it is particularly important to consider plastic-zone contribution to Δa, since the shape of the R-curve is affected strongly and, hence, has a marked influence on the indicated point of tangency between crack-growth resistance and crack driving force curve. Figure 22 shows an R-curve for an X-60 grade of line pipe steel that was fit to crack driving force for a 48-in. diameter pipe pressurized to 1240 psi (50 ksi hoop stress). Here, crack drive is dependent upon pipe curvature and the Folias correction was applied [*10*]. The model predicts that an initial physical crack half length of 2.05-in. will propagate to 2.5 in. and become unstable at a pressurization of 50 ksi hoop stress. Although confirming tests were not available in this study, results available in the literature from full-scale pipe tests confirm the reasonableness of the prediction [*11*].

A second example is provided by a wide plate test made on the quenched and tempered grade of carbon-manganese steel tested by CLWL and reported in Fig. 20. The material is a 1/4-in.-thick plate, heat treated to 110 ksi yield strength. The test was made at room temperature on a 48-in.-wide plate containing a 29-in. central crack. Matching crack driving force curves to the room temperature R-curve predicted a failure load of 462 kips. In test, the panel failed at 459 kips. The crack-growth resistance curve obtained from the panel is compared to the CLWL R-curve in Fig. 23. Unfortunately, the wide panel test had been interrupted due to a panel buckling problem which developed after about 0.5 in. of effective crack

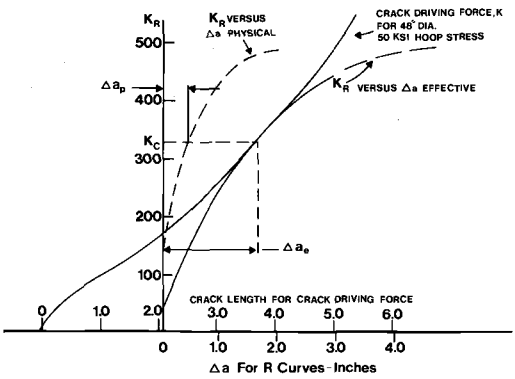

FIG. 22—*R-curve and crack driving force curve matchup for instability prediction.*

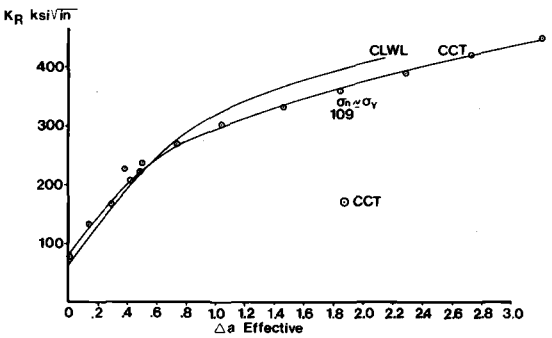

FIG. 23—*Comparison of R-curves obtained by CLWL and by center cracked panel test.*

propagation. Additional reinforcements were added, and the test was resumed to failure. Despite this problem, and the fact that the panel ultimately failed in net section yield, R-curves derived by both methods were reasonably comparable.

Summary and Discussion

The purpose of this work has been to describe a test method which was used to develop R-curves for low-strength and high-toughness materials. Since the specimens generally develop full plastic flow at some stage in the test, a CTOD technique was introduced to extend the determinations into the domain of general yield mechanics. The relationship between COS and K_R as given by Eq 3 has been simplified here by assuming plane-stress conditions throughout. A more general form would be to use $K_R^2 = n \times \sigma_y \times \text{COS} \times E$, where n is a plastic stress-intensification factor vary-

ing between 1 for plane stress and 2.1 for plane-strain conditions [*12*]. One could expect to find certain cases where intermediate values of n would apply, but, so far, the pure plane-stress assumption has provided a continuous transition between elastic and plastic K_R determinations.

Comparisons of K_R values determined by COS and plastic hinging with J-integral values determined according to the procedure outlined earlier are given in Figs. 24 and 25 for a 2024 aluminum alloy and a high-strength, low-alloy steel.

In Fig. 24, the 2C and 7C size specimens (see Fig. 2) were used to study specimen size effects on the 1/4-in.-thick aluminum plate. The large specimens provided a nearly complete R-curve for the material using the conventional elastic small-scale plastic techniques. Data points shown are from the small specimen which displaced in dominant plastic flow for about half of the slow-stable crack propagation life. Both the COS and J-integral computational procedures gave K_R determination in good agreement with the R-curve determined by the elastic small-scale plastic method described in the ASTM Tentative Recommended Practice for R-Curve Determination (E 561-76T). In Fig. 25, tests on a low-alloy steel of 50 ksi

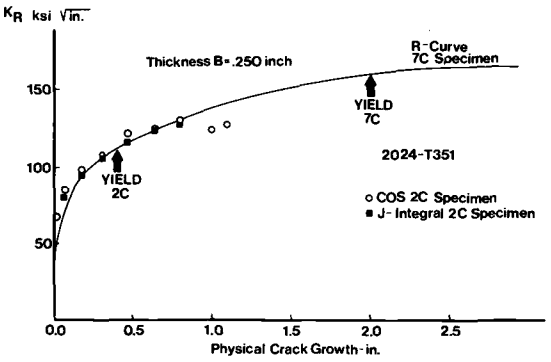

FIG. 24—*R-curve for 2024-T531 aluminum from 7C and 2C size CLWL specimens; comparison of elastic, COS, and J-integral analysis.*

yield strength displaced almost entirely under dominant plastic flow even with the larger 7C size specimen. The comparison shown, therefore, is essentially between two plastic analysis procedures. Here the solid lines represent R-curves developed by COS analysis, and a minor specimen size effect is indicated. J-integral values converted to K_R are represented by the data points shown. Although there is some data scatter, the comparison between the two methods is most encouraging.

A note of caution to be entered at this point, however, is that the method of J determination used here has not been justified from an energy distribution standpoint, and the values reported should for the present be

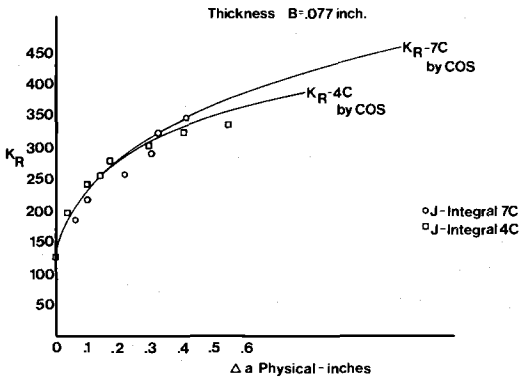

FIG. 25—*R-curve for 50 ksi yield strength steel; comparison of specimen size effect and analysis method.*

regarded only as reasonable approximations to values obtained by more rigorous methods.

A point to be made about R-curve technology that is demonstrated by the foregoing is that R-curve is a method of analysis which is not considered to be competitive with certain accepted computational procedures. The R-curve can be regarded as a representation of the slow-stable crack extension history of a material which is commonly seen in laboratory tests and in service. The properties that are considered to be basic to R-curves, such as independence of the specimen type, size, and starting crack length, have been disputed, and this will probably continue to be the case until optimum experimental practices are established and boarder experience is obtained. Aside from these considerations, the R-curve can be used to demonstrate the reason for certain observed specimen dimensional effects on instability or as a ranking procedure to evaluate material toughness critically. The implication from R-curve technology is clear, however, that instability values of stress-intensity factor K, Griffith G, J-integral, or COS—under conditions other than plane strain—are not singular material-toughness values, but they depend to a significant degree upon the crack driving force associated with the structure. This has been demonstrated in the past on high-strength sheet materials, and the present need is for demonstration of this principle in applications involving structural grades of materials.

Acknowledgments

The author gratefully acknowledges the helpful discussions with P. O. Metz, D. A. Sarno, D. M. Bench, R. J. Glodowski, and C. F. Berold and for the use of the wide plate test results conducted under the direction of P. O. Metz.

References

[1] Fearnehough, G. D., Lees, G. M., Lowes, J. M., and Weiner, R. T., "The Role of Stable Ductile Crack Growth in Failure of Structures," Applied Mechanics Group Conference, Dec. 1970.

[2] McCabe, D. W. and Heyer, R. H. in *Fracture Toughness Evaluation by R-Curve Methods, ASTM STP 527,* American Society for Testing and Materials, 1973, pp. 17–35.

[3] Green, A. P. and Hundy, B. B., *Journal of Mechanics and Physics of Solids,* Vol. 4, 1956, p. 128.

[4] Harrison, T. C., "Gas Council Engineering Report," Station Report T311, United Kingdom Council Engineering Research, June 1970.

[5] Hayes, D. J. and Turner, C. E., *An Application of Finite Element Techniques to Post-Yield Analysis of a Practical Fracture Test Specimen,* Imperial College of Science and Technology, London, England.

[6] Tetelman, A. S., "The Critical Crack Tip Opening Displacement and Microfracture and Macrofracture Criteria for Metals," Technical Report Eng 7360, University of California at Los Angeles, Aug. 1973.

[7] Begley, J. A. and Landes, J. D. in *Fracture Toughness, ASTM STP 514,* American Society for Testing and Materials, 1972, pp. 1–20.

[8] Landes, J. D. and Begley, J. A. in *Fracture Toughness, ASTM STP 514,* American Society for Testing and Materials, 1972, pp. 24–39.

[9] Heyer, R. H. and McCabe, D. E., *English Fracture Mechanics,* Vol. 4, 1972, pp. 393–412.

[10] Folias, E. S., *International Journal of Fracture Mechanics,* Vol. 1, 1965, p. 104.

[11] Dolan, T. J., "Fracture from Large Flaws in Pipeline Steels," Report to American Iron and Steel Institute Subcommittee on Line Pipe Research, University of Illinois, Nov. 1973.

[12] Wells, A. A., "The Status of COD in Fracture Mechanics," Proceedings of the Canadian National Congress on Applied Mechanics, Calgary, Alberta, Canada, May, 1971.

R. Roberts,[1] *G. V. Krishna,*[2] *and G. R. Irwin*[3]

Fracture Behavior of Bridge Steels

REFERENCE: Roberts, R., Krishna, G. V., and Irwin, G. R., "**Fracture Behavior of Bridge Steels,**" *Flaw Growth and Fracture, ASTM STP 631,* American Society for Testing and Materials, 1977, pp. 267-284.

ABSTRACT: The results of a recent study of the dynamic and static fracture toughness behavior, over a wide-temperature range, of eight different bridge steels are presented. These results are discussed in connection with current toughness requirements for bridge steels. Strain rate and temperature effects on fracture toughness are examined.

KEY WORDS: crack propagation, steels, impact tests, bridge design, toughness

It has been assumed by the general public and many segments of the engineering community that large civil engineering structures such as bridges are designed and fabricated in the United States so that they are safe from sudden failures. The fundamental truth of this belief is, to a great extent, demonstrated by past satisfactory operating experience. However, the 1967 failure of the Point Pleasant Bridge [*1*][4] raised serious questions as to the safety of existing steel bridges. In response to these questions and concerns, as related to bridge safety, the Federal Highway Administration of the U.S. Department of Transportation sponsored a series of studies on the fracture, fatigue-crack propagation, and stress-corrosion response of bridge steels. The program, designed to evaluate the fracture resistance of steels typical of those used in older bridge structures and in current designs, was carried out at Lehigh University. The results of this study are reported here.

The particular steels reported on in this paper are ASTM steels A7, A36, A242, A440, A441, A588, A514, and SAE grade 1035. These steels represent a yield strength range of 250 to 830 MPa (36 to 110 ksi). For

[1]Professor of Mechanical Engineering and Mechanics, Lehigh University, Materials Research Center, Bethlehem, Pa. 18015.

[2]Senior engineer, Cryogenic Systems Division, Air Products and Chemicals, Inc., Allentown, Pa. 18105.

[3]Visiting professor, Mechanical Engineering Department, University of Maryland, College Park, Md. 20742.

[4]The italic numbers in brackets refer to the list of references appended to this paper.

each steel, except A7, the fracture resistance of three thicknesses of plate 12.7 mm, 25.4 mm, and 50.8 mm was studied over a wide range of temperatures and loading rates. The temperatures ranged from approximately −150 to 20°C. The loading rates were varied between impact and approximately static loading. This corresponded to a time to failure of 0.001 and 1.0 s, respectively. The fracture response of each plate was characterized primarily by its Charpy V-notch (CVN) performance, its 1 s fracture toughness, as measured by K_{Ic}, and its dynamic fracture toughness as measured by K_{ID}. The 1 s loading tests correspond roughly to the maximum loading rates encountered in bridges. Along with the CVN and K testing, a series of resistance or R-curve determinations were undertaken for each steel type and thickness.

General Fracture Behavior of Structural Steels

Structural grade steels had not been the subject of extensive fracture-mechanics type studies prior to the period of 1967 to 1970. The work of Shoemaker and Rolfe [*2*], Barsom and Rolfe [*3,4*] at U.S. Steel, and the work of Madison [*5*] at Lehigh University were the primary sources of information relative to the fracture performance of structural grade steels. At the time the work plan was developed for the fracture results described in this paper, it was known that the fracture behavior of structural grade or bridge steel was affected by plate thickness, temperature, and loading rate [*4,5*]. These influences are represented schematically in Fig. 1. There, it is seen—using a critical stress-intensity level, K_c, to measure fracture toughness—that as temperature increases toughness increases. Also, as loading speed increases, toughness decreases at a fixed temperature. In this paper, the symbol K_c is used to indicate a critical stress-intensity level which does not necessarily meet ASTM requirements. The basic effect of thickness, aside from plane-strain, plane-stress effects on toughness, is that, for specimens of equal size taken from different thicknesses of plate from the same heat of steel, the toughness of the plates generally decreases with increasing thickness.

The dynamic and static K_c curves shown in Fig. 1 are separated generally along the temperature axis by a fixed temperature differential which is dependent on yield strength [*4*]. The static curve corresponds to loading times of the order of 60 s. Barsom [*6*] currently expresses this as

$$T_s = 215 - 1.5\sigma_y \tag{1}$$

where

T_s = temperature shift °F, and
σ_y = yield strength.

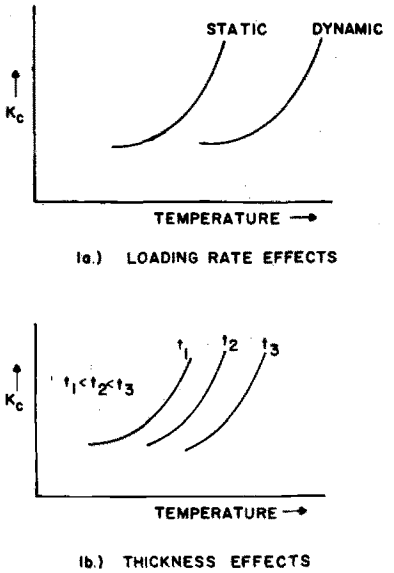

FIG. 1—*Effects of temperature, loading rate, and thickness on* K_c.

Furthermore the plateau or lower shelf of the K_c curves are the same for both the static and dynamic loading rates. Thus, if one of the K curves is known, the other curve can be constructed by shifting the known curve by the temperature differential indicated by Eq 1.

It had also been pointed up by Barsom and Rolfe [*4*] that the potential for correlating the fracture behavior of structural steels as measured by fracture-mechanics type specimens with CVN test results was quite good. They observed that the temperature-transition regions of the dynamic K_c and standard dynamic CVN curves corresponded. This correspondence of temperature-transition regions also was observed for static K_c and very slowly loaded CVN specimens. This is shown schematically in Fig. 2. It was this type of observation which gave courage to Barsom and Rolfe to attempt correlations of K_c and CVN results aside from the obvious economics and practical implications of being able to use a simple CVN test in place of complex K_c tests. Their efforts [*4*] led to a correlation in the temperature-transition region of the form

$$K_{Ic} = \sqrt{AE(\text{CVN})} \tag{2}$$

where

A = a constant,
E = Young's modulus in psi,

CVN = Charpy energy in foot-pound, and
K_{Ic} = plane-strain fracture toughness in psi $\sqrt{\text{in.}}$.

To estimate a dynamic K_{Ic} value from Eq 2 at a specific temperature in the temperature-transition region, one uses the dynamic CVN value at that temperature. Similarly, to estimate a static K_{Ic} level, one would use a CVN energy value obtained from slow-loading tests of CVN specimens. Barsom [*6*] currently proposes a value of 5 for A in Eq 2. Barsom and Rolfe [*4*] also developed a correlation between the room-temperature K_{Ic} response of structural steels and the upper shelf CVN energies of the steels. This will not be discussed here.

Coupled with the foregoing general understanding of structural steel, fracture performance was a real concern that plane-strain fracture mechanics, as embodied in K_{Ic} testing, would not be applicable to real structural steel applications. Most envisioned problem areas were in thicknesses of plate and temperature regions where plane-stress behavior would be expected. To examine some of the implications of this, pilot studies of specialized K_c (plane stress) measurement techniques as well as R-curve determination were carried out in the program described here.

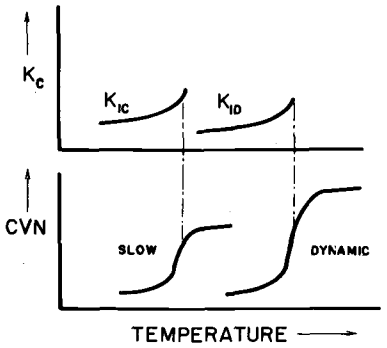

FIG. 2—*Schematic representation of correspondence of temperature transition regions of* K *and CVN curves.*

Experimental Details

Material Properties

Three thicknesses of plate, 12.7, 25.4, and 50.8 mm, were tested for the A36, A242, A440, A441, A588, A514, and SAE1035 steels. A single thickness, 12.7 mm, was tested for the A7 steel. The chemical composition, yield strength, ultimate strength, and percent elongation were de-

termined for each piece of plate tested. These results are reported in Tables 1 and 2.

CVN Tests

Standard CVN specimens were prepared from the quarter thickness point of each plate studied. These were tested over an approximate temperature range of −150 to +20°C in accordance with ASTM Recommended Practice for Notched Bar Impact Testing of Metallic Materials (E 23-72). All specimens were of the L-T orientation (ASTM Test for Plane-Strain Fracture Toughness of Metallic Materials (E 399-74)) where the notch is perpendicular to the rolling direction. Specific CVN results are presented and discussed in the next section on Experimental Results.

K *Testing*

The initial phase of the research project reported herein was concerned primarily with the dynamic fracture behavior of the A36, A441, and A514 steels. However, both the 1 s and dynamic K response was determined for the A441 material. A number of nonstandard methods for measuring K were attempted for these three steels. The details of these tests are given in Refs *7* and *8*. The remaining steels—A7, A242, A440, A588, and SAE1035—were evaluated for both their 1 s and dynamic K response with primary emphasis placed on dynamic loading. As with the CVN testing, the K tests covered a temperature range of about −150 to +20°C. All K tests discussed in this paper were made with the crack perpendicular to the rolling direction, the L-T orientation.

All K tests were conducted with a three-point-bend specimen approximately 300 mm long by 76.2 mm high by the plate thickness. The initial cracks were about 25.4 mm long with the tips sharpened by low-amplitude fatigue loading. Reference *7* gives a detailed discussion of specimen preparation and testing. All K values reported in the remaining sections of this paper have been corrected for plastic-zone size, r_y, as described in Ref *7*.

R-Curve Tests

In a series of recent papers, Heyer and McCabe [*9,10*] have described a procedure for obtaining R-curves from crack-line loaded compact tension specimens. Their test consisted of wedge loading a compact tension specimen while monitoring the crack-surface displacements at two definite positions relative to the load line. In this study, a test apparatus similar to the one employed by Heyer and McCabe was used. A crack-line loaded compact tension specimen was employed for the determination of R-curves.

TABLE 1—*Chemistry summary of plates tested.*

Plate Grade	Plate Thickness, in.	C	Mn	P	S	Si	Cu	V	Ni	Cr	Mo	B	Heat No.
A7	½	0.22	0.44	0.014	0.038	0.02	0.01	< 0.002	0.045	0.01	< 0.02	< 0.001	...
A36	½	0.21	0.54	0.008	0.021	0.05	...	...	...	...	...	...	490B5631
	1	0.18	0.95	0.009	0.015	0.05	...	...	...	...	...	...	490C0461
	2	0.20	1.00	0.011	0.018	0.24	...	...	...	...	...	...	422B3861
A242	½	0.10	0.75	0.07	0.023	0.30	0.29	...	0.33	0.58	...	...	401C6101
	1	0.10	0.73	0.08	0.030	0.31	0.27	...	0.37	0.53	...	...	481B1981
	2	0.10	0.85	0.056	0.024	0.28	0.28	...	0.34	0.53	...	...	481C0061
A440	½	0.18	1.14	0.009	0.025	0.15	0.26	...	...	...	...	...	487C0381
	1	0.18	1.14	0.009	0.025	0.15	0.26	...	...	...	...	...	487C0381
	2	0.16	1.13	0.012	0.021	0.23	0.23	...	...	...	...	...	412C5233
A441	½	0.20	1.08	0.017	0.025	0.21	0.23	0.051	0.02	0.03	0.002	...	482T0241
	1	0.20	1.08	0.017	0.025	0.21	0.23	0.051	0.02	0.03	0.002	...	482T0241
	2	0.20	1.08	0.017	0.025	0.21	0.23	0.051	0.02	0.03	0.002	...	482T0241
A514M	½	0.19	0.65	0.008	0.026	0.27	...	...	1.38	...	0.59	0.002	533Z0023
A514P	1	0.10	0.58	0.009	0.023	0.30	...	...	1.40	0.91	0.56	0.005	521X0027
A514M	2	0.18	0.65	0.010	0.032	0.27	...	...	1.39	...	0.59	0.005	532Z0265
A558B	½	0.15	1.15	0.014	0.026	0.23	0.30	0.027	0.30	0.56	...	...	432B2371
	1	0.13	1.05	0.013	0.030	0.26	0.31	0.029	0.31	0.52	...	...	401C2251
	2	0.15	1.15	0.014	0.026	0.23	0.30	0.027	0.30	0.56	...	...	432B2371
SAE 1035	½	0.38	0.61	0.008	0.021	0.17	...	...	...	...	...	...	422B5674
	1	0.38	0.61	0.008	0.021	0.17	...	...	...	...	...	...	422B5674
	2	0.38	0.74	0.016	0.019	0.21	...	...	...	...	...	...	402C2991

TABLE 2—*Data summary.*

Material	Thickness, in.	T_{15}, °F	$_{15}\Delta T_{SH}$, °F	T_s, °F	$0.75T_s$, °F	$0.75T^*_s$, °F	A	σ_y, ksi	σ_u, ksi	Elongation, %
A7	½	100	~ 75	162	122	...	35	35.5	63.0	27.5
A36	½	50	~ 75	158	119	...	8	37.5	62.0	30.0
A36	1	60	~ 75	152	114	...	8	42.5	65.0	31.0
A36	2	60	~ 75	148	111	...	8	45.0	76.0	...
SAE 1035	½	70	~ 75	147	111	75	9	45.3	80.7	23.0
SAE 1035	1	55	~ 75	155	116	75	9	39.7	76.2	25.0
SAE 1035	2	50	> 100	148	111	...	9	44.3	89.7	...
A242	½	− 65	~ 75	134	101	100	5	53.9	73.5	26.0
A242	1	25	~ 75	138	104	50	5	50.9	74.8	23.0
A242	2	35	> 100	148	111	...	5	45.0	72.0	...
A440	½	− 25	~ 75	121	91	100	20	62.6	83.2	23.0
A440	1	0	~ 75	137	103	100	7	51.8	78.8	28.0
A440	2	70	> 100	121	91	125	7	62.5	82.0	...
A441	½	− 15	~ 75	130	98	80	5	56.7	82.3	27.2
A441	1	− 10	> 100	130	98	100	5	55.9	87.0	...
A441	2	40	> 100	130	98	80	5	55.0	94.0	29.0
A588-B	½	− 10	~ 75	112	84	75	15	68.5	94.0	20.0
A588-B	1	− 75	> 100	111	83	75	5	69.1	80.5	20.0
A588-B	2	− 15	> 100	121	91	...	5	62.5	87.0	...
A514-M	½	−150	~ 75	24	18	...	...	127.0	131.5	...
A514-M	1	−100	> 100	52	39	...	...	108.0	121.8	...
A514-M	2	−125	~ 75	55	41	...	...	106.0	117.0	...

NOTE—T_{15} = Temperature corresponding to the 15 ft·lb energy level from a test of standard CVN specimens.
$_{15}\Delta T_{SH}$ = Difference in temperature going from the 15 ft·lb to the upper shelf energy level in a standard CVN test.
T_s = $(215 - 1.5\ \sigma_y)$ where σ_y is the room temperature yield strength.
$0.75T^*_s$ = Estimate of $0.75\ T_s$ from data where possible.
A = Estimate of best fit A value for Eq 2.
σ_y = Yield strength.
σ_u = Ultimate strength.

The specimen had an h/W ratio of 0.6. W was 486.8 mm and h was 292.1 mm. These proportions correspond to those recommended in ASTM Standard Method E 399-74. The specific details of the test apparatus testing procedure and data reduction can be found in Ref *7*. All tests were run at loading rates which produced failure times of about 30 to 60 s. Also, K data from the R-curve tests reported in the next section were based on r_y corrected crack lengths as was the case of the dynamic and static K_c data.

Experimental Results

Due to the extensive nature of the data presented in this paper, each grade of steel will not be discussed separately in this section. Only certain specifics will be presented. The implications and broad trends found in the data will be taken up in the next section on American Association of State Highway and Transportation Officials (AASHTO) Requirements and Fracture Safe Design.

Before proceeding to discuss the fracture performance of the steels tested, some general comments on the R-curve results are appropriate. It had been expected, due to the wedge loading system, that as the load was applied to the R-curve specimens, it would be possible to observe some region of slow-stable fracturing. This was expected to produce an R-curve similar to those reported by Heyer and McCabe [*9,10*]. However, this was not the case for the majority of the R-curve tests. Rather, the specimens failed very suddenly and produced only a single test point. Also, in most tests, the fracture occurred in such a manner that there was enough stored energy in the system at the point of fracture to produce very sudden crack extensions and crack velocities sufficient to cause crack branching. Due to this, the K levels measured are reported as just single data points on the 1 s K_c curve.

Along with the previous comments, it should be noted that the comparisons between dynamic K prediction, based on Eq 2, and actual measured K values are, in reality, a comparison of CVN data with K level, which range from valid K_{Ic} results to nonplane-strain K_c type behavior. Equation 2 has been proposed for only K_{Ic}-CVN correlations [*4*]. However, as will be seen, Eq 2 still gives reasonable results for K_c-CVN correlations.

Figures 3 through 12 present the results of the CVN and K tests for all steels tested except the A36, A441, and A514 materials. These data have been presented elsewhere [*11*]. Only trend lines are shown for the Charpy results. The temperatures corresponding to the 20 J (15 ft·lb) CVN levels denoted as T_{15} are tabulated in Table 2. Along with these values are the temperature differentials which occur going from the T_{15} level to the CVN upper shelf. This difference is labeled ${}_{15}\Delta T_{SH}$. These two specific properties

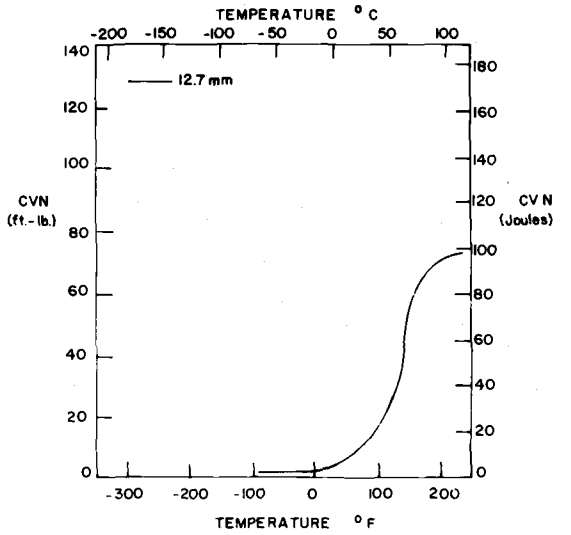

FIG. 3—*CVN results A7 steel.*

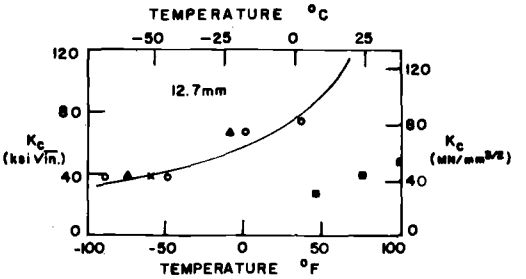

FIG. 4—K *data A7 steel—▲ =* R *values,* o = *dynamic* K *values,* • = *static* K *values, and* ■ = *estimate from Eq 2,* × *point of maximum valid* K.

of the CVN curves, T_{15} and ${}_{15}\Delta T_{SH}$, are important to the later discussion of the AASHTO CVN requirements. As can be seen in Table 2, the majority of the plates tested had a ${}_{15}\Delta T_{SH}$ of approximately 42°C while the remaining plates had a ${}_{15}\Delta T_{SH}$ greater than 55°C.

In general, the figures of K versus temperature show the actual data points as well as proposed trend lines. The terminology K_c has been applied to all K results, since for the most part the thickness of the specimens does not meet the requirements for valid plane-strain measurements (ASTM Method E 399-74).

Along with the K data shown in the figures, the results of the R-curve tests are shown where the scale of the figures allow this to be done. The individual R-curve data are tabulated in Table 3. Generally, the K levels,

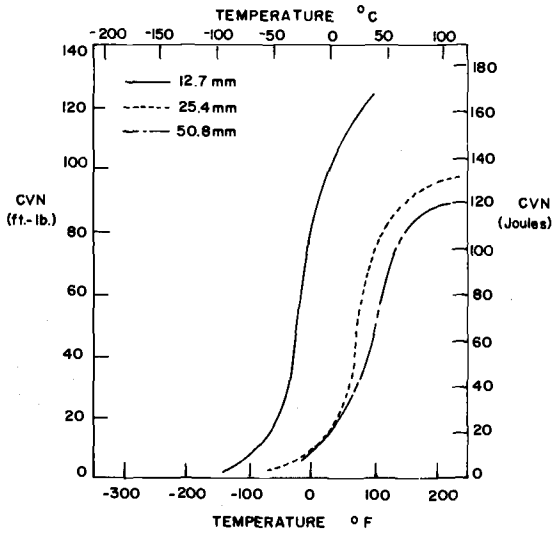

FIG. 5—*CVN results A242 steel.*

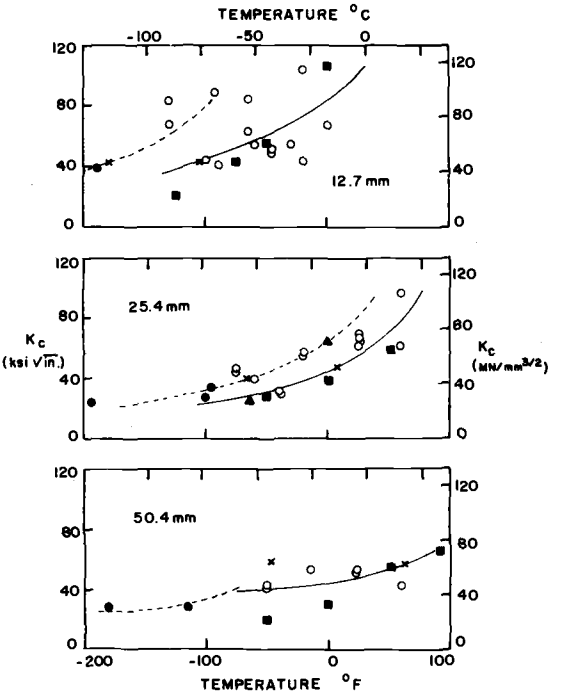

FIG. 6—K *data A242 steel*—▲ = R *values,* o = *dynamic* K *values,* • = *static* K *values, and* ■ = *estimate from Eq 2,* × *point of maximum valid* K.

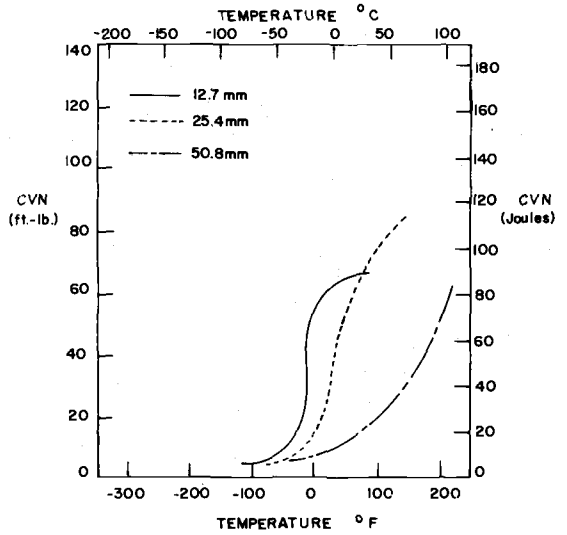

FIG. 7—*CVN results A440 steel.*

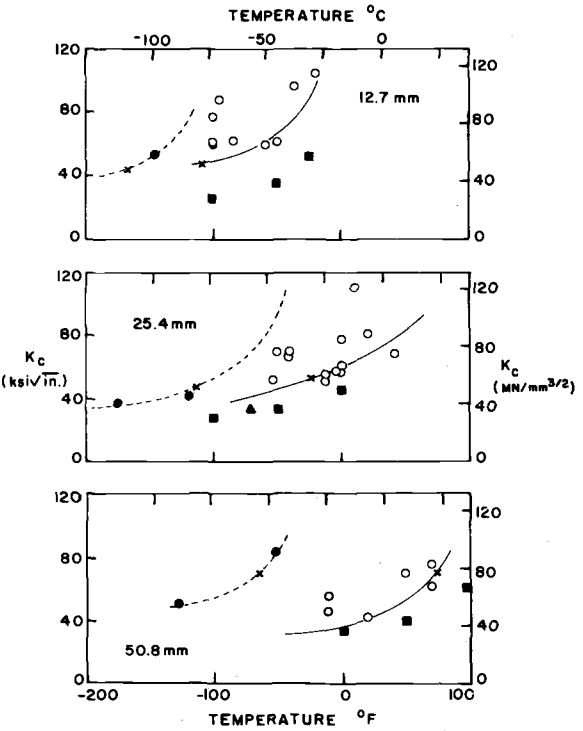

FIG. 8—K *data A440 steel—*Δ = R *values,* o = *dynamic* K *values,* • = *static* K *values, and* ■ = *estimate from Eq 2,* × *point of maximum valid* K.

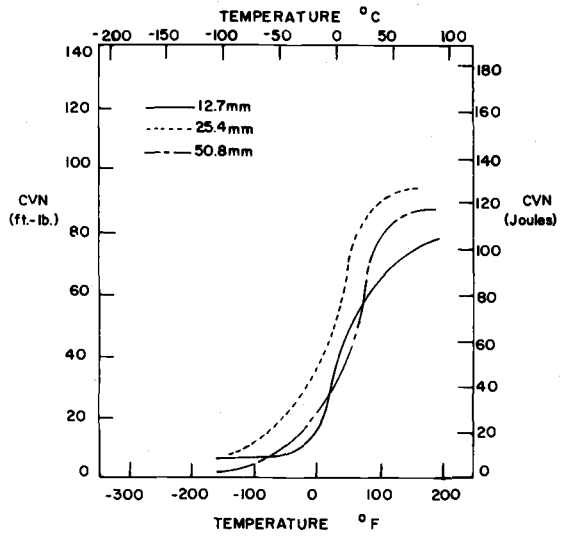

FIG. 9—*CVN results A588 steel.*

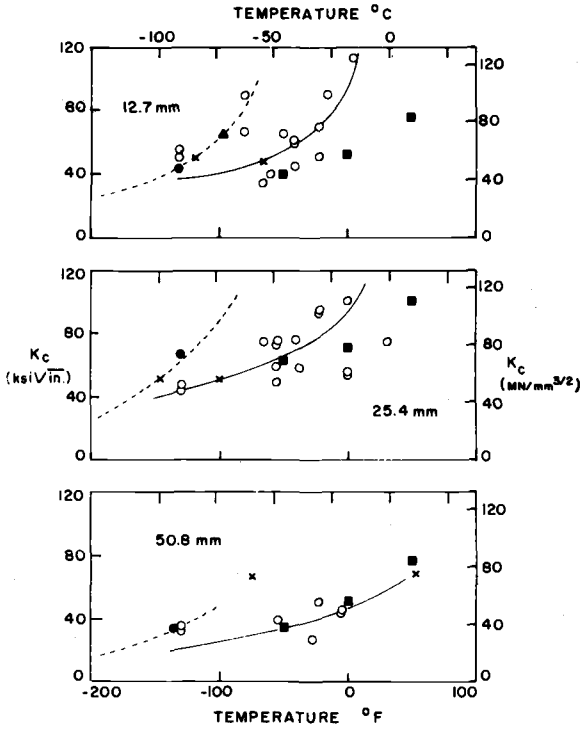

FIG. 10—K *data A588 steel—▲ = R values,* o = *dynamic* K *values,* • = *static* K *values, and* ■ = *estimate from Eq 2,* × *point of maximum valid* K.

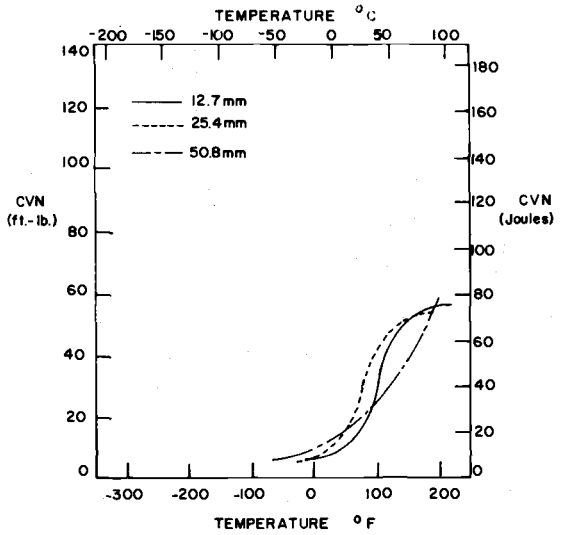

FIG. 11—*CVN results SAE1035 steel.*

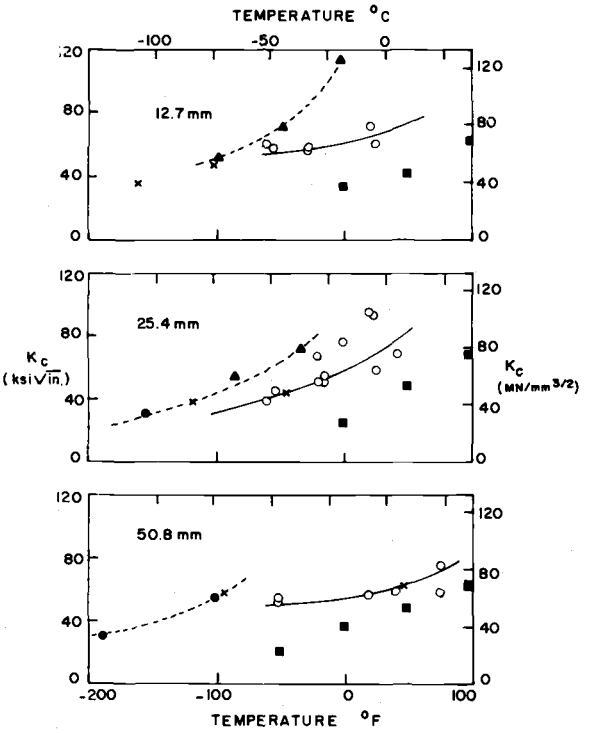

FIG. 12—K *data SAE1035 steel—▲ = R values, o = dynamic* K *values, • = static* K *values, and ■ = estimate from Eq 2, × point of maximum valid* K.

TABLE 3—R *results.*

Material	Thickness, in.	Test Temperature, °F	K_R, psi$\sqrt{\text{in.}}$
A7	½	− 75	30 700
A7	½	− 10	66 700
A36	1	− 44	169 900
A36	½	− 47	116 700
A36	½	− 100	46 400
SAE 1035	1	− 85	54 100
SAE 1035	1	− 32	71 400
SAE 1035	½	− 47	71 400
SAE 1035	½	− 3	114 000
SAE 1035	½	− 98	51 700
A242	1	0	62 100
A242	1	− 55	24 000
A242	½	− 50	224 900
A440	1	− 70	33 200
A440	1	− 48	154 600
A440	½	− 100	350 400
A441	½	− 50	169 400
A441	½	− 95	66 100
A588	½	− 95	63 800
A588	½	− 40	135 500
A588	½	− 10	347 100
A588	1	− 50	217 000
A588	1	− 40	150 000

as measured in the R-curve tests, were used to assist in estimating the 1 s K_c temperature response curve. This seemed to be an acceptable procedure for many of the plates tested, since the R-curve tests were also conducted at slow rates of loading. However, some of the results seem to produce anomalous behavior as can be seen in the figures. In the specific case of the single A7 plate tested, the R-curve results fell on the dynamic K_c curve. Due to convergences problem in the data reduction procedures, no static three-point-bend K_c values were available for the A7 material. Also, in some cases, the use of the R-curve results to estimate the 1 s K_c trend lines could produce some of the very low estimated temperature shift results. As an example, consider the 25.4 mm and A242 material. For this case, the R-curve result actually governs the observed temperature shift between the dynamic and static trend K_c curves.

Equation 1 gives a value of the temperature shift, T_s, as a function of yield strength. Barsom proposed that the temperature shift between 1 s and 0.001 s fracture times should be of the order of $0.75T_s$ [*12*]. These levels are reported in Table 2 for the measured yield strengths of the plate. Observed temperature shifts also are reported in Table 2. As mentioned previously, some of the discrepancies between the predicted and observed levels could be due to the use of the R-curve results. Also, the limited nature of the K data for some plates places some of the estimate of T_s in doubt.

One item of particular importance is the ability of Eq 2 to predict the dynamic K_c response from CVN test results. For most of the plates tested, the value predicted by Eq 2, using a value of $A = 5$, are shown on the K_c-temperature figures. The use of Eq 2 generally gave conservative results. Table 2 shows the value of A needed to match Eq 2 and the observed dynamic K_c levels.

AASHTO Requirements and Fracture Safe Bridge Design

The current AASHTO CVN requirements for bridge steels are stated in Table 4. This specification represents a set of CVN requirements at certain temperatures for the various steels. This specification, coupled with good design and fabrication procedures, hopefully provides a reasonable margin of safety against fracture.

The AASHTO requirements, as found in Table 4, were developed around the CVN test rather than a fracture-mechanics type K test due to the simplicity and low cost of CVN testing. However, these requirements were derived from fracture-mechanics principles as described by Barsom [*12,13*]. The general intent was to guarantee enough toughness in bridge steels so nonplane-strain behavior would occur for the lowest expected operating temperature and the maximum expected loading rate. In the case of bridges, this maximum loading rate corresponds to the 1 s loading

TABLE 4—*AASHTO fracture-toughness specifications for bridge steels.*

ASTM Designation	Thickness	Energy Absorbed, ft·lb at °F		
		Zone 1 [a]	Zone 2 [b]	Zone 3 [c]
A36	...	15 at 70	15 at 40	15 at 10
A572 [d]	up to 4 in. mechanically fastened	15 at 70	15 at 40	15 at 10
	up to 2 in. welded	15 at 70	15 at 40	15 at 10
A440	...	15 at 70	15 at 40	15 at 10
A441	...	15 at 70	15 at 40	15 at 10
A242	...	15 at 70	15 at 40	15 at 10
A588 [d]	up to 4 in. mechanically fastened	15 at 70	15 at 40	15 at 10
	up to 2 in. welded	15 at 70	15 at 40	15 at 10
	over 2 in. welded	20 at 70	20 at 40	20 at 10
A514	up to 4 in. mechanically fastened	25 at 30	25 at 0	25 at 30
	up to 21/2 in. welded	25 at 30	25 at 0	25 at 30
	over 21/2 to 4 in. welded	35 at 30	35 at 0	35 at 30

[a] Zone 1 = minimum service temperature 0 °F and above.
[b] Zone 2 = minimum service temperature from − 1 to − 30 °F.
[c] Zone 3 = minimum service temperature from − 31 to − 60 °F.
[d] If the yield point of the material exceeds 65 ksi, the temperature for the CVN value for acceptability shall be reduced by 15 °F for each increment of 10 ksi above 65 ksi.

tests. This desired toughness performance then can be related to the CVN tests through a series of correlations. First, for the data considered, Barsom proposed that nonplane-strain behavior would occur for all loading rates at a temperature which is approximately 28 °C above the temperature-transition point on a K versus temperature plot. Thus, if the knee of the K versus temperature curve is known, the region of nonplane-strain behavior can be estimated. It was also assumed that the knee or temperature-transition point on the dynamic K versus temperature curve can be conservatively estimated by the 20 J (15 ft·lb) CVN level temperature. This information, when used in conjunction with the temperature-shift concept, provides the basis for setting CVN requirements for the various steels.

Consider the case of a hypothetical steel with a 250 MPa (36 ksi) yield strength to be used for a lowest expected service temperature of −17.8 °C. For bridge loading rates, the 1 s K curve should exhibit a knee at −45.8 °C to guarantee the nonplane-strain behavior at −17.8 °C. Using the temperature shift between the 1 s and dynamic loading rate, the knee of the dynamic K versus temperature curve can be located. This shift corresponds to $0.75T_s$ where T_s depends on the particular yield strength. Knowing the temperature-transition point of the dynamic curve allows for the 20 J (15 ft·lb) CVN temperature to be set. Thus, the AASHTO CVN requirements were established with the intent of producing nonplane-strain behavior at a desired temperature and loading rate.

At this point, the concept of fracture safe bridge design can be considered. For new welded bridge construction, it is well documented [*14, 15*] that fatigue cracks emanating from the welds are the limiting problem, and, that when these cracks are of the order of the plate thickness, the majority of the fatigue life of the structure has been exhausted. Thus, for a properly designed and fabricated bridge, detail cracks will exist of the order of the plate thickness at the end of the design life. In this type of situation, the AASHTO requirements can be shown to provide adequate toughness. Furthermore, the utilization of the AASHTO requirements provides steel which allows for safe fabrication and erection of the structures. Prior to this specification, it was possible for steel of very very low toughness to find its way into a structure and cause severe problems during fabrication and erection.

To fully consider fracture safe bridge design and all of its facets is clearly not the intent of this paper. However, one other aspect of the question should be raised here. That is, the point of multiple load paths. If a structure is such that the failure of a single member could cause total collapse of the structure, then a certain degree or level of toughness should be required in that member. If the structure is such that the loads can be shifted safely to other members, then a lower level of toughness can be required. Most of the steel in bridges are employed in regions where the

loads can be shifted so that more moderate toughness requirements are reasonable.

The data collected in this study were of a very broad nature, whereby the magnitude of potential bridge problems might be examined. There was neither the time nor the funds to study each material in depth and investigate anomolous results or departures from expected performance. However, the general results were suitable for use as part of the justification for the current AASHTO specifications. As shown in the figures of K versus temperature, there is reasonable agreement with the estimate of $0.75Ts$ for the 1 s to dynamic temperature shift where the data are sufficient to make these estimates. Also, as highlighted in Table 2, the quantity ${}_{15}\Delta T_{SH}$ is generally about 41.5°C. This implies that 28°C above the T_{15}, these materials are giving 60 to 70 percent shear performances in terms of CVN test results. This lends strong support to the argument of 28°C above the T_{15} temperature for nonplane-strain behavior. Furthermore, for the eight plates tested where ${}_{15}\Delta T_{SH}$ was greater, $\backsim$ 55°C, a 50 percent shear performance would be expected. It was also noted in the present study that correlation of dynamic K behavior with CVN results is a reasonable procedure.

As already indicated, the results of the current study were used as part of the data base to develop the CVN requirements currently imposed by the AASHTO on all steel purchased for new bridge construction. The general conclusion of the Lehigh Study [7] in terms of bridge design was that there appear to be two major roles for fracture-toughness evaluations of bridge steels. That is (*a*) elimination of very brittle steels which cause unnecessary expense during fabrication and produce potentially hazardous conditions if used for tensile load bearing members of a bridge, and (*b*) careful assessment of the fracture reliability of nonredundant tensile load bearing bridge components.

Standard CVN tests appear to be as suitable for the foregoing (*a*). In the case of bridge steels used in nonredundant (single load path) components, careful evaluation of the steel toughness is needed. Unless employed with very conservative interpretations, CVN tests are not recommended for this purpose. It is recommended that some attention be given to instrumented fracture tests with specimen sizes large enough to permit K_c or K_{Ic} determinations for critical members. The actual extent of the testing needed will have to be determined from studies of the statistics associated with K_c testing. The current program did not evaluate this question. It should be recognized that although K_c testing is more costly than qualifying a material by CVN results, the amount of such testing should be small, since most of the structural members will not be critical nonredundant members. Thus, the total cost of a job should not be affected.

Acknowledgments

The authors would like to acknowledge support from the Federal Highway Administration through contract DOT-FH-11-7664 for the work discussed in this paper.

References

[1] "Collapse of U.S. 35 Highway Bridge, Point Pleasant, West Virginia, December 15, 1967," Highway Accident Report NTSB-HAR-71-1, National Transportation Safety Board, 1971.

[2] Shoemaker, A. K. and Rolfe, S. T., "The Static and Dynamic Low-Temperature Crack-Toughness Performance of Seven Structural Steels," *Engineering Fracture Mechanics,* Vol. 2, No. 4, June 1971.

[3] Barsom, J. M. and Rolfe, S. T., "K_{Ic} Transition-Temperature Behavior of A517-F Steel," *Engineering Fracture Mechanics,* Vol. 2, No. 4, June 1971.

[4] Barsom, J. M. and Rolfe, S. T., *Impact Testing of Metals, ASTM STP 466,* American Society for Testing and Materials, 1970, p. 281.

[5] Madison, R. B., "Application of Fracture Mechanics to Bridges," Ph.D. dissertation, Lehigh University, 1969, Fritz Engineering Laboratory Report 335.2.

[6] Barsom, J. M., "Toughness Criteria for Bridge Steels," Technical Report No. 5, American Iron and Steel Institute, Project 168, 8 Feb. 1973.

[7] Roberts, R., Irwin, G., Krishna, G., and Yen, B., "Fracture Toughness of Bridge Steels—Phase II Report," Technical Report No. FHWA-RD-74-59, Federal Highway Administration Office of Research and Development, Washington, D.C., Sept. 1974.

[8] Irwin, G. R. and Pietrzak, K., "Fracture Toughness Evaluation of Structural Steels," Fritz Engineering Laboratory Report 366.2, June 1971.

[9] Heyer, R. H. and McCabe, D. E., "Crack Growth Resistance in Plane-Stress Fracture Testing," Presented at the Fourth National Symposium on Fracture Mechanics, Carnegie-Mellon Institute, 24–26 Aug. 1970.

[10] Heyer, R. H. and McCabe, D. E., "R-Curve Determination Using a Crack-Line-Wedge-Loaded (CLWL) Specimen," Presented at ASTM E-24 Meeting, Hawthorne, California, September 29, 1971.

[11] Roberts, R. and Irwin, G., *Journal of the Structural Division of the American Society of Civil Engineers,* Vol. 102, No. ST2, Feb. 1976, pp. 337–353.

[12] Barsom, J. M., Sovak, J. F., and Novak, S. R., "Fracture Toughness of A36 Steel," Technical Report No. 1, American Iron and Steel Institute Project 168, 1 May 1972.

[13] Barsom, J. M., *Engineering Fracture Mechanics,* Vol. 7, No. 3, Sept. 1975, pp. 605–618.

[14] Fisher, J. W., Frank, K. H., Hirt, M. A., and McNamee, B. M., "Effect of Weldments on the Fatigue Strength of Steel Beams," NCHRP Report 102, Highway Research Board, 1970.

[15] Fisher, J. W., Albrecht, P. A., Yen, B. T., Klingerman, D. J., and McNamee, B. M., "Fatigue Strength of Steel Beams with Welded Stiffeners and Attachments," NCHRP Report 147, Highway Research Board, 1974.

F. G. Nelson[1] *and D. J. Brownhill*[1]

Fracture Characteristics of Plain and Welded 3-In.-Thick Aluminum Alloy Plate at Various Temperatures

REFERENCE: Nelson, F. G. and Brownhill, D. J., **"Fracture Characteristics of Plain and Welded 3-In.-Thick Aluminum Alloy Plate at Various Temperatures,"** *Flaw Growth and Fracture, ASTM STP 631,* American Society for Testing and Materials, 1977, pp. 285–309.

ABSTRACT: The tensile, notch tensile, tear, and, in some cases, fracture-toughness properties (K_Q and K_{Ic}, ksi $\sqrt{\text{in.}}$) have been evaluated for 3-in.-thick 5083-H321, 5086-H32, 6061-T651, and 7005-T6351 plain plate and gas metal arc (GMA) welds in 5083-H321 (5183 filler), 6061-T651 (4043 and 5356 fillers), and 7005-T6351 (5356 filler) with no subsequent thermal treatment. The tests were made in the longitudinal, long-transverse and short-transverse orientations for the plain plate and in the "cross-weld" orientation for the welded panels. The tests were made at room temperature and generally at −100 and −320°F.

The fracture indexes, that is, notch-yield ratio and unit-propagation energy values, rank the plate and welds. The K_Q and K_{Ic} values have been developed for the 6061-T651 and 7005-T6351 plate.

For the relatively tough materials in this investigation, the notch-yield ratio versus K_{Ic} relationship was not useful in estimating K_{Ic} values. However, the unit-propagation energy values versus K_{Ic} relationship does appear to provide a satisfactory means of estimating K_{Ic} values. Estimates of K_{Ic} values for all the materials tested in this program have been made from this correlation.

KEY WORDS: crack propagation, fracture properties, tensile properties, aluminum alloys, weldments

In 1971, the Metal Properties Council sponsored a program at Alcoa Laboratories in which an attempt was made to determine the plane-strain fracture toughness of plain and welded 3-in.-thick 5083-H321, 5086-H32, 6061-T651, and 7005-T6351 plate at room temperature [*1*].[2] Because of their very high toughnesses, it was not possible to measure the plane-strain fracture toughness (K_{Ic}) for most of these alloys and welds. The two

[1] Senior engineers, Engineering Properties and Design Division, Alcoa Laboratories, Alcoa Center, Pa. 15069.

[2] The italic numbers in brackets refer to the list of references appended to this paper.

aluminum-magnesium (Al-Mg) alloys (5083 and 5086) and the aluminum-magnesium-silicon (Al-Mg-Si) alloy (6061) were so tough that even when using large, full-thickness specimens valid measurements of K_{Ic} could not be obtained. For the 7005, valid values of K_{Ic} were obtained for the plate in all orientations. The development of valid K_{Ic} values from the welded panels of each of the alloys also was virtually impossible because of their extreme toughness.

Since all of these alloys are of considerable interest for cryogenic applications, the Metal Properties Council extended this program to include the determination of related properties at −100 and −320°F. For the higher strength alloys 6061-T651 and 7005-T6351, plane-strain, fracture-toughness tests were made at −100 and −320°F, and, for all of the alloys tensile, notch tension and tear tests also were made at room temperature, −100 and −320°F, with the expectation that the latter would be useful in estimating the fracture toughness for these materials for which valid K_{Ic} measurements could not be made directly.

It is the object of this report to describe the test procedures and present the results of tests to determine notch toughness, tear, and, in some cases, the fracture toughness of these materials and use the relationships among these types of data to estimate values of the plane-strain fracture toughness for those materials for which valid K_{Ic} values could not be obtained.

Material

Plate

The same lots of commercially produced 3-in.-thick plate of 5083-H321, 5086-H32, 6061-T651, and 7005-T6351 used for the previous program [*1*] were used for the tests described herein.

The nominal compositions of these alloys are as follows.

Alloy	Si	Cu	Mn	Mg	Cr	Zn	Ti	Zr
5083	...	...	0.6	4.45	0.15	...	...	...
5086	...	...	0.45	4.0	0.15	...	...	...
6061	0.6	0.27	...	1.0	0.20	...	...	...
7005	...	...	0.5	1.4	0.13	4.5	0.04	0.13

The tensile properties of these four alloys, determined in accordance with ASTM Tension Testing of Metallic Materials (E 8-69) and ASTM Tension Testing Wrought and Cast Aluminum and Magnesium Alloy Products (B 557-74), are shown in Table 1 with the corresponding specified minimum tensile properties. The properties of all four alloys equalled or exceeded the respective minimum properties.

Welded Panels

Welded panels were prepared in the "as-welded" condition for three of the four alloys as follows.

Base Alloy and Temper	Filler Alloy
5083-H321	5183
6061-T651	4043, 5356
7005-T6351	5356

Thirty-six, inch long panels of each base alloy and filler alloy combination were made in the down-hand position by the gas metal arc (GMAW) method by the Joining Division of the Alcoa Laboratories. A 60-deg deep double "V" without an abutting land was utilized. The details of the welding procedures are as follows.

Base Metal	5083-H321	6061-T651		7005-T6351
Filler Wire	5183	4043	5356	5356
Welding current, amps	340 to 380	325 to 370	355 to 385	355 to 385
Welding voltage, volts	28 to 34	33 to 35	33 to 36	33 to 36
Welding speed, in./min	24 to 30	24 to 30	24	24
Number of passes	38	38	29	29

NOTE—Electrode diameter = 3/32 in., joint type = butt, double V-60 deg, no land, gas flow = 60 ft^3/h (40 He, 20A), and interpass temperature = 150°F

All welds were radiographed in accordance with Division 2 of Section VIII of the American Society of Mechanical Engineers (ASME) Boiler and Pressure Vessel Code [*2*]. Each panel met the radiographic requirements stated in the Code.

To further check the quality of the welds, duplicate reduced section tension specimens were prepared from each panel. The specimens were tested at room temperature in accordance with Section IX of the ASME Code [*3*]. The results of these tests are as follows.

Base Alloy and Temper	Filler Metal	Tensile Strength, ksi	Location of Fracture
5083-H321	5183	41.7	through weld
		44.8	through weld
		43.2	
Qualification value [*3*]		39.0	
6061-T651	4043	30.4	through weld
		30.6	through weld
		30.5	

Base Alloy and Temper	Filler Metal	Tensile Strength, ksi	Location of Fracture
	5356	34.6	through weld
		35.0	through weld
		34.8	
Qualification value [3]		24.0	
7005-T6351	5356	40.4	through weld
		39.9	through weld
		40.2	

For the 5083 and 6061 panels, the strengths exceeded the qualification value shown in Section IX of the Code [3]; there is no qualification value for 7005. The strength of the 7005 panel was representative of what might be expected for this combination of 3-in.-thick material and filler.

Procedure

Tension, Notch-Tension, and Tear Tests

Tension, notch-tension, and tear properties were determined at room temperature, −100°F, and −320°F with specimens cut from the T/4 and T/2 locations from the orientations shown in Fig. 1.

Tension tests were made of smooth 1/2-in.-diameter specimens (L and L-T orientations) and subsize smooth specimens (S-T orientation) of the types shown in Fig. 8 of ASTM Method E 8-69. For the tests at −100 and −320°F, the testing procedures were essentially the same as those at room temperature except that the specimens and grips were enveloped in the vapors of boiling liquid nitrogen (LN_2) for the tests at −100°F and immersed in boiling LN_2 for the tests at −320°F. The tensile yield strengths were obtained from autographically recorded load-strain diagrams. For the tests at −100 and −320°F, yield strengths were obtained from load-deformation diagrams developed using a strain-transfer device in conjunction with an autographic extensometer. The elongations were measured over a gage length of 4D.

Notch-tension tests were made of 1/2-in.-diameter specimens of the type shown in Fig. 2 in accordance with the ASTM Method for Sharp-Notch Tension Testing of Thick-Section Materials with Cylindrical Specimens (E 602-76T). The tests at −100 and −320°F were made in the same manner as those at room temperature except that at −100°F, the specimens and grips were enveloped in the vapors of LN_2 boiling at a controlled rate, and at −320°F, immersed in LN_2.

The notch-tensile strengths were determined by dividing the maximum

load at failure by the original net cross-sectional area at the root of the notch. The ratios of the notch-tensile strength to the tensile yield strength (notch-yield ratio (NYR) = notch-tensile strength, ksi/tensile yield strength, ksi) were also determined. The NYR is a relative measure of a materials notch toughness, that is, its ability to deform plastically and thereby avoid cracking in the presence of a severe stress raiser. Therefore, the higher the ratio, the greater the resistance to crack initiation or cracking in the presence of severe stress raisers.

Tear tests of 0.1-in.-thick specimens of the types shown in Fig. 2 were made [*4*]. The tests at subzero temperatures were made with the specimens and grips enveloped in the vapors of boiling LN_2 for the tests at $-100\,°F$ and immersed in boiling LN_2 for the tests at $-320\,°F$. Load-deformation diagrams were obtained autographically, and the energies required to initiate and propagate the crack in the specimen were determined from measurements of the appropriate areas under the load-deformation diagrams [*4*]. The unit-propagation energies (UPE) were calculated. The UPE is a relative measure of the resistance of a material to the propagation of a crack once initiated.

Fracture-Toughness Tests

Fracture-toughness tests were made of full-thickness specimens (3-in. thick) from the L-T and T-L orientations and of 1.250 or 1.000-in.-thick specimens from the S-L orientation. The type of specimen used was the standard compact specimen in Fig. 5 of ASTM Method E 399-74. Prior to testing, all of the specimens were fatigue precracked. For specimens with L-T and T-L orientations, the fatigue cracks were initiated and propagated to the desired length (about 0.1 in.) with about 60 000 cycles at a stress intensity of about 14 ksi $\sqrt{\text{in.}}$ The fatigue cracks for specimens with the S-L orientation were initiated and propagated to the desired length with about 9000 cycles at a stress intensity of about 15 ksi $\sqrt{\text{in.}}$ All tests were made in accordance with ASTM Method E 399-74. The tests at $-320\,°F$ were made by essentially the same techniques as at room temperature, except that during the tests at $-100\,°F$, the test section of the specimens were enveloped in the vapors of boiling LN_2, and, at $-320\,°F$, they were immersed in LN_2.

For each test, a load crack opening displacement (COD) curve was obtained on an *x-y* plotter, and the curve was analyzed in accordance with established procedures (ASTM Method E 399-74). A 5 percent secant offset line was constructed, the secant intercept load determined, and a K_Q value (candidate value of K_{Ic}) was calculated with the equation from ASTM Method E 399-74.

All of the criteria in ASTM Method E 399-74 were utilized in judging

TABLE 1—*Results of tension tests*[a] *of some 3-in.-thick*

Alloy and Temper	Test Temperature, °F	Longitudinal (T/4) Tensile Strength, ksi	Yield Strength,[b] ksi	Elongation in 4D, %	Reduction of area, %
5083-H321	Room	45.0	33.6	22.0	38
		45.4	33.7	21.5	36
	Avg	45.2	33.6	21.8	37
	Minimum[c] (1.501-3.000-in.)	41.0	29.0	12.0	...
	−100	47.6	34.1	21.0	43
		47.0	34.0	21.5	44
	Avg	47.3	34.0	21.2	44
	−320	63.3	39.7	32.5	30
		61.6	39.4	33.5	32
	Avg	62.4	39.6	33.0	31
5086-H32	Room	39.8	30.1	23.0	46
		40.2	29.9	23.0	43
	Avg	40.0	30.0	23.0	44
	Minimum[c] (0.250-2.000-in.)	40.0	28.0	12.0	...
	−100	41.4	30.4	24.0	52
		41.3	30.4	24.5	53
	Avg	41.4	30.4	24.2	52
	−320	57.0	34.6	40.0	45
		57.0	34.6	39.5	45
	Avg	57.0	34.6	39.8	45
6061-T651	Room	45.5	42.3	15.5	36
		45.4	42.2	15.5	38
	Avg	45.4	42.2	15.5	37
	Minimum[c] (2.001-4.000-in.)	...	...	...	...
	−100	52.1	45.7	12.5	23
		51.7	46.0	12.0	23
	Avg	51.9	45.8	12.2	23
	−320	63.5	51.0	15.5	23
		62.9	51.1	15.5	22
	Avg	63.2	51.0	15.5	22
7005-T6351	Room	54.7	48.4	17.0	44
		54.3	48.1	16.0	43
	Avg	54.5	48.2	16.5	44
	Minimum[d] (0.250-3.000-in.)	...	...	...	...
	−100	62.3	53.6	15.5	35
		62.2	53.5	15.5	35
	Avg	62.2	53.6	15.5	35
	−320	74.1	59.7	17.5	25
		73.4	59.0	17.0	27
	Avg	73.8	59.4	17.2	26

[a] L and L-T specimens from T/4 location, S-T specimens from T/2 location.
[b] Offset equals 0.2 percent.
[c] Aluminum Standards and Data, 1974–75 Edition, The Aluminum Association.
[d] Alcoa Green Letter GL198, Aluminum Alloy 7005, Sept. 1974.

aluminum alloy plate at room temperature, −100 and −320°F.

Long-Transverse (T/4)				Short-Transverse (T/2)			
Tensile Strength, ksi	Yield Strength,[b] ksi	Elongation in 4D, %	Reduction of Area, %	Tensile Strength, ksi	Yield Strength,[b] ksi	Elongation in 4D, %	Reduction of Area, %
47.9	32.1	18.0	29	44.7	29.6	9.0	27
48.8	32.3	18.0	29	...	...	...	...
48.4	32.2	18.0	29	44.7	29.6	9.0	27
...	...	...	...	...	...	...	...
48.5	32.6	18.0	32	46.0	31.1	9.3	14
48.9	32.2	18.5	34	46.2	30.9	9.3	12
48.7	32.4	18.2	33	46.1	31.0	9.3	13
64.4	37.4	25.5	24	53.8	35.8	6.7	6
64.4	37.2	25.0	23	54.7	35.5	6.7	6
64.4	37.3	25.2	24	54.2	35.6	6.7	6
41.6	28.5	22.0	38	39.3	26.3	12.0	21
41.5	28.4	20.0	39	...	...	...	...
41.6	28.4	21.0	38	39.3	26.3	12.0	21
...	...	...	...	...	...	...	...
42.7	28.6	20.5	44	40.9	27.8	17.3	25
42.7	28.3	20.5	44	40.6	27.1	16.0	25
42.7	28.4	20.5	44	40.8	27.4	16.6	25
59.5	32.8	33.0	35	55.9	32.7	16.0	17
59.5	32.3	32.5	34	56.2	32.8	16.0	16
59.5	32.6	32.8	34	56.0	32.8	16.0	16
46.6	41.5	13.0	30	45.8	39.6	10.0	29
46.7	41.5	13.0	26	...	...	...	...
46.6	41.5	13.0	28	45.8	39.6	10.0	29
42.0	35.0	6.0	...	...	...	...	...
51.4	47.9	14.5	33	52.0	44.5	9.3	17
51.7	48.8	14.5	34	52.2	44.2	10.7	17
51.6	48.4	14.5	34	52.1	44.4	10.0	17
62.0	52.9	20.0	34	62.0	49.6	12.0	12
62.1	53.0	19.5	34	62.0	49.5	12.0	14
62.0	53.0	19.8	34	62.0	49.6	12.0	13
55.9	49.4	15.0	39	56.4	47.5	7.0	11
55.4	48.7	15.0	40	...	...	...	...
55.6	49.0	15.0	40	56.4	47.5	7.0	11
47.0	38.0	7.0	...	...	...	...	...
63.5	54.2	14.5	30	62.4	52.0	5.3	6
63.2	54.0	14.5	28	61.5	51.7	5.3	6
63.4	54.1	14.5	29	62.0	51.8	5.3	6
74.6	59.8	15.0	23	70.0	58.4	4.0	5
74.7	60.3	15.5	23	72.8	58.3	4.0	5
74.6	60.0	15.2	23	71.4	58.4	4.0	5

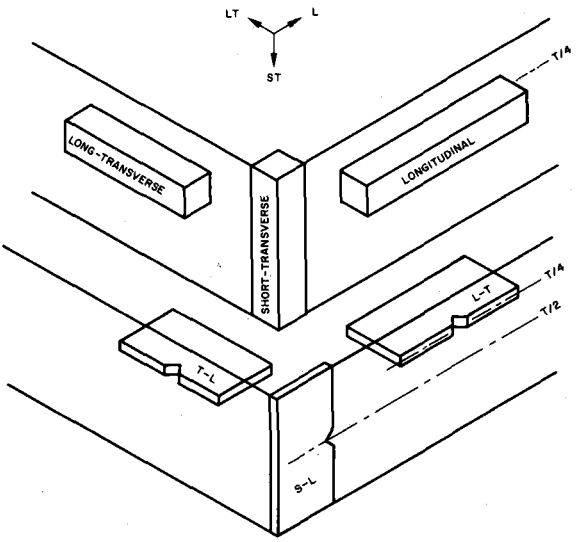

FIG. 1—*Orientation of tension, notch tension, and tear specimens in 3-in.-thick aluminum alloy plate.*

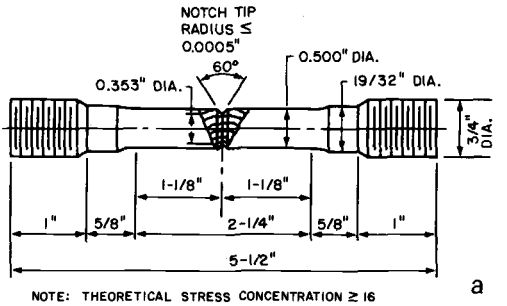

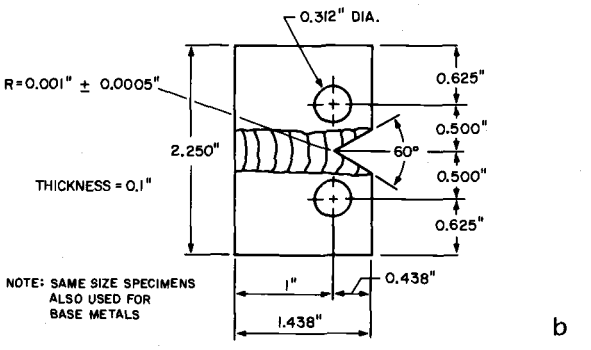

FIG. 2—(a) *Notch tension specimen, and* (b) *tear test specimen.*

the validity of the results. A K_{max} was also calculated using the same equation except that the P_{max} (the maximum load developed by the specimen) was substituted for the P_5 load in the aforementioned equation.

The specimen strength ratio for compact specimens, R_{sc}, was calculated with the equation from ASTM Method E 399-74. This is the ratio of the maximum nominal net-section stress developed at the crack tip by the specimen to the tensile yield strength. The ratio is a relative measure of toughness and is useful from a screening standpoint when a valid value of K_{Ic} is not obtained.

Discussion of Results

Tensile, Notch Tensile and Tear Properties of Plain Plate

Tensile Properties—The individual and average results of the tension tests of 5083-H321, 5086-H32, 6061-T651, and 7005-T6351 plate are shown in Table 1. For all four alloys at room temperature, the tensile properties in the longitudinal and long-transverse orientations are generally higher than those in the short-transverse orientation; short-transverse elongations are 1/2 to 2/3 of the values in the other two orientations. Of the four alloys tested, 7005-T6351 has the highest strengths by a significant margin. Of the other three, 6061-T651 has the highest yield strengths, and 5086-H32 has the lowest, but there is little spread in tensile strengths. Alloy 5086-H32 generally has the highest values of elongation and reduction of area, and 7005-T6351 generally has the lowest.

For the 5083-H321 and 5086-H32, there appears to be little change in tensile properties at −100°F from those at room temperature. For the 6061-T651 and 7005-T6351 the strengths are higher at −100°F than those at room temperature; the elongations are about the same at −100°F and room temperature. For all four alloys at −100 and −320°F and in all three orientations (longitudinal, long-transverse, and short-transverse), the tensile properties at −320°F are generally higher than those at room temperature.

Notch Tensile Properties—The average NYR's are plotted in Fig. 3. At room temperature, the long-transverse ratios for 5083-H321 and 5086-H32 are higher than the longitudinal ratios; for 6061-T651 and 7005-T6351, the reverse is true. For all alloys, the short-transverse ratios are the lowest.

For 5083-H321 and 5086-H32, the NYR's regardless of orientation, tend to be higher at −100°F than at room temperature or −320°F. For 6061-T651 and 7005-T6351, the value at both subzero temperatures are generally lower than the room-temperature values.

Tear Properties—The average UPE values are plotted in Fig. 4. At all test temperatures, the values are the highest in the longitudinal orientation and lowest in the short-transverse orientation.

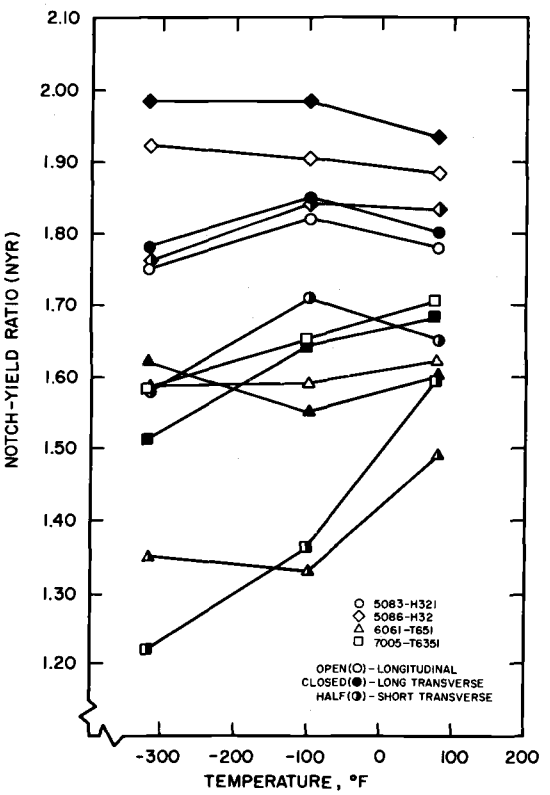

FIG. 3—*Notch-yield ratio (NYR) versus temperature for 3-in.-thick aluminum alloy plate.*

For 5086-H32, the UPE values at subzero temperatures are significantly higher than those at room temperature. For 5083-H321 and 6061-T651, the values at subzero temperatures are generally as high as or higher than those at room temperature. For 7005-T6351, the UPE values at −320°F are significantly lower than those at room temperature. The UPE values for 5086-H32 in all three orientations are highest while those for the 6061-T651 are the lowest.

Tensile, Notch Tensile and Tear Properties of Welded Panels

Tensile Properties—The individual and average results of the tension tests of the 5083-H321 [5183], 6061-T651 [4043], 6061-T651 [5356], and 7005-T6351 [5356] welded panels are shown in Table 2. At room temperature, the tensile properties, in general, reflect the strength of the filler metal. The tensile properties developed by the 5183 weld in 5083-H321

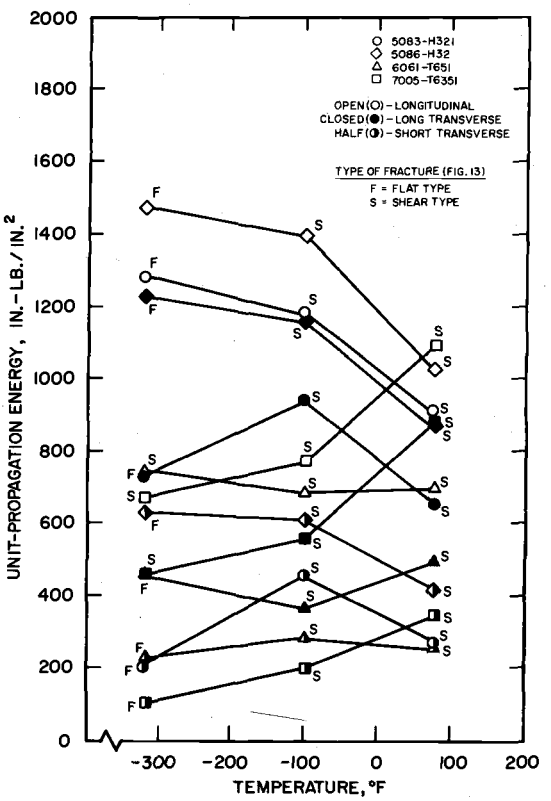

FIG. 4—*Unit-propagation energy (UPE) versus temperature for 3-in.-thick aluminum alloy plate.*

are higher than those of the other panels; the tensile properties developed by the 4043 weld in 6061-T651 are the lowest.

The tensile properties at −100°F are about equal to the room-temperature values, while those at −320°F are generally higher.

Notch Tensile Properties—The average NYR's of the four welded panels are plotted in Fig. 5. The NYR's of the 6061-T651 [5356] are the highest at all temperatures; the ratios for the 5083-H321 [5183] and 6061-T651 [4043] are about the same and are lowest.

The NYR's at the subzero temperatures are higher than those at room temperature, with those at −100°F being the highest.

Tear Properties—The average UPE values of the four welded panels are plotted in Fig. 6. The 5356 welds in 6061-T651 and 7005-T6351 generally have the highest UPE values, with the 5183 weld in 5083-H321 averaging 20 percent lower; the 4043 weld in 6061-T651 has the lowest values.

At −100°F, the UPE values are higher than the comparable values at

TABLE 2—*Results of tension tests at room temperature, −100 and −320°F of groove welded 3-in.-thick aluminum alloy plate welded by the GMAW method.*

Alloy and Temper	Filler Metal	Test Temperature, °F	Tensile Strength, ksi	Yield Strength,[a] ksi	Elongation in 2 in., %	Reduction of Area, %	Location of Fracture
5083-H321	5183	Room	42.7	24.5	10.5	15	through weld
			44.9	24.6	17.0	24	through weld
		Avg	43.8	24.5	13.8	20	
		−100	40.7	24.6	9.5	18	through weld
			45.0	24.4	16.5	34	edge of weld
		Avg	42.8	24.5	13.0	26	
		−320	60.8	28.5	18.0	15	through weld
			60.8	29.5	18.0	16	through weld
		Avg	60.8	29.0	18.0	16	
6061-T651	4043	Room	28.7	17.0	8.0	20	through weld
			28.7	17.0	7.0	20	through weld
		Avg	28.7	17.0	7.5	20	
		−100	30.3	16.7	8.0	19	through weld
			30.3	17.1	7.5	20	through weld
		Avg	30.3	16.9	7.8	20	
		−320	42.1	20.3	7.0	12	through weld
			41.9	19.6	6.5	13	through weld
		Avg	42.0	20.0	6.8	12	

6061-T651	5356	Room	33.6	20.7	7.0	14	edge of weld
			33.5	21.4	6.5	9	edge of weld
		Avg	33.6	21.0	6.8	12	
		−100	35.8	21.4	8.5	15	outside weld
			36.2	21.1	8.5	18	outside weld
		Avg	36.0	21.2	8.5	16	
		−320	49.9	24.6	16.0	31	outside weld
			49.9	24.6	16.5	26	outside weld
		Avg	49.9	24.6	16.2	28	
7005-T6351	5356	Room	40.1	22.6	13.5	34	through weld
			40.3	22.3	11.0	28	through weld
		Avg	40.2	22.4	12.2	31	
		−100	40.9	21.9	14.5	39	through weld
			41.3	22.3	15.0	36	through weld
		Avg	41.1	22.1	14.8	38	
		−320	55.5	26.2	9.5	16	edge and through weld
			47.1	26.1	4.5	10	edge and through weld
		Avg	51.3	26.2	7.0	13	

[a] Offset equals 0.2 percent.

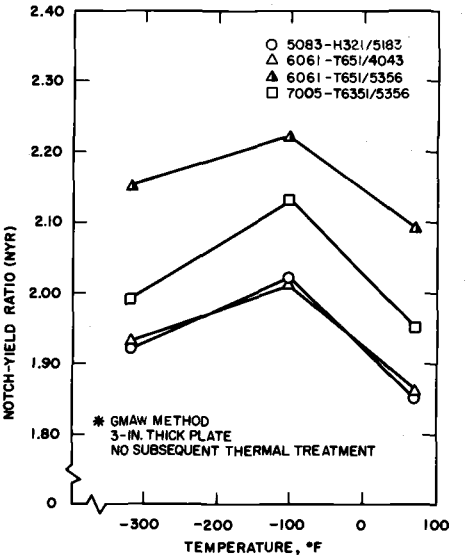

FIG. 5—*Notch-yield ratio (NYR) versus temperature for groove welded* plate.*

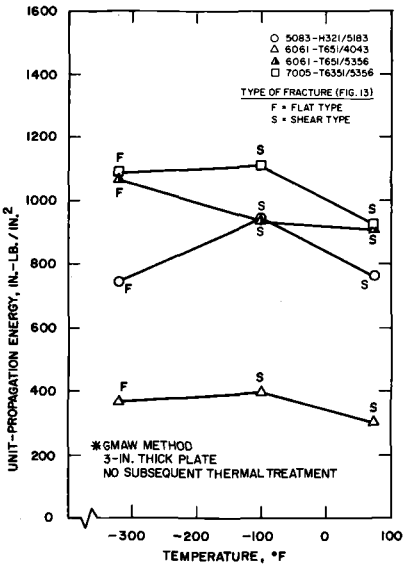

FIG. 6—*Unit-propagation energy (UPE) versus temperature for groove welded* panels.*

room temperature. At −320°F the UPE values are generally lower than the comparable values at −100°F but are about equal to or higher than the values at room temperature.

Fracture Toughness of Plain Plate

The average results of the compact fracture-toughness tests of the 6061-T651 and 7005-T6351 plate in all three orientations are plotted in Fig. 7. The room-temperature data for the S-L orientation were previously published [*1*] but have been included in this report for comparative purposes.

Representative fracture surfaces of the fracture toughness specimens are shown in Figs. 8 (6061-T651) and 9 (7005-T6351). There usually are two distinct regions in the fracture surfaces which are shown in the photographs; that is, the surface developed during the fatigue precracking, and the failure surface created during the load K_{Ic} tests. In addition, the lamellar fracture surface of the 7005-T6351 specimens developed in tests at −320°F is shown clearly.

Representative load-deformation diagrams for the compact specimens are schematically reproduced in Fig. 10 to illustrate the shapes of the original diagrams.

As indicated in Table 3, valid K_{Ic} values were obtained only for (*a*) the 6061-T651 plate in the S-L orientation at room temperature and in the T-L and S-L orientations at −320°F and (*b*) for the 7005-T6351 plate in the T-L and S-L orientations at room temperature and in the S-L orientation at −320°F. However, most of the other values for both alloys in the

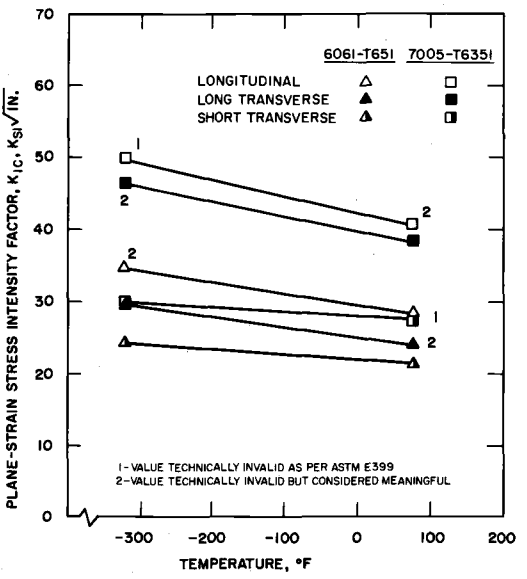

FIG. 7—*Plane-strain, stress-intensity factor* (K_{Ic}) *versus temperature for 6061-T651 and 7005-T6351 plate, 3-in. thick.*

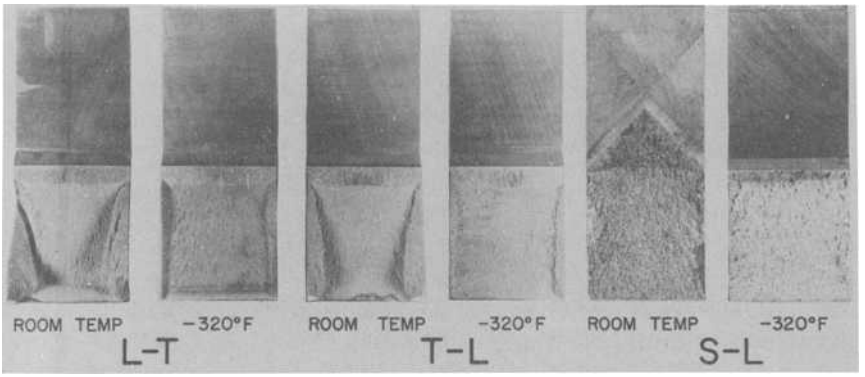

FIG. 8—*Fracture surfaces of compact fracture toughness specimens from 6061-T651 aluminum alloy plate, 3-in. thick.*

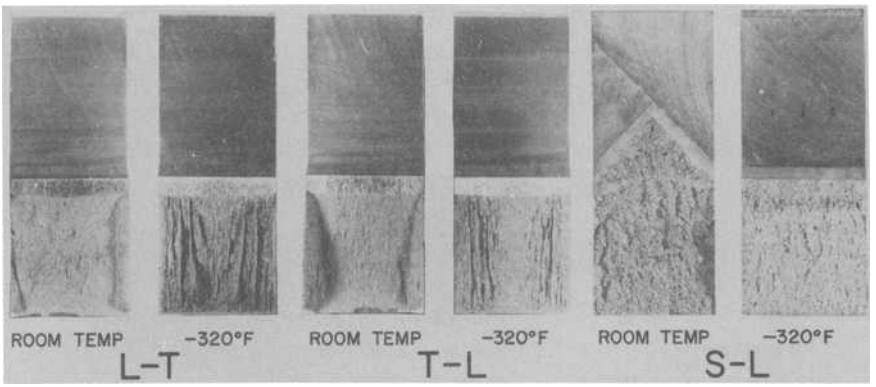

FIG. 9—*Fracture surfaces of compact fracture toughness specimens from 7005-T6351 aluminum plate, 3-in. thick.*

other orientations exceeded the ASTM Method E 399-74 validity criteria by only a very small margin and can be considered meaningful. The limits for meaningful data when applicable are shown in the footnotes in Table 3. For both alloys, the P_{max}/P_5 relationship indicated that slightly larger specimens would be required to ensure plane-strain conditions in the L-T and T-L orientations.

The data have been plotted in Fig. 7 to indicate the influence of temperature on valid K_{Ic} or meaningful K_Q values. Two invalid values also are shown merely to indicate the trend. For all orientations of both alloys, the K_{Ic} or K_{max} values at -320°F are higher than the corresponding room-temperature values.

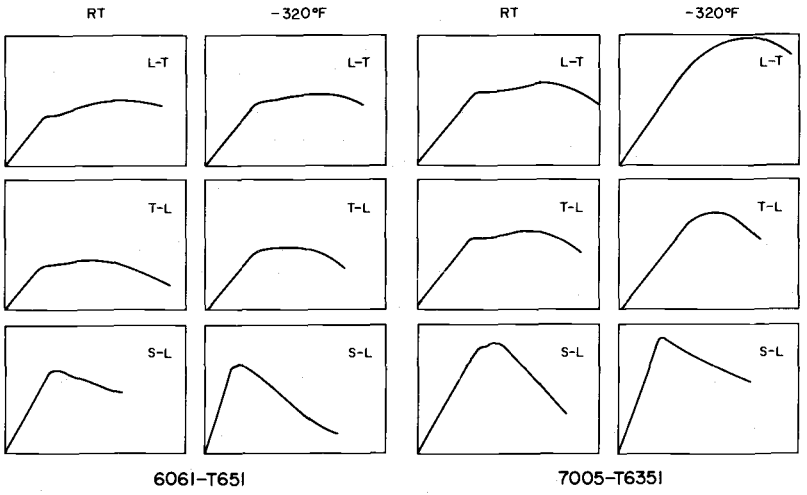

FIG. 10—*Load displacement curves for compact fracture toughness tests of some 6061-T651 and 7005-T6351 plate, 3-in. thick (L-T, T-L, and S-L orientations).*

Summary and Relationships of Fracture Indexes to Fracture Toughness

The summaries of fracture indexes for plain and welded plate are shown in Tables 3 and 4, respectively.

When valid K_{Ic} values cannot be obtained using standard specimens which are tested and evaluated in accordance with the requirements of ASTM Method E 399-74, the results of notch tension and tear tests can be used to estimate approximate K_{Ic} levels from values of the NYR and UPE values, which have been shown previously to relate to the fracture toughness, K_{Ic} [*4,5*].

The published relationship [*6,7*] between NYR and valid measures of K_{Ic}, together with the data generated in this program, is shown in Fig. 11. As indicated, the data illustrate that for ratios above about 1.4, the correlation is not a useful one.

The published relationship [*7,8*] between UPE and K_{Ic} together with data from this program are shown in Fig. 12. In the course of this investigation, it was observed that the mode of fracture greatly influences the correlation, that is, data developed from the flat-type and shear-type fractures (Fig. 13) of the tear specimen appear to be related directly to K_{Ic} by two different relationships as illustrated in Fig. 12. In utilizing the correlation, the appropriate band must be used, dependent upon the nature of the fracture in the tear specimen.

Estimation of Fracture Toughness From Unit-Propagation Energy Values

Based on the relationship of UPE versus K_{Ic} as shown in Fig. 12, K_{Ic}

TABLE 3—*Summary of fracture indexes for 3-in.-thick aluminum alloy plate.*

Alloy and Temper	Temperature, °F	Notch Yield Ratio	Unit Propagation Energy, in·lb/in.^{2}	K_{Ic}, ksi $\sqrt{\text{in.}}$	K_{max}, ksi $\sqrt{\text{in.}}$	Specimen Strength Ratio, R_{sc}
			Longitudinal (L-T)			
5083-H321	Room	1.78	910	...	...	...
	−100	1.82	1158	...	...	...
	−320	1.75	1285	...	...	...
5086-H32	Room	1.88	1020	...	...	...
	−100	1.90	1390	...	...	...
	−320	1.92	1470	...	...	...
6061-T651	Room	1.62	645	27.7[a]	36.0	0.76
	−100	1.59	680	...	...	...
	−320	1.58	745	34.6[b]	38.8	0.67
7005-T6351	Room	1.70	1095	40.8[b]	46.6	0.85
	−100	1.65	775	...	...	...
	−320	1.58	675	50.0[a]	68.0	1.01
			Long-Transverse (T-L)			
5083-H321	Room	1.80	655	...	...	...
	−100	1.85	940	...	...	...
	−320	1.78	730	...	...	...

5086-H32	Room	1.93	860	...	...	...
	−100	1.98	1155	...	...	...
	−320	1.98	1225	...	...	...
6061-T651	Room	1.60	490	24.0 [b,c]	28.1	0.60
	−100	1.55	365	...	...	...
	−320	1.62	460	29.8	32.2	0.54
7005-T6351	Room	1.68	880	38.2	42.0	0.75
	−100	1.64	560	...	...	...
	−320	1.51	460	46.4 [b]	52.7	0.78
				Short-Transverse (S-L)		
5083-H321	Room	1.65	270	...	23.3	0.98
	−100	1.71	455	...	...	...
	−320	1.58	205	...	...	...
5086-H32	Room	1.83	410	...	26.2	1.26
	−100	1.84	605	...	...	...
	−320	1.76	625	...	...	...
6061-T651	Room	1.49	250	21.3	21.8	0.70
	−100	1.33	280	...	...	...
	−320	1.35	230	24.2	24.8	0.75
7005-T6351	Room	1.59	345	27.0	28.8	0.76
	−100	1.36	200	...	...	...
	−320	1.22	105	30.0	30.0	0.78

[a] $P_{max}/P_5 > 1.10$; technically invalid as per ASTM E 399-74.
[b] P_{max}/P_5 between 1.105 and 1.200; technically invalid as per ASTM E 399-74 but value considered meaningful.
[c] K_F between 0.605 and 0.700; technically invalid as per ASTM E 399-74 but value considered meaningful.

TABLE 4—*Summary of fracture indexes for GMA welds in 3-in.-thick aluminum alloy plate.*

Alloy and Temper	Filler	Room Temperature		−100 °F		−320 °F	
		Notch Yield Ratio	Unit Propagation Energy, in·lb/in.^{2}	Notch Yield Ratio	Unit Propagation Energy, in·lb/in.^{2}	Notch Yield Ratio	Unit Propagation Energy, in·lb/in.^{2}
5083-H321	5183	1.85	765	2.02	945	1.92	745
6061-T651	4043	1.86	300	2.01	395	1.93	365
	5356	2.09	910	2.22	935	2.15	1065
7005-T6351	5356	1.95	925	2.13	1120	1.99	1085

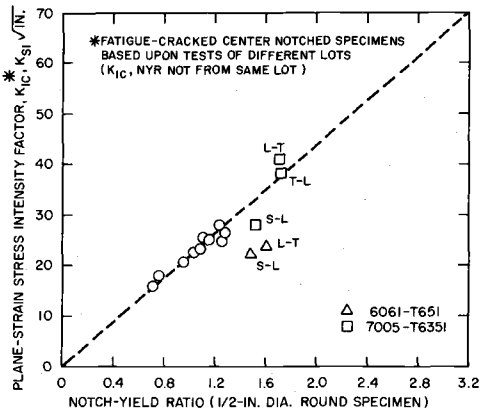

FIG. 11—*Relationship between plane-strain fracture toughness and notch-yield ratio.*

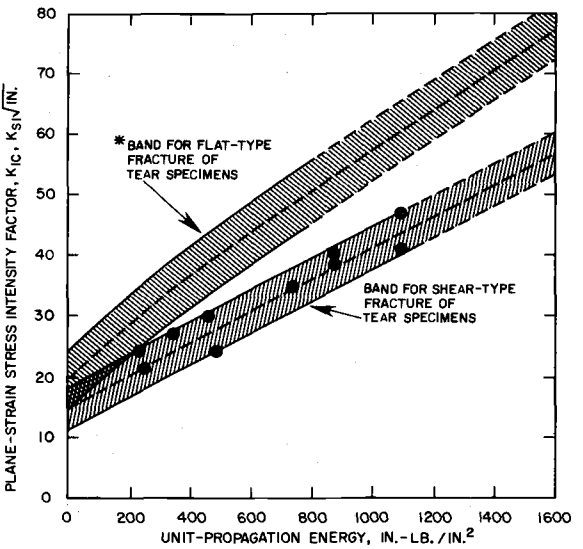

FIG. 12—*Relationship between plane-strain fracture toughness and unit-propagation energy from tear tests.*

values were estimated for the materials tested in this investigation and are shown in Table 5 together with the measured values where they were available. The estimated K_{Ic} values appear to be in fair agreement with the measured values in most cases.

For the two 5XXX series alloys, the estimated K_{Ic} values increase, and, in some cases, significantly as the temperature decreases from room temperature to −320°F. Of the two alloys (5083-H321 and 5086-H32), the

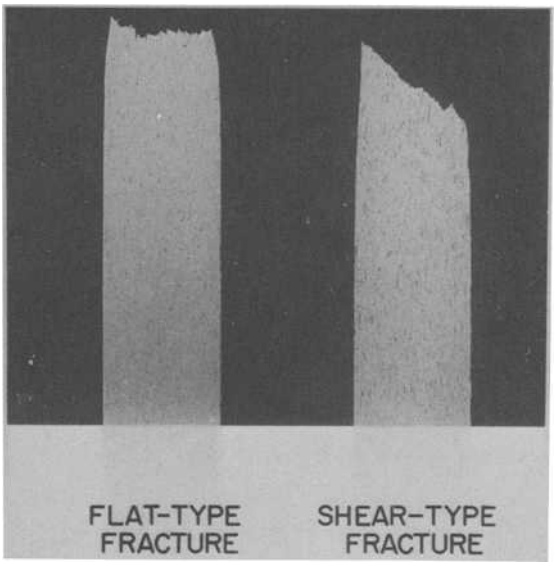

FIG. 13—*Types of fracture modes of tear test specimens.*

5086-H32 is indicated to have higher fracture toughness at all temperatures and orientations. For the two heat-treatable alloys (6061-T651 and 7005-T6351), the estimated K_{Ic} values for each alloy are generally about the same for all temperatures for each orientation; 7005-T6351 ranks the higher of the two alloys.

The toughness data for weldments ranked the filler alloys from highest to lowest: (1) 5356, (2) 5183, and (3) 4043. The estimated toughness values for the two 5XXX series alloy filler metals were in the same general range of values that were developed for the two 5XXX parent metals. For the 4043 welds in 6061-T651 plate, the estimated K_{Ic} values were in the same general range as developed for the parent metal, however, the values for 5356 welds in either 6061-T651 or 7005-T6351 were higher than that of the parent metal.

Conclusions

The following conclusions appear warranted on the basis of the results of tension, notch tension, tear, and, in some cases, compact fracture-toughness tests of 3-in.-thick plain and welded plate at room temperature, −100°F, and −320°F of several aluminum alloys.

1. The tensile properties of the plain plate in three orientations (L, L-T, and S-T) and the welds in one orientation (cross-weld) at the three test temperatures indicate that for the 5XXX alloys, and welds in all

TABLE 5—*Estimated*[a] *fracture toughness values* (K_{Ic}) *based on unit-propagation energy values* (UPE).

Alloy and Temper	Filler Alloy	Longitudinal (L-T)			Long-Transverse (T-L)			Short-Transverse (S-L)		
		Room	−100°F	−320°F	Room	−100°F	−320°F	Room	−100°F	−320°F
5083-H321	...	39	46	67	32	40	48	22	27	29
5086-H32	...	41	51	72	37	45	64	26	31	44
6061-T651	...	32	33	35(34.6)	28(24.0)	25	27(29.8)	22(21.3)	23	30(24.2)
7005-T6351	...	43(40.8)	35	33	38(38.2)	30	38(46.4)	24(27.0)	20	25(30.0)
5083-H321	5183	...	...	...	35	40	48	...	...	...
6061-T651	4043	...	...	...	23	25	35	...	...	...
	5356	...	...	...	39	40	59	..	...	...
7005-T6351	5356	...	...	...	39	44	60	...	...	...

[a] Numbers in parentheses are K_{Ic} or K_Q (meaningful) values from actual tests.

alloys, the strengths are about the same at room temperature and −100°F but are higher at −320°F. For the plain 6061-T651 and 7005-T6351, the strengths increase consistently with decrease in temperature.

2. Overall consideration of values of NYR (a measure of the ability of a material to deform plastically in the presence of a stress raiser) and the UPE, (a measure of the ability of a material to resist the propagation of a crack once initiated) leads to a ranking of the alloys regardless of orientation and temperature as follows.

Plain Plate	As-Welded Panels
5086-H32 (toughest)	7005-T6351 [5356] (toughest)
5083-H321	6061-T651 [5356]
7005-T6351	5083-H321 [5183]
6061-T651	6061-T651 [4043]

3. For the 6061-T651 and 7005-T6351, the K_Q or K_{Ic} values developed with compact fracture specimens are as follows.

	K_{Ic}, ksi $\sqrt{\text{in.}}$			
	6061-T651		7005-T6351	
Orientation	Room Temperature	−320°F	Room Temperature	−320°F
L-T	27.7[a]	34.6[b]	40.8[b]	50.0[a]
T-L	24.0[b]	29.8	38.2	46.4[b]
S-L	21.3	24.2	27.0	30.0

[a] Technically invalid per ASTM Method E 399-74.
[b] Technically invalid per ASTM Method E 399-74 but considered meaningful.

4. Relationships between UPE and K_{Ic} are related to the fracture mode of the tear test specimen. When fracture appearance is incorporated, values are about in the same general range as the actual K_{Ic} values where both could be compared, and so useful estimates of approximate K_{Ic} can be made.

5. Estimated K_{Ic} values for 5083-H321 and 5086-H32 in the L-T, T-L, and S-L orientations and at various temperatures are as follows.

	Estimated (Approximate) K_{Ic}, ksi $\sqrt{\text{in.}}$					
	5083-H321			5086-H32		
Orientation	Room Temperature	−100°F	−320°F	Room Temperature	−100°F	−320°F
L-T	39	46	67	41	51	72
T-L	32	40	48	37	45	64
S-L	22	27	29	26	31	44

6. Estimated K_{Ic} values for the welded panels in the cross-weld orientation and at various temperatures are as follows.

		Estimated K_{Ic}, ksi $\sqrt{\text{in.}}$		
Alloy and Temper	Filler Metal	Room Temperature	−100°F	−320°F
5083-H321	5183	35	40	48
6061-T651	4043	23	25	35
	5356	39	40	59
7005-T6351	5356	39	44	60

7. The use of the NYR to estimate values of K_{Ic} for these alloys is not justified; a larger diameter notch-tension specimen may provide a better correlation with K_{Ic}.

References

[1] Nelson, F. G. and Kaufman, J. G. in *Progress in Flaw Growth and Fracture Toughness Testing, ASTM STP 536,* American Society for Testing and Materials, 1973, pp. 350–376.

[2] "Pressure Vessels," ASME Boiler and Pressure Vessel Code, Division 2 of Section VIII, 1975 edition.

[3] "Welding Qualifications," ASME Boiler and Pressure Vessel Code, Section IX, 1975 edition.

[4] Kaufman, J. G. and Holt, M., "Fracture Characteristics of Aluminum Alloys," Technical Report No. 18, The Aluminum Company of America, Alcoa Laboratories, 1965.

[5] Holt, M. and Kaufman, J. G., "Indices of Fracture Characteristics of Aluminum Alloys Under Different Types of Loading" *Current Engineering Practice,* Vol. 16, No. 3, 1973.

[6] Nelson, F. G., Kaufman, J. G., and Holt, M., "Fracture Characteristics of Welds in Aluminum Alloys," *Welding Journal,* July 1966.

[7] Kaufman, J. G., Nelson, F. G., and Wanderer, E. T., "Mechanical Properties and Fracture Characteristics of 5083-0 Products and 5183 Welds in 5083 Products," Vol. 1, Proceedings of the XIII International Congress of Refrigeration, Washington, D. C., 1971.

[8] Nelson, F. G., Kaufman, J. G., and Wanderer, E. T., "Tear Tests of 5083 Plate and of 5183 Welds in 5083 Plate and Extrusions," Vol. 15, *Advance in Cyrogenics Engineering,* 1970.

Satish Gaggar[1] *and L. J. Broutman*[1]

Fracture Toughness of Random Glass Fiber Epoxy Composites: An Experimental Investigation

REFERENCE: Gaggar, S. and Broutman, L. J., **"Fracture Toughness of Random Glass Fiber Epoxy Composites: An Experimental Investigation,"** *Flaw Growth and Fracture, ASTM STP 631,* American Society for Testing and Materials, 1977, pp. 310–330.

ABSTRACT: An experimental investigation to determine the applicability of linear-elastic fracture mechanics to a randomly oriented, discontinuous fiber epoxy composite is described. Two epoxy resins differing in ductility were reinforced by a glass fiber mat such that the volume fraction of glass could be varied from 20 to 45 percent. The candidate stress-intensity factor (K_Q) was measured using single-edge notched (SEN), double-edge notched (DEN), and notched bend tests (NBT). The effect of specimen thickness, notch-root radius, and a/w ratio was investigated. It is suggested that a conservative value of stress-intensity factor representative of the onset of fiber-matrix debonding (K_D) be utilized for design purposes. It is shown that good correlation for K_Q exists between the various types of specimens and that K_Q is independent of specimen thickness. K_Q is also independent of the a/w ratio for DEN and NBT specimens. It is also shown by calculation that the magnitude of the fracture energy is dominated by the fiber-matrix debonding energy and the fiber pull-out energy.

KEY WORDS: crack propagation, fractures (materials), glass fibers

The fracture properties of composite materials have been studied by a number of investigators in recent years. Some investigators [*1–3*][2] have approached the problem by studying microfracture mechanisms, whereas others have tried to apply conventional linear-elastic fracture mechanics (LEFM) to these materials to study the effect of a crack on fracture properties. Such a characterization of material, with respect to crack initiation and propagation, is important for any potential structural and engineering application. Following the work of Wu [*4*], a number of papers have been

[1]Research Associate and professor of materials engineering, respectively, Illinois Institute of Technology, Chicago, Ill. 60616; Mr. Gaggar is now a research scientist at Borg-Warner Chemical Co., Washington, W.Va.

[2]The italic numbers in brackets refer to the list of references appended to this paper.

published in recent years dealing with the application of LEFM to predict the fracture properties of composites containing notches. Wu considered the case of a unidirectional glass reinforced epoxy resin with a crack parallel to the direction of the fibers and reported that the critical stress-intensity factor, K_c, did not vary significantly with the crack length. Konish et al [5] studied a wide variety of composites and concluded that the failure mechanism of the specimens tested was crack dominated in most cases, and the procedures of LEFM could be applied even where the overt failure mechanism was not so obviously dominated by the starter crack. Owen and Bishop [6] have carried out fracture-toughness tests on polyester resin containing various forms of reinforcement. It was concluded that K_c values, in most cases, were not independent of crack size, but a method similar to the plastic-zone correction in metals was used to obtain K_c values independent of the crack length. Ellis and Harris [7] studied the effect of specimen size and other test variables on the fracture properties of some fiber reinforced epoxy resins. It was concluded that the work of fracture values depended on the dimensions of the test specimens, crack length, and the type of fracture test. Beaumont and Phillips [8] investigated random glass fiber polyester composites with respect to the application of LEFM and the effect of strain rate, crack length, and test methods on fracture properties. It was reported that the stress-intensity factor did not vary significantly with the crack length when the specimens were fractured in a three-point-bending mode. More recently, Mandell et al [9] have shown that the candidate stress-intensity factor, K_Q, is almost insensitive to the thickness of the specimen for the combined roving-mat type of composites. The purpose of this study is to evaluate the fracture properties of random glass fiber epoxy composites by using various experimental techniques and then to study the effect of various material and test variables on the fracture behavior of such composites.

Material Preparation and Experimental Procedure

Materials

The matrix materials used in this study were a brittle epoxy resin, DER 334, and a flexible epoxy resin, DER 736 (Dow Chemical Co.). The two resins are compatible, and they can be physically blended in various proportions to form resin matrices having a range of properties. Generally, as DER 736 is added to DER 334, the yield point and modulus of elasticity decrease while the elongation to failure increases. Curing agent Z (20 percent by weight) was used for curing the epoxy resins. The glass reinforcement was in the form of chopped strand mat (M700) having a weight of 1½ oz./ft^2 bonded together with a high-solubility polyester resin. The chopped fibers are about 2 in. in length. The details of molding compos-

ite plates can be found elsewhere [*10*]. Specimens were cut from the molded plates using a water cooled diamond cutting wheel.

Fracture Tests—Fig. 1 shows the specimen geometries for the various types of fracture tests. The specimen thickness was maintained at 0.1 in. in all cases. The load-displacement records were obtained by using an Instron transverse strain sensor to monitor the crack mouth opening displacement. The strain sensor (G 57-12) is quite sensitive, and displacement values up to 1×10^{-4} in. could be measured easily from the chart recording. The load-displacement records obtained during the fracture tests were analyzed in accordance with the procedures recommended in ASTM Test for Plane-Strain Fracture Toughness of Metallic Materials (E 399-74), and a candidate stress-intensity factor was calculated using the appropriate K-equations [*11*].

The compliance of the specimen at various crack lengths was determined using two strips bonded to the specimen at the longitudinal centerline, ¼ in. on each side of the crack line. The displacement was monitored also using an Instron transverse strain sensor (G 57-11) which is more sensitive than the one used for crack-opening displacement measurements. The load-displacement records were obtained for specimens having cracks of various lengths, all produced by machining. Compliance values were determined for crack intervals of 0.05 in.

It should be pointed up that the machined slot necessary to simulate a crack does not provide exactly the same specimen compliance as a natural crack. In the ideal case, Srawley [*12*] has observed that although the compliance of a slotted specimen will slightly exceed that of a specimen with a natural crack, the derivative of compliance with respect to crack length may be approximately the same. In this study, the machined crack in the compliance specimen and the fracture test specimens were of the same type, and, hence, it is expected that the compliance specimen will simulate the behavior of the fracture-test specimen. The strain energy release rate is given by the following relation

$$G = \frac{P^2}{2t}\frac{dC}{da}$$

where P is the fracture load as obtained from the load displacement record, t is the thickness of the sample, and dC/da is the rate of change of compliance with the crack length.

Results and Discussion

The tensile and fracture properties of two blended epoxy resins are shown in Table 1. It is seen that the elongation to failure is increased

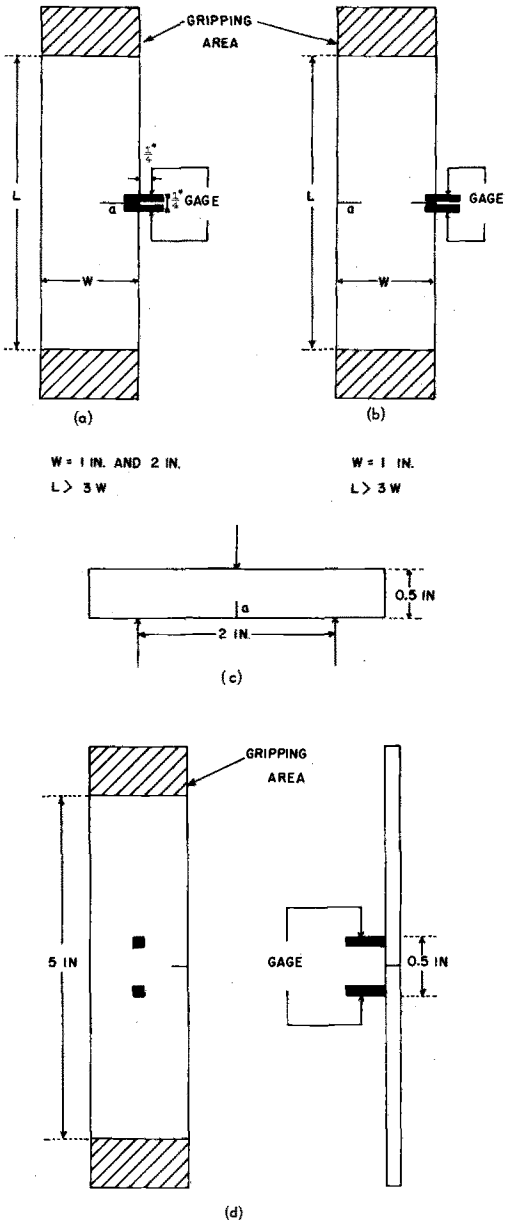

(*a*) SEN specimen.
(*b*) DEN specimen.
(*c*) NBT specimen.
(*d*) SEN compliance specimen.
FIG. 1—*Fracture test specimens.*

TABLE 1—*Tensile and fracture properties of resin materials.*

Material	Tensile Yield Strength, psi	Modulus of Elasticity	Strain to Failure, %	K_Q, ksi·in.$^{1/2}$ (a/w = 0.2)
70% DER 334 30% DER 736 (brittle resin) Material A	9 000 to 10 500	4.3 to 4.75 × 10^5	2.5 to 4.2	2.25
70% DER 736 30% DER 334 (flexible resin) Material C	3 300 to 5 000	2.8 to 3.6 × 10^5	25 to 80	2.27

greatly for the highly flexibilized epoxy blend. It has been reported earlier [*10*] that the tensile strength and modulus of composites with the two resin matrices were different, but the elongation to failure was observed to be almost independent of the resin elongation. This indicates that the toughness parameters for the two types of composites may not be much different. The candidate stress-intensity factors for the two resin blends are identical, indicating that the notch sensitivity of the blends is not changed by the addition of the more flexible resin.

Table 2 lists the effect of loading conditions on the candidate stress-intensity factor and the notch strength of the brittle epoxy composite. For the pin-loading arrangement, two 1-in. square pieces were bonded to the specimen ends to avoid bearing failure at the loading points. The minimum gage length used was $3w$ where w is the width of the specimen. It is seen from these results that the K_Q values are identical for the two end conditions. It was, thus, decided to use wedge grip loading with the gage length greater than $3w$ for all subsequent tests.

TABLE 2—*Effect of loading conditions on fracture results of brittle epoxy composite* (v_f = *0.29,* a/w = *0.4*).

Wedge Grip Loaded, Gage Length			Pin Loaded, Gage Length
7 in.	5 in.	3 in.	3 in.
		K_Q ksi·in.$^{1/2}$	
9.3	9.3	9.3	9.9
10.5	10.2	9.6	9.8
9.2	9.3	9.8	9.7
9.2	9.7	10.4	9.7
		σ_A psi	
4300	4900	4675	4500
4825	5000	5400	4500
4550	5000	5260	4700
4500	4750	4840	4150

The load displacement records for the brittle and flexible epoxy composites (V_f = 29 percent) are shown in Fig. 2 for comparison purposes. It is found that the crack mouth opening displacement for the flexible epoxy composite is greater than that for the brittle resin composite. This implies that the deformation, or damage, at the crack tip prior to unstable crack propagation is greater in the case of the flexible resin composite. This is possible because when fiber-matrix debonding initiates at the crack tip, the constraint provided by the fibers to the resin rich area is decreased, and the more flexible resin may undergo larger deformation at the crack tip than the brittle resin. Debonding of the fibers ahead of the crack in these type of composites is known to occur at about 65 percent of the fracture load [*13*]. Figure 3 shows the K_Q values plotted against the crack size for the brittle and flexible resin composites. The candidate stress-intensity factor decreases as a/w decreases. Four specimens were tested at each crack length. At larger crack lengths ($a/w > 0.2$), the K_Q values are almost independent of the starter crack length. This is in agreement with the behavior of many metallic materials. The lower K_Q values, at very small crack lengths for metals, results from the increased amount of deformation or gross section yielding which produces fracture at a lower value of critical load. In the case of these composites, it can be thought that a greater amount of debonding at the crack tip, or gross section debonding, may occur which, in turn, results in a lower value of critical load. It is also noted from Fig. 3 that the flexible resin composite shows only slightly higher K_Q at all crack lengths which may be due to the greater

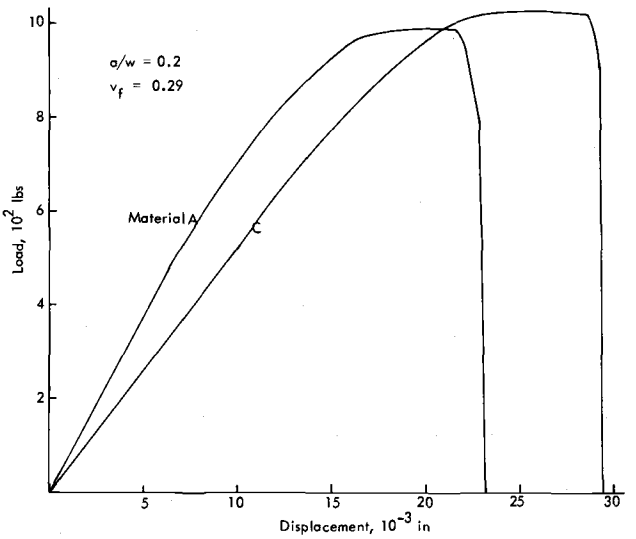

FIG. 2—*Load displacement records for epoxy-resin composites.*

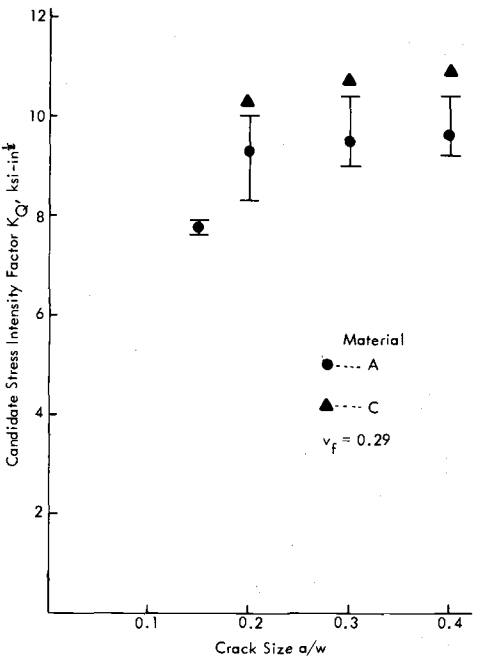

FIG. 3—*Variation of* K_Q *with crack size for single-edge, notched specimens.*

amount of debonding at the crack tip in the flexible epoxy composites as compared to the brittle epoxy composites.

Effect of Fiber Concentration

Figure 4 shows the variation of the K_Q values with fiber volume fraction for these materials. The K_Q values increase with increasing fiber concentration. The strength of the composite also increases with increasing fiber concentration. Thus, in this class of materials, one has the effect of increasing tensile strength corresponding to an increase in fracture toughness.

Figure 5 shows the notched tensile strength as a function of crack size for these materials. It is clear from this figure that both types of composites are notch sensitive, and their notched strengths are almost identical at each crack length although the unnotched tensile strength of the brittle epoxy composite is slightly higher than that of the flexible epoxy composite. It appears that the fracture behavior of random fiber epoxy composites is crack dominated, and, thus, the LEFM approach should be applicable to these materials, providing that the recommended guidelines for specimen geometry are followed.

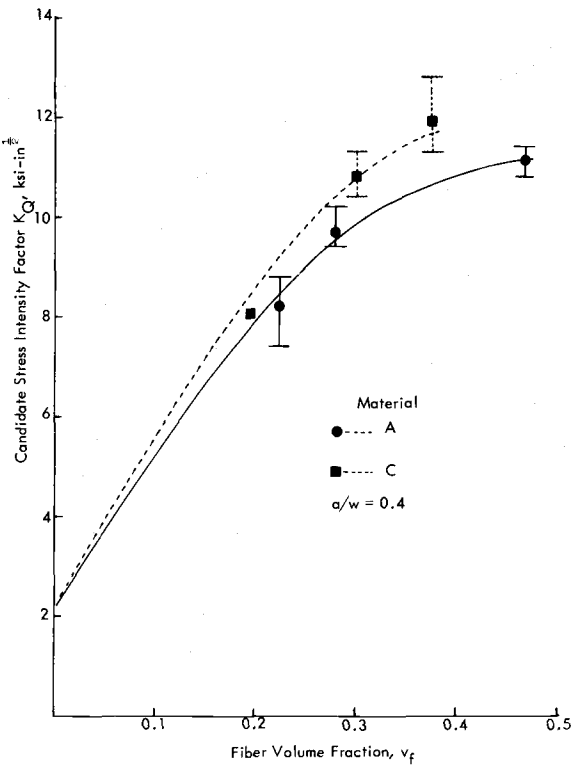

FIG. 4—*Variation of* K_Q *with fiber volume fraction for epoxy composites.*

To study the effect of specimen size on the notched tensile strength and fracture toughness, specimens with varying widths (a/w ratio kept constant) were tested. Figure 6 shows the notched tensile strength as a function of specimen width. It seems that the notched tensile strength decreases as the width is increased. Table 3 shows the candidate stress-intensity factor values for 1 and 2-in.-wide specimens. A minimum of three specimens were tested at each specimen width. The average K_Q values are lower for the 2-in.-wide specimens than for the 1-in.-wide specimens. This behavior is consistent with the notched tensile strength behavior. The reason for this behavior may also be explained by gross section debonding occurring at small a/w values as described earlier.

Effect of Notch-Root Radius

The effect of notch-tip radius on the fracture toughness of metallic materials is well known. The fracture toughness increases as the notch-tip radius is increased above a certain critical notch-tip radius. For typical

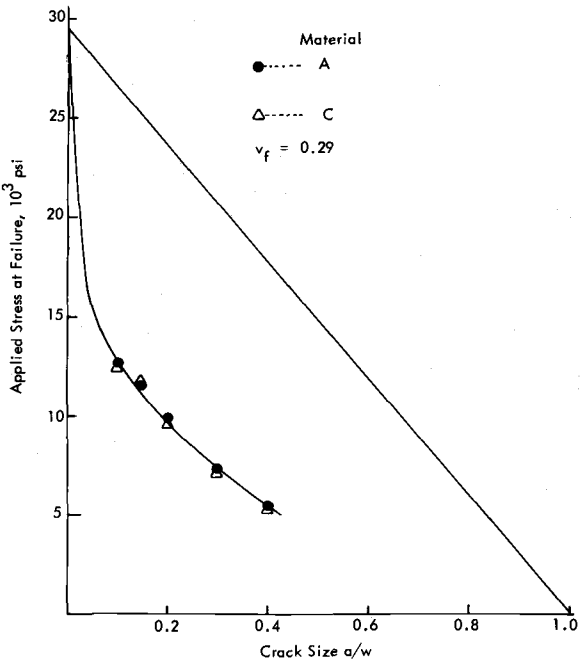

FIG. 5—*Notched tensile strength versus crack size for epoxy.*

high-strength metals, the critical notch-tip radius is reported to be in the range of 10^{-4} to 10^{-2} in. Some work has been reported on the effect of the notch-tip radius on the toughness of polyester resins and it has been shown that the toughness of the polyester resin increases as the radius of the notch root increases [*14*]. Similar observations have been made for some metal matrix composites. In resin composite materials, the situation is different. It has been reported that for chopped and woven fabric composites, the fracture stress is independent of notch-root radius below a value of $r = 0.10$ in. [*9*]. Although the value of critical notch-tip radius will be a function of the structure of the composite, the critical notch-root radius in a composite seems to be at least an order of magnitude greater than that in most metallic materials.

To vary the notch-tip radius, small holes of different sizes were drilled at the tip of a machined notch. The candidate stress-intensity factor and the strength results for different crack-tip radii are presented in Table 4. It is seen that in the range of notch-root radii considered in this study, the K_Q values and strength values were insensitive to the notch sharpness. These results suggest that extra sharpening of notches is not necessary for the materials, and machined notches will give useful fracture results.

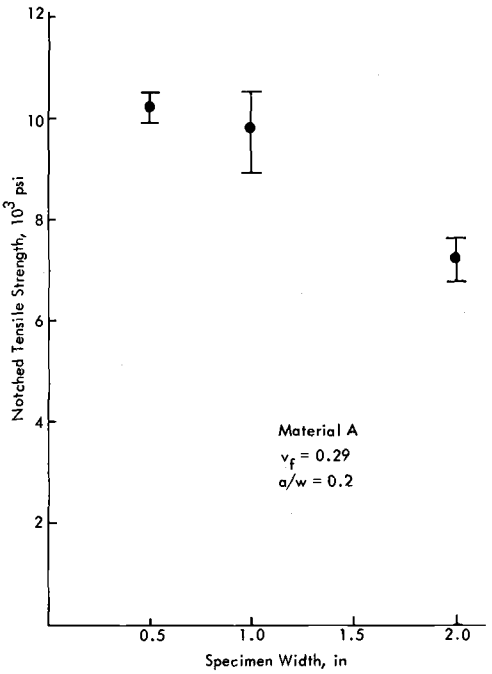

FIG. 6—*Notched tensile strength as a function of specimen width for composite using brittle epoxy matrix.*

Thickness Effects

The fracture toughness of metallic materials is known to depend on the thickness of the test specimen. Plane-stress conditions exist at the crack tip for very thin specimens, whereas for thicker specimens, plane-strain conditions can exist in the center of the sheet at the crack tip. In composite materials, very little is known about the effect of thickness on the toughness parameters. Tests were conducted for specimens having a range of thicknesses to study the fracture behavior of the material as a function

TABLE 3—*Effect of specimen width on fracture results.*

Material	*a/w*	Average K_Q, ksi·in.$^{1/2}$	Average Fracture Stress, psi	Crack Mouth Displacement, in.
		Brittle Resin Composites, $v_f = 0.29$		
1 in. wide	0.2	9.3	10 000	0.023
2 in. wide	0.2	8.05	7 200	0.022
		Flexible Resin Composites, $v_f = 0.29$		
1 in. wide	0.2	10.20	10 500	0.030
2 in. wide	0.2	8.50	7 300	0.030

TABLE 4—*Effect of notch root radius on fracture results* ($v_f = 0.29$).

Notch Root Radius, in.	Brittle Resin Composites				Flexible Resin Composites			
	K_Q, ksi·in.$^{1/2}$	Average	σ_A, psi	Average	K_Q, ksi·in.$^{1/2}$	Average	σ_A, psi	Average
0.007	7.4		4700		9.1		5000	
	11.0		5800		10.7		5450	
	10.2	9.5	5120	5270	10.0	10.0	5250	5230
0.010	10.0		4620		8.7		4720	
	10.8		5800		11.3		5550	
	9.6	10.1	4575	4995	10.5	10.2	4800	5025
0.012	9.5		4960		11.0		5600	
	11.0		5400		11.1		5550	
	10.2	10.2	5225	5200	10.8	11.0	4975	5370
0.020	10.3		4500		10.7		5130	
	8.8		4950		10.2		5000	
	10.5	9.8	5300	4915	11.2	10.7	5400	5175

of thickness. Thin specimens were obtained by reducing the number of mat layers in the composite. For obtaining very thick plates, two or more plates were bonded together using the matrix materials as an adhesive. Figure 7 shows the candidate stress-intensity factor as a function of specimen thickness for the brittle resin composite. The values of K_Q are independent of the thickness in the range of thicknesses considered here. The crack propagation was in the plane of the notch in all cases.

The behavior of these composites is in contrast with the behavior of most metallic materials in that no transition of fracture behavior from plane stress to plane strain takes place in the normally encountered thickness range. It appears that microfailure of these composites takes place under plane-strain conditions due to the existence of triaxial stresses in the matrix material resulting from fiber constraint. This was evidenced in an earlier study [*10*].

In all of the previous experiments, it was observed that massive damage occurs at the crack tip prior to unstable crack growth. This damage is characterized by fiber-matrix debonding and is known to occur in almost all composite materials. The debonding at the crack tip initiates at loads much lower than the maximum fracture loads. In the present study, the development of this debonding zone was observed using transmitted light

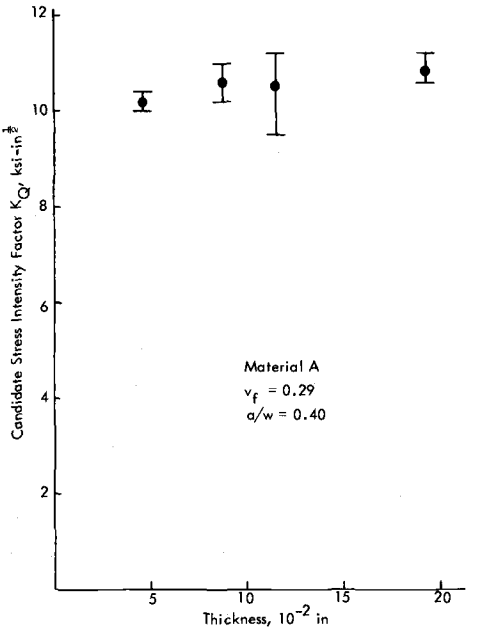

FIG. 7—*Variation of* K_Q *with specimen thickness for brittle composite using brittle epoxy matrix.*

to illuminate the specimen while under load. Initially, the crack-tip zone is quite transparent, and, when the load is gradually increased, a translucent zone initiates at the crack tip. The size of this translucent zone increases as the load is increased and finally spreads along the plane of the crack to such an extent that unstable fracture occurs. The damage is a result of debonding of the fibers from the matrix material and matrix cracking ahead of the crack tip. The initiation of damage at the crack tip was established by loading a notched specimen ($a/w = 0.2$) to various fractions of its ultimate fracture load and by then microscopically examining polished cross sections of the region near the crack tip. It was established by this procedure that the damage initiates at 65 percent of the fracture load [*13*]. This is an approximate value for this type of composite and will depend somewhat on the a/w ratio. Also, it was shown that the size of the debonded zone and its shape was comparable to the plastic zone in a metal and that the radius of the debonded zone could be calculated using the same equations for calculating the radius of plastic zones [*14*].

Since the critical stress-intensity factor should correspond to the crack-initiation point, it can be argued that K_Q should be based on the load corresponding to the onset of debonding in the material. If the stress-intensity factor corresponding to debonding is denoted by K_D, its value can be calculated by substituting 65 percent of the maximum load in the appropriate K equation. Table 5 shows the stress-intensity factor K_D at various crack lengths and is compared with the K_Q values obtained earlier. The K_D values are lower than the K_Q values, and it is interesting to note that the K_D values seem to be independent of crack length, whereas the K_Q values show a slight dependence on initial crack lengths. In some

TABLE 5—*Comparisons of* $K_{D(Debonding)}$ *with* K_Q *for brittle epoxy composites* ($v_f = 0.29$).

a/w	$K_{D(Debonding)}$, ksi·in.$^{1/2}$	Average	K_Q, ksi·in.$^{1/2}$	Average
0.15	6.6		7.8	
	7.4		7.6	
	7.2	7.1	7.5	7.7
0.20	8.0		10.0	
	6.3		8.3	
	7.6	7.3	9.9	9.4
0.30	7.0		10.3	
	7.5		9.4	
	7.4		10.4	
	7.5	7.4	9.0	9.8
0.40	7.4		9.3	
	7.7		10.2	
	7.7		9.3	
	7.3	7.6	9.7	9.7

composites, where debonding starts at a much earlier stage of the fracture process, the K_D values can be significantly lower than the K_Q values. In random fiber polyester composites, K_D values are as low as one third of K_Q values [*16*]. The more conservative K_D values may be more appropriate if used in design applications.

Effect of Measurement Technique

Compliance Technique—The K_Q values obtained from the analytical technique, as described previously, and the stress-intensity factor values obtained from a compliance test refer to the resistance of a material to crack initiation and, thus, measure the same material property. In the analytical technique, an assumption is made regarding the material isotropy, but the compliance technique does not involve such an assumption. It has been shown that the compliance method of measuring strain energy release rate is applicable to anisotropic or orthotropic materials [*4*]. The materials considered in this study are macroscopically isotropic, and, thus, the relations developed (K equations) for isotropic materials were used in calculating the stress-intensity factor. The validity of using these relations thus can be checked by determining K_Q values from the compliance method.

Thus, the compliance method was used here, and the compliance of the fracture specimen at various crack lengths was determined (see Fig. 1*a*) from the load displacement records at various crack lengths. The compliance value at each crack length is obtained and plotted as a function of crack length as shown in Fig. 8. The slope of the curve at any crack length will give the rate of change of compliance with respect to a/w. Table 6 lists the critical strain energy release rate and stress-intensity factor at various crack lengths. The toughness parameters seem to be almost independent of the crack length. The K_{Qc} values are about 20 percent lower than the K_Q values obtained earlier.

Double-Edge Notch Tension (DEN) Tests

As stated earlier, an objective of this study has been to determine the applicability of LEFM techniques to characterize the fracture behavior of random fiber composites. It was, thus, necessary to evaluate a number of experimental measurement techniques. DEN tests for the determination of stress-intensity factors are used widely for conventional metallic materials. It has been reported that this technique can be applied successfully to many composite materials and yields results which are consistent with other experimental techniques such as the compliance method [*17*]. Figure 9 shows the candidate stress-intensity factors for the brittle resin and flexible resin composites. The K_Q values are independent of crack length

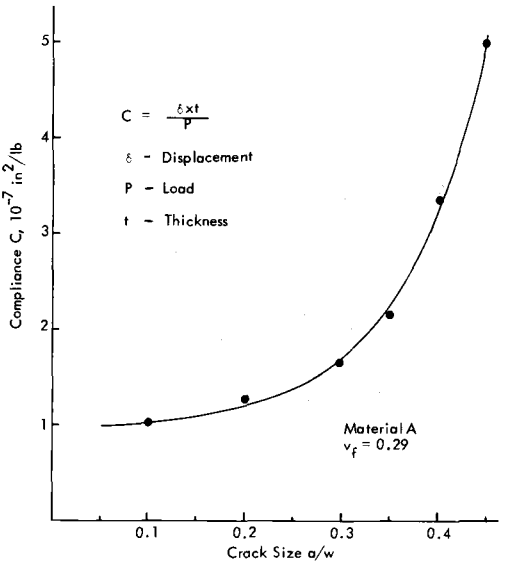

FIG. 8—*Compliance of a specimen as a function of crack size.*

TABLE 6—*Compliance results as a function of crack length.*

a/w	$\frac{E}{2}\frac{dc}{d(a/w)}$	K_{QC}[a] ksi·in.$^{1/2}$	K_{QC}[a] Average	G,[b] in·lb/in.^{2}
0.2	0.445	7.7		
		7.6		
		6.7		
		7.3	7.4	28.6
0.3	1.24	7.9		
		8.0		
		8.3		
		7.8	8.0	36
0.4	2.0	8.0		
		8.0		
		6.9		
		7.4	7.6	33.1

[a] $K_{QC} = p/wt\,(1-\gamma^2)\sqrt{(E/2)[dc/d(a/w)]}$.
[b] $G = [K_{QC}^2(1-\gamma^2)/E]$.

except at very small crack lengths. The K_Q values from the DEN tests are comparable to the K_Q values obtained from the compliance test but are lower than those obtained from single-edge notch (SEN) tests. It is possible that the determination of the fracture load, P_Q, from the load displacement records in the DEN and SEN tests may not correspond to the

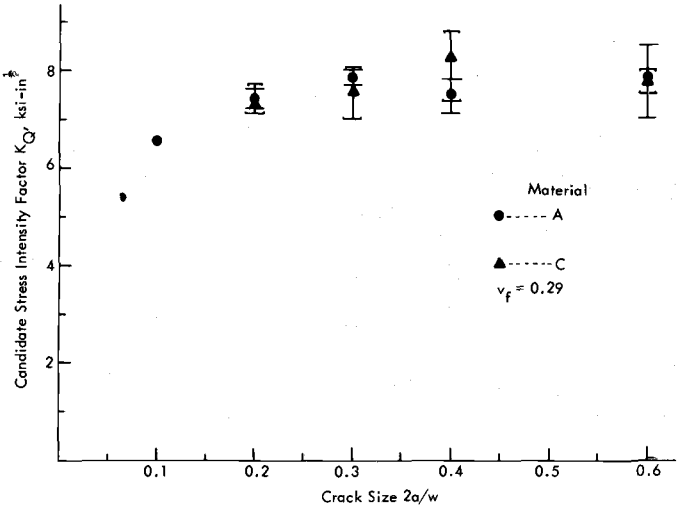

FIG. 9—*Variation of* K_Q *with crack size for epoxy composites using DEN specimen.*

same stage or extent of crack growth or damage. The load, P_Q, in the DEN test may correspond to a smaller amount of crack-tip damage than that in the SEN tests, and this may result in lower K_Q values for DEN tests.

Notch-Bend Tests

The load deflection curves obtained from three-point, notch-bend tests were analyzed to obtain the candidate stress-intensity factor K_Q. The values of K_Q for the two composites are shown in Fig. 10 as a function of crack length. It is seen that the K_Q values are independent of crack length within the experimental scatter. The flexible resin composite gives slightly higher values of K_Q as compared to the K_Q values for the brittle resin composite. The K_Q values measured by the notch-bend tests agree more closely with the DEN test results than with the SEN results.

Fracture-Toughness Mechanisms

As mentioned earlier, the debonding process in random fiber composites seems to be the most dominant energy absorbing mechanism. Figures 11 and 12 show scanning electron micrographs (SEM) of the fracture surfaces of SEN specimens. Both these figures clearly show that fiber debonding and fiber pull-out mechanisms are operative in these composites. Figure 11 also shows debonding and pullout of fibers which were

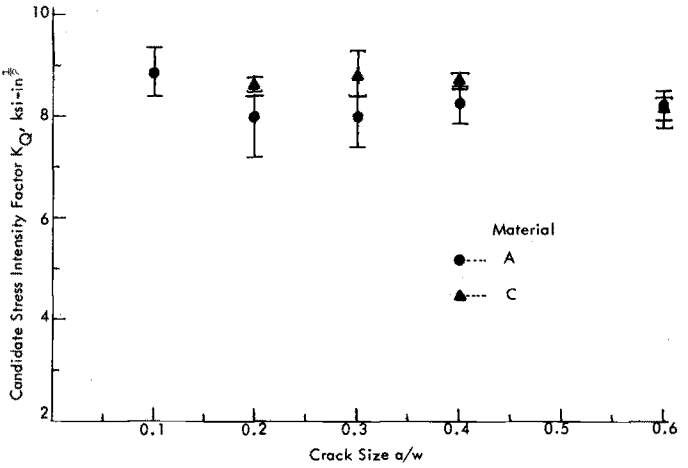

FIG. 10—*Variation of* K_Q *with crack size for epoxy composites using NBT specimen.*

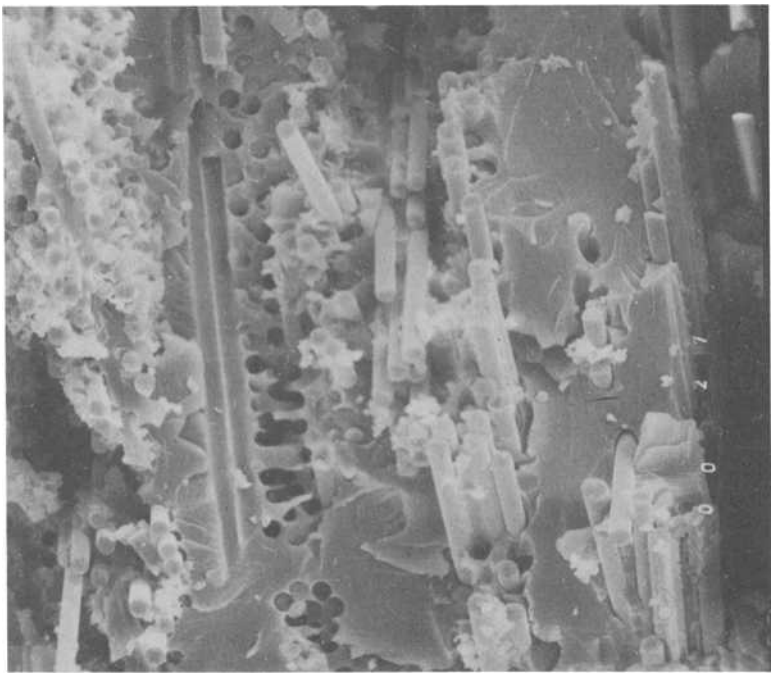

FIG. 11—*Fracture surface of a brittle epoxy composite (SEN) near the crack tip* (×300).

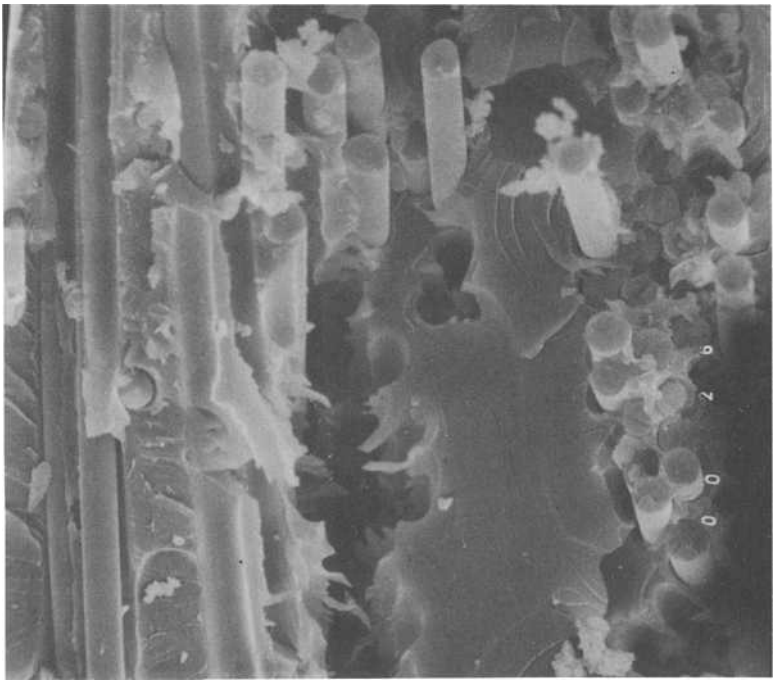

FIG. 12—*Matrix crack formed due to debonding and pull out of fibers* (×600).

transverse to the load direction. The total fracture energy of the system can be written as follows

$$\gamma_{\text{composite}} = \alpha \gamma_D + \alpha \gamma_{PO} + V_m \gamma_m + V_f \gamma_f$$

where γ_D and γ_{PO} are the absorbed energy values for fiber debonding and pullout, respectively, and γ_m and γ_f are the fracture-energy values of the matrix and fibers, respectively. Since the fibers are randomly oriented, not all the fibers constitute towards the debonding and pull-out energy, and, thus, a factor α is introduced. The expressions for debonding energy and pull-out energy are as follows [*16*]

$$\gamma_D = \frac{V_f \sigma_f^2 Y}{4 E_f}$$

$$\gamma_{PO} = \frac{V_f \sigma_f l_c^2}{24 l} \quad (l > l_c)$$

where

V_f = fiber volume fraction,
σ_f = fiber strength,
E_f = modulus of fibers,
Y = debonded length,
l_c = critical transfer length, and
l = length of fibers.

It should be pointed up that these expressions have been derived for unidirectional fiber composites and, thus, application of these expressions to evaluate the fracture energy for random fiber composites only can be approximate. Recently [*18*], it has been argued that the foregoing expression for pull-out energy should be applicable for any fiber orientation. It was suggested that the frictional forces which oppose pullout will always act along a fiber regardless of its orientation, and the fiber will not pull out until the stress in the fiber direction reaches the value equivalent to that for uniaxial fibers. Hence, provided only a small fraction of fibers are oriented near the crack plane, it is to be expected that the foregoing expressions for energy absorption will be reasonable approximations. Thus, for these calculations, the value of α in the previous equation can be taken to be unity. Although some work also will be done during the interfacial tensile failure of transverse fibers, it can be thought that this work will be of the order of the work done in fracturing an equivalent area of matrix material. If the value of α is taken as unity, then the debonding and pull-out work will be slightly overestimated whereas $V_m \gamma_m$ will be slightly underestimated.

To evaluate γ_D, the debonded length Y has to be estimated from the optical micrographs of fracture specimens and the visual observation of debonding at the crack tip. The value of Y is estimated to be about 0.075 in. If the value of σ_f and E_f is taken to be 250 000 psi and 10.5×10^6 psi, respectively

$$\gamma_D = \frac{0.29 \times (250\,000)^2 \times 0.075}{4 \times 10.5 \times 10^6} = 32.6 \text{ in·lb/in.}^2 (57 \times 10^5 \text{ erg/cm}^2)$$

To estimate the pull-out energy, it can be thought that the fibers having their ends within the debonded region will pull out. It should be mentioned that the fiber matrix shear strength falls to some smaller value τ after debonding, because the load transfer can take place due to the presence of frictional forces at the interface. If this is the case, then there may be some fibers which do not break at the crack plane but break some distance from the crack plane in the debonded zone, and, thus, some pull-out work will be done in the pulling out of such fibers. It can, however, be assumed that if fibers are uniformly strong, they will break at the

crack plane where they are stressed at a maximum. Substitution of l_c, l, σ_f and V_f in the pull-out energy equation yields

$$\gamma_{PO} = \frac{0.29 \times 250\,000 \times (0.075)^2}{24 \times 2} = 8.6 \text{ in·lb/in.}^2 (15 \times 10^5 \text{ erg/cm}^2)$$

The $V_m \gamma_m$ and $V_f \gamma_f$ terms will be comparatively small. In the case of the matrix, it has been shown previously [*10*] that as a result of triaxial constraint imposed by the random closely packed fibers, even the flexible resin behaves in a brittle fashion. SEM photographs of fracture surfaces have confirmed the brittle behavior of the matrix [*10*]. It has been determined that the value of γ_m for the matrix is approximately 2 in·lb/in.^{2} [*10*]. The theoretically estimated value of γ_c is, thus, reasonably comparable to the experimentally observed values of γ_f which ranged from 31 to 46 in·lb/in.^{2} as determined from notch bend tests [*16*].

The previous calculations show that the debonding mechanism and pull-out mechanism can be used to estimate the fracture energy of random fiber composites. These calculations also show that the debonding mechanism is more dominant as compared to the pull-out mechanism in random fiber composites.

Conclusion

The values of the candidate stress-intensity factor, as obtained from three different tests, are listed in Table 7. Also shown is the average K_Q determined from all tests and the variation of K_Q for each test from the average K_Q. The individual results are within 11 percent of the average and, thus, indicate that the stress-intensity approach is suitable to characterize the fracture behavior of random fiber composites. The DEN and notch-bend test methods give more conservative values of K_Q than does the SEN test. Furthermore, it is suggested that the stress-intensity factor corresponding to the initiation of debonding be used as a design param-

TABLE 7—*Average* K_Q *values for brittle epoxy composites.*

Fracture Test	Average K_Q (overall a/w ratio) ksi·in.$^{1/2}$	Average $\bar{K}_Q$ of all Tests	Percent Variation of K_Q from $\bar{K}_Q$
Single-Edge Notch Tension	9.39	...	−11
Double-Edge Notch Tension	7.70	8.46	−9
Notch-Bend Test	8.30	...	−1.9

eter providing that further studies demonstrate its independence of specimen geometric variables.

It can also be concluded that for this class of random short fiber composites, the value of candidate stress-intensity factor, K_Q, is independent of specimen thickness. The value of K_Q is independent of crack length in the notch-bend test and DEN test and in the SEN specimen for a/w values above 0.2. It was also concluded that K_Q is independent of notch-root radius between values of 0.007 and 0.020 in.

Acknowledgments

The authors would like to acknowledge the support of the U.S. Air Force Office of Scientific Research under Grant No. AFOSR-72-2214F.

References

[1] Outwater, J. O. and Murphy, M C., "On the Fracture Energy of Unidirectional Laminates," 24th Annual Technical Conference, Society of the Plastics Industry, 1969, pp. 1-8.

[2] Cooper, G. A. and Kelly, A., *Journal of the Mechanics of Physics and Solids,* Vol. 15, 1967, p. 279.

[3] Zweben, C., *Journal of the Mechanics of Physics and Solids,* Vol. 19, 1971, p. 103.

[4] Wu, E. M., "Fracture Mechanics of Anisotropic Plates," Composite Materials Workshop, Technomic Publishing Co., Inc., 1968, p. 20.

[5] Konish, H. J., Swedlow, J. L., and Cruse, T. A., *Journal of Composite Materials,* Vol. 6, 1972, p. 114.

[6] Owen, M. J. and Bishop, P. T., *Journal of Composite Materials,* Vol. 7, April 1973, p. 146.

[7] Ellis, C. D. and Harris, B. H., *Journal of Composite Materials,* Vol. 7, Jan. 1973, p. 76.

[8] Beaumont, P. W. R. and Phillips, D. C., *Journal of Materials Science,* Vol. 7, 1972, pp. 682-686.

[9] Mandell, J. F., McGarry, F. J., Kashihara, R., and Bishop, W. R., "Engineering Aspects of Fracture Toughness: Fiber Reinforced Laminates," 29th Annual Technical Conference, Society of the Plastics Industry, Feb. 1974, 17-D, pp. 1-11.

[10] Gaggar, S. K. and Broutman, L. J., "Strength Properties of Random Fiber Mat Composites," 29th Annual Technical Conference Society of the Plastics Industry, 1974, 17E.

[11] Brown, W. F. and Srawley, J. E., *"Plane Strain Crack Toughness Testing of High Strength Metallic Materials," ASTM STP 410,* American Society for Testing and Materials, 1966.

[12] Srawley, J. E. "Plane Strain Fracture Toughness," *Fracture,* M. Liebowitz, Ed., Academic Press, 1969, pp. 45-69.

[13] Gaggar, S. and Broutman, J., "Crack Growth Resistance of Random Fiber Composites," *Journal of Composite Materials,* Vol. 9, July 1975.

[14] Gaggar, S. and Broutman, L. J., *International Journal of Fracture,* Vol. 10, 1974, p. 606.

[15] Harris, B. and de Ferran, E. M., *Journal of Material Science,* Vol. 4, 1969, p. 1023.

[16] Gaggar, S., "Strength and Fracture Properties of Random Glass Fiber Composites," Ph.D. thesis, Illinois Institute of Technology, Chicago, Ill., May 1974.

[17] Trachte, K. L. and Dibenedetto, A., *International Journal of Polymeric Materials,* Vol. 1, 1971, pp. 75-94.

[18] Williams, T., Allen, G., and Kaufman, M. S., *Journal of Materials Science,* Vol. 8, 1973, pp. 1765-1787.

W. G. Clark, Jr.[1]

Effect of Cold Working on K_{Iscc} in a 4340 Steel

REFERENCE: Clark, W. G., Jr., **"Effect of Cold Working on K_{Iscc} in a 4340 Steel,"** *Flaw Growth and Fracture, ASTM STP 631,* American Society for Testing and Materials, 1977, pp. 331-344.

ABSTRACT: The effects of cold working on the stress-corrosion cracking performance of a 140 ksi (965 MPa) yield strength type 4340 steel are evaluated. Compact-toughness specimens representing 0, 10, 25, and 50 percent cold-worked material were subjected to an accelerated stress-corrosion test in hydrogen sulfide gas and the results expressed in terms of fracture mechanics parameters. The effect of mechanical strenghtening on K_{Iscc} is compared with the effect of metallurgical strengthening, and the influence of stress relieving and crack-plane orientation are considered. Results show that mechanical and metallurgical strengthening have a similar influence on K_{Iscc}, and stress relieving can improve the stress-corrosion resistance of cold-worked 4340 steel. No significant effect of crack-plane orientation on K_{Iscc} was observed.

KEY WORDS: crack propagation, environments, heat treatment, growth, cold working, stresses, corrosion, fractures (materials)

It is well recognized that the susceptibility of structural alloys to stress-corrosion cracking is a strength dependent phenomenon [*1,2*].[2] In general, as the strength of a given alloy increases, the susceptibility to stress-corrosion cracking also increases. This observation is based primarily on the evaluation of the effect of metallurgical strengthening (heat treating) on stress-corrosion performance. However, there are many applications where the inherent strength of an alloy can be increased as the result of mechanical deformation (cold working) associated with either the fabrication or operation of a component. Consequently, it is equally important to recognize the potential influence of mechanical strengthening on stress-corrosion cracking susceptibility.

This paper presents the results of an investigation designed to evaluate the effect of cold working on the stress-corrosion cracking performance of a 140 ksi (965 MPa) yield strength type 4340 steel. Fatigue precracked

[1]Fellow engineer, Mechanics Department, Westinghouse Research Laboratories, Pittsburgh, Pa. 15235.

[2]The italic numbers in brackets refer to the list of references appended to this paper.

compact-toughness specimens prepared from material which had been cold worked at various amounts (0, 10, 25 and 50 percent through the thickness) were exposed to a 50 psig (344.7 kPa) hydrogen sulfide (H_2S) gas environment and the fracture performance evaluated. The results of the tests are expressed in terms of the fracture mechanics stress-corrosion susceptibility parameter, K_{Iscc}, and the value of the plane-strain, stress-intensity factor below which an existing crack will not grow due to stress corrosion [*2*].

The effect of mechanical strengthening on K_{Iscc} is compared with the effect of metallurgical strengthening, and a limited evaluation of the effect of stress relieving is included. The influence of crack-plane orientation in the cold-rolled plates is evaluated, and the results of a fractographic examination of the test specimens also are included.

Material and Specimen Preparation

The material involved in this investigation was taken from a 6.5 in. (16.5 cm) diameter by 24 in. (61 cm) long quenched and tempered American Iron and Steel Institute (AISI) type 4340 (ASTM A540, type B24) steel bar forging. The chemical composition and heat treatment are given next.

The chemical composition (weight percent) of the material was carbon—0.41; manganese—0.81; phosphorus—0.008; sulfur—0.011; silicon—0.23; chromium—0.86; nickel—1.77; molybdenum—0.39; copper—0.14; and iron—the balance.

The heat treatment was normalized at 1650°F (900°C) for 1 h, austenitized at 1500°F (816°C) for 1.5 h, oil quenched, tempered at 1080°F (582°C) for 8 h, and stress relieved at 1000°F (538°C) for 8 h (after straightening). The room-temperature tensile properties of the "as-received" (0 percent cold work) material are given in Table 1.

A 1.5-in. (3.8-cm) thick plate was cut from 6.5 in. (16.5 cm) diameter bar forging at the one-half radius location as noted in Fig. 1. This plate was then cut into smaller sections and various pieces cold rolled to 10, 25, and 50 percent reduction in thickness (B). The initial and final thickness of each test plate are noted next.

Plate No.	Initial Thickness	Final Thickness	Percent Cold Work
1	1.35 in. (3.43 cm)	1.22 in. (3.10 cm)	9.6
2	1.50 in. (3.81 cm)	1.125 in. (2.86 cm)	25
3	1.125 in. (2.86 cm)	0.60 in. (1.52 cm)	47

TABLE 1—*Room temperature tensile properties of test material.*

Condition	L-T Orientation				T-T Orientation			
	0.2% Yield Strength, ksi	Tensile Strength, ksi	Elongation, %	Reduction in Area, %	0.2% Yield Strength, ksi	Tensile Strength, ksi	Elongation, %	Reduction in Area, %
As received (0% cold worked)	139 (958 MPa)	151 (1040 MPa)	18	56	143 (985 MPa)	155 (1068 MPa)	16	44
10% cold worked	146 (1006 MPa)	160 (1102 MPa)	13	56	139 (958 MPa)	155 (1068 MPa)	11	34
25% cold worked	162 (1116 MPa)	171 (1178 MPa)	13	50	151 (1040 MPa)	169 (1164 MPa)	8	26
50% cold worked	171 (1178 MPa)	188 (1295 MPa)	11	45	159 (1095 MPa)	181 (1247 MPa)	7.2	17.4
25% cold worked + stress relief	...	...	...	...	155 (1068 MPa)	159 (1095 MPa)	18.5	57
50% cold worked + stress relief	...	...	...	...	172 (1185 MPa)	172 (1185 MPa)	16.5	54

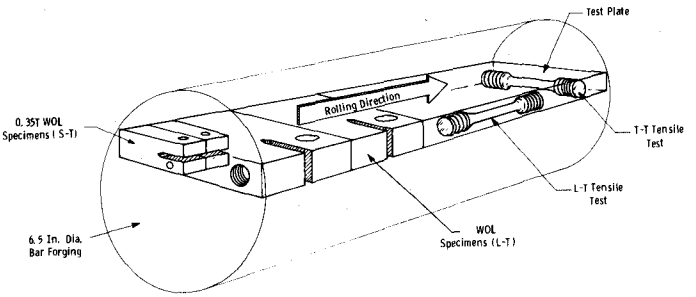

FIG. 1—*Layout of test specimens in original forging.*

$$\text{percent cold work} = \frac{B_{(\text{initial})} - B_{(\text{final})}}{B_{(\text{initial})}} \times 100$$

After cold rolling, wedge opening loading (WOL) type compact-toughness specimens (Fig. 2) were cut from the test plates. Two test specimen orientations were included. In one case, the specimens were prepared such that the plane of the notch was parallel to the long transverse direction of the plate and perpendicular to the major axis of the forging (L-T crack-plane orientation, see Fig. 1). In the other specimens, the notch plane was parallel to the major axis of the forging and perpendicular to the long transverse direction of the plate (T-L orientation). The test specimens taken from the 10 and 25 percent cold-worked plates were 1 in. (2.54 cm) thick and machined to the relative dimensions noted in Fig. 2. The test specimens taken from the 50 percent cold-worked plate were 0.5 in. (1.27 cm) thick with the same in-plane dimensions as a 1-in. (2.54-cm) thick specimen. Three 0.35-in. (0.89-cm) thick WOL specimens oriented in the S-T direction (Fig. 1) were also tested in this investigation. These specimens were machined from the broken halves of the as tested 1-in. (2.54-cm) thick WOL specimens from the 25 percent cold-worked plate. Tension test specimens (0.252 in., 0.64 cm diameter) were taken from each cold-worked test plate as noted in Fig. 1. The results of these tests are summarized in Table 1. Figure 3 shows the microstructure of the as received 25 and 50 percent cold-worked test plates. All of the WOL test specimens involved in this investigation were fatigue precracked in air prior to testing in the H_2S gas environment. The maximum stress-intensity factor associated with the precracking operation did not exceed 20 ksi$\sqrt{\text{in.}}$ (22 MPa$\sqrt{\text{m}}$), and the corresponding stress ratio (minimum stress/maximum stress) did not exceed 0.1.

Experimental Procedure

The stress-corrosion susceptibility testing involved in this investigation

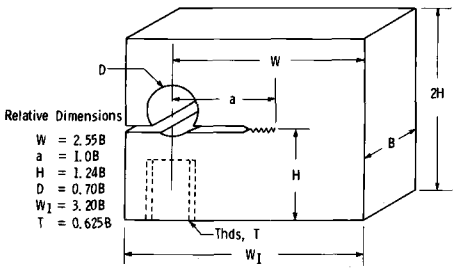

FIG. 2—*WOL type compact fracture toughness specimen (relative dimensions in terms of thickness* B).

was conducted at room temperature (80°F, 26.7°C) in a 50 psig (344.7 kPa) H_2S gas (99.6 volume percent (liquid phase) H_2S, typically 31 ppm water) environment in accordance with the rising load K_{Iscc} test procedure described by Clark and Landes [*3*]. Specifically, the test specimens were subjected to slow-rate tensile loading in the H_2S gas and the onset of subcritical crack growth determined from the corresponding load-deflection record. The rising load H_2S gas tests were conducted at a loading rate corresponding to a rate of change in stress intensity, $\dot{K}_I$, of 0.1 ksi$\sqrt{\text{in.}}$/min (0.11 MPa$\sqrt{\text{m}}$/min).

In addition to the rising load H_2S gas tests, one specimen (L-T orientation) from each test plate was subjected to a conventional room-temperature, air-environment fracture toughness test (K_{Ic} test) in accordance with ASTM Test for Plane-Strain Fracture Toughness of Metallic Materials (E 399-74).

One T-L orientation test specimen from both the 25 and 50 percent cold-worked plates also was subjected to a stress-relief heat treatment (8 h at 1000°F, 538°C) prior to testing in the H_2S environment. These tests were used to evaluate the influence of stress relieving on the stress-corrosion susceptibility of cold-worked 4340 steel. Following the K_{Iscc} testing, selected specimens were subjected to a detailed fractographic analysis with the scanning electron microscope.

Experimental Results

K_{Ic} and K_{Iscc} Testing

The results of the K_{Ic} and rising load H_2S gas tests are summarized in Table 2. Note that in all cases the critical toughness tests did not yield valid K_{Ic} values in that gross plastic deformation of the specimen occurred prior to failure. Test specimens much larger than those used in this program would be required to establish the room-temperature K_{Ic} of the 4340 steel in the as-received and cold-worked conditions involved here.

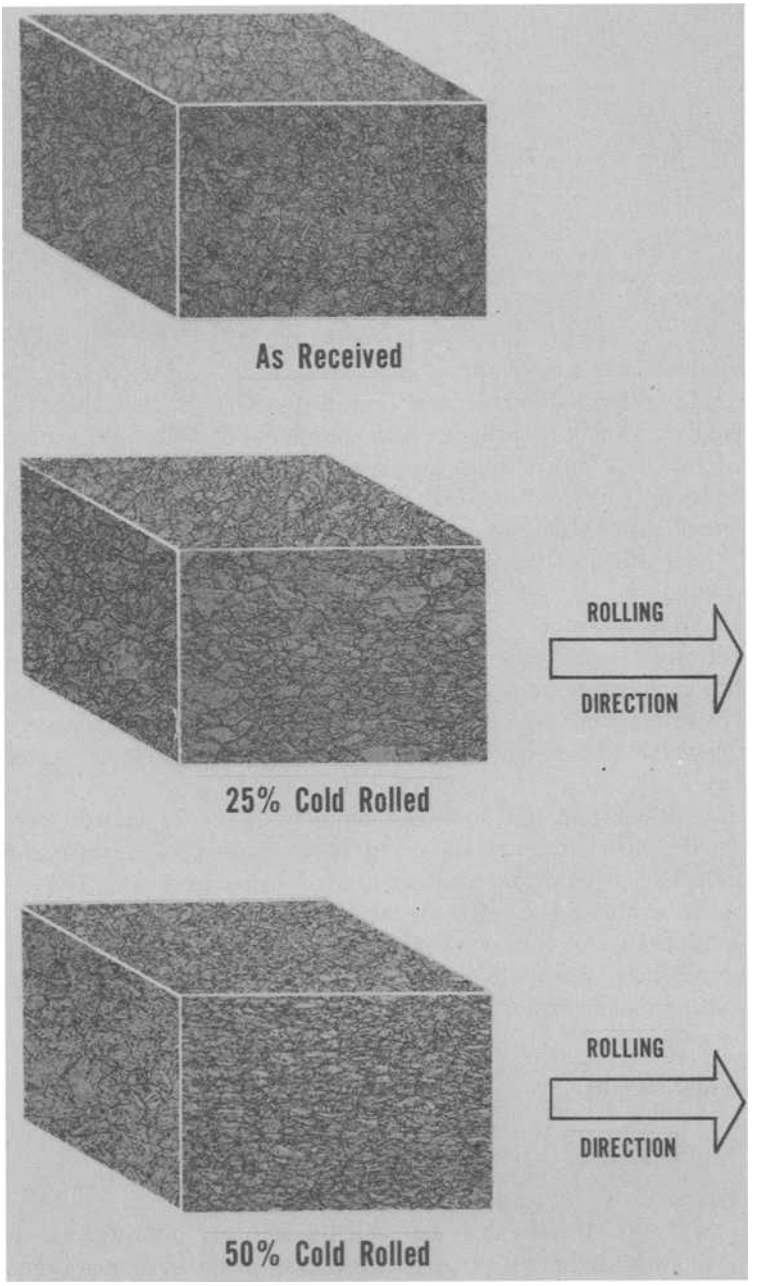

FIG. 3—*Microstructure of test plates* (×*355*).

TABLE 2—*Summary of* K_{Ic} *and* K_{Iscc} *test results.*

Specification Identification	Specimen Thickness	Cold Work, %	Specimen Orientation	Test Environment	Test Results
125-0-1	1 in. (2.54 cm)	0	L-T	air	gross plastic failure
125-0-2	1 in. (2.54 cm)	0	L-T	H_2S [a]	K_{Iscc} [b] = 106 ksi$\sqrt{\text{in.}}$ (116 MPa$\sqrt{\text{m}}$)
124-1	1 in. (2.54 cm)	0	L-T	H_2S	K_{Iscc} = 102 ksi$\sqrt{\text{in.}}$ (112 MPa$\sqrt{\text{m}}$)
124-2	1 in. (2.54 cm)	0	L-T	H_2S	K_{Iscc} = 104 ksi$\sqrt{\text{in.}}$ (114 MPa$\sqrt{\text{m}}$)
125-10-1	1 in. (2.54 cm)	10	L-T	H_2S	K_{Iscc} = 69 ksi$\sqrt{\text{in.}}$ (75.8 MPa$\sqrt{\text{m}}$)
125-10-2	1 in. (2.54 cm)	10	L-T	H_2S	K_{Iscc} = 72 ksi$\sqrt{\text{in.}}$ (79.1 MPa$\sqrt{\text{m}}$)
25-1	1 in. (2.54 cm)	25	L-T	H_2S	K_{Iscc} = 36 ksi$\sqrt{\text{in.}}$ (39.6 MPa$\sqrt{\text{m}}$)
25-2	1 in. (2.54 cm)	25	L-T	air	gross plastic failure
25-3	1 in. (2.54 cm)	25	T-L	H_2S	K_{Iscc} = 31 ksi$\sqrt{\text{in.}}$ (34.1 MPa$\sqrt{\text{m}}$)
25-4	1 in. (2.54 cm)	25 (stress relieved) [c]	T-L	H_2S	K_{Iscc} = 56 ksi$\sqrt{\text{in.}}$ (61.5 MPa$\sqrt{\text{m}}$)
25-1-1	0.35 in. (0.89 cm)	25	S-T	H_2S	K_{Iscc} = 36 ksi$\sqrt{\text{in.}}$ 39.6 MPa$\sqrt{\text{m}}$)
25-1-2	0.35 in. (0.89 cm)	25	S-T	H_2S	K_{Iscc} = 40 ksi$\sqrt{\text{in.}}$ (44 MPa$\sqrt{\text{m}}$)
25-1-3	0.35 in. (0.89 cm)	25	S-T	H_2S	K_{Iscc} = 32 ksi$\sqrt{\text{in.}}$ (35.2 MPa$\sqrt{\text{m}}$)
50-1	0.5 in. (1.27 cm)	50	L-T	H_2S	K_{Iscc} = 29 ksi$\sqrt{\text{in.}}$ (32 MPa$\sqrt{\text{m}}$)
50-2	0.5 in. (1.27 cm)	50	L-T	air	gross plastic failure
50-3	0.5 in. (1.27 cm)	50	T-L	H_2S	K_{Iscc} = 25 ksi$\sqrt{\text{in.}}$ (27.5 MPa$\sqrt{\text{m}}$)
50-4	0.5 in. (1.27 cm)	50 (stress relieved) [c]	T-L	H_2S	K_{Iscc} = 35 ksi$\sqrt{\text{in.}}$ (38.5 MPa$\sqrt{\text{m}}$)

[a] 50 psig (345 kPa) H_2S gas, 80°F (26.7°C).
[b] Apparent K_{Iscc}.
[c] 8 h at 1000°F (538°C).

Figure 4 presents a graphical summary of the rising load H_2S gas tests. Note that the apparent K_{Iscc}[3] measured in the H_2S gas is inversely related to the amount of cold work. Note also that the test specimen orientation in the 25 and 50 percent cold-worked plates does not appear to have a significant effect on the fracture performance measured in the H_2S environment. Table 2 and Fig. 4 also show that stress relieving the cold-worked material can improve the resistance to stress-corrosion cracking.

Figure 5 presents the results of the H_2S environment stress-corrosion testing plotted as a function of the 0.2 percent offset yield strength (L-T direction) measured for each test plate (Table 1). These data clearly show that the susceptibility to stress-corrosion cracking increases (decreasing K_{Iscc}) as the extent of mechanical strengthening increases. The dashed line in Fig. 5 shows the relationship between the apparent K_{Iscc} in H_2S gas and the yield strength of 4340 steel heat treated to various strength levels [*4*]. Note that the apparent K_{Iscc} versus yield strength behavior is essentially independent of the strengthening mechanism. Specifically, for the 4340

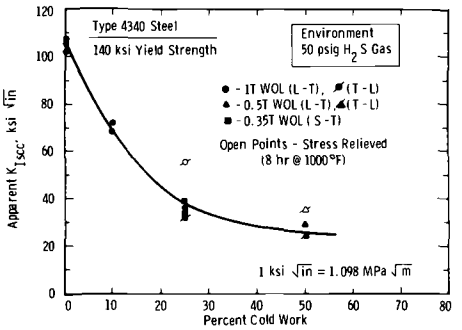

FIG. 4—*Effect of cold working on apparent* K_{Iscc}.

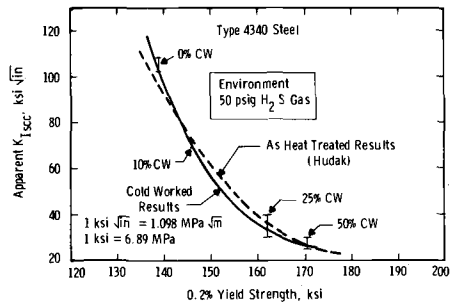

FIG. 5—*Effect of yield strength on apparent* K_{Iscc}.

[3]The term "apparent K_{Iscc}" instead of K_{Iscc} is used in this investigation to distinguish between results developed under rising load conditions and results obtained by means of long time, constant load, or constant displacement testing.

steel involved here, mechanical strengthening or metallurgical strengthening to a common yield strength level results in essentially the same value of apparent K_{Iscc}.

Fractographic Examination

Figure 6 shows the variation in macroscopic fracture appearance with the amount of cold work for specimens tested in the H_2S gas environment. Note that an extensive amount of through-the-thickness delaminating occurred in the 25 and 50 percent cold-worked test specimens (both L-T and T-L crack-plane tests). The delaminations adjacent to the fatigue precrack were developed in conjunction with the stress corrosion induced subcritical crack growth. Such delaminations did not occur in the air test of the 25 percent cold-worked material but did occur in both the air and H_2S gas tests with the 50 percent cold-worked material. However, the extent of delamination was much greater in the H_2S tests.

The 0.35-in. (0.89-cm) thick WOL specimens taken from the broken halves of the 25 percent cold-worked specimens, so that the crack plane was in the S-T direction (see Fig. 1), did not develop delaminations. This is to be expected since the crack plane in these tests is parallel to the delaminations developed in the larger specimens. However, it is interesting to note that essentially the same value of apparent K_{Iscc} was measured for the 25 percent cold-worked material regardless of the crack-plane orientation (see Fig. 4).

Figures 7 and 8 show the fractographic appearance of the 0 and 25 per-

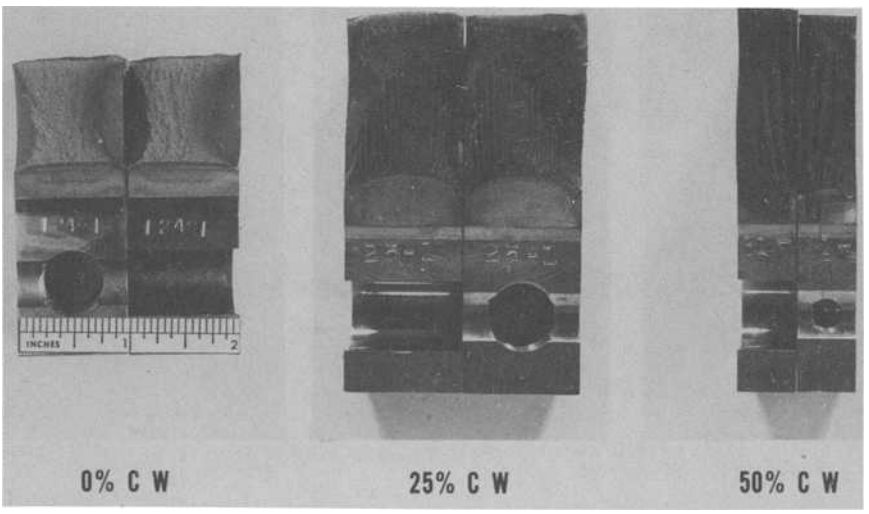

FIG. 6—*Variation in fracture appearance with amount of cold work (50 psig H_2S gas environment).*

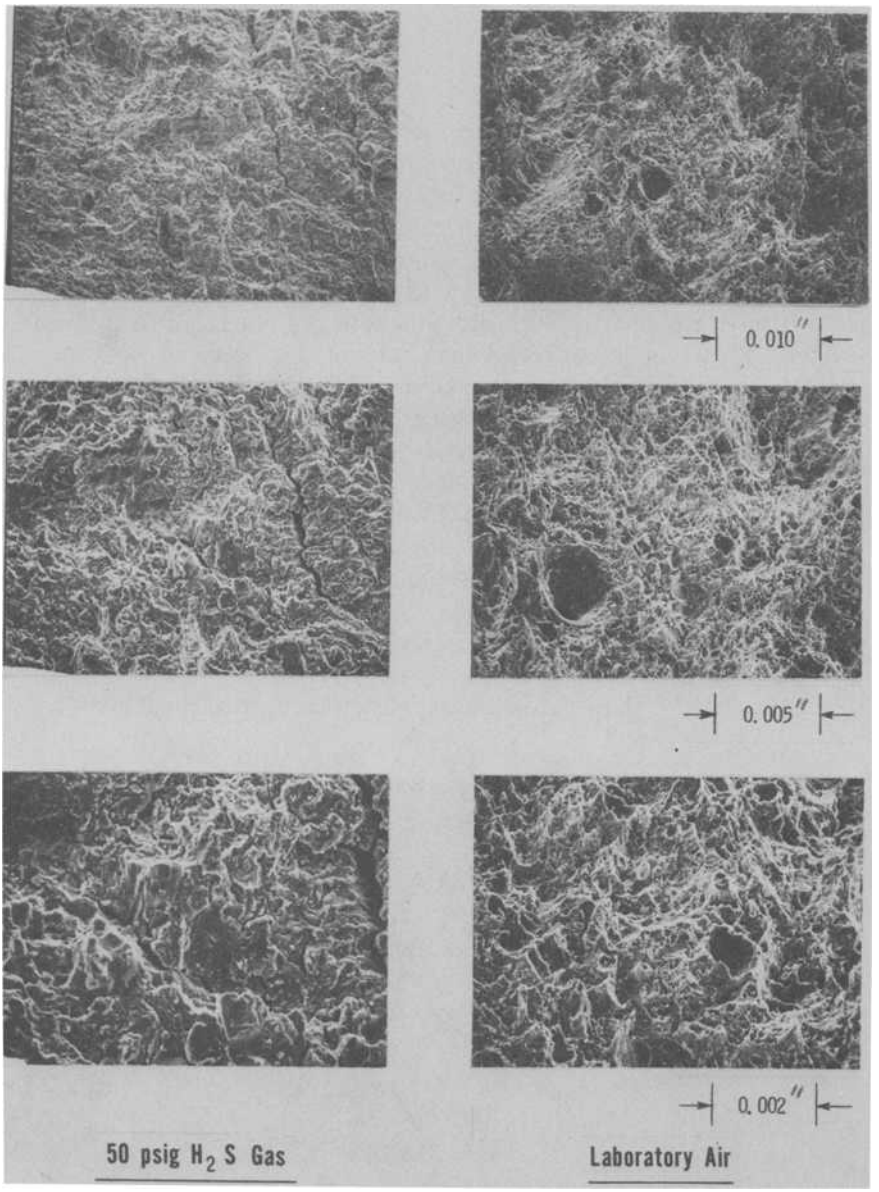

FIG. 7—*Effect of environment on the fractographic appearance of as received (0 percent cold worked) specimens.*

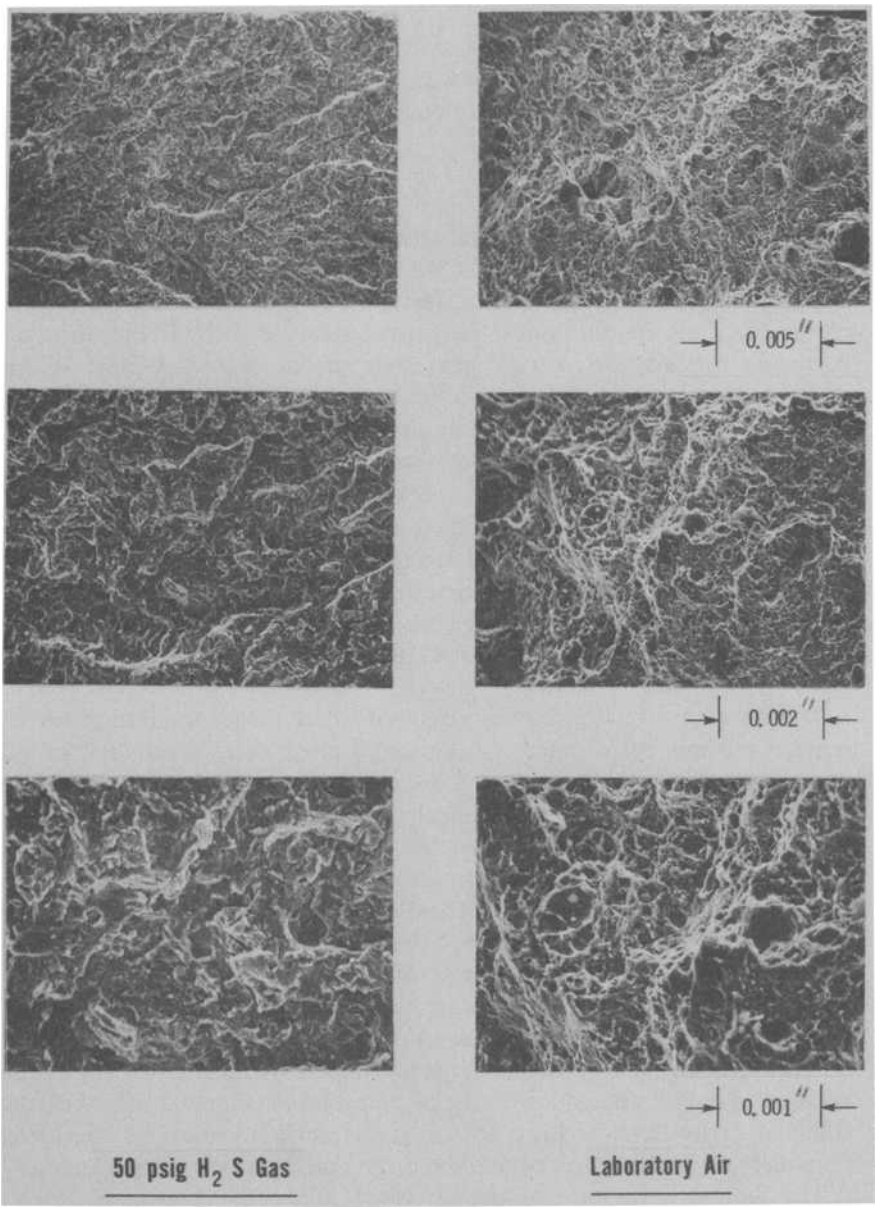

FIG. 8—*Effect of environment on the fractographic appearance of 25 percent cold worked specimens.*

cent cold-worked specimens (L-T orientation) tested in both air and H_2S gas. Note that in both cases, there is a distinct difference between the fractographic features observed in the air and H_2S environments. The H_2S gas tests consistently yield cleavage-like features characteristic of brittle fracture, whereas the features of the air tests are predominantly dimples representing a much more ductile failure mechanism.

Discussion

The results of this investigation clearly show that, at least for the 140 ksi (965 MPa) yield strength 4340 steel evaluated here, mechanical strengthening has a detrimental effect on the susceptibility to stress-corrosion cracking. In addition, it was shown that the susceptibility to stress-corrosion cracking in a H_2S gas environment is independent of the strengthening mechanism (cold working versus heat treating) and primarily dependent on the 0.2 percent offset yield strength of the test material. Although the rising load H_2S gas tests used in this investigation to evaluate stress-corrosion performance represent an extremely severe environment and only can be used to estimate K_{Iscc}, sufficient data have been developed for relatively high-strength 4340 steels which show that the accelerated K_{Iscc} test provides an accurate estimate of K_{Iscc} in other hydrogen bearing environments [*3–5*]. Consequently, we can assume that the effect of cold working on the apparent K_{Iscc} noted here is applicable to other environments.

The absence of a significant effect of crack-plane orientation on the stress-corrosion performance of the cold-rolled plates evaluated in this investigation is very surprising. One normally would expect substantial directional effects on the mechanical properties of a plate cold rolled to 25 percent reduction in thickness, and the tensile properties summarized in Table 1 show such effects. In addition, the extensive amount of delaminating associated with subcritical crack growth in the L-T and T-L orientation specimens tested in H_2S would appear to indicate very weak planes in the through-the-thickness direction. It is not possible at this time to explain the absence of directional effects on the apparent K_{Iscc} measurements. However, it is very important to recognize the practical implications of such behavior. It would appear from the test results developed in this investigation that the potential detrimental effect of mechanical strengthing on stress-corrosion susceptibility must be considered regardless of the direction of loading on the member being considered.

The limited evaluation of the effect of stress relieving on the stress-corrosion susceptibility of cold-worked 4340 steel clearly showed that stress relieving could improve the resistance to stress-corrosion cracking. However, the stress-relief treatment involved here obviously did not restore the original stress-corrosion resistance. From these limited results,

we can speculate that for the case of cold-worked material, both the residual stresses associated with cold working and the microscopic material damage contribute to the stress-corrosion performance. Apparently, a stress-relief heat treatment can remove detrimental residual stresses, but the inherent material damage remains.

The tension test results shown in Table 1 indicate that the stress-relief treatment had a very significant effect on the tensile elongation and reduction in area properties of the plate. In addition, the tensile strength decreased as the result of stress relieving but the yield strength increased. Such data clearly indicate that stress-corrosion susceptibility is not a function of yield strength alone.

These results illustrate the complex interactions of mechanical performance and stress-corrosion behavior. Obviously, more substantial work is required to characterize the stress-corrosion phenomenon adequately.

Conclusions

The pertinent conclusions associated with this investigation are summarized next.

1. Mechanical strengthening has a detrimental effect on the stress-corrosion susceptibility of 140 ksi (965 MPa) type 4340 steel.

2. The susceptibility to stress-corrosion cracking is essentially independent of the strengthening mechanism (cold working versus heat treating) and primarily dependent upon the inherent yield strength of the material. Specifically, type 4340 steel heat treated or mechanically worked to a given strength level yields similar stress-corrosion behavior.

3. Crack-plane orientation does not have a significant effect on the stress-corrosion performance of 140 ksi (965 MPa) yield strength 4340 steel cold rolled to 25 percent through the thickness.

4. Stress relieving can improve the stress-corrosion resistance of cold-worked type 4340 steel.

Acknowledgments

The experimental testing associated with this investigation was conducted by W. H. Halligan and F. X. Gradich under the direction of D. R. Young of the Fracture Mechanics Laboratory. The work was sponsored by the Westinghouse Large Rotating Apparatus Division.

References

[*1*] *Stress Corrosion Cracking of Metals—A State of the Art, ASTM STP 518,* American Society for Testing and Materials, 1972.

[*2*] Wei, R. P., Novak, S. R., and Williams, D. P., "Some Important Considerations in

the Development of Stress Corrosion Cracking Test Methods," *Material Research and Standards,* Vol. 12, No. 4, 1972.

[3] Clark, W. G., Jr., and Landes, J. D. in *Stress Corrosion—New Approaches, ASTM STP 610,* American Society for Testing and Materials, 1976, pp. 108–127.

[4] Hudak, S. J., unpublished Westinghouse Research Laboratories data.

[5] Clark, W. G., Jr., "The Effect of Temperature and Pressure on Hydrogen Cracking in 180 ksi Yield Strength 4340 Steel," presented at the American Institute of Mechanical Engineers' Symposium on the Effect of Hydrogen on Behavior of Materials, Sept. 1975, to be published.

W. E. Krupp,[1] *J. T. Ryder,*[1] *D. E. Pettit*[1] *and*
D. W. Hoeppner[2]

Corrosion Fatigue Properties of Ti-6Al-6V-2Sn (STOA)

REFERENCE: Krupp, W. E., Ryder, J. T., Pettit, D. E., and Hoeppner, D. W., **"Corrosion Fatigue Properties of Ti-6A1-6V-2Sn (STOA),"** *Flaw Growth and Fracture, ASTM STP 631,* American Society for Testing and Materials, 1977, pp. 345–364.

ABSTRACT: The corrosion fatigue crack properties of Ti-6A1-6V-2Sn (STOA) were studied in room-temperature laboratory air, dry air, high-humidity air, and 3.5 percent sodium-chloride solution environments. The alloy was characterized by chemical, microstructural, tensile, and fracture-toughness properties. Corrosion fatigue tests were conducted using wedge-open load (WOL), center-cracked-through (CCT) and part-through-cracked (PTC) specimens. Frequency and environmental interactions were studied as well as the effects of orientation and stress ratio. The effect of frequency was to increase the fatigue crack growth rate as the frequency was decreased. A severe effect of frequency was noted in salt water where at 0.1 Hz, crack-growth rates increased to such a high level that failure occurred at K_{max} levels significantly below the stress-corrosion cracking threshold. Fractographic studies showed no apparent cause of this unexpected phenomenon.

KEY WORDS: crack propagation, corrosion fatigue, titanium, frequency, environment

The problem of subcritical flaw growth and subsequent fracture of aircraft structural materials has been recognized as a challenge in maintenance of aircraft structural integrity [*1*].[3] Recent experiences in military aircraft have indicated that a greater amount of information pertaining to the fracture and subcritical flaw-growth behavior of engineering materials is required in order to prevent early failures and ensure the safe service life of a structural component [*2*].

This report summarizes corrosion fatigue crack propagation studies conducted for Ti-6A1-6V-2Sn (STOA) titanium. The report is based upon the results of a contract [*3*] supported by the U.S. Air Force, Air Force

[1]Group engineer, research scientist, and research scientist, respectively, Lockheed-California Company, Rye Canyon Research Laboratory, Valencia, Calif.
[2]Professor of Engineering, University of Missouri, Columbia, Mo.
[3]The italic numbers in brackets refer to the list of references appended to this paper.

Materials Laboratory, Wright-Patterson Air Force Base, Ohio. This titanium alloy was chosen for study as typical of fittings, attachments, planks, doublers, and other similar aircraft components. The STOA alloy typically has high strength, but lower fracture-toughness properties as compared to an alloy such as recrystalized annealed Ti-6Al-4V-2Sn (RA).

This fatigue crack propagation study was separated into two main tasks. The first task was determination of the influence of cyclic frequency on the fatigue crack growth behavior of this titanium alloy in the suspected most aggressive environment of those to be tested, here selected as 3.5 percent sodium-chloride solution. This initial frequency screening was conducted using wedge-open-load (WOL) specimens. Based on these results test frequencies for the second task were determined. In the second task, the influence of environment (laboratory air, dry air, high humidity, and 3.5 percent sodium-chloride solution), test frequency, orientation, and stress ratio on fatigue crack growth behavior was evaluated.

For these fatigue crack propagation tests, surface flaws (part-through-cracked (PTC)) were used as the main flaw geometry because of the frequency with which they are encountered in service problems. In addition, through-cracked center-cracked tension (CCT) panels were also tested for comparison with the PTC results to examine the effect of crack orientation within the parent material.

Material Characterization

Chemistry and Microstructure

STOA alloy was purchased from Titanium Metals Corporation of America, West Caldwell, New Jersey, in two product forms: ⅛ by 36 by 96-in. (0.318 by 91.4 by 243.8-cm) plate, heat K9207 and ⅜ by 36 by 96-in. (0.952 by 91.4 by 243.8-cm) plate, heat K9197.

The solution treated and overaged (STOA) condition was obtained by the following heat treatment cycle: heat at 1700°F (927°C) for 1 h and water quench; anneal at 1400°F (760°C) for 1 h and air cool. This heat treatment, combined with an effort to lower the copper and iron content, was selected as an attempt to obtain high fracture-toughness material [*4*]. Samples were removed from the corner of each plate, submitted for chemical analysis, and the results compared to specification requirements. As shown in Table 1, the material met the specification requirements for each element within apropriate limits.

Microstructure of the ⅛-in. (0.318-cm) plate was primary alpha particles in a matrix of transformed beta. Surface sections showed 35 to 45 percent primary alpha, while center sections showed 15 to 25 percent primary alpha. This was a result of the lower temperatures and higher amount of

TABLE 1—*Chemical analysis of Ti-6Al-6V-2Sn(STOA) products by weight.*

Material	Al	V	Sn	Fe	Cu	C	O	N	H	T
⅜ in. (0.952 cm) plate	5.4	5.6	1.8	0.54	0.54	0.022	0.18	0.017	0.009	Remainder
⅛ in. (0.318-cm) plate	5.7	5.4	1.9	0.52	0.50	0.022	0.16	0.015	0.009	Remainder

work imparted to the surface during forming of the ⅛-in. (0.318-cm) sheet, both leading to primary alpha coarsening. Microstructure of the ⅜-in. (0.952-cm) plate showed primary alpha particles in a matrix of transformed beta, with the amount of primary alpha increasing from 30 percent at the center to 40 percent at the surface. Primary alpha at the surface showed a nonuniform distribution. There were large prior beta grains that were deficient in primary alpha, and some grain boundary alpha present. This may have been due to overheating during rolling or to a beta-rich region in the ingot.

Tensile and Fracture-Toughness Properties

Flat tension specimens were machined from the ⅛ and ⅜-in. (0.318 and 0.952-cm) plates. All tests were conducted in a Baldwin universal testing machine in accordance with ASTM Tension Testing of Metallic Materials (E 8-69). The ⅛-in. (0.318-cm) thick plate had the following properties: longitudinal direction, ultimate strength, σ_{ult} = 141.4 ksi (975 MPa), 0.2 percent yield strength, σ_y = 132.9 ksi (916 MPa), percent elongation in 2 in. (5.08 cm), e = 12.8; transverse direction, σ_{ult} = 143.0 ksi (986 MPa), σ_y = 137.4 ksi (947 MPa), e = 12.2. The ⅜-in. (0.952-cm) thick plate tensile properties were: longitudinal, σ_{ult} = 167.2 ksi (1153 MPa), σ_y = 156.5 ksi (1029 MPa), e = 14.7; transverse, σ_{ult} = 167.8 ksi (1156 MPa), σ_y = 160.3 ksi (1105 MPa), e = 14.8. These results are the average of the three tests conducted in each orientation. No orientation effect was observed in either plate.

The STOA fracture-toughness tests were conducted according to ASTM Test for Plane-Strain Fracture Toughness of Metallic Materials (E 399-74). The range of K_{Ic} values measured was within the expected range for the material. The toughness results for the ⅛-in. (0.318-cm) thick plate were: WR orientation, K_Q = 56.9 ksi $\sqrt{\text{in.}}$ (62.5 MPa $\sqrt{\text{m}}$), R_{sc} = 0.794; RW orientation, K_Q = 54.8 ksi $\sqrt{\text{in.}}$ (60.3 MPa $\sqrt{\text{m}}$), R_{sc} = 0.755. For the ⅜-in. (0.952-cm) thick plate, toughness results were: WR orientation, K_{Ic} = 46.1 ksi $\sqrt{\text{in.}}$ (50.7 MPa $\sqrt{\text{m}}$); RW orientation, K_{Ic} = 42.9 ksi $\sqrt{\text{in.}}$ (47.2 MPa$\sqrt{\text{m}}$). These results were based on three coupons tested at each condition.

Fatigue Crack Propagation Test Procedures

Three specimen geometries were used in this fatigue crack propagation study: the WOL specimen (Fig. 1), used for frequency screening tests; the PTC specimen (Fig. 2), used for the majority of the tests; and the CCT specimen (Fig. 2), used as a secondary specimen geometry. Stress intensities for the WOL geometry were calculated using the typical equation for WOL coupons [5]. For PTC specimens, stress intensity was computed using the equation of Irwin [6]. No back surface correction was used for basic analysis of the surface flaw due to the large number of proposed corrections available—none of which have been shown to be applicable for fatigue crack propagation studies over a range of materials and testing conditions. For the range of crack lengths used in the majority of this program, a maximum 10 percent difference in K would have resulted from applying a correction factor, and, in general, the difference would be much less than 10 percent. The CCT specimen geometry was the same as that for the PTC specimen with the exception of the starter crack which was a ⅛-in. (0.318-cm) diameter slotted hole in the center of the panel. For CCT specimens, stress intensity was computed using the equation of Federson [7].

Prior to testing, all specimens were fatigue precracked at 20 Hz at a load ratio of $R = +0.1$ in laboratory air. Loads were stepped down such that the final 0.020 in. (0.5 mm) of growth occurred at a maximum stress intensity equal to that at which subsequent testing was to be started. All precracking and fatigue crack propagation tests were conducted in closed loop electrohydraulic testing machines. Each machine was equipped with peak and valley detectors which controlled the load to ±1 percent on both the maximum and minimum loads, any exceedance of these levels

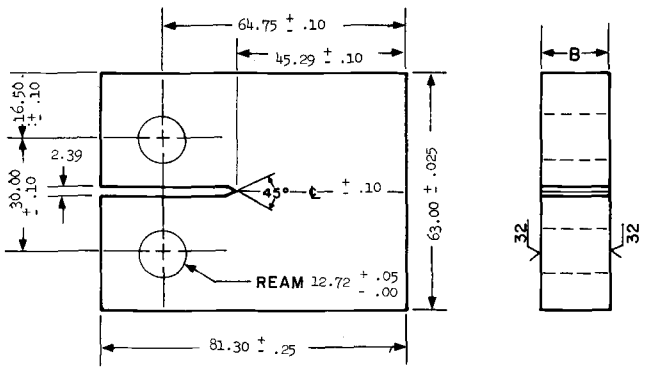

(All Dimensions in mm)

FIG. 1—*Wedge-open-load (WOL) specimen configuration.*

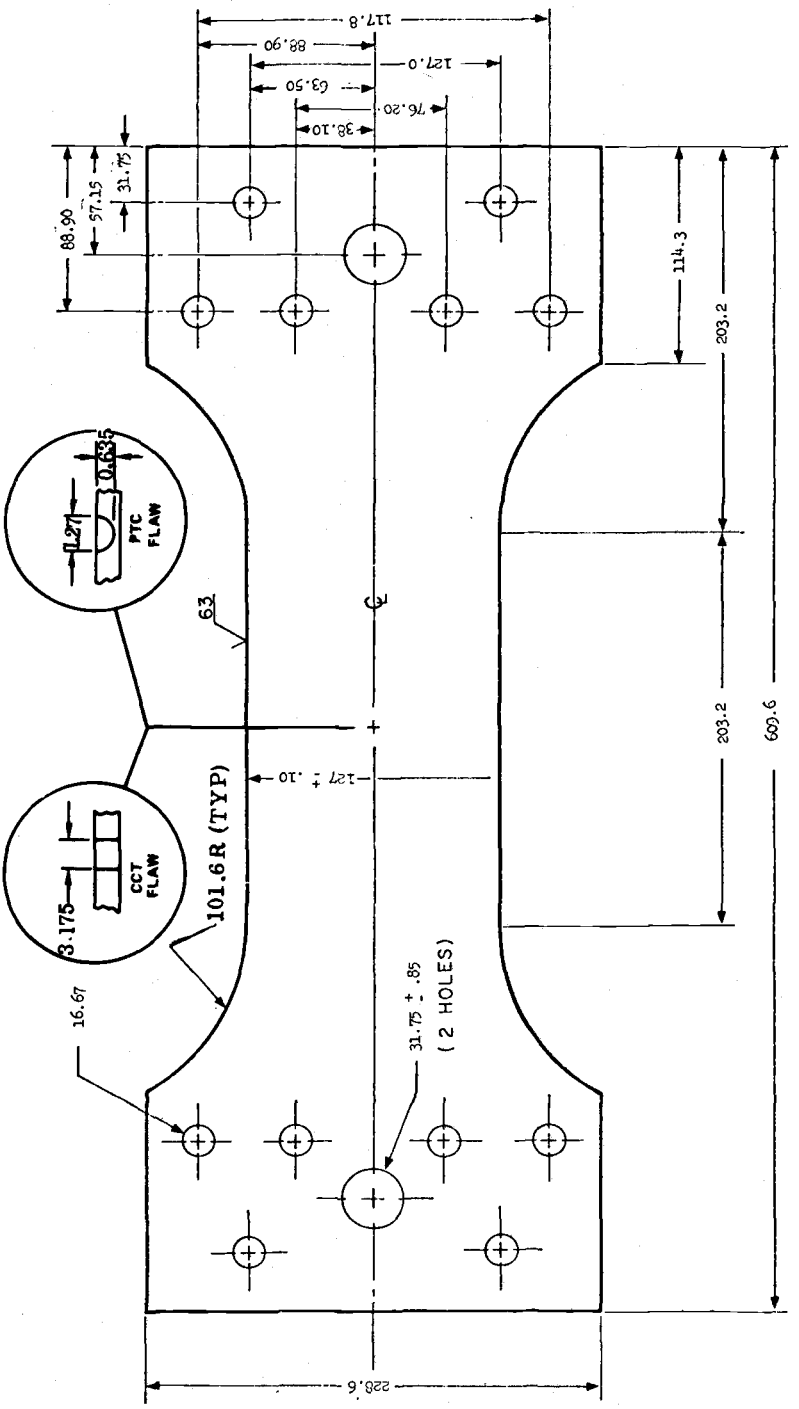

FIG. 2—*Part-through-cracked specimen geometry for fracture toughness and fatigue crack propagation tests.*

resulting in a dumping of the load signal to zero and the sounding of an alarm. The test waveform used was the sine wave.

The fatigue crack propagation tests were all conducted at room temperature, 22 ± 2°C (72 ± 5°F), in controlled environments. These environments were: laboratory air—laboratory air was at 40 ± 10 percent relative humidity; dry air—10 percent, or less, relative humidity was obtained by enclosing the specimen in a moisture-proof container with freshly dried desiccant (MIL-D-3464, Type I); high humidity—environment of ≥ 85 percent relative humidity was achieved by bubbling argon gas through distilled water; 3.5 percent sodium-chloride solution—solution was made by adding sodium-chloride to deionized water such that a 3.5 percent sodium-chloride solution was achieved.

The environments were circulated around the entire crack region of each specimen. The high-humidity environment was contained by placing a clear plastic bag around the entire crack region of the specimen. A chamber formed of silicon rubber and clear glass was installed around the crack for the 3.5 percent sodium-chloride liquid environment. The 3.5 percent sodium-chloride solution was continuously circulated past the crack region at the rate of 0.008 gal/min ($7.886 \times 10^{-3} m^3/s$).

Crack length measurements were made on the front surface of the PTC specimens, until crack breakthrough occurred, and on both front and back surfaces of the WOL and CCT specimens. Crack lengths were measured to ± 0.001 in. (± 0.0254 mm) using a toolmaker's microscope and appropriate illumination. For PTC specimens, the maximum stress ratio was periodically lowered for 0.02 in. (0.508 mm) of growth to mark the crack length. Following completion of each test, the specimen was fractured and correlations made between surface crack length, $2C$, and corresponding crack depth, a, as measured from fracture surface markings. Fracture surfaces of all specimens were sprayed with a clear plastic lacquer (Krylon) subsequent to failure to preserve the fracture surface for subsequent fractography.

All data analysis was performed by computer programs, using as input the measured crack length (or crack depth for PTC samples) versus cycles data, specimen geometry, loading conditions, and appropriate stress-intensity expressions for each specimen type. Crack depth values for PTC specimens were computed by hand based on the correlation of $a/2C$ versus measured $2C$ values as determined from the fracture surface markings for each specimen. The computer analysis computed incremental crack growth rates, da/dN or dC/dN depending on specimen type, and stress-intensity parameters at average crack length in the specific crack length interval. A tabulation of the results was printed out and a plot of da/dN or dC/dN versus the alternating stress intensity factor, ΔK, printed.

Results

The experimental variables studied included environment, frequency, orientation, stress ratio, and microstructure. The test matrix is summarized in Table 2. Results of these tests are discussed in the following subsections. In the figures which accompany these subsections, smooth curves through the data are shown to aid in visualizing trends. Specific data points for each coupon are plotted in Ref *3*. Trend curves were used because the large number of data points per coupon would have unnecessarily cluttered the graphs. The data scatter for each coupon was generally quite small (see Ref *3*) as indicated for one data set.

Environment/Frequency Effects

For the ⅜-in. (0.952-cm) thick material, test results for WOL, CCT, and PTC coupons at $R = 0.1$ at 10 Hz in dry air, laboratory air, and high-humidity environments were compared. No discernable difference between the crack-growth rates for these flaw geometries was found. Therefore, this scatter band was defined as a baseline for comparing other test results. Figure 3 shows the baseline scatter band compared to the data for different geometries tested at 10 Hz, $R = 0.1$ in 3.5 percent sodium-chloride solution. An increase in crack-growth rates was observed for the WOL and CCT coupons, but only an insignificant increase for the PTC coupon.

Figure 4 shows the same baseline compared to the data at 0.1 Hz. The data for different orientations at 0.1 Hz were similar and faster than the baseline data above $\Delta K \cong 18$ ksi $\sqrt{\text{in.}}$ (19.8 MPa $\sqrt{\text{m}}$). The data of Fig. 4 clearly show that at 0.1 Hz, the crack-growth rate did not return to the baseline rate at high ΔK levels. These coupons at 0.1 Hz in salt water essentially failed at $\Delta K \cong 18$ ksi $\sqrt{\text{in.}}$ (19.8 MPa $\sqrt{\text{m}}$) as opposed to those

TABLE 2—*Summary of fatigue crack propagation tests for Ti-6Al-6V-2Sn(STOA).*

Material	Environment				Test Frequency			Stress Ratio		Orientation		
Specimen Geometry	Dry Air	Lab Air	Humid Air	3.5% NaCl	0.1	1	10	0.1	0.5	WR	WT	RT
⅜ in. plate (0.318 cm)												
WOL		X		X	X	X	X	X		X		
CCT			X	X	X		X	X	X	X		
PTC	X		X	X	X		X	X	X		X	X
⅛ in. sheet (0.952 cm)												
CCT			X	X	X		X	X		X		

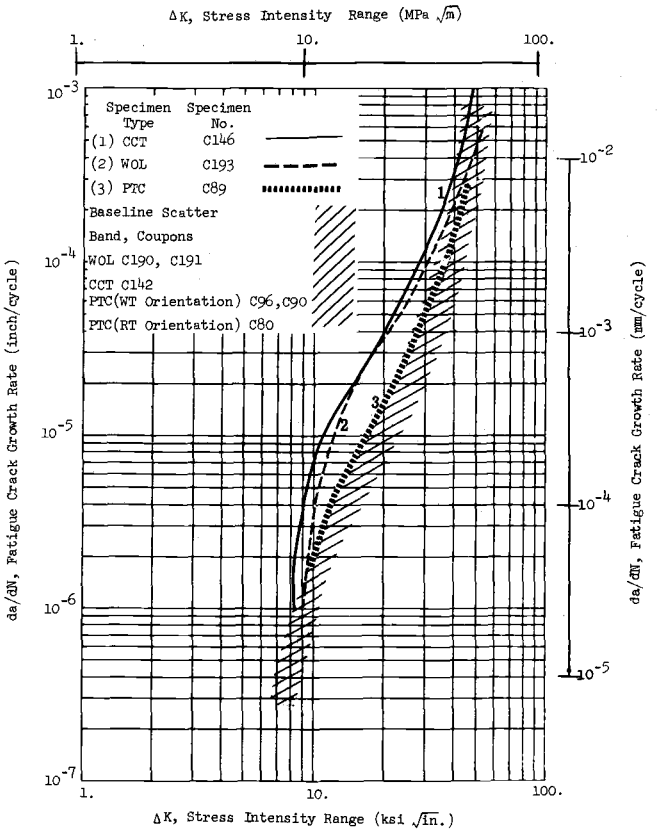

FIG. 3—*Fatigue crack propagation results for* ⅜-in. *(0.952-cm) STOA using various specimen geometries,* R = *0.1, 10 Hz in 3.5 percent sodium-chloride solution, WT, or WR orientations.*

at 10 Hz (Fig. 3) which failed at $\Delta K \cong 45$ ksi $\sqrt{\text{in.}}$ (49.5 MPa $\sqrt{\text{m}}$). This severe reduction in K_{max} at failure observed at 0.1 Hz was unexpected and suggested a possibly severe restriction on application of this alloy in aggressive environments.

To investigate further the effect of frequency and environment interaction, additional tests were conducted using WOL and PTC coupons. Results of the ⅜ in. (0.952 cm) WOL frequency screening tests are presented in Fig. 5. The introduction of a 3.5 percent sodium-chloride solution at 10 Hz produced the normally observed increase in fatigue crack-growth rates in the intermediate ΔK range when compared to baseline data. As the test frequency was decreased to 1 and 0.1 Hz in 3.5 percent sodium-chloride solution, the crack-growth rates exhibited an extremely rapid acceleration at $\Delta K \backsim 17$ ksi $\sqrt{\text{in.}}$ (18.7 MPa $\sqrt{\text{m}}$), the 0.1 Hz and 1 Hz

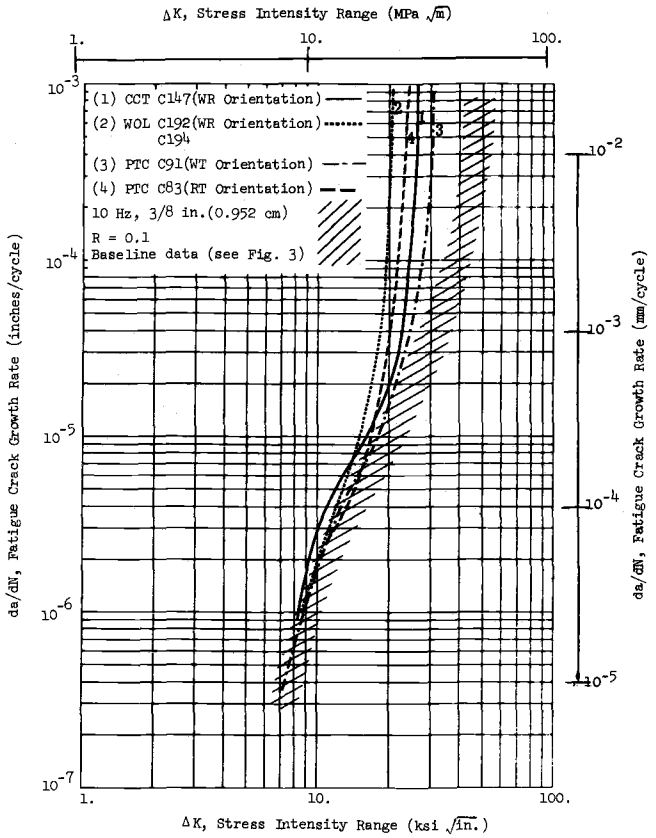

FIG. 4—*Fatigue crack propagation results for ⅜-in. (0.952-cm) STOA using various specimen geometries,* R = *0.1, 0.1 Hz in 3.5 percent sodium-chloride solution.*

rates rapidly increasing. The 1 Hz rates showed a slowing trend at rates above 2×10^{-4} in./cycle (5×10^{-3} mm/cycle)—the rates remaining about one order of magnitude faster than the 10 Hz salt solution results. Note that the 1 Hz and 0.1 Hz rates fell below the 10 Hz, 3.5 sodium-chloride percent solution results in the range of $\Delta K \leq 15$ ksi $\sqrt{\text{in.}}$ (16.5 MPa $\sqrt{\text{m}}$) —their values approaching the laboratory air results. As will be shown later, this was not an isolated observation but a general trend shown by all of the STOA data.

Frequency screening effects in 3.5 percent sodium-chloride solution environment on the ⅜-in. (0.952-cm) PTC (WT orientation) specimens are shown in Fig. 6. The general trends previously noted on the WOL specimens (WR orientation) were noted also for these PTC specimens (WT orientation). The general accelerating effect of lower frequencies in 3.5 percent sodium-chloride solution was observed; the 0.1 Hz results

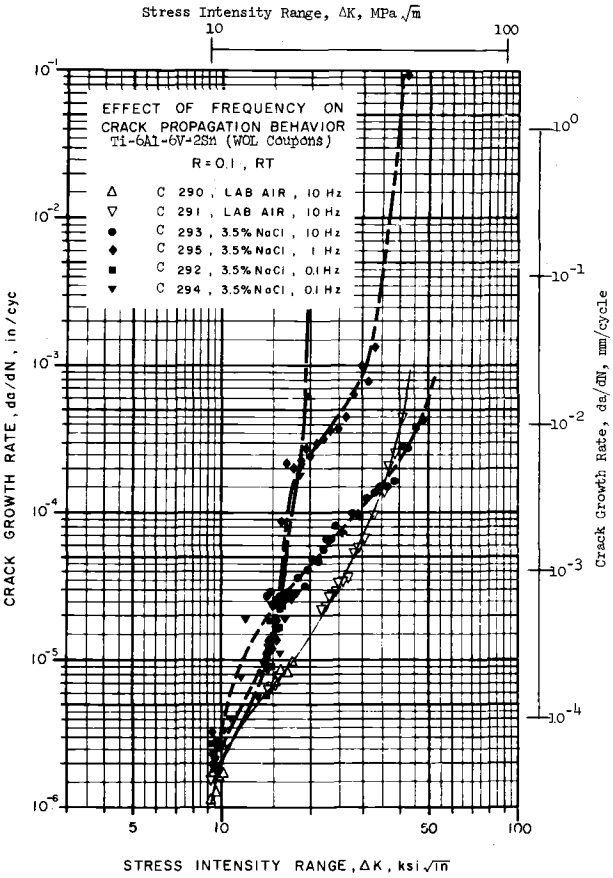

FIG. 5—*Frequency screening results for ⅜-in. (0.952-cm) STOA WOL specimens,* R = *0.1, WR orientation.*

again showing a point of rapid acceleration (here at $\Delta K \sim 25$ ksi $\sqrt{\text{in.}}$, 27.5 MPa $\sqrt{\text{m}}$). Crack-growth rates also were lower than those observed at 10 Hz in 3.5 percent sodium-chloride solution in the intermediate range $9 \leq \Delta K \leq 20$ ksi $\sqrt{\text{in.}}$ ($9.9 \leq \Delta K \leq 22$ MPa $\sqrt{\text{m}}$), the rates being equivalent at $\Delta K \leq 9$ ksi $\sqrt{\text{in.}}$ (9.9 MPa $\sqrt{\text{m}}$).

For the ⅛-in. (0.318-cm) CCT panel test results (WR), the same general effects of frequency were again observed as shown in Fig. 7. For the ⅛-in. (0.318-cm) material, the 10 Hz high-humidity results were slower than the fatigue crack-growth rates observed in the ⅜-in. (0.952-cm) material. However, the 10 Hz 3.5 percent sodium-chloride solution tests agreed very well with the ⅜-in. (0.952-cm) material results for $\Delta K < 30$ ksi $\sqrt{\text{in.}}$ (33 MPa $\sqrt{\text{m}}$), the ⅛-in. (0.318-cm) material showing lower rates above this level.

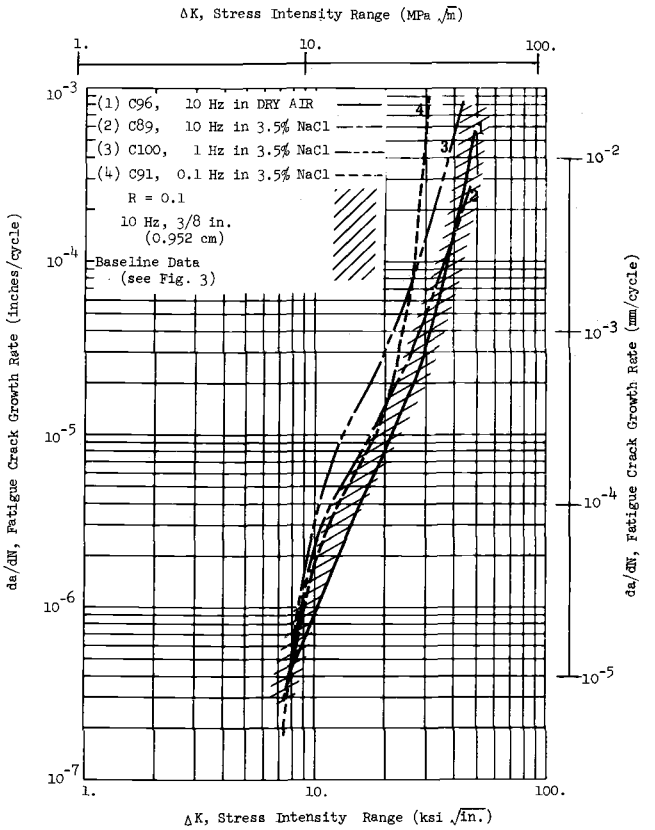

FIG. 6—*Frequency screening results for ⅜-in. (0.952-cm) STOA PTC specimens in sodium-chloride solution,* R = *0.1, WT orientation.*

The 0.1 Hz results in 3.5 percent sodium-chloride solution again showed the trends noted in the ⅜-in. (0.952-cm) thick material—the major difference being the more gradually increasing crack growth rate and the higher ΔK level to which finite rates ($< 10^{-2}$ in./cycle ($< 2.54 \times 10^{-3}$mm/cycle)) were measured. The lower crack growth rates are believed to be due to the inability to develop substantial regions of plane-strain conditions in the ⅛-in. (0.318-cm) thickness.

Results for ⅜-in. (0.952-cm) PTC specimens (WT orientation) tested in air are shown in Fig. 8. At 10 Hz, the effect of changing the humidity from < 10 percent to > 90 percent had no significant effect on the STOA material. However, as the frequency was lowered from 10 Hz to 0.1 Hz in high humidity, an increase in fatigue crack-growth rates in the intermediate range $10 \leq \Delta K \leq 40$ ksi $\sqrt{\text{in.}}$ (44 MPa $\sqrt{\text{m}}$) was noted. This result

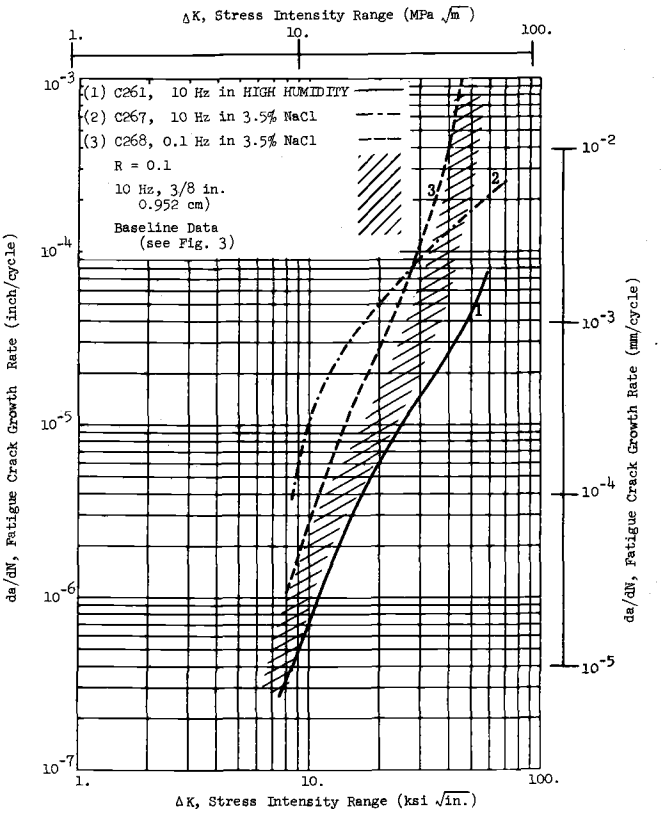

FIG. 7—*Fatigue crack propagation results for ⅛-in. (0.318-cm) STOA CCT specimens, R = 0.1, WR orientation.*

demonstrated the detrimental nature of even the high-humidity environment on STOA material.

The effect of PTC specimen orientation was investigated. The 10 Hz and 0.1 Hz high-humidity results for the RT orientation agreed very well with the WT orientation 10 Hz dry air and high-humidity results and indicated less of a low-frequency humidity sensitivity in the RT orientation than was found in the WT orientation at 0.1 Hz. The effect of 3.5 percent sodium-chloride solution showed the same trends previously noted in the other orientations. The 0.1 Hz data again crossed below the 10 Hz 3.5 percent sodium chloride solution data below $\Delta K \sim 17$ ksi $\sqrt{\text{in.}}$ (18.7 MPa $\sqrt{\text{m}}$) and showed a rapid acceleration in the fatigue crack-growth rate at $\Delta K > 20$ ksi $\sqrt{\text{in.}}$ (22 MPa $\sqrt{\text{m}}$).

Stress Ratio Effects

The $R = +0.5$ results for the ⅜ and ⅛-in. (0.952 and 0.318-cm) thick

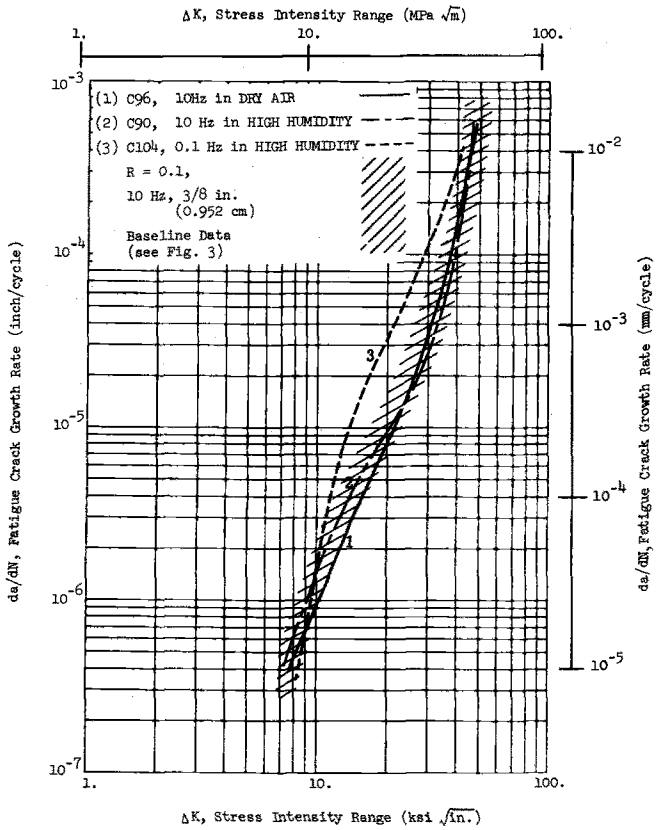

FIG. 8—*Fatigue crack propagation results for ⅜-in. (0.952-cm) STOA PTC specimens in air,* R = *0.1, WT orientation.*

CCT specimens (WR orientation) are shown in Fig. 9. For 10 Hz high-humidity results of the ⅜-in. (0.952-cm) thick material, the maximum effect of $R = 0.5$ occurred at high- and low-ΔK values—the results in the range of $9 \leq \Delta K \leq 15$ ksi $\sqrt{\text{in.}}$ ($9.9 \leq \Delta K \leq 16.5$ MPa$\sqrt{\text{m}}$) being nearly equivalent to the $R = 0.1$ results. The ⅛-in. (0.318-cm) STOA material showed a somewhat different response, the $R = 0.5$ results lying above and nearly parallel to the $R = 0.1$ results over the range of data available. The shift amounted to a factor of three increase in the fatigue crack propagation rate. The increased effect of stress ratio at high-ΔK values was not yet reached with the available data, due to the higher K_Q of the ⅛-in. (0.318-cm) material. The increased effect at low-ΔK appeared extended to the end of the range of data ($\backsim 10^{-7}$ in./cycle (2.54×10^{-6} mm/cycle)). Also evident in Fig. 9 is the lower crack-growth rates of the ⅛-in. (0.318-cm) thick material compared to the ⅜-in. (0.952-cm) thick material.

The effect of frequency in 3.5 percent sodium-chloride solution at R =

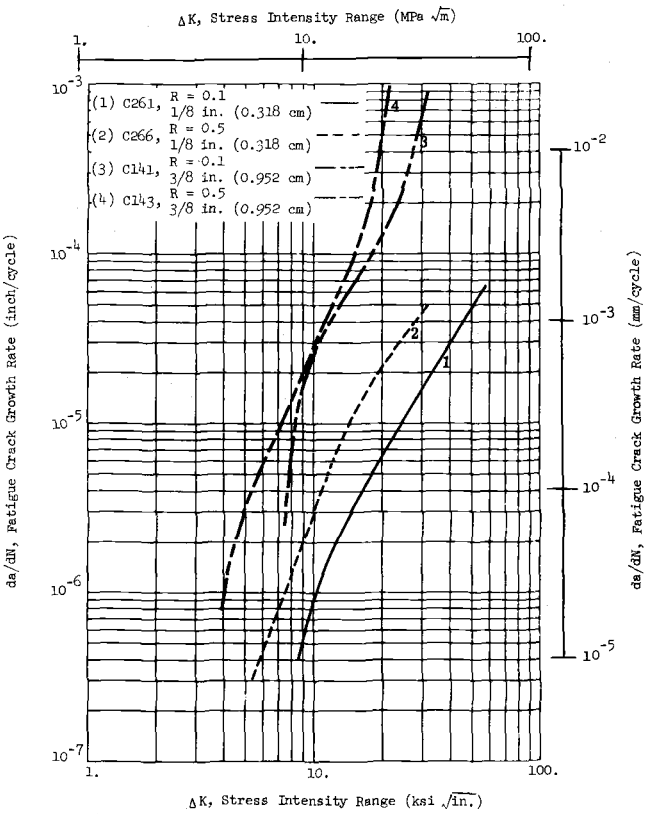

FIG. 9—*Effect of stress ratio for STOA CCT specimens, 10 Hz in high humidity, WR orientation.*

+ 0.5 for the ⅜-in. (0.952-cm) PTC specimens of STOA (WT orientation) is presented in Fig. 10. As shown in Fig. 10, no significant effect of frequency was observed. When the R = + 0.5 results were compared with the 10 Hz salt solution R = 0.1 data, the same trends observed for the comparable CCT data were seen; that is, the major effects occurring at high- and low-ΔK values with only minor effects at the intermediate ΔK range. The results in high-humidity air for the ⅜-in. (0.952-cm) PTC STOA specimens (WT orientation) also showed no significant frequency effects at R = + 0.5. At 10 Hz, the stress-ratio effect was of the same basic form previously noted. When the 0.1 Hz data at R = + 0.1 and R = + 0.5 were compared, as shown in Fig. 11, the only observed difference in previous trends was the parallel nature of the curves at high-ΔK values. Note in Fig. 11, that the R = + 0.5, 3.5 percent sodium-chloride solution results were the same as the R = + 0.5, 0.1 Hz high-humidity results, thus, indicating that at R = 0.5 most of the environ-

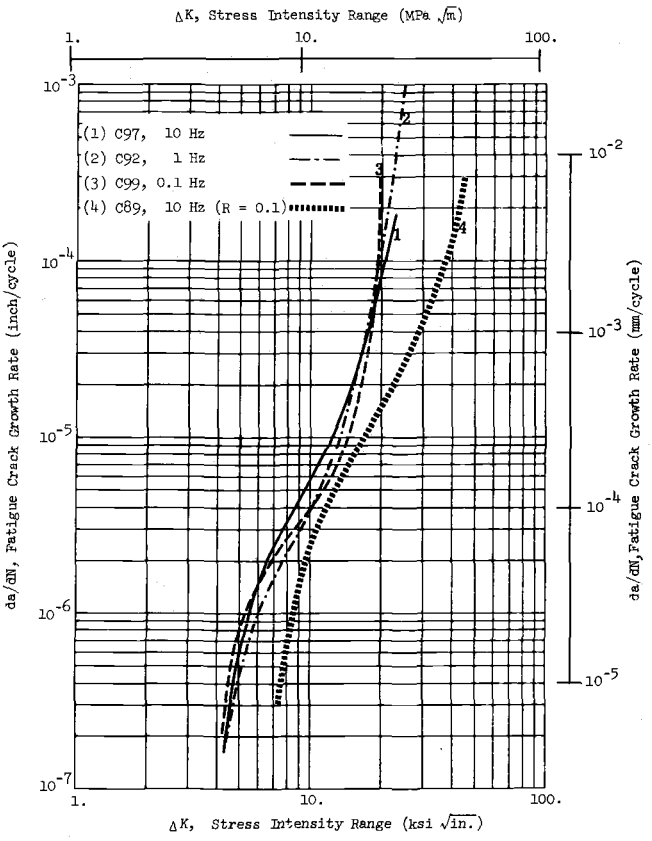

FIG. 10—*Frequency screening results for ⅜-in. (0.952-cm) STOA PTC specimens,* R = *0.5, in 3.5 percent sodium-chloride solution, WT orientation.*

mental effect has saturated at the low-frequency, high-humidity conditions.

Discussion

The two product forms, ⅛ and ⅜-in. (0.318 and 0.952-cm) plate, exhibited a lack of marked directionality in their tensile and fracture-toughness properties. The main variation was the somewhat lower fracture toughness of the ⅜-in. (0.952-cm) plate as compared to the ⅛-in. (0.318-cm) material.

At 10 Hz, the effect of a severely aggressive environment such as 3.5 percent sodium-chloride solution was to increase the crack-growth rate relative to the 10 Hz air results in the intermediate ΔK range; the high-ΔK and low-ΔK values remaining basically unchanged. At slow frequencies

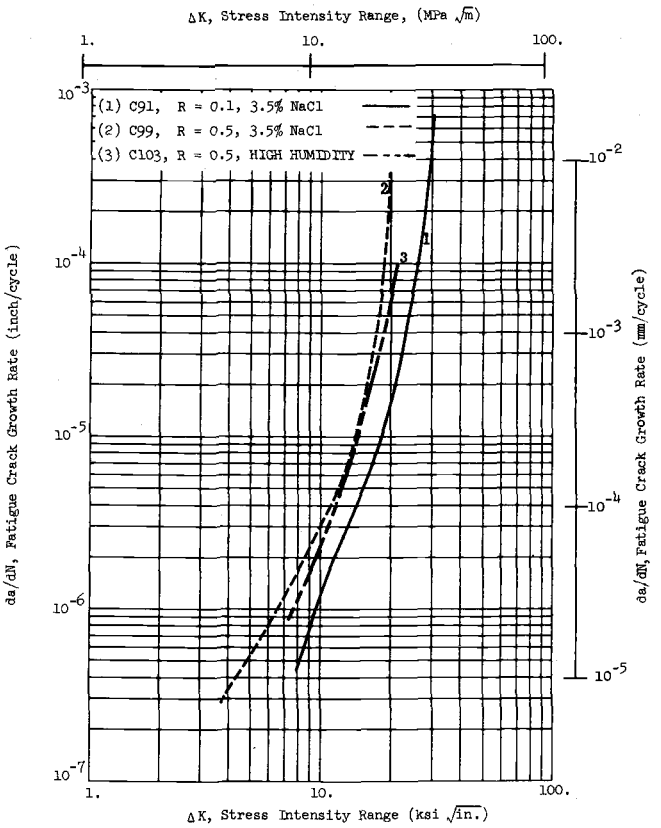

FIG. 11—*Effect of stress ratio for ⅜-in. (0.952-cm) STOA PTC specimens, 0.1 Hz, WT orientation.*

in detrimental environments (including high humidity), this alloy showed a frequency effect typified by a crossover at low-ΔK levels of the slow frequency (0.1 Hz) *da/dN* curve with the 10 Hz *da/dN* data in the same environment. As a result, the ΔK level at which a rate of 1×10^{-5} in./cycle (2.54×10^{-3} mm/cycle) occurred was a significantly higher ΔK value for 0.1 Hz than for 10 Hz.

This effect was discussed in detail in Ref *3* and also was reported by Dawson and Pelloux [*8*]. Kraft has suggested a physical explanation of this cross-over effect [*9*] and used the 1973 data of Pettit, Krupp, Ryder, and Hoeppner [*10*] for RA material to support his conclusion. Essentially, to quote Kraft [*9*], the effect of frequency and environment on crack propagation is analyzed as a special case of the tensile ligament instability model. The model is further discussed by Kraft in Ref *11*.

The steep slope of the fatigue crack growth rate data for ⅜-in. (0.952-

cm) material at 0.1 Hz in 3.5 percent sodium-chloride solution showed that once a value of $\Delta K > \sim 18$ ksi $\sqrt{\text{in.}}$ (20 MPa $\sqrt{\text{m}}$) was reached (for $R = 0.1$) little useful life remained. This ΔK level for crack instability was considerably below the apparent sustained load flaw growth threshold of 30 ksi $\sqrt{\text{in.}}$ (33 MPa $\sqrt{\text{m}}$) for fracture [*12*]. High-humidity results exhibited a similar although less severe effect as the frequency was lowered to 0.1 Hz. Even at the low frequencies in 3.5 percent sodium-chloride solution, the crack-growth rates for $\Delta K < 9$ to 15 ksi $\sqrt{\text{in.}}$ (9.9 to 16.5 MPa $\sqrt{\text{m}}$) were essentially equivalent to those measured at 10 Hz in air.

For the ⅛-in. (0.318-cm) material, similar fatigue crack growth trends were noted. However, the 0.1 Hz, 3.5 percent sodium-chloride solution curve did not exhibit the rapid acceleration in rate until $\Delta K \sim 45$ ksi $\sqrt{\text{in.}}$ (49.5 MPa $\sqrt{\text{m}}$). This is believed to be due to the large plastic-zone size relative to the thickness in the ⅛-in. (0.318-cm) material which does not permit development of a significant region of plane-strain constraint at the crack tip.

A fractographic comparison between two WOL specimens used for frequency screening in 3.5 percent sodium-chloride solution, one at 10 Hz and the other at 1 Hz, was conducted. Specimen C293 (10 Hz) did not experience an instability in crack growth in 3.5 percent sodium-chloride solution, while in specimen C295 (1 Hz) an acceleration in rates occurred at a $\Delta K \cong 16$ ksi $\sqrt{\text{in.}}$ (17.6 MPa $\sqrt{\text{m}}$). However, fractography results showed no significant difference between the specimen fracture surfaces at magnifications up to $\times 1000$. Some increase in amount of secondary cracking at the higher crack growth rate appeared to have occurred at the lower frequency.

To further investigate the differences between those specimens which went unstable and those which did not, metallographic sections were taken of specimens C290 and C294. For specimen C290, which did not exhibit a rapid acceleration in crack growth at 10 Hz in laboratory air, the extent of cracking in the coarse alpha appeared to increase as the growth rate increased to instability. In the same region of specimen C294 which suffered instability at 0.1 Hz in 3.5 percent sodium chloride solution, severe subsurface, secondary cracking occurred which appeared to have been unconnected to the main crack front. These secondary cracks mainly propagated by transgranular cleavage in the fine acicular alpha phase and along the interface of the coarse alpha-beta regions. This type of secondary cracking, here observed in corrosion fatigue, is similar to that observed by Cowgill et al [*13*] for stress corrosion of Ti-8A1-1Mo-1V where secondary cracking along the alpha-beta interface and in the coarse alpha also occurred.

These results are consistent with other work which showed that in typical alpha-beta alloys, transgranular cleavage normally occurs in the alpha

phase [*14–16*] on or near the (0001) planes [*16*] and occasionally at the alpha-beta interface [*13–17*]. The effect of the microstructural parameters that have been observed indicates that the acicular alpha microstructure has better resistance to corrosion-fatigue cracking than larger equiaxed alpha microstructures. This is believed to be due to smaller alpha particle size which requires additional cleavage cracks to be developed to extend the primary crack a given increment. However, the effectiveness of the acicular microstructure is also dependent on the strength and characteristics of the beta matrix material.

As the stress ratio was increased from 0.1 to 0.5, the fatigue crack growth rates were found to increase most markedly at low-ΔK values and at high-ΔK values, with relatively little change in the intermediate ΔK range. The increased rates at high-ΔK values were typical and result from the K_{max} of the load cycle approaching the K_Q of the material. Increased rates at low-ΔK values would appear to suggest that in this region the maximum stress intensity may no longer be a secondary variable to the alternating stress intensity.

Conclusions

For this alloy, the following conclusions can be drawn.

In general, decreasing frequency resulted in an increase in fatigue crack growth rate. This effect was enhanced as the aggressiveness of the environment was intensified.

At low-ΔK levels in detrimental environments (including high humidity), the frequency effect was typified by a crossover of the slowest frequency (0.1 Hz) *da/dN* curve and the 10 Hz *da/dN* data.

For ⅜-in. (0.952-cm) thick material tested at $R = 0.1$, a rapid instability in crack growth rate at low frequencies was observed in 3.5 percent sodium-chloride solution at a $K_{max} \cong 18$ to 20 ksi $\sqrt{\text{in.}}$ (20 to 22 MPa $\sqrt{\text{m}}$). Failure occurred in only a few cycles once this value of K_{max} was reached. This ΔK level for rapid crack acceleration was considerably below the apparent sustained load flaw growth threshold of 30 ksi $\sqrt{\text{in.}}$ (33 MPa $\sqrt{\text{m}}$) for fracture in 3.5 percent sodium-chloride solution in 300 h.

In high humidity, laboratory air, and dry air environments, the fatigue crack growth rates at $R = 0.1$, 10 Hz were independent of flaw type.

In 3.5 percent sodium-chloride solution, crack-growth rates at $R = 0.1$, 10 Hz in WOL and CCT coupons increased relative to baseline rates, but growth rates in PTC coupons did not increase.

Increasing the stress ratio from 0.1 to 0.5 increased the fatigue crack growth rates in ⅜-in. (0.952-cm) material at low- and at high-ΔK values with relatively little change in the intermediate ΔK range. Observed increased rates at low-ΔK values shifted the apparent threshold value to

lower ΔK levels and would suggest that in this region the maximum stress intensity/environment interaction may no longer be a secondary variable compared to the effect of alternating stress intensity.

For the ⅛-in. (0.318-cm) material, similar fatigue crack growth trends were noted. However, the 0.1 Hz 3.5 percent sodium-chloride solution curve for the thin material did not exhibit rapid acceleration in rates until the fracture toughness value was reached. This was probably due to decreased constraint in the ⅛-in. (0.318-cm) thick material.

Fatigue crack growth rates of the ⅛-in. (0.318-cm) thick coupons were slower than for ⅜-in. (0.952-cm) thick coupons tested at the same load ratio and frequency and in the same environment.

Acknowledgments

This report is based on part of the results of a contract, No. AF33615-71-C-1688 supported by the U.S. Air Force, Air Force Materials Laboratory, Wright-Patterson Air Force Base, Ohio.

References

[1] Hardrath, H. F., "Fatigue and Fracture Mechanics," AIAA Paper 70-512, American Institute of Aeronautics and Astronautics, Denver, Col., 1970.

[2] Hinder, U. A., "F-111 Design Experience—Use of High Strength Steel," AIAA Paper 70-884, American Institute of Aeronautics and Astronautics, Los Angeles, Calif., 1970.

[3] Pettit, D. E., Ryder, J. T., Krupp, W. E., and Hoeppner, D. W., "Investigation of the Effects of Stress and Chemical Environments on the Prediction of Fracture in Aircraft Structural Materials," Technical Report AFML-TR-74-183, Air Force Materials Laboratory, Dec., 1974.

[4] Hall, J. A., Pierce, C. M., Ruckle, D. L., and Sprague, R. A., "Property-Microstructure Relationships in the Ti-6Al-2Sn-4Zr-6Mo Alloy," *Materials Science and Engineering,* Vol. 9, 1972.

[5] Wessel, E. T., *Engineering Fracture Mechanics,* Vol. 1, 1968, pp. 77–101.

[6] Irwin, G. R., *Journal of Applied Mechanics,* Vol. 85, 1962, pp. 651–654.

[7] Federson, G. E. in *Plane Strain Crack Toughness Testing, ASTM STP 410,* American Society for Testing and Materials, 1969, pp. 77–79.

[8] Dawson, D. B. and Pelloux, R. M., *Mettalurgy Transactions,* Vol. 5, March 1974, pp. 723–731.

[9] Kraft, J. M., *Transactions,* American Society of Mechanical Engineers; *Journal of Engineering Materials and Technology,* Vol. 96, Series H, No. 4, Oct., 1974, pp. 275–282.

[10] Pettit, D. E., Krupp, W. E., Ryder, J. T., and Hoeppner, D. W., "Investigation of the Effects of Stress and Chemical Environments on the Prediction of Fracture in Aircraft Structural Materials," Technical Report LR 26026, Lockheed-California Company, July 1973.

[11] Kraft, J. M., "Method for Relating Plastic Flow Properties to Fatigue Crack Propagation Including Effects of Stress Ratio," NRL Memorandum Report 2980, Naval Research Laboratory, Jan. 1975.

[12] Ryder, J. T., Krupp, W. E., Pettit, D. E., and Hoeppner, D. W., "Stress Corrosion Crack Growth in Aircraft Alloys," submitted to *Journal of Testing and Evaluation.*

[13] Cowgill, D. S., Fritzen, J. S., Krystkowiak, S., and Weber, K. E., "Crack Morphology

Studies in the Ti-8Al-1V-1Mo Alloy," paper presented at ASTM-ARPA Symposium on Stress Corrosion and Corrosion Principles, Atlanta, 1968.

[*14*] Curtix, R. E. and Spurr, W. F., *Transactions,* American Society for Metals, Vol. 61, 1968, pp. 115–127.

[*15*] Powell, D. T. and Scully, J. C. in *The Science, Technology, and Application of Titanium,* Pergamon Press, New York, 1968, pp. 247–256.

[*16*] Fager, D. N. and Spurr, W. F. in *The Science, Technology, and Application of Titanium,* Pergamon Press, New York, 1968 pp. 259–626.

[*17*] Piper, D. E., Smith, S., and Carter, G. C., Stress Corrosion Cracking in Aqueous Environments," *Metals Engineering Quarterly,* Vol. 8, No. 3, Aug. 1968, p. 50.

G. R. Chanani[1]

Effect of Thickness on Retardation Behavior of 7075 and 2024 Aluminum Alloys

REFERENCE: Chanani, G. R., **"Effect of Thickness on Retardation Behavior of 7075 and 2024 Aluminum Alloys,"** *Flaw Growth and Fracture, ASTM STP 631,* American Society for Testing and Materials, 1977, pp. 365–387.

ABSTRACT: The effect of specimen thickness on retardation behavior was investigated by using 12.7, 6.4, and 1.6-mm thick single-edge notched specimens of 7075 alloy in the T6 and T73 conditions and 2024 alloy in the T3 and T8 conditions. Single overload cycles were used with two different overload ratios, and interferometry was used to measure the surface plastic-zone size. The cyclic hardening exponents for all four materials were determined by obtaining cyclic stress-strain curves using incremental strain-cycling tests on 6.4-mm diameter cylindrical specimens. Test results indicated that the amount of retardation decreases with increasing specimen thickness. However, the relative decrease was more predominant in the 7075 alloy and at the higher overload ratio, 2.0. The effect of thickness on the retardation behavior of the 2024-T8 alloy was not conclusive. It appeared that thickness changes have only a minor effect on the retardation behavior of the 2024-T8 alloy. Fractography was used to study the micromechanisms of crack growth. Well-defined striations and changes in the striation spacings after an overload cycle were not seen in all specimens studied, and no striations were observed immediately following the overload cycle. The lack of discernable striations could be due to: abrasion, difficulty in resolving striations associated with relatively low crack-growth rates, change in crack-propagation mode, or a combination of all of these factors. However, the agreement between the measured *da/dN* and the striation spacings was good for all the specimens in which striations were discernable.

KEY WORDS: crack propagation, fracture (materials), aluminum alloys

Retardation of fatigue-crack growth due to tensile overloads is well established [*1–8*].[2] However, the mechanisms of overload retardation have not been well understood. Several empirical models which take retardation into account have been developed to predict the fatigue-crack growth

[1]Engineering specialist, Metallics Research Department, Northrop Corporation, Hawthorne, Calif. 90250.

[2]The italic numbers in brackets refer to the list of references appended to this paper.

under variable amplitude loading [*9–13*]. Most of these models are based on the changes in the plastic-zone size at the crack tip. Since thickness affects the plastic zone size [*14*], it seems plausible to assume that thickness may have an effect on retardation behavior. Some work has been reported on this aspect of retardation behavior. Mills and Hertzberg [*15*] found that a decrease in thickness increased the number of delay cycles in 2024-T3 alloy at an overload ratio (OLR) of 2.0, while at an OLR of 1.5, the thickness effect was small. Shih [*16*] also found a decrease in the number of delay cycles with an increase in thickness in 7075-T6 alloy. However, Sharpe et al [*17*] did not find any effect of thickness on the number of delay cycles in the 2024-T851 alloy. Hence, it appears that there is considerable uncertainty about the effect of thickness on retardation behavior, depending on the alloy and testing parameters used.

In the present investigation, 12.7 mm, 6.4 mm, and 1.6-mm-thick, single-edge notched (SEN) specimens of two aluminum alloys in four heat treat conditions were used with the 7075 alloy in the T6 and T73 conditions and the 2024 alloy in the T3 and T8 conditions. In this work, only single overload cycles were used. The changes in the size of the surface plastic-zone at the crack tip were determined by optical interferometry. These interferometry results were correlated with the retardation behavior. Fractography also was employed to understand the micromechanisms of failure in different thicknesses and alloys.

Experimental Procedure

SEN specimens (Fig. 1) with three different thicknesses, 1.6, 6.4, and 12.7 mm, were used for this investigation. The 6.4-mm-thick specimens were obtained from the center of the same stock as the 12.7-mm specimens. The 1.6-mm specimens were obtained from a different heat of material than the 6.4 and 12.7-mm specimens.

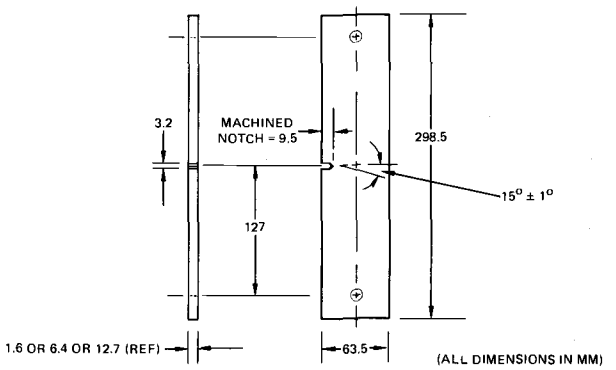

FIG. 1—*SEN aluminum specimen, LT (RW) orientation.*

The effects of single overloads on the fatigue crack growth behavior were determined using a simple, two-level spectrum of the type shown in Fig. 2 in a controlled laboratory atmosphere (22 °C ± 3 °C and 50 ± 5 percent relative humidity). All of the constant-amplitude load cycles were conducted at an R ratio (P_{min}/P_{max}) of 0.1 and a frequency of 5 Hz, while the overload cycles were run at 0.1 Hz. The number of constant-amplitude cycles was sufficient for complete recovery of the unretarded crack-growth rate. The crack lengths were measured using imprinted photogrids (intergrid spacings of 0.5 mm) with a filar eyepiece in a high-magnification traveling microscope. Generally, crack lengths were similar on both faces of each specimen. However, in some of the thick specimens, the crack front did not grow uniformly on both faces; that is, the crack front on one face lagged behind the crack front on the other face. In those tests where the crack on one face lagged the other by a small amount, an average of both the measurements was taken. If the difference in crack length between the two faces was larger than 2.5 mm, the data were considered invalid.

A Zeiss interference microscope with thallium spectrum lamp was used to observe the surface plastic-zone size at the crack tip for all three thicknesses of the four alloys. With this procedure, one can measure surface thickness changes as small as 0.03 μ(300Å).

Changes in the morphology of the fracture surfaces due to overload cycles were determined using the scanning electron microscope (SEM) for each thickness. Fracture surfaces were cleaned by replication and then gold-shadowed before SEM observation.

Results and Discussion

Table 1 lists the tensile properties of the four alloys obtained from both 1.6-mm-thick sheets and 12.7-mm-thick plates. Since the 6.4-mm-thick specimens were obtained by machining the 12.7-mm-thick plates, their

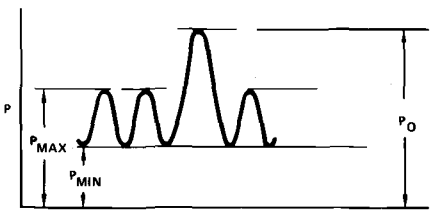

FIG. 2—*Schematic representation of the test spectrum.*

TABLE 1—*Tensile properties of the aluminum alloys.* [a,b]

Alloy and Heat Treatment	Thickness, mm	0.2% YS, MN/m^2	UTS, MN/m^2	Elongation, %	Monotonic Strain Hardening Exponent	Cyclic Hardening Exponent
7075-T6	1.6	504	553	12.5	0.071	...
7075-T651	12.7	502	541	12.6	...	0.07
7075-T73	1.6	419	491	12.3	0.133	...
7075-T7351	12.7	445	512	15.0	...	0.09
2024-T3	1.6	356	471	18.6	0.163	...
2024-T351	12.7	361	457	18.8	...	0.06
2024-T8	1.6	422	471	10.0	0.083	...
2024-T851	12.7	485	519	10.3	...	0.13

[a] For 1.6 mm thick sheet, flat specimens of 50.8 mm gage length were used, while for 12.7 mm thick plate, cylindrical specimens of 25.4 mm gage-length were used.

[b] The reported values are the average of three tests.

tensile properties are essentially the same as those for the 12.7-mm-thick specimens. The yield and tensile strengths of both the thick (6.4 mm and 12.7 mm) and thin (1.6 mm) material were generally within 5 percent of each other for three of the four alloys investigated. A significant difference in the yield strength, approximately 13 percent between the thick and thin conditions, was found only for the 2024-T8 alloy. The chemical compositions and mechanical properties of both the thicknesses of 2024-T8 were within the acceptable specifications. Hence, the difference in the yield strength of the two conditions can be attributed to the heat-to-heat variations within the normal procurement specifications. The implications of this difference in determining the effect of thickness on the retardation behavior of the 2024-T8 alloy are discussed later.

The retardation results are summarized in Tables 2 and 3. The number of delay cycles, N^*, and affected crack length, a^*, refer to the number of cycles and crack length over which the retardation occurs, respectively. Figure 3*a* schematically shows how the number of delay cycles and affected crack length were determined, while Fig. 3*b* shows typical crack length versus number of cycles for the three thicknesses of the 2024-T3 alloy after single overload cycles with an OLR of 2.0. These are typical of all the tests conducted. For the 1.6-mm-thick specimens, baseline reference data for no overload conditions were obtained by conducting constant-amplitude load tests, while for the 6.4 and 12.7-mm-thick specimens, da/dN was obtained from the retardation tests once crack growth had stabilized. Due to the difficulty of obtaining a unique slope at the end of the delay region, a straight crack front, particularly for the thicker specimens and the inherent scatter in the crack-growth rate after the overload cycle, a small difference in number of delay cycles between any two tests should not be considered significant.

The retardation, interferometry, and fractographic results are described and discussed next.

Retardation Test Results

7075-T73 Alloy—Figure 4 shows the amount of delay for a given stress-intensity factor as a function of thickness for the 7075-T73 alloy. In this figure, the minimum recommended thickness (ASTM Test for Plane-Strain Fracture Toughness of Metallic Materials (E 399-74)) to obtain a plane-strain condition for each case is denoted by an X. The approximate thickness for plane strain was calculated from the formula per ASTM Method E 399-74

$$B_0 \geq 2.5 \left(\frac{K_0}{\sigma_{ys}}\right)^2 \tag{1}$$

TABLE 2—*Summary of retardation results in air for different thicknesses of 7075-T73 and T6 alloys.*

$$\frac{P_{max}\text{ (baseline max load)}}{B\text{ (thickness)}} = 1401\text{ N/mm}$$

B, mm	Specimen No.	OLR	K_{max}, MN/m$^{-3/2}$	a_i, mm	a^*, mm	N^*, 1000	ACCL[a]
			7075-T73				
12.7	HT73THK1	1.5	6.7	14.5	0.08	12.5	a
			9.7	20.3	0.15	4	a
			13.6	26.1	0.46	3	c
	HT73THK2	2.0	6.7	14.5	0.03	20	a
			9.7	20.3	0.51	12.5	c
			13.6	26.1	0.88	8	c
6.4	HT73THK3	1.5	6.7	14.5	0.23	15	a
			9.7	20.3	0.30	5	b
			13.6	26.1	0.63	3	a
	HT73THK4	2.0	7.0	15.0	0.13	20	a
			10.0	20.9	0.91	15	a
			14.2	26.6	1.36	10	b
1.6	DT73OLC1	1.5	6.7	14.5	0.31	17.5	a
			8.5	18.1	0.23	6	a
	DT73OLC2	2.0	5.9	12.7	0.48	55	a
			8.5	18.2	0.64	25	a
			11.2	23.0	1.10	20	b

7075-T6

12.7	HT6THK1	1.5	7.0	15.0	0.06	8	a
			8.7	18.5	0.15	5	a
			10.8	22.0	0.08	1.5	a
	HT6THK2	2.0	7.0[b]	15.0	...	...	a
			8.7	18.5	0.69	9	a
			10.8	22.0	0.33	3	a
6.4	HT6THK3	1.5	7.0	15.0	0.15	8	c
			8.7	18.5	0.14	4	a
			10.8	22.0	0.58	1	b
	HT6THK4	2.0	6.7[b]	14.5	...	...	a
			8.4	17.7	0.21	12.5	b
			10.2	21.3	0.37	8	b
1.6	DT6OLC1	1.5	6.7	14.5	0.28	17.5	a
			8.4	18.0	0.25	6	b
			10.2	21.5	0.30	4	a
	DT6OLC2	2.0	6.2	13.0	0.10	25	a
			8.1	17.7	0.27	12.5	b
			11.1	22.8	0.54	10	a

[a]a = No crack growth during overload cycle and no initial acceleration.
b = Crack growth during overload cycle.
c = Initial acceleration after the overload cycle.
[b]Crack grew only on one surface, making data invalid.

TABLE 3—*Summary of retardation results in air for different thicknesses of 2024-T8 and T3 alloys.*

$$\frac{P_{max}\text{ (baseline max load)}}{B\text{ (thickness)}} = 1401\text{ N/mm}$$

B, mm	Specimen No.	OLR	K_{max}, MN/m$^{-3/2}$	a_i, mm	a^*, mm	N^*, 1000	ACCL[a]
			2024-T8				
12.7	HT8THK1	1.5	6.7[b]	14.5	...	...	a
			11.2	22.9	0.76	4	b
			14.3	26.9	0.30	2	b
	HT8THK2	2.0	6.7	14.5	0.41	25	a
			9.6	20.1	0.25	10	b
			13.6	25.9	1.68	8	b, c
6.4	HT8THK3	1.5	6.7	14.5	0.05	8	a
			9.7	20.3	0.06	1.5	a
			13.6	26.1	0.37	2	b
	HT8THK4	2.0	6.7	14.5	0.12	35	a
			9.7	20.3	0.29	15	a
			13.6	26.1	1.93	15	b
1.6	DT8OLC1	1.5	6.7	14.5	0.26	12.5	a
			8.7	18.5	0.07	5	a
			12.2	24.4	0.11	2	a
	DT8OLC2	2.0	6.7	14.5	0.83	30	b
			8.7	18.6	0.38	20	b
			10.8	22.3	1.07	15	b

2024-T3

12.7	HT3THK1	1.5	6.9	14.7	0.08	40	a
			9.7	20.3	0.23	15	a
			13.8	26.4	0.53	4	a
	HT3THK2	2.0	6.7	14.5	0.13	175	a
			9.7	20.3	0.66	60	b, c
			13.6	26.1	1.16	17.5	b
6.4	HT3THK3	1.5	6.7	14.5	0.08	50	a
			9.6	20.1	0.43	15	b
			13.8	26.2	0.71	5	a
	HT3THK4	2.0	6.7	14.5	0.66	185	a
			9.6	20.1	0.84	50	b
			13.8	26.2	1.93	80	a
1.6	DT3OLC1	1.5	6.7	14.5	0.29	55	a
			8.4	17.9	0.39	20	a
			10.7	22.0	0.60	12.5	c
	DT3OLC2	2.0	6.7	14.5	0.80	240	a
			8.5	18.1	1.12	145	b
			10.3	21.5	1.02	130	a

[a]a = No crack growth during overload cycle and no initial acceleration.
b = Crack growth during overload cycle.
c = Initial acceleration after the overload cycle.
[b]Crack grew only on one surface, making data invalid.

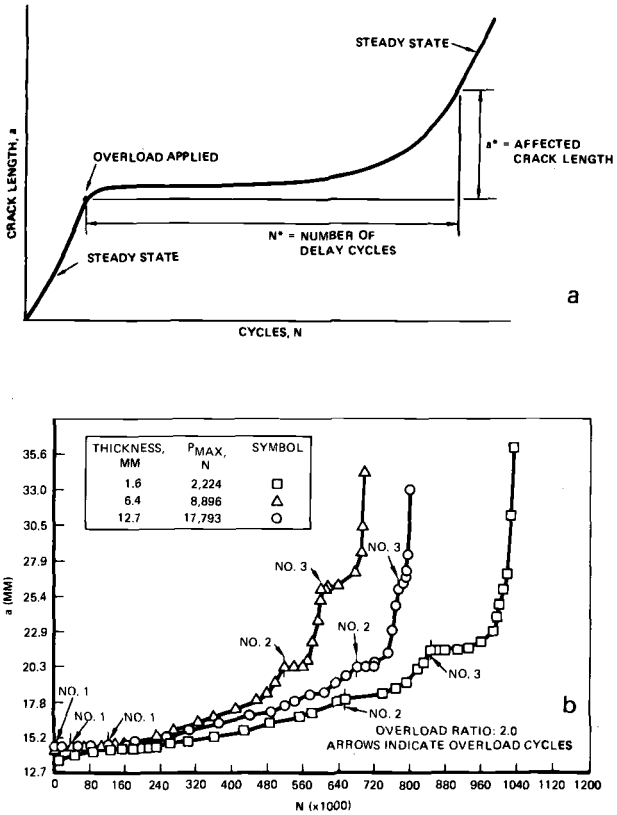

FIG. 3—(a) *Crack-growth rate curve resulting from application of a single overload, and* (b) *crack length versus number of cycles for three thicknesses of 2024-T3 alloy at an overload ratio of 2.0.*

where

B_0 = plane-strain thickness,
σ_{ys} = yield strength of the alloy, and
K_o = overload stress-intensity factor.

In these and subsequent figures showing retardation behavior for other alloys, whenever the stress-intensity level for any particular data point was significantly different from those of other points, it was shown as a number in parenthesis next to that particular data point.

The number of delay cycles decreased with increasing thickness and decreasing OLR. Furthermore, at a given OLR, the number of delay cycles decreased as the baseline stress intensity increased, even though the affected crack-length, a^*, (Table 2) increased. This was probably due to a higher baseline crack-growth rate and faster recovery of unretarded crack-

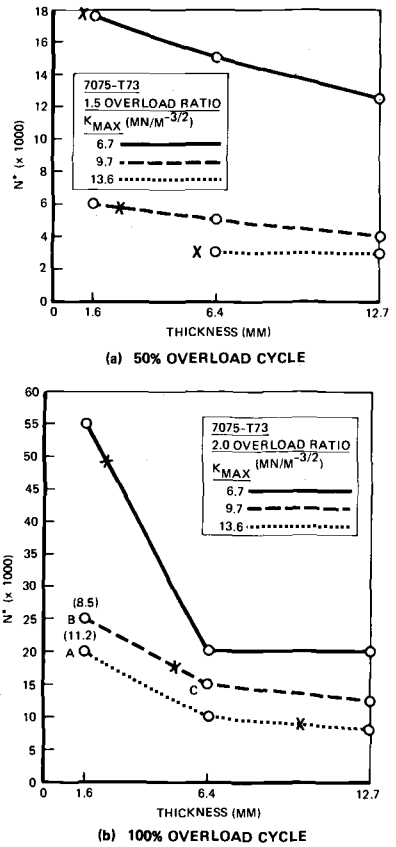

FIG. 4—*Effect of thickness on delay for 7075-T73 alloy; the X denotes ASTM Method E 399-74 plane-strain thickness requirement.*

growth rate which caused the crack to grow through the overload plastic zone in relatively fewer cycles.

Even though the K_{max} for two of the data points (*A* and *B* in Figure 4*b*) are not completely consistent with other data points, the basic conclusions remain the same. This is so because, if we interpolate between *A* and *B* to obtain an approximate N^* at a K_{max} of 9.7 MN/(m)$^{-3/2}$ for the 1.6-mm-thick specimen, the value of N^* thus obtained will still be higher than that for the 6.4-mm-thick specimen which corresponds to point *C* in the figure. This difference in K_{max} simply means that the drop in N^* as the thickness changes from 1.6 to 6.4 mm may not be as large as shown.

The observed thickness effect on the number of delay cycles at a given *K* level is probably due to an increase in the plastic-zone associated with a decrease in thickness. The approximate plastic-zone size, R_p, under plane-stress conditions is

$$R_p = \frac{1}{\pi}\left(\frac{K_o}{\sigma_{ys}}\right)^2 \tag{2}$$

while under plane-strain conditions, the plastic-zone size, R^*_p, is one third of the foregoing value and given as

$$R^*_p = \frac{1}{3\pi}\left(\frac{K_o}{\sigma_{ys}}\right)^2 \tag{3}$$

The crack tips were under a plane-stress condition during the overload cycle in almost all of the 1.6-mm-thick specimens, as confirmed by the interferometry measurements described in the next section. For mixed mode, the plastic-zone size is between the plane-stress and plane-strain values. The larger plastic-zone sizes under plane-stress conditions cause larger plastic strains and residual stresses at the crack tip and also give rise to severely blunted cracks. For this reason, more retardation was observed in thin specimens of this alloy. However, other factors such as fracture toughness besides the state of stress play a role in determining the thickness effect. This is indicated by the fact that the 2024 alloy did not behave in the same manner as the 7075 alloy.

7075-T6 Alloy—Figure 5 illustrates the thickness effect on the retardation behavior of this alloy. Here too, with an increase in OLR and a dedrease in K_{max} levels, the number of delay cycles increased. The effect of thickness was as expected. However, the results are not as large as those for the 7075-T73 alloy. The reason could be that here the plane-strain condition of Eq 1 is achieved at a much lower thickness because of the higher yield strength of the 7075-T6 alloy as compared to that for the 7075-T73 alloy. Also, since the number of delay cycles is fewer for this heat treatment, the experimental scatter may have masked some of the thickness effect in this alloy.

2024-T8 Alloy—Figure 6 shows the effects of thickness on the number of delay cycles for this alloy. However, the thickness effect on the 2024-T8 alloy is less than that for the 7075 alloys, except for one point at OLR of 1.5, which is probably due to the difficulty of obtaining a straight crack front in this thickness for the 2024-T8 alloy at low-K values. In this case, the thickness effect is even less when we consider that the 6.4 and 12.7-mm-thick specimens had a higher yield strength (Table 1) than the 1.6-mm-thick specimens. Hence, the 6.4 and 12.7-mm-thick 2024-T8 specimens have plastic-zone sizes even smaller than they would have had if the only change was in going from a plane-stress condition to a plane-strain condition. Therefore, the higher yield strength of 6.4 and 12.7-mm-thick 2024-T8 alloy should enhance the thickness effects, if any, in this alloy. Furthermore, some of the observed differences in the number of delay cycles

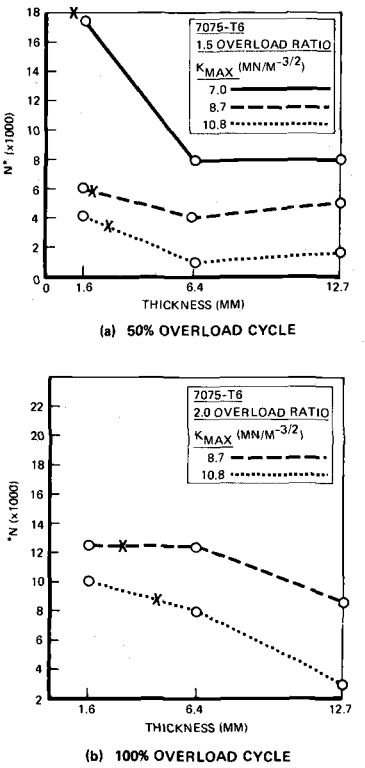

FIG. 5—*Effect of thickness on delay for 7075-T6 alloy; the X denotes ASTM Method E 399-74 plane-strain thickness requirement.*

with changes in thickness in these tests become much less if the K_{max} differences in the corresponding tests are taken into account. Because of the difficulty of obtaining a straight crack front, the tests on the 2024-T8 alloy could not be conducted at corresponding K_{max} levels for all three thicknesses. When these K_{max} differences are taken into account, as discussed for the 7075-T73 alloy, the point *A* in Figure 6*a* will probably become lower while point *C* will move up, indicating practically no decrease in delay cycles with increase in thickness. Similarly, the difference between points *D* and *E* in Figure 6*b* also becomes less. We also should note that N^* for the data under discussion is of the order of only 2000 to 4000 cycles. Hence, the results on thickness effect in the 2024-T8 alloy are inconclusive, even though they suggest that in this alloy there may be less thickness effect.

2024-T3 Alloy—The trend here (Fig. 7) is essentially similar to that for the 7075-T6 and 7075-T73 alloys. The basic conclusions at OLR of 2.0 remain the same even though the K_{max} values are not exactly similar

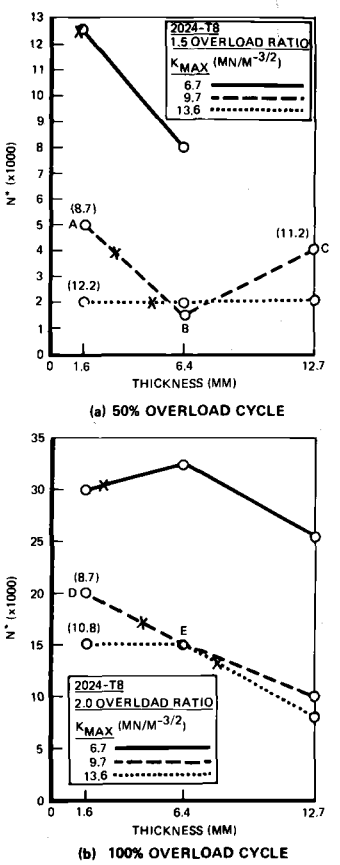

FIG. 6—*Effect of thickness on delay for 2024-T8 alloy; the X denotes ASTM Method E 399-74 plane-strain thickness requirement.*

for all the data points, because the trend is similar to that for the 7075-T73 alloy; that is, the relationship between *A, B,* and *C* in Fig. 7*b* is similar to the corresponding points in Fig. 4*b*. However, at an OLR of 1.5, a similar argument indicates relatively less effect of thickness at a K_{max} of 9.7 MN/(m)$^{-3/2}$ and 13.8 MN/(m)$^{-3/2}$.

The anomalous behavior of one 12.7-mm point (*L*) in Fig. 7*b* could be due to either scatter or the difficulty of getting a straight crack front across the 12.7-mm-thick 2024 alloy at the lower *K* values or a combination of both. In all the other alloys, the 12.7-mm thickness was adequate for obtaining plane strain at all the *K* values tested. However, in the 2024-T3 alloy, the plane-strain condition was not reached at the K_{max} of 13.8 MN/(m)$^{-3/2}$, even for 12.7-mm-thick specimens. This is reflected by the fact that the number of delay cycles had not reached a minimum at 12.7 mm

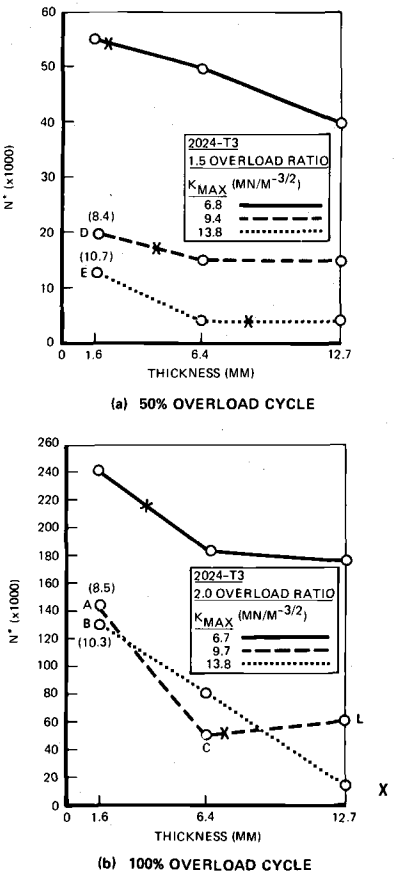

FIG. 7—*Effect of thickness on delay for 2024-T3 alloy; the X denotes ASTM Method E 399-74 plane-strain thickness requirement.*

at a K_{max} of 13.8 MN/(m)$^{-3/2}$ in the 2024-T3 alloy as had happened in all the other alloys.

Microstructural Differences and Summarization of Retardation Test Results

In general, a decrease in the number of delay cycles was observed with increase in thickness. However, the results were not uniform or conclusive, particularly for the 2024-T8 alloy. With the 2024-T8 alloy, there appeared to be less thickness effect.

The cyclic hardening exponents for all four alloys are listed in Table 1. They were determined by obtaining cyclic stress-strain curves. These curves were obtained by the incremental strain-cycling method described

by Landgraf et al [*18*] using 6.4-mm-diameter cylindrical specimens obtained from the 12.7-mm-thick stock. As seen in Table 1, the 2024-T8 alloy does have a completely different cyclic hardening exponent. The cyclic hardening exponent apparently influences the plastic-zone size, because, as shown in Table 4, the measured plane-stress plastic zone for the 1.6-mm-thick 2024-T8 specimen is smaller than that for the 1.6-mm-thick 7075-T73, even though they both have the same yield strength. The reason for this difference in cyclic hardening exponent is probably due to the nature of the precipitates in the 2024-T8 alloy, which are essentially S' and not Guinier-Preston (GP) zones as in the 2024-T3 or η' and GP zones as in the 7075-T6 alloy. This difference in precipitate nature and morphology is probably responsible for the fact that, in this case, the number of delay cycles did not decrease with increase in thickness, and, also, the number of delay cycles was generally lower for the 1.6-mm-2024-T8 alloy than that for the 1.6-mm-7075-T73 alloy, even though they both have a similar yield strength in this thickness. Hence, the microstructural differences are probably the key to differences in observed retardation behavior. A more detailed metallurgical study should provide a definite answer. Nevertheless, these results indicate that for improved prediction models, one has to take thickness and microstructural factors into consideration in addition to the yield strength and applied K.

Interferometry Results

As previously reported [*1*], the optical interference technique gives a reliable measurement of the surface plastic-zone size for the SEN specimens. Here, interferometry patterns were obtained in each of the three thicknesses for all four alloys after 100 percent overload cycles. Table 4 summarizes measured overload plastic-zone sizes from these observations.

The agreement between measured and calculated plastic-zone size is very good for the 1.6-mm-thick specimens as shown in Table 4. Except for the 2024-T8 alloy, no alloy showed a consistent decrease in surface plastic-zone size with increase in thickness. However, the changes in plastic-zone size with change in thickness were manifested in fractographic observations described in the next section. This was so because the interferometry measures surface plastic zone, and, for specimens of any thickness, a pure plane-strain condition does not exist at the surface because of the lack of a three-dimensional constraint at the surface. Hence, the changes in interferometry patterns as the crack passes through the plastic zone can be correlated accurately with the retardation behavior only for the 1.6-mm thickness.

For this purpose, patterns were obtained (*a*) immediately after the overload cycle, (*b*) when the crack was halfway through the plastic zone, and (*c*) when the crack was beyond the plastic-zone. The retardation behavior

TABLE 4—*Comparison of calculated and measured plastic-zone sizes in the four alloys.* [a,b]

Alloy	B_o, Min Plane-Strain Thickness Eq 1, mm	Calculated R_p Plane-Stress Eq 2 ⌢mm	Orientation	Approximately Measured Overload Plastic-Zone, mm: Specimen Thickness 1.6 mm	6.4 mm	12.7 mm	Calculated R_p* Plane-Strain Eq 3 ⌢mm
2024-T3	7.3	0.93	X	0.76 ± 0.33	0.87 ± 0.66	0.72 ± 0.53	0.30
			Y	0.99 ± 0.08	1.23 ± 0.04	1.14 ± 0.10	
2024-T8	5.2	0.66	X	0.50 ± 0.05	0.28 ± 0.02	0.22 ± 0.02	0.17
			Y	0.63 ± 0.04	0.41 ± 0.03	0.29 ± 0.03	
7075-T73	5.3	0.67	X	0.56 ± 0.04	0.42 ± 0.02	0.41 ± 0.19	0.20
			Y	0.80 ± 0.17	0.54 ± 0.06	0.54 ± 0.09	
7075-T6	3.6	0.46	X	0.43 ± 0.03	0.64 ± 0.08	0.52 ± 0.04	0.15
			Y	0.64 ± 0.04	0.61 ± 0.03	0.60 ± 0.08	

[a] Orientation: 

[b] All the measurements were made after an OLR of 2.0 and at a baseline K_{max} of 9.6 $MN/m^{-3/2}$.

of these same specimens also was measured. Figure 8 shows such a correlation for the 7075-T6 alloy after a 100 percent overload cycle. The figure clearly shows an excellent correlation between the retardation behavior, affected crack length, and the overload plastic zone.

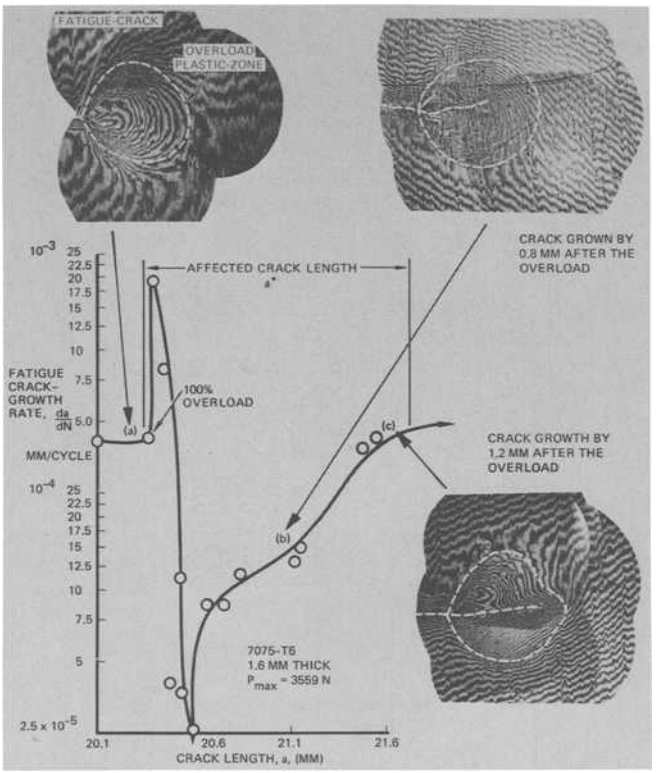

FIG. 8—*Interference patterns at different stages of crack growth after a 100 percent overload cycle.*

Fractographic Results

The fracture surfaces of selected retardation specimens from each alloy and thickness were examined to understand the micromechanisms of crack growth due to the overload cycles with special attention to the following.

1. The nature and size of the overload region, the occurrence of stretch zones, dimples, abrasion, etc., and their relationship to the plastic-zone size for the three thicknesses tested.

2. The effect of single overload cycles on the microscopic crack-growth rate as indicated by the changes in striation spacings.

For this purpose, fractographs were obtained (*a*) before overload, (*b*) in the overload stretch-band, and (*c*) at several locations in the retardation zone. The overload cycle manifested itself as a stretch band across the thickness of the failed specimens in almost all the cases. The width of the overload stretch zone and associated retardation region increased with decreasing thickness and increasing applied K level. It increases from a barely visible thin line at low-K levels and larger thicknesses to a wide band overload zone which exhibits more dimpling and tunneling at lower thicknesses and higher K values. This increased stretch band is a direct manifestation of the overload plastic-zone size which increases with decreasing thickness and increasing K.

Figure 9 shows the results for a 1.6-mm-thick 2024-T3 specimen. Here, as the stress-intensity level went up, the width of the overload zone increased because the plastic-zone size is directly proportional to the square of applied K as shown in Eq 2.

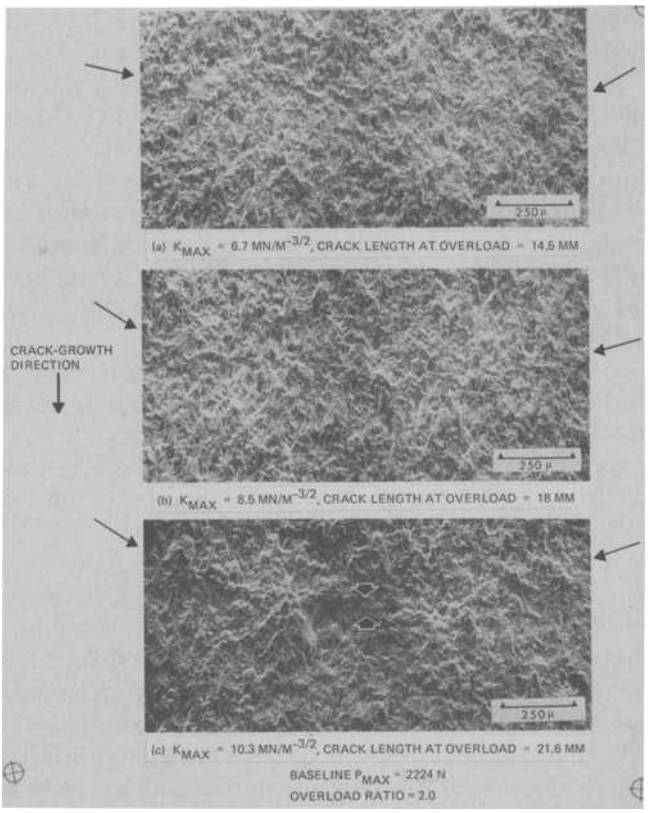

FIG. 9—*Fractographs showing effect of stress intensity on overload marking after a 100 percent single overload cycle in a 1.6-mm 2024-T3 specimen.*

The overload band or stretch zone associated with the incremental crack growth during the rising load portion of the overload cycle is marked by a dimpled region (Fig. 9*c*). The tunneling effect in the stretch zone, particularly for 1.6-mm-thick specimens, as shown in Fig. 9*b* and *c*, is due to the relatively plane-strain condition along the midsection of the specimen. Immediately following the stretch marking is the retardation zone marked by a rather smooth topography, characteristic of a very low fatigue crack-growth rate. Evidence of abrasion and fatigue striations also was observed in these regions in some cases. As one proceeds further from the overload region, the topography of the fracture surface becomes increasingly similar to that before the overload due to the recovery of constant-amplitude, crack-growth rate.

For 1.6-mm-thick specimens, the overload marking was clearly visible, while for 6.4 mm, it was somewhat less marked, and, at a thickness of 12.7 mm, it was barely visible. This behavior was similar for all the alloys at both OLR. Only the degree of marking was different at OLR of 1.5. At the lowest K, there was no distinct marking for 12.7-mm-thick specimens. Instead, only a change in topography was seen. The change in marking is a direct result of the stress state at the crack tip, which gives rise to a much smaller plastic zone. The 2024-T3 had the best marking, because it has the lowest yield strength of the four alloys.

The abrasion was generally higher in the thin specimens, which could be due to higher compressive levels or crack closure, as suggested by Mills and Hertzberg [*15*]. The crack closure does explain, qualitatively, the occurrence of abrasion. However, the degree of abrasion cannot be explained. Furthermore, controversy exists about whether crack closure can explain quantitatively the observed retardation [*17,19–21*].

In comparing the overload regions and associated affected zones of the 2024 alloy with the 7075 alloy, the 7075-T6 and T73 fall in between those for the 2024-T3 and T8. This behavior is in agreement with the delay behavior observed during testing. The 2024-T8 alloy shows the least amount of delay, while the 2024-T3 alloy shows maximum delay with the 7075-T6 and T73 alloys falling somewhere in between.

Changes in striation spacings across the retardation zone were noted, in some cases, depending on the baseline K. The striation spacings were correlated with measured da/dN. Figure 10 shows typical results from 6.4 and 12.7-mm-thick 7075-T73 specimens tested at an OLR of 2.0. Similar results were obtained for several more specimens. No striations were observed immediately after the overload cycle and at crack-growth rates below 5×10^{-5}mm/cycle. This lack of discernable striations in many cases could be due to abrasion or the difficulty in resolving striations associated with the relatively low crack growth rates or a change in crack-propagation mode or a combination of all these factors. Nevertheless, for the specimens in which striations were discernable, the agreement between measured da/dN and striation spacings was good.

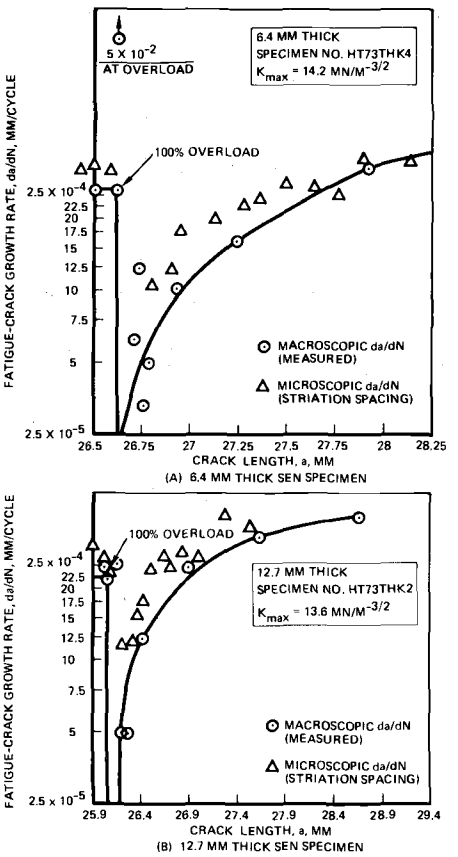

FIG. 10—*Microscopic and macroscopic crack-growth behavior after 100 percent overload cycle in 7075-T73 alloy.*

Summary and Conclusions

1. The number of delay cycles was found to decrease with an increase in thickness, and, hence, in development of models for prediction of fatigue-crack growth under variable loading, consideration should be given to the thickness of structure. However, the results on thickness effect in the 2024-T8 alloy were inconclusive.

2. For a given OLR, the number of delay cycles decreased as the baseline stress-intensity factor was increased, even though the affected crack-length increased.

3. A good agreement between plastic-zone size measured by interferometry and that calculated under plane-stress condition was found for the 1.6-mm-thick specimens of all four alloys.

4. The results showed the applicability of the optical interference technique for investigating the crack-growth behavior as the crack progresses

through the plastic zone under plane-stress conditions and also confirmed that retardation occurs primarily in the overload plastic zone.

5. The overload cycle manifests itself as a stretch band across the thickness of the failed specimens. The width of the overload-stretch zone and the associated retardation region increased with a decrease in thickness and an increase in applied stress-intensity level.

6. In many cases, striations were not observed in the retardation zone. For those specimens with discernable striations, the correlation between measured *da/dN* rates and changes in striation spacing was good.

Acknowledgments

This work was supported, in part, by the Air Force Materials Laboratory, Air Force Systems Command, U.S. Air Force, Wright-Patterson Air Force Base, Ohio, under Contract F33615-74-C-5126, with Dr. D. M. Corbly as the Project Engineer. Thanks are due to J. Clift and B. J. Mays for mechanical testing, T. P. Remmel for fractography, and D. P. Wilhem for a critical review of the manuscript.

References

[1] Chanani, G. R., *Metallurgical Engineering Quarterly,* Vol. 15, 1975, p. 40.

[2] Schijve, J., "Fatigue Crack Propagation in Light Alloy Sheet Materials and Structures," Technical Report MP-195, National Luchtvaartlaboratorium, Amsterdam, Netherlands, 1960.

[3] Hudson, C. M. and Raju, K. N., "Investigation of Fatigue-Crack Growth Under Simple Variable-Amplitude Loading," NASA Report TN D-5702, National Aeronautics and Space Administration, Washington, D.C., March 1970.

[4] Hardrath, H. F., "Cumulative Damage," *Fatigue—Interdisciplinary Approach,* Syracuse University Press, Syracuse, New York, 1964.

[5] Von Euw, E. F. J., Hertzberg, R. W., and Roberts, R., in *Stress Analysis and Growth of Cracks, ASTM STP 513,* American Society for Testing and Materials, 1972, p. 230.

[6] Corbly, D. M. and Packman, P. F., *Engineering Fracture Mechanics,* Vol. 5, 1972, p. 479.

[7] Rice, R. C. and Stephens, R. I., in *Progress in Flaw Growth and Fracture Toughness Testing, ASTM STP 536,* American Society for Testing and Materials, 1973, p. 95.

[8] Schijve, J., *Engineering Fracture Mechanics,* Vol. 5, 1973, p. 269.

[9] Wheeler, O. E., *Transactions,* American Society of Mechanical Engineers, *Journal of Basic Engineering,* Paper No. 71-Met-X.

[10] Willenborg, J., Engle, R. M., and Wood, H. A., "A Crack Growth Retardation Model Using an Effective Stress Concept," Technical Report TM-71-1 FBR, Wright-Patterson Air Force Base, Ohio, 1971.

[11] Porter, T. R., *Engineering Fracture Mechanics,* Vol. 4, 1972, p. 717.

[12] Bell, P. D., and Creager, M., "Crack-Growth Analysis for Arbitrary Spectrum Loading," Technical Report AFFDL-TR-74-129, Oct. 1974.

[13] Antolovich, S. D., Saxena, A., and Chanani, G. R., *Engineering Fracture Mechanics,* Vol. 7, 1975, p. 649.

[14] Liu, H. W., Discussion to a paper of W. Weibull, *Proceedings of the Crack Propagation Symposium,* Vol. 11, Cranfield, 1961, p. 514.

[15] Mills, W. J., and Hertzberg, R. W., *Engineering Fracture Mechanics,* Vol. 7, 1975, p. 705.

[16] Shih, T. T., "Fatigue-Crack Growth Under Variable Amplitude Loading," PhD thesis, Lehigh University, 1974.
[17] Sharpe, W. N., Corbly, D. M., and Grandt, A. F. in *Fatigue Crack Growth Under Spectrum Loads, ASTM STP 595,* American Soeicty for Testing and Materials, 1976, p. 61.
[18] Landgraf, R. W., Morrow, Jo Dean, and Endo, T., *Journal of Materials,* Vol. 4, No. 1, 1969, p. 176.
[19] Chanani, G. R., "Fundamental Investigation of Fatigue-Crack Growth Retardation in Aluminum Alloys," Technical Report AFML-TR-76-156, Sept. 1976.
[20] Chanani, G. R., and Mays, B. J., *Engineering Fracture Mechanics,* Vol. 9, 1977, p. 65.
[21] Shih, T. T. and Wei, R. P., *Engineering Fracture Mechanics,* Vol. 6, 1974, p. 19.

R. J. Bucci[1]

Spectrum Loading—A Useful Tool to Screen Effects of Microstructure on Fatigue Crack-Growth Resistance

REFERENCE: Bucci, R. J., **"Spectrum Loading—A Useful Tool to Screen Effects of Microstructure on Fatigue Crack-Growth Resistance,"** *Flaw Growth and Fracture, ASTM STP 631,* American Society for Testing and Materials, 1977, pp. 388–401.

ABSTRACT: The purpose of this paper is to promote consideration of variable amplitude or spectrum fatigue loading as a useful tool for screening effects of alloy microstructure on fatigue crack-propagation resistance. Increased sensitivity to microstructure, practical interpretation, and economy of testing are offered as rationale for advantageous use of this type of test.

KEY WORDS: fatigue (materials), microstructure, crack propagation, alloys

Though conceptual improvements for the fatigue resistance of metals exist, only limited success has been achieved in improvement of structural fatigue performance in commercial alloys. The present dilemma results from basic limitations in our understanding of the role of alloy microstructure and its relationship to design for a fatigue resistant component. For this reason, fracture control for fatigue has been treated, in part, primarily as a design problem; the design of reliable structures requires a provision that material flaws or cracks will not propagate under cyclic loading to a critical size, whereupon unstable fracture results.

The damage-tolerant design approach strives to limit or retard flaw growth so that the largest possible flaw missed at one inspection will be detected within a later inspection interval; thus, catastrophic failure is avoided. Therefore, fatigue crack-propagation characteristics of aircraft materials are important for development of aircraft structural integrity. For many fatigue critical aircraft applications, potential improvements in fatigue life, aircraft performance, structural efficiency, and fleet maintenance requirements offer ample incentive for both selection and develop-

[1]Staff engineer, Engineering Properties and Design Division, Aluminum Company of America, Alcoa Laboratories, Alcoa Center, Pa. 15069.

ment of high-strength alloys with improved fatigue crack-propagation resistance. However, there is a general lack of consensus among users as to what constitutes significant improvement in fatigue crack-propagation resistance. Comparison of fatigue crack-propagation performance among alloys tends to be qualitative rather than quantitative.

Current adopted methods employed to characterize fatigue crack-propagation behavior of metals involve either determination of crack length, a, versus number of applied stress cycles, N, or the rate of cyclic crack growth, $\Delta a/\Delta N$. The latter is often used in linear-elastic fracture mechanics interpretation, and it is expressed generally as a function of ΔK, the crack-tip, stress-intensity factor range, which essentially measures the cyclic range of localized opening mode crack-tip stresses [*1,2*].[2] Figure 1*a* shows the typical relationship between fatigue crack-growth rate and ΔK observed for most structural alloys when tested in a nonhostile environment. Log-log presentation of the data is used most commonly. Figure 1*b* [*3*] shows typical data which fit the general trend.

For many aerospace engineering problems, crack-propagation data of

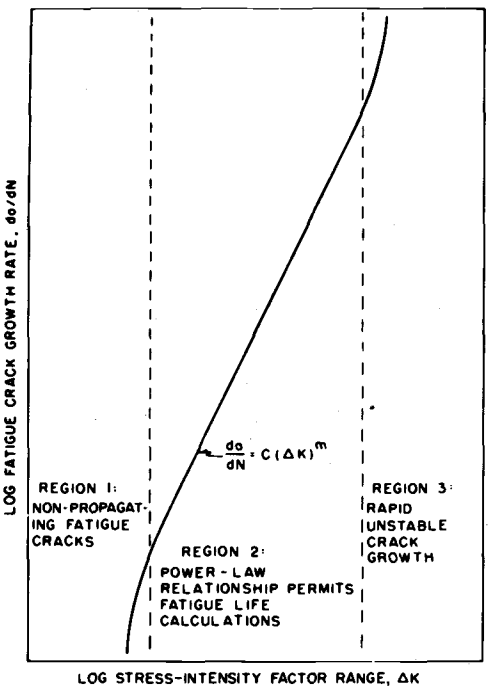

FIG. 1*a*—*Schematic representation of fatigue crack propagation behavior in a nonhostile environment.*

[2] The italic numbers in brackets refer to the list of references appended to this paper.

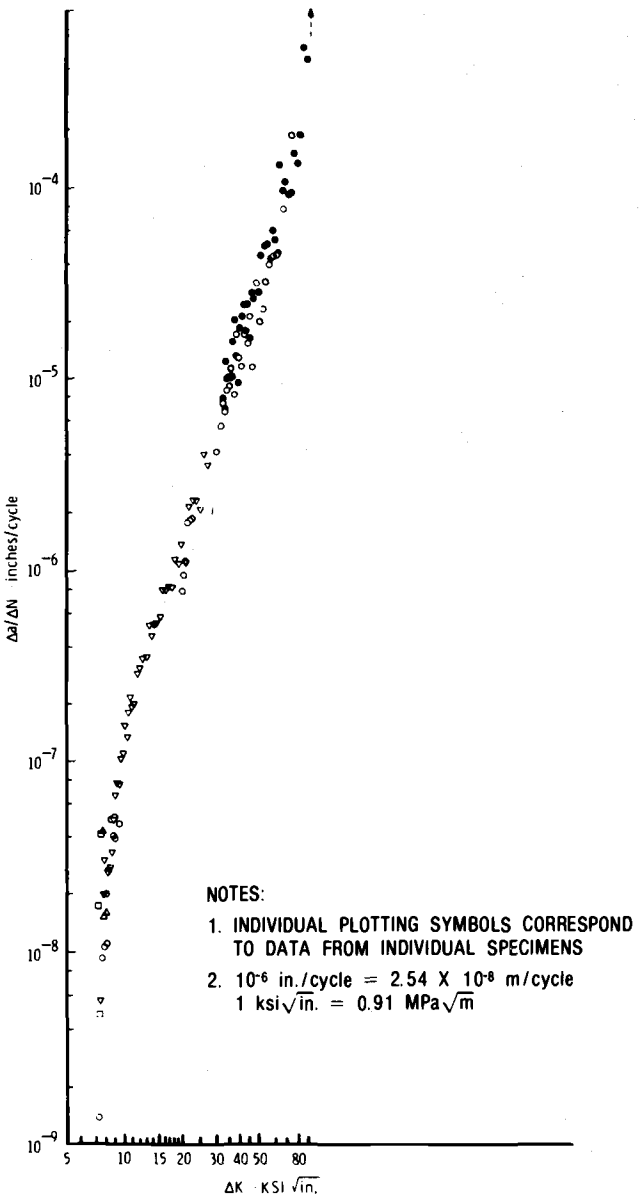

FIG. 1*b*—*Wide range of fatigue crack propagation of ASTM A533 B-1 steel,* R = *0.10; ambient room air 75°F* [3].

Region 2 (Fig. 1*a*), where fatigue crack-growth behavior is often characterized by a linear relationship between log $\Delta a/\Delta N$ and log ΔK, is of greatest practical interest. Within Region 2, the rate of fatigue-crack growth

obtained in inert or innocuous environment (under constant amplitude tension-tension loading) reportedly falls within distinct bands for a wide range of alloys of a given metal system, namely, aluminum, steel, titanium [*4,5*]. For structural steels, the band width is relatively tight, varying by a factor of four for a wide variety of strength, microstructure, and toughness levels [*5,6*]. For aluminum and titanium alloys, the band width is appreciably greater. Clark [*5*], incorporating data of Crooker [*4*], has estimated crack-growth rate scatter band limits for a wide variety of structural aluminum alloys tested in ambient air (Fig. 2). The width of Clark's

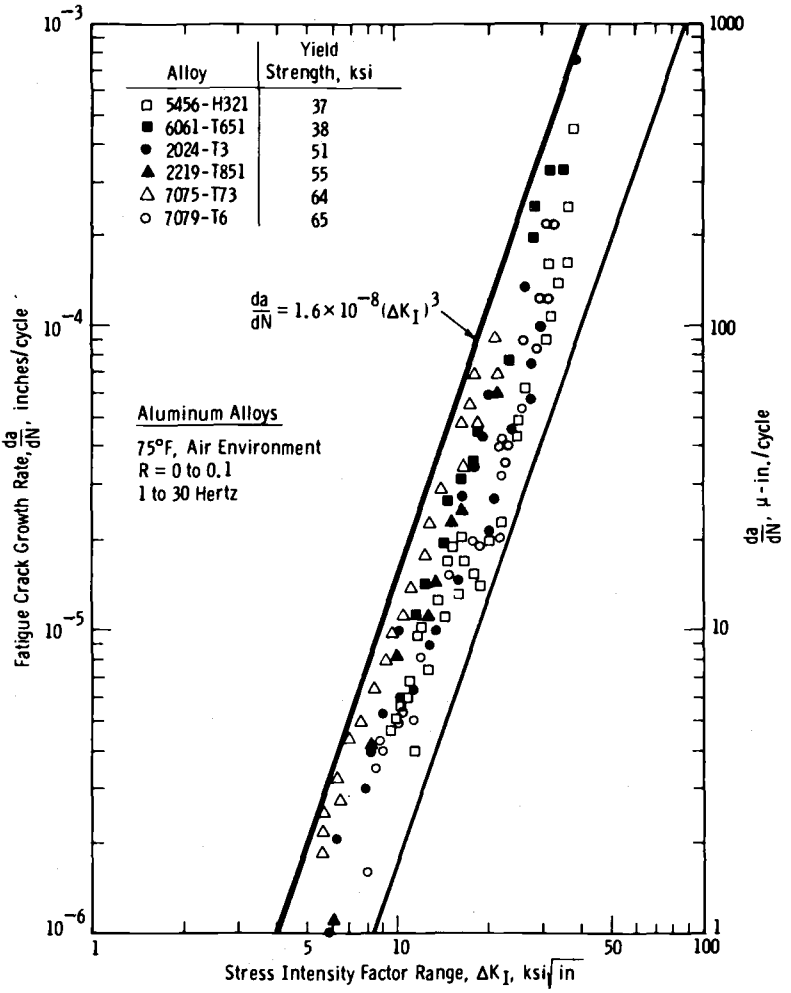

FIG. 2—*Scatter band limits for fatigue crack growth rate behavior for a range of aluminum alloys* [5] (*1μin./cycle = 2.54 × 10⁻⁸ m/cycle, 1 ksi√in. = 0.91 MPa√in.*).

scatter band represents a factor of ten in crack-growth rate at a given ΔK level. A band of this width implies that the linear cumulative damage fatigue life estimate for a structural component can vary as much as a factor of ten based upon use of the limiting bounds of crack-propagation data in the life calculation. This appreciable band width does suggest that significant improvement in fatigue performance may be derived if particular alloys can be selected or developed with propagation behavior confined to the lower bound of crack-growth rate scatter for the given alloy system. A more recent comprehensive study on fatigue crack-propagation resistance of high-strength 2XXX and 7XXX sheet type aluminum alloys was successful at identifying significant effects of microstructural variants, including composition, size, type and morphology of second phase particles on constant amplitude fatigue crack-growth behavior in the linear growth rate region [7]. (Significance was defined at the 95 percent confidence level and was based upon comparison of both propagation life (a versus N) and crack-growth rates, $\Delta a/\Delta N$, at discrete values of ΔK determined from a highly controlled and statistically designed set of fatigue-crack growth experiments.) In this latter investigation, the bound of scatter in growth rates was again found to be approximately one order of magnitude for all microstructures.

In general, replicate constant amplitude tests of a given alloy-temper combination almost always generate growth-rate scatter somewhat less than one order of magnitude. There is, nonetheless, sufficient variability in both the test method and the material (lot to lot) to confound ranking of fatigue crack-growth rate performance of different alloy microstructure possessing similar crack-propagation characteristics.

When plotted as log ΔK versus log $\Delta a/\Delta N$, the somewhat less than dramatic shifts in mean crack-growth performance produced by metallurgical variants within a given metal system have led some researchers to conclude that fatigue crack-propagation behavior of alloys tested in innocuous environments are essentially similar, and they cannot be significantly improved by conventional alloy and process development techniques. However, most aerospace designers will concede that either a 50 percent improvement in component fatigue life or a 10 percent weight reduction afforded by increasing design allowable stresses without reduction in fatigue strength is significant. In many instances, damage tolerant design computations will indicate that the shift in the mean crack-growth rate (log ΔK versus log $\Delta a/\Delta N$) need not be very dramatic to suggest the previous improvements in life or structural efficiency. Therefore, what is needed are screening methods possessing increased sensitivity to alloy microstructure on alloy fatigue crack-propagation performance. In addition, it is desirable that these methods be representative of intended alloy usage.

The real life situation in most fatigue critical applications is variable

amplitude or spectrum loading, rather than constant amplitude tension-tension loading predominantly used in previous investigations. Under variable load history, metallurgical variables can interact with high-tensile fatigue overloads to provide significant delays in crack growth during subsequent fatigue cycle at lower stress amplitudes. This phenomenon, known as crack-growth retardation, is synergistic, that is, the interaction of metallurgical and design variables can far outweight main effects produced by each variable if considered separately.

Crack-growth retardation and the importance of prior stress history on producing retardation effects have been well documented [*8–48*]. To date, proposed mechanisms which explain crack-growth retardation phenomena may be subdivided into two basic categories: crack-geometry effects and the material condition at the tip of the crack. Crack-geometry effects consider such factors as crack length; the curvature of the crack front (straight or curved); the orientation of the crack (slant versus flat); the shape of the crack tip (sharp, blunted, or branched); and the crack closure (plastic deformation in the wake of the crack). The crack-tip material condition includes factors such as plastic deformation in the crack-tip zone, resultant magnitudes, and distributions of residual stresses or strains or both, and cyclic strain hardening or softening. One feature common to all of the proposed mechanisms is that attention is focused upon the current state as well as prior history of plastic deformation in the vicinity of the crack tip. That is, upon application of a large tensile overload, crack-tip deformation and the development of a highly deformed region surrounding the crack make subsequent crack growth at lower stress levels more difficult. The extent of deformation at the crack tip and the size and microstructural characteristics suggest controlling parameters which may vary significantly the magnitude of the crack retardation. Moreover, the material's fracture toughness, that is, ability to survive high-tensile load excursions without significant or catastrophic crack advance, also can influence significantly the fatigue life. That is, alloys which resist failure at high stress-intensity levels generally will produce significant retardation at lower stress-intensity levels. Of course, microstructure controls the character of plastic deformation at, and in the vicinity of, the crack tip, as well as the material's fracture toughness, and, hence, the level of retardation. (Fracture toughness has been noted to vary with product size and form (that is, sheet, plate, forging, extrusion, etc.), where difference in fabrication history may imply differences in microstructure. Differences in variable amplitude loading propagation life with varying product form are, therefore, possible.) Yet, the role and effects of microstructure that control the nature and history of crack-tip deformation have not been well established, nor are the probable important interactions between microstructure and stress history appropriately accounted for in the constant amplitude test.

Emerging experimental evidence suggests that microstructure does indeed have a much greater effect on crack growth under spectrum loading than under constant amplitude loading.

Figure 3 [*49*], for example, illustrates the complicated interaction of microstructure as affected by alloy, temper, plate thickness, and specimen thickness (design variable) on fatigue-crack propagation in several aluminum alloys tested under identical conditions. The crack length versus cycles (or flights) curves shown represent the arithmetic mean of three replicate tests. The cyclic lives of the seven material conditions rank quite differently when tested under constant amplitude and flight by flight spectrum with the greatest range in cyclic lives observed for the spectrum tests. An alternate presentation of the 7075-T7351 and 7050-T73651 data of Fig. 3 is shown in Fig. 4. Linear damage estimates of flight by flight fatigue life calculated from constant amplitude data of 7075 and 7050 alloys are essentially identical. However, comparison of actual fatigue lives of 7050 and 7075 at comparable specimen thickness (6 mm) and product thickness (90 and 100 mm) show 7050 to have longer life in addition to a 15 percent greater yield strength over 7075. (The occurrence of increased life with decreasing specimen thickness observed in 7075 spectrum tests but not in constant amplitude tests has been verified by others [*42,43*]. Potential variation of fracture toughness (microstructure) with product size and a possible interaction with variable load history offers rationale that differences in actual fatigue lives of 100 and 150 mm 7050 plate may have a plausible explanation, other than being attributed solely to test variability. Note that constant amplitude life estimates for both 7050 plate sizes are identical.)

If weight rather than life is the critical design factor, then the flight by flight test data of Fig. 3 can be used to estimate allowable stresses for a given component life. For example, Fig. 5 shows that substituting 7050 for 7075 will allow, σ_0, the minimum spectrum stress to be increased from 196 to 225 N/mm^2 for a life of 5300 flights. (Life predictions were made by employing crack length versus flight information analogous to use of crack length versus cycles information generated from constant amplitude fatigue crack-propagation tests to predict fatigue life as a function of applied stress cycles.) Assuming that minimum part thickness was not controlled by some other factor such as stiffness, this increase in allowable stress would imply a weight savings on the order of 15 percent. For a nonplane-strain stress state, which is common to thin plate and sheet applications, a thickness reduction would offer additional advantages of increasing component fracture toughness, K_c, and increasing the magnitude of retardation (refer to relationship of 7075 spectrum life versus product thickness, Fig. 4). These latter advantages were not considered in the foregoing estimate of weight savings.

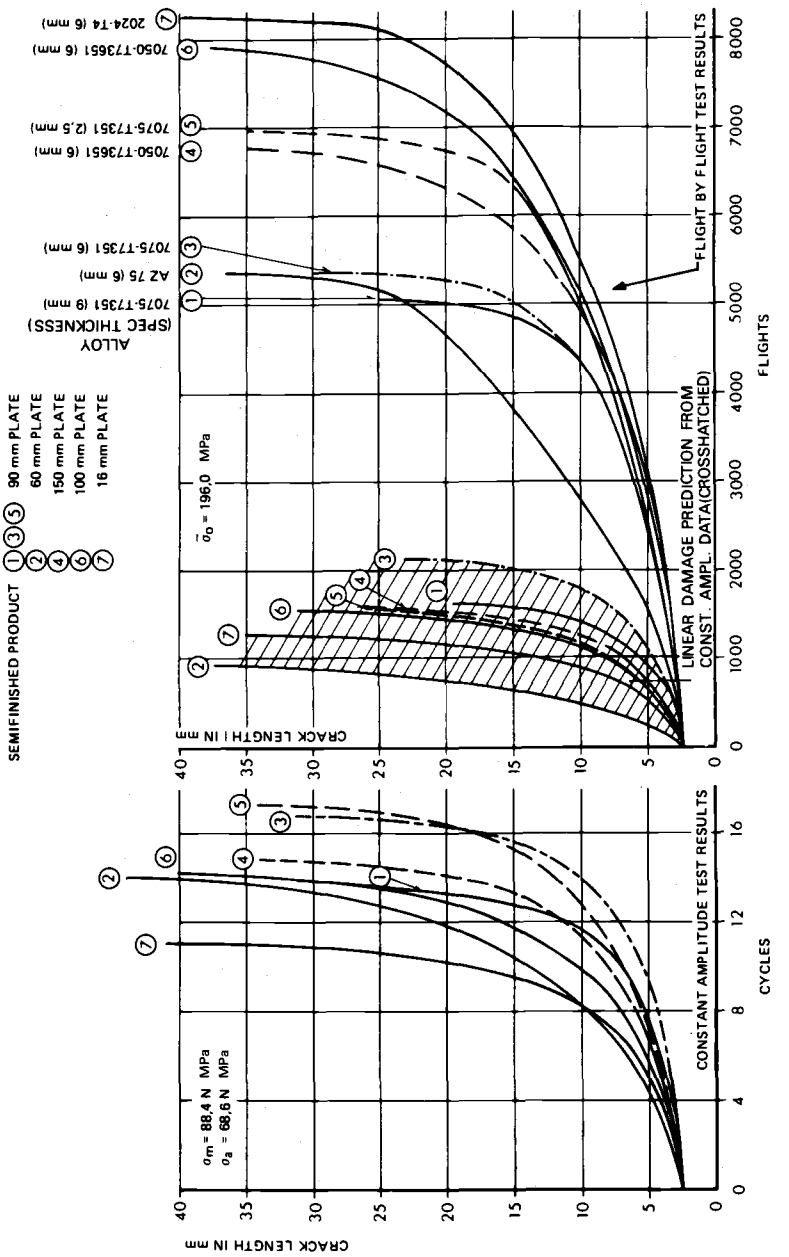

FIG. 3—*Crack propagation tests under flight by flight and constant amplitude loading for different aluminum alloys* [49].

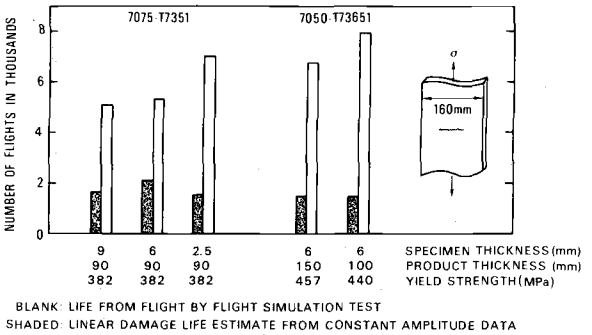

FIG. 4—*Fatigue crack propagation of aluminum alloys under flight simulation loading* [49].

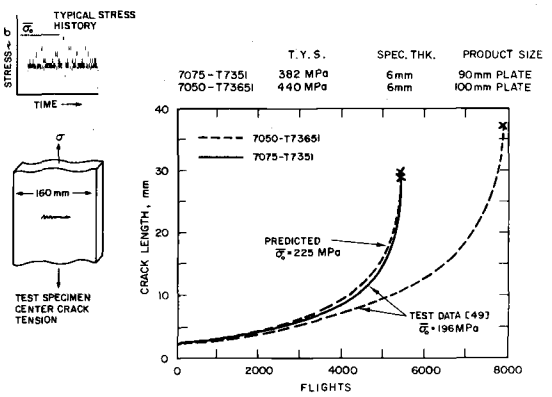

FIG. 5—*Fatigue crack propagation of aluminum alloys under flight simulation loading.*

Flaw tolerability affords an alternate criteria for ranking alloy fatigue crack-propagation performance. Figure 6 shows that for equivalent lives of 5300 flights at $\sigma_0 = 196$ N/mm^2, alloy 7050 will support an initial flaw nearly twice that of 7075, thereby permitting improved structural reliability along with opportunity for significant reductions in inspection and fleet maintenance costs.

Additional results of National Aerospace Labs, Netherlands [*50*], further demonstrate the complexity of interaction of alloy microstructure and variable load history as shown in Fig. 7. For two aluminum alloys, this figure demonstrates a general trend of increased life under spectrum loading with decreased yield strength. Johnson et al [*51*] showed overaging aluminum alloy 7475-T651 ($\sigma_{ys} = 482$ MPa) to 7475-T7351 ($\sigma_{ys} = 427$ MPa) produced longer spectrum fatigue crack-growth life due to better retardation characteristics of the lower strength temper. Gallagher and Hughes [*39*] reported a similar effect of strength level on fatigue crack-growth life

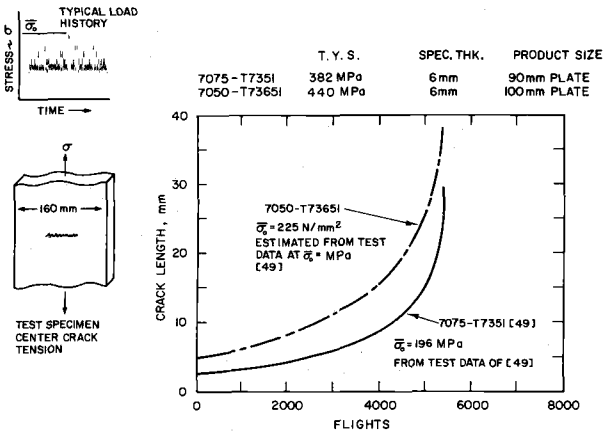

FIG. 6—*Initial flaw size for equivalent crack propagation life under flight simulation loading.*

of a 4340 steel alloy subjected to tensile overloads. In contrast constant amplitude fatigue crack-growth rates for a wide variety of metal alloys have been shown to be rather insensitive to tensile strength (except at high-stress levels where excessive net section yielding is apparent); see for example, Fig. 2. Therefore, alloy comparisons under spectrum loading should be made at comparable strengths. Though current somewhat successful fatigue crack-growth prediction models [*19,46–48*] account for the trend of increased crack growth retardation with decreased yield strength, they may not correctly identify differences in alloy performance under spectrum loading since constant amplitude information is used as basic input in the flaw-growth prediction scheme. For example, the spectrum fatigue life improvement at a given yield strength demonstrated by alloy 7050-T736 in Fig. 7 would not be predicted by current flaw-growth models [*19,46,47*], since the constant amplitude crack-growth rate information for the alloys considered overlap one another.

An implication of the foregoing is that ductility is a factor of major significance in controlling the amount of crack-growth retardation. However, microstructure controls characteristics of material ductility and, as such, would be expected to be important in development of crack-growth resistance under variable load history.

In summary, it appears that there is an important interaction between microstructure and crack growth under variable amplitude cyclic loading which is not appropriately accounted for by the constant amplitude test. Alloys similar to those considered in the preceding discussion, when ranked solely on a constant amplitude crack propagation basis, do not show differences as clearly in crack-growth performance. For example, limited data suggest aluminum alloy 7050 offers good resistance to fatigue-crack

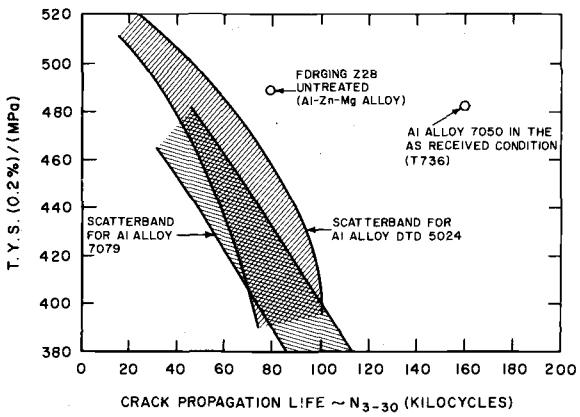

FIG. 7—*The relationship between tensile yield stress and fatigue crack propagation life for gust load flight simulation test spectrum* [50].

propagation under variable load history. This conclusions is not readily apparent from constant amplitude results (see for example, Fig. 4). Though not completely understood, favorable response of 7050 to spectrum loading may be attributed to improved crack-growth retardation capability of the alloys—a characteristic which would not be recognized from the constant amplitude test.

Assuming truth for the previous rationale, then the variable amplitude test should be more sensitive to alloy differences and, on that basis, provide certain advantages for screening alloy-fatigue performance. The user, however, must have a good understanding of the stress history for his particular application (that is not always possible) so that conclusions from his spectrum test(s) will be meaningful for the intended application. Improved fundamental understanding of interactions between load history and microstructure are required for studies which aim to optimize alloy performance and make initial assessments of trade-offs in design and mechanical properties. Here, simple load histories (namely, single and multiple spike overloads) might be used advantageously as a basic material evaluation and screening tool. Moreover, results of these tests also might be used to establish additional guidance for improvement of present analytical flaw-growth prediction schemes and their implementation into design methodology. Fatigue crack-propagation data generated under more complex and realistic spectra would be suggested for verification of fundamental concepts and finalization of material selection and design criteria for fatigue critical applications. With the latter, identification of the proper stress spectrum becomes more critical.

Since programmed load capability is readily available in many modern fatigue laboratories possessing electrohydraulic fatigue test equipment,

acquisition of test data in terms of crack length versus life (cycles, blocks, flights, etc.) is relatively straightforward and ideally suited for efficient control of testing, data assimilation, and processing through automation. All of the foregoing can be translated into time and cost savings. For alloy screening purposes, the precision of crack-length measurement need not be as stringent as that required for generation of conventional crack-growth rate, $\Delta a/\Delta N$, for use in design and handbooks (for example, MIL-Handbook-5). Interpretation and comparison of results in terms of cyclic life is both practical and meaningful for alloy screening purposes. In addition, use of crack length versus block (flights) data from spectrum crack-propagation test affords good opportunity to analyze and compare alloy crack-propagation performance in terms of meaningful design parameters (namely, life, weight savings, tolerable flaw sizes) as illustrated herewith.

In summary, the variable amplitude crack-propagation test offers the following advantages: (*a*) increased sensitivity to microstructure, (*b*) relevancy to design through consideration of important effects of load history, (*c*) practical interpretation when results expressed in terms of crack size versus life, and (*d*) suitability for automated testing and analysis. Thus, the variable amplitude crack-propagation test is an effective, practical, and economical means of screening effects of microstructure on alloy fatigue crack-propagation performance.

References

[*1*] Johnson, H. H. and Paris, P. C., "Sub-Critical Flaw Growth," *Engineering Fracture Mechanics,* Vol. 1, No. 1, June 1968.

[*2*] Clark, W. G., Jr., "Fracture Mechanics in Fatigue," *Experimental Mechanics,* Sept. 1971.

[*3*] Paris, P. C., Bucci, R. J., Wessel, E. T., Clark, W. G., and Mager, T. R., in *Stress Analysis and Growth of Cracks, ASTM STP 513,* American Society for Testing and Materials, 1973, pp. 141–176.

[*4*] Crooker, T. W., "Crack Propagation in Aluminum Alloys Under High Amplitude Cyclic Load," NRL Report 7286, July 1971.

[*5*] Clark, W. G., Jr., "How Fatigue Crack Initiation and Growth Properties Affect Material Selection and Design Criteria," *Metals Engineering Quarterly,* Aug. 1974.

[*6*] Barsom, J. M., Imhof, E. J., and Rolfe, S. T., "Fatigue-Crack Propagation in High Yield Strength Steels," *Engineering Fracture Mechanics,* Vol. 2, No. 4, 1971.

[*7*] Truckner, W. G., Staley, J. T., Bucci, R. J., and Thakker, A. B., "Effects of Microstructure on Fatigue Crack Growth of High Strength Aluminum Alloys," Technical Report AFML-TR-76-169, Air Force Materials Laboratory, Dec. 1976.

[*8*] Christensen, R. H., *Metal Fatigue,* McGraw Hill, New York, 1959.

[*9*] Hardrath, H. F. and McEvily, A. T., *Proceeding of the Crack Propagation Symposium,* Vol. 1, Canfield, England, Oct. 1961.

[*10*] Hudson, C. M. and Hardrath, H. F., "Effects of Changing Stress Amplitude on the Rate of Fatigue Crack Propagation of Two Aluminum Alloys," NASA Technical Note D-960, Sept. 1961.

[*11*] Schijve, J., *Advances in Aeronautical Sciences,* Vol. 3, 1961, p. 387.

[*12*] Schijve, J. and Broek, D., *Aircraft Engineering,* Vol. 34, 1962, p. 314.

[13] Schijve, J., Broek, D., and de Rijk, P., "Crack Propagation Under Variable Amplitude Loading," NLR Report M2094, Jan. 1962.
[14] Smith, S. H. in *Structural Fatigue in Aircraft, ASTM STP 404,* American Society for Testing and Materials, 1966, p. 74.
[15] Hudson, C. M. and Raju, K., "Investigation of Fatigue Crack Growth Under Simple Variable Amplitude Loading," NASA Report TND-5072, National Aeronautics and Space Administration, March 1970.
[16] Elber, W. in *Damage Tolerance in Aircraft Structures, ASTM STP 486,* American Society for Testing and Materials, 1971, p. 230.
[17] Jonas, O. and Wei, R. P., *International Journal of Fracture Mechanics,* Vol. 7, 1971, p. 116.
[18] Mathews, W. T., Baratta, F. I., and Driscoll, G. W., *International Journal of Fracture Mechanics,* Vol. 7, 1971, p. 224.
[19] Wheeler, O. E., *Journal of Basic Engineering Transactions,* American Society of Mechanical Engineers, Series D, Vol. 94, March 1972, p. 181.
[20] von Euw, E. F. J., Hertzberg, R. W., and Roberts, Richard, *Stress Analysis and Growth of Cracks, ASTM STP 513,* American Society for Testing and Materials, 1972, p. 230.
[21] Schijve, J., "The Accumulation of Fatigue Damage in Aircraft Materials and Structures," AGARD-AG-157, Jan. 1972.
[22] Trebules, V. W., Roberts, R., and Hertzberg, R. W. in *Progress in Flaw Growth and Fracture Toughness Testing, ASTM STP 536,* American Society for Testing and Materials, 1973, p. 115.
[23] Schijve, J., *Engineering Fracture Mechanics,* Vol. 5, 1973, p. 269.
[24] Wei, R. P., Shih, T. T., and Fitzgerald, J. H., "Load Interaction Effects on Fatigue Crack Growth in Ti-6Al-4V Alloy," NASA Report Cr-2239, National Aeronautics and Space Administration, 1973.
[25] Buck, O., Ho, C. L., and Marcus, H. L., "Plasticity Effects in Crack Propagation," *Engineering Fracture Mechanics,* Vol. 5, No. 1, Feb. 1973.
[26] Rice, R. C. and Stephens, R. I. in *Progress in Flaw Growth and Fracture Toughness Testing, ASTM STP 536,* American Society for Testing and Materials, 1973, p. 95.
[27] Vargas, L. G. and Stephens, R. I., "Subcritical Crack Growth Under Intermittent Overloading in Cold-Rolled Steel," *Third International Conference on Fracture,* Munich, Germany, 1973.
[28] Jones, R. E., *Engineering Fracture Mechanics,* Vol. 5, 1973, p. 585.
[29] Corbly, D. M. and Packman, P. F., *Engineering Fracture Mechanics,* Vol. 5, 1973, p. 479.
[30] Probst, E. P. and Hillberry, B. M., *American Institute of Aeronautics and Astronautics Journal,* Vol. 12, 1974, p. 330.
[31] Katcher, M., *Engineering Fracture Mechanics,* Vol. 5, 1973, p. 793.
[32] Stephens, R. I., McBurney, G. W., and Oliphant, L. J., *International Journal of Fracture,* Vol. 10, 1974, p. 587.
[33] Shih, T. T., "Fatigue Crack Growth Under Variable Amplitude Loading," Ph.D. dissertation, Lehigh University, 1974.
[34] Schijve, J., *Engineering Fracture Mechanics,* Vol. 6, 1974, p. 245.
[35] Pitoniak, F. J., Grandt, A. F., Montulli, L. T., and Packman, P. F., *Engineering Fracture Mechanics,* Vol. 6, 1974, p. 663.
[36] Petrak, G. J., *Engineering Fracture Mechanics,* Vol. 6, 1974, p. 725.
[37] Himmelein, M K. and Hillberry, B. M., "Effects of Stress Ratio and Overload Ratio on Fatigue Crack Delay," presented at 8th National Symposium on Fracture Mechanics, Providence, Rhode Island, Aug. 1974.
[38] Schijve, J., "Fatigue Crack Growth Under Variable Amplitude Loading," presented at Conference on Prospects of Advanced Fracture Mechanics, Delft, Netherlands, June 1974.
[39] Gallagher, J. P. and Hughes, T. F., "Influence of Yield Strength on Overload Affected Fatigue Crack Growth Behavior in 4340 Steel," Technical Report AFFDL-TR-74-27, 1974.
[40] Shih, T. T. and Wei, R. P., *Journal of Testing and Evaluation,* Vol. 3, No. 1, Jan. 1975, p. 46.

[41] Chanani, G. R., "Retardation of Fatigue Crack Growth in 7075 Aluminum," *Metals Engineering Quarterly,* Feb. 1975.
[42] Shih, T. T. and Wei, R. P., "Effect of Specimen Thickness on Delay in Fatigue Crack Growth," *Journal of Testing and Evaluation,* Vol. 3, No. 1, Jan. 1975.
[43] Mills, W. J., "Load Interaction Effects on Fatigue Crack Growth in 2024-T3 Aluminum and A514F Steel Alloys," Ph.D. dissertation, Lehigh Univeristy, 1975.
[44] Lankford, J. and Davidson, D. L., *Journal of Engineering Materials and Technology,* Vol. 98, 1976, p. 17.
[45] *Fatigue Crack Growth Under Spectrum Loads, ASTM STP 595,* American Society for Testing and Materials, 1976.
[46] Willenborg, J., Engle, R. M., and Wood, H. A., "A Crack Growth Retardation Model Using an Effective Stress Concept," Technical Report TM-71-1-FBR, January 1971.
[47] Vroman, G., "Analytical Preduction of Crack Growth Retardation Using a Critical Stress Intensity Concept," Technical Report TFR 71-701, Los Angeles Division, North American Rockwell, 1971.
[48] Wood, H. A., Gallagher, J. P., Engle, R. M., and Potter, J. M., "Current Practice on Estimating Crack Growth Damage Accumulation with Specific Application to Structural Safety Durability and Reliability," Technical Report AFFDL-TR-75-32, Air Force Flight Dynamics Laboratory Jan. 1976.
[49] Sippel, K. O. and Weisgerber, D., "Crack Propagation in Flight by Flight Tests on Different Materials," presented at the 1975 International Conference on Aeronautical Fatigue, Lausanne, 5 June 1975.
[50] Schijve, J., "Review of Aeronautical Fatigue Investigations in the Netherlands During the Period April 1973–March 1975," Technical Report NLR-MP-75011U, National Aerospace Lab, NLR the Netherlands, May 1975.
[51] Johnson, W. S., Morrow, J. W., Little, C. D., "Damage Tolerance Crack Growth Characterization of 7475 Aluminum Material," General Dynamic Convair Aerospace Division Research Report ERR-FW-1753, Dec. 1976.

J. H. Underwood,[1] *L. P. Pook,*[2] *and J. K. Sharples*[2]

Fatigue-Crack Propagation Through a Measured Residual Stress Field in Alloy Steel

REFERENCE: Underwood, J. H., Pook. L. P., and Sharples, J. K., **"Fatigue-Crack Propagation Through a Measured Residual Stress Field in Alloy Steel,"** *Flaw Growth and Fracture, ASTM STP 631,* American Society for Testing and Materials, 1977, pp. 402–415.

ABSTRACT: Fatigue crack-propagation tests were performed using 5 by 30 mm cross-section bend specimens of a nickel-chromium-molybdenum steel. The fatigue crack-propagation rate was determined from a group of stress-free specimens by measuring crack length on the specimen surfaces at intervals during cycling. Residual stress was produced in a second group of specimens by using a localized plastic deformation process. Resistance strain gages were first applied near one edge of each specimen along the line of intended crack growth. A series of 1-mm-deep plastic indentations was then made along the opposite edge of the specimen using a 25-mm-diameter pin. The strain gages provided a direct, accurate measure of the elastic, residual stress produced on one side of the specimen due to the local plastic deformation on the opposite side.

Measured crack-propagation rates in the specimens with residual stress are compared with rates in residual stress-free specimens. Crack-propagation rates are lower, as expected, near the edge of the specimen where the initial residual stress is compressive. Propagation rates remain lower even as the crack grows deeper into the specimen where the initial residual stress is tensile, which is not what would be expected from a simple superposition of stresses. However, an analysis involving the combination of the applied stress-intensity factor with that estimated from a redistribution of the residual stress in the specimens can account for the lower crack-propagation rates.

KEY WORDS: crack propagation, fracture (materials), alloys

Nomenclature

- a Crack depth
- B Specimen thickness

[1]Research engineer, Materials Engineering Division, U.S. Army, Benet Weapons Laboratory, Watervliet, N.Y. 12189.

[2]Principal scientific officer and higher scientific officer, respectively, National Engineering Laboratory, East Kilbride, Glasgow, Scotland.

K_I Opening mode stress-intensity factor
K_{max} K_I at maximum load in fatigue cycle
K_{min} K_I at minimum load in fatigue cycle
K_a K_I corresponding to the amplitude of alternating load in fatigue cycle
K_R K_I corresponding to the residual stress distribution at maximum load in fatigue cycle
K_{op} K_I corresponding to the residual stress distribution at minimum load in fatigue cycle
ΔK Range of K_I in fatigue cycle
ΔK_R Range of K_I in fatigue cycle including effect of residual stress
N Number of fatigue cycles
P_a Amplitude of alternating load in fatigue cycle
P_m Mean load in fatigue cycle
W Specimen depth
y Distance from notched edge of specimen
y_o y at the point of zero residual stress
σ_R Residual stress at $y = 0$
σ_R^1 Bending component of residual stress at $y = 0$
$\sigma_{R\text{-ave}}$ Average residual stress over the range $a/2 < y < 3a/2$

Fatigue-crack propagation in metal samples which contain residual stress is a subject of considerable interest. In most cases, however, the distribution and magnitude of residual stress are not known with much certainty. The uncertainty is caused by the fact that the processes which produce residual stress in a specimen, such as plastic deformation, thermal treatment, and metallurgical phase change, nearly always preclude an accurate calculation or measurement of residual stress. Linear-elastic analyses seldom can be used directly to determine the residual stress which results from these processes because they involve nonlinear deformations.

Even if the residual stress present in a sample were known with certainty, its effect on the fatigue crack-propagation rate would be difficult to assess. Methods for including the effect of residual stress in fracture mechanics descriptions of fatigue crack-propagation rate are not at all well developed. The approach often taken is simply adding the residual stress to the applied stress on the sample and using such a modified stress to calculate K_I, which is then used to describe the fatigue crack-propagation rate in the usual manner. This approach seems correct for sufficiently shallow cracks, that is, for crack depths which are small relative to sample dimensions and relative to the depth of the residual stress distribution. For other than shallow cracks, and most real situations are in this category, the addition of stress approach is merely an estimate of unknown accuracy, because the presence of the crack may cause a basic change in the residual stress distribution.

Based on the foregoing rationale, we planned a series of experiments in which the effect of an accurately measured residual stress on fatigue crack-propagation rate could be measured, and we planned to use the results to indicate an improved approach for including residual stress effects in a fracture-mechanics description of crack-propagation rate. The specific objectives of the work are (*a*) to produce a residual stress distribution in specimens of a high-strength steel and obtain an accurate measurement of the distribution, (*b*) measure fatigue crack-growth rate in the specimens and in stress-free comparison specimens, and (*c*) describe the crack-propagation rate using a superposition of applied stress intensity and the stress intensity determined from the residual stress distribution.

Test Procedures

Specimens

Ten specimens were machined from a single piece of forged steel of the following composition: 0.35C, 3.4Ni, 1.8Cr, 0.6Mo, 0.5Mn, 0.1V. The yield strength, tensile strength, and fracture toughness of the steel are 1210 MN/m^2, 1370 MN/m^2, 145 $MN/m^{3/2}$, respectively. The specimens were made to the following dimensions: thickness, B, 5.1 mm, depth, W, 30.0 mm, and length, 200 mm. A 0.3-mm-deep notch with a 0.05-mm root radius was cut across the thickness of each specimen at midlength. A photo of the center portion of one of the specimens is shown as Fig. 1.

Producing the Residual Stress

Residual stress was produced in six of the test specimens by using a

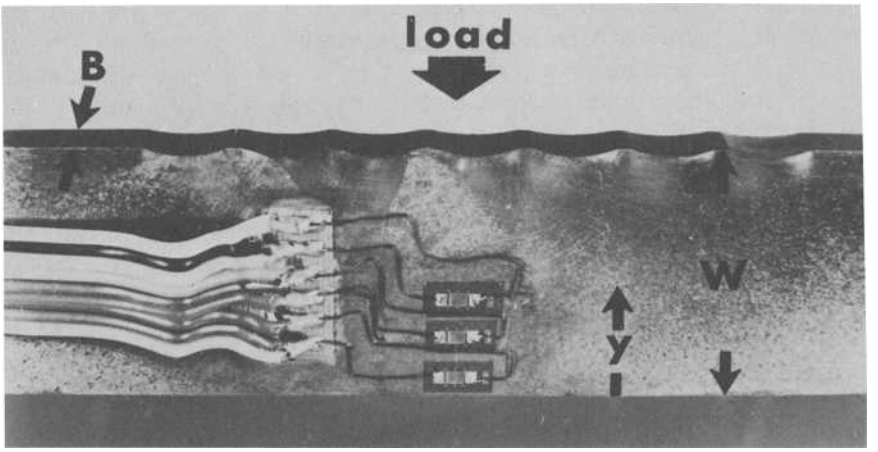

FIG. 1—*Photograph of specimen.*

localized plastic deformation process. Resistance strain gages were first applied to both sides of the specimen along the line of intended fatigue-crack growth. In general, three gages were applied to each side in the area near the notched edge of the specimen (see Fig. 1). A series of 1-mm deep, 5-mm long plastic indentations were then made along the opposite edge of the specimen using a 25-mm diameter pin mounted in a universal testing machine. The plastic indentations can be visualized as roughly equivalent to a series of wedges driven into the edge of the specimen. The strain gages provide a direct, accurate measurement of the elastic residual stress produced near one edge of the specimen due to the local plastic deformation along the opposite edge. The plastic deformation appeared to extend inward from the edge about 4 mm, while the strain gages were placed 15 to 30 mm from the deformed edge. So we are quite sure that no direct effect of the plastic deformation is recorded by the gages but only the induced elastic, residual deformation of the specimen.

The measured residual stress data are shown in Fig. 2. Each point represents the average strain from two gages on opposite sides which has been converted to a stress value using the elastic modulus. The data are well represented by the straight line shown, with the exception of the data from specimen T-5 which can be represented by a quite similar line. We attribute the difference for T-5 to a higher indentation load for this specimen.

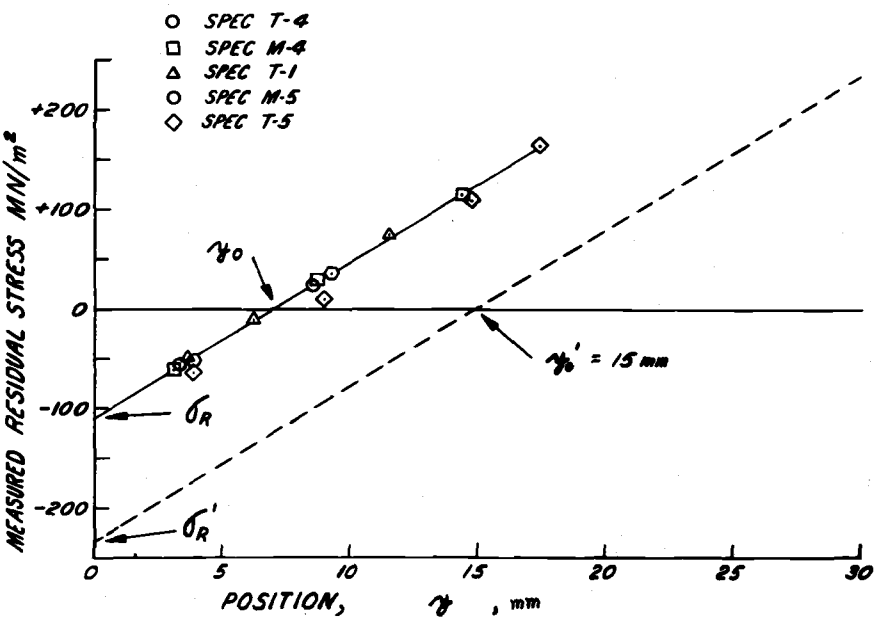

FIG. 2—*Measured residual stress distribution.*

The measured residual stress distribution is quite linear to beyond the specimen midpoint, $y/W = 0.5$. Then, the stress must drop sharply at some point, possibly at $y/W = 0.8$, pass through zero a second time, and approach a negative value about equal to the yield strength at the deformed edge, $y/W = 1.0$. A stress distribution of this sort meets the basic requirements that forces and moments be in balance. Balance of forces requires that the total area above and below the zero stress line be equal. Balance of moments requires that there be at least three separate areas above and below the zero stress line, because it is easy to show that two equal areas with one above and one below the zero stress line will always produce an unbalanced moment.

The actual stress distribution as just discussed would be difficult to include in a fracture-mechanics analysis. In the analysis used here, we assume that the residual stress distribution remains linear across the full width of the specimen. While this is not true, it may be a good approximation for describing the effect of residual stress on fatigue crack growth rate up to the specimen midpoint. In addition, a linear residual stress distribution can be represented exactly by the superposition of two familiar stress distributions; namely, a pure bending stress distribution shown as the dashed line in Fig. 2, and a uniform tension stress distribution which represents the difference between the two lines in Fig. 2. Further details will be discussed later.

Fatigue Tests

The fatigue crack-propagation tests were performed in three-point bending using a lower support span of 120 mm. The upper load point was centered on the span and directly over the strain gage and notch location (see Fig. 1). The load was applied to the specimen, and the specimen was supported by means of the blunt knife edges with a tip radius of about 1.0 mm which were supplied with the fatigue testing machine used for the tests. An electromagnetic fatigue machine was used, operating at 130 Hz at room temperature. The test conditions are listed in Table 1, including the alternating and mean loads and the measured residual stress information for each specimen. For three of the specimens containing residual stress, the notch was deepened much beyond the initial 0.3 mm depth. This caused a significant change in the fatigue crack-propagation rate for equivalent total notch plus crack depths as shown later.

The crack length was measured at intervals during the test on both sides of the specimen using a seven power microscope. For most of the data, the crack length readings from the two sides varied by less than 0.5 mm. The average values were plotted against number of cycles, a smooth curve was drawn through the points, and the slope of the curve was measured at intervals. We make no apology for this manual procedure. When it is

TABLE 1—*Test conditions.*

Specimen Number	Alternating Load, P_a, kN	Mean Load, P_m, kN	Residual Stress at $y = 0$, σ_R, MN/m^2	Position at zero residual stress, y_0, mm	Notch Depth, mm
			Stress Free		
M-1	1.25	1.50	0	...	0.3
M-6	2.50	3.00	0	...	0.3
T-2	2.50	3.00	0	...	0.3
T-6	3.50	4.20	0	...	0.3
			Residual Stress		
T-4	1.25	1.50	−108	7.1	0.3
M-4	2.00	2.40	−108	7.1	0.3
T-3	3.50	4.20	−108	7.1	0.3
			Residual Stress With Deep Notch		
T-1	1.50	1.70	−108	7.1	7.9
M-5	1.75	2.10	−108	7.1	5.0
T-5	2.50	3.00	−124	8.0	4.6

done properly, the results are every bit as reliable as those using computer aided methods. Plots of crack length, a, against number of cycles, N, are shown in Fig. 3 for six of the specimens tested. The zero point for N is arbitrary, since the concern here is with da/dN for a given crack length, loading, and residual stress condition.

Test Results and Analysis

Stress-Free Specimens

Crack-propagation tests were performed with the stress-free specimens to obtain results with which to compare the results from specimens containing residual stress. The a versus N data are shown in Fig. 3, including two specimens tested at the same load. The good agreement between the two repeat specimens is apparent in the a versus N plot and in the log ΔK versus da/dN plot shown in Fig. 4*a*. The straight line, upper bound to the growth-rate data in Fig. 4*a*, is typical of this material [*1*].[3] The deviations from the straight line are larger than we would expect for tests of this type, and the deviations appear to be systematic with a/W, as can be seen by the values of a/W shown in Fig. 4*a* which correspond to the beginning, middle, and end of the tests. For a/W values above 0.3 the deviations from the straight line become significant, as indicated by the dashed lines.

[3] The italic numbers in brackets refer to the list of references appended to this paper.

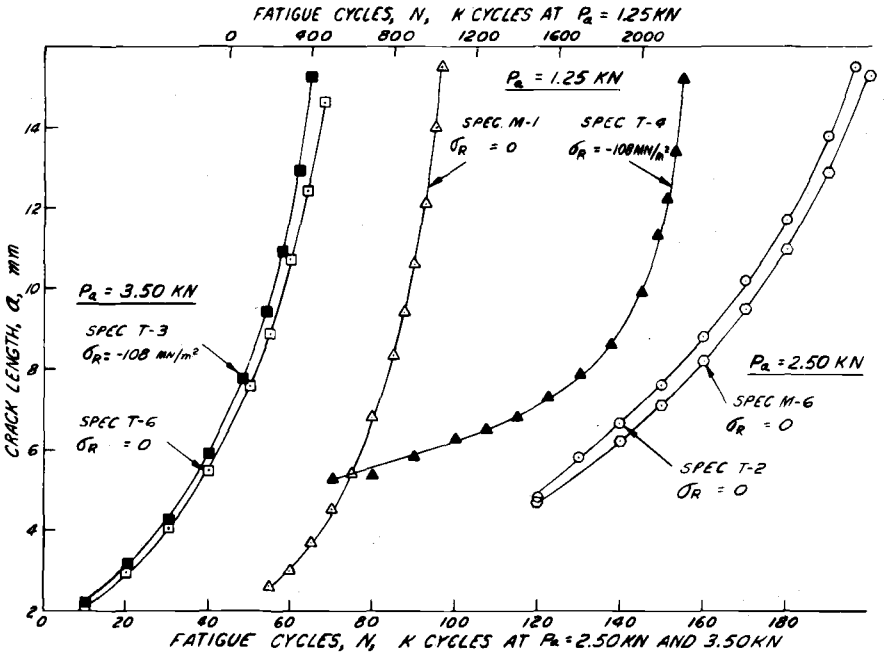

FIG. 3—*Measured crack length versus number of cycles.*

Crack Length Effect on da/dN

The deviations from the straight line in the data of Fig. 4*a* can be well represented by using the following modified ΔK function in the log ΔK versus log da/dN plot

$$\Delta K_{\text{mod}} = (1 - [a/W]^2)\Delta K \tag{1}$$

The ΔK values are calculated in the usual manner using the K relations from Ref *2*. When the modified ΔK expression is used to plot the results from the stress-free specimens, the data are all close to the expected straight line relation (see Fig. 4*b*). This result led us to the conclusion that for our tests there is a crack length effect on da/dN which is independent of the variation of ΔK with crack length.

The form of Eq 1 was chosen arbitrarily to fit the data. But Eq 1 also could be a representation of a crack-closure effect as proposed by Elber [*3*]. Crack length is one of the variables suggested by Elber with potential effect on crack-propagation rate through crack closure. And although crack length was not a significant variable in Elber's tension-fatigue tests with

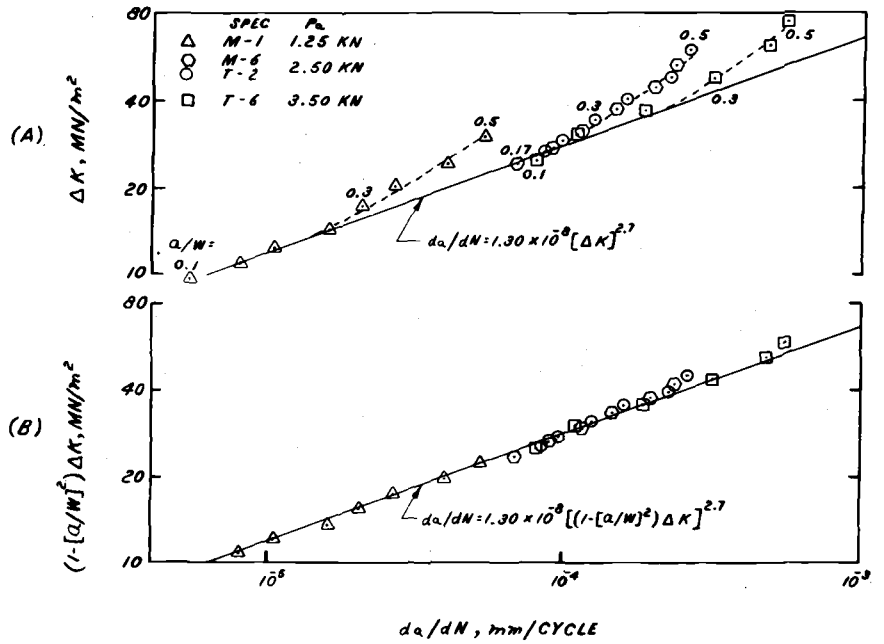

FIG. 4—ΔK *versus growth rate for stress free specimens*; (a) *conventional* ΔK *and* (b) *modified* ΔK *function.*

an aluminum alloy, the bend tests with a steel alloy in this work could be affected by crack length. Alternatively, Eq 1 could be a representation of an R-curve effect in fatigue-crack propagation. Pook and Greenan [*4*] have suggested that the resistance to fatigue-crack growth can increase with the amount of crack growth in a similar manner to the R-curve effect observed in monotonic loading of thin plate and sheet. Finally, a suggestion by an anonymous reviewer of this paper is that the deviation from the straight line in Fig. 4*a* for large *a/W* could be the result of an axial restraint applied to the specimen due to the friction at the specimen supports. Particularly, as the rotation of the specimen halves becomes significant at large *a/W*, the friction between the fixed specimen supports and the specimen could limit the rotation and cause a reduction in the value of *K* at maximum load and, thus, a reduction in the ΔK applied to the specimen.

It is not our intention here to relate the crack-length effect on *da/dN* to any particular process or model. It is only necessary to describe the crack-length effect so that it can be separated from the effect of residual stress on fatigue crack-propagation rate, the main topic of interest. So the modified ΔK function is used in the subsequent plots of ΔK versus *da/dN*.

Specimens Containing Residual Stress

The results from crack-propagation tests in three specimens containing residual stress and with a 0.3-mm notch are shown in Fig. 5. Results from similar specimens, but with much deeper notches of about 5 mm, are shown in Fig. 6. The data are plotted using the modified ΔK function, and

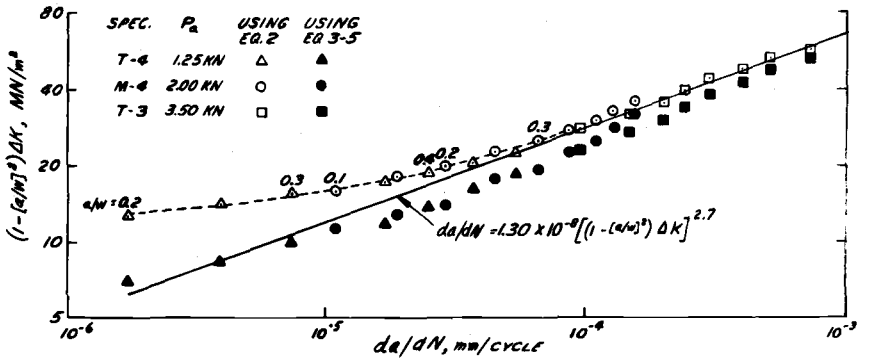

FIG. 5—*Modified* ΔK *function versus growth rate for specimens with residual stress and a shallow notch.*

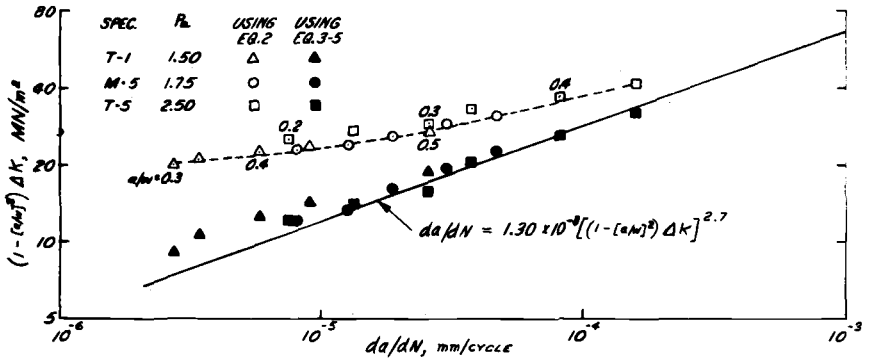

FIG. 6—*Modified* ΔK *function versus growth rate for specimens with residual stress and a deep notch.*

the straight line shown is the line which represents the stress-free results in Fig. 4. The ΔK values are calculated in two ways in Figs. 5 and 6. One is the conventional method. With the mean load positive and larger than the alternating load, and if the effect of residual stress is ignored, then ΔK has the straightforward definition

$$\Delta K = 2K_a \text{ for } P_m > P_a,\ \sigma_R = 0 \tag{2}$$

where K_a is the K_I value which corresponds to the alternating load on the specimen.

The second method for calculating ΔK includes an attempt to account for the effect of residual stress and is outlined as follows

$$\Delta K_R = (K_{max} + K_R) - (K_{min} + K_{op}) \quad (3)$$

where ΔK_R is the ΔK including the effects of residual stress, K_{max} and K_{min} have the usual definitions of the maximum and minimum K_I applied during the fatigue cycle, K_R is the K_I value which simulates the effect of the residual stress at the point of maximum load during the fatigue cycle, and K_{op} is the K_I value which simulates the effect of residual stress at the point of minimum load during the cycle. The approach used here is patterned after the Elber [3] model, but the situation is somewhat different. In the tests here, the amount of crack-tip plastic deformation, as measured by the ratio of ΔK to yield strength, is very much lower than in Elber's tests. Still, crack closure is believed to have occurred in the tests here but due to presence of residual stress rather than crack-tip plastic deformation. The first term in Eq 3 represents the reduction in the amount of crack opening at maximum load due to the presence of residual stress, and the second term represents the delayed opening of the crack at some point in the cycle above minimum load due to the presence of residual stress.

Redistribution of Residual Stress

The procedure for determining values for K_R and K_{op} in Eq 3 is discussed in relation to the sketches in Fig. 7. Shown here are the redistributed residual-stress gradients that we expect at maximum and minimum loads in specimens with very short and very long notches. The sketches depict the situation in which the total length of notch plus crack is in the same order of size as y_0, which is the situation for much of the test data presented here.

In Fig. 7, and the related discussions, we describe how the original residual stress distribution in the specimens as shown in Fig. 2 could become shifted or redistributed due to the combined effect of the notch plus crack arrangement and the load condition of the specimen.

Referring to Fig. 7 (*a* and *b*), we expect that a redistribution of residual stress has occurred at maximum load in the fatigue cycle and that the final redistributed stress is the same for specimens which are predominantly notched or cracked. At maximum load neither the now opened crack nor the notch can support any residual stress, but neither can they relieve any residual stress because the source of the residual stress is on the opposite side of the specimen. So as an estimate, we expect that the residual-stress distribution formally present with no crack or notch is still present but is

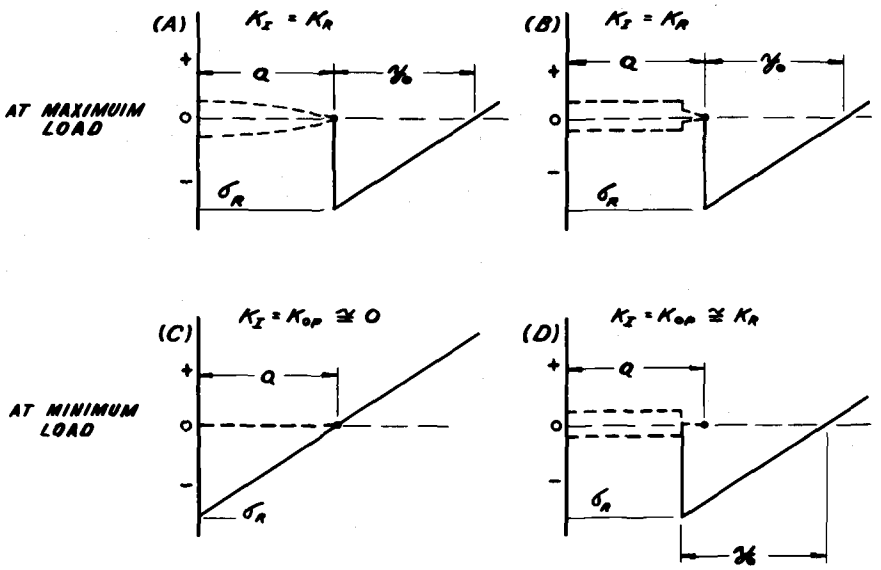

FIG. 7—*Expected residual stress distribution for various test conditions.*

shifted ahead to the crack tip as shown in Fig. 7 (*a* and *b*). And the K_I which corresponds to the shifted residual-stress distribution is the K_R in Eq 3.

Referring to Fig. 7*c*, at minimum load in the fatigue cycle in a cracked specimen, we expect that the residual stress distribution is unchanged from the uncracked situation because the crack has no effect on the compressive residual stress. And for this same reason there is no K_I in this situation.

Referring to Fig. 7*d*, at minimum load in a specimen which is predominantly notched, we expect that the stress distribution is shifted to the tip of the notch; the K_I which corresponds to this shifted stress distribution is the K_{op} in Eq 3 and, in addition, is approximately equal to K_R. This is a reasonable estimate in the limit as the crack ahead of the notch becomes very small, and it may remain a useful estimate for most of the test results here.

If the rationale discussed in relation to Fig. 7 is accepted, then Eq 3 can be rewritten as follows

$$\Delta K_R = 2K_a + K_R \quad \text{for cracked specimens}$$
$$\Delta K_R = 2K_a + 2K_R \quad \text{for notched specimens} \tag{4}$$

For a cracked specimen with a negligibly small notch, Eq 4 describes the reduction in ΔK caused by the addition of a negative K_I due to the residual stress. For a notched specimen with a small crack ahead, Eq 4 describes a

larger reduction in K, because the negative K_I due to the residual stress can affect the applied K_I at low applied loads as well as high.

In order to determine ΔK_R from Eq 4, an expression for K_R is needed. Since the stress distribution in Fig. 7 which is to be represented by K_R is a discontinuous distribution and is only an estimate, then a simple expression for K_R is called for and is given as follows

$$K_R = \sigma_{R\text{-ave}}(\pi a)^{1/2} \tag{5}$$

where $\sigma_{R\text{-ave}}$ is the average value of the redistributed residual stress near the crack tip, that is, over the range $a/2 < y < 3a/2$. Values of K_R calculated from Eq 5 assuming a shifted residual-stress distribution as indicated in Fig. 7 and using $\sigma_R = -108$ MN/m^2 are listed in Table 2. Also listed

TABLE 2—*Values of* K_R, *the* K_I *which simulates residual stress.*

a, mm	a/W	K_R from Eq 5 with redistribution MN/m$^{3/2}$	K_R from Eq 6 no redistribution MN/m$^{3/2}$
3	0.1	−4.7	−11.3
6	0.2	−5.9	−14.5
9	0.3	−6.3	−18.2
12	0.4	−6.0	−22.5
15	0.5	−5.5	−27.2

are values from the following expression for K_R based on the assumption that the residual-stress distribution remains unchanged during fatigue crack growth

$$(K_R)_{a\to 0} = 1/6\,\sigma_R' Y_B(a)^{1/2} + (\sigma_R' - \sigma_R)\, Y_T(a)^{1/2} \tag{6}$$

In Eq 6, σ_R' is the outer fiber stress due to the pure bending component of the residual stress distribution (see Fig. 2), and Y_B and Y_T are the dimensionless K_I factors for pure bending and uniform tension [*2,5*]. Because of the assumption of a residual-stress distribution which does not redistribute with crack growth, Eq 6 is expected to be most appropriate for small values of a. Equation 6 describes a superposition of the K_I from the pure bending component of the residual-stress distribution and the K_I from the uniform tension component of the distribution (see Fig. 2). Together, these simulate the K_I which would be produced by the linear portion of the measured residual-stress distribution. It would be tempting to use Eq 6 to represent K_R since it is a bit more elegant. But it does not include the effect of redistribution of residual stress, and, as will be discussed shortly, it is not supported by the test results.

Results with Redistribution of Residual Stress

Returning to the discussion of Figs. 5 and 6, the data plotted using Eq 2, which is the conventional method for determining ΔK, result in da/dN values at low-ΔK which are lower, by up to a factor of 10, than those from stress-free specimens represented by the straight line. Further, it is interesting to note that the da/dN values remain significantly lower even at crack depths beyond $a/W = 0.3$. Considering that the residual stress at points beyond $a/W = 0.24$ in the uncracked specimen was a tensile stress, a simple superposition of stress would predict a higher da/dN. When the data are plotted using the method indicated by Eqs 3 through 5 which includes the effect of residual stress and a redistribution of residual stress, then the da/dN values are in reasonable agreement with the stress-free results. If the effect of residual stress were included but without the assumption of redistribution of stress, that is, using Eq 6, the result would not make sense. In fact, if the Eq 6 values are used to calculate ΔK, negative ΔK values result in some cases.

One further point regarding the results in Figs. 5 and 6 should be discussed. The data plotted using the conventional method give a clear indication that the effect of residual stress is independent of crack depth. Adjacent points on the smooth curve through the data often correspond to crack depths which differ by a factor of two to three, as indicated by the a/W values shown for selected data points. We view this crack depth independence as further support for the residual-stress-redistribution model used to interpret the results. Crack depth independence of K_I associated with the residual stress can be visualized if the stress distribution is considered as a local closing effect on the crack tip which occurs over an area which is small relative to crack length. For relatively deep cracks, this may be close to correct. It is interesting, although perhaps fortuitous, that the residual-stress redistribution approach of Eq 5 produces a K_I which is relatively independent of crack length for deep cracks (see Table 2).

Closing

The nature of the results obtained in the tests here and the relevancy of the analysis used to interpret the results are both highly dependent on the process which was used to produce the residual stress. In the process used here, the plastic deformation which caused the residual stress was remote from the area of fatigue cracking. A remote source of residual stress is a basic requirement for the redistribution model discussed here. A plastic deformation process can be conceived which would produce a similar initial residual-stress distribution, as that measured in the specimens here, but which would include plastic deformation in the area of subsequent fatigue cracking. Then, as the crack grows through the area of plastic

deformation, which is also the source of the residual stress, a combination of relief of residual stress and redistribution of residual stress will occur. The effect on the crack-growth rate could be quite different than that in the specimens here with a remote source of residual stress.

Although a rigorous analysis has not been possible in this work, the results obtained demonstrate that the behavior of fatigue cracks in residual stress fields can be described using fracture-mechanics methods. Further progress will depend at least as much on obtaining a fuller understanding of the applied mechanics of situations of interest, as on the accumulation of further experimental data. Of central importance will be the determination of the nature of residual stress redistribution in loaded, cracked bodies.

Acknowledgments

The authors are happy to acknowledge the help of J. A. Mackinnon of the National Engineering Laboratory for his help in planning and conducting the experiments described here.

Mr. Underwood acknowledges the support of the Secretary of the U.S. Army Research and Study Fellowship program which sponsored this work.

References

[*1*] Frost, N. E., Marsh, K. J., and Pook, L. P., *Metal Fatigue*, Claredon Press, Oxford, 1974.

[*2*] Srawley, J. E. and Gross, B., *Engineering Fracture Mechanics*, Vol. 4, 1972, pp. 587–589.

[*3*] Elber, Wolf in *Damage Tolerance in Aircraft Structures, ASTM STP 486*, American Society for Testing and Materials, 1971, pp. 230–242.

[*4*] Pook, L. P. and Grennan, A. F., "Various Aspects of the Fatigue Crack Growth Threshold in Mild Steel," presented at Conference on Fatigue Testing and Design, City University, London, England, April 1976, Society of Environmental Engineers Fatigue Group.

[*5*] Brown, W. F. and Srawley, J. E., *Plane Strain Crack Toughness Testing of High Strength Metallic Materials, ASTM STP 410*, American Society for Testing and Materials, 1966.

C. S. Davis[1]

Automated Design of Stiffened Panels Against Crack Growth and Fracture Among Other Design Constraints

REFERENCE: Davis, C. S., **"Automated Design of Stiffened Panels Against Crack Growth and Fracture Among Other Design Constraints,"** *Flaw Growth and Fracture, ASTM STP 631,* American Society for Testing and Materials, 1977, pp. 416–445.

ABSTRACT: A Fortran IV computer program has been developed to design integrally stiffened two-panel boxes subject to fatigue-crack growth and fracture as well as side constraints, displacements, yielding, and local and general buckling. For crack growth and fracture, stress-intensity factors are compounded from available solutions, and final crack sizes are estimated using R-curve methods for the fracture constraints. An average and integrate strategy is employed for life prediction. Mathematical programming is used for design optimization, and approximation concepts reduce the constraint calculation effort. In the design procedure, multilayered constraint deletion and replacement of original constraint analyses by approximate substitutes define a sequence of approximate subproblems for design solution. For each subproblem, an extended Fiacco-McCormick penalty function is used with a modified Davidon-Fletcher-Powell deflected gradient algorithm for the unconstrained minimizations. The effective slope of crack growth with respect to stress-intensity factor is central to the success of procedures developed. This slope provides a normalizing exponent for the design constraints and a weighting exponent for efficient interpolation and quadrature to predict crack-growth lives. Probabilistic treatment of identified uncertainties in the crack growth ahd fracture analysis, in place of across the board safety factors, has improved design efficiency.

KEY WORDS: crack propagation, fatigue life, fracture strength, fracture mechanics, mathematical prediction, optimum design, automated design, probabilistic design, reliability, safety factor, computer programs, aircraft panels, structural design, numerical quadrature

Structural design is done to define a structure to perform its intended function at minimum cost within prescribed limits without failure under anticipated usage. Two sets of terms describe a structure. The first are

[1]Assistant professor, School of Engineering, University of New Orleans, New Orleans, La. 70122 and consultant, Fracture Control, Martin Marietta Aerospace, Michoud Operations, New Orleans, La. 70189.

design variables, $\vec{D} = (D_1, \ldots, D_N)$, with values subject to design change. The remaining terms have fixed or preassigned values. In this paper, the weight of a structure, $W(\vec{D})$, represents the cost to be minimized. The prescribed limits and behavior of a structure under usage loadings are formulated as design constraints, $g_l(\vec{D})$, $l = 1, \ldots, l_L$ where negative values signify failure. Thus, the design problem is to

$$\begin{aligned} &\text{find } \vec{D} \\ &\text{such that } W(\vec{D}) \text{ is a minimum} \\ &\text{subject to } g_l(\vec{D}) \geq 0 \text{ for } l = 1, \ldots, l_L \end{aligned} \tag{1}$$

Use of mathematical programming for general structures design on the computer (Eq 1) was first presented by Schmit [*1*][2] in 1960. Since then, mathematical programming has been applied to increasingly important structural design problems [*2–4*]. These have included plate and shell buckling [*5,6*], dynamic response [*7,8*], flutter [*9,10*], and probabilistically defined constraints [*11*]. Inevitably, formidable difficulties arose with the numbers of trial designs, design variables, and complex design constraints in many practical structures. More recently, reduction of design variables by reduced basis concepts, constraint ranking and deletion, replacement of constraints by approximate substitutes, etc., have improved automated design efficiency [*4,12*] (for other approaches see Refs *13* and *14*).

However, before this investigation, methods to incorporate fatigue, crack growth, and fracture technology in automated design of structures were not observed in the literature. Nevertheless, the need and possibility for inclusion of fatigue-crack growth and fracture analysis in larger automated design systems has been recognized [*15,16*]. Moreover, development of this technology to reduce the uncertainties that might hinder confidence in automated design results is well underway [*17–19*]. Criteria for design against crack growth have been developed [*20,21*]. A modified form of these criteria is used here.

For this investigation, an integrally stiffened two panel box (Fig. 1) provides a representative structure for design against crack growth and fracture. This structure produces a variety of initial crack sites and stress-intensity-factor analysis problems as well as skin, stiffener, and panel buckling problems. Figure 1 indicates the eight design variables ($D_{11}, \ldots, D_{42}$) chosen. In addition, uncertainties in R-curve level for fracture, crack growth rate, initial crack sizes, and various points in the stress-intensity factor analysis are identified as parameters $\vec{\theta} = (\theta_1, \ldots, \theta_{21})$ to observe their impact on reliability.

In particular, design constraints

[2]The italic numbers in brackets refer to the list of references appended to this paper.

$$g_l(\vec{D}) = 1 - \frac{\text{computed}}{\text{max allowed}} \geq 0 \tag{2}$$

are prescribed for geometric realizability and against displacement and yield-stress limits; panel, skin, and stiffener buckling; and crack growth and fracture. For crack growth and fracture, a structure must reliably survive one usage life before a 0.08-in. crack grows to a fracture failure. Moreover, at least one of three inspection systems (Fig. 1) must catch, with sufficient reliability, any larger crack before the occurrence of failure.

For this design problem, automated design and crack growth and fracture analysis methods were developed and used. In this paper, the objectives are:

1. To outline the approximate analysis techniques that were applied so that crack growth and fracture analysis could be successfully incorporated with other constraints in an automated design system.

2. To present design results to demonstrate the methodology on typical integrally stiffened panels.

3. To indicate how remaining uncertainties in material properties and analysis methods can be treated to produce more efficient but safe designs

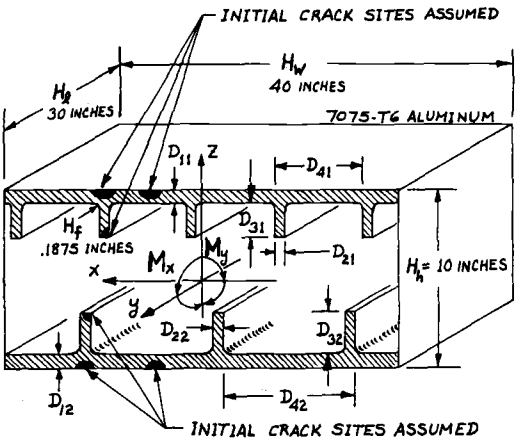

REQUIREMENT	INITIAL CRACK SIZE (INCHES)	REQUIRED NUMBER OF BLOCKS BEFORE FAILURE
1. DURABILITY	.08	4000 (FULL LIFE)
SATISFY AT LEAST ONE OF THE FOLLOWING		
2. OVERHAUL INSPECTION	.25	1000
3. CLOSE VISUAL INSPECTION	1.00	400
4. WALKAROUND INSPECTION	4.00 [a]	10

a SIZE AS MEASURED ALONG OUTSIDE OF 2 PANEL BOX

FIG. 1—*Stiffened two-panel box and life requirements.*

and identify which of the uncertainties treated require research attention and which do not.

Crack Growth and Fracture

Analysis Problem

The crack growth constraints for design are

$$g(\vec{D}) = 1 - \left(\frac{L_{\text{req}}}{L}\right)^{1/\bar{\Theta}} \Omega_L \geq 0 \tag{3}$$

where L_{req} is required life (Fig. 1), L is predicted life and $\bar{\Theta}$ is a normalizing exponent (see Eq 27). The safety factor, Ω_L, derives from the uncertainty parameters, $\vec{\theta}$, (see Eqs 28, 29, and 30). For predicted life, L, a crack grows from a specified though uncertain initial size (Fig. 1) to a final size. The crack then extends by the worst static design load to a critical size for which the fracture design constraint

$$g(\vec{D}) = 1 - \left(\frac{K}{R_c}\right) \Omega_F \geq 0 \tag{4}$$

is computed (see section on Fracture Mechanics). In Eq 4, K is applied stress-intensity factor, R_c is critical resistance to crack extension and Ω_F is the safety factor from the parameters, $\vec{\theta}$. The critical crack sizes are chosen on the basis that a minimum weight structure presupposes maximized values for critical sizes consonant with nonnegative fracture constraints.

In this investigation, crack growth is restricted to symmetric cracks growing straight across the panels so that crack size becomes a single variable, V_1. The loading histories used are periodic and plastic-zone size, V_2, is the only secondary physical state treated. Further, this physical state is always formulated to directly compute its initial value, V_{21}, for any crack size upon starting a loading block. Thus, crack growth, ΔV_1 takes the form [*22*]

$$\Delta V_{1i} = \mathcal{V}_1(\vec{k}_i(V_{1i}), V_{2i}, \vec{\theta})\, \Delta t_i \text{ for crack size} \tag{5}$$

$$\Delta V_{2i} = \mathcal{V}_2(\vec{k}_i(V_{1i}), V_{2i}, \vec{\theta})\, \Delta t_i \text{ for plastic zone size} \tag{6}$$

where $\vec{k}_i(V_{1i})$ are stress-intensity factors for load event i, and an explicit expression gives the initial plastic-zone size.

To predict lives under crack growth modeled by Eqs 5 and 6, an aver-

age and integrate strategy similar to that of Brussat [*23*] is suggested. First, by holding crack size constant at $V_1 = V_{11}$ for a block of loadings, Eq 6 can be solved for V_{2i} for each loading i as a function of V_{11} alone. This permits Eq 5 to be summed and divided by the time for one block of loadings at selected crack sizes. Thus, for periodic loading histories, averaged crack growth per unit time

$$\frac{dV_1}{dt} = \frac{\sum_{i=1}^{1} \Delta V_{1i}}{\sum_{i=1}^{1} \Delta t_i} = \mathcal{U}(\vec{\alpha}(V_1), \vec{\theta}) \tag{7}$$

is obtained as a function of crack size, V_1, and hence of stress-intensity coefficient, $\alpha(V_1)$, since with τ as stress

$$K = \tau\alpha \tag{8}$$

Eq 7 is then solved for life from an initial to a final crack size by evaluating the integral

$$L = \int_{t=0}^{L} dt = \int_{V_1 = V_{\text{initial}}}^{V_{\text{final}}} \frac{dV_1}{\mathcal{U}(\vec{\alpha}(V_1), \vec{\theta})} \tag{9}$$

For the integrally stiffened panels of Fig. 1, the computational task to obtain stress-intensity factors and solve Eqs 5 and 6 for crack-growth life can be formidable. This is of particular concern since for every trial design of the structure, these life predictions must be repeated for several crack sites, loading histories, uncertainty parameter gradients $dL/d\theta_i$ for the safety factor Ω_L, and design variable gradients $dg(\vec{D})/dD_i$ to direct redesign. Consequently, for automated design against crack growth and fracture to be feasible, both the number of trial designs analyzed and the computational effort for life prediction must be minimized. The rest of this section is devoted to methods for achieving some of the needed efficiency for crack growth and fracture analysis.

Fracture Mechanics

In each stiffened panel, three initial crack sites (Fig. 1) were selected to represent possible symmetrically located cracks [*22*]. In Fig. 2, the crack path from each site is divided into crack-size regions. For any geometry of cracked structure represented by these regions, methods are in use for computing elastic stress-intensity factors [*24,25*]. However, direct methods to solve for stress-intensity factors often require extensive analysis. As a short cut, stress-intensity factors may often be compounded

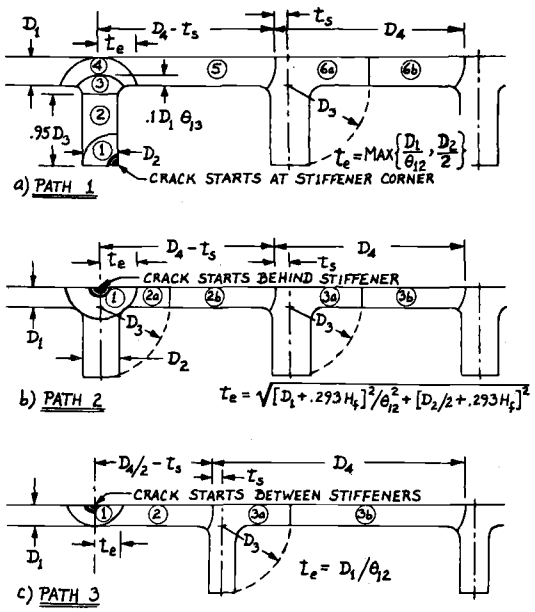

$t_s = \theta_{11} D_2/2$ WHERE θ_{11} IS UNCERTAINTY PARAMETER FOR t_s. SYMMETRIC CRACKS MEAN GROWTH TO LEFT IS SAME AS TO RIGHT.

FIG. 2—*Crack-size regions for paths chosen.*

from available results on simple configurations of crack, load and structure [*26–29*].

For regions 1, 2, 5, and 6b of path 1, regions 2b and 3b of path 2, and regions 1, 2, and 3b of path 3, the literature provides sufficient results to construct satisfactory stress-intensity factors. These results include correction factors for edge crack in a plate [*30*], surface flaw in a plate [*31*], corner flaw [*29*], finite width of plate [*32*], skin crack through a broken stiffener [*33*], skin crack near an unbroken stiffener [*34*], and crack in sheet with stiffened edges [*35*]. In the latter three cases, only numerical values are available so that computable expressions for automated design use had to be derived by curve fitting. For the remaining regions, results were not available so that stress-intensity factors were interpolated. For region 6a in path 1, regions 2a, 3a in path 2, and region 3a in path 3 (Fig. 2), Poe [*36*] conservatively suggested letting the crack grow through stiffener and skin at the same rate with the stress-intensity factors linearly interpolated from adjacent regions. A surface crack behind a stiffener (region 1 in path 2) is treated as a surface flaw in a plate whose thickness falls between stiffener depth and skin thickness. Regions 3 and 4 of path 1 are interpolated between an edge crack in the stiffener sheet with

stiffening skin (region 2) and a skin crack through a broken stiffener (region 5).

Crack resistance properties for sheet materials are given by R-curve plots of stress-intensity factor resistance versus crack extension and sheet thickness (Fig. 3). In this paper, fracture failure is instable crack extension to collapse of a structure before crack arrest under the worst static design loading. The fracture design constraint (Eq 4) defines imminence of instable crack extension. From Griffith [*37*], Irwin and others [*38,39*], frac-

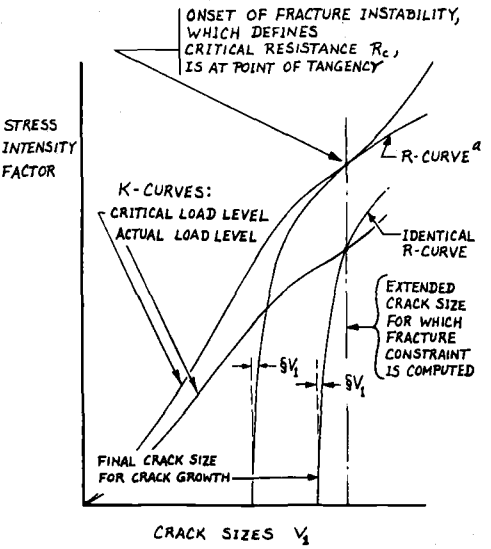

FIG. 3—*R-curve concept for fracture constraints.*

ture instability occurs if stress-intensity factor K increases faster than crack-growth resistance R can rise with increasing crack size V_1 under an applied loading (Fig. 3). That is, instable fracture occurs if

$$K = R \quad \text{and} \quad \frac{dK}{dV_1} \geq \frac{dR}{dV_1} \tag{10}$$

where equality (tangency point in Fig. 3) defines critical resistance R_c.

Eq 8 ($K = \tau\alpha$) implies that the ratio $[(dK/dV_1)/K]$ is constant for all load levels at any given crack size. For any fracture-resistance data, an R-curve exists such that $[(dR/dV_1)/R]$ monotonically decreases as R increases and such that values equal or smaller than those observed are pre-

dicted for R_c at every value of crack extension. On this basis, a single valued and conservative expression [*22*]

$$R_c = \theta_3 f\left(\frac{dK}{dV_1}\Big/ K,\ t\right) \tag{11}$$

to be viewed as an R-slope curve was derived from available 7075-T6 aluminum fracture data [*40–44*] for use in Eq 4. In Eq 11, t is material thickness and θ_3 represents uncertainty in the R-curve level.

The critical crack sizes are obtained as follows [*22*]. First, the highest crack-size region (Fig. 2) is found whose lowest crack size has a positive fracture constraint. Second, the largest crack size with a positive fracture constraint found in this region defines the critical crack size. For the worst design load, subtracting crack extension from the critical size gives a final crack size for crack growth lives.

Crack Growth Laws Used

The crack growth modeling used is state of the art. While only cracks growing straight across the panels are considered, some torsional loadings are employed. Cracks are assumed to grow normal to the direction of the most positive stresses in a loading cycle [*45*]. Thus, the maximum stress-intensity factor $K_{\max}$ governing crack growth direction is

$$K_{\max} = \sqrt{\frac{K_{Mj}^2}{4} + K_{Tj}^2} + \frac{K_{Mj}}{2} \tag{12}$$

where K_{Mj}, K_{Tj} are the stress-intensity factors due to bending and torsion, respectively, and j is either 1 or 2 for whichever load condition in the loading cycle maximizes $K_{\max}$.

Crack growth is corrected to its projected direction across the panel by

$$\cos\psi = \sqrt{\frac{c+1}{2}} \tag{13}$$

where

$$c = \frac{1}{2} K_{Mj}\Big/ \sqrt{\frac{K_{Mj}^2}{4} + K_{Tj}^2}$$

and j refers to the same load condition as in Eq 12.

For varying stress in a load cycle, an octahedral shear criterion is used as the root mean square of resolved shear stress for all possible slip directions [*46*]. That is, the varying stress-intensity factor is

$$\Delta K = \sqrt{\Delta K_A^2 + 3\,(K_{T1} - K_{T2})^2}$$

where

$$\Delta K_A = K_{A\max} - \text{Max}\{K_{A\min}, -0.12\,K_{A\max}\} \tag{14}$$

and

$$K_{A\max} = \text{Max}\{0, K_{M1}, K_{M2}\}$$

$$K_{A\min} = \text{Min}\{K_{M1}, K_{M2}\}$$

with subscripts 1 and 2 referring to the first and second conditions in the loading cycles. In Eq 14, axial loadings close 7075-T6 aluminum cracks at − 12 percent of the maximum load in a cycle [*47*].

For the design studies, the two crack growth laws used are curve fits of arbitrarily selected 7075-T6 aluminum data. The first uses a relationship by Forman, Kearney and Engle [*48*] fitted by Hudson [*49*] to crack growth data at National Aeronautics and Space Administration (NASA). This datum enjoys recognition in the aircraft industry which makes it an attractive standard for comparison. Here, crack growth in inches per cycle is

$$\left.\frac{\Delta V_1}{\Delta t}\right|_i = \frac{91 \times 10^{-8}\,\theta_6\,\Delta K^{2.21}\,K_{\max}}{K_{cr} - K_{\max}} \tag{15}$$

where K_{cr} is a reference value for critical stress-intensity factor adjusted for material thickness (pp. 57, 70 of Ref *22*). Uncertainty in the crack-growth rate is represented here by the parameter, θ_6. The second model is from data reported by Walker [*50*] for dry and moist air. A plot of crack growth versus stress-intensity factor for this data fits a curve broken into three segments. This gives an added test for convergence capabilities of the life prediction methods used. For moist air, crack growth in inches per cycle is given by

$$\left.\frac{\Delta V_1}{\Delta t}\right|_i = \text{Max}\left\{\delta V_{1a}, \frac{\delta V_{1b}\,\delta V_{1c}}{\delta V_{1b} + \delta V_{1c}}\right\}$$

where

$$\delta V_{1a} = 0.04 \times 10^{-8}\,\theta_6\,(K_{\max}\Delta K)^2 \tag{16}$$

$$\delta V_{1b} = 82 \times 10^{-8}\,\theta_6\,(K_{\max}\Delta K)^{0.87}$$

$$\delta V_{1c} = 0.0272 \times 10^{-8}\,\theta_6\,(K_{\max}\Delta K)^{2.5}$$

for both models, if $\sqrt{K_{max}\Delta K}$ exceeds 26.9815 ksi $\sqrt{\text{in.}}$, then crack growth may exceed that given by Eq 15 and 16. In this investigation, the R-curve (Fig. 3 and p. 72 of Ref *22*) is used as a more realistic model for crack growth when K exceeds 26.9815 ksi $\sqrt{\text{in.}}$

For interaction effects of sequential loadings on crack growth, the Wheeler model (See Eqs 3 to 5 in Ref *51*) is used in the absence of realistic modeling of such effects. To speed calculations, the Wheeler model was reduced to the form of Eqs 5 and 6 and solved for one block of loadings. For the q^{th} layer of n_q equal loadings in a block, crack growth is computed in one step with [*22*]

$$\Delta V_{1n_q} = \begin{cases} V_2 - R_{yq} + (n_q - n_{\text{decay } q}) \left.\dfrac{\Delta V_1}{\Delta t}\right|_q & \text{if } n_q \geq n_{\text{decay } q} \\ V_2 - V_{2n_q} & \text{if } n_q < n_{\text{decay } q} \\ \left. n_q \dfrac{\Delta V_1}{\Delta t}\right|_q & \text{if } V_2 \leq R_{yq} \end{cases}$$

where

$$n_{\text{decay } q} = \frac{V_2 (V_2/R_{yq})^m - R_{yq}}{(m+1)\left.(\Delta V_1/\Delta t)\right|_q} \tag{17}$$

$$V_{2n_q} = \left[V_2^{m+1} - (m+1) n_q \left.\frac{\Delta V_1}{\Delta t}\right|_q R_{yq}^{\,m} \right]^{1/(m+1)}$$

$$V_2 = \begin{cases} R_{yq-1} - \left.\dfrac{\Delta V_1}{\Delta t}\right|_{q-1} & \text{if first layer or } n_{q-1} \geq n_{\text{decay } q-1} \\ V_{2n_{q-1}} & \text{if } n_{q-1} < n_{\text{decay } q-1} \end{cases}$$

$$R_{yq} = \frac{K_{max}^2}{4\sqrt{2}\,\pi F_{ty}^2}$$

and F_{ty} is yield limit and m is Wheeler's exponent for strength of crack retardation. The plastic zone size V_2 is initiated by starting with the layer of largest loadings in the block.

Prediction Method

Prediction of crack growth life is completed by integrating Eq 9. Since calculation of reciprocal crack growth per block, $\mathcal{U}_r(V_1) = 1/\mathcal{U}(\alpha(V_1), \theta)$,

is so extensive, numerical quadrature is necessary. Quadrature proceeds by fitting an easily integrated function to an integrand at selected points and integrating the fit to approximate the desired integral. For Hermite quadrature, a cubic polynomial

$$Z(V_1) = A_0 + A_1 x + A_2 x^2 + A_3 x^3 ; \; x = \frac{V_1 - V_{1i}}{V_{1i+1} - V_{1i}} \tag{18}$$

is equated to the integrand and its derivative at successive points, V_{1i} and V_{1i+1}. However, reciprocal crack growth, $\mathfrak{V}_r(V_1)$, is proportional to $\alpha^{-\Theta_i}$ or $V_1^{-C_i}$ where Θ_i is the slope of log crack growth versus log stress-intensity factor and C_i is the corresponding slope for crack size from V_{1i} to V_{1i+1} (that is, $C_i = -d \log \mathfrak{V}_r(V_1)/d \log V_1|_{V_1 = V_{1i}}$). Consequently, a weighted polynomial, $w(V_1)Z(V_1) = V_1^{-C_i} Z(V_1)$ should produce a closer fit to the integrand, $\mathfrak{V}_r(V_1)$, than $Z(V_1)$.

In this way, the integral (Eq 9) is approximated in each interval by

$$\begin{aligned} \int_{V_1 = V_{1i}}^{V_{1i+1}} \mathfrak{V}_r(V_1) dV_1 &\approx \int_{V_1 = V_{1i}}^{V_{1i+1}} V_1^{-C_i} Z(V_1) dV_1 \\ &= \sum_{p=0}^{1} \mathfrak{K}_{i(p)} \mathfrak{V}_r(V_{1i+p}) + \bar{\mathfrak{K}}_{i(p)} \mathfrak{V}'_r(V_{1i+p}) \end{aligned} \tag{19}$$

where $\mathfrak{V}_r(V_{1i+p})$, $\mathfrak{V}'_r(V_{1i+p})$ with $p = 0, 1$ are reciprocal of crack growth per block and its derivative with respect to crack size at V_{1i} and V_{1i+1}. The weighted quadrature coefficients are computed by [*22*]

$$\mathfrak{K}_{i(0)} = h_{i(0)} + \frac{C_i}{V_{1i}} \bar{\mathfrak{K}}_{i(0)}$$

$$\mathfrak{K}_{i(1)} = h_{i(1)} + \frac{C_i}{r_i V_{1i}} \bar{\mathfrak{K}}_{i(1)}$$

$$\bar{\mathfrak{K}}_{i(0)} = \frac{V_{1i}^2}{(r_i - 1)^2} [- r_i^2 \mathfrak{L}_{1i} + r_i(r_i + 2)\mathfrak{L}_{2i} - (2r_i + 1)\mathfrak{L}_{3i} + \mathfrak{L}_{4i}]$$

$$\bar{\mathfrak{K}}_{i(1)} = \frac{r_i^{C_i} V_{1i}^2}{(r_i - 1)^2} [- r_i \mathfrak{L}_{1i} + (1 - 2r_i)\mathfrak{L}_{2i} - (2 + r_i)\mathfrak{L}_{3i} + \mathfrak{L}_{4i}]$$

where

(20)

$$h_{i(0)} = \frac{V_{1i}}{(r_i - 1)^3}[r_i^2(r_i - 3)\mathfrak{L}_{1i} + 6r_i\mathfrak{L}_{2i} - 3(r_i + 1)\mathfrak{L}_{3i} + 2\mathfrak{L}_{4i}]$$

$$h_{i(1)} = \frac{r_i^{C_i}V_{1i}}{(r_i - 1)^3}[(3r_i - 1)\mathfrak{L}_{1i} - 6r_i\mathfrak{L}_{2i} + 3(r_i + 1)\mathfrak{L}_{3i} - 2\mathfrak{L}_{4i}]$$

with

$$\mathfrak{L}_{ki} = \begin{cases} \log_e r_i & \text{if } C_i = k \\ (r_i^{k-C_i} - 1)/(k - C_i) & \text{if } C_i \neq k \end{cases}$$

and $r_i = V_{1i+1}/V_{1i}$

Crack growth lives have been predicted with Eqs 17, 19, and 20 for surface flaws in D6ac steel under repeated blocks of Wheeler's 13 layer spectrum of loadings (Table 1) [*51*]. Since this D6ac steel followed a simple Paris law for crack growth, a one step calculation per layer of equal loadings similar to Eq 17 was derived for the Willenborg [*52*] model for crack growth retardation (See Appendix D of Ref *22*). In all three cases (Table 1), a single interval of weighted quadrature achieved an accuracy comparable with previously published predictions. Computer speed was increased ten fold over the next best numerical procedure on the same equipment. Unweighted quadrature ($C_i = 0$) required 4 intervals to achieve the accuracy of one interval with weighted quadrature. For a center-through-crack growing from 1 to 60 percent of a plate width, the advantages of weighted over unweighted quadrature (Table 1) are more dramatic.

In integrally stiffened panels, stress-intensity coefficients do not increase regularly with crack size as in a surface flaw. However, some regularity can be had by integrating crack growth on a crack size region-by-region basis (See Fig. 2). At the few locations where regularity fails, the use of upper and lower quadrature bounds limit the possible error [*22*].

Within a crack-size region, crack growth varies more regularly with stress-intensity coefficients than with crack size. Consequently, reciprocal crack growth, $\mathcal{V}_r(\alpha)$, is computed for a few stress-intensity coefficient levels along the crack path in each region and then interpolated to the coefficient levels, α, corresponding to the crack sizes used as quadrature points. Since crack growth is proportional to α^Θ, a cubic polynomial with $\log\alpha$ replacing V_1 in Eq 18 is weighted by $\alpha^{-\Theta}$ so that

$$\log \mathcal{V}_r = Z(\log\alpha) - \Theta \log\alpha \tag{21}$$

TABLE 1—*Comparison of predicted crack growth lives.* [a]

	No Crack Retardation, $m = 0$, use α_1	Wheeler Model for Retardation, $m = 1.3$, use α_1	Willenborg Model for Retardation, use α_2	Center-Through Crack (Irwin), 1 Load Per Block, $\frac{\Delta V_1}{\Delta t} = \left[\frac{2}{\pi} \tan \frac{\pi V_1}{2}\right]$
Growth Law for D6ac Steel is $\Delta V_1/\Delta t = 0.22 \times 10^{-8} \Delta K^{2.55}$	Crack grows from 0.14 to 0.69 in. deep in 0.69 in. D6ac steel plate, yield stress = 206 ksi, under 13 layer spectrum of Wheeler [*51*]			Crack grows from $V_1 = 0.01$ to $V_1 = 0.60$
		Weighted Quadrature		
1 Interval computer time	20.2666 3 s	26.424 3 s	31.319 4 s	97.359
2 Intervals	20.204	26.445	31.622	97.383
4 Intervals	20.194	26.440	31.653	97.393
20 Intervals	20.194	26.442	31.652	97.395
		Unweighted Quadrature ($C_i = 0$)		
1 Interval	4.732	4.561	13.906	− 54897.
2 Intervals	19.457	25.391	30.804	− 466.
4 Intervals	20.152	26.382	31.608	76.230
20 Intervals	20.194	26.442	31.652	97.372
Exact Integration				97.395
		Results of Others		
Wheeler [*51*]	20.2	26		
Willenborg [*52*]			32.2	
Brussat [*23*]		26.24	31.45	
Brussat time		40 s	50 s	

NOTE—Stress-intensity coefficients used

$\alpha_1 = 1.243 \sqrt{V_1} [0.899 + (V_1/t)(.184 + (V_1/t)(.279 + .108 (V_1/t))]$

$\alpha_2 = 1.243 \sqrt{V_1} [1.0037 + (V_1/t)(-.0383 + .1408 (V_1/t)^2)]$

[a] Lives in blocks from initial to final size.

To evaluate the constants of Z ($\log\alpha$), this expression and its derivative with respect to $\log \alpha$ are equated to exact values of $\log \mathcal{U}_r$ and $d \log \mathcal{U}_r/d \log \alpha$ at successive levels of α [*22*]. Use of Eq 21 to interpolate $\mathcal{U}_r$ saves analysis time for both the original crack growth constraints and the constraint gradients to construct probabilistic safety factors and redirect design. Reanalysis of $\mathcal{U}_r$ is avoided for numerical gradients aside from those of uncertainty parameters which appear in the crack growth modeling.

For computing gradients, varied stress-intensity coefficients from varied design variables or uncertainty parameters can also be interpolated. The variation of stress-intensity coefficients is assumed to follow

$$\log \alpha^{+}(V_1) = \log \alpha(V_1) + Z(V_1) \tag{22}$$

where the + indicates the varied coefficient α and the unweighted cubic polynomial, $Z(V_1)$, is defined by Eq 18 [*22*].

In automated design, the most significant fact about crack-growth constraints is that life, L, varies as stress, $\tau = P/A$, raised to a variable power Θ which values roughly from 2 to 5 (See Eqs 7, 8, 9, 15, 16, and 21). Early work indicated that if stress-like and life-ratio design constraints are mixed, then life constraints will severely oscillate above and below stress constraints and each other with even small changes in design. Such behavior can badly confuse a design system. Consequently, life constraints must be normalized to respond like stress constraints to design change.

To derive a normalizing exponent, let area A in stress, P/A, be subject to design change and let an average slope, $\bar{\Theta}$, exist such that

$$L = bA^{\bar{\Theta}} \tag{23}$$

where b is constant for small changes in A. If small changes in design are considered by equating the derivatives of Eqs 23 and 19, then

$$\frac{dL}{dA} = \sum_{i=1}^{I} \int_{V_1 = V_{1i}}^{V_{1i+1}} \frac{d\mathcal{V}_r(V_1)}{dA}\, dV_1 = \sum_{i=1}^{I} \int_{V_1 = V_{1i}}^{V_{1i+1}} \frac{\Theta(V_1)\mathcal{V}_r(V_1)}{A}\, dV_1 = \bar{\Theta}\, L/A \tag{24}$$

Finally, if $\Theta(V_1)$ is replaced by $[\Theta(V_{1i}) + \Theta(V_{1i+1})]/2$ in each interval, then the average slope becomes

$$\bar{\Theta} = \sum_{i=1}^{I} [\Theta(V_{1i}) + \Theta(V_{1i+1})] \int_{V_1 = V_{1i}}^{V_{1i+1}} \mathcal{V}_r(V_1) dV_1 / 2L \tag{25}$$

where

$$L = \sum_{i=1}^{I} \int_{V_1 = V_{1i}}^{V_{1i+1}} \mathcal{V}_r(V_1) dV_1 \text{ and } \Theta(V_{1i}) = -\left. \frac{d \log \mathcal{V}_r(\alpha)}{d \log \alpha(V_1)} \right|_{V_1 = V_{1i}}$$

From Eq 23, the life weighted average slope $\bar{\Theta}$ defined by Eq 25 can be seen to provide the desired normalizing exponent for the crack-growth design constraint (Eq 3).

Probabilistic Analysis

For the crack-growth constraints to reflect the impact of various uncertainties, $\vec{\theta}$, in the analysis, a probabilistic analysis is used to compute the safety factors Ω_L, Ω_F of Eqs 3 and 4. Here, the whole of the analyses applied to compute crack-growth life or stress-intensity factor over critical

resistance defines an engineering mathematical model. This model was first converted into a corresponding statistical mathematical model which is assumed to take the regression form

$$y = f(\vec{\xi}, \vec{\theta}) + \epsilon \tag{26}$$

Here, the prediction model is represented by

$$f(\vec{\xi}, \vec{\theta}) = \begin{cases} \log [(L_{\text{req}}/L)^{1/\bar{\Theta}}] & \text{for crack growth} \\ \log [K/R_c] & \text{for fracture} \end{cases} \tag{27}$$

and y is a possible outcome with ϵ as random error. In Eq 26, $\vec{\xi}$ is an array of numbers for all controlled variables including the applied static design and normal usage loadings, the design variables, and the preassigned parameters. After some analysis, a reliable value for the safety factor Ω becomes [*22*]

$$\Omega = \exp \left\{ t_R \left[s^2 + \sum_{j=1}^{Z} \sum_{i=1}^{Z} \frac{df(\vec{\xi}^\circ, \hat{\theta})}{d\theta_i} S_{ij} \frac{df(\vec{\xi}^\circ, \theta)}{d\theta j} \right]^{1/2} \right\} \tag{28}$$

In Eq 28, t_R is a coefficient corresponding to some reliability R, s^2 is the estimated variance on future outcomes of y, Z is the number of uncertainty parameters θ_i, $\vec{\xi}^\circ$ is the array of control variable values for which a prediction is made and S_{ij} is the i by j element of the variance-covariance matrix. In this investigation, the values $t_R = 3$ and $s^2 = 0.0036$ were used for all design examples. The matrix of variances and covariances S_{ij} defines the amounts of uncertainty in the estimates $\hat{\theta}$ for the parameters $\vec{\theta}$ as obtained from experiment and prior experience (see Ref *22* for values of $\sqrt{S_{ij}}$ used here).

Variation in some uncertainty parameters can influence predicted crack-growth lives through the fracture analysis and, hence, critical crack sizes. A natural approach is to combine all sources of random variation including fracture into a single probability distribution on crack-growth life. However, if a critical crack size were near a stiffener just strong enough to arrest the crack, then a slight uncertainty parameter change could cut the critical crack size back to the preceding stiffener. This cut would cut crack-growth life so that a probability density on crack-growth life would be discontinuous. Such unpredictable discontinuities undermine the usefulness of any safety factors computed. To avoid the situation, safety factors for crack growth and fracture are computed separately. As a result, the critical crack sizes used already contain any cuts in critical size appropriate to a desired reliability level. In this way, a probability distribution on

crack-growth life can satisfy the necessary regularity conditions so that safety factors can be meaningful.

If safety factors (Eq 28) are varied in response to varied design variables for gradients, then the potential computational effort is enormous. When only nine uncertainty parameters define safety factors for the original analysis plus the eight design variables used here, than 90 separate constraint values are needed for one crack-life constraint and its design gradients. For more parameters and design variables, the situation is increasingly worse. However, safety factors should not change drastically with redesign. Consequently, safety factors are not revised when computing design gradients. Thus, for nine parameters and eight design variables, only 18 constraint values are used here to define a crack-growth constraint with its gradients.

Automated Design Procedure

Mathematical programming is used to solve the design problem of Eq 1 for the integrally stiffened two panel box [*22*]. An extended version of the penalty function method of Fiacco and McCormick is used to construct a sequence of unconstrained minimization problems which converge to a local minimum weight design [*53,54*]. A modified Davidon-Fletcher-Powell deflected gradient algorithm is employed for unconstrained minimizations [*55,56*].

The design constraints against buckling, crack growth, and fracture involve extensive numerical analysis. With six crack paths, four initial crack sizes and two loading histories, 48 crack-growth constraints are generated for analysis. The stiffened two-panel box generates eight design variables. With this computational burden, direct analysis of these constraints must be avoided as much as possible during design. This is particularly important if larger structures, more static load conditions, and longer loading histories are required in future applications.

Schmit and his co-workers [*4,6,12*] have employed constraint deletion and approximate substitutes for constraints to reduce calculations for design of structures against displacement, stress, buckling, and dynamic failure mode constraints. Constraint deletion (also known as relaxation [*57*]) is the retention for design of only the more critical constraints calculated before each design stage. Linear Taylor expansions of retained constraints, with respect to the design variables, create explicit approximations to replace the original analyses during subsequent design synthesis. These techniques are used here to replace the extensive original design problem with a sequence of subproblems having fewer and more easily computed constraints.

For efficient use of constraint analysis effort, a multistaged approach to subproblem definition is employed [*22*] (Fig. 4). As an outer or survey

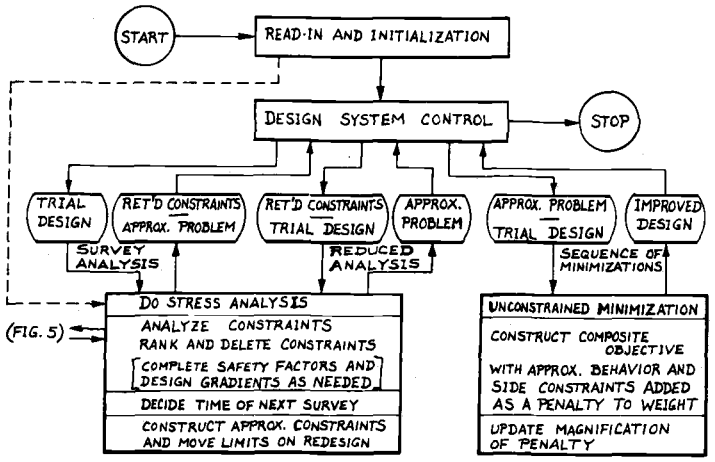

FIG. 4—*Outline of design procedure.*

stage, all constraints are calculated and those unlikely to become critical are deleted. Only retained constraints are treated in subsequent (reduced analysis) stages until the next survey. Return to a survey analysis occurs if observed changes in relative constraint rankings indicate that ignored constraints could be critical. With each reduced analysis, the retained constraints are reanalyzed and sorted for constraints to retain in the current penalty function. Only for constraints in the penalty function are gradients and move limits computed to construct approximate analyses to use in subsequent minimizations. In addition, the criterion to reanalyze probabilistic safety factors is more restrictive in reduced analyses than in survey analyses. In survey or reduced analyses, constraints are sorted using both their past and current values. Side constraints for geometric realizability are computed only during subsequent minimizations.

Design Problems and Results

Automated Design Capability

The design procedure and the crack growth and fracture methods outlined in this paper have been applied to an integrally stiffened two panel box (Fig. 1) in a computer program [*22*]. The program is coded in FORTRAN IV for the G compiler on the University of California, Los Angeles (UCLA) Campus Computing Network's IBM System 360/91 computer. The program runs entirely within 400 000 bytes of core memory in the computer. The design procedure operates as shown on Fig. 4.

The coding for the crack-growth constraints is more fully flow charted

on Fig. 5. The constraint analysis initiates in subroutine CSIZE which finds the critical crack size for each crack path. Subroutine FRACT (Fig. 5) provides the fracture-design constraints (Eq 4 with probabilistic safety factors, Ω_F, as needed) at each crack size used to find critical crack size. The crack-growth resistance properties of 7075-T6 aluminum are provided and used in the subroutine to evaluate the fracture constraints. Stress-intensity coefficients for any crack size on the three crack paths (Fig. 2) are given by subroutine KCOEF.

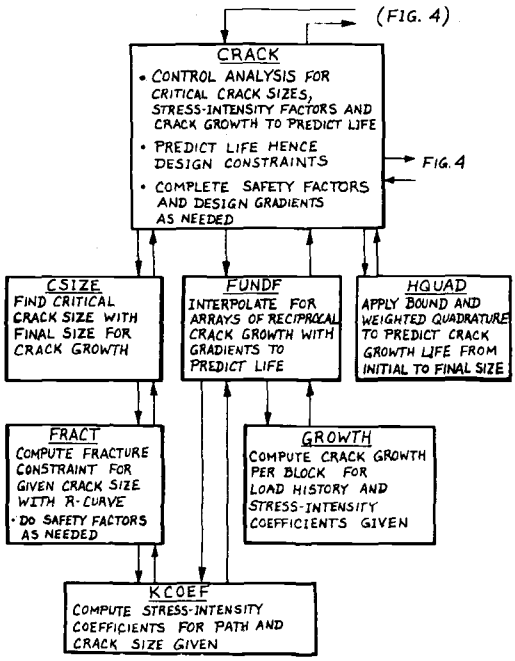

FIG. 5—*Flowchart for crack-growth constraints.*

For each stress-intensity coefficient level, subroutine GROWTH computes crack growth for one block of loadings (Eqs 12 to 17) with two alternative sets of crack-growth data for 7075-T6 aluminum (Eqs 15 and 16). Subroutine FUNDF implements the interpolations used to replace the crack growth and stress-intensity coefficient analyses at many of the crack sizes used for quadrature (Eqs 21 and 22). A weighted piecewise Hermite quadrature procedure using Eqs 19 and 20 but with built-in upper and lower bounds is provided in subroutine HQUAD to predict crack-growth life from initial to final crack size.

Once predictions are completed, subroutine CRACK computes probabilistic safety factors Ω_L if a specified change in constraint value would

make a positive constraint negative or vice versa. If the crack-growth constraint is to be retained in the penalty after sorting, then perturbed values of the constraint are computed upon variation of each design variable. These calculations depend heavily on the interpolations of subroutine FUNDF for efficient use of information from the original unperturbed analysis.

The computer program also computes behavior constraints against stiffener, skin, and orthotropic panel buckling as well as box displacements, yielding, and crack growth.

Description of Design Examples

To demonstrate the design procedure and the feasibility of including crack growth and fracture design constraints, 32 design examples were treated for the integrally stiffened two-panel box [*22*] (Fig. 1). For the first example, a known solution is afforded by constraints on minimum and maximum dimensions acting alone. With this example, the design system was found to converge satisfactorily since the design settled smoothly to within 4 percent of the solution after 10 minimizations and to 3 significant figure accuracy after 20 minimizations.

For 31 design examples, the static-design loading conditions, initial designs, constraint limits, buckling mode limits, and material properties appear in Table 2. The preassigned parameters for all the examples are shown in Fig. 1. Two examples among the 31 are devoted to design against buckling and other constraints but without any consideration of crack growth or fracture. These two examples provide a basis of design comparison for the later designs against crack growth and fracture. The use of two different starting designs provide alternative design trajectories (double point) which should produce the same final designs (which did occur in this case) if the system is working, the gradients are accurate, and only one minimum attracts the designs.

The remaining 29 design examples should demonstrate the feasibility of including the crack growth and fracture capability in the automated design system. These examples are generated by the loading histories, crack growth modeling, variance-covariance matrices, quadrature interval sizing, and initial designs assumed. The 29 examples are categorized among seven crack-growth design cases (Table 3). In each case, two alternative sets of two loading histories each are considered. The first history is shown in Table 4. For histories 2, 3, and 4, the bending moments are made more positive by 100, 200, and 300 kip·in., respectively, and, for histories 2 and 3, the number of taxi, flight, and braking loads are doubled. Both the Forman (Eq 15) and Walker (Eq 16) crack-growth laws are considered in each design case. For the design results obtained, both laws are appended by an R-curve for high stress-intensity factors and Wheeler's model (Eq 17) is used for crack retardation.

TABLE 2—*Static design loads and constraint limits.*

Static Design Loads

Condition	Torsion, kip, in., M_y	Bending, kip, in., M_x
1	0	− 2000
2	1200	− 1200
3	0	1200

Initial Designs

	Panel	Skin Thickness, D_1 (in.)	Stiffener Thickness, D_2 (in.)	Stiffener Depth, D_3 (in.)	Stiffener Spacing D_1 (in.)
Basic	1	0.1	0.25	2.0	5.0
	2	0.1	0.25	2.0	5.0
Double	1	0.225	0.140	1.6	4.0
	2	0.250	0.120	1.6	5.0
2 in. Double	1	0.225	0.140	1.6	2.0
	2	0.250	0.120	1.6	2.0

Side Constraint Limits

Minimum values	0.032	0.032	0.2

Behavior Constraint Limits

	Symbol	Dimension	Value
Allowable torsional twist	$u_{\max 1}$	radians	0.02
Allowable bending rotation	$u_{\max 2}$	radians	0.02
Yield stress (7075-T6 aluminum)	F_{ty}	ksi	70

Material Properties

Weight density	ρ	lb/in.^{3}	0.101
Elastic modulus	E	ksi	10 000
Poisson's ratio	μ		0.3

Buckling Mode Limits

	No. of Modes
Cross panel modes (skin buckling)	4
Longitudinal modes (skin buckling)	6
Cross panel modes (panel buckling)	6
Longitudinal modes (panel buckling)	4

In case 1 (Table 3), the skin and panel buckling constraints are ignored to see what designs the crack growth and other constraints acting alone would lead to. All design constraints are considered simultaneously in the remaining cases. Between cases 2 and 3 and in cases 6 and 7 the effect of refining the quadrature interval sizing on design convergence was compared. The influence of initial designs chosen from Table 2 are compared between cases 3 and 4 and cases 6 and 7 (Table 3). The basic initial design

TABLE 3—*Outline of design examples.*

Case	Variance Covariance Matrix	Quadrature Interval Sizing	Initial Design	Example or Run	Crack Growth Model	Loading Histories	Computer Time, s	No. of Design Stages	Final Design Weight
A[a]	...	...	basic	9-4-74	...	...	...	...	0.9097
B[b]	...	...	basic	1-30	...	...	31	12-conv	40.84[d]
			double	2-8b	...	...	26	11-conv	40.82
1[c]	first	refined	basic	2-16a	Forman	1,4	289	11-good	62.74
				2-16b	Forman	2,3	304	10-good	57.92
				2-16	Walker	1,4	267	11-conv	50.96[d]
				2-17	Walker	2,3	281	12-good	46.64
2	first	gross	basic	1-20	Forman	1,4	255	12-good	63.51
				1-26a	Forman	2,3	251	11-good	60.43
				1-21	Walker	1,4	230	11-conv	52.89[d]
				1-25a	Walker	2,3	253	12-conv	50.03
3	first	refined	basic	2-17e	Forman	1,4	282	12-conv	63.40
				2-17c	Forman	2,3	295	12-conv	59.89
				2-15a	Walker	1,4	248	11-conv	52.65[d]
				2-17a	Walker	2,3	297	12-good	49.19
4	first	refined	double	2-17f	Forman	1,4	185	11-conv	74.87
			double	2-17d	Forman	2,3	200	10-good	67.55
			double	2-15	Walker	1,4	218	11-conv	54.87
			double	2-17b	Walker	2,3	245	10-good	50.36
4a			2 in. double	2-27	Forman	1,4	317	12-conv	63.17
			2 in. double	2-28	Forman	2,3	228	9-good	59.71
5	second	gross	basic	2-1a	Forman	1,4	229	12-good	60.35
				1-28	Forman	2,3	248	12-conv	57.21
				2-1	Walker	1,4	222	11-conv	51.58
				1-29	Walker	2,3	242	11-conv	49.16
6	across-the-	gross	basic	2-1b	Forman	1,4	141	11-conv	72.20
	board safety	midsize		2-8a	Forman	2,3	161	12-good	67.42
	factor	midsize		2-7	Walker	1,4	182	12-good	57.87[d]
		midsize		2-8	Walker	2,3	172	12-conv	53.10
7	across-the-	midsize	double	2-9	Forman	1,4	144	12-good	73.54
	board safety	refined	2 in. double	3-1	Forman	1,4	194	12-good	70.42
	factor	refined	2 in. double	3-2	Forman	2,3	192	12-good	64.39

[a]Case A: Side constraints only.
[b]Case B: Designed for buckling since crack growth and fracture are ignored.
[c]Case 1: Skin and panel buckling are ignored so that design is for crack growth and fracture alone.
[d]See Figs. 6 and 7.

TABLE 4—*One block of history No. 1* [a]

Layer	Number of Cycles in Layer	Bending Moment, kip, in.		Torsion Moment, kip, in.	
		First Condition	Second Condition	First Condition	Second Condition
		Taxi Loadings			
1	100	20	− 220	10	50
2	6	100	− 300	− 10	70
3	30	60	− 260	0	60
4	300	− 20	− 180	20	40
		Transition			
5	1	− 100	− 300	30	0
		Flight Loadings			
6	2	− 200	− 400	0	0
7	200	− 100	− 300	0	0
8	2	300	− 700	0	0
9	30	60	− 460	0	0
10	15	− 180	− 300	0	100
11	12	160	− 520	0	0
12	5	− 180	− 400	0	200
13	80	20	− 340	0	0
14	4	260	− 580	0	0
15	2	− 160	− 360	0	0
		Landing Loads			
16	1	50	− 350	− 400	400
17	3	0	− 240	− 200	200
		Braking Loads			
18	3	− 20	− 180	− 30	− 400
19	10	− 60	− 140	− 30	− 300
20	20	− 80	− 120	− 30	− 200

[a] The loadings are arranged as in an aircraft flight.

was invariably infeasible with negative design constraints. The second (double) with wide stiffener spacing provided a double point for the examples. The third initial design (2 in. double) provided a narrow stiffener spacing for an alternative double point where needed.

The impact of probabilistically computed safety factors can be compared with across-the-board safety factor designs on comparison of cases 3 and 5 with cases 6 and 7 (Table 3). Two alternative variance-covariance matrices are used for computing crack growth and fracture safety factors. Each of the two matrices provides for the influence of nine uncertainty parameters six of which appear in both matrices. For the deterministic designs, across-the-board safety factors of $\Omega_L = 1.5$ on crack growth and $\Omega_F =$

1.23 on fracture were chosen as producing a reliability roughly equivalent to that for the first variance-covariance matrix.

Design Results

For each example run, the computer time and number of design stages to settle on a final design and the final design weight are given in Table 3. For the probabilistic crack growth examples (cases 1 to 5) computer time ranged from 185 to 317 s for an average of 254 s. The deterministic crack-growth design runs (cases 6 and 7) took from 141 to 194 s for an average of 169 s. This means that perhaps 85 s of a probabilistic design run may go to computing uncertainty parameter gradients and safety factors. Comparison of cases 4 and 4a with Case 3 and of Case 6 with Case 7 indicates that sometimes different final designs can result from different starting designs when design gradients are inaccurate. Except for runs 2-17f, 2-17d, and 2-9, the use of alternate starting designs did not significantly alter the final designs obtained in this investigation.

Typical design histories of weight and level of analysis conducted at each stage are presented on Fig. 6. These design histories show the classic pattern of design. First, a safe starting design is established in the early stages. Next, a rapid weight loss is followed by a transition to the later

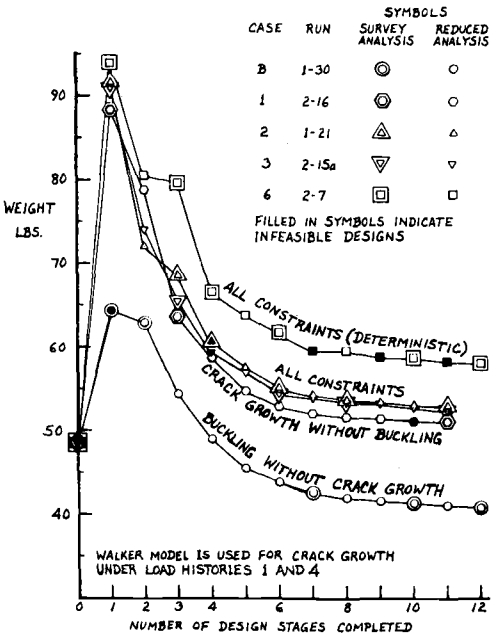

FIG. 6—*Typical design histories.*

stages when the design settles gradually into a final configuration. Twelve stages, including only 4 to 7 full survey analyses of all constraints, have appeared sufficient to allow settlement on final design configurations. Comparison of case 2 with case 3 shows that more accurate gradients through refined quadrature interval sizing does lead to improved design trajectories (Fig. 6) and lighter-weight final designs (Table 3). Here, the effect on design was slight (less than 1 percent). With designs that went astray, alternative starting designs were sometimes used with improved gradients to help lead the design to a minimum weight (compare case 4 with 3 and 4a and case 6 with 7 in Table 3).

The results for the designs followed in Fig. 6 are shown on Fig. 7. For the loading histories and crack-growth models considered, the design results of Fig. 7 are typical in showing the interactive impact of buckling and crack growth on design. The top half of Fig. 7 shows the designs for buckling without crack growth (case B) and for crack growth without skin and panel buckling (case 1). Without panel buckling as a constraint, satisfaction of crack growth and fracture constraints did lead to minimum

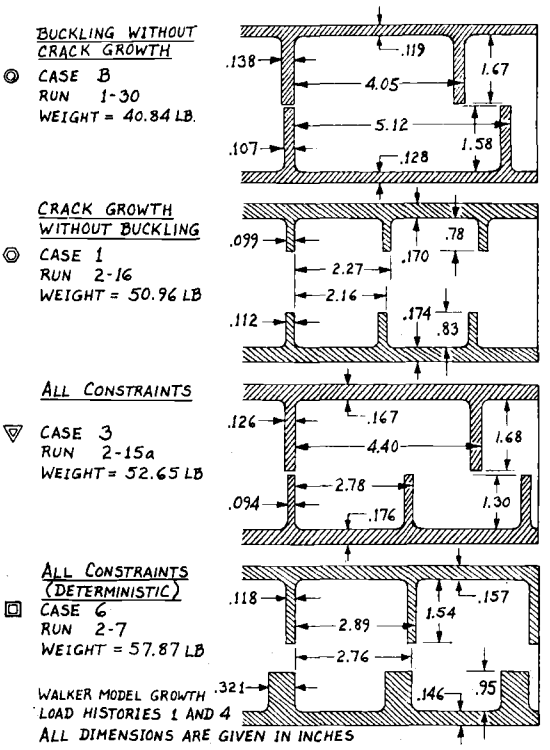

FIG. 7—*Typical design results.*

weight designs. These designs were characterized by small, closely spaced stiffeners (Fig. 7). This contrasted with the deeper more widely spaced stiffeners for buckling. Designs resulting from simultaneous imposition of buckling and crack growth appear in the lower half of Fig. 7. In these designs, the stiffeners are heavier and further apart than with crack-growth constraints alone but usually not so far apart as with buckling alone. In all examples with both buckling and crack growth constraints, the buckling constraints were just as critical as the crack growth constraints to the final designs reported [*22*]. Without reference to the design results of Fig. 7, it is not clear how design results for buckling or crack growth alone could provide proper guidance on design with both buckling and crack growth as design constraints.

Among the examples studied, the final crack sizes obtained by considering fracture ranged from 2.01 in. half length with 3.25 in. stiffener spacing to 9.16 in. half length with 2.13 in. spacing [*22*]. Thus, anywhere from one to eight or nine broken stiffeners were safe or critical depending on the design situation.

Critical constraints for crack growth included every crack path on Fig. 2 [*22*]. Both durability and inspection requirements were critical. Among the inspection alternatives (Fig. 1), only walk-around and overhaul inspections appeared to govern the final designs. The close visual inspection did, however, emerge as a governing constraint for a number of the intermediate designs prior to termination of design in most cases.

The results in Fig. 6 and Table 3 show that designs with probabilistic constraints based on the first variance-covariance matrix (case 3) are from 7 to 10 percent lighter than the best designs obtainable with equivalently reliable deterministic constraints (cases 6 and 7).

Sensitivity Study Results

To consider the impact of selected uncertainties, $\vec{\theta}$, on uncertainty in the predicted lives of final designs, the probabilistic analysis (Eq 28) is used. Essentially, each uncertainty parameter is treated alone in Eq 28 with $s^2 = 0$ to compute component safety factors. In this way, the contributions of individual uncertainties to a total uncertainty in predicted lives can be studied and compared. The 12 uncertainty parameters treated are described and assigned estimated mean and standard deviation values in Fig. 8.

Component safety factors, Ω_z, derived for the various final designs (See Table 3 for design examples treated) are plotted in Fig. 8. For each uncertainty parameter studied, the component factors for designs obtained using Forman's crack growth model are plotted on top with the Walker model results right below. A rough assessment of the results follows two rules of thumb. If most safety factors plotted for an uncertainty parame-

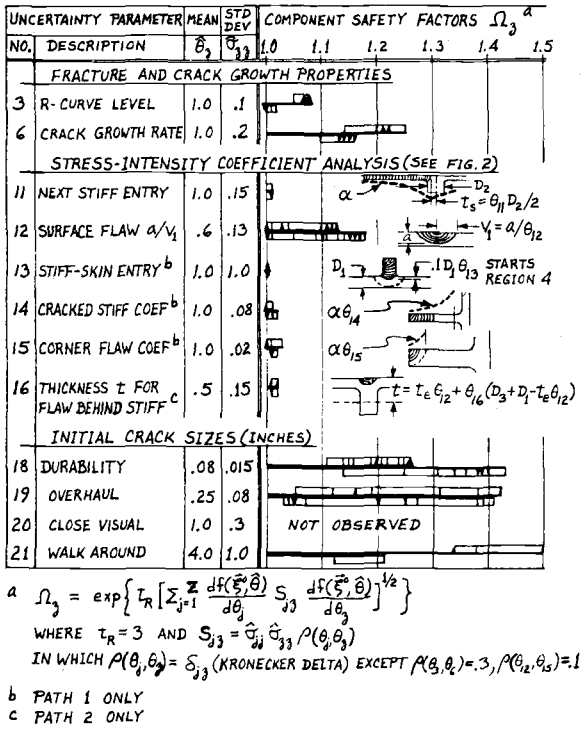

FIG. 8—*Sensitivity study results.*

ter exceed 1.10, then that parameter is considered significant. If none exceed 1.02 and no special circumstances intervene, then the effect of the parameter is considered negligible.

By the first rule, Fig. 8 indicates that uncertainties in the initial crack sizes (θ_{18}, θ_{19}, θ_{21}) are very significant. By inference, uncertainty in what initial crack size, θ_{20}, is discoverable by close visual inspection is also significant. In addition, uncertainties concerning crack-growth properties, θ_6 (as expected) and the surface crack depth over half length ratio, θ_{12}, are significant.

Figure 8 shows by the second rule that the following uncertainties are negligible. These include crack entry to a subsequent stiffener θ_{11}, stiffener into skin flaw size θ_{13}, the Isida model for stiffener edge cracks θ_{14} [*35*], and the effective thickness for a behind stiffener surface flaw θ_{16}. It appears that if the stress-intensity coefficients for cracks with fronts in the stiffener-skin intersections are within an order of magnitude to being correct, then further accuracy is unnecessary for the design cases studied.

The corner flaw parameter θ_{15} also appears negligible. However, the smallest initial crack sizes used here have been almost the size of the stiff-

ener thicknesses for the final designs. Consequently, smaller initial crack sizes or heavier stiffeners should induce greater significance for the corner flaw parameter θ_{15}.

Uncertainty in crack-extension resistance, θ_3, appears negligible except with Forman's model. This apparent significance arises from Forman's denominator K_{cr}-K_{max} in Eq 15. One intent of this denominator is to produce an improved fit for crack-growth data as the stress-intensity factor reaches critical levels [*48,49*]. However, if the R-curve is used to define crack growth for high stress-intensity factors, then the need for a K_{cr}-K_{max} denominator in Eq 15 is no longer apparent.

While uncertainty in resistance θ_3 has little effect on life, it does directly affect the fracture constraints used to compute critical crack sizes (see Eq 11). Particularly with small initial crack sizes, critical crack size should have little influence on life (apply Eqs 7, 8, 15, and 16 to Eq 9). Nevertheless, earlier design studies indicated that if variation of critical crack size in response to varied design was ignored, then the resulting approximate analysis would often lead the design astray [*22*].

Conclusions

1. Crack growth and fracture technology has been incorporated in automated design for the first time.

2. Realistic design criteria were applied using parallel and consecutively related constraints in addition to the usual series related chain of design constraints. The parallel constraints arise from the alternative inspection criteria for initial crack sizes. The critical crack sizes define the consecutive link between crack growth and fracture.

3. Systematic use of constraint deletion and replacement of analysis by various interpolations has reduced computer time sufficiently for feasible design without loss of analysis integrity. Computer time averaged 250 s with four to seven full survey analyses out of 12 to 13 analyses to settle on a design.

4. The slope of crack growth with respect to stress-intensity factor is crucial in providing (*a*) a normalizing exponent for life constraints so they can respond at the same rate as stress constraints to design changes, and (*b*) a weighting exponent for quadrature and interpolation to predict crack growth lives.

5. Probabilistic treatment of identified uncertainties in place of across-the-board safety factors reduced weight 7 to 10 percent for equivalent reliability. With nine uncertainty parameters, computer time increased only by 50 percent.

Acknowledgments

The author wishes to express his appreciation to his faculty advisor and doctoral committee chairman, Professor Lucien A. Schmit of UCLA, for his enthusiastic assistance and encouragement throughout all phases of this investigation.

References

[1] Schmit, L. A., *Proceedings of the 2nd National Conference on Electronic Computation, Structural Division,* American Society of Civil Engineers, Pittsburgh, Pa., pp. 105–132, Sept. 1960.

[2] Sheu, C. Y. and Prager, W., *Applied Mechanics Reviews,* Vol. 21, No. 10, Oct. 1968, pp. 985–992.

[3] Pope, G. G. and Schmit, L. A., Eds., "Structural Design Applications of Mathematical Programming Techniques," 2nd Ed., AGARD-AG-149, Advisory Group for Aerospace Research and Development, North Atlantic Treaty Organization, Neuilly Sur Seine, France, Feb. 1972.

[4] Schmit, L. A. and Miura, H., "Approximation Concepts for Efficient Structural Synthesis," University of California, Los Angeles, Calif., prepared under Grant No. NGR-05-007-337; NASA Report CR-2552, National Aeronautics and Space Administration, Washington, D.C., May 1975.

[5] Schmit, L. A., Kicher, T. P. and Morrow, W. M., *American Institute of Aeronautics and Astronautics Journal,* Vol. 1, No. 12, Dec. 1963, pp. 2820–2836.

[6] Morrow, W. M. and Schmit, L. A., "Structural Synthesis of a Stiffened Cylinder," Case Western Reserve University, Cleveland, Ohio, prepared under Grant No. NsG 110-61; NASA Report CR-1217, National Aeronautics and Space Administration, Washington, D.C., Dec. 1968.

[7] Fox, R. L. and Kapoor, M. P., *American Institute of Aeronautics and Astronautics Journal,* Vol. 8, No. 10, Oct. 1970, pp. 1798–1804.

[8] Cassis, J. H., "Optimum Design of Structures Subjected to Dynamic Loads," Ph.D. dissertation, University of California, Los Angeles, Calif., March 1974.

[9] Turner, M. J., *American Institute of Aeronautics and Astronautics Journal,* Vol. 7, No. 5, May 1969, pp. 945–951.

[10] Gwinn, L. B. and Taylor, R. F., *American Institute of Aeronautics and Astronautics Journal,* Vol. 11, No. 12, Dec. 1973, pp. 1612–1617.

[11] Moses, F. and Kinser, D. E., *American Institute of Aeronautics and Astronautics Journal,* Vol. 6, No. 6, June 1967, pp. 1152–1158.

[12] Schmit, L. A. and Farshi, B., *American Institute of Aeronautics and Astronautics Journal,* Vol. 12, No. 5, May 1974, pp. 692–699.

[13] Gallagher, R. H. and Zienkiewicz, O. C., Eds., *Optimum Structural Design Theory and Applications,* John Wiley & Sons, London, England, 1973.

[14] Venkayya, V. B., Khot, N. S., and Berke, L., "Application of Optimality Criteria Approaches to Automated Design of Large Practical Structures," *AGARD Conference Proceedings No. 123, 2nd Symposium on Structural Optimization,* Milan, Italy, April 1973.

[15] Brooks, G. W., "Structural Technologies—Systems Challenges and NASA Thrusts," *American Institute of Aeronautics and Astronautics* Paper No. 73-17, New York, January 1973.

[16] Fulton, R. E., Sobieszczanski, J., Storaasli, O., Landrum, E. J., and Loendorf, D., "Application of Computer-Aided Aircraft Design in a Multidisciplinary Environment," *American Institute of Aeronautics and Astronautics* Paper No. 73-353, New York, March 1973.

[17] Davidson, J. R., *Engineering Fracture Mechanics,* Vol. 4, No. 4, Dec. 1972, pp. 777–788.

[18] Hardrath, H. F., *Journal of Testing and Evaluation*, Vol. 1, No. 1, Jan. 1973, pp. 3-12.
[19] Wood, H. A. and Trapp, W. J., *Engineering Fracture Mechanics*, Vol. 5 No. 1, Feb. 1973, pp. 119-146.
[20] Ekvall, J. C., Brussat, T. R., Liu, A. F., and Creager, M., "Preliminary Design of Aircraft Structures to Meet Structural Integrity Requirements," *American Institute of Aeronautics and Astronautics* Paper No. 73-374, New York, March 1973.
[21] "Airplane Damage Tolerance Design Requirement," Military Specification MIL-A-83444, United States Air Force, May 1974.
[22] Davis, C. S., "Inclusion of Crack Growth and Fracture Constraints in Automated Design," Ph.D. dissertation, University of California, Los Angeles, Calif., March 1976.
[23] Brussat, T. R. in *Fracture Toughness and Slow-Stable Cracking, ASTM STP 559*, American Society for Testing and Materials, 1974, pp. 298-311.
[24] Sih, G. C., Ed., *Mechanics of Fracture I—Methods of Analysis and Solution of Crack Problems*, Noordhoff, Leyden, 1973.
[25] Poe, C. C., Jr., "Stress Intensity Factor for a Cracked Sheet with Riveted and Uniformly Spaced Stringers," NASA Report TR-R-358, Langley Research Center, Hampton, Va., National Aeronautics and Space Administration, Washington, D.C., May 1971.
[26] Paris, P. C. and Sih, G. C. in *Fracture Toughness Testing and Its Applications, ASTM STP 381*, American Society for Testing and Materials, 1965, pp. 30-83.
[27] Sih, G. C., *Handbook of Stress Intensity Factors*, Vol. I, Lehigh University, Bethlehem, Pa., 1973.
[28] Tada, H., Paris, P. C., and Irwin, G. R., *The Stress Analysis of Cracks Handbook*, Del Research Corporation, Hellertown, Pa., 1973.
[29] Liu, A. F., *Engineering Fracture Mechanics*, Vol. 4, No. 1, March 1972, pp. 175-179.
[30] Wigglesworth, L. A., *Mathematika*, Vol. 4, Part I, No. 7, June 1957, pp. 76-96.
[31] Newman, J. C., *Engineering Fracture Mechanics*, Vol. 5, No. 3, Sept. 1973, pp. 667-690.
[32] Brown, W. F., Jr. and Srawley, J. E., *Plane Strain Crack Toughness Testing of High Strength Metallic Materials, ASTM STP 410*, American Society for Testing and Materials, 1967, pp. 77-79.
[33] Sanders, J. L., Jr., "Effect of a Stringer on the Stress Concentration Due to a Crack in a Thin Sheet," NASA Report TR-R-13, Langley Research Center, Langley Field, Virginia, National Aeronautics and Space Administration, Washington, D.C., 1959.
[34] Grief, R. and J. L. Sanders, *Journal of Applied Mechanics*, Vol. 32, No. 1, March 1965, pp. 59-66.
[35] Isida, M., *Engineering Fracture Mechanics*, Vol. 5, No. 3, Sept. 1973, pp. 647-665.
[36] Poe, C. C., Jr., in *Damage Tolerance in Aircraft Structures, ASTM STP 486*, American Society for Testing and Materials, 1971, pp. 79-97.
[37] Griffith, A. A., *Philosophical Transactions*, Royal Society of London, Series A, Vol. 221, No. VI, March 1921, pp. 163-198.
[38] *ASTM Bulletin*, No. 243, Jan. 1960, pp. 29-40.
[39] Irwin, G. R., "Fracture Testing of High Strength Materials Under Conditions Appropriate for Stress Analysis," Naval Research Laboratory Report No. 5486, 27 July 1960.
[40] Krafft, J. M., Sullivan, A. M., and Boyle, R. W., "Effect of Dimensions on Fast Fracture Instability of Notched Sheets," *Proceedings of the Crack Propagation Symposium*, Vol. 1, College of Aeronautics, Cranfield, England, Sept. 1961, pp. 8-26.
[41] Carman, C. M. in *Fracture Toughness Evaluation by R-Curve Methods, ASTM STP 527*, American Society for Testing and Materials, 1973, pp. 62-84.
[42] Srawley, J. E. and Brown, W. F., Jr., *Fracture Toughness Testing and Its Applications, ASTM STP 381*, American Society for Testing and Materials, 1965, pp. 133-198.
[43] Weiss, V. and Yukawa, S., *Fracture Toughness Testing and Its Applications, ASTM STP 381*, American Society for Testing and Materials, 1965, pp. 1-29.
[44] Wilhem, D. P., "Fracture Mechanics Guidelines for Aircraft Structural Applications," Technical Report AFFDL-TR-69-111, Flight Dynamics Laboratory, Wright Patterson Air Force Base, Dayton, Ohio, Feb. 1970.

[45] Iida, S. and Kobayashi, A. S., *Journal of Basic Engineering*, Vol. 91, No. 4, Dec. 1969, pp. 746–769.
[46] Sines, George, *Journal of Materials*, Vol. 4, No. 2, June 1969, pp. 377–392.
[47] Brussat, T. R. in *Damage Tolerance in Aircraft Structures, ASTM STP 486*, American Society for Testing and Materials, 1971, pp. 122–143.
[48] Forman, R. G., Kearney, V. E., and Engle, R. M., *Journal of Basic Engineering*, Vol. 89, No. 3, Sept. 1967, pp. 459–464.
[49] Hudson, C. M., "Effects of Stress Ratio on Fatigue Crack Growth in 7075-T6 and 2024-T3 Aluminum Alloy Specimens," NASA Report TN D-5390, Langley Research Center, Hampton, Virginia, National Aeronautics and Space Administration, Washington, D.C., Aug. 1969.
[50] Walker, K. in *Effects of Environment and Complex Load History on Fatigue Life, ASTM STP 462*, American Society for Testing and Materials, 1970, pp. 1–14.
[51] Wheeler, O. E., *Journal of Basic Engineering*, Vol. 94, No. 1, March 1972, pp. 181–186.
[52] Willenborg, J. D., Engle, R. M., and Wood, H. A., "A Crack Growth Retardation Model Using an Effective Stress Concept," Technical Report AFFDL-TM-FBR-71-1, Flight Dynamics Laboratory, Wright Patterson Air Force Base, Dayton, Ohio, Jan. 1971.
[53] Fiacco, A. V. and McCormick, G. P., *Nonlinear Programming: Sequential Unconstrained Minimization Techniques*, John Wiley & Sons, New York, 1968.
[54] Kavlie, D. and Moe, J., *Journal of Structural Division*, American Society of Civil Engineers, Vol. 97, No. ST1, Jan. 1971, pp. 33–62.
[55] Oren, S. S. and Luenberger, D. G., "The Self-Scaling Variable Metric Algorithm (SSVM)," *Proceedings*, 5th Hawaii International Conference on System Sciences, University of Hawaii, Honolulu, Hawaii, 11–13 Jan. 1972, pp. 130–132.
[56] Luenberger, D. G., *Introduction to Linear and Nonlinear Programming*, Addison-Wesley, Reading, Massachusetts, 1973.
[57] Lasdon, L. S., *Optimization Theory for Large Systems*, MacMillan, New York, 1970.

W. L. Server,[1] *R. A. Wullaert,*[1] *and J. W. Sheckherd*[1]

Evaluation of Current Procedures for Dynamic Fracture-Toughness Testing

REFERENCE: Server, W. L., Wullaert, R. A., and Sheckherd, J. W., "**Evaluation of Current Procedures for Dynamic Fracture-Toughness Testing,**" *Flaw Growth and Fracture, ASTM STP 631,* American Society for Testing and Materials, 1977, pp. 446-461.

ABSTRACT: Instrumented impact test requirements for impact velocity, inertial loading, time to fracture, and frequency response were developed as a part of a large testing program sponsored by the Electric Power Research Institute (EPRI). These test procedures relied heavily on current ASTM standards plus the composite experience of investigators throughout the world. This paper provides experimental verification of the EPRI developed procedures and clarifies some of the empirical relationships used in the procedures. The material investigated was a 4340 steel (R_c52) which was relatively insensitive to loading rate. Load-time information obtained simultaneously from an instrumented tup and strain-gaged specimen was analyzed for tests performed at various impact velocities. The results indicate that the EPRI developed procedures are conservative and allow reliable fracture-toughness measurements to be made.

KEY WORDS: crack propagation, evaluation, impact tests, frequency response, fractures (materials)

Instrumented impact loading is an attractive method for obtaining dynamic plane-strain fracture toughness (K_{Id}) at a stress intensification loading rate ($\dot{K}$) near 10^6 ksi·in$^{1/2}$/s (10^6 MN·m$^{-3/2}$/s). The calculations of K_{Id} and $\dot{K}$ from dynamic loading require reliable measurements of the force applied at the instant of fracture and the loading time associated with the fracture event. In the past, interpretation of the impact load-time record has led to certain ambiguities with respect to the reliability of the measurements derived from impact tests [*1-4*].[2] The relationships between impact velocity, inertial loading, time to fracture, and frequency response are now well understood, such that test procedures have been developed as a

[1]Vice president, president, and manager of Testing Services, respectively, Fracture Control Corporation, Goleta, Calif. 93017.

[2]The italic numbers in brackets refer to the list of references appended to this paper.

part of a large testing program sponsored by the Electric Power Research Institute (EPRI). These dynamic test procedures were derived from many sources including the International Institute of Welding Task Group on Dynamic Testing [2], the Metal Properties Council/Pressure Vessel Research Committee (MPC/PVRC) Task Group on instrumented precracked Charpy testing of nuclear pressure vessel materials [5], ASTM E24.03.03 Task Group on Precracked Charpy Testing of Committee E-24 on Fracture Testing of Metals [6], appropriate ASTM standards [ASTM Test for Plane-Strain Fracture Toughness of Metallic Materials (E 399-74) and ASTM Standard Method for Notched Bar Impact Testing of Metallic Materials (E 23-72)], and the composite experiences of other investigators [7].

The procedures developed for the EPRI Fracture Toughness Program [8] were designed hopefully to be more restrictive than necessary to ensure reliable and conservative measurements of dynamic fracture toughness. The purpose of this paper is to add insight into the EPRI developed dynamic testing procedures and possibly clarify certain ambiguous areas related to the procedures. The material investigated was a 4340 steel (R_c52) which was relatively insensitive to loading rate for the rates examined. Comparisons were made between the tup output signal and signals obtained from strain gages mounted on the specimens.

Material and Specimen Preparation

The material used in this investigation was an oil-quenched 4340 steel. Standard Charpy V-notch, 1.00-in. (2.54-cm) square Charpy-type, and 2.00-in. (5.08-cm) square Charpy-type samples were machined in the LT orientation from a conventional 3-in. (7.6-cm) thick 4340 plate in the annealed form. The samples were then heat treated and oil quenched; the hardness after quenching was an average value of R_c52. (There was a slight variation in R_c for different sample types as will be discussed later.)

All of the samples were fatigued precracked at a maximum stress intensity K_f(max) of 15 to 16 ksi·in$^{1/2}$ (15 to 16 MN·m$^{-3/2}$). The 4340 samples were precracked to a crack length (a) to width (W) ratio greater than 0.327, which corresponds to at least 0.050 in. (0.127 cm) of crack growth.

The 4340 samples which were strain gaged had semiconductor gages mounted on the top tensile surface of the specimen midway between the center notch and the end anvil support on one side; this gage location is referred to as the ¼-point location. A full set of four gages was used to complete the necessary wheatstone bridge with the inactive gages mounted perpendicular to the active tensile gages. The inactive gages therefore only see a small Poisson's ratio effect which is additive. All of the gaged samples were calibrated in a static manner using a conventional tensile machine with the same anvils to be used during the impact tests (except

for the precracked Charpy tests). The specimen gages were calibrated as load cells with direct readings in analog pounds rather than voltage. The samples were loaded to a stress-intensity level of 20 ksi·in$^{1/2}$(22.0 MN·m$^{-3/2}$ during calibration. This calibration was then linearly extrapolated to the load at fracture.

Testing Equipment

All of the precracked Charpy tests were performed using a Satec 240 ft·lbf (1068 J) (model SI-1C) pendulum impact machine with Dynatup (model 500) instrumentation. A Nicolet (model 1090/93) digital oscilloscope was used as an auxiliary recording device. The larger three-point-bend samples were tested using a drop tower with the same instrumentation as the pendulum impact machine. The weight of the drop tower head was maintained at 270 lbf (366 N). The dimensions for the anvils and tups met current ASTM requirements except that free rollers were not used.

Discussion of EPRI Dynamic Test Procedures

The EPRI impact testing procedures relied heavily on existing ASTM Methods E 399-74 and E 23-72 as they pertained to instrumented impact testing. The measurement criteria related to sample geometry and dimensions, crack length and shape, fatigue precracking, and testing jig requirements were maintained as much as possible.

The load signal measured from an instrumented tup during an impact test oscillates about the actual load required to deform the sample. Therefore, the signal analysis procedure employed should minimize the deviation of the apparent load from the actual specimen deformation load. A simplistic view of the impact event allows three major areas for test specification to be identified: inertial loading, limited frequency response, and electronic curve fitting.

The impact of an unsupported specimen will create inertial oscillations in the contact load between tup and specimen, and a time approximately equal to 2τ is required for the load to be dissipated. τ is related to the period of the apparent specimen oscillations and can be predicted for a span to width ratio of 4 by [9]

$$\tau = 3.36 \frac{W}{C_0} (EBC_s)^{1/2} \tag{1}$$

where

W = beam width
B = beam thickness

C_s = specimen compliance
E = Young's modulus, and
C_0 = speed of sound in the specimen.

The value of 3.36 in Eq 1 is an empirical fit to data generated using aluminum, beryllium, and steel samples with varying spans and a/W ratios. Theoretically, for a free-standing wave it can be shown that Eq 1 is valid when the factor is $4/n$, where n is the mode of oscillation. Since the oscillation pattern during impact appears to be a combination of mode 1 and mode 3 with mode 1 dominating, the empirical factor of 3.36 seems quite reasonable.

The appearance of the tup signal during the time 2τ is nearly the same as that for an unsupported specimen. When any time τ is less than 2τ, it is not possible to use the tup signal to measure the specimen load (and therefore determine fracture toughness) due to inertial effects. A tentative specification for reliable load or time evaluation is

$$t \geq 3\tau \tag{2}$$

where t designates the time to fracture in an elastic fracture (t corresponds to the shortest time to be measured; therefore, in a postgeneral yield fracture, t would represent the time to general yield). The constant 3 in Eq 2 may be as low as 2.3 to 2.5 without adversely affecting the test results if the curve-fitting technique described next is followed [*10*], but conservatively a value of 3 was chosen.

The potential problem of limited frequency response of the transducer amplifier is avoided by specifying

$$t \geq 1.1\ T_R \tag{3}$$

where T_R is defined as the 0.915 *dB* response time of the instrumentation, that is

$$T_R = \frac{0.35}{f_{0.915dB}} \tag{4}$$

where $f_{0.915dB}$ is the frequency at 0.915 *dB* (10 percent) attenuation. The specification in Eq 3 results in approximately 4 percent amplitude attenuation of a sine wave signal at a rise time equal to 3τ if $T_R = 2\tau$. This upper limit attenuation level does not appear to effect the maximum load response for instrumented impact tests [*9,10*]. It is important to note that the electronic attenuation must be indicative of an RC circuit.

The curve fitting of the oscillations is achieved by specifying a minimum T_R such that the amplitude of the oscillations is reduced to make a mini-

mal disparity between tup contact load and the effective specimen midspan load. For the bend test, it has been empirically found [*9*] that

$$T_R \geq 2\tau \tag{5}$$

is adequate for the curve fitting. However, more recent work on A533B-1 steel [*10*] has shown that the constant 2 may be reduced to 1.4 (which corresponds to an equivalent 0.445 *dB* (5 percent) attenuation) without affecting the results. Another alternative to Eq 5 is to curve fit lower T_R data by computer techniques. Also, it has been shown that filtering below a level of 1.4τ when the requirement of Eq 2 is met causes less than a 5 percent increase in the load measured [*10*].

The most concise manner to state these requirements related to inertial effects, limited frequency response, and curve fitting is

$$t \geq 3\tau \tag{2}$$

$$2\tau \leq T_R \leq 0.9t \tag{6}$$

Equation 2 satisfies the inertial effects criterion, and Eq 6 requires that the signal is not over filtered (see Eq 3), but the filtering is sufficient to electronically curve fit the signal oscillations (see Eq 5). Note that Eq 6 can be modified using 1.4τ rather than 2τ.

The requirements for obtaining acceptable load-time records (in particular, Eq 2) result in the need to control the impact velocity (V_0). In controlling the impact velocity, a corresponding control of the total available energy (E_0) is inherent. The reduction in tup velocity during the impact loading of the specimen should, therefore, be minimized. A conservative requirement is

$$E_0 \geq 3W_M \tag{7}$$

where W_M is the energy dissipated to maximum load. This requirement ensures that the tup velocity is not reduced by more than 20 percent during the initiation fracture event. A total fracture energy criterion is important if total energy values are desired. It is then important that the sample be completely fractured, in addition to the requirement of Eq 7, that is

$$E_0 > \Delta E_0 \tag{8}$$

where ΔE_0 is the energy consumed in completely breaking the sample.

Results

The results from the 4340 static fracture-toughness (K_{Ic}) tests are listed in Table 1. The maximum load (P_M) values obtained from the tensile machine load cell were used to calculate fracture toughness since the clip gage response showed little or no nonlinearity; the Z factor corresponds to the geometry multiplier used to calculate K_{Ic} in English units, that is, $K_{Ic} = P_M \times Z$. The three static precracked Charpy values are quite consistent with a mean value of 40.3 ksi·in$^{1/2}$ (44.3 MN·m$^{-3/2}$). The 1-in. (2.54-cm) scaled Charpy test results exhibit more scatter and a higher mean value of 45.6 ksi·in$^{1/2}$ (50.1 MN·m$^{-3/2}$); the fast tensile machine result (sample B6) was used in the average since it is consistent with the two slower rate values. The 2-in. Charpy-type samples gave an average toughness of 46.1 ksi·in$^{1/2}$ (50.7 MN·m$^{-3/2}$) with slightly more data scatter. To check this data spread between different sample sizes, hardness tests were performed corresponding to an area below the fatigue precrack using typical samples of each size. These results are also listed in Table 1. There is a decrease in R_c from 54 to 50 with increasing thickness as might be expected from the individual heat treatment for each sample. This decrease in R_c results in a decrease in ultimate strength [*11*] and the corresponding yield strength ($\sim$ 20 ksi less than ultimate strength). This decrease can correspond to the small increase in toughness seen for these different thickness samples [*12*]. The static scatter bands for the slow-bend precracked Charpy test and the total data spread from all tests will be used for comparison with the dynamic data. All of the toughness values for this material are low enough that even the small precracked Charpy tests are valid by ASTM Method E 399-74.

The static 1 and 2-in. Charpy-type samples were also gaged at the ¼ point and calibrated as discussed earlier, and the linear calibration was extrapolated to the load at facture. Results from these gages are also shown in Table 1. The comparison of the gage output to the tensile machine load is in most cases consistent.

Tables 2 and 3 list the dynamic precracked Charpy and 1-in. (2.54-cm) Charpy-type sample results over a range of impact velocities. No 2-in. (5.08-cm) samples were tested dynamically. Some of the dynamic bend samples were gaged at the ¼-point location, and some of the tests were performed at conditions violating Eqs 2 and 5. Shown in Fig. 1 is a typical oscillographic test result for the precracked Charpy tests, and Fig. 2 shows test records for the dynamic 1-in. (2.54-cm) Charpy-type tests. The dynamic fracture-toughness values were calculated in the same manner as the static, using maximum load and the geometry factor Z. The toughness results from Tables 2 and 3 are plotted in Figs. 3 through 6. The acceptable results for the tup signal (following the EPRI procedures)

TABLE 1—*Slow bend data for 4340 steel.*

Sample No.	R_c[a]	B, in.	W, in.	a/W	Z	P_m, lb	K_{IC}, ksi·in.$^{1/2}$	$\dot{K}$, ksi·in$^{1/2}$/s
1	54.0	0.394	0.394	0.446	36.4	1110	40.4	3.1
11	54.0	0.394	0.394	0.470	39.0	1065	41.5	3.4
30	54.0	0.394	0.394	0.330	26.5	1475	39.1	3.6
B2	53.8	1.000	1.000	0.383	7.54	5750(5500)[b]	43.3(41.5)[b]	2.3
B4	53.8	1.000	1.000	0.408	8.08	5880(5070)[b]	47.5(41.0)[b]	2.1
B6	53.8	1.000	1.000	0.377	7.43	6200(5750)[b]	46.1(42.7)[b]	102[c]
A4	51.9	2.000	2.000	0.385	2.68	16 830(16 980)[b]	45.1(45.5)[b]	1.2
A7	51.9	2.000	2.000	0.406	2.83	17 280(17 460)[b]	48.9(49.4)[b]	1.2
A9	51.9	2.000	2.000	0.411	2.88	15 360	44.2	1.3

[a]Average of nine interior measurements at and below the fatigue precrack as measured on a typical sample of each type.
[b]Load and toughness analog values from quarter-point gages mounted on the sample.
[c]Obtained by running the crosshead of the tensile machine at 10 in/min—data recorded on oscilloscope.

TABLE 2—*Dynamic precracked charpy toughness results for 4340 steel* (R_c54).

Sample No.	V_0, ft/s	a/W	Z	t, μs	$P_{m\text{-tup}}$, lb		$P_{m\text{-gage}}$, lb, T_R = 10 μs	$K_{Id\ tup}$, ksi·in.$^{1/2}$		$K_{Id\text{-gage}}$, ksi·in.$^{1/2}$	$\dot{K}$, ksi·in$^{1/2}$/s × 10^5		
					T_R[a] = 62.5 μs	T_R[a] = 10 μs		T_R = 62.5 μs	T_R = 10 μs		Tup, T_R = 62.5 μs	Tup, T_R = 10 μs	Specimen Gage
3	2.0	0.515	45.1	355	885	885	...	39.9	39.9	...	1.1	1.1	...
5	2.0	0.466	37.5	350	1160	1200	1260	43.5	45.0	47.3	1.2	1.3	1.4
9	4.5	0.400	32.0	180	1310	...	1325	41.9	...	42.4	2.3	...	2.4
14	4.5	0.368	29.2	220	1580	...	...	46.1	...	...	2.1	...	...
20	4.5	0.378	30.1	175	1340	1475	...	40.3	44.4	...	2.3	2.5	...
23	4.5	0.407	32.5	120	1120	...	...	36.4	...	...	3.0	...	...
29	4.5	0.447	36.4	160	1195	...	...	43.5	...	...	2.7	...	...
33	4.5	0.324	26.2	180	1480	...	...	38.8	...	...	2.2	...	...
8	6.0	0.327	26.3	135	1630	1900	...	42.9	50.0	...	3.2	3.7	...
15	6.0	0.370	29.3	130	1450[b]	1525	1500[b]	42.5	44.7	44.0	3.3	3.4	3.4
10	11.0	0.401	32.0	60	1185	1740	...	37.9	55.7	...	6.3	9.3	...
17	11.0	0.391	31.1	65	...	1995	1350[c]	...	62.0	42.0		9.5	5.3
18	17.0	0.350	28.0	50	1890	2615	1405[c]	52.9	73.2	39.3	10.6	14.6	7.9
21	17.0	0.373	29.7	65	1765	2600	...	52.3	77.1	...	8.0	11.9	...

[a]Signal attenuated 0.915 dB at response time T_R.
[b]The last 7% of the trace had to be extrapolated to find P_m.
[c]The maximum load had a strange topped off appearance.

TABLE 3—*Dynamic 1-in. Charpy-type toughness results for 4340 steel* (R_c*53.8*).

Sample No.	V_0, ft/s	a/W	Z	t, μs	$P_{m\text{-tup}}$, lb [b]		$P_{m\text{-gage}}$, lb, T_R [a] = 10 μs	$K_{Id\text{-tup}}$, ksi·in$^{1/2}$		$K_{Id\text{-gage}}$, ksi·in$^{1/2}$	$\dot{K}$, ksi·in$^{1/2}$/s × 10^5		
					T_R [a] = 185 μs	T_R [a] = 10 μs		T_R = 185 μs	T_R = 10 μs		Tup, T_R = 185 μs	Tup, T_R = 10 μs	Specimen Gage
B7	2.2	0.406	8.04	620	...	6780	6460	...	54.5	51.9	...	0.88	0.84
B9	2.2	0.377	7.43	500	...	6020	5000	...	44.7	37.2	...	0.89	0.74
B13	2.2	0.389	7.65	600	7000	...	6000	53.6	...	45.9	0.89	...	0.77
B1	4.3	0.331	6.58	290	...	7230	6835	...	47.6	45.0	...	1.6	1.6
B10	4.3	0.371	7.29	290	6760	7410	5750	49.3	54.0	41.9	1.7	1.9	1.4

[a] Signal attenuated 0.915 *dB* at response time T_R.
[b] Original tup data was suspect to calibration errors and later corrected by 10 percent as listed here.

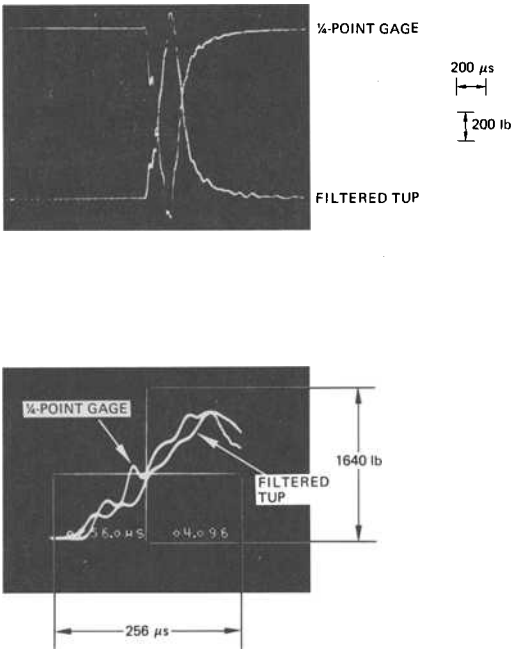

FIG. 1—*Acceptable tup signal and ¼-point gage signal for 4340 sample 9 tested at 4.5 ft/s.*

and the specimen ¼-point gage results are plotted in Figs. 3 and 4, while the unacceptable tup values which did not meet the acceptance criteria are shown in Figs. 5 and 6.

It is obvious from Figs. 3 and 4 that the ¼-point gage and acceptable tup data are in good agreement with the static trend bands, but there is more scatter in the dynamic case, and the data are skewed toward higher values. These observations are consistent with results on 4340 ($\backsim R_c 52$) obtained by Burnett [*12*]. Note that the highest velocity precracked Charpy tests exhibited a strange topped-off appearance for the ¼-point gage output (as noted in Table 2), although the dynamic toughness results were consistent with the lower velocity tests. From Figs. 1 and 2, it is obvious that the ¼-point gage response exhibits oscillations similar to those seen in the tup signal, which are indicative of the specimen period (Eq 1). It also should be stated that the initial inertial oscillation for the specimen ¼-point location is a compressive (negative) signal which relates to the first initial elastic stress wave sensed at the ¼-point location.

The trends of the data in Figs. 5 and 6 show that at the high-impact velocities (low t and high $\dot{K}$) where $t < 3\tau$, the data start to deviate markedly from the trend band. Only the precracked Charpy data violated the

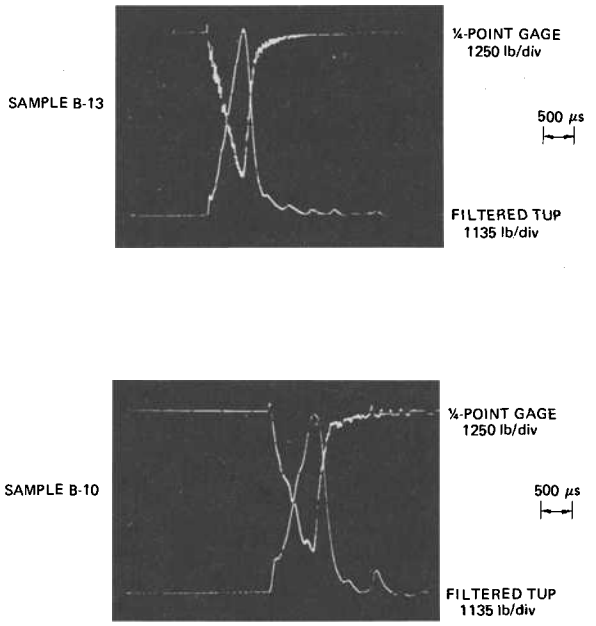

FIG. 2—*Comparison of tup signals and ¼-point gage signals for 1-in. 4340 Charpy-type samples B-13 and B-10.* (V_0 = *2.2 ft/s and 4.3 ft/s respectively*).

$t < 3\tau$ criterion. This deviation from the trend band does not occur until $t < 2\tau$ for the precracked Charpy data due to the gap in data. The extremely high-toughness values for raw signal data (T_R = 10 μs, therefore $T_R < 2\tau$) are due to inertial effects (closed stars in Figs. 5 and 6). When these high inertia affected signals are filtered (closed diamonds), the signals tend to drop closer to the expected values. It is interesting to note in Figs. 5 and 6 that for fracture times greater than 3τ (open stars and open diamonds), the effect of filtering is small, and the data are as consistent with the trend for acceptable (static) data as the acceptable filtered tup data shown in Figs. 3 and 4.

Conclusions and Recommendations

The dynamic fracture toughness results for the 4340 tests performed in accordance with the EPRI procedures were in agreement with static results for the same material. There was, however, an increase in data scatter for the dynamic tests as compared to the static.

The comparison of the tup and the specimen ¼-point gage signals was consistent for $t \geq 3\tau$ for both precracked Charpy and 1-in. (2.54-cm) thick

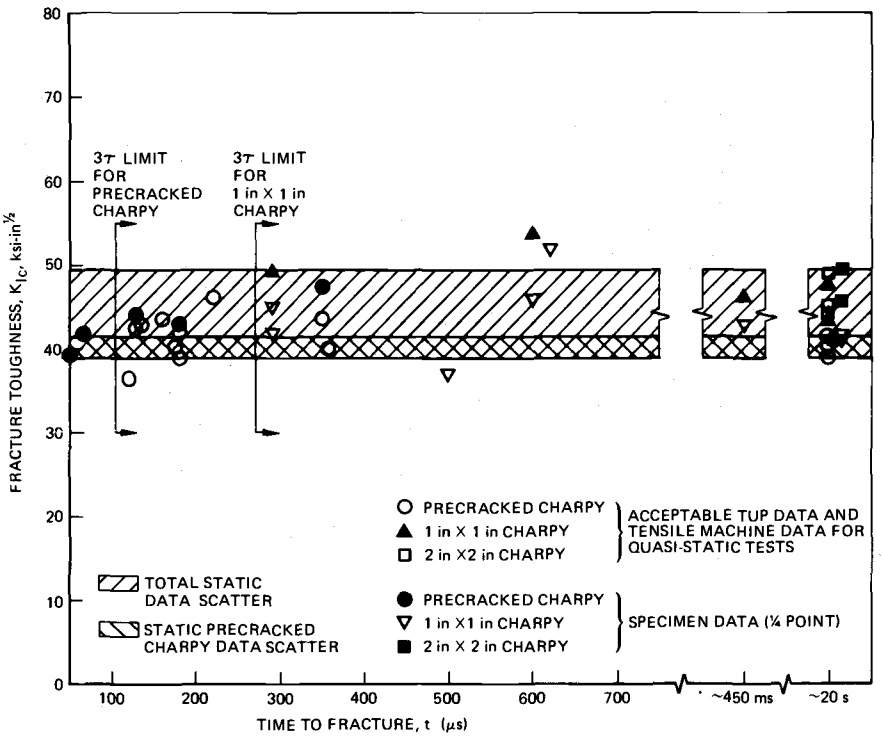

FIG. 3—*Acceptable toughness results for 4340 steel as a function of time to fracture.*

samples. For times less than 3τ, the ¼-point gages produced toughness results consistent with the static values. However, it is possible that limitations relating to some multiple of τ may also be necessary for ¼-point specimen gages.

The comparison between the properly filtered tup signal and a much less filtered tup signal showed little or no difference in toughness results with $t \geq 3\tau$. However, when $t < 3\tau$, it is necessary to curve fit the high-magnitude oscillatory nature of the load-time trace. Thus, if t is always kept greater than 3τ, the only other criterion which should be satisfied is that of limited frequency response (Eq 3).

Future impact procedures may, therefore, specify only that $t \geq 3\tau$ and that $t \geq 1.1T_R$. However, for most cases in which the 3τ criterion cannot be satisfied (but t must still be greater than $\sim 2.3\tau$), the electronic filtering criterion also should be specified. Alternately, it is possible to gage each individual sample, but it is also obvious that gaging every sample is expensive and time consuming. If tests are conducted properly using the tup output signal, then the only need for gaging samples is to check the tup

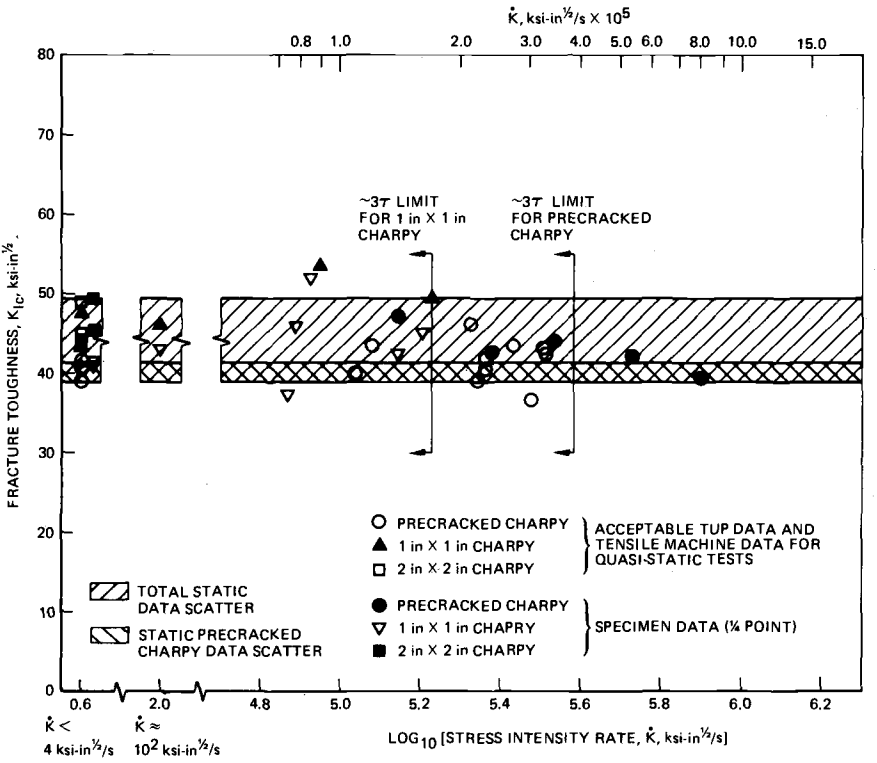

FIG. 4—*Acceptable toughness results for 4340 steel as a function of stress-intensity rate.*

signal in crucial experiments (or when violating the velocity requirements is unavoidable). The most obvious case where the 3τ criterion may not be obtainable is that for a light head impact machine in which the only way to have enough total available energy to meet the requirements of Eq 7 (and Eq 8, if desired) is by increasing the impact velocity.

The effects of violating the limited frequency response criterion (Eq 3) were not investigated in the time range greater than 3τ; the known response would have resulted in a reduced value of maximum load (and hence toughness). It is always important to ensure that the frequency response of an electronic package is adequate to measure a particular transient pulse, without attenuating the pulse signal by an unacceptable amount.

As mentioned previously, the high-rate tensile machine result ($t \sim 450$ ms; $K \sim 10^2$ ksi·in$^{1/2}$/s [$\sim 10^2$ MN·m$^{-3/2}$/s]) for the 1-in. (2.54-cm) scaled Charpy sample was quite consistent with the standard quasistatic values ($t \sim 20$ ms, $K \sim 2$ ksi·in$^{1/2}$/s [~ 2 MN·m$^{-3/2}$/s]). The intermediate $\dot{K}$ range of $10^2 - 10^5$ ksi·in$^{1/2}$/s ($10^2 - 10^5$ MN·m$^{-3/2}$/s) was not studied, but these

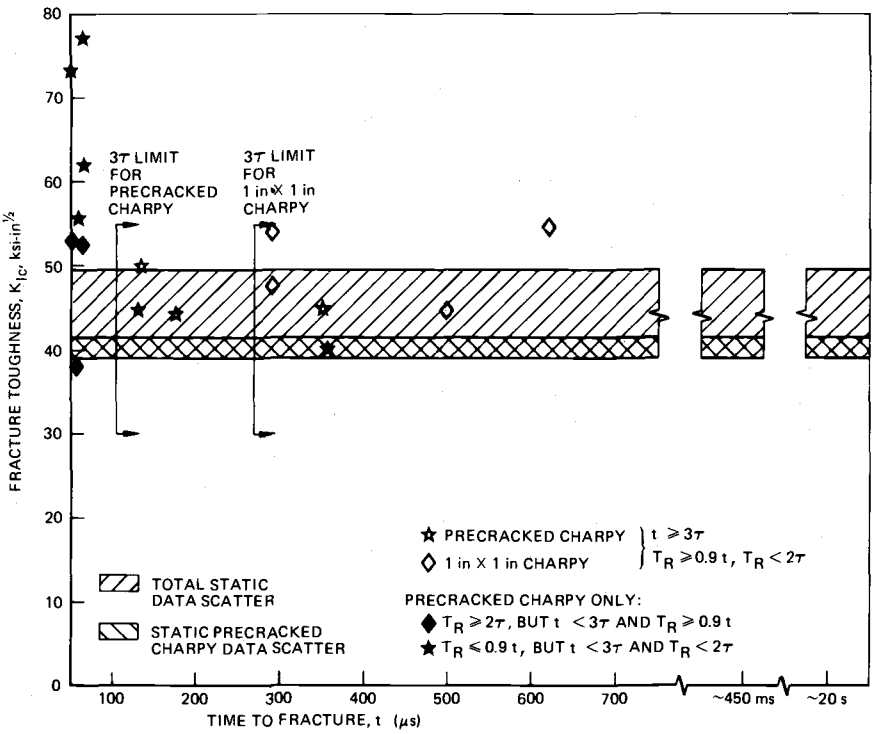

FIG. 5—*Unacceptable toughness results for 4340 steel as a function of time to fracture.*

loading rates can be achieved by using a closed-loop hydraulic machine. The procedures developed for the impact tests performed at approximately 10^5 ksi·in$^{1/2}$/s (10^5 MN·m$^{-3/2}$/s) may well apply at the high end of the range covered by closed-loop hydraulic machines. Therefore, the procedures developed for impact testing should be incorporated into this other dynamic test technique, with specific attention given to the problem of limited frequency response.

Since a prescribed set of procedures exists for obtaining the dynamic load response obtained from an instrumented tup, and the acceptable dynamic fracture-toughness results agree with the static data for a loading rate insensitive material, it seems appropriate that somebody should take these procedures and incorporate them into a standard test method. This method would then ensure consistent results from various laboratories throughout the United States and the world.

Acknowledgments

This study was performed under contract from the Electric Power Re-

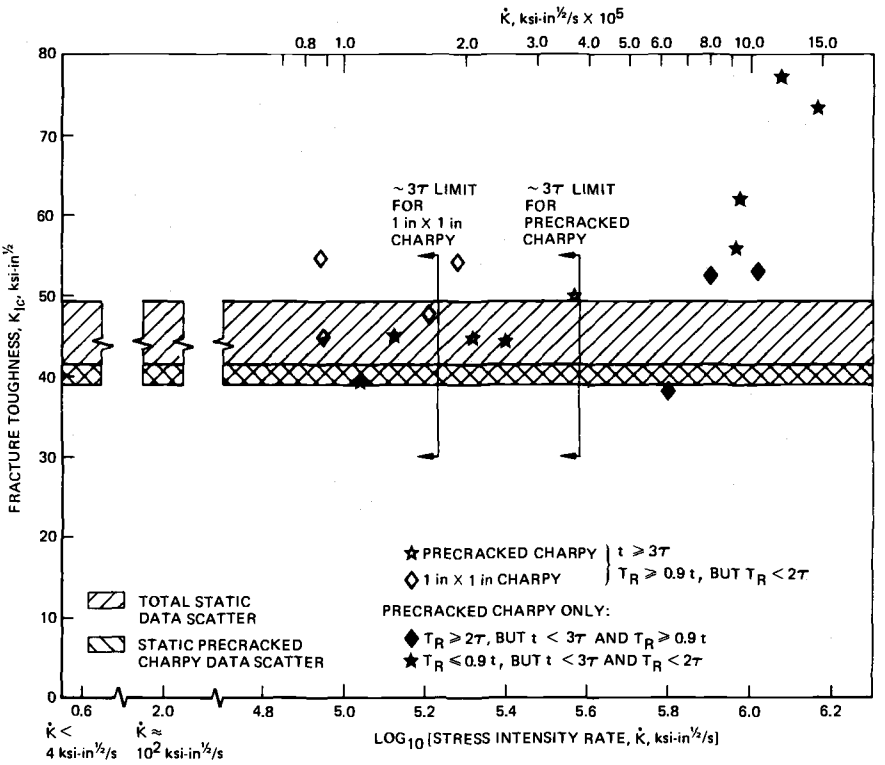

FIG. 6—*Unacceptable toughness results for 4340 steel as a function of stress-intensity rate.*

search Institute (RP 232-1). The authors wish to express gratitude to Dr. T. R. Wilshaw and K. Imhoff for their helpful suggestions during this work.

References

[1] Buys, E. C. J. and Cowan, A., "Interpretation of the Instrumented Impact Test," Document X-459-68, International Institute of Welding, July 1968.

[2] *Impact Testing of Metals, ASTM STP 466,* American Society for Testing and Materials, 1970.

[3] Nash, G. E., "An Analysis of the Forces and Bending Moments Generated During the NRL Dynamic Tear Test," Technical Report 6864, Naval Research Laboratory, Jan. 1969.

[4] Turner, C. E., Kennish, P., Culver, L. E., and Radon, J. C., "A Study of the Mechanics of Notched-Bar Impact Tests," Mechanical Engineering Department, Imperial College, London, England, June 1970.

[5] Metal Properties Council/Pressure Vessel Research Committee, Working Group on Instrumented Precracked Charpy Test, Chairman C. Buchalet, Task Group on Fracture Toughness Properties for Nuclear Components.

[6] ASTM Task Group E24.03.03 on Precracked Charpy Standardization of Committee E-24 on Fracture Testing of Metals, Chairman C. E. Hartbower.
[7] *Instrumented Impact Testing, ASTM STP 563,* American Society for Testing and Materials, 1974.
[8] Ireland, D. R., Server, W. L., and Wullaert, R. A., "Procedures for Testing and Data Analysis," Technical Report TR 75-43, Effects Technology, Inc., Oct. 1975.
[9] Ireland, D. R., "Comments on EPRI Instrumented Impact Procedures," Technical Report TR 75-37, EPRI Fracture Toughness Program Information Meeting, May 1975, Effects Technology, Inc.
[10] Server, W. L., Wullaert, R. A., and Sheckherd, J. W., "Verification of the EPRI Dynamic Fracture Toughness Testing Procedures," Technical Report TR 75-42, Effects Technology, Inc., Oct. 1975.
[11] *Metals Handbook,* 1948 ed., The American Society for Metals, Cleveland, Ohio, 1952.
[12] Burnett, A., paper presented at the ASM-IIWG Technical Session on Instrumented Impact Testing and Analysis of Materials, Detroit, Mich., Oct. 1974.

B. Marandet[1] *and G. Sanz*[1]

Experimental Verification of the J_{Ic} and Equivalent Energy Methods for the Evaluation of the Fracture Toughness of Steels

REFERENCE: Marandet, B. and Sanz, G., "**Experimental Verification of the J_{Ic} and Equivalent Energy Methods for the Evaluation of the Fracture Toughness of Steels,**" *Flaw Growth and Fracture, ASTM STP 631,* American Society for Testing and Materials, 1977, pp. 462–476.

ABSTRACT: The critical value J_{Ic} and the apparent fracture toughness K_{Bd} are measured with a single small specimen (compact tension or three-point-bend bar) loaded in the elastic-plastic range. Initiation is detected during loading by an electrical potential method.

For the steels studied here (2.25Cr-1Mo, electroslag weld, manganese cast steel), the K_{Ic} values deduced from J_{Ic} are in agreement with the K_{Ic} values directly measured with thick specimens in the transition-temperature range. Furthermore, the equivalent energy procedure gives the same results as those obtained by the J-integral method.

KEY WORDS: crack propagation, fracture properties, toughness, crack initiation, steels

The application of linear-elastic fracture mechanics to high-toughness, low-yield strength materials is often impractical. Large-size specimens must be used generally for the experimental determination of the plane-strain fracture toughness K_{Ic}. For example, Wessel [*1*][2] demonstrated that K_{Ic} values of A533 Grade B, Class 1 steel were measurable only up to about + 10°C, even when using 300-mm-thick specimens. From a practical point of view, it is not feasible or economical to obtain valid K_{Ic} in the transition range or at elevated temperature. Some recent investigations have, therefore, attempted to evaluate K_{Ic} from tests on smaller specimens. Two fracture criteria for elastic-plastic behavior of metals recently have

[1]Research engineer and head of Steels Properties Group, respectively, Institut de Recherches de la Sidérurgie Francaise, Saint Germain en Laye, France.

[2]The italic numbers in brackets refer to the list of references appended to this paper.

been proposed—the J-integral fracture criterion and the equivalent energy concept.

The J_{Ic} fracture criterion as introduced and developed by Begley and Landes [*2,3*] is based largely on the path-independent J-integral proposed by Rice [*4,5*]. This criterion attempts to characterize the elastic-plastic field. Begley and Landes have checked that the initial value J_{Ic} measured with a small specimen at the maximum load [*2*] or, more accurately, at the onset of slow-crack growth [*6*] is in good agreement with the fracture toughness K_{Ic} measured with a large specimen.

The equivalent energy method devised by Witt [*7–9*] gives a lower bound fracture toughness K_{Bd}. With increasing specimen thickness, K_B values approach to K_{Ic} [*10*]. It has been demonstrated analytically [*11,12*] that for deeply cracked bend bars or compact specimens, the J_{Ic} criterion and the equivalent energy procedure may give identical results.

The purpose of this investigation was to determine experimentally the critical value J_{Ic} with a single specimen (compact tension or bend bar) and compare the elastic-plastic fracture toughness K_{IJ} with the plane-strain fracture toughness K_{Ic} measured in accordance with ASTM Test for Plane-Strain Fracture Toughness of Metallic Materials (E 399-74). The onset of the stable crack growth was detected during loading of the specimen by an electrical potential method. The critical value J_{Ic} and the lower bound K_{Bd} were calculated from the energy supplied to the specimen until stable cracking occurred. It was then possible to compare the values K_{IJ} with the values K_{Bd} calculated at initiation.

Materials and Experimental Methods

Materials

The materials investigated include a 10CD9-10 steel (2.25-Cr-1Mo), 10CD9-10 electroslag weld, and manganese-molybdenum cast steel (15MDV04-03M).

The heat treatments and chemical compositions of these steels are given in Table 1. The mechanical properties measured at room temperature are given in Table 2.

Elastic-plastic fracture toughness tests were performed with 15-mm-thick or 25-mm-thick compact tension specimens, and with three-point-bend bars (cross section 10 by 20 mm or 20 by 20 mm). They were taken from the center of either broken halves of 100-mm-thick compact tension specimens (steel-Reference C) or blocks of the same dimensions and properties (steels-Reference A and B).

The specimens were fatigue precracked according to the recommendations of the ASTM E 399-74 standard, except for the crack length which was such that $0.6 < a/W < 0.7$.

TABLE 1—*Chemical compositions and heat treatments of steels.*

Material	Heat Treatment	Chemical Composition, weight percent							
		C	Mn	Si	P	S	Cr	Mo	Ni
10CD9-10 Reference A	940°C 1 h/water quenched + 700°C 1 h/air	0.110	0.455	0.275	0.014	0.025	2.10	1.05	0.115
10CD9-10 Reference B	925°C 5 h/air-electroslag welding + 925°C 5 h/water quenched + 640°C 12 h/air	0.124	0.50	0.122	0.013	0.010	2.72	1.06	0.105
15MDV04-03 (cast steel) Reference C	960°C 4 h/air + 650°C 3 h/air	0.140	1.50	0.50	< 0.02 < 0.02		...	0.3	...

TABLE 2—*Mechanical properties of steels at room temperature.*

Material	σ_Y		Ultimate Tensile Strength		Elongation, %	Reduction in Area, %
	N/mm^2	(ksi)	N/mm^2	(ksi)		
A	510	74	641	93	24.0	76.8
B	584	84.7	703	102	20.0	78.0
C	377	54.6	523	75.8	24.1	43.7

Measurement of J_{Ic} with a Single Specimen by the Electrical Potential Method

Principle [13]—We devised an electrical device making it possible to detect, with high sensitivity, the initiation of stable crack growth during loading of a precracked specimen (Fig. 1).

A high-intensity alternating current (I adjustable from 0 to 50 A; F = 50 Hz) passes through two identical specimen series connected in a Thomson bridge. One of the specimens is active and the other is used as a reference. In each of them, the a-c potential drop, between two points on either side of the mechanical notch, is recorded. These voltages are in an opposite phase; they are amplified, filtered, and detected separately. At the beginning of the test, the two specimens being at rest, the bridge is balanced by means of the potentiometer summation device at the two circuit outputs. As soon as a mechanical action is applied to the specimen being tested, the bridge becomes unbalanced. The unbalanced voltage is amplified and filtered; it is applied to a conventional analog recorder.

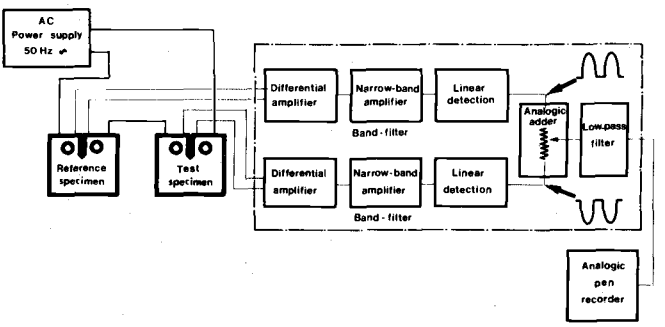

FIG. 1—*Diagram of the circuit used to detect the onset of stable-crack growth.*

The differential a-c system is much less sensitive to drift effects, thermocouple effects, and temperature changes than the generally used d-c systems. We believe that the high accuracy of this method is connected to an appreciable skin effect. At the frequency used, 60 percent of the intensity is concentrated next to the specimen surface (2.2 mm depth).

Apparatus Used—The test specimen must be carefully electrically insulated from the frame of the tension machine during mechanical loading.

A general view of the system used for three-point-bend tests is shown in Fig. 2. The current leads are screwed to the bar on the edges of the specimen and the potential connectors are spot welded on both sides of the notch. The instrumented punch and rollers are insulated by means of a plastic sheet. The displacement is measured by an inductive transducer (linear variable differential transducer).

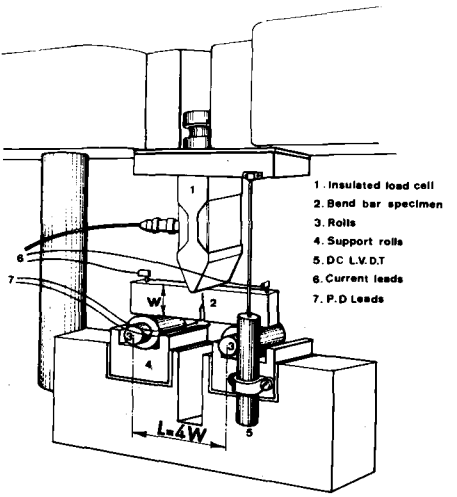

FIG. 2—*General view of the apparatus used for three-point bending specimens.*

The compact tension specimen is attached on the fastening line of the tension machine with insulated grips (Fig. 3). The displacement is measured by the parallelogram developed at Institut de Recherches de la Sidérurgie Francaise (IRSID) for hot tension tests [*14*]. The displacement of the sides of the specimen in the load line is transmitted to the two arms of the parallelogram via two steel or silica rods. The leverage is such that the displacement is multiplied by 2.5. This is measured between two sliding parts by means of an inductive transducer. A spring maintains the pressure between the rods and the sides of the specimen. Preliminary tests confirmed that the displacement measurement by the parallelogram arrangement is identical to that made by the clip-on gage placed on the specimen between two small machined knives.

The advantage of the parallelogram appears particularly in low-temperature tests. The compact specimen is immersed in a tank filled with freon. This organic liquid does not conduct electricity. The freon bath is cooled by liquid nitrogen circulating in a coil. Thus, J_{Ic} can be measured at temperatures between − 40°C and − 196°C. For obtaining a temperature between + 20°C and − 40°C, the specimen is simply left in the cold atmosphere created by the nitrogen circulating in the coil.

Detection of Initiation—The applied load and the unbalance voltage

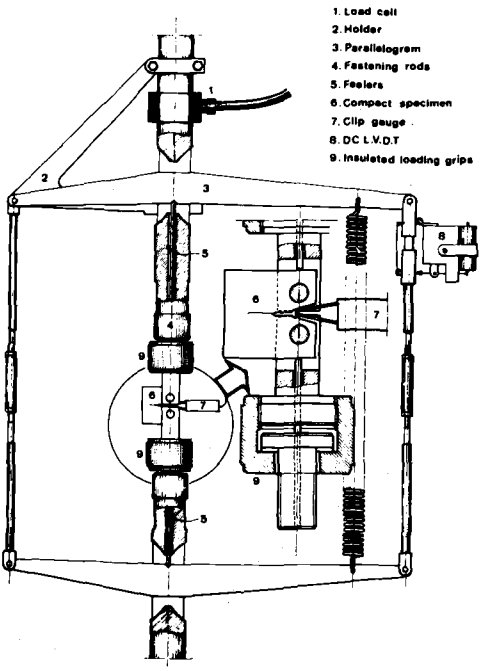

FIG. 3—*General view of the apparatus used for compact specimens.*

ΔV of the bridge versus the load displacement are recorded on the same graph. An example of a typical record is presented in Fig. 4. The experimental ΔV-displacement curve can be divided into three zones.

1. At the beginning of loading (Zone 1), the apparent impedance of the specimen increases. We believe that this variation is related to the fact that both sides of the fatigue crack are actually in partial contact. When a small load is applied to the specimen, the sides of the fatigue crack separate, resulting in an increase of the apparent impedance. In cases where only a mechanical notch is present, this first part of the recording disappears.

2. During the loading in the pseudoelastic range (Zone 2), the apparent impedance decreases. The variation is linear with the applied load, and the signal is reversible on unloading. From results with various materials of different magnetic permeability factors μ, we believe that this variation is due to an inverse magnetostriction phenomenon.

3. Finally, at the onset of plastic yielding, the curve deviates from linearity; it goes through a minimum, and, afterwards, the apparent impedance increases until fracture (Zone 3). We checked that initiation of stable crack growth occurs at the minimum of the ΔV-displacement curve.

In the lower temperature range, the fracture mechanism becomes fully brittle. Then, fracture occurs suddenly—either after a small-stable crack extension (Fig. 4*b*) or before the minimum (Fig. 4*c*). In some circumstances (transition region), the fracture mechanism is mixed: the crack propagates suddenly step by step during loading. At each step, the load drops and the output voltage increases simultaneously; the crack propagates slowly between two "pops."

Figure 5 shows that the output voltage ΔV_p measured beyond the minimum is proportional to the relative increase $\Delta a/a$ of the crack length. We see that the calibration curve does not pass through the origin of the diagram. For $\Delta V_p = 0$ (minimum), the relative crack growth measured on the broken halves specimens, corresponds approximately to the stretched zone width.

Calculation of J_{Ic}—The critical value J_{Ic} is calculated by the approximation formula proposed by Rice et al [*15*] for deep-cracked bend specimens

$$J_{Ic} = \frac{2U^*}{B(W - a)}$$

where U^* is proportional to the area under the load versus displacement curve up to the initiation point, B is specimen thickness, and $(W - a)$ is the length of the uncracked ligament.

Note that in the case of the three-point bend bar, the energy U_e supplied to the unnotched specimen is appreciable and has to be eliminated. Pelissier-Tanon et al [*16*] showed clearly that the correction cannot be neglect-

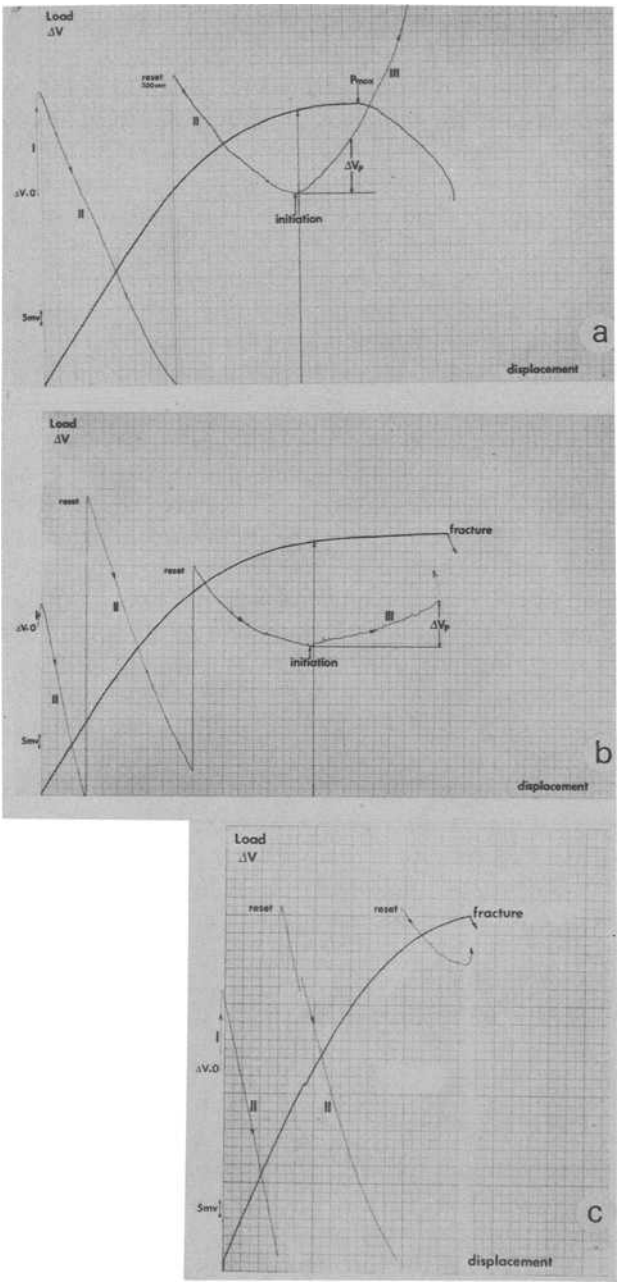

FIG. 4—*Typical load and output voltage versus displacement records.*

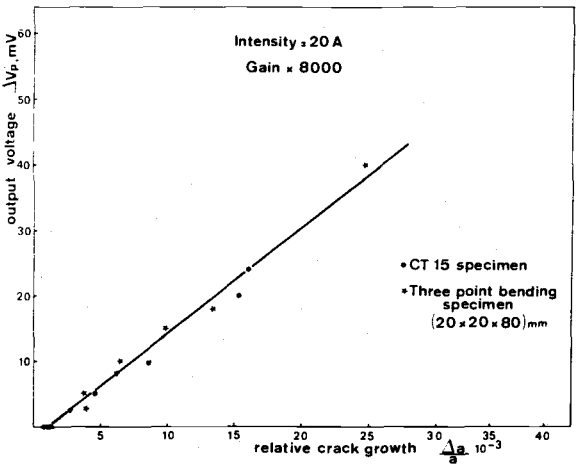

FIG. 5—*Correlation between the output voltage and the relative amount of stable-crack growth.*

ed. In the case of a compact tension specimen, however, the energy U_e is negligible and J_{Ic} may be evaluated by using directly the energy U subtended by the load versus displacement curve up to the initiation point.

Experimental Results

Type 10CD9-10 Steel, Quenched and Tempered at 700°C (Reference A)

Tests were performed on 10 and 20-mm-thick, three-point-bend bars at room temperature. The J_{Ic} values determined by the electrical potential method are compared (Fig. 6) with those found by the conventional interrupted loading method proposed by Begley and Landes [*6*]. One may observe that the J values measured at the intersection between the experimental J versus crack growth curves and the theoretical stretch zone line $J = 2\sigma_{flow}\Delta a$ are slightly different for the two types of specimens (J = 0.113 MJ/m^2 and 0.136 MJ/m^2). Next, it appears that J calculated at the maximum of the load displacement curve (J_m) is much larger than J at initiation (J_m = 0.138 MJ/m^2 and 0.170 MJ/m^2); J_m increases as the size of the specimen increases. Consequently, these values cannot be taken as measurement points for J_{Ic}. However, we see that the critical values J_{Ic} directly measured by the electrical potential method are almost identical for the two types of specimens (0.109 MJ/m^2 < J_{Ic} < 0.111 MJ/m^2). Initiation is detected just at the knee of the experimental crack growth resistance curve. Further, in this work, we have thus systematically used

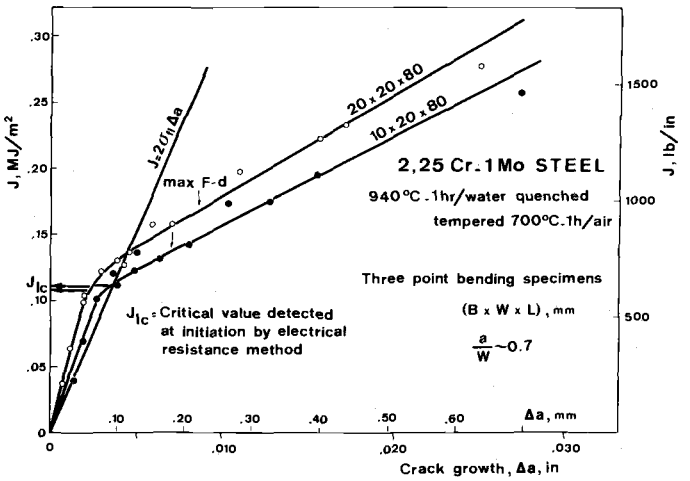

FIG. 6—*Experimental determination of* J_{Ic} *for 10CD9-10 steel quenched and tempered at 700°C by using two types of specimens.*

the electrical potential method for determining the J_{Ic} fracture criterion at the initiation of slow-crack growth.

Electroslag Weld of 10CD9-10 Steel (Reference B)

Valid K_{Ic} values were measured on 150-mm-thick compact tension specimens. In the temperature range considered ($-50°C < T < +50°C$), the fracture toughness of this material goes from 50 MPa $\sqrt{m}$ to about 150 MPa $\sqrt{m}$.

J_{Ic} tests were performed on three-point-bend bars and compact tension specimens of various sizes (Fig. 7). These were taken from the welded joint in the same way as large specimens used for K_{Ic} tests. The electrical potential method was used to detect initiation of slow-crack growth during loading. At room temperature, a small stable crack extension is detected before fracture. In the lower temperature range, fracture occurs without any stable crack extension. In the upper temperature range, the beginning of tear fracture is detected just before the maximum of the load displacement curve.

In the temperature range considered here, there is an excellent agreement between K_{Ic} values calculated from J_{Ic} and directly measured K_{Ic} values (Fig. 7).

15MDV04-03M Cast Steel (Reference C)

J_{Ic} tests were conducted on 15 and 25-mm-thick compact tension speci-

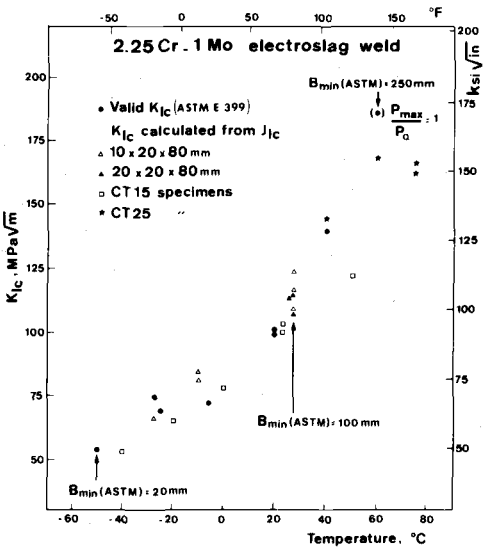

FIG. 7—*Variation of* K_{Ic} *(actual values and calculated from* J_{Ic} *values) with temperature for an electroslag weld.*

mens machined from the broken halves of 100-mm-thick compact tension specimens previously used for K_{Ic} tests. Valid fracture-toughness values were measured at temperatures between − 130°C and − 10°C (Fig. 8).

The mechanism of fracture changes with temperature. Initiation and stable crack extension was observed only at temperatures higher than − 10°C (15-mm compact tension specimen) or + 20°C (25-mm compact tension specimen). At lower temperatures, fracture occurred suddenly during loading.

The fracture toughness values calculated from J_{Ic} tests are plotted along with valid K_{Ic} values (Fig. 8). It may be noticed that, in the lower temperature range, there is a fairly good agreement between calculated and measured fracture-toughness values. In the transition temperature range, the comparison is doubtful because K_{Ic} values are not strictly valid according to ASTM Method E 399-74 since the size requirement is not exactly fulfilled. However, it must be emphasized that J_{Ic} increases very rapidly at temperatures above − 10°C.

Discussion

The fracture-toughness values K_{IJ} deduced from J_{Ic} tests on small specimens, are plotted (Fig. 9) against the corresponding fracture-toughness values K_{Ic} measured under ASTM specifications. Results obtained by other laboratories [*2,17,18*] are also included in this diagram. Taking into ac-

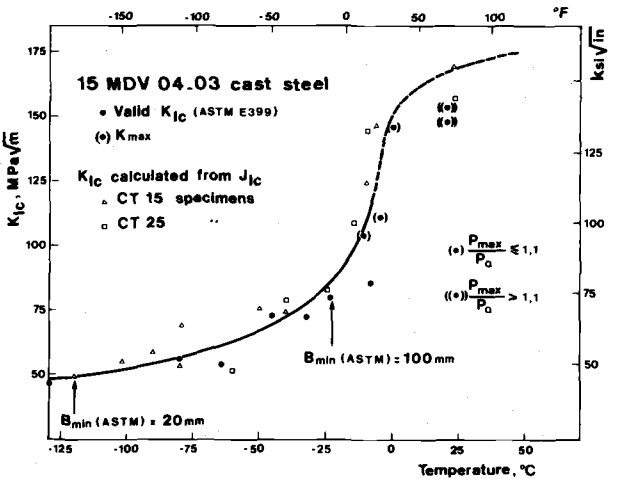

FIG. 8—*Variation of* K_{Ic} *(actual values and calculated from* J_{Ic} *values) with temperature for a 15MDV04-03 cast steel.*

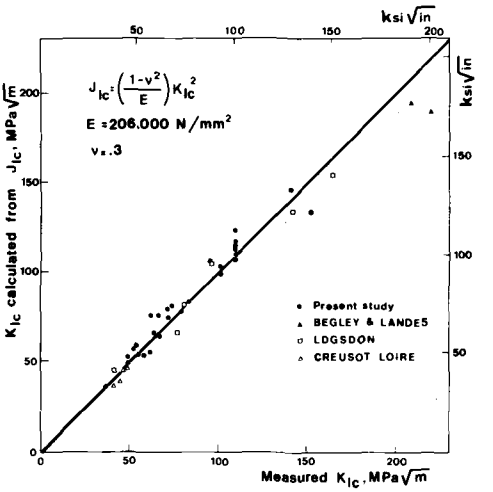

FIG. 9—*Correlation between* K_{Ic} *values calculated from* J_{Ic} *and actual* K_{Ic} *values.*

count the size differences between J_{Ic} and K_{Ic} test specimens and possible heterogeneities in materials studied, the agreement between measured and calculated values can be considered as quite good from an engineering point of view. However, it should be pointed up that almost all these results were obtained in the transition region of the K_{Ic} versus temperature

curve. Under these conditions, the mechanism of fracture is essentially brittle. In the upper region of the K_{Ic} versus temperature curve, the elastic-plastic fracture toughness calculated from J_{Ic} was found to be much lower than the elastic fracture toughness K_{Ic} [*17*].

Application of the Equivalent Energy Method

Some authors [*11,12*] have postulated that for deep-cracked bend bar or compact tension specimens, the J_{Ic} fracture criterion and the equivalent energy concept must be identical. Riccardella and Swedlow have shown recently that these two methods can be used to predict the fracture toughness of the A533 Grade B steel at room temperature [*19*].

Our aim in this work was to compare the K_{Ic} values deduced from J_{Ic} measurements previously made on small specimens and K_{Bd} values found by the equivalent energy method. The latter were determined from the experimental load versus displacement curves which had been recorded during the J_{Ic} tests.

Experimental Estimation of K_{Bd}

Witt and Mager [*8–10*] have proposed a simple method of measuring the lower bound K_{Bd} from a load-displacement record made with a compact specimen of thickness d.

1. The area E_A subtended by the experimental loading curve up to the maximum load is measured. The latter is assumed to correspond to the onset of stable cracking. In fact, as we have seen, initiation can occur before the maximum, and, in our calculations, we preferred to use the area subtended by the loading curve up to the critical displacement which corresponds to the initiation detected by the electrical method.
2. For any point on the linear part of the load-displacement curve, the area E_B subtended by the curve up to this point is measured.
3. The ratio E_A/E_B of the areas thus measured is called b.
4. From the load P_B at point B, K_{Bd} is calculated by means of the following equation [*5*]

$$K_{Bd} = \frac{P_B\sqrt{b}}{d\sqrt{2d}} F\left(\frac{a}{W}\right)$$

where d is the thickness of the specimen.

$F(a/W)$ is the polynomial function used in K_{Ic} determination.

It easily can be shown that the value of K_{Bd} is independent of the point chosen on the linear part of the experimental curve.

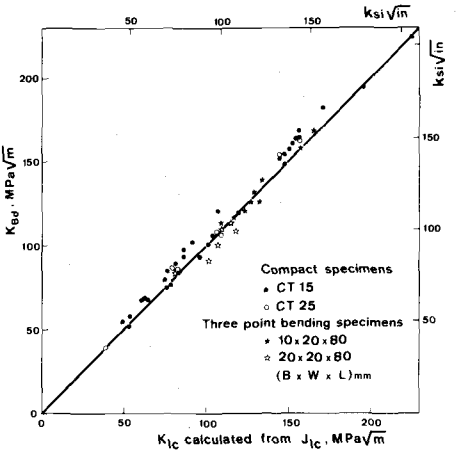

FIG. 10—*Correlation between* K_{Bd} *and* K_{Ic} *values calculated from* J_{Ic}.

Discussion

Apparent fracture-toughness values calculated by the equivalent energy method (K_{Bd}) are plotted in Fig. 10 against the fracture-toughness values deduced from the corresponding J_{Ic} measurements on small specimens.

It appears that the two methods of analyzing the experimental load-displacement curves give almost identical results, provided that the same measurement point is used for both calculations. If one uses the area subtended by the experimental load-displacement curve up to the maximum load, the apparent fracture-toughness value K_{Bd} obviously would be higher than the value calculated up to the initiation point. It is generally observed that J at the maximum of the load-displacement curve (J_m) increases as the dimensions of the specimen increase. Consequently, the lower bound fracture toughness K_{Bd} would be increasing with the thickness d of the specimen as observed by some authors at the plateau of the K_{Ic} versus temperature curve [*8,10*].

Conclusions

J-integral method and equivalent energy procedure were used to characterize the fracture toughness K_{Ic} of medium-strength steels. Tests were performed on small specimens loaded in the elastic-plastic range. The critical values J_{Ic} were calculated from the area subtended by the experimental load-displacement curves up to the onset of stable crack growth using the deep crack formula proposed by Rice. An electrical resistance method developed by IRSID was used for the detection of initiation

during loading. Thus, it was possible to measure J_{Ic} at any temperature with only one small specimen.

For the steels studied here (2.25-Cr-1Mo, electroslag weld, manganese-molybdenum cast steel), the K_{Ic} values deduced from J_{Ic} are in agreement with the actual K_{Ic} values measured on thick specimens in the transition temperature range.

The apparent fracture toughness K_{Bd} were calculated by means of the equivalent energy concept, considering not the maximum of the load-displacement curves but the load at the onset of stable crack growth. A direct comparison between the K_{Bd} values and the K_{Ic} values deduced from J_{Ic} confirms that the equivalent energy and the J-integral concepts lead to identical results in the case of bend bars and compact tension specimens deeply cracked.

These results show that with a single, small specimen loaded in the elastic-plastic range, it is possible to characterize the fracture toughness K_{Ic} of medium-strength steels in the lower region or in the transition zone of the K_{Ic} versus temperature curve.

References

[1] Wessel, E. T., Clark, W. G., and Pryle, W. H., *Proceedings*, Second International Conference on Fracture, Brighton, April 1969, Chapman and Hall LTD, London, England part VI, pp. 825–850.

[2] Begley, J. A. and Landes, J. D., in *Fracture Toughness, ASTM STP 514*, American Society for Testing and Materials, 1972, pp. 1–20.

[3] Landes, J. D. and Begley, J. A. in *Fracture Toughness, ASTM STP 514*, American Society for Testing and Materials, 1972, pp. 24–39.

[4] Rice, J. R., *Journal of Applied Mechanics and Physics of Solids*, Vol. 16, 1968, pp. 1–12.

[5] Rice, J. R., in *Fracture*, H. L. Liebowitz, Ed., Vol. 2, Academic Press, New York, 1968, pp. 191–311.

[6] Landes, J. D. and Begley, J. A., in *Fracture Analysis, ASTM STP 560*, American Society for Testing and Materials, 1973, pp. 170–186.

[7] Witt, F. J., Fourth National Symposium on Fracture Mechanics, Carnegie Mellon University, Aug. 1970.

[8] Witt, F. J. and Mager, T. R., *Nuclear Engineering and Design*, Vol. 17, No. 91, 1971 p. 102.

[9] Witt, F. J. and Mager, T. R., "A Procedure for Determining Bounding Values of Fracture Toughness K_{IC} at Any Temperature," Technical Report ORNL-TM 3894, Oct. 1975.

[10] Buchalet, C. and Mager, T. R., in *Progress in Flaw Growth and Fracture Toughness Testing, ASTM STP 536*, American Society for Testing and Materials, 1973, pp. 281–296.

[11] Begley, J. A. and Landes, J. D., in *Progress in Flaw Growth and Fracture Toughness Testing, ASTM STP 536*, American Society for Testing and Materials, 1973, pp. 246–263.

[12] Merkle, J. G. and Corten, H. T., *Transactions*, American Society of Mechanical Engineers, Nov. 1974, pp. 286–292.

[13] "Procédé et dispositif de détection de la fissuration dans une éprouvette," Patent AFBI-509.

[14] Constant, A., Pomey, G., and Grumbach, M., *Revue de Metallurgie*, July-Aug. 1966, Vol. 63, No. 7/8, pp. 597–604.

[15] Rice, J. R., Paris, P. C., and Merkle, J. G. in *Progress in Flaw Growth and Fracture Toughness Testing, ASTM STP 536,* American Society for Testing and Materials, 1973, pp. 231–245.

[16] Pellissier-Tanon, A., Miannay, D., Ponsot, A., Royer, J., and Tissot, J., "J_{IC} Testing with Three Point Bend Specimens on a 2.25 Cr 1 Mo Steel," presented at the Ninth National Symposium on Fracture Mechanics, 1975.

[17] Logsdon, W. A., "Elastic-Plastic (J_{IC}) Fracture Toughness Values: Their Experimental Determination and Comparison with Conventional Linear Elastic (K_{IC}) Fracture Toughness Values for Five Materials," Technical Report 74—1E7-FM-PWR-P1 Westinghouse, 1974.

[18] Ponsot, J., "Results Obtained During the Contract No. 72-7-0602.00.221. 75.01 of the French Délégation à la Recherche Scientifique et Technique."

[19] Riccardella, P. C. and Swedlow, J. L., "A Combined Analytical Experimental Fracture Study of the Two Leading Theories of Elastic-Plastic Fracture (J-Integral and Equivalent Energy), HSST program," Technical Report No. 33, WCAP-8224, Oct. 1973.

W. A. Logsdon[1] *and J. A. Begley*[1]

Dynamic Fracture Toughness of SA533 Grade A Class 2 Base Plate and Weldments

REFERENCE: Logsdon, W. A., and Begley, J. A., **"Dynamic Fracture Toughness of SA533 Grade A Class 2 Base Plate and Weldments,"** *Flaw Growth and Fracture, ASTM STP 631,* American Society for Testing and Materials, 1977, pp. 477-492.

ABSTRACT: Dynamic fracture toughness tests were performed on four base plate heats and six weldments of SA533 Gr A Cl 2 pressure vessel steel. Linear elastic K_{Id} results were obtained at low temperatures while J-integral techniques were utilized to evaluate dynamic toughness over the transition and upper shelf temperature ranges. Loading rates in terms of $\dot{K}$ were on the order of 2 to 4 $\times$ 10^4 ksi $\sqrt{\text{in.}}$/s (2.2 to 4.4 $\times$ 10^4 MPa $\sqrt{\text{m}}$/s). Charpy and drop weight nil-ductility transition (NDT) tests were performed to permit a comparison of toughness results with the American Society of Mechanical Engineers (ASME) code reference toughness K_{IR} curve. Dynamic instrumented precracked Charpy tests on base plate material were included for a comparison with compact toughness (CT) specimen results. All dynamic fracture-toughness values of SA533 Gr A Cl 2 base, weld, and heat affected zone (HAZ) material exceeded the ASME code reference toughness K_{IR} curve. Fracture-toughness values obtained via small specimen dynamic J_{Id} tests (1.0 in. (2.5 cm) thick CT specimens) compared well with previously developed large specimen K_{Id} values. Dynamic instrumented precracked Charpy toughness values were also comparable at low temperatures but failed to meet minimum J specimen size limitations midway into the transition-temperature range. At this point, Charpy toughness values increased dramatically compared to J_{Id} results meeting a 25 J_{Id}/σ_f size criterion and, thus, should not be considered a valid representation of fracture toughness. True upper shelf dynamic fracture-toughness results are also presented. The point of crack initiation (which provides the minimum measured value of J_{Id}) was identified rather than the typical maximum load point.

KEY WORDS: crack propagation, fractures (materials), steels, alloys

The fail safe performance of pressure retaining vessels involved in nuclear applications (pressurized water reactors, etc.) can depend greatly on the ability of various structural materials to sustain high stress/strain in the presence of flaws. Pressure retaining materials for vessels involving

[1]Mechanics Department, Westinghouse Research Laboratories, Pittsburgh, Pa. 15235; J. A. Begley is presently a professor at The Ohio State University, Department of Metallurgical Engineering, Columbus, Ohio.

nuclear applications must pass minimum dynamic fracture-toughness standards as set forth in Sections III and XI of the American Society of Mechanical Engineers (ASME) Boiler and Pressure Vessel Code [*1*].[2] In brief, for a particular selected material, the dynamic fracture toughness must lie above a specified minimum K_{IR} reference toughness curve temperature corrected based on drop weight nil-ductility transition (NDT) tests and Charpy impact tests [*1,2*]. This K_{IR} concept is based on the lower bound of a substantial amount of dynamic fracture toughness data generated on materials such as ASTM A533 Gr B Cl 1 and ASTM A508 Cl 2 and can be considered as a very conservative representation of the dynamic fracture toughness of those reactor vessel materials with nominal (minimum) yield strengths up to 50 ksi (345 MPa).

The present state of the art in nuclear pressure vessel technology calls for higher strength materials such as SA533 Gr A Cl 2 (minimum yield strength equals 70 ksi (483 MPa)). The ASME Boiler and Pressure Vessel Code permits the use of higher strength materials (greater than 50 ksi (345 MPa) minimum specified yield strength) for pressure vessels; however, Appendix G of the Code indicates that dynamic fracture-toughness (K_{ID}) data needs to be developed to enable verification and use of the K_{IR} curve relative to these new materials.

To develop this data base relative to SA533 Gr A Cl 2 pressure vessel steel, dynamic fracture-toughness tests were performed on four base plate heats and six weldments. Linear-elastic K_{Id} results were obtained at low temperatures while J-integral techniques were utilized to evaluate dynamic toughness over the transition and upper shelf temperature ranges. Support tests (tension, Charpy, and drop weight NDT) were performed to permit a comparison of toughness results with the ASME code reference toughness K_{IR} curve. To further verify the application of J-integral techniques to dynamic fracture-toughness testing, a series of dynamic fracture-toughness tests were conducted on specimens of A533 Gr B Cl 1 steel removed from the HSST 02 dynamic base plate. This is the identical plate of steel investigated by Shabbits [*3*], who employed large specimens (up to 8.0 in. (20 cm) thick) to generate linear-elastic K_{Id} data which greatly influenced K_{IR} curve development. Dynamic instrumented precracked Charpy tests on base plate material also were included for a comparison with compact toughness (CT) specimen results.

Material, Mechanical Properties and Weld Parameters

SA533 Gr A Cl 2 is a manganese-molybdenum alloy steel for use in the quenched and tempered condition for the construction of welded pressure vessels. Tensile requirements for this material call for a minimum yield

[2]The italic numbers in brackets refer to the list of references appended to this paper.

TABLE 1—*Chemical compositions of SA533 Gr A Cl 2 base plate and weld wire.* [a]

TO-No.	Base Plate or Weld Wire	C	Mn	P	S	Si	Ni	Cr	Mo	V	Cu	Al
2864	Base Plate	0.22	1.39	0.016	0.017	0.22	...	...	0.55	...	...	...
2899	Base Plate	0.23	1.30	0.010	0.015	0.26	...	...	0.54	...	...	...
3272	Base Plate	0.22	1.35	0.009	0.015	0.25	...	...	0.58	...	...	...
3312	Base Plate	0.22	1.47	0.010	0.015	0.22	...	...	0.57	...	...	...
3742	Base Plate	0.22	1.35	0.003	0.015	0.27	...	...	0.58	...	...	...
4335	Base Plate	0.23	1.39	0.010	0.013	0.27	...	...	0.57	...	...	...
4336	Base Plate	0.22	1.31	0.013	0.012	0.27	...	...	0.58	...	...	...
3881	Weld Wire	0.177	1.96	0.013	0.005	0.03	0.67	0.05	0.53	0.008	0.01	0.02
4098	Weld Wire	0.170	2.10	0.008	0.005	0.03	0.62	0.07	0.49	< 0.01	0.03	0.01
4113	Weld Wire	0.153	1.99	0.009	0.013	0.06	0.65	0.06	0.47	< 0.01	0.03	0.02

[a]Chemical composition, weight percent.

TABLE 2—*Heat treatments of SA533 Gr A Cl 2 pressure vessel steel.*

TO-No.	Heat Treatment
2864	Heated to 1660°F (904°C), held 3 h and water quenched; tempered 1240°F (671°C) and held 4.3 h.
2899	Heated to 1660°F (904°C), held 3 h and water quenched; tempered 1260°F (682°C) and held 4.4 h.
3272 and 3312	Heated to 1625/1675°F (885/913°C), held ¾ h/in. min and air cooled; tempered 1210°F (654°C), held 1 h/in. min and air cooled.
3742[a]	Heated to 1625/1675°F (885/913°C), held 1 h/in. min and water quenched; tempered 1210°F (654°C), held 1 h/in. min and air cooled.
4335[a] and 4336[a]	Heated to 1625/1675°F (885/913°C), held 1 h/in. min and water quenched; tempered 1200°F (649°C), held 1 h/in. min and water quenched.

[a]Post weld heat treated at 1125°F (607°C), held 3/3.5 h.

strength of 70 ksi (485 MPa), a range in ultimate strength of 90 to 115 ksi (620 to 795 MPa), and a minimum total elongation of 16 percent. Chemical compositions of the seven base plates and three weld wires are presented in Table 1 while the various heat treatments are outlined in Table 2. Note each weld was postweld stress relieved at 1125°F (607°C) for 3 to 3.5 h.

Table 3 summarizes the mechanical properties of SA533 Gr A Cl 2 base plate and weldments. Room-temperature yield strengths of the four base plates ranged from 69.4 ksi (478 MPa) to 82.3 ksi (567 MPa), while their ultimate strengths ranged from 89.5 ksi (617 MPa) to 102.0 ksi (703 MPa). Plate 3312 demonstrated yield and ultimate strengths slightly below the specified minimum. Room-temperature elongation averaged 25.2 percent and was well above the specified minimum. Weldment room-temperature yield and ultimate strengths were, in general, superior to those of the base plates. Percent elongation demonstrated by the weld and heat affected zone (HAZ) material equalled nearly twice that of the base material in five of six cases.

Table 3 also summarizes the drop weight and Charpy V-notch (CV) impact properties necessary to determine the reference temperatures (RT_{NDT}) relative to SA533 Gr A Cl 2 base plate and weldments. The method for establishing a RT_{NDT} is outlined in detail in Section III, Division I and Subsection NB-2331 of the ASME Boiler and Pressure Vessel Code [*1*]. Dynamic fracture toughness data are typically plotted versus $T - RT_{NDT}$ for comparison with the ASME code reference toughness K_{IR} curve. Obviously, the lower the RT_{NDT}, the smaller the amount of conservatism built into the particular dynamic fracture toughness data.

Parameters describing the automatic submerged arc weldments are presented in Table 4. Throughout this paper the weldments are identified as follows: TO-material/TO-weld wire, weld, or HAZ.

TABLE 3—*Mechanical, drop weight, and impact properties of SA533 Gr A Cl 2 pressure vessel steel.*

TO-No.	Base, Weld, or HAZ	NDT Temperature °F	NDT Temperature °C	50 ft·lb Energy Temperature °F	50 ft·lb Energy Temperature °C	35 mil Lateral Exp. Temperature °F	35 mil Lateral Exp. Temperature °C	RT_{NDT} °F	RT_{NDT} °C	Mechanical Properties (Room Temperature) σ_{ys} ksi	σ_{ys} MPa	σ_{ut} ksi	σ_{ut} MPa	Elongation, %
2864	Base	30	− 1	20	− 7	20	− 7	30	− 1	82.3	567.4	102.0	703.3	22.8
2899	Base	− 20	− 29	− 25	− 32	− 30	− 34	− 20	− 29	79.6	548.8	101.4	699.1	26.1
3272	Base	10	− 12	15	− 9	15	− 9	10	− 12	74.0	510.2	94.5	651.6	25.6
3312	Base	− 20	− 29	− 15	− 26	− 25	− 32	− 20	− 29	69.4	478.5	89.5	617.1	26.4
4336/4098	Weld	− 80	− 62	25	− 4	15	− 9	− 35	− 37	89.9	619.8	105.8	729.5	23.6
4335/4098	Weld	− 50	− 46	40	4	40	4	− 20	− 29	90.9	626.7	106.5	734.3	56.2
3742/3881	Weld	− 60	− 51	35	2	25	− 4	− 25	− 32	81.6	562.6	98.9	681.9	56.8
4335/4098	HAZ	− 30	− 34	0	− 18	0	− 18	− 30	− 34	97.4	671.5	114.2	787.4	48.8
4336/4113	HAZ	− 90	− 68	− 20	− 29	− 20	− 29	− 80	− 62	93.9	647.4	113.8	784.6	49.4
3742/4113	HAZ	− 60	− 51	0	− 18	15	− 9	− 45	− 43	84.4	581.9	100.5	692.9	56.4

TABLE 4—*Parameters for automatic submerged arc weldments.*

Name of process	Single wire dc (automatic submerged arc)
Welding process specification	82148 RR
Electrode size and type	5/32 in. (0.4 cm), MnMoNi
Flux type	Linde 0091
Flux test numbers	
All weldments except 4335/4098 weld	4553
Weldment 4335/4098 weld	3970
Current and polarity	600 dc
Arc voltage	32
Travel speed, in./min (cm/min)	12 (30)
Welding position	Downhand
Preheat temperature	250 °F (121 °C)
Interpass temperature	500 °F (260 °C)
Postweld heat treatment	1125 °F (607 °C) hold 3/3.5 hours
Inspection after fabrication	Magnetic particle, radiography

Experimental Procedures

The majority of base metal dynamic toughness tests were conducted on 3-in. (7.6-cm) thick CT specimens, while all weldment tests and a single series of base metal tests were performed on 1-in. (2.5-cm) thick CT specimens. All specimens were precracked and oriented with their notch directions perpendicular to the plate rolling direction (orientation L-T per ASTM Test for Fracture Toughness of Metallic Materials (E 399-74)). The larger CT specimens were tested in a facility previously described by Shabbits [*3*].

The small CT specimens were modified to allow placement of a spring loaded clip gage capable of measuring centerline of loading displacements. These tests were conducted on a servo-hydraulic MTS machine with load frame and load cell capacities of 50 kips (22680 kg) and 20 kips (9072 kg), respectively. Dynamic capability was realized by employing a 90 g/min (341 litres/min) MTS Teem value (two stage with feedback). Loading rates in terms of $\dot{K}$ were on the order of 2 to 4 $\times$ 10^4 ksi $\sqrt{\text{in.}}$/s (2.2 to 4.4 $\times$ 10^4 MPa $\sqrt{\text{m}}$/s). Load versus time, displacement versus time, and load versus displacement traces were recorded for each test.

Some specimens tested at low temperatures were linear elastic and similar to those described by previous investigators [*3–5*]. The majority of test specimens, however, were in the elastic-plastic regime where J-integral test techniques applied [*6–8*]. Dynamic elastic-plastic (J) test techniques can be divided into two categories: (1) load to failure and (2) dynamic resistance curve. Each of these test techniques will be described separately along with the dynamic instrumented precracked Charpy test technique.

Load to Failure

All SA533 Gr A Cl 2 specimens tested at temperatures below that where upper shelf fracture toughness behavior was first experienced were loaded dynamically to failure and sustained cleavage controlled fractures. The onset of crack extension was abrupt and unambiguous. There was no stable growth. A sudden drop in the load-deflection curve occurred at the fracture point. Inertial loading effects were negligible at the testing speed utilized. Actual test records illustrating the various types of failures are shown in Fig. 1. At low temperatures, the load versus displacement records were linear and the fracture toughness was calculated directly from the failure load as outlined in ASTM Method E 399-74, although in many cases the specified size criterion was not met by the 1-in. (2.5-cm) thick CT specimens.

At transition temperatures, nonlinear load versus displacement records were possible although the specimen fractures were cleavage controlled (see Fig. 1). For these tests, J was calculated from the estimation method outlined by Rice et al [*9*]

$$J = \frac{2A}{B(w - a)}$$

where A is the area under the load-displacement curve taken at the displacement of interest, B is the specimen thickness, and $(w - a)$ (often referred to as b) is the remaining uncracked ligament. Corresponding K_{Id} values were calculated from the relationship between elastic-plastic and linear-elastic fracture mechanics parameters [*8*]

$$J_{Id} = \frac{1 - \nu^2}{E} K_{Id}^2$$

where ν is Poisson's ratio and E is Young's modulus. Thus, in dynamic fracture-toughness testing, it is possible to obtain nonlinear load versus displacement records and cleavage controlled fractures without some form of slow stable crack growth (ductile tearing). This dynamic fracture behavior can occur at transition temperatures where ductile tearing controlled fractures and slow stable crack growth would be likely in quasi-static fracture-toughness tests.

At upper shelf temperatures, specimens loaded dynamically to failure experienced fractures which were controlled by ductile tearing. The point of crack initiation was not apparent from the load-displacement records. Calculating a fracture toughness based on maximum load clearly is not related to the point of crack growth initiation. Crack growth may in fact occur prior to or after the maximum load.

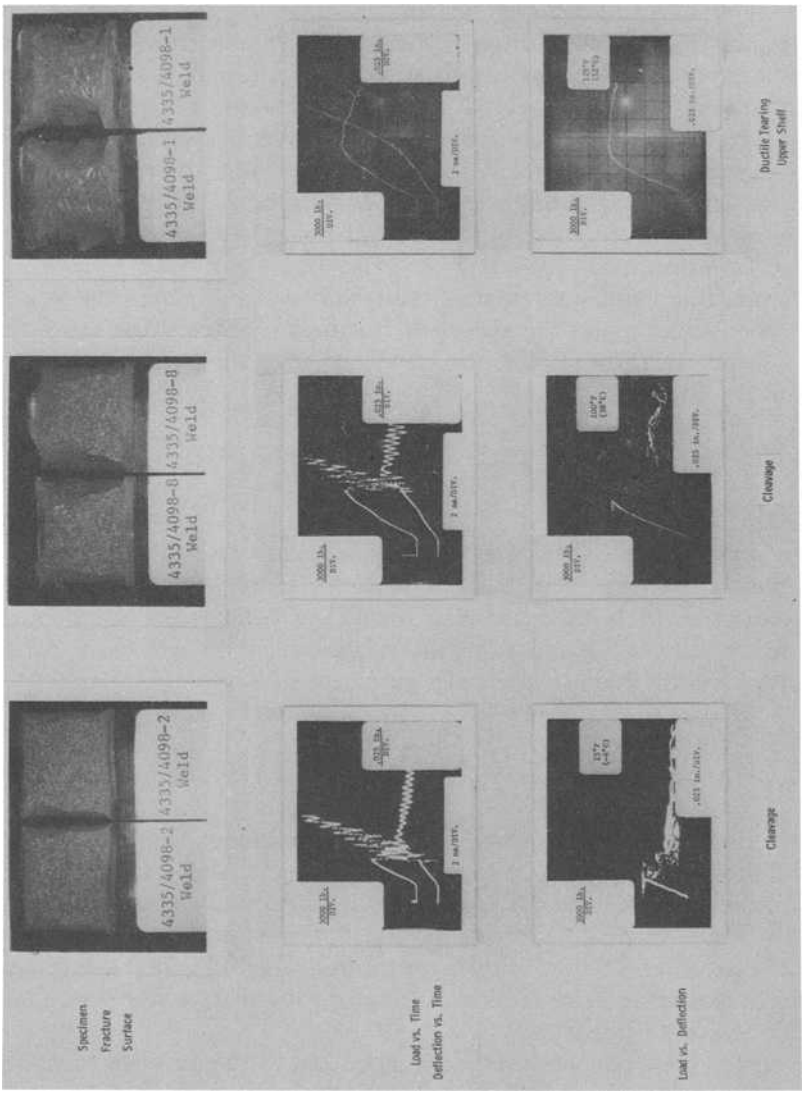

FIG. 1—*Test records for SA533 Gr A Cl 2 weld metal (4335/4098) specimens illustrating various types of failures.*

Dynamic Resistance Curve

To obtain clearly defined dynamic fracture-toughness values at upper shelf temperatures, it was necessary to employ a resistance curve test technique identical to that set forth by Landes and Begley in Ref *8* for quasi-static fracture toughness testing. This technique is applicable to the ductile tearing upper shelf fracture regime where the onset of crack growth cannot be ascertained from the appearance of the load-deflection record. CT specimens were dynamically loaded to a specific displacement (not to failure), unloaded, heat tinted, and broken open to reveal the amount of stable crack growth. Actual test records for two SA533 Gr A Cl 2 HAZ specimens tested at 100°F (38°C) are illustrated in Fig. 2, while the corresponding resistance curve is presented in Fig. 3. These 1.0-in. (2.5-cm) thick specimens were loaded to their final displacements and loads in

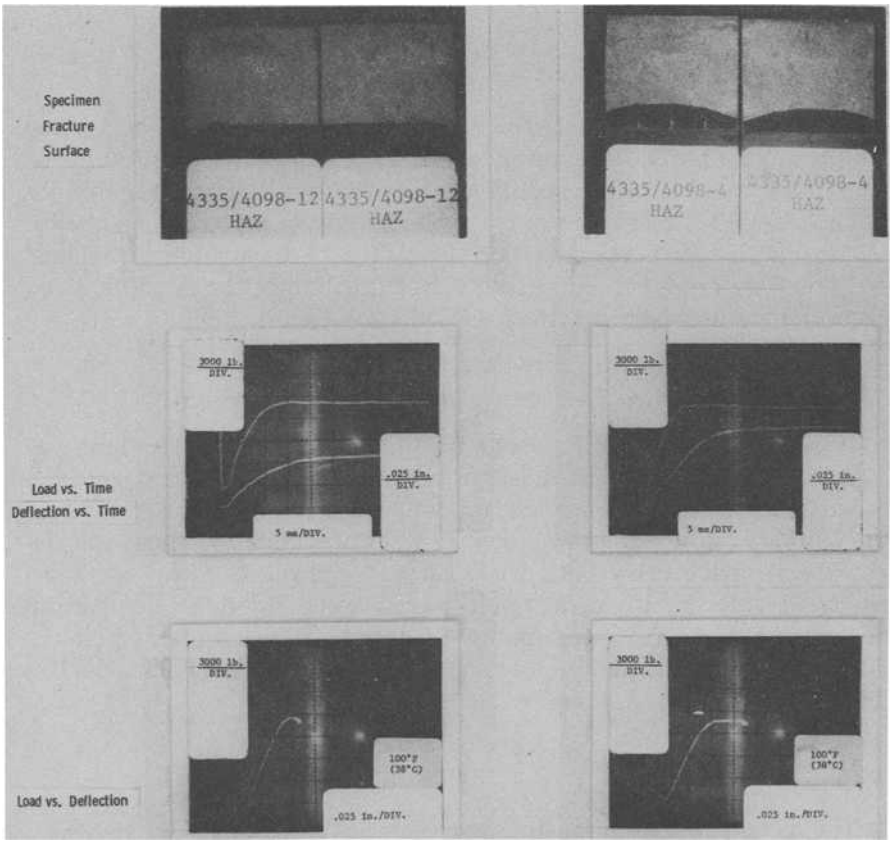

FIG. 2—*Test records for SA533 Gr A Cl 2 HAZ (4335/4098) specimens illustrating loading to specific displacements.*

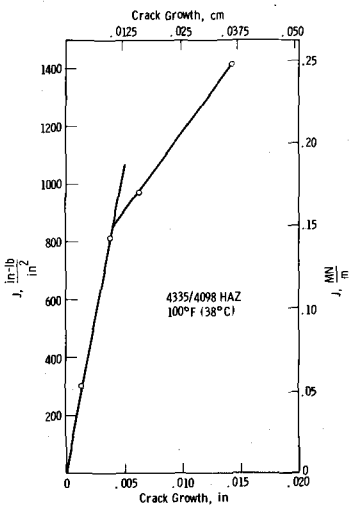

FIG. 3—J-*resistance curve for SA533 Gr A Cl 2 HAZ material.*

approximately 18 to 20 ms. The critical value of dynamic J (J_{1d}) based on the initiation of crack growth for this HAZ material equals 850 in·lb/in.^{2} (0.149 MN/m). This corresponds to a fracture toughness of 167 ksi $\sqrt{\text{in.}}$ (185 MPa $\sqrt{\text{m}}$). Therefore, a dynamic resistance curve technique for J_{1d} testing has been developed whereby tests can be dynamically interrupted to allow heat tinting and thus permit an evaluation of the extent of crack growth at various points on the load-deflection record.

Dynamic Instrumented Precracked Charpy Tests

In addition to the CT geometry fracture tests, a series of fatigue precracked CV specimens machined from SA533 Gr A Cl 2 base material were tested utilizing an instrumented impact testing machine. Load-time curves were recorded on a transient recorder. Fracture-toughness calculations were made using both J-integral and equivalent energy methods, although only the J-integral results were plotted for direct comparison with elastic-plastic CT specimen results. J values were calculated from the area under the load-deflection curve to the point of maximum load in both linear-elastic and elastic-plastic tests.

Results

The dynamic fracture-toughness values generated on SA533 Gr A Cl 2 base plate and weldments are plotted versus $T - \text{RT}_{\text{NDT}}$ for comparison with the ASME code reference toughness K_{IR} curve in Figs. 4 and 5, re-

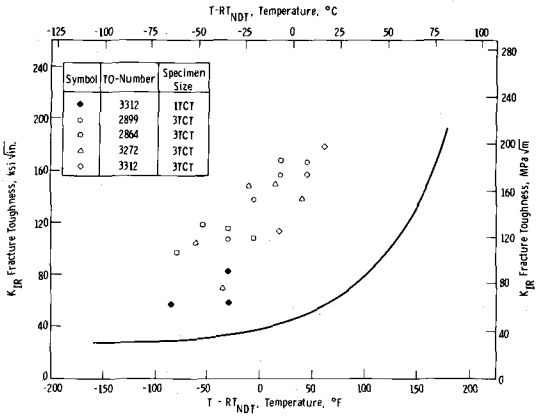

FIG. 4—K_{IR} *reference toughness curve for SA533 Gr A Cl 2 base material.*

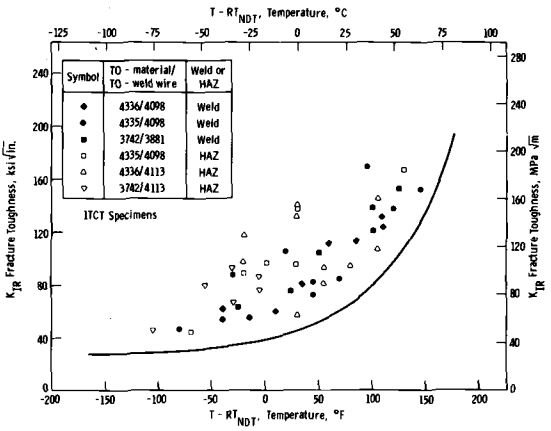

FIG. 5—K_{IR} *reference toughness curve for SA533 Gr A Cl 2 weld and HAZ material.*

spectively. The single upper shelf dynamic fracture-toughness value generated with the dynamic resistance curve test technique on 4335/4098 HAZ is plotted at a $T - RT_{NDT}$ temperature of 130°F (54°C) in Fig. 5. In all cases, the dynamic fracture toughness of SA533 Gr A Cl 2 base plate and weldments exceeded the ASME code reference toughness K_{IR} curve. Therefore, this 70 ksi (485 MPa) minimum yield strength material is acceptable for nuclear pressure vessel structural applications from a dynamic fracture toughness standpoint.

The SA533 Gr A Cl 2 base plate dynamic fracture toughness is substantially conservative compared with the corresponding weldment fracture toughness when plotted versus the K_{IR} curve. At any given test tem-

perature, the average base plate dynamic fracture toughness exceeds that of the weldments by approximately 30 percent. In addition, the lower reference temperatures demonstrated by the weldments compared with the base material, in a sense, penalized the weldment dynamic fracture-toughness values by shifting them significantly closer to the K_{IR} curve.

Both SA533 Gr A Cl 2 base plate and weldment dynamic fracture-toughness data exhibited relatively large scatter. Some CT specimens demonstrated step type crack fronts (especially 4336/4098 HAZ) as the fracture plane, which normally remained in the weld or HAZ material, searched out the path of least resistance. This typically produced higher dynamic fracture toughness values than when the fracture plane was identical with that of the fatigue precrack.

Instrumented precracked CV versus CT specimen dynamic fracture-toughness data are presented for each heat of SA533 Gr A Cl 2 base material in Fig. 6. Low-temperature, dynamic fracture-toughness results

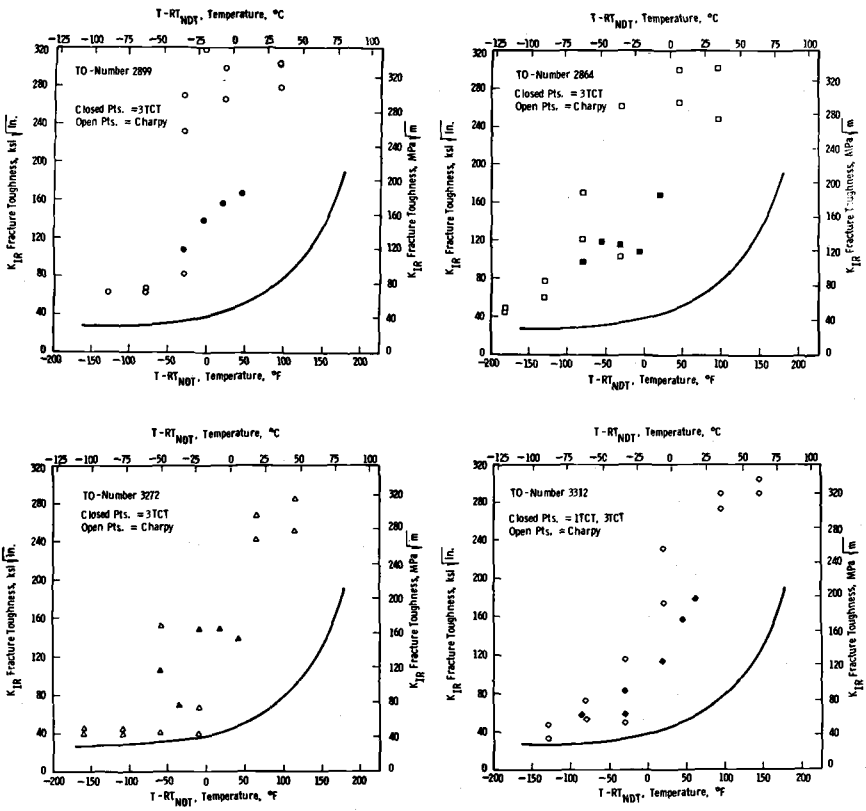

FIG. 6—K_{IR} *reference toughness curves for SA533 Gr A Cl 2 base material illustrating data generated with instrumented precracked Charpy versus CT specimens.*

were independent of whether instrumented precracked CV or CT specimens were utilized. At temperatures midway into the transition-temperature range, CV toughness values increased dramatically and are considerably higher than CT specimen dynamic J_{Id} results. This was caused by a violation of the J test size criterion as toughness and maximum load increased with temperature [8]

$$a,\ B,\ b \geq 25\ \frac{J_{Id}}{\sigma_f}$$

where a is the crack length and σ_f is a flow stress midway between the material's yield and ultimate stresses. Obviously, dynamic tensile properties should be utilized in evaluating dynamic toughness tests. The high-temperature CV toughness values violate the J test size criterion by such a sufficient margin, however, that dynamic tensile properties are not imperative and were not employed in this investigation. Based on critical dimensions for a and b equivalent to one half the specimen thickness and an average base metal room-temperature static flow stress of 86.6 ksi (597 MPa), the maximum measurable toughness with the 0.394-in. (1.0-cm) thick CV specimens equalled 150 ksi $\sqrt{\text{in.}}$ (166 MPa $\sqrt{\text{m}}$).

An increase in toughness may be expected from the fact that the CV test necessarily uses a maximum load measurement point rather than the point of crack-growth initiation. This is only of concern, however, if the fracture is not cleavage controlled. The transition range CV toughness values are considered invalid because a violation of the J size criterion resulted in a change in fracture mode compared to the CT J_{Ic} specimens. Had the measurement point for the transition range CV tests been consistent with the J_{Ic} approach, the toughness values would still be too high as a result of a ductile fracture mode in the CV bars versus cleavage fracture of the CT specimens.

Finally, a slight $\dot{K}$ effect (approximately one order of magnitude) could account for a small portion of the higher toughness exhibited by the CV tests in comparison with the CT specimen results.

Therefore, low-temperature, dynamic fracture-toughness values generated via instrumented precracked CV specimens can be regarded as a valid measure of a material's toughness. Dynamic fracture-toughness values generated via instrumented precracked CV specimens at temperatures midway into the transition-temperature range or higher should be approached with caution as they most likely significantly overestimate a material's actual toughness.

Discussion

Supplemental support can be directed toward the utilization of J-inte-

gral test techniques (whether load to failure or dynamic resistance curve) as a primary method of obtaining dynamic fracture-toughness values. Figure 7 illustrates a comparison of the dynamic fracture-toughness properties of A533 Gr B Cl 1 HSST 02 base plate developed via large specimen K_{Id} tests versus small specimen load to failure J_{Id} tests. This large specimen K_{Id} data generated by Shabbits [*3*] had a large influence on development of the ASME code reference toughness K_{IR} curve [*2*].

The agreement between valid K_{Id} test results and equivalent K_{Id} values obtained from small specimen J_{Id} tests is very good. There is perhaps increased scatter with the J_{Id} derived toughness data, but this is due in part to the presence of a Weibull type size effect. Larger specimens are more likely to contain weak areas leading to lower fracture toughness in the absence of any stress state effect. This type of weak-link analogy is appropriate for the cleavage fracture test results presented in Fig. 7. An additional factor in comparing test results of large and small specimens is a drastically reduced likelihood of obtaining invalid J_{Id} values. In K_{Id} testing of a particular size specimen, a test result exceeding the measurement capacity is termed invalid and discarded. Generally, no mention is made that the test did in fact reveal a toughness higher than the measurement capacity. Hence, the size of a K_{Id} specimen automatically limits the maximum reportable toughness value.

Support relative to the dynamic resistance curve test technique is demonstrated through Fig. 8, which illustrates a modified resistance curve developed on a 88.3 ksi (105.5 MPa) yield strength SA508 Cl 2a pressure

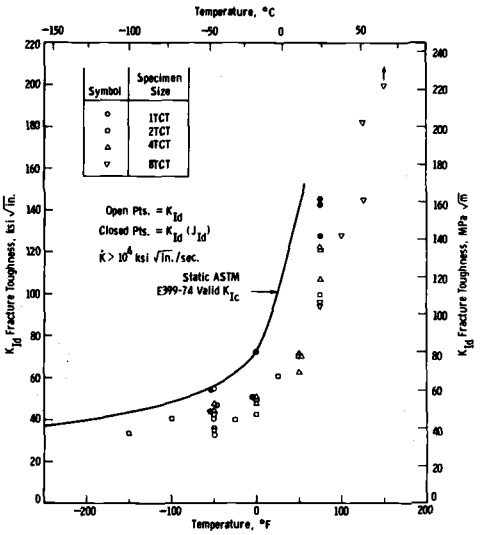

FIG. 7—*Dynamic fracture toughness properties of A533 Gr B Cl 1 HSST 02 baseplate.*

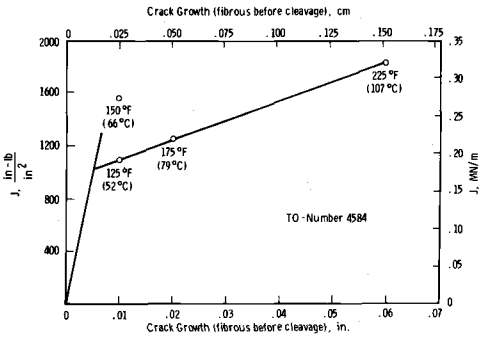

FIG. 8—*J-resistance curve for SA508 Cl 2a base material.*

vessel steel. Each of the four specimens which make up this resistance curve were loaded dynamically to failure. Since upper shelf ductile tearing fractures occurred in each of these tests, the point on the load-deflection curves where crack extension first initiated was not obvious, and calculating individual J_{Id} values was impossible. Each of the fracture surfaces were similar to the upper shelf fracture illustrated in Fig. 1, whereby a small region of ductile tearing (slow stable crack extension) occurred immediately adjacent to the precrack followed by an area of cleavage fracture. Measuring this ductile crack extension and plotting it versus J (calculated based on the total area under the load-deflection curve to abrupt failure) resulted in the resistance curve pictured in Fig. 8. The K_{Id} resulting from this modified resistance curve equalled 183 ksi $\sqrt{\text{in.}}$ (203 MPa $\sqrt{\text{m}}$). This compares quite favorably with the upper shelf toughness of 167 ksi $\sqrt{\text{in.}}$ (185 MPa $\sqrt{\text{m}}$) for the 4335/4098 HAZ material generated via dynamically interrupted tests. No deceleration occurred for the SA508 Cl 2a tests where the extent of ductile growth was fortunately marked by a change in fracture mode. The similarity of test results supports the contention that deceleration does not unduly affect J_{Id} values in dynamically interrupted tests.

Conclusions

1. All dynamic fracture-toughness values of SA533 Gr A Cl 2 base, weld, and HAZ material exceeded the ASME code reference toughness K_{IR} curve. Therefore, this 70 ksi (485 MPa) minimum yield strength material is acceptable for nuclear pressure vessel structural applications from a dynamic fracture-toughness standpoint.

2. Fracture-toughness values obtained via small specimen dynamic J_{Id} tests (1.0-in. (2.5-cm) thick CT specimens) compared well with previously developed large specimen K_{Id} values. Hence, massive linear-elastic speci-

mens are not required to develop a complete dynamic fracture toughness versus temperature curve.

3. A technique was devised to develop upper shelf dynamic J resistance curves and thus provide an unambiguous measure of the point of crack-growth initiation.

4. Instrumented precracked CV specimens could not meet minimum J specimen size limitations at temperatures midway into the transition-temperature range. CV toughness values increased dramatically at these temperatures and were considerably higher than CT specimen dynamic J_{Id} results.

Acknowledgments

The authors gratefully wish to acknowledge D. R. Young, P. J. Barsotti, and W. H. Pryle of the Westinghouse Research Laboratories for their contributions toward development of the dynamic test facilities and for performing the elastic-plastic (J) fracture toughness tests. The authors are particularly indebted to A. J. Bush and R. B. Stouffer, also of the Westinghouse Research Laboratories, for conducting the instrumented precracked Charpy tests.

References

[1] *ASME Boiler and Pressure Vessel Code,* American Society of Mechanical Engineers, New York, 1974.

[2] "Derivation of K_{IR} Curve," Appendix 1, *PVRC Recommendations on Toughness Requirements for Ferritic Materials,* WRC Bulletin 175, Welding Research Council, Aug. 1972.

[3] Shabbits, W. O., "Dynamic Fracture Toughness Properties of Heavy Section A533 Gr B Cl 1 Steel Plate," Technical Report No. 13, Heavy Section Steel Technology Program, Dec. 1970.

[4] Bush, A. J. in *Impact Testing of Metals, ASTM STP 466,* American Society for Testing and Materials, 1970, pp. 259–280.

[5] Paris, P. C., Bucci, R. J., and Loushin, L. L. in *Fracture Toughness and Slow-Stable Cracking, ASTM STP 559,* American Society for Testing and Materials, 1974, pp. 86–98.

[6] Begley, J. A. and Landes, J. D. in *Fracture Toughness, Proceedings of the 1971 National Symposium on Fracture Mechanics, Part II, ASTM STP 514,* American Society for Testing and Materials, 1972, pp. 1–20.

[7] Landes, J. D. and Begley, J. A. in *Fracture Toughness, Proceedings of the 1971 National Symposium on Fracture Mechanics, Part II, ASTM STP 514,* American Society for Testing and Materials, 1972, pp. 24–39.

[8] Landes, J. D. and Begley, J. A. in *Fracture Analysis, ASTM STP 560,* American Society for Testing and Materials, 1974, pp. 170–186.

[9] Rice, J. R., Paris, P. C., and Merkle, J. G. in *Progress in Flaw Growth and Fracture Toughness Testing, ASTM STP 536,* American Society for Testing and Materials, 1973, pp. 231–245.

T. Iwadate,[1] *T. Karaushi,*[1] *and J. Watanabe*[1]

Prediction of Fracture Toughness K_{Ic} of 2¼Cr-1Mo Pressure Steels from Charpy V-Notch Test Results

REFERENCE: Iwadate, T., Karaushi, T., and Watanabe, J., "**Prediction of Fracture Toughness K_{Ic} of 2¼Cr-1Mo Pressure Vessel Steels from Charpy V-Notch Test Results,**" *Flaw Growth and Fracture, ASTM STP 631,* American Society for Testing and Materials, 1977, pp. 493-506.

ABSTRACT: The validity of the Barsom, Rolfe, and Novak correlation between Charpy energy, yield strength, and K_{Ic} in the upper-shelf region has been confirmed for 2¼Cr-1Mo pressure vessel steels. The relationship between the excess temperature and $K_{Ic}/K_{Ic\text{-upper shelf}}$ has also been developed. Based on these relationships, K_{Ic} transition curves may be predicted from Charpy V-notch test results of 2¼Cr-1Mo pressure vessel steels.

KEY WORDS: crack propagation, steels, fracture strength, toughness, transition temperature, impact strength, yield strength

It has been increasingly recognized that pressure vessels made of 2¼Cr-1Mo steel require a fracture safe analysis for their safe operation, since the steel may be temper embrittled during service [*1,2*].[2] Linear fracture mechanics is used commonly and is a very useful tool for a fracture safe analysis, while fracture toughness K_{Ic} is the material property to be used for the analysis.

Measurement of K_{Ic} of 2¼Cr-1Mo pressure vessel steels with low-yield strength—45 ksi (310 MPa) minimum at room temperature per ASTM A387, 22 Class 2 and A336, F22—requires large specimens to obtain valid K_{Ic} value per ASTM Test for Plane-Strain Fracture Toughness of Metallic Materials (E 399-74). At the temperatures in question, 30 to 260°F (0 to 130°C), about 20-in.-thick specimens are required for unembrittled steels. This specimen size almost prohibits routine measurement of K_{Ic} of 2¼Cr-

[1]Research engineers and general manager, respectively, Research Laboratory, Muroran Plant, The Japan Steel Works, Muroran, Japan 051.

[2]The italic numbers in brackets refer to the list of references appended to this paper.

1Mo pressure vessel steels. In order to overcome the inconvenience, the J-integral method, which is being studied very extensively [*3,4*], may be a good alternate because of much smaller specimen size required.

Prediction of K_{Ic} from Charpy V-notch (CVN) test results also has been proposed [*5–7*]. It is clear that a single and generalized correlation may not be established between these two tests results [*8*]. However, if a reliable method is available for a specific material grade, it would be very useful. As for 2¼Cr-1Mo steel, many pressure vessels presently in service were built using this steel. The only available toughness data of the steels used for these reactors are the Charpy impact test results, and past data on temper embrittlement of the steel also have been obtained mainly by CVN test.

This paper presents an empirical method to predict K_{Ic} of 2¼Cr-1Mo steels from CVN test results covering the entire temperature range, from upper shelf to lower shelf. In principle, the method is a combination of the Barsom, Rolfe, and Novak upper shelf correlation [*5*] and the excess temperature versus K_{Ic} relationship developed by Brothers, Newhouse, and Wundt [*9*].

Materials and Experimental Procedure

Materials

The materials tested in this study include four 2¼Cr-1Mo pressure vessel steels and a nickel-molybdenum-vanadium rotor steel. The chemical compositions of these materials are listed in Table 1, and the tensile properties are listed in Table 2. The 2¼Cr-1Mo steels A, B, and C were taken from the same forging and different locations with different temper embrittlement during their service exposure [*2*].

Test Specimens

K_{Ic} *Specimens*—2.5T compact tension (CT) specimens from the 2¼Cr-1Mo material B, 3T bend specimens from the 2¼Cr-1Mo material D, and 3T bend specimens from the rotor steel were prepared in accordance with ASTM Method E 399-74. The orientation of the specimens and notches were L-R and C-R orientation per ASTM Method E 399-74 for the 2¼Cr-1Mo steels and rotor steel, respectively.

J_{Ic} *Specimens*—For the 2¼Cr-1Mo steels, bend-bar specimens, of which size ranges from 0.39 by 0.39 in. (10 by 10 mm) to 2 by 4 in. (51 by 102 mm), were prepared in accordance with the tentative J_{Ic} test method recommended by Landes and Begley [*3*]. For the nickel-molybdenum-vanadium rotor steel, 1T-CT specimens were prepared in accordance with the

TABLE 1—*Chemical composition of 2¼Cr-1Mo pressure vessel steels and a nickel-molybdenum-vanadium rotor steel investigated (check analysis), percent.*

Material	C	Mn	P	S	Si	Ni	Cr	Mo	V	As	Sn	Sb
2¼Cr-1Mo pressure vessel steel												
A[a]	0.16	0.61	0.010	0.010	0.26	0.17	2.32	1.11	...	0.015	0.022	0.0047
B[a]	0.16	0.60	0.010	0.009	0.25	0.17	2.31	1.12	...	0.016	0.023	0.0045
C[a]	0.15	0.59	0.009	0.009	0.26	0.17	2.30	1.09	...	0.015	0.022	0.0045
D[b]	0.15	0.57	0.011	0.007	0.05	0.18	2.49	1.07	...	0.008	0.014	0.0041
Ni-Mo-V rotor steel	0.25	0.38	0.013	0.009	0.24	3.95	0.56	0.42	0.12	...	...	...

[a]Taken out of a pressure vessel after 30 000 h service [2].
[b]Temper embrittled by a step cooling.

TABLE 2—*Mechanical properties of 2¼Cr-1Mo pressure vessel steels and a nickel-molybdenum-vanadium rotor steel at 75°F.*

Material	0.2 % Yield Strength, ksi	Tensile Strength, ksi	Elongation in 2 in., %	Reduction of Area, %	Charpy V-Notch	
					Energy Absorption, ft·lb	FATT,[a] °F
2¼Cr-1Mo pressure vessel steel						
A	63	88	32	73	21	203
B	62	87	31	73	32	163
C	59	85	32	74	56	140
D	85	105	20	74	61	81
Ni-Mo-V rotor steel	90	110	30	59	23	115

[a]50 percent shear fracture appearance transition temperature.

same recommended practice [3]. The orientation of the specimens and notches were the same as those used for the K_{Ic} specimens. Fatigue crack lengths of all specimens, a/w—where a is the crack length and w is the specimen width—were about 0.6. Final precracking stress intensity (K_f) was controlled to limit the amount of crack-tip plasticity less than 25 ksi $\sqrt{\text{in.}}$ (27.5 MPa $\sqrt{\text{m}}$).

CVN Specimens—Conventional ASTM A370-75, Type A, CVN specimens were tested. The orientation of the specimens and notches were the same as those used for the K_{Ic} and J_{Ic} specimens.

Experimental Procedure

K_{Ic} *Tests*—K_{Ic} specimens were tested in accordance with ASTM Method E 399-74. The validity of the test results was examined, and it was found that the results were valid up to −40°F (−40°C) for the 2¼Cr-1Mo steel B, −90°F (−68°C) for the steel D, and 95°F (35°C) for the nickel-molybdenum-vanadium rotor steel.

J_{Ic} *Tests*—For the 2¼Cr-1Mo steel D in the upper shelf region, the tentative J_{Ic} test method recommended by Landes and Begley [3] was used. 0.6 by 1.2 in. (15 by 30 mm), 1 by 2 in. (25 by 51 mm) and 2 by 4 in. (51 by 102 mm) bend bar specimens were used, and the smallest one could not meet the specimen size requirement. Figure 1 presents the relationship between J and the crack extension.

For all other measurements, the fractographic method [4] was used instead of the heat tinting method. The stretched zone width of 10 to 29 areas at the middle portion of each specimen was measured by a scanning electron microscope with the angle of 30 deg to the fatigue cracked plane. Figure 2 presents an example of J versus stretched zone width relationship of the rotor steel. It has been found in this study that the measurement of the stretched zone width is much more time consuming but more

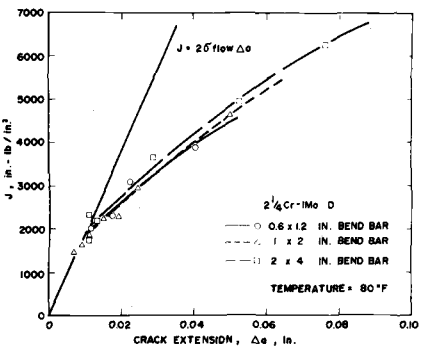

FIG. 1—J *versus crack extension of 2¼Cr-1Mo steel D.*

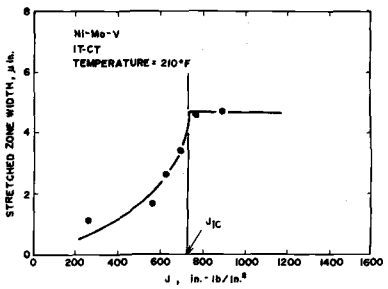

FIG. 2—J *versus stretched zone width of nickel-molybdenum-vanadium rotor steel.*

reliable for the measurement of J_{Ic}, especially in the transition-temperature range. The validity of the test results was examined by the size criteria given by Landes and Begley [*3*].

Fracture toughness J was calculated by using the equation developed by Rice et al

$$J = \frac{2A}{Bb} \tag{1}$$

where

A = area under the load-displacement curve taken at the displacement of interest,
B = specimen thickness, and
b = remaining uncracked ligament.

The critical value of J (J_{Ic}) was defined as J at the point of zero crack extension due to actual material separation. K_{Ic} values of the steels were obtained by converting J_{Ic} to K_{Ic} by using the equation

$$K_{Ic}^2 = \frac{J_{Ic}E}{1 - \mu^2} \tag{2}$$

where E is Young's modulus and μ is Poisson's ratio.

CVN tests—Impact tests were conducted at various temperatures, and the energy absorption and fibrous fracture were measured as functions of temperature.

Results and Discussion

K_{Ic} *and CVN Correlation in the Upper Shelf Region*

An empirical relationship obtained by Barsom, Rolfe, and Novak [*5*]

between upper shelf Charpy energy, yield strength, and K_{Ic} for steels with yield strengths between 110 and 246 ksi (758 and 1696 MPa) has been observed to be valid by Begley and Toolin [*10*] for intermediate yield strength nickel-chromium-molybdenum-vanadium rotor steels (Fig. 3). The yield strength of the rotor steels ranges between 134 and 160 ksi (924 and 1103 MPa). A theoretical explanation of this relationship has been given by Rice, Paris, and Merkle [*11*]. In the present study, the validity of this relationship is examined in 2¼Cr-1Mo pressure vessel steels and a nickel-molybdenum-vanadium rotor steel with much lower yield strengths between 59 and 90 ksi (407 and 621 MPa).

The CVN test results are presented in Table 2, and the CVN transition curves are shown in Fig. 4. The fracture toughness versus temperature

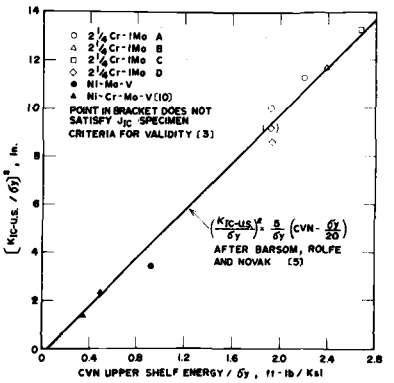

FIG. 3—*Relationship between* K_{Ic} *and CVN energy in the upper shelf region.*

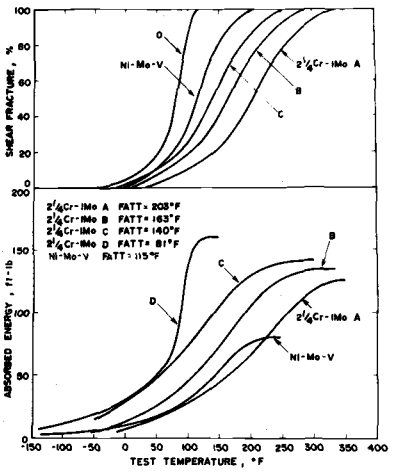

FIG. 4—*CVN transition curves.*

behaviors relative to the 2¼Cr-1Mo steels and the rotor steel are illustrated in Figs. 5 through 9, respectively. In these figures, the specimen size and testing method are also shown.

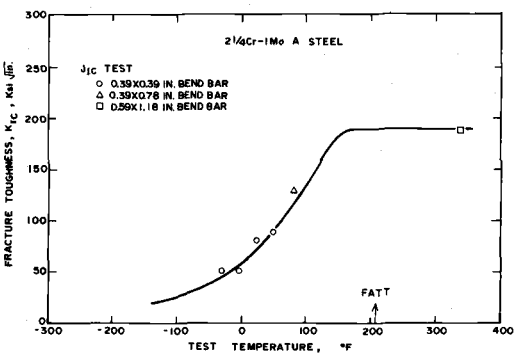

FIG. 5—*Fracture toughness versus temperature behavior of 2¼Cr-1Mo steel A.*

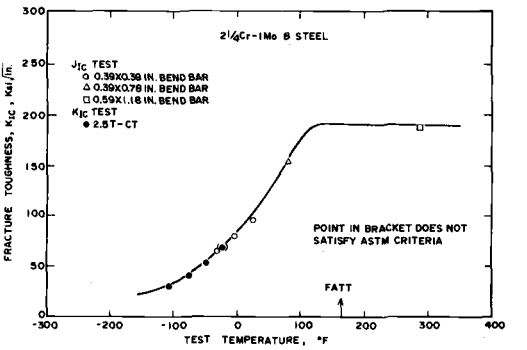

FIG. 6—*Fracture toughness versus temperature behavior of 2¼Cr-1Mo steel B.*

The temperatures where CVN specimens first experience zero percent brittle fracture were determined from the CVN test results. These temperatures are known in this paper as the upper shelf temperatures. The fracture toughness K_{Ic} values at these temperatures, which were obtained from Figs. 5 through 9, are known in this paper as $K_{Ic\text{-upper shelf}}$ ($K_{Ic\text{-us}}$). CVN values and yield strengths also were obtained at the same temperatures. These properties at the upper shelf temperature are presented in Table 3.

Figure 3 presents a plot of $[K_{Ic\text{-us}}/\sigma_y]^2$ versus CVN/σ_y. The experimental results coincide with the Barsom, Rolfe, and Novak correlation very well,

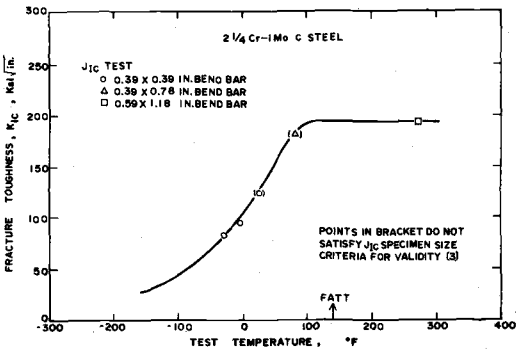

FIG. 7—*Fracture toughness versus temperature behavior of 2¼Cr-1Mo steel C.*

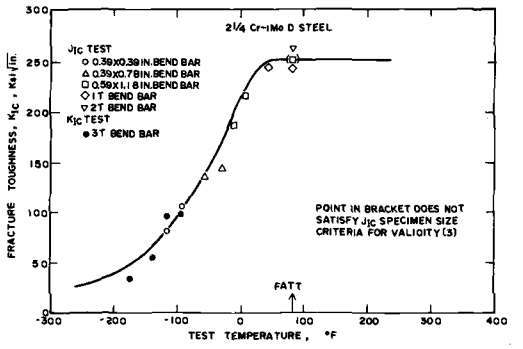

FIG. 8—*Fracture toughness versus temperature behavior of 2¼Cr-1Mo steel D.*

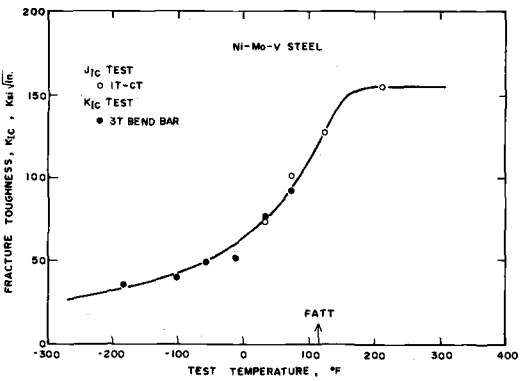

FIG. 9—*Fracture toughness versus temperature behavior of nickel-molybdenum-vanadium rotor steel.*

TABLE 3—*Properties at the upper shelf temperature.*

Material	Upper Shelf Temperature, °F	0.2% Yield Strength, ksi	CVN Energy, ft·lb	$K_{Ic\text{-}us}$[a] ksi $\sqrt{in.}$
2¼Cr-1Mo pressure vessel steel				
A	330	56	124	190
B	280	56	133	191
C	265	53	141	195
D	110	82	157	242
				261
				250[b]
Ni-Mo-V rotor steel	210	85	78	155

[a]Converted from J_{Ic}.
[b]J_{Ic} specimen size criteria for validity is not satisfied [3].

and it has been confirmed that the correlation is valid for 59 to 85 ksi (407 to 586 MPa) yield strengths 2¼Cr-1Mo pressure vessel steels.

K_{Ic} *Versus Excess Temperature Correlation in 2¼Cr-1Mo Pressure Vessel Steels*

When the K_{Ic} values of the 2¼Cr-1Mo steels shown in Figs. 5 through 8 are normalized using the excess temperature and $K_{Ic}/K_{Ic\text{-}us}$, where the excess temperature is test temperature minus fracture appearance transition temperature (FATT) (CVN 50 percent FATT) [9], Fig. 10 is obtained. In this figure, much less scatter is observed and a single master curve can be drawn as shown in the figure.

Prediction of K_{Ic} *from CVN Test Results*

K_{Ic} versus temperature curves of 2¼Cr-1Mo pressure vessel steels can be estimated using the following procedure.

1. Perform the CVN test and obtain temperature versus energy and fracture appearance curves.
2. Decide the 50 percent FATT and the 100 percent ductile fracture appearance temperature. The latter temperature is known in this paper as the upper shelf temperature.
3. Perform the tension test at the upper shelf temperature and obtain the yield strength.
4. Obtain the $K_{Ic\text{-}us}$ from Fig. 3 or Eq 3.

$$\left(\frac{K_{Ic\text{-}us}}{\sigma_y}\right)^2 = \frac{5}{\sigma_y}\left(\text{CVN} - \frac{\sigma_y}{20}\right) \tag{3}$$

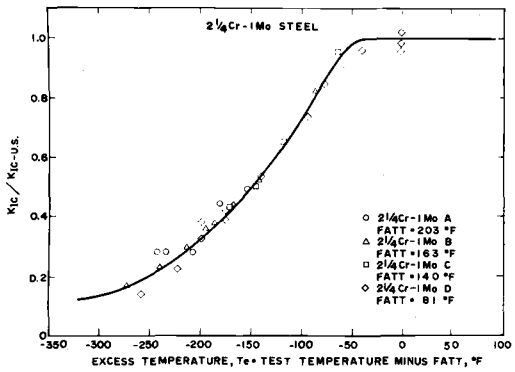

FIG. 10—*Relationship between excess temperature and* $K_{Ic}/K_{Ic\text{-}us}$ *of 2¼Cr-1Mo pressure vessel steels. (FATT: CVN 50 percent fracture appearance transition temperature,* $K_{Ic\text{-}us}$: K_{Ic} *in the upper shelf region.)*

5. Form a predicted K_{Ic} versus temperature curve using the master curve (Fig. 10), $K_{Ic\text{-}us}$ and FATT.

An example of the prediction is illustrated in Fig. 11 for the 2¼Cr-1Mo steel A. The K_{Ic} versus temperature curves predicted by this method are shown in Fig. 12, and they coincide with the test results very well.

Discussion

Figure 12 shows that fairly good prediction of K_{Ic} in the transition and upper shelf temperature regions can be made empirically for 2¼Cr-1Mo pressure vessel steels. The possibility of extending the same procedure to another low-alloyed medium to low-yield strength steels was examined. Figure 13 shows the excess temperature versus K_{Ic} relationship for various steels, and it shows a very wide scatter indicating that a master curve as shown in Fig. 10 cannot be developed. When the same test results are plotted in Fig. 14 as the relationship between $T - To$ and $K_{Ic}/K_{Ic\text{-}us}$, a much narrower scatter band is observed, where T is test temperature and To is the temperature where $K_{Ic}/K_{Ic\text{-}us}$ is 0.50.

Begley and Logsdon [7] have obtained for nickel-chromium-molybdenum-vanadium, nickel-molybdenum-vanadium, and chromium-molybdenum-vanadium rotor steels

$$\frac{K_{Ic}}{\sigma_y} = 0.45 \tag{4}$$

at the temperature which corresponds to the 100 percent brittle fracture appearance temperature in CVN test. When similar equation(s) is developed for other steels, prediction of K_{Ic} from CVN and tension test re-

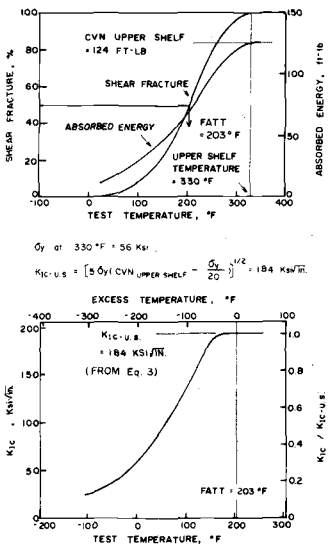

FIG. 11—*Prediction of the* K_{Ic} *values versus temperature curve of the 2¼Cr-1Mo steel A.*

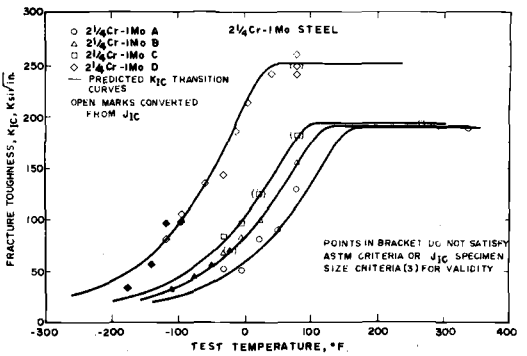

FIG. 12—*Measured and predicted* K_{Ic} *of 2¼Cr-1Mo pressure vessel steels.*

sults is possible for various steels using the equation(s) together with Figs. 3 and 14.

Summary

In order to predict K_{Ic} values of 2¼Cr-1Mo pressure vessel steels from CVN test results, the fracture properties of four 2¼Cr-1Mo steels with approximate yield strengths ranging from 59 to 85 ksi (407 to 586 MPa) were studied. The results may be summarized as follows.

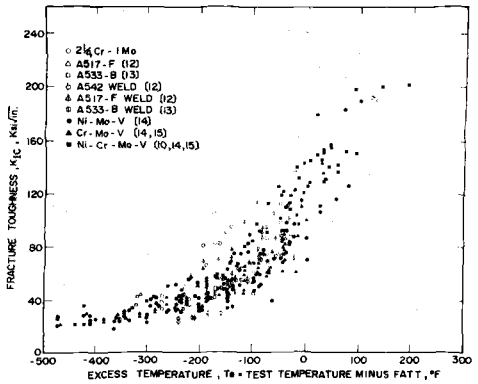

FIG. 13—*Relationship between excess temperature and* K_{Ic} *for various steels.*

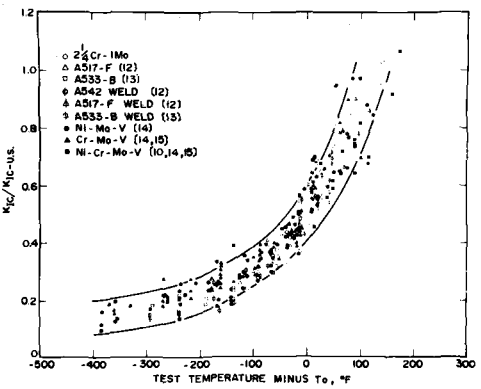

FIG. 14—*Relationship between* (T-To) *and* $K_{Ic}/K_{Ic\text{-}us}$ (T: *test temperature,* To: *temperature where* $K_{Ic}/K_{Ic\text{-}us}$ *is 0.50*).

1. It has been confirmed that the Barsom-Rolfe-Novak relationship between upper shelf CVN energy, yield strength, and K_{Ic} is valid for the steels studied.

2. Relationship between the excess temperature and $K_{Ic}/K_{Ic\text{-}us}$ has been established for 2¼Cr-1Mo steels.

Based on these results, K_{Ic} versus temperature curves may be predicted for 2¼Cr-1Mo pressure vessel steels.

For other low alloyed low- to medium-strength steels, a modification of the method developed by Begley and Logsdon was presented.

Acknowledgments

The authors wish to thank M. Kashihara, General Manager, Muroran

Plant, The Japan Steel Works, Ltd., for encouragement given to this study. They also acknowledge the cooperation of M. Horiuchi and K. Nakao.

References

[1] Emmer, L. G., Clauser, C. D., and Low, J. R., Jr., "Critical Literature Review of Embrittlement in 2¼Cr-1Mo Steel," WRC Bulletin, No. 183, Welding Research Council, May 1973.

[2] Watanabe, J., Shindo, Y., Murakami, Y., Adachi, T., Ajiki, S. and Miyano, K., "Temper Embrittlement of 2¼Cr-1Mo Pressure Vessel Steel," presented at the ASME 29th Petroleum Mechanical Engineering Conference, Dallas, Tex., American Society of Mechanical Engineers, Sept. 1974.

[3] Landes, J. D. and Begley, J. A. in *Fracture Analysis, ASTM STP 560,* American Society for Testing and Materials, 1974, pp. 170–186.

[4] Kobayashi, H., Hirano, K. and Nakazawa, H., "Fractographic Study on Evaluation of Fracture Toughness," presented at the Fifty Third National Meeting of Japan Society for Mechanical Engineers, Sendai, Japan, Oct. 1975.

[5] Barsom, J. M. and Rolfe, S. T. in *Impact Testing of Metals, ASTM STP 466,* American Society for Testing and Materials, 1970, pp. 281–302.

[6] Sailors, R. H. and Corten, H. T. in *Fracture Toughness, ASTM STP 514,* American Society for Testing and Materials, 1972, pp. 164–191.

[7] Begley, J. A. and Logsdon, W. A., "Correlation of Fracture Toughness and Charpy Properties for Rotor Steels," Scientific Paper 71-1E7-MSLRF-P1, Westinghouse Research Laboratories, July 1971.

[8] Wullaert, R. A., Ireland, D. R., and Tetelman A. S., "The Use of the Precracked Charpy Specimen in Fracture Toughness Testing," presented at the Fracture Prevention and Control Symposium, WESTEC 72 Meeting, Los Angeles, Calif., American Society for Metals, March 1972.

[9] Brothers, A. J., Newhouse, D. L., and Wundt, B. M., "Results of Bursting Tests of Alloy Steel Disks and Their Applications to Design against Brittle Fracture," presented at the ASTM Annual Meeting, Philadelphia, Pa., 1965.

[10] Begley, J. A. and Toolin, P. R., *International Journal of Fracture,* Vol. 9, 1973, pp. 243–253.

[11] Rice, J. R., Paris, P. C., and Merkle, J. G., in *Progress in Flaw Growth and Fracture Toughness Testing, ASTM STP 536,* American Society for Testing and Materials, 1973, pp. 231–245.

[12] Gentilicore, V. J., Pense, A. W. and Stout, R. D., *Welding Journal Research Supplement,* Vol. 49, 1970, pp. 341–353.

[13] Shabbits, W. O., Pryle, W. H., and Wessel, E. T., "Heavy Section Fracture Toughness Properties of A533 Grade B Class 1 Steel," HSST-TR-6, Westinghouse Electric Corp., Dec. 1969.

[14] Greenberg, H. D., Wessel, E. T., Clark, W. G., Jr., and Pryle, W. H., "Critical Flaw Sizes for Brittle Fracture of Large Turbine Generator Rotor Forgings," Scientific Paper 69-1D9-MEMTL-P2, Westinghouse Research Laboratories, Dec. 1969.

[15] Kumeno, K., Nishimura, M., Mitsuda, D. and Iwasaki, T., "Defects and Fracture Strength of Large Rotor Forgings for Steam Turbines," ASME Paper No. 75-Pwr-10, presented at the Joint Power Conference, Portland, Ore., American Society of Mechanical Engineers, Sept. 1975.

S. R. Varanasi[1]

Analysis of Stable and Catastrophic Crack Growth Under Rising Load

REFERENCE: Varanasi, S. R., **"Analysis of Stable and Catastrophic Crack Growth Under Rising Load,"** *Flaw Growth and Fracture, ASTM STP 631,* 1977, pp. 507-519.

ABSTRACT: Some metals exhibit slow crack growth prior to instability under rising load. This paper is concerned with an elastic-plastic finite element plane-stress analysis of stable and catastrophic crack growth in a center-cracked panel of a ductile material, subjected to a monotonically increasing applied stress. The stable crack growth phenomenon is modeled by incorporating a local failure criterion in the stress-analysis procedure. An automatic reidealization procedure is developed to refine the finite element mesh at the new crack-tip position before external load is increased. The method is applied to study the crack-growth behavior of geometrically similar panels of different material stress-strain curves, and results are compared with experiment. The effects of some important parameters on crack growth and stability under rising load are discussed.

KEY WORDS: crack propagation, fractures (materials), rising load, elasto-plasticity, failure criterion, aluminum

Experimental evidence shows that some metals exhibit slow crack growth prior to instability under rising load, where the plastic region behind the advancing crack tip is unloaded while the region ahead of the crack tip is being loaded. The analytical model required for the study of this phenomenon must be able to account for both the changing kinematic boundary conditions associated with crack extension and the hereditary properties of the elastic-plastic material. Theoretically, it has been possible to study the phenomenon of stable crack growth only in the case of antiplane shear case (Mode III) [*1,2*].[2] No theoretical solution exists for the opening mode (Mode I) stable crack growth of an elastic-plastic material with arbitrary strain hardening; therefore, a finite element method is used in this investigation.

Finite element methods were applied previously in the studies of a

[1]Specialist engineer, Stress and Fatigue Research, Boeing Commerical Airplane Company, Seattle, Wash. 98124.

[2]The italic numbers in brackets refer to the list of references appended to this paper.

steadily growing crack under monotonically increasing load [*3–6*] and fatigue crack growth under cyclic loading [*7*]. Reference *3* involved the numerical calculation of the J-integral but did not utilize any failure criterion for crack extension. The criterion for crack extension in Ref *4* is the opening angle between the two finite element sides that represent the crack tip. Reference *6* describes an initial attempt to explore crack stability concepts under rising load, utilizing a material dependent criterion; in this paper, a more accurate and efficient finite element method is used to investigate crack extension and crack stability. This paper also shows the results of application of the method to panels of different materials and demonstrates the role of basic material strength parameters in ductile fracture.

Finite Element Analysis

The problem of stable and catastrophic crack growth in a center-cracked panel of a ductile material, subjected to a monotonically increasing uniform applied stress, is considered here. An incremental elastic-plastic, plane-stress analysis of this cracked panel is performed using a finite element program [*8*]. Due to symmetry, only a quarter panel is discretized by an assemblage of 377 constant strain triangles with 225 nodes. A fine mesh is used in the vicinity of the crack tip. Away from the crack tip, the mesh size is gradually increased (Fig. 1). The panel material is assumed to be isotropically strain hardening, characterized by Von Mises yield condition and Prandtl-Reuss incremental stress-strain relations.

Tangent Stiffness Method of Elastic-Plastic Analysis

In this method, the external load is applied in small steps. The matrix equation which governs the response of a discretized structure for n^{th} load step is given by

$$[K_t]^{(n)}\{\Delta U\}^{(n)} = \{\Delta P\}^{(n)} \tag{1}$$

where $[K_t]^{(n)}$ is the tangent stiffness matrix, $\{\Delta P\}^{(n)}$ is the applied load step vector, and $\{\Delta U\}^{(n)}$ is the resulting incremental nodal displacement vector for the n^{th} step. The tangent stiffness matrix $[K_t]^{(n)}$ is a function of the existing state of stress; therefore, it is calculated for each load step prior to the solution of Eq 1. Structural response is assumed to be elastic for the first load step.

For a finite load step $\{\Delta P\}^{(n)}$, the utilization of a tangent stiffness $[K_t]^{(n)}$ calculated at the beginning of the load step (the end of the $(n-1)^{\text{th}}$ step) may be inappropriate. For this reason, this finite element program uses the tangent stiffness calculated at the midpoint of the load step. This re-

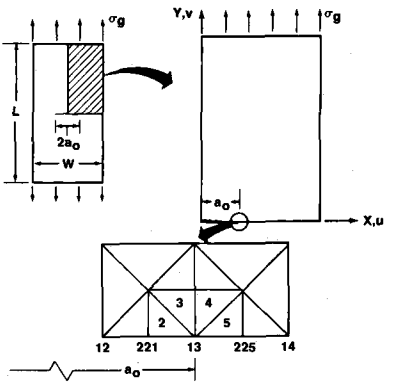

FIG. 1—*Center-cracked panel geometry and finite element idealization.*

quires two solutions of the stiffness Eq 1 for each load step. This approach was shown to be analogous to that of a two-step Runge-Kutta integration scheme to solve a set of first order ordinary nonlinear differential equations [*9*]. The tangent stiffness method is very suitable for the study of stable crack growth problem, because the load-unload material behavior involved in crack extension can be modeled conveniently by this method.

In Ref *6*, the solution for any load step was obtained as the average of two solutions determined by using the tangent stiffness at the beginning and end of the load step. This method of using the tangent stiffness at the midpoint of the load step is found to be more accurate in the vicinity of crack tip. Additionally, in this program, convergence is improved in the analysis of structures with nonhardening materials.

Crack Extension Procedure and Local Failure Criterion

Stable crack growth is modeled by incorporating a local failure criterion in the stress analysis procedure. The failure criterion used is that the crack would grow when the maximum principal stress σ_1, at the crack-tip node reaches the material tensile ultimate strength, F_{tu}. At the end of the stress analysis for any load step, this failure criterion is applied to ascertain whether crack growth is indicated. If crack growth is not indicated, the stress analysis proceeds with the application of the next load increment. Otherwise, the following procedure is used for unloading the newly created crack surface and calculating the resulting redistribution of stresses (Fig. 2).

1. The crack-tip node, which is constrained in the direction perpendicular to the crack line, is released, and the crack tip advances to the next node on the crack line.

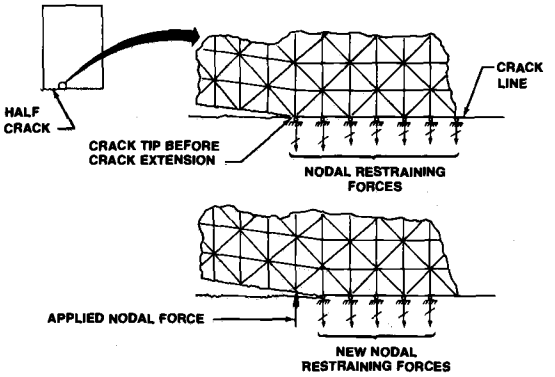

FIG. 2—*Crack extension procedure.*

2. The accumulated restraining force at the previous crack tip is relaxed elastoplastically by the next step of the finite element analysis as follows. The newly released crack-tip node is subjected to a force equal in magnitude but opposite in direction to the accumulated restraining force at that node. A stress analysis of the cracked sheet is performed with this nodal force as the only external load.

3. The failure criterion is applied again to determine if further crack growth is indicated. If so, the forementioned procedure (Steps 1 and 2) is repeated. If a crack extension causes successive crack extensions to panel edge, then the process is considered as having reached the point of instability. If there is no further crack growth after a redistribution of stresses, then it is a stable crack, and the external load has to be increased for further crack growth. The application of this failure criterion to determine the stable and catastrophic growth is similar conceptually to that used in Ref *2*, although the specific failure criteria used in Ref *2* and this investigation differ.

Modeling of Finite Element Loading-Unloading Behavior

In Step 2, the relaxation of the crack-tip nodal force produces unloading of the newly created crack surface behind the new crack tip, while increasing the loading on the region ahead of the crack tip. This redistribution of forces necessitates the inclusion of the routines for changing the element stiffness according to an incremental theory of plasticity in the stress analysis procedure.

During the crack growth, the determination of whether an element loads or unloads is done iteratively by a trial application of Step 2. Initially, the loads on all elements are assumed to increase, and Eq 1 is solved; the incremental stresses due to this trial step are accumulated in

the usual way. Then, for each element, the equivalent stress, $\bar{\sigma}_2$ is compared with its equivalent stress, $\bar{\sigma}_1$ prior to the application of this trial step. If $\bar{\sigma}_2 \geq \bar{\sigma}_1$, then the load on the element is assumed to have increased; otherwise, the element is assumed to unload elastically. Two iterations of this process were used in this investigation to determine the load-unload behavior of each element. After this determination, the stress state prior to this step is reestablished and the crack is extended by Step 2.

Automatic Reidealization Procedure

For computational economy, a mesh size which gradually varies from fine at the crack tip to coarse away from the crack tip is used in the finite element discretization of the cracked panel. A procedure for automatic extension of the fine mesh surrounding the crack tip as the crack grows was developed (Fig. 3). The quadrant is divided into three zones along the crack line; namely, a crack-tip zone surrounding the crack tip where a fine mesh is used, a forward zone which extends from the crack-tip zone to the free edge of the panel, and an aft zone which extends from the crack-tip zone to the crack center. Following the stable crack growth, the discretization is automatically revised by a mapping routine as follows. The crack-tip zone is translated along the crack line by the amount of the stable crack growth, so that the new crack tip is surrounded by the same arrangement of finite elements as the initial crack tip. The forward zone is correspondingly compressed, and the aft zone is correspondingly elongated along the crack line by the amount of stable crack growth. The stress state for the revised discretization is obtained from that of the previous discretization by interpolation. Thus, with a fine mesh at the new crack tip, the stress analysis is resumed.

Results

The developed finite element program was applied to study the crack-growth behavior of four center-cracked panels. The first panel is a 2024-T3 aluminum test panel [*10*]. The second and third panels have this test panel geometry but are assumed to be made of different materials to assess the role of basic material strength parameters on ductile fracture. The second panel material is representative of a 7075-T6 aluminum. The third panel material has the same ductility as the 7075-T6 aluminum, but its strain hardening characteristics are similar to those of the 2024-T3 aluminum. The fourth panel is another 2024-T3 aluminum test panel [*11*].

The same finite element model (Fig. 1) was used for all the panels by appropriately modifying the nodal data to get the geometry of each panel. The elements surrounding the crack tip have sides which are of length equal to 0.8 mm (1.25 percent of half-crack length) for Panels 1 through 3

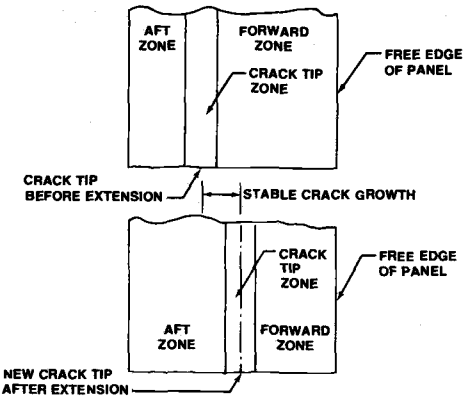

FIG. 3—*Stable crack-tip mesh refinement.*

and 0.2 mm (0.68 percent of half-crack length) for Panel 4. This resulted in elastic-stress concentration factors (ratio of normal stress σ_y to applied stress σ_g) of 9.87 for Panels 1 through 3 and 15.60 for Panel 4. The uniaxial stress-strain curves of the four materials are represented by Ramberg-Osgood relationships (Fig. 4). The load increments used in the analyses of all the panels correspond to gross stress increments of 6.895 MN/m^2 (1 ksi).

Finite Element Results for Panel 1 (Test Panel 1)

For Panel 1, the maximum principal stress at the crack-tip node reaches the material tensile ultimate strength, F_{tu}, at an applied gross stress of 124.1 MN/m^2 (18 ksi). According to the assumed failure criterion, the

MATERIAL NO.	TENS. ULT. F_{tu}(MN/m^2)	TENS. YEILD F_{ty} (MN/m^2)	ELONG. e	MODULUS E(MN/m^2)
1	474	335	0.195	72400
2	606	569	0.095	72400
3	606	441	0.095	72400
4	494	371	0.200	72400

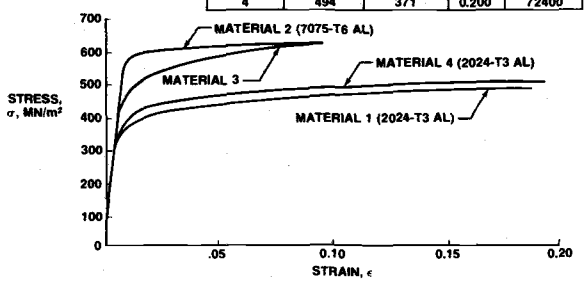

FIG. 4—*Uniaxial stress-strain curve of panel materials (Ramberg-Osgood representation).*

crack is extended one element length by releasing the crack-tip node, 13, (Fig. 1) and relaxing the crack-tip restraining force in ten equal steps. The resulting redistribution of stresses causes the maximum principal stress at the new crack-tip node, 225, to exceed the material tensile ultimate strength. Again, the crack is extended by releasing node 225 and relaxing its restraining force in ten equal steps. The crack is then found to be stable at the next crack tip node, 14, with a half-crack length of 6.51 cm. Figures 5 through 7 show some of the details of this crack extension and stabilization. Figure 5 shows the elastic-plastic, load-unload behavior of the elements in the vicinity of the crack tip. Figures 6 and 7 show the distributions of principal stress on the net section and crack surface separation displacements, respectively, in the vicinity of the crack tip. For comparison, another finite element analysis (with the same idealization

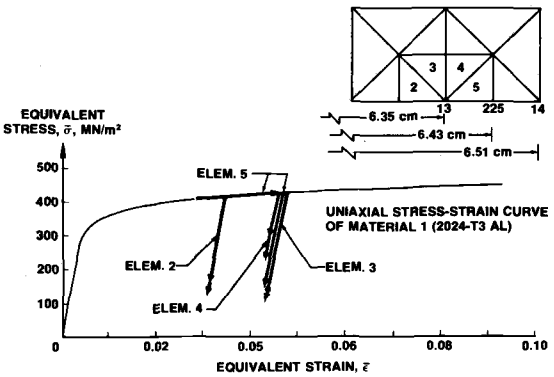

FIG. 5—*Crack-tip elements behavior for crack extension.*

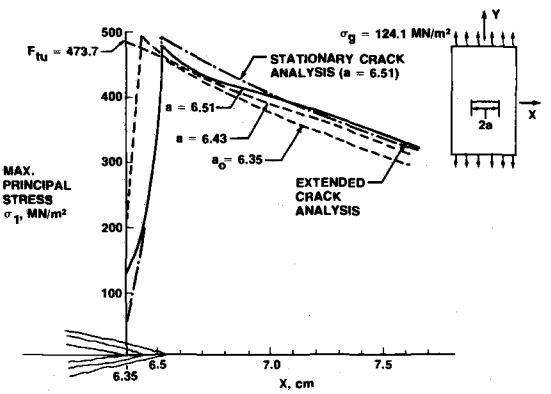

FIG. 6—*Maximum principal stress on net section for crack extension under constant applied stress (Panel 1).*

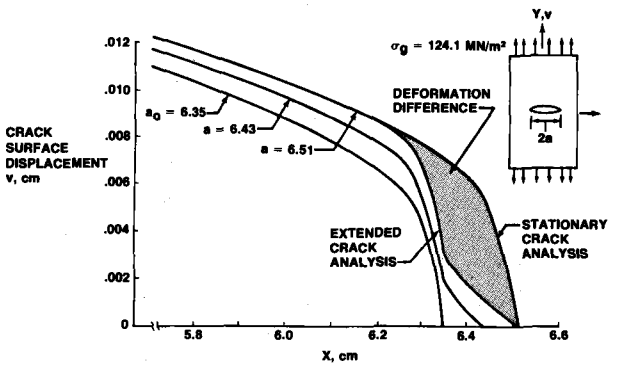

FIG. 7—*Crack-surface displacements for crack extension under constant applied stress (Panel 1).*

in the crack-tip zone) was made for a panel with a stationary crack of half-length 6.51 cm (that is, the same half-crack length at which crack stability occurred at applied stress of 124.1 MN/m² (18 ksi) in the analysis of Panel 1). The results of this stationary crack analysis are also shown in Figs. 6 and 7 to illustrate the marked difference between the results of a stationary crack analysis and a moving crack analysis for crack-tip stress and deformation fields.

As the crack extends at constant applied stress, unloading of the newly created crack surface results in the translation of the plastic zone ahead of the crack. Since the material responds elastically for unloading from a plastic state, a wake of residual plastic strain is left behind a moving crack tip (Fig. 8).

The determination of the elastoplastic, load-unload characteristics of the finite element assemblage during crack extension process is one of the vital elements in the formulation of a crack stability concept for a ductile material. Figure 9 compares the results of elastoplastic relaxation of the crack-tip restraining force at node 13, with those for the relaxation of the same restraining force under the assumption of elastic behavior for all elements. It may be seen from Fig. 9 that there is a marked difference between these simulations of elastic-plastic and elastic-crack extension processes. When a crack extends elastically, the effect of the unloading of the newly created crack surface is to load the new crack-tip region so intensely that the failure criterion is met inevitably at the new crack tip. Thus, for an elastic material, crack initiation results in immediate instability. In contrast, when a crack extends elastoplastically, the loading of the region ahead of the new crack tip is more broadly distributed and much less intense in the immediate vicinity of the tip. This is a consequence of the low-tangent modulus of the material in the plastic zone in the vicinity of the crack tip. Thus, when a crack extends in an elastic-plastic

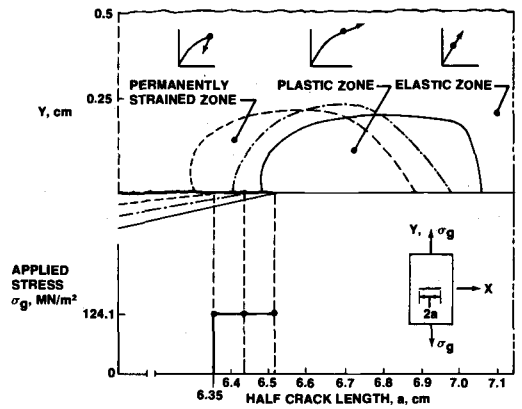

FIG. 8—*Plastic-zone shift under constant applied stress (Panel 1).*

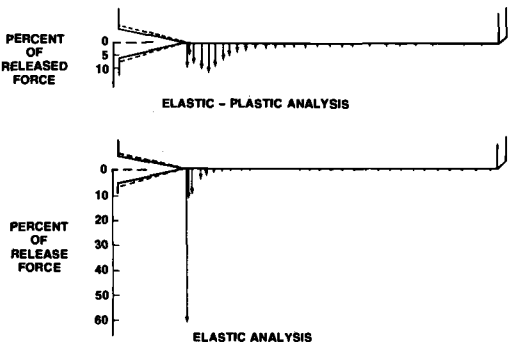

FIG. 9—*Comparison of elastic-plastic and elastic-crack extension processes for the release of the same crack-tip force.*

material, the unloading of the crack surface behind the advancing crack tip does not necessarily cause the failure criterion to be met at the new crack tip. Conditions for continued growth depend on such factors as material strain-hardening, stress, and deformation history.

The finite element results are compared with test panel results in Fig. 10. The analytically calculated panel failure stresses are 193.1 MN/m² (28 ksi) for one-step relaxation of crack-tip force and 206.9 MN/m² (30 ksi) for ten-step relaxation. These compare to the test panel failure stress of 163.4 MN/m² (23.7 ksi). Measurements of slow crack growth prior to instability for this test panel are not available for comparison. However, the finite element results are typical of observed slow crack growth in tests of 2024-T3 aluminum panels.

The effect of the step size for relaxation of crack-tip force is shown in

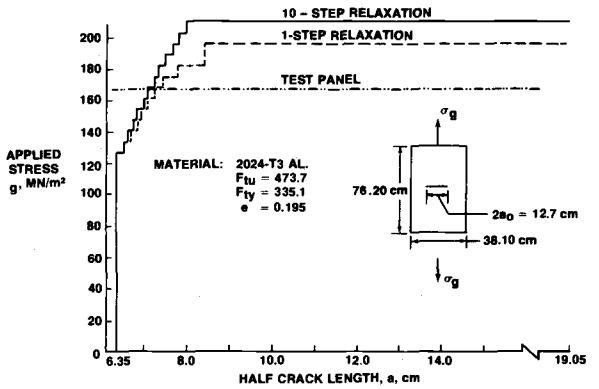

FIG. 10—*Comparison of analysis results with test results (Panel 1).*

Fig. 11. The crack-tip force is relaxed in a single step and a number of equal steps for the first crack extension in the analysis of two panels. After four steps, there is no appreciable change in the accumulated restraining force and the maximum principal stress at the new crack tip.

Finite Element Results for Panels 2 and 3

The results of application of the developed finite element technique to Panels 2 and 3 are shown in Fig. 12. The results of Panel 1 also are included in Fig. 12 for comparison. The second panel, which is made of a 7075-T6 aluminum, shows the lowest panel failure stress and the smallest applied stress range for slow crack growth. Since this material does not show appreciable strain hardening, the crack begins to grow according

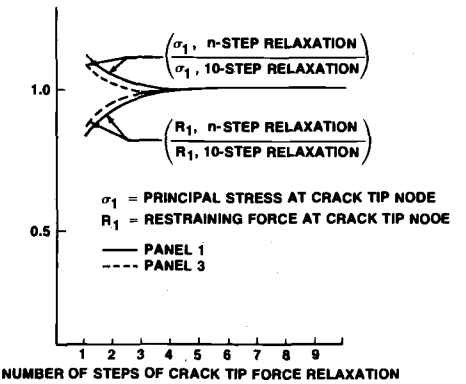

FIG. 11—*The effect of step size for crack-tip force relaxation.*

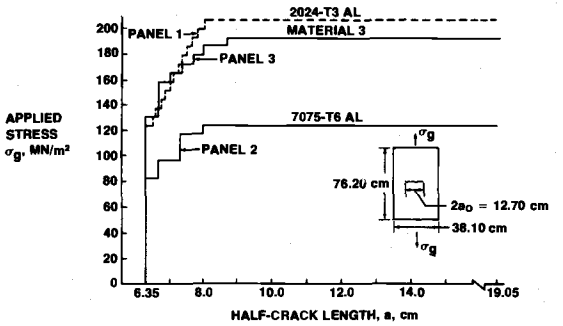

FIG. 12—*Finite element results of slow crack growth to instability for Panels 1 through 3 (ten-step relaxation of crack-tip restraining force).*

to the assumed criterion at a low applied stress of 82.7 MN/m² (12 ksi). This panel shows larger crack extensions at lower stresses compared to the other panels and rapidly attains catastrophic growth. This is typical of the fracture behavior of a 7075-T6 aluminum panel.

The third panel does not show crack extension until the gross stress reaches 131 MN/m² (19 ksi). This panel material has the same high-tensile strength as the second material, but it has a yield stress which is lower than that of the second material. The crack growth behavior of this panel is more like that of the first panel than the second because of the similarity in the strain hardening characteristics of these two materials. Figure 12 shows that the applied stress range during which a cracked panel exhibits slow crack growth depends primarily on the strain hardening behavior of the panel material; cracked panels made of strain-hardening materials exhibit more slow crack growth than cracked panels with non-hardening materials.

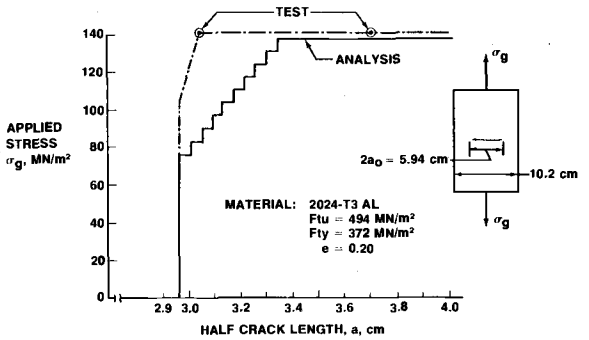

FIG. 13—*Comparison of analysis results with test results (Panel 4).*

Finite Element Results for Panel 4 (Test Panel 2)

In the finite element analysis of this panel, the crack-tip restraining forces are relaxed in four equal steps since earlier results indicated (Fig. 11) this number to be optimum. The analysis results are compared with test results in Fig. 13. Although the agreement between the results of the analysis and test is not very good for the threshold stress for stable crack growth, the agreement is very good for critical crack length and panel failure stress. Since it is very difficult to measure the critical crack length exactly, two final crack lengths of 6.1 cm (2.4 in.) and 7.4 cm (2.9 in.) were measured in the test to bracket the critical crack length. The measured panel failure stress was 141.3 MN/m^2 (20.5 ksi). These compare very favorably with the predicted critical crack length of 6.70 cm (2.64 in.) and predicted failure stress of 137.9 MN/m^2 (20 ksi).

Concluding Remarks

1. A two-dimensional finite element analysis has been developed to model successfully the slow crack growth prior to instability under rising load.
2. The results of application of the analysis compare reasonably well with test results and show expected trends for crack growth and residual strength behavior.
3. The automated reidealization scheme, developed as a part of the analysis, saves considerable computational time.
4. The postulated criterion for crack extension is that the principal stress at the crack tip reaches the ultimate tensile strength of the material. The results are consistent with the observed effects of basic material strength properties on slow crack growth behavior.
5. The determination of the character of the elastoplastic load redistribution process during crack extension is one of the vital elements in the formulation of a crack stability concept for a ductile material.
6. The analysis illustrates the development of the residual plastic zone behind the moving crack tip in addition to the growth of the advanced plastic zone as crack extension progresses toward catastrophic failure.
7. This method of simulation of crack extension behavior is somewhat sensitive to the step size for the relaxation of the crack-tip forces. In the particular applications, crack-tip force relaxation in four or five steps were sufficient to optimize the results. The step size for crack-tip force relaxation did not have an appreciable effect on the catastrophic failure load.
8. The analysis scheme is versatile enough to permit ready incorporation of any alternative local failure criterion for crack extension.

Further work is necessary to study the effect of finite element mesh size

on slow crack growth prior to instability. Any failure criterion which is based on the values of field variables in the vicinity of the crack tip is affected by the finite element mesh size surrounding the crack tip. For example, if the element size in the crack-tip zone were smaller, the assumed failure criterion in this analysis would show crack extension at a lower applied stress. However, the crack tip restraining force and crack extension step would also be smaller for such an idealization. If finite element mesh size has a pronounced effect, it would be desirable to examine an alternative criterion (for example, the J-integral) which is not appreciably affected by inaccuracies in numerical computations of crack-tip stress strain field. With an analytical technique for stable crack growth, it should be possible to characterize fracture in the presence of large-scale yielding and, thus, to develop standard procedures for the fracture-toughness testing on small-scale specimens where unstable fracture occurs near general yield.

References

[1] Chitaley, A. D. and McClintock, F. A., *Journal of Mechanics and Physics of Solids,* Vol. 19, 1971, pp. 147–163.

[2] McClintock, F. A., *Journal of Applied Mechanics; Transactions,* American Society of Mechanical Engineers, Dec. 1958, pp. 582–588.

[3] Kobayashi, A. S., Chiu, S. T., and Beeuwkes, R., *Engineering Fracture Mechanics,* Vol. 5, 1973, pp. 293–305.

[4] Anderson, H., *Journal of Mechanics and Physics of Solids,* Vol. 21, 1973, pp. 337–356.

[5] Anderson, H., *International Journal of Fracture*, Vol. 9, 1973, pp. 231–233.

[6] Miller, R. E., Backman, B. F., Hansteen, H. B., Lewis, C. M., Samuel, R. A., and Varanasi, S. R., "Recent Advances in Computerized Aerospace Structural Analysis and Design," Second National Symposium on Computerized Structural Analysis and Design, Washington, D.C., 29–31 March 1976.

[7] Newman, J. C., Jr., "A Finite Element Analysis of Fatigue Crack Closure," ASTM Eighth National Symposium on Fracture Mechanics Providence, R.I., 26–28 Aug. 1974.

[8] Varanasi, S. R. and Carey, G. F., "Elasto-Plastic Analysis of Plane Structures by the Finite Element Displacement Method," Boeing Co. Document No. D6-24524, Dec. 1970.

[9] Tocher, J. L. and Varansi, S. R., "Finite Element Analysis of Plasticity Problems," ASCE Joint Specialty Conference on Optimization and Nonlinear Problems, Chicago, 18–20 April 1968.

[10] Kaufman, J. G. and Holt, M., "Fracture Characteristics of Aluminum Alloys," Technical Report No. 18, ALCOA Research Laboratory.

[11] Feddersen, C. E., Simonen, F. A., Hulbert, L. E., and Hyler, W. S., "An Experimental and Theoretical Investigation of Plane Stress Fracture of 2024-T351 Aluminum Alloy," NASA Report CR-1678, National Aeronautics and Space Administration, Washington, D.C., Sept. 1970.